TURBULENT FLOW IN AN IDEALIZED WING-BODY JUNCTION

by

Ibrahim Mohamed Mohamed Aly SHABAKA
B.Sc. (Cairo), M.Sc. (Ain Shams)

A Thesis Submitted for the Degree of
Doctor of Philosophy of the University of London

Department of Aeronautics
Imperial College of Science and Technology
Exhibition Road
London, S.W.7

April, 1979

To Hoda and Amr,

my Wife and Son.

ABSTRACT

The flow along the streamwise corners between an aerofoil and the body on which it is mounted is found in many practical applications, e.g. in turbomachinery and aeronautics. It is a complex turbulent flow in which the two turbulent boundary layers formed on the corner walls interact.

The present work is an experimental study of the interaction between the two boundary layers in the corner of an idealized wing-body junction. An uncambered wing of constant thickness downstream of a half-elliptic nose was fixed to the tunnel floor, which simulated the body surface, and spanned the full height of the tunnel.

In addition to the measurements of the three mean velocity components, the six elements of the Reynolds stress tensor, and the triple products of the fluctuating velocities, made at three cross-sectional planes, the experiment included measurements of the distribution of body wall-static pressure and wall shear stress on both surfaces. Some surface oil-film flow visualization tests were carried out at the beginning.

The present experimental work is thought to represent a full coverage of the flow field in the test region. It is hoped that the results will serve as data for testing and improvement of future calculation methods.

The lateral skewing of streamlines in the tunnel floor boundary layer, caused by the wing leading edge, induces streamwise vorticity in the corner region. The results show that this induced vortex overwhelms the stress-induced secondary flow over the entire region of measurement (about 25 wing thicknesses downstream of the leading edge). Reynolds stresses, indeed, act to attenuate this skew-induced secondary flow in

the wing-body junction. Regions where the body-oriented and wing-oriented shear stresses attain negative values were detected; in parts of these areas the mean shear gradient is positive. This leads to the conclusion that eddy-viscosity or mixing-length models are unsuitable for treating the present type of flow. The two-dimensionality and local equilibrium of the inner layers of the body and wing boundary layers are not affected by the presence of the streamwise vortex except very near to the wing leading edge and in the vicinity of the corner. The ratio between the shear stress and the turbulent kinetic energy is constant over most of the flow except close to the corner.

بِسْمِ اللَّهِ الرَّحْمَٰنِ الرَّحِيمِ

وَقُل رَّبِّ زِدْنِي عِلْمًا

صَدَقَ اللَّهُ الْعَظِيمُ

In the name of God, Most Gracious

Most Merciful

Say: Oh, My Lord! Advance me in Knowledge.

ACKNOWLEDGEMENTS

It is with pleasure that I record my sincere gratitude to Professor P. Bradshaw for his excellent supervision and untiring encouragement. His dynamic enthusiasm and depth of insight have been a constant source of inspiration.

I am also indebted to all other members of the Aeronautics Department of Imperial College who have helped in many different ways to enable the completion of this work. In particular, Dr. M. S. Kareem for many helpful suggestions during the course of this research and for his assistance in producing the graphs. For many stimulating discussions and checking the manuscript, I thank Mr. D. H. Wood and Dr. P. H. Hoffmann. Thanks are due to Dr. H. E. Mahgoub for the supply of the AMOS program.

I also thank the technical staff of the Department, especially Mr. J. E. Coles and Mr. L. Eals for their help during the experimental work, Mr. J. P. O'Leary for taking the photographs and Miss S. Lawrence for persistence when searching for many obscure references.

Thanks are also due to Mrs. R. Fairhurst for typing the captions for the figures.

Mrs. H. A. Bastin deserves a special mention for typing the thesis efficiently and very quickly.

The receipt of a grant from the Faculty of Engineering, Cairo University, Egypt, is gratefully acknowledged.

Finally, I must thank my Wife, Hoda, for moral support and continuous encouragement.

CONTENTS

LIST OF FIGURES

LIST OF SYMBOLS

A	Area or Constant in hot-wire response equation: $E^2 = AU^n + B$ or Constant in the log-law: $U/u_\tau = A \log_{10} y^+ + B$ or Constant in the relation $U = Ax^n$
A_c	Area enclosed by the contour C
$A_{max/2}$	Area enclosed by the contour $\xi = 0.5\xi_{max}$
A_1, A_2, A_3	Coefficients in Lagrange three-point differentiation (see Appendix E)
B	Constant in the hot-wire response equation or in the log-law (see above)
C	Convection term in the streamwise vorticity Equation (1.3) or Constant in the hot-wire response equation $E^2 = A + BU^n + CU^{2n}$
C_f	Skin friction coefficient = $\tau_w / \frac{1}{2} \rho U_e^2$
C_p	Local static pressure coefficient = $(p - p_{at}) / \frac{1}{2} \rho U_{ref}^2$
D	Diffusion term in the streamwise vorticity Equation(1.3)
E	Hot-wire mean voltage output
e	Hot-wire fluctuating voltage output
F_{u_i}	Flatness factor of the velocity component u_i
F_u, F_v, F_w	Flatness factors of the velocity components u, v and w respectively
f	Function
h	Half the width of a rectangular duct
i, j, k, ℓ	Tensor indices
$\underline{i}$, $\underline{j}$, $\underline{k}$	Unit vectors in the x, y, z directions
K	von Karman constant = 0.41
ℓ	Length scale

n	Exponent in the hot-wire response law (see above) or Exponent in the relation $U = Ax^n$ or Station number
p	Mean static pressure
p'	Fluctuating static pressure
P_1, P_2, P_3, P_4	"Production" terms in the streamwise vorticity (Equation (1.3))
p_{ref}	Reference static pressure
q^2	$= \overline{u^2} + \overline{v^2} + \overline{w^2}$ = 2 x turbulent kinetic energy per unit mass
R	$= R_w/R_o$ = Hot-wire overheat ratio
R_o	Wire cold resistance
R_w	Wire resistance at operation
R_θ	Momentum thickness Reynolds number
S_{u_i}	Skewness factor of the component u_i
S_u, S_v, S_w	Skewness factor of the components u, v, w respectively
s	Arc length in the y-z plane
T	Averaging time
t	Time
U, V, W	Mean velocity components in the x-, y-, z-directions respectively, see Fig. (1.1)
u, v, w	Fluctuating velocity components in the x-, y-, z-directions respectively, see Fig. (1.1)
U_i, U_j, U_k	Mean velocity components in the x_i, x_j, x_k directions respectively
u_i, u_j, u_k	Fluctuating velocity components in the x_i, x_j, x_k directions respectively
U_e	Free stream velocity
u_τ	Friction velocity = $\sqrt{\tau_w/\rho}$

V_s	Secondary flow velocity = $\sqrt{V^2 + W^2}$
v_α, v_β	Fluctuating velocity components in the arbitrary α-β axes system (in the normal plane, see Fig. (1.1))
X, Y, Z or x, y, z	Cartesian axes, for full definition see Fig. (1.1)
y^+	$= \frac{u_\tau y}{\nu}$
z^+	$= \frac{u_\tau z}{\nu}$

Greek Symbols

α	Angle or
	Temperature coefficient of resistivity
α, β	Arbitrary axes in the plane normal to the x-axis (see Fig. (1.1))
Γ_x	Streamwise component of circulation
γ	Intermittency factor
Δ	Change (e.g. $\Delta\theta$ = change in temperature)
δ	Boundary layer thickness or
	Cross-wire yaw angle
δ_b	Body-boundary layer thickness away from the wing
δ_w	Wing-boundary layer thickness away from the body
δ_{cr}	Critical boundary layer thickness
ε	Dissipation rate of the turbulent kinetic energy
ξ, η, ζ	Vorticity components in the x, y, z directions respectively
θ	Temperature or
	Boundary layer momentum thickness or
	Angles of cross-wire plane relative to y- or z-axes
ν	Kinematic viscosity
ρ	Density

σ_i	$= \sqrt{\overline{u_i^2}} = \sqrt{\text{Variance of the fluctuating velocity } u_i}$
τ	$= \sqrt{\overline{uv}^2 + \overline{uw}^2}$ = Turbulent shear stress in the y-z plane
τ_w	Wall shear stress (wall skin friction)
ψ	Hot-wire angle

Subscripts

at	Atmospheric
b	Related to the body
c	Along the contour C
cr	Critical value
e	Free stream value
eff	Effective value
i	In the direction x_i
s	Along the secondary flow (V_s) direction
m	Measured value
max	Maximum value
max/2	Corresponding to 0.5 of the maximum value
u, v, w	Related to the velocity components u, v, w respectively
w	Related to the wing or
	Related to the wall
α	Along the α-direction
β	Along the β-direction
τ	Friction value
2D	Two-dimensional
1, 2	For cross-wire sensing elements 1 and 2 respectively
∞	Value far upstream
x, y, z	In the x, y, z directions respectively

Superscript

$\overline{\quad}$	Time averaged $= \frac{1}{T}\int_0^T dt$

Abbreviations

rms	Root mean square
wrt	With respect to

CHAPTER 1

INTRODUCTION

Interaction between two shear layers is an important aspect in which turbulent shear layers in turbomachines are different from turbulent boundary layers on isolated aerofoils. The flow near the wake centreline and the effect of a blade wake on a following blade are examples of such interaction. In the streamwise corner between blades and the hub, or casing, lies an important example of interaction between two shear layers inclined to each other.

Turbomachines are only one example where the problem of flow along "wing-body" junctions plays an important role. The mutual interference between wings and fuselage is the oldest of the interference problems in aeronautics, yet it has not been completely solved. Schlichting (1946) and Flax and Lawrence (1951) showed the great variety of problems involved and the methods so far employed in dealing with them. It is, of course, expected that the corner where wings and fuselage meet is the region of this inherent interference. In the world of heat transfer, an example is found in the corners between fins, at their roots, and the heat exchanger body.

"Wing-body" corner flow was thus classified by Bradshaw (1976) as a real life "complex" turbulent flow. Flow along streamwise "wing-body" corners is a "slender" three-dimensional flow; that is, the crosswise* gradients ($\partial/\partial z$) are comparable to the normal ($\partial/\partial y$) gradients,

---

* In the present work, the wing was mounted with its span vertical on the tunnel floor which formed the body. Throughout the thesis, we will use "crosswise" for the tunnel spanwise direction (z) to avoid confusion with the spanwise wing direction (y).

and only the streamwise gradients ($\partial/\partial x$) are small. In this flow, normal and extra shear stress gradients are important and a wide variety of boundary layer shapes are likely to occur in practice. A general calculation method is thus still unattainable. Bradshaw (1968) has stated that "in order to make any useful progress, a much better understanding of corner flow is needed and the main need is for more experiments". During the last decade, the problem of corner flow has attracted the attention of many workers, e.g. Zamir and Young (1970), Perkins (1970a, 1970b), Mojola (1972) and Chu and Young (1975) among others. However, all the detailed turbulence studies were devoted to the flow along corners of non-circular ducts and corners between two flat plates at an angle.

The present work is intended as a thorough study of the turbulent flow along the "wing-body" corner. The two main targets are: a better physical understanding of this type of flow and the collection of comprehensive data to serve in the improvement of prediction methods.

A feature common to all corner flows is the existence of secondary flow currents. Accordingly, it seems useful to begin with a short review of the subject.

1.1 Secondary Flows

The time-mean flow of a three-dimensional field with a certain predominant direction is usually divided into a main (primary or "streamwise") flow in the x-direction, say, (see Fig. (1.1) for the axes used in this thesis), and secondary flows. "Secondary flows" represent the developing components in the cross plane (y-z) normal to the main flow.

Secondary flow analysis is most fruitfully approached via the streamwise component of vorticity. The equation for the vorticity is

derived from the time-averaged Navier-Stokes (momentum) equations of motion by eliminating the pressure terms between the three equations in x, y and z directions and the use of the continuity (mass conservation) equation. The equation for the mean streamwise (ξ) component of vorticity in incompressible flow is:-

$$\frac{D}{Dt}\xi = \frac{\partial \xi}{\partial t} + U\frac{\partial \xi}{\partial x} + V\frac{\partial \xi}{\partial y} + W\frac{\partial \xi}{\partial z} = \xi\frac{\partial U}{\partial x} + \eta\frac{\partial U}{\partial y} + \zeta\frac{\partial U}{\partial z} + \frac{\partial}{\partial x}\left[\frac{\partial}{\partial z}\overline{uv} - \frac{\partial}{\partial y}\overline{uw}\right] +$$

$$+ \left[\frac{\partial^2}{\partial y^2} - \frac{\partial^2}{\partial z^2}\right](-\overline{vw}) + \frac{\partial^2}{\partial y \partial z}(\overline{v^2} - \overline{w^2}) + \nu\left[\frac{\partial^2}{\partial x^2} + \frac{\partial^2}{\partial y^2} + \frac{\partial^2}{\partial z^2}\right]\xi \qquad (1.1)$$

where:
$$\left.\begin{aligned} \xi &= \frac{\partial W}{\partial y} - \frac{\partial V}{\partial z}\,, \\ \eta &= \frac{\partial U}{\partial z} - \frac{\partial W}{\partial x}\,, \text{ and} \\ \zeta &= \frac{\partial V}{\partial x} - \frac{\partial U}{\partial y} \end{aligned}\right\} \qquad (1.2)$$

are the three components of mean vorticity in x, y and z-direction respectively (see Fig. (1.1)).

For steady slender shear flows ($\partial/\partial y \sim \partial/\partial z >> \partial/\partial x$), the equation becomes:-

$$\overbrace{U\frac{\partial \xi}{\partial x} + V\frac{\partial \xi}{\partial y} + W\frac{\partial \xi}{\partial z}}^{C} = \overbrace{\xi\frac{\partial U}{\partial x}}^{P_1} + \overbrace{\eta\frac{\partial U}{\partial y} + \zeta\frac{\partial U}{\partial z}}^{P_2} + \overbrace{\left[\frac{\partial^2}{\partial y^2} - \frac{\partial^2}{\partial z^2}\right](-\overline{vw}) + \frac{\partial^2}{\partial y \partial z}(\overline{v^2} - \overline{w^2})}^{P_3} + \overbrace{\nu\left[\frac{\partial^2}{\partial y^2} + \frac{\partial^2}{\partial z^2}\right]\xi}^{D} \qquad (1.3)$$

(c.f. Cebeci and Bradshaw, 1977 - page 319)

Terms (C) on the left hand side of the equation represent the convection of the streamwise vorticity ξ by the mean flow components, U, V, W. Terms on the right hand side represent the contributions of different mechanisms that play parts in changing the ξ component of vorticity. $P_1 = \xi \frac{\partial U}{\partial x}$ represents the rate of change (intensification) of ξ by streamwise stretching in accelerating flows (positive $\partial U/\partial x$). The interaction between the remaining main shear rates ($\partial U/\partial y$ and $\partial U/\partial z$) and the η and ζ vorticity components is expressed by the term P_2. $P_2 = \{\eta \frac{\partial U}{\partial y} + \zeta \frac{\partial U}{\partial z} = \frac{\partial U}{\partial z}\frac{\partial V}{\partial x} - \frac{\partial U}{\partial y}\frac{\partial W}{\partial x}\}$ thus represents the rate of increase in streamwise vorticity ξ as a result of skewing the mean shear by the action of a transverse pressure gradient or body forces. The two terms, P_3 and P_4, only existing in turbulent flows, represent the production rate of streamwise vorticity component as a result of inhomogeneity and anisotropy of turbulence in the cross plane (terms P_3 & P_4). In fact, P_3 and P_4, strictly speaking, represent transport rather than production of vorticity since the integral of these Reynolds stress terms over the whole y-z plane is zero. The remaining term in the equation, D, represents the rate of diffusion of the streamwise vorticity by viscosity.

Prandtl (1952) was the first to differentiate between two mechanisms for secondary flow induction (i.e. production of streamwise vorticity). He separated them into two* categories:-

(a) Secondary Flow of the First Kind

This is present both in laminar and in turbulent flows and is a result of skewing of the vorticity vector by the mean shear (P_2

---

* The eddying flows associated with the oscillatory motion of a body are categorized as secondary flow of the third kind (c.f. Young, 1977).

in Equation (1.3)). Secondary currents produced by this mechanism were noticed in the flow along meandering river beds and curved channels during the last quarter of the nineteenth century (c.f. Perkins, 1970a) and still in discussion (c.f. Hey and Thorne, 1975). The mechanism is also responsible for the production of streamwise vorticity as a result of the deflection of the inviscid core of flow through highly curved ducts, e.g. S-shaped ducts (discussed by Bansod and Bradshaw, 1972), and also near the walls in the centre plane of two-dimensional contractions of wind tunnels (c.f. Cebeci and Bradshaw, 1977). Secondary flow of the first kind results also from the intensification of the lateral (z-direction) component of vorticity as a result of lateral stretching, $\partial W/\partial z$, in a two-dimensional shear layer when it flows over a bluff obstacle. The flow separates just upstream of the obstacle leading edge at a "saddle point" of skin friction lines where the separated shear layer rolls up forming a horseshoe vortex that wraps around the leading edge. Vasanta Ram (1963), Bělik (1973) and Werlé (1975) were among those who studied this secondary flow about circular cylinders immersed in boundary layers. Flow near the leading edge of a wing at its junction with a body is an important practical example, studied in the present work.

Squire and Winter (1951) and Hawthorne (1951) in their early simplified theoretical studies of the problem of secondary flow, have shown for an inviscid flow that flow deflection through an angle α in a plane containing the streamline and the vorticity component ζ (i.e. x-z plane) rotates the vorticity vector through α towards the flow direction, i.e. produces streamwise vorticity = $-2\alpha\zeta$.

(b) Secondary Flows of the Second Kind

These are produced by the time-averaged action of anisotropic

inhomogeneous turbulence as expressed by terms P_3 and P_4 in Equation (1.3). An isotropic viscosity does not produce secondary flow. Terms P_3 and P_4 collectively represent the sum effect of the time-averaged convection of turbulent vorticity by the turbulence and the time-averaged production of turbulent vorticity. Following Townsend (1956) and Brundrett and Baines (1964) among others, the time-averaged production of turbulent vorticity is a result of unsteady macroscale interactions identical to those expressed by Equation (1.3). Anisotropic wall turbulence in any boundary layer situation is potentially a source of secondary flows of the second kind when the flow is strongly inhomogeneous in the spanwise direction. This occurs in ducts of non-circular cross-sections (e.g. Brundrett and Baines, 1964) and in boundary regions such as the streamwise corners (e.g. Mojola, 1972) or at edges of surfaces (e.g. Bray, 1967; Perkins, 1970a, 1970b), or even changes in surface roughness (e.g. Hinze, 1967). Secondary flows of the second kind were first postulated by Prandtl to explain the distortions in Nikuradse's (1926) and Schiller's (1923) isovels (contours of constant streamwise mean velocity).

Use of the terms "Prandtl's secondary flow of the first kind" and "Prandtl's secondary flow of the second kind" continues although it is clearer (c.f. Cebeci and Bradshaw, 1977) to describe the two different kinds of secondary flow by the mnemonic terms "skew-induced secondary flows" and "stress-induced secondary flows".

1.2 Review of Previous Work

In what follows, a review of the work done in the field of corner flow is given. Only incompressible flow work is reviewed but laminar and turbulent cases are discussed.

1.2.1 Flow in Ducts, Channels and Unbounded Corners

1.2.1.1 Laminar Corner Flow

(a) Theoretical Analyses and Predictions

The first theoretical study of the problem of laminar flow in streamwise corners is that of Carrier (1947). He has evaluated the change in Blasius flow caused by the corner through solving the streamwise momentum and continuity equations, but his analysis is considered incomplete since the streamwise vorticity was not taken into account. Kemp (1951) has criticized Carrier's work in some aspects while Dowdell (1952) tried to estimate the error in U by linearizing the boundary layer equations about Carrier's solution, but only minor modifications were suggested. Other contributions are those of Sowerby (1951), Gersten (1959), Oman (1959), who presented an integral method analysis of constant-density flow in a 90^{o}-corner including pressure gradient, and Irvine and Eckert (1959) who analysed the flow within wedge-shaped grooves of finite end walls using a constant-density integral method.

The streamwise vorticity was first included by satisfying the cross flow momentum equation, by Pearson (1957) but the problem was systematically formulated, and the existence of secondary flow towards the corner reported by Rubin (1966). The asymptotic features of the corner flows were demonstrated by Pal and Rubin (1971). They suggested that all the corner layer flow variables exhibit algebraic, rather than exponential, decay into the boundary layer away from the corner and that the cross flow velocities decay algebraically into the outer potential flow. They also showed that the streamwise velocity and vorticity decay exponentially from the corner into the potential flow. This analysis made it possible to define boundary conditions for

a limited region in the corner. This was done in a numerical calculation by Rubin and Grossman (1971) who applied the Gauss Seidel method of successive iterations. Zamir (1968, 1970 and 1973) has devised a new approach independent of the coordinate system. He formulated the problem in a curvilinear coordinate system, rather than the Cartesian one used by Rubin (1966), of which one family approximates roughly to the expected isovels (without secondary flow) including the plate surfaces. The first trials of the method by Zamir was to determine the flow in the corner plane of symmetry for a range of pressure gradients using the form $U = Ax^n$ for the mainstream velocity. The interesting results showed that the streamwise pressure gradient has a great effect on the sign and magnitude of the secondary flow: the velocity component in the plane of symmetry is directed towards the corner for n greater than 1/2 and away from the corner for n less than 1/2. A curvilinear system was found by Desai and Mangler (1974) in which the corner layer equation took the form of the Blasius equation in the two-dimensional region.

Arbitrary corner angles were studied by Dowdell (1968). Barclay (1971) has formulated the problem by assuming a form of relationship between the cross flow and the streamwise velocity component which he used instead of the cross flow momentum equations.

The above calculations are either algebraic or, if numerical, of restricted range. More general numerical work has been done recently. Ghia and Davis (1974), Ghia (1975) and Patel and Goglia (1977) have used the alternating direction implicit method (ADI) developed by Peaceman and Rachford (1955) in solving the governing equations of the incompressible laminar boundary flow in axial corners. Patel and Goglia (1977) have found good agreement between their results and those of Rubin and Grossman (1971) only for large values of axial distances.

The bulge of isovels predicted by Zamir (1968) (see the experimental investigation in (b) below) were not predicted by Ghia's (1975) analysis.

(b) Experimental Investigations

As may be seen from the above short review, a massive amount of theoretical work has been done on the laminar corner problem over the past four decades. Comparatively little effort has been devoted to investigating the problem experimentally. This may be attributed to practical difficulties in maintaining the flow in corners in the laminar state even at very low speeds.

Some limited measurements have been carried out by Oman (1959), Nomura (1962) and Wallis (1968) in 90^{o} corner laminar flow but the most important investigation in this field is due to Zamir (1968) and Zamir and Young (1970). This work, which is considered the first detailed study of the problem, offers carefully obtained extensive results for the laminar flow along a 90^{o} corner. They have displayed the behaviour of the flow in developing laminar corner flow and explained for the first time that it is accompanied by a "secondary flow" opposite in direction to that found in turbulent flows (see Fig. (1.2)). They have also pointed out a progressive distortion in the velocity profiles with distance from the leading edge. Barclay (1971 and 1973) has carried out an experimental study of the laminar flow along a 135^{o} corner. His measurements were taken in the same wind tunnel as Zamir and Young but with sharp leading edges rather than the rounded leading edges used by his predecessors. He has reported distortions of the isovels near the plane of symmetry of his 135^{o} corner similar to, but less severe than, those observed by Zamir. Contrary to what Zamir and Young found, Barclay's results showed that the distortion damped out with downstream distance. Barclay has attributed the difference

to change in the leading edge shape between the two investigations. He has found that the analytical solution of Carrier (1947) gives a good representation of the flow in the 135^0 corner. This implies that Carrier's neglect of streamwise vorticity was adequate for ideal corner flows. Barclay also held a comparison between his experimental results and the theoretical work of Rubin and Grossman (1971) and Desai and Mangler (1974).

Among the most recent experiments carried out on laminar corner flow are those of El-Gamal (1977) and El-Gamal and Barclay (1978) who studied the flow along a streamwise rectangular corner with sharp leading edges, both in zero and in slightly favourable pressure gradients. Profile distortions of the kind noted by Zamir and Young were completely absent from their results. This was again referred by them to the change of the corner leading edges used in each work.

The main conclusion that could be drawn from the above-reviewed work, which agrees with Equation (1.3), is that secondary flows do not exist in laminar corner flows except if streamwise vorticity was generated by the first mechanism (term P_2 in Equation (1.3)) due to shear flow skewness at rounded leading edges which wraps horseshoe vortices around them. This is a first warning that skew-induced vorticity can dominate a flow field!

1.2.1.2 Turbulent Corner Flow

Laminar flow is purely a numerical problem in which calculations and theoretical analysis should throw light on experiments and their deficiencies; in turbulent flow, on the other hand, experiments must precede the development of turbulence models and consequent improvements in prediction methods. Hence in this section, on turbulent corner flows, we start with a discussion of experiments.

(a) Experimental Investigations

Schiller (1923) and Nikuradse (1926) were possibly the first to observe the tendency of the isovels of their measured streamwise velocities to penetrate the corner region of straight non-circular ducts (see Fig. (1.2)). As mentioned before in Section 1.2, a mechanism was then given by Prandtl (1927) who showed that the existence of secondary flow in the corner is the result of anisotropy of the transverse normal Reynolds stresses in the corner (term P_4, Equation (1.3)). Nikuradse (1930) confirmed through his flow visualization the existence of secondary flow in the corners of non-circular ducts. Eckert and Irvine (1955) did some flow visualization tests on flow in the corners of triangular ducts of height to base ratio of 5 : 1 and noticed that laminar flow existed in the narrow apex angle of the duct cross-section together with turbulent flow over its base. While working on fully-developed flow in trapezoidal ducts, Rodet (1958, 1960) again reported the bulging of isovels towards corners as a result of secondary flow. He also noticed more marked distortions in the contours of turbulent fluctuation components. Rodet was the first to measure the six components of the Reynolds stress tensor by rotating a single inclined hot wire sensor in the flow to eight different positions. The method has poor accuracy (Perkins, 1970a) in measuring $\overline{vw}$ and $(\overline{v^2} - \overline{w^2})$, the two values responsible for secondary flow induction (see Equation (1.3)).

The nine variables U, V, W, and the six Reynolds stresses were also measured by Brundrett (1963) for fully developed flow along a straight square duct and rectangular ducts. He applied Rodet's method for measuring the stress tensor. The detected values of $\overline{vw}$ were approximately zero everywhere except in the immediate neighbourhood of the corner bisector. He attempted to deduce the form of terms in the streamwise vorticity, Equation (1.3). His results were highly

inaccurate, especially for term P_4, because of the great deal of scatter in his data.

Fully-developed turbulent flow was investigated by Hoagland (1960) and Gilbert (1960) in rectangular ducts. The maximum value of crossflow velocity measured was 1.5% of the streamwise velocity component. The observed distribution of secondary flow was independent of Reynolds number.

Gessner and Jones (1961) have carried out a preliminary study of turbulence characteristics in the corner of a duct with no pressure gradient. They have concluded that the isovel patterns are independent of free-stream turbulence, in their tested range of turbulence intensity (0.8 - 2.3%). They found that the ratio $\overline{v_\alpha^2}/\overline{v_\beta^2}$ (referred to an arbitrary coordinate system x, α, β, Fig. (1.1)) takes its maximum when (α, β) coordinates are located roughly parallel and perpendicular to the local isovels. The ratio is always greater than one and increases with increase in isovels' curvature. The measurements thus confirmed Prandtl's hypothesis.

Wall shear stress (τ_w) measured by Leutheusser (1963) in the corner regions of square and rectangular ducts showed only small circumferential variation except in the vicinity of the corners where it fell rapidly to zero. The experimental measurements of Ahmed and Brundrett (1971) taken in the developing flow through square ducts have also shown that τ_w is very nearly uniform around the duct perimeter, except for small distances near the corners. Leutheusser's measurements have shown a static pressure rise of about 0.01 x $\frac{1}{2}\rho U_\infty^2$ between the wall and the duct centreline (no corrections were applied to the cylindrical static tube measurements to account for secondary flows or turbulent fluctuations). Leutheusser suggested that secondary flows and their associated transverse convection did not affect the two-

dimensionality of the inner layer ($y/h \lesssim 0.1$)*. The extent of inner law correlation diminishes rapidly in the vicinity of corners. This finding agreed with Bragg's (1965, 1969) results obtained in developing flow along unbounded 90^{o}-corners under zero and adverse pressure gradients.

The measurements of Gessner (1964) and Gessner and Jones (1965) in square and rectangular ducts of aspect ratio 2, an extension of their 1961 work, have shown, in contrast to the findings of Brundrett and Baines (1964), a decrease in secondary flow velocity, when normalized by the centreline mean velocity, as Reynolds number increases. The use of an "X"-wire probe in conjunction with an adding/subtracting circuit gave considerable improvement in accuracy for stresses $\overline{vw}$ and $(\overline{v^2} - \overline{w^2})$. In both ducts, the $\overline{vw}$ component took its maximum value along the corner bisector. It was found to be very small or to vanish elsewhere. The directional properties of $\overline{v_\alpha v_\beta}$ (in the general coordinate system x, α, β, Fig. (1.1)) were studied to locate planes of zero correlation. Such planes were found not to be normal to the isovels, a result which agrees with the later analysis by Perkins (1970a). The study of Launder and Ying (1971) made at different values of wall shear stress τ_w, obtained in smooth and rough walls, has shown that these changes in the secondary flow are considerably reduced if the secondary velocity V_s is normalized by u_τ rather than the centreline velocity. This is, of course, what we would expect; wall-law or defect-law ideas should still apply in slender flows although the resulting formulae may be more complicated than in two dimensions.

A more comprehensive experimental program was carried out by Mojola and Young (1971) and Mojola (1972) (reported also in short by

---

* Duct cross-section height = 2h

Young, 1977) on developing flow in unbounded 90^0-corners under zero and adverse pressure gradients. Separation at a free stream speed of about 30 m/sec with adverse pressure gradient was noticed at the corner. The onset of separation receded downstream with increasing spanwise distance from the corner. The isovels of mean velocity showed the expected bulging in the corner and the secondary flow measurements (taken by X-wire probes) showed the direction of the accompanying secondary flow. Measurements of wall shear stress τ_w distribution showed peaks near the corner, as shown in Fig. (1.3), as a result of secondary flow currents. In comparison to the findings of Zamir and Young (1970), Mojola and Young's results showed that the turbulent boundary layer is much more stable than the laminar one. This proved to be true in spite of the vanishing wall shear stress τ_w at the corner. They also found out that the rate of boundary layer growth was the same at the corner as away from the corner where the layers asymptote to their two-dimensional profiles.

The most recent work is that of Melling (1975) and Melling and Whitelaw (1973) who, aiming mainly at testing the reliability of Laser-Doppler anemometry in investigating complex turbulent flows, studied developing turbulent flow of water in a square duct. Their results supplement some of the previously reported work. The $\overline{vw}$ shear stress component could not be measured due to the complexity of the necessary optical system. Melling has reported that the accuracy of his measurements is comparable with those obtained by hot wires. Also the shear stress measurements appeared to be compatible with the necessary boundary conditions while secondary mean velocity data were no more reliable than those previously existing.

(b) Theoretical Analyses and Predictions

(i) Integral Methods of Calculation

Nikuradse (1930), Loitsianskii and Bolshakov (1951) and Eichelbrenner (1961) tried to generalise the n^{th} power law in order to describe the mean velocity profile in the corner region. By the use of the power law and Blasius-type formulae for wall shear in the momentum integral equation, Loitsianskii and Bolshakov, and Eichelbrenner could relate the corner layer thickness to the asymptotic two-dimensional boundary layer far from the corner. Eichelbrenner (1965) attempted a perturbation analysis for the local change in the streamwise velocity brought about by secondary convections. A further modification to the n^{th} law and the resulting isovels model of Eichelbrenner was made afterwards by Toan (1968) who used the Ludwieg-Tillman (1949) skin friction law to predict the distortion in the U-contours caused by the secondary flow. Toan introduced an arbitrary exponent in the n^{th} law, whereby he could increase the penetration of the isovels into the corner to match the experimental behaviour. To analyse their data on 90^{o} open channel flow, Liggett, Chiu and Miao (1965) transformed the n^{th} power law to a curvilinear coordinate system parallel and normal to the isovels in the cross plane. These elementary analyses are now of little relevance.

Bragg (1965, 1969) has suggested a modified wall law both far from the corner and very close to it. He defined a new velocity scale, analogous to the friction velocity u_{τ} but taking into account the mean velocity gradients normal to <u>both</u> walls (i.e. $\partial U/\partial y$ and $\partial U/\partial z$). He has also shown the validity of the log-law over much of the fully-turbulent inner layer of a 90^{o} corner under zero and mild adverse pressure gradient. This was proved to be the case except very near to the corner where he suggested a three-dimensional form of the law. In fact, the validity of a log-law region in the corner has been

assumed by many other workers before Bragg; for example: Deissler and Taylor (1959), in their analysis of flow and heat transfer in fully-developed flow, have assumed the log-law to hold along rays normal to the isovels. They devised an ingenious graphical technique for calculating the approximate isovel field. Nevertheless, because of the neglect of secondary velocity flow in this analysis, the resulting isovels in triangular and rectangular ducts did not exhibit any bulge towards the corners. In contrast to Deissler and Taylor's method, Perkins (1967), discussed in Perkins (1970a), selected a fixed coordinate system, not necessarily parallel to the isovels and attempted to find a model for the velocity field taking into account the effect of the secondary flows. He used a set of concentric duct profiles and their orthogonals as coordinate system in which the orthogonals simulated radial rays of circular pipes. Unfortunately, this system was not suitable for rectangular ducts (sharp corners) because of the discontinuity of the rays at $y = z$ and also because the log and wake laws lose their meaning along the corner bisector where $u_\tau\big|_{y=z} = 0$.

The validity of the Coles' (1956) wake model in the outer corner layer has been studied byMauer (1961) who has suggested a new empirical wake function. Different forms of empirical wake functions then followed by Bragg (1965) and Perkins (1970a).

Another way of attacking the problem has been used to derive an "interference" momentum-integral equation to allow for the presence of two adjacent walls. Among those who tried this approach were Gersten (1959), Bragg (1965) and Perkins (1970a). Ahmed and Brundrett (1971) have devised a momentum-integral technique for calculating the spanwise-averaged skin friction as a function of the development length for steady incompressible flow in rectangular ducts. On the other hand, the attempts of Toan (1971) to apply a momentum-integral

technique did not appear to be promising.

Mojola (1972), who gave a more comprehensive review of some of the above-mentioned work, discussed the extent to which his experimental data supported each approach. He has also carried out an extensive theoretical analysis work in which he arrived analytically at a relation for the mean streamwise velocity in the corner sublayer identical to that proposed by Bragg (1965), and an approximation for the mean secondary velocity in the viscous sublayer near the corner. Mojola derived an expression for $\overline{u^2}$ showing that its value does not vanish at the corner as the corner is approached along the bisector, which contradicts previous speculations. The most important contribution of Mojola is the use of curvilinear coordinate system (parallel and normal to the isovels) to predict a "unified" velocity correlation for the mean velocity in the corner wall region. He showed that the relation seemed to correlate all of the cases over a wide range of Reynolds number and for different corner angles, except for very narrow corners. Mojola also discussed the possibility of using a non-Newtonian laminar flow analysis to model turbulent flow in corners.

(ii) The Use of Eddy Viscosity and Mixing Length Models in Corner Flow Calculation

A considerable amount of effort has been, and is still being, devoted towards predicting the turbulent corner flow through the solution of the equations of motion using different postulated models. Ibragimove et al (1969) and Gerard (1970), among others, have developed an empirical model for the Reynolds stress terms in the equations in order to effect closure. Another model has been developed by Klinksiek (1972) for zero pressure gradient corner flow. He used the Boussinesq's (1877) model of eddy viscosity which he related to the mixing length via a formulation

originally suggested by Prandtl for three-dimensional flows (see Goldstein, 1965). Unfortunately, the predicted values of $\overline{v^2}$, $\overline{w^2}$, $\overline{vw}$ were under-estimated by two orders of magnitude compared to experimental results.

Fully-developed turbulent flow in square ducts was predicted by Launder and Ying (1973). In their solution, they took account of the secondary flow in corners. $(\overline{v^2} - \overline{w^2})$ and $\overline{vw}$ (see Equation (1.3) for importance of terms in inducing secondary flow) were related to $\overline{uv}$ and $\overline{uw}$ on the basis of a simplified Reynolds stress transport equation. $\overline{uv}$ and $\overline{uw}$ were then modelled with the eddy viscosity. Their system of equations was then closed by solving the kinetic energy equation and specifying a length scale distribution which was originally suggested by Buleev (1963). Numerical results based on this model predicted isovel patterns and secondary flow streamlines which agreed well with experimental results. On the other hand, their predicted turbulent kinetic energy was less than experiments and also the difference $(\overline{v^2} - \overline{w^2})$ was underestimated by at least an order of magnitude (see comments by Kacher, 1973).

Gessner and Emery (1976) developed a Reynolds stress model relating all the six components to mean rates of strain. The model was proposed to be used for solving the problem of incompressible turbulent flow along streamwise corners. It was based on Launder and Ying's model (1973) and used an extended form of the relation between shear stress and turbulent kinetic energy originally postulated by Bradshaw et al (1967). Later, Gessner and Po (1976) used the experimental results of Gessner (1964) and Tracy (1965) to fit the values for the model's two empirical constants and to help formulate the global mixing length representation. However, the model was strongly criticized by So (1977).

The most recent work in this direction is again due to Gessner and Emery (1977) who proposed a three-dimensional mixing length for modelling local Reynolds stress behaviour of developing and fully-developed flow in 90^{0}-corners. Gessner and Emery's new model is just a modification to the previous one of 1976. In this model, they used the experimental data of Po (1975) on square duct flow and of Klebanoff (1954) on asymmetric two-dimensional layers to develop an analytical expression for mixing length rather than using Buleev's (1963) model. However, the model could not eliminate the inconsistency between predicted and experimental values of $(\overline{v^2} - \overline{w^2})$, see Equation (1.3). Bradshaw (1977), in his discussion of this paper, has attributed this discrepancy to the "capricious" behaviour of streamwise vorticity (which should be included in modelling corner flows, see Section 1.1). Gessner and Emery agreed with Bradshaw's comment that the model is only reliable for 90^{0}-corners that comprise symmetry around the corner bisector, and is not at present adequate to describe decay of skew-induced vorticity.

(iii) Numerical Solution of Reynolds Stress Transport Equations

The case of fully-developed square-duct flow was also predicted by Naot et al (1974) using a Reynolds stress model similar to that of Launder and Ying except that the stresses were modelled by means of transport equations rather than algebraic relationships. The model was tested against measurements by Leutheusser (1963), Brundrett and Baines (1964) and Gessner and Jones (1965). The predicted degree of isovel distortion was over-emphasized in the vicinity of the corner as compared to Leutheusser's results, while the contours of kinetic energy in the transverse plane exhibited much less distortion than those of Brundrett and Baines. The predicted values of $(\overline{v^2} - \overline{w^2})$ were of

the same order as the experimental results.

Tatchell (1975) used a modification of Launder and Ying's model in his prediction of developing and fully-developed flow in square ducts. He solved the transport equation of ε (the viscous dissipation of turbulent kinetic energy) and $\overline{q^2}$ (the turbulent kinetic energy) rather than specifying a length scale distribution. The model was tested against the results of Ahmed and Brundrett (1971), Gessner (1964) and Brundrett and Baines (1964) in addition to those of Tatchell himself. The model did not account sufficiently for the bulging of the isovels towards the corners in developing flow. Predicted profiles of $\overline{q^2}$ agreed with measurements except as the walls were approached, where they exceeded the experimental values. These were attributed to slower predicted rate of secondary flow development as compared to the measured rate.

It is now obvious from the aforementioned review that turbulent flow in streamwise corners of straight ducts, channels or along the corner between two flat plates is dominated by secondary flow induced as a result of the anisotropy of Reynolds stresses (second kind). The conditions in which secondary flows are induced under the action of Reynolds stresses has been studied by more than one person to find out the mechanism of secondary flow induction. The first of them was Prandtl (1952) who suggested that turbulent fluctuations tangential to isovels ($\overline{v_\alpha^2}$) are larger than those normal to them ($\overline{v_\beta^2}$) which was found in measurements (c.f. Gessner and Jones, 1961). As a result of momentum exchange between a fluid element in a region of an isovel curvature, and its surroundings, a net force proportional to the isovel curvature, acts in the direction from concave towards the convex sides of the isovel producing secondary flow in its direction. Townsend (1956) has suggested

the same mechanism postulated by Prandtl. He suggested that the inequality in $\overline{v^2}$ and $\overline{w^2}$, rather than $\overline{v_\alpha^2}$ and $\overline{v_\beta^2}$, to be the driving force. He has also demonstrated that the return flows along the walls are also driven by secondary flow and do not occur by virtue of continuity as suggested by Prandtl. The analyses of Einstein and Li (1958), Hoagland (1960) and Tracy (1965) of the streamwise vorticity Equation (1.2) led them to an agreement with the Prandtl-Townsend mechanism. Hinze (1967) examined the turbulent kinetic energy equation in a region near but "not too close to the walls" and considered the relative magnitudes of the various terms. He suggested that secondary currents of the second kind are produced by the non-uniformities in anisotropic wall turbulence. Secondary flow, in Hinze's mechanism, transport turbulent kinetic energy in directions that balance the inequality between production and dissipation. Perkins (1970a) attributed the production of mean streamwise vorticity to anisotropy of the turbulence when a transverse gradient arises in wall shear stress (τ_w) and/or ℓ (a chosen length = δ or the distance at which $\overline{v^2} = \overline{w^2}$). Based on the evaluation of terms of both the energy and vorticity equations, Gessner (1973) has suggested another mechanism for initiation of secondary flow in developing turbulent corner flow. He suggested that secondary flow directed towards the corner results directly from shear stress gradients normal to the bisector rather than the anisotropy of the turbulent normal stresses which, he suggested, do not play a major role.

1.2.2 Flow in Wing-Body Junctions

We now proceed to study the flow in corners, concentrating this time on corner flows where skew-induced secondary flows dominate the flow. We will start by describing previous contributions in the field

of turbomachinery and by then discussing the flow in the corner of a single wing joined to a body.

1.2.2.1 Wing-Body Junctions in Turbomachinery

One of the most important topics that interests designers and researchers in turbomachinery is the end wall losses. It is well known (e.g. Dunham, 1970) that cascade secondary losses, which result from the interaction between the annulus wall (body) boundary layer and the blade (wing) rows, represent roughly half the total losses in axial-flow turbines and more than that in compressors. However, the extreme complexity of the three-dimensional flow in moving or stationary cascade passages close to the end wall, which cannot be denied, made it very difficult to predict, or even describe properly, this type of flow.

The postulates of Carter and Cohen (1946), Ainley and Mathieson (1951), Smith (1955) and Stewart et al (1960), among others, were reviewed by Dunham (1970). The flow visualization of Hertzig et al (1953) showed the complexity of end wall flow and indicated the existence of a "passage vortex", generated as a result of the three-dimensional deflection of the end wall boundary layer. The size of the vortex and its strength depended upon the main stream turning in the cascade passage. Hertzig et al investigated very thin blades so that the horseshoe vortices (see below) were weak. The effects of changes in the upstream wall boundary layer were studied by a number of workers. Higher losses were reported by Armstrong (1955) (who used a large-scale cascade to improve measurement accuracy) as a result of a thicker upstream wall boundary layer, while complete removal of the upstream wall boundary layer by Turner (1957) resulted in lower losses but no change in the flow pattern was observed. An

interesting work is that of Louis (1958) who measured the losses due to an inlet free shear layer (no end wall) passing through a compressor cascade and found them to be very low. Senoo (1958a), who studied the effect of the upstream boundary layer and the internal boundary layer developing on the wall within the cascade, showed that the relative importance of the two boundary layers depends on the cascade geometry. Wolf (1961), who analysed the results of his own as well as others' experiments, concluded that increasing the upstream boundary layer thickness extended the zone in which the secondary loss vortex dominated the flow behind the cascade. Wolf arrived at a certain critical boundary layer thickness δ_{cr}, after which any further increase in δ has no effect. Wolf suggested that δ_{cr} corresponds to the condition when the deflection of upstream boundary layer causes all the layer fluid to reach the next blade surface. Recent work on this topic included the detailed inlet and outlet total-pressure surveys done by Came (1973) on a large-scale turbine cascade with variable inlet boundary layer thickness and incidence and by Carrick (1975) who has found that inlet skew in the boundary layer intensifies the secondary flow which causes stronger roll-up of the Bernoulli surfaces (surfaces of constant total pressure).

Armstrong (1957) was one of the earliest to give an account of the horseshoe vortices that were formed ahead of compressor blades. The flow visualization of Prümper (1972) showed evidence of a saddle point of separation and Bělik (1972) reported the evidence of the horseshoe vortex (nose vortex, as he termed it) developed as a result of three-dimensional separation at the saddle point. Wagner and Owczarek (1974) conducted some experiments in two planar nozzles of different contours. In analysing their data, together with those of Owczarek et al (1970, 1972), they discussed the side wall boundary

layer migration caused by the cross-flow and its accumulation in the corner between the side wall and nozzle walls at its exit. They presented a model for the roll-up of the passage vortex and discussed the effect of Reynolds number, concluding that an increase in Reynolds number results in a decrease in the extent of the corner secondary flow and an increase in the roll-up angle of the side wall boundary layer caused by the main stream pressure gradient.

The studies of Sjolander (1975) and Langston et al (1975) are probably the first to demonstrate experimentally the importance of the horseshoe vortex in turbine cascades. In the Langston et al investigation, the three-dimensional flow in a turbine cascade was studied. They used thick blades of 110 degrees turning angle and concluded that three-dimensional separation is an important feature of the end wall flow. They have showed clearly, by flow visualization, that the inlet boundary layer separates on the end wall at a saddle point and rolls up forming a horseshoe vortex. One leg of the resulting vortex crosses the passage and encounters the suction surface at its point of minimum potential flow pressure (the point of passage vortex initiation - see Hertzig et al, 1953), while the other leg enters the adjacent passage. Bradshaw, Cebeci and Whitelaw (1977) considered this as an extreme case; as with thinner blades and/or smaller turning angles, the horseshoe leg would move only part way across the passage. Smoke flow visualization was carried out by Marchal and Sieverding (1977) using the light sheet technique in taking their photographs, in addition to oil flow visualization and 5-hole probe tests. Their results confirm basically the results of Langston and Sjolander. They have explained the mechanism in which the horseshoe vortex (leading edge vortex, as they named it) is formed as a result of the presence of the blade leading edge and showed that

the vortex leg on the suction side of the blade rotates in the opposite direction to the secondary flow generated by the cross-channel pressure gradient, and thus its size diminishes rapidly. On the other hand, the pressure-side leg initiates the passage secondary flow and rapidly develops into the passage vortex. Comparing their findings in turbine blades with those of Salvage (1974) on compressor cascades, Marchal and Sieverding concluded that the horseshoe vortex and its associated phenomena are much more significant in turbines than in compressors and that the skewness of the inlet boundary layer is also more important in turbines.

The effect of sharp corners at the junction between end walls and compressor cascades on secondary flow was investigated by Penken (1977). By superposition of the duct corner flow (as described by Mojola and Young, 1971) onto the potential flow due to pressure gradient from the suction to the pressure sides, he schematically postulated the flow pattern in the passage. He attributed the considerable contribution of the corner layer to the cascade secondary flow to the sharp corners and suggested that a "very simple" rounding of this corner should reduce the secondary flow.

1.2.2.2 Isolated and Simplified Wing-Body Junctions

It is now evident from the previous surveyed work on turbomachinery that a logical step towards better understanding of the nature of flow in the blade-wall corner is to isolate the corner from other effects like, for instance, the presence of pressure gradients, blade camber and interference from nearby blades. With this in mind, some workers carried out their investigations on what may be called simplified wing-body junctions.

Amongst the first to do so was Vasanta Ram (1963b) who

extended his work of 1963a on the junction between a circular cylinder and a plane surface and studied the flow in the corner between a symmetrical aerofoil at zero incidence and the flat surface. East and Hoxey (1968) have conducted some experiments in the corner of a simplified wing-body junction. Their wing had a circular arc nose followed by a short constant thickness portion, after which the thickness reduces linearly and symmetrically to a sharp trailing edge. Their experimental investigation comprised some surface oil flow visualization and limited measurements of static pressure, total pressure and cross-flow distributions which they measured using a three-hole yaw probe. They concluded that the turbulent boundary layer on the flat plate separates ahead of the wing leading edge to form a separated region extending round the edge and trailing downstream along each of the wing sides in a single concentration of vorticity "similar" to a vortex. They predicted the approximate location of the vortex centre to be 0.5 δ (δ = thickness of body boundary layer) away from the body and 1.5 δ from the wing at its parallel sides section. Surface pressure distribution was modified to a small extent by the existence of the vortex. This work was later extended by the same workers (1969) on the same configuration in order to collect data for improving integral calculation methods. East and Hoxey (1971) reported both results together. Comparing their results with two- and three-dimensional boundary layers, they found: (i) in the region of the separation line, the normal boundary layer approximation was not valid; (ii) agreement with Johnston's (1960) secondary flow model was obtained only ahead of the free stream inflection, and, (iii) the logarithmic law seemed to fit the data satisfactorily. Flow visualization studies were carried out by Winkelmann (1971) on the junction between a cylindrically blunted, unswept, unyawed fin and a

flat plate. The fin was immersed in the flat plate turbulent boundary layer and tested at Mach no. = 5. A pair of horseshoe vortices were detected from the flow visualization.

The above work concentrates mainly on the leading edge region where the flow is quasi-inviscid. However, the horseshoe vortex exists far downstream, as turbomachinery studies show.

The work done recently in Queen Mary College by Sepri (1973) and Chu and Young (1975) and reported also by Young (1977), represents an important contribution. The NACA 0012 wing section was connected to a circular flat plate with which it formed the investigated corner. Sepri started his investigations with some smoke and surface oil flow visualization covering a range of incidence angles. Again, evidence of the plate boundary layer separation together with the roll-up of the accompanying horseshoe vortex was noticed. According to Sepri's suggested vortex pattern, in the region of separated flow ahead of the wing leading edge, Young explained that the formation of one or more vortices depends on the flow Reynolds number. It has been noticed that the distance between the "main" vortex and the wing surface increases slightly as it proceeds downstream. The small vortex, which is in the opposite direction to the main one, seemed to grow in size with the downstream distance as a result of the increase in pressure gradient normal to the wing surface. At incidence, the same features were noticed (except that, of course, the horseshoe was not symmetrical around the wing). The suction surface leg was kept closer to the wing surface while the other vortex leg was swept away from the wing pressure surface. Again, this was attributed to the differences in pressure gradients on both wing surfaces. Surface oil flow pictures also indicated that the leading edge horseshoe vortex continues downstream of the trailing edge. This ensured that the complex structure of the

leading-edge vortices and separation lines influence the total corner region including the wake. Some limited surface static pressure measurements were made ahead of the leading edge and at some isolated stations on the wing and plate surfaces. Static pressure was also measured along the trailing edge and downstream of it. Mean values of the three velocity components together with static pressure profiles in the corner region were measured at and near the trailing edge using a conventional five-tube yaw meter. Some checks on the yaw meter secondary flow measurements were made by a hot wire from which the turbulence quantities u and w resulted as by-products. However, no analysis was made of the turbulence quantities' profiles.

In a trial to collect more comprehensive data (on the same wing-body configuration), Chu (1975) replaced the five-tube yaw meter with a single 45^{o} chamfered-mouth tube which could be rotated around its axis in 90^{o} steps. The tube was also supplied with an outer tube that covered the chamfered-mouth to transform the tube into a Pitot tube. This arrangement, of course, eliminates the effect of mean velocity gradients that affect multi-tube probes. Chu's measurements covered the trailing edge region and the wing wake, together with some traverses at the wing mid-chord plane. For zero incidence, the streamwise velocity cross-distribution showed two regions of low velocity on either sides of the wing, as a result of the extended legs of the horseshoe vortex, in addition to a central low velocity region corresponding to the wing wake proper. The V-velocity component showed approximate symmetry about the wing plane of symmetry. The V-velocity distributions measured near the plate surface showed shallow peaks away from the central region and troughs near the centre, while the opposite proved to be true for planes far from the plate surface. At 9.5^{o} incidence angle, Chu's measurements showed that the vortex from the

suction side was strengthened with incidence and remained close to the continuation of the wake, whilst that from the pressure side was weakened and moved somewhat away from the wake. The results also indicated that the location of the centreline of the wing wake region remained practically unchanged throughout the plate boundary layer.

Wing-body junctions in which the wing is attached to a cylindrical body or a body of revolution is another very important configuration as it simulates simply the practical wing-fuselage configuration. Simplified wing-body junctions of this type have been studied by some workers (e.g. Stanbrook, 1957; Weber, 1975 and Naranjit, 1976). Here, we are going to consider only the two studies made by Stanbrook (1957) and recently by Naranjit (1976) on simplified junctions.

Stanbrook (1957) (reported 1959) carried out his experiments on various wing-body junction combinations in which he tested different shapes and lengths of conical noses fitted to a cylindrical body to which the different types of wings (swept and unswept) were joined. He also tried both rounded and sharp leading edges. His experiments, which were conducted at both subsonic and supersonic ranges of speeds, included flow visualization and total pressure distributions. Again, the rolling up of the separated body boundary layer ahead of the wing nose formed a horseshoe vortex. He also predicted the same effects of incidence on vortex asymmetry, as did Sepri (1973). However, the most striking result of Stanbrook was the effect of the wing leading edge shape on the generation of the horseshoe vortex, i.e. that the vortices were present with both swept and unswept rounded leading edges at subsonic and supersonic speeds, but were not found with sharp edges at zero incidence.

The latest work due to Naranjit (1976) was on a simple wing-

body combination in which he measured the pressure over the combination including detailed measurements in the wing wake and body boundary layer both immediately behind the wing trailing edge and just behind the fuselage tail. From Naranjit's total pressure contours just behind the wing trailing edge at 9^{o} incidence, it was predicted that the wing wake merged without much distortion with the fuselage boundary layer. His results also showed clear evidence of the associated streamwise vortex on both sides of the wing wake. Behind the body trailing edge, the "fuselage" boundary layer and the wing wake did not merge smoothly due to the downwash distribution in this region which kept the main part of the wing wake above the "fuselage" boundary layer.

1.3 Conclusion

From the above review of previous work, specially on turbulent flow, it has been shown that the problem of interference occurring in the junction between a body and a wing is far from being completely or even partially understood. Even a thorough knowledge of the very simplified combination is still lacking.

The logical steps that should be followed towards the solution of the problem seem to start with more detailed experimentation devoted to much more simplified configurations in order to detect the fundamental processes that govern flow in corners.

1.4 Present Work

It was thus decided to carry out the present work on a much simplified configuration of wing-body junction. In this configuration, the tunnel floor simulates the body flat surface. The wing, which is described in much more detail in the following chapter, was designed to give the minimum possible complications. It has straight,

uncambered parallel sides. The leading edge has an elliptic-shaped nose and the trailing edge is blunt. The junction itself was arranged in an "idealized" form, namely, with the wing spanning the whole height of the tunnel and fixed at zero incidence to the flow.

All the work was directed towards studying this single configuration in order to collect the maximum possible amount of data. Tests performed in the present investigation comprised preliminary flow visualizations and a full survey of all the mean and fluctuating flow parameters including all the six components of the Reynolds stress tensor.

1.5 Outline of the Thesis

The following chapter of the thesis deals with the experimental arrangements and techniques utilized during the course of experiments. Experimental results are presented in Chapter 3, together with some preliminary discussions. Chapter 4 includes the main discussion and the higher order results. The conclusions extracted from the present investigations are given in the last chapter of the thesis.

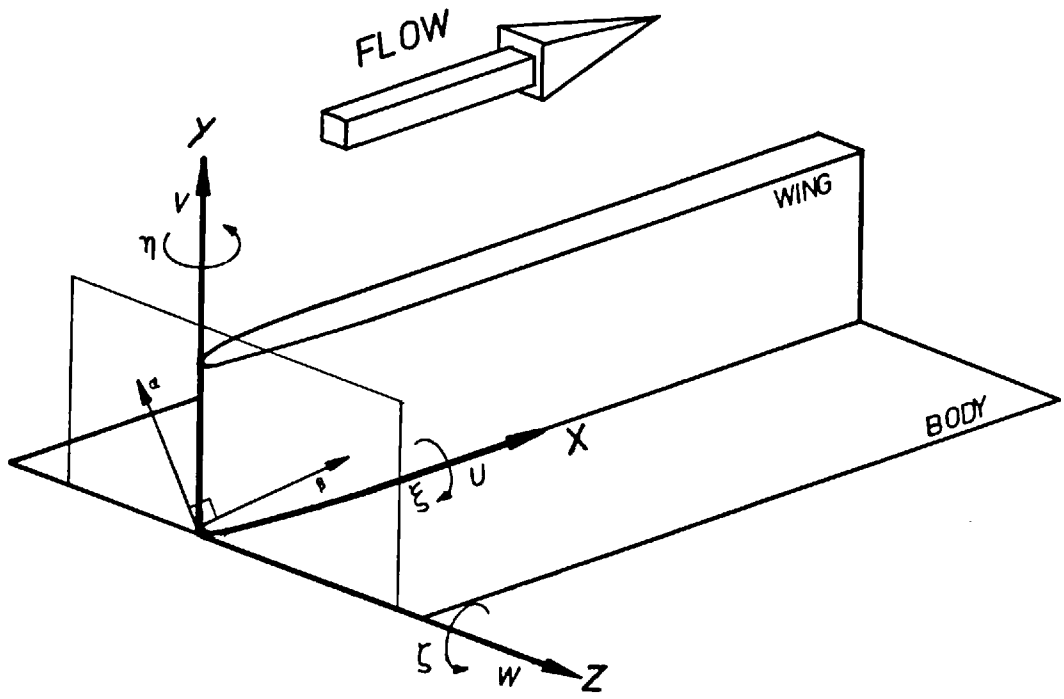

FIG.(1.1) THE IDEALIZED WING-BODY JUNCTION

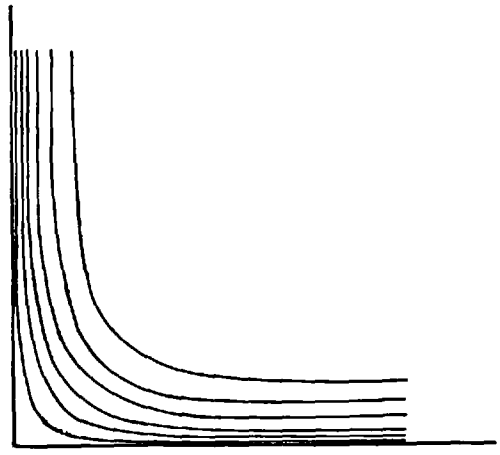

(a) Laminar Corner Flow with No Secondary Currents

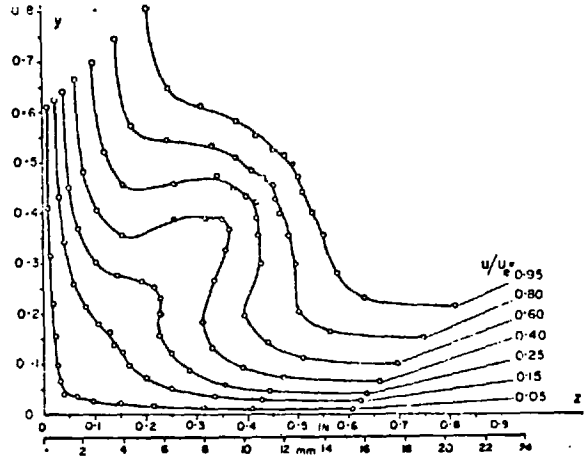

(b) Laminar Corner Flow with Secondary Currents
(after Zamir & Young, 1970)

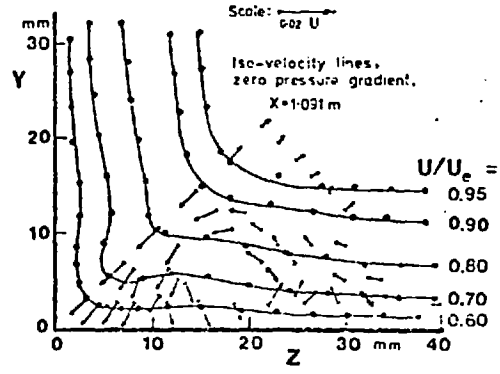

(c) Turbulent Corner Flow (after Mojola, 1972)

FIG.(1.2) ISOVELS (LINES OF CONSTANT STREAMWISE VELOCITY), and SECONDARY FLOWS IN CORNERS

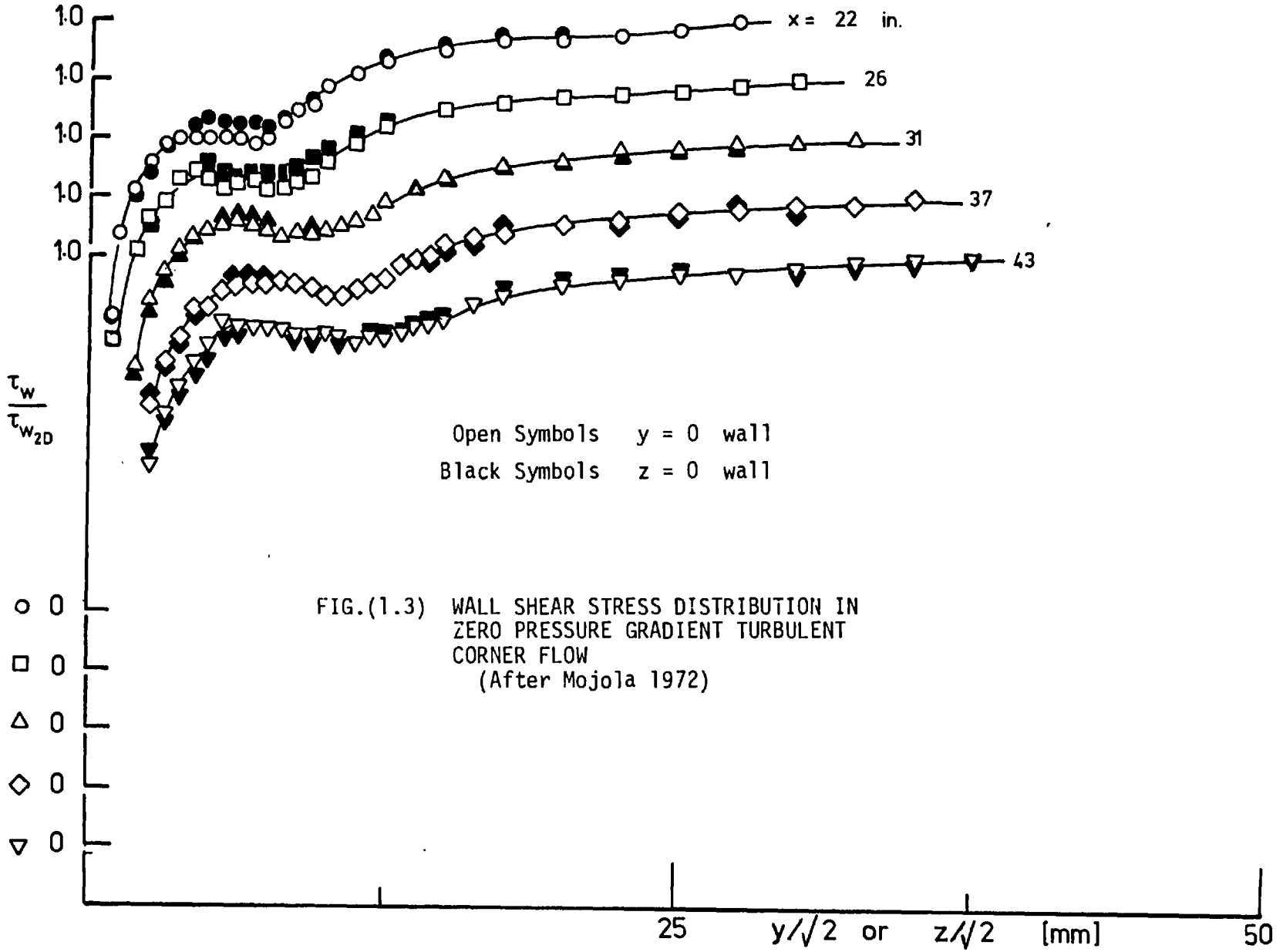

FIG.(1.3) WALL SHEAR STRESS DISTRIBUTION IN ZERO PRESSURE GRADIENT TURBULENT CORNER FLOW
(After Mojola 1972)

CHAPTER 2

EXPERIMENTAL ARRANGEMENT, INSTRUMENTATION AND TECHNIQUES

2.1 Introduction

To achieve the main two objectives of the present work, namely, a better understanding of the flow in the wing-body junction, and the supply of a nearer to complete set of experimental data to be used in future development of prediction methods, it was planned to measure as many of the flow parameters as time and available experimental facilities allowed, including all relevant second- and third-order mean products of velocity fluctuations.

The experimental programme started with oil-film flow visualization, using the standard techniques (see Sub-section 2.2.7). The first set of quantitative measurements comprised wall static pressure distributions on the "body" surface (the tunnel floor). This was followed by Pitot-tube measurements from which streamwise mean velocity profiles were deduced. Preston tube measurements of wall shear stress (skin friction) were made on both "wing" and "body" surfaces. A single hot-wire probe (U-wire) was then used to measure the streamwise turbulence intensity $\overline{u^2}$ with real-time analogue processing. A full survey of all the turbulent flow parameters was carried out, at a number of cross planes, using a cross-wire probe, with later digital processing. Some tests were then carried out, using pitch- and yaw-meters for measuring the secondary flow components V and W, but results were not accurate and thus dropped. Also, some trials were made of a cross-heated element, in which the angular rotation of a heated sheet of air convected from a thin hot wire is measured by a temperature wire set downstream of the heating element, as a method for

measuring the streamwise vorticity component but the practical difficulties proved to be insoluble.

The different experimental arrangements and instrumentation used in the present programme are described in the following sections. Some of the sections in this chapter are devoted to explaining the techniques used in collecting and processing the experimental data. The calibration procedures used in connection with the different instruments are also described in this chapter.

2.2 Experimental Arrangements and Instrumentation

2.2.1 The Wind Tunnel

2.2.1.1 General Description

The present experimental work was carried out in the 30" x 5" boundary layer wind tunnel of the Aeronautics Department at Imperial College. The wind tunnel is shown in Plate (2.1a), and sketched in Fig. (2.1b). It is an open-circuit design with an aerofoil-type centrifugal blower (Airscrew-Weyroc. Ltd. Type HEBA/B 27 in.)driven by a DC motor (Electrical Construction Co. Ltd. "Varispeed Mk 10" thyristor drive) fitted at its entry. High quality flow is ensured by the use of an aerofoil-type blower at the tunnel entry (Bradshaw, 1966). The blower is followed by a straight-sided wide-angle diffuser supplied with two screens for flow refraction into the expansion. Flow discharges from the diffuser into a settling chamber made up of frames, each of 2" thickness, carrying the honeycomb and screens and bolted together by drawbolts. The honeycomb is "Aeroweb" aluminium honeycomb with $\frac{3}{8}$" hexagonal cells, 2" deep, and the screens are 14 mesh, 28 swg (0.0148"

diameter). The settling chamber is followed by a two-dimensional contraction leading to a 5" high, 30" wide working section.

The tunnel working section is composed of two identical parts, each 4' 9" long. The test section floor is an aluminium sheet ($\frac{1}{2}$" thick) supplied with removable brass discs ($3\frac{1}{2}$" diameter) fitted flush to the surface at 6" pitch. The discs are interchangeable and carry traverse gears, Pitot tubes, Preston tubes, etc. Wall static pressure could also be measured simply through drilled tappings in the disc surfaces. Having circular arc-slots on their circumference, the discs are designed to be rotated around their centres with the retaining nuts slightly loosened. The test section roof is adjustable to allow any desired pressure gradient to be set up by trial. It is made of transparent PVC sheets 1/16" thick strengthened by spanwise wood bars, 1" square. Test section walls are made of $\frac{1}{2}$" thick perspex screwed to the floor with an $\frac{1}{8}$" gap for insertion of probes or applying suction to the tunnel corner boundary layers. The roof can be removed to give access to the working section for fitting trip wires, painting tunnel floor, fixing test models, etc.

A dust filter, made up of five 2' x 2' filter panels (Altair Ltd. Type 101/PP), is fitted to the blower suction side.

2.2.1.2 Tunnel Specification and Performance

Important items defining the tunnel specifications and performance are summarised as follows:-

(i) Working section dimensions : 30" x 5" x 9.5' (76.2 x 12.7 x 289.56 cm.)

(ii) Maximum tunnel flow speed : 45 ms^{-1} (the present measurements were made at about 30 ms^{-1})

(iii) Driving motor power : 12.5 kW

(iv) Maximum motor speed : 1500 rpm

(v) Turbulence level : 0.07%

(vi) Boundary layer at the contraction exit (upstream of trip wire) : laminar, 3 mm. thick (at 30 ms^{-1})

(vii) Spatial variation of total pressure at contraction exit : 0.2% of the dynamic pressure, (within experimental scatter)

(viii) The tunnel roof and floor boundary layers are tripped at the contraction exit.

(ix) The tunnel is supplied with a manual and an automatic control unit for flow speed adjustment. Details of the construction of the automatic speed control unit are given by Chandrsuda (1976).

The tunnel is described in more detail by Bradshaw (1972).

2.2.2 The Test Rig

The test rig was simply composed of the 30" x 5" tunnel working sections with the wing model fixed in the rear one. The roof height was set to a constant value of 5". Special arrangements were made, using the removable discs, for measuring wall static pressure and for fitting traverse gears.

The present experiments were carried out on a wooden wing model constructed by the Aeronautics Department Workshop. Model dimensions and configuration are shown in Fig. (2.2) (taken from Shabaka, 1975). The wing has an elliptic-nose leading edge (2.54, 15.24 cm. (1", 6") semi axes). The two parallel sides of the model are made of 12 mm thickness plywood tied together with wooden spacing pieces. The nose-

side surfaces are made of a thin sheet of metal wrapped around wooden semi-elliptic templates. This construction was preferred as it allows the model thickness to be changed, for future use, simply by replacing the spacing pieces and the nose templates. The wing span is 12.7 cm. (5"), its chord is 157.48 cm. (62"), and it is 5.08 cm. (2") thick. Five inches span, which the tunnel height allows, is enough to ensure the existence of a potential core between the tunnel floor and roof boundary layers. The maximum thickness to which each boundary layer grows at the exit from the working section is only two inches.

Another model of the same chord and span, but smaller thickness, was used in the preliminary flow visualization tests. This second model was made of a sheet of plywood, 6.4 mm ($\frac{1}{4}$") thick, with a chamfered leading edge.

The thick model (the main one) was placed in the rear test section of the tunnel with its leading edge at the section entrance and its chord parallel to the tunnel centre line, i.e. at zero incidence to the nominal flow direction (see Fig. (2.2)). It was placed with one of its surfaces covering equal small sectors of the removable discs of the tunnel floor. This allowed measurements to be taken in a region extending from the wing surface to about 65 mm. in the direction normal to the wing. This distance was found sufficient to cover the whole region where three-dimensional effects were detected. The thin model was used only for flow visualization experiment during which it was placed parallel to the thick model at the other side of the working section as shown in Fig. (2.2). All the surfaces in the hatched zones were painted black to give better contrast. Trip wires, 0.7 mm. diameter, were stuck to the surfaces of each wing, along their spans, at about 1" downstream of the leading edges. Hence, the boundary layers on the wing surfaces were made turbulent very near to their leading edges.

After the flow visualization was completed, the thin wing was removed from the working section. The main set of experiments was then carried out in the corner region formed by the surface of the thick wing and the tunnel floor.

2.2.3 Arrangement for Pressure Measurements

2.2.3.1 Surface Static Pressure Taps

Static pressure distribution on the tunnel floor was surveyed both in the axial (x) and the crosswise (z) directions*. Thirteen taps were drilled along the diameter of one of the 3½" diameter removable discs. Each of these taps is 1 mm. diameter. The ports are drilled at 6.4 mm. intervals, starting from the disc centre. Fitting this disc into any of the nine rings along the corner, or the nine rings upstream of the wing leading edge, made it possible for the static pressure to be measured at different stations to a sufficient distance away from the corner.

2.2.3.2 Pitot and Preston Tubes

Pitot and Preston tubes used in the present work, Fig. (2.3), were manufactured by the Department Workshop. The Pitot tube is of 0.624 mm. inner diameter, 1.05 mm. outer diameter, and 41.54 mm. overhanging length. The tube is soldered to a series of tubes of increasing diameter, ending with a 4 mm. diameter stem suitable for fitting in the traverse gear collet. The tube's overhanging length is angled very slightly towards the tunnel floor and sideways towards the wing surface. This allowed measurements to be taken with the tube lying in contact

---

* See Fig. (2.2) for axes system

with any of the two surfaces. A second tube having the same dimensions but with 53 mm. overhanging length was used as a Preston tube. This longer overhanging length ensures that the tube rests on the tunnel floor ahead of the edge of its mounting disc.

2.2.3.3 Manometers

Three types of manometers were used for pressure measurements in the present work:-

(i) An "AVA" Betz manometer was used to set and monitor the tunnel reference dynamic pressure at the entrance to the working section. This type of manometer makes it possible to read to the nearest 0.01 mm. water gauge resulting in an accuracy better than 0.02% in the range of dynamic pressure of the present experiments.

(ii) A "TEM" multi-tube manometer was used for measuring the surface static pressure distribution and for taking readings of the Preston tube. In the preliminary set of experiments, the Pitot tube was connected to the multi-tube manometer. This multi-tube manometer, when set to an angle of 18^{o} to the horizontal, gives an accuracy of about 0.2% of the reference dynamic pressure. A separate zero was recorded for each tube.

(iii) The Pitot tube was connected to a Furness Controls Type MDC multi-range capacitor micromanometer for traversing the total pressure in the corner region. A data logging system (see Subsection 2.2.5) produced the micromanometer out-

put on a punched paper tape. This arrangement resulted in an accuracy in the total pressure measurement of 0.4% of the reference dynamic pressure.

2.2.4 Traverse Gear Arrangement

The traverse system was designed to give motion in two directions, the vertical (y) direction away from the tunnel floor and the crosswise horizontal (z) direction normal to the wing surface (in its straight-sided section). As for the streamwise (x) direction, no motion is needed. Use can always be made of the tunnel removable discs facility to survey the flow along this direction.

The specially designed arrangement, shown in Fig. (2.4), was designed by the author and manufactured in the Department Workshop. An aluminium base A was fitted to one of the tunnel removable discs, B. The traverse gear C which holds the probe D and gives its vertical (y-wise) movement is fixed to a small base E that slides in the groove F of the main base, A. This traverse gear together with its base E are moved in the z-direction by the horizontal traverse gear G via a push rod, H. A slot 8 mm. wide was milled diametrically in the disc face to allow the probe to move in the z-direction. This slot, not apparent in the figure, was covered on its internal walls with self-adhesive foam rubber tape to mimimize leakage and to prevent metal contact between the probe stem and the disc. For the purpose of yaw-calibration, (see Sub-section 2.3.4b), a small hole I was drilled in the outer face of the disc. In this way the yaw-calibration could be performed with the probes in the measurement station by yawing the whole arrangement against the saddle J.

The two existing traverse gears (C and G) offering the two required motions and fitted to the above-described arrangement are of

the "slide rule" type, in which the "cursor" K carrying the probe stem is driven up or down the "stock" by a leadscrew L. Each has a stroke of 15 cm. (6"), is driven by a 12 V-DC electric motor M, Portescap Type P26, and is fitted to a Sakae linear potentiometer N, Type 20LP100*. This type of potentiometer is 10 cm. stroke and of 0.04 mm. resolution. One remote control box or power supply per traverse feeds both the motor and the potentiometer. The box also contains a voltage stabilizer and a zero potentiometer adjustment. Distance travelled by each traverse gear was monitored on a Solartron LM1420.2 digital voltmeter (DVM) measuring the potentiometer outputs.

2.2.5 The Data Logging System

The data logging system of the Aeronautics Department was used for recording the Pitot tube mean stagnation pressure profiles. A diagrammatic sketch showing the electrical connections of its components is given in Fig. (2.5). The system is composed mainly of a Solartron Data Transfer Unit (DTU), a Solartron LM1420.2 Digital Volt-Meter (DVM) and a Teletype ASR33 Teleprinter. Three extra DVMs were included for convenience: two were used for setting the traverse gears' voltages, i.e. specifying the Pitot tube location in the y-z plane, and the third acted as a monitor for the capacitor manometer output to check its steadiness before scanning a reading. In the present arrangement, the DTU simultaneously receives input signals from the two traverse gears (to input channels 0 and 2), the capacitor manometer (to channel 1) and the "coder box" (to channel 4). The remaining input channel (channel 3) was shorted out. The system's

---

* The potentiometers shown in Fig. (2.4) are, in fact, of the CIC Type 111 which were fitted to the traverse gears after finishing the experiment.

output device, the teletype, prints the readings and produces them punched in ISO/ASCII* code on a paper tape.

The "coder box", which is just a discrete potentiometer, fed from a separate power supply unit, provides an extra input voltage for later use during computer processing. Each of the twelve discrete control voltages that the box can provide defines the way in which the computer program handles a data record, e.g. it defines the points on the velocity profile, the points in the free stream, deletes a mistaken point, etc. More details on the program are found in Bradshaw (1973) and de Brederode (1973).

2.2.6 Hot Wire Anemometry

Turbulence quantities were all measured in the present work using constant temperature hot wires. The measurements were carried out in two stages: the first was the use of single wires (U-wires) for measurement of the longitudinal turbulence intensity $\overline{u^2}$, and the second was the use of the cross wires (X-wires) for measuring all the six independent components of the Reynolds stress tensor $\overline{u_i u_j}$ and higher-order velocity products.

2.2.6.1 Anemometers and Hot-Wire Probes

"DISA" anemometers and probes were used for all the tests. Both types of "DISA" constant temperature anemometers, namely, "55D01" and "55M01", were used. There is little effective difference between them except that the first has more control facilities, i.e. more flexibility, while the latter is easier to use. The "D01" type was used for all cross-wire measurements because it has a much lower out-

---

* ASCII : American Standard Code for Information Interchange

put impedance and is, therefore, more suitable for use with the filters (made in the Department) used when tape-recording hot wire signals. Longitudinal turbulence intensity was measured using DISA U-probes Type "55P01" with home-made 5 μm platinum (Wollaston) wires. The wire overall length is 3 mm. and its active part is approximately 1 mm. long. DISA miniature cross-wire probe Type "55A38" with DISA original gold-plated tungsten wires were used for some of the measurements while Wollaston wires were home soldered to DISA probes and used when original wires were not available. They proved to be better from the point of view of calibration drift, but they are more fragile.

2.2.6.2 Single-Wire Arrangement

Fig. (2.6a) is a block diagram of the experimental set-up used in connection with U-wires. The anemometer output was low-pass-filtered at 1 Hz and the mean voltage was read from a Solartron "LM1420.2" DVM. A "DATRON" true RMS meter was used to measure the signal rms value after filtering its DC component (high-pass filter set at 1 Hz) and high frequency noise (low-pass filter set at 20 kHz). The signal was always monitored on an oscilloscope as a check.

2.2.6.3 Cross-Wire Arrangement

(a) Analogue Measurements Set-Up

Some analogue cross-wire check measurements were taken using a variable-gain sum-and-difference unit, made in the Department, to obtain voltages proportional to u and v (with the cross-wires in the x-y plane). These measurements were used for preliminary comparison of cross- and U-wire results for the u-component intensity before proceeding to the main cross-wire measurements, and also as a check on the accuracy of the recorded data.

The analogue measuring system, shown in Fig. (2.6b) inside the dotted-line box, consisted of two DISA 55D10 linearizers, two "PHI" type operational amplifiers, a multiplier and an integrator, in addition to the sum-and-difference unit. A "PHI" console (Servicon Ltd.) with common ± 15 V power supply accommodated these plug-in units. Integration time was set by a WATESTA timer.

(b) Analogue Recording and Processing Equipment

(i) Analogue Recording Equipment

Non-linearized cross-wire signals were recorded throughout the course of the experiments. The wires' analogue output has been recorded on 1" magnetic tapes using an "Ampex FR1300", 14-channel, Analogue Tape Recorder. The recorder has 6 speeds ranging from $1\frac{7}{8}$ in. sec^{-1} to 60 in. sec^{-1} and increasing in geometric steps of base 2. 30 in. sec^{-1} speed was used for recording the X-wire data. The maximum and minimum values of + 1 V and - 1 V that the recorder can handle without distortion put limits on the amplifications applied to wires' signals. The total number of analogue tapes used in the present investigation is twelve; correspondingly, a total track length of about 604800 feet was recorded.

The recorded signals were played back at the same time and checked with the original signals by viewing them simultaneously on a multi-channel "Tektronix" oscilloscope. A sine wave signal of known amplitude and frequency was produced by a "Farnell" wave generator and recorded on both channels before and after every few traverses. This signal was later used for calibration purposes.

A block diagram of the above arrangement is shown in Fig. (2.6b). In this diagram, the analogue measurement equipment is sketched inside a dotted line box. This part of the equipment was disconnected during

the main recording processes.

Each cross-wire signal was filtered in the same way as the U-wire signal (passband 1 Hz to 20 kHz). Operational amplifiers (PHI type) were then used for signal amplification before recording. System complication was reduced by using a passive filter in filtering both wires' signals and to separate their DC and AC components. The DC components of the two wires were monitored on the same DVM using a selector switch in the passive filter unit.

(ii) Digitization Equipment

The process of reproducing analogue information in the form of discrete data points suitable for handling by digital computers is known as digitization. The Departmental Data-Logging System was used in digitizing the previously-recorded cross-wire signals. The system was described in full detail by Weir and Bradshaw (1974) and, together with its operating instructions, by Bradshaw (1975). Fig. (2.7), quoted from the above-cited references, shows a block diagram of the system. The system consists of an "Ampex FR1300" portable analogue tape recorder (on which recorded data was replayed at $7\frac{1}{2}$ in. sec^{-1}), a Data Laboratories Ltd. Simultaneous "Sample and Hold" Type 800, a "multiplexer", a Data Laboratories Ltd. "A/D Converter" 710, a Digital Equipment Co. Ltd. "PDP-8/L" minicomputer, an interface unit built by "DEC", and an "Ampex TM 16" Digital Recorder. A crystal clock sets the rate of transfer from the A/D converter to the core store of the minicomputer. The system is supplied with optional input "PHI" operational amplifiers. The input signal was low-pass filtered at 5 kHz*,

---

* With 20 kHz total sampling rate, filter is set to (10/n) kHz where n = number of channels to avoid aliasing.

and high-pass filtered at 1 Hz to cut out any recorded DC component. The system which handles up to 12 parallel input channels of analogue voltages (of amplitudes between ± 1 V), converts them into 10-bit binary numbers. It then records them in pure binary form on a 7-track ½" digital magnetic tape in "block IBM" format compatible with the Imperial College and University of London CDC computers. The system conversion rate is adjustable up to approximately 25,000 samples/sec. In the present work, a rate of 20,000 (10,000 samples/sec per channel) was used.

2.2.7 Oil Flow Visualization Mixture

The surface oil film technique was used for flow visualization on the tunnel floor in the corner regions of both wing models and upstream of the thick model leading edge. The oil mixture used by de Brederode (1975) was also used in the present work. It was formed from:-

- "Plus-Gas", formula "A" penetrating oil,
- "Speedivac" Grade 16 vacuum pump oil,
- titanium dioxide, and,
- oleic acid

and mixed according to the approximate volumetric ratios of 8 : 4 : 3 : 1 respectively. The mixture was then applied with a brush to the painted areas of the tunnel floor.

2.3 Calibration Procedures and Techniques

2.3.1 Multitube Manometer Calibration

The "TEM" multitube inclined manometer used in the present

investigation was calibrated against the "Betz" manometer. Calibration, in this case, meant defining a proportionality constant to transform columns of liquid on the inclined manometer into pressure measured in mm of water. This replaces working out the constant from the manometer inclination and the specific gravity of its liquid. The "Betz" projection manometer and two of the inclined manometer tubes were kept connected to the tunnel dynamic pressure throughout the experiment, and thus the calibration constant could be checked frequently. No change in the calibration was noticed except, of course, when the manometer angle changed.

2.3.2 Calibration of the Capacitor Micromanometer

The capacitor micromanometer used in the Pitot tube traverses was calibrated against the Betz manometer by connecting both of them to the same pressures simultaneously. The actual value of pressure, read in mm of water off the Betz, was then plotted against the micromanometer response in volts as monitored on the DVM. The micromanometer and the DVM connected to it was calibrated as one unit; in other words, the same DVM was connected to the manometer during both calibration and measurements. Fig. (2.8) gives a typical calibration curve. A least-squares method, performed on a pocket calculator, fitted a straight line passing through all the points except the first (to avoid any zero error effects).

Calibration was carried out before and after traversing each station and an average value was used for both the line slope and the intercept, provided that not more than 1% change was noticed. Measurements were repeated in the few cases where the calibration constant changed by more than 1%.

2.3.3 Traverse Gear Calibration

Each of the two traverse gears connected to the arrangement described in Sub-section 2.2.4 was calibrated against slip gauges. Every calibration started with some preliminary trials to set a potentiometer output of approximately 0.02 V per mm of travel. The least-squares algorithm was then applied (on a pocket calculator) to fit the best straight line (traverse gears are fitted with linear potentiometers) to the points of the main calibration. Calibration was performed before, and checked after, every set of tests. Only small changes (less than 0.6%) in the line slope were noticed, but the average slope was used. At the time of experiment, the location of the measurement points relative to the surfaces of the body and the wing (y and z) were chosen by inspection of the potentiometer voltages. Electrical contact was used for determining the potentiometer's zero readings. Pitot tube and hot-wire probe holders were electrically insulated from the traverse gears and their carrying disc. Contact of the Pitot tube tip or hot wire holders with the tunnel floor, which was detected by an electrical buzzer, defined the location $y = 0$. $z = 0$ was defined as the point of contact between the probes and a metallic strip stuck to the wing surface. This copper strip (12 mm wide and 0.1 mm thick) was fitted along the wing chord at height $y = 65$ mm and was electrically connected to the tunnel floor. The thickness of the strip was taken into account.

2.3.4 Hot-Wires' Calibration

(a) Velocity Calibration

Only static velocity calibration of both U- and X-wires were performed during the present work since Chandrsuda (1976) has shown that careful differentiation of a static calibration curve and the

dynamic calibration give the same $\partial E/\partial U$ within experimental error. He has also come to the conclusion that the calibration law:-

$$E^2 = A + BU^n + CU^{2n} \qquad (2.1)$$

where:- E : anemometer voltage reading (Volts)

U : flow velocity ($m.sec^{-1}$)

A, B, C and n : constants

proposed by Davies and Patrick (Cockrell, 1972) is unnecessary with the ranges of speeds found in the present work, because over the 2 : 1 range of speeds to which ordinary-size probes are limited in a boundary layer ($0.5 < U/U_e < 1$) the effect of the third term is negligible. Chandrsuda has suggested that the exponent n can be carefully chosen to produce a good straight line in the speed range up to approximately 30 ms^{-1}.

According to these findings, hot wires were statically calibrated to fit the law:-

$$E^2 = A + BU^n \qquad (2.2)$$

with n = 0.45.

Velocity calibrations were performed at the same stations as the measurements with the wires located in the free stream outside the boundary region. This was ensured by placing the wire in the tunnel mid-plane as far from the wing surface as possible. The local dynamic pressure was measured on the "Betz" manometer of which the high pressure side was connected to the tunnel inlet Pitot tube (i.e. neglecting any losses in the total pressure up to the calibration station, which is a

very good approximation), and its low-pressure side was connected to a surface static pressure tap just below the calibrated wire. The best straight line was fitted between E^2 and $U^{0.45}$ after removing points of noticeable experimental error, if any. Fitting was done on a pocket calculator using the least-squares algorithm. Typical U-wire and X-wire velocity calibration curves may be found in Figs. (2.9) and (2.10).

(b) Cross-Wire Yaw Calibration

The standard technique used in the Imperial College Aeronautics Department to measure the effective X-wire yaw response was applied in the present investigation. Details of the technique can be found in Castro (1973). Appendix A of this thesis gives a short account. The probe was placed in the free stream with the plane of wires laying horizontally. A specially designed circular arc (saddle) piece (see Fig. (2.4)), available in the Department, was used to yaw the probe at known angles to the flow, and the mean wire voltages were then monitored on the DVMs. The brass saddle-piece contains seven holes (only five of them could be used in the present investigation due to limitations of the traverse gear arrangement) on the arc of a circle whose centre lies at the centre of the disc holding the traverse gears. The holes are equi-spaced at intervals of 4.67°. When in position, the saddle is fixed to the tunnel co-axially with the disc. The disc, together with traverse gears and the probe, may be rotated in the x-z plane until the hole (see Sub-section 2.2.4) in the disc lines up with one of the saddle holes. Insertion of a peg locates the assembly in position until a reading is taken. The calibration curves, of which Fig. (2.11) is a typical one, was then plotted and the effective wire angles ψ_1 and ψ_2 were determined.

(c) Hot Wire Calibration Drift

To eliminate the effect of calibration drift, the U-wire was calibrated before and after every run of measurements or every three hours of measurements in longer runs. Frequent calibrations of cross-wires were also performed as indicated in Sub-section 2.4.6.2b. Calibration was even more frequently carried out when it seemed desirable.

If the drift in any of the constants A or B (Equation (2.2)) or wires' angles ψ_1, ψ_2 between successive calibrations was larger than 4%, the measurement taken between the two calibration processes was repeated. For less percentage drift, the change in constants was distributed linearly among the traverses (not points) done between calibrations.

(d) Effect of Changes of Flow Temperature

Owing to the fact that the hot wire principle is based on forced-convective heat transfer from the wire to the flow, it is expected that changes in flow temperature affect hot wire readings. The problem was discussed by Bearman (1971) who has suggested the following formula:-

$$\frac{\Delta E}{E} = \frac{-\alpha}{2(R-1)} \Delta\theta \qquad (2.3)$$

where:- ΔE : correction in hot wire voltage due to change $\Delta\theta$ (degrees) in ambient flow temperature.

α : temperature coefficient of resistivity, $(\text{deg K})^{-1}$

$= 0.0052$ for tungsten

and $= 0.0039$ for platinum

R : wire overheat ratio = R_w/R_o = ratio of wire resistance at operation condition to its cold resistance (set to 1.8 in the present work)

It can be shown from this relation that a change of one degree centigrade in flow temperature produces an error of - 0.33% in E for a tungsten wire and of - 0.24% for a platinum one.

In spite of the percentage errors being small, temperature corrections were performed for traverses having average temperature changes of more than $2^{o}C$ from calibration temperature.

2.4 Experimental Techniques

2.4.1 The Tunnel Flow Conditions

The present study was carried out at a tunnel inlet flow velocity around 30.5 $m.sec^{-1}$ (about 100 ft/sec). On one hand, it was found difficult to maintain the speed precisely at constant value owing to the continuous changes in the ambient conditions throughout a test day. Since the flow is not too sensitive to Reynolds number, in this range of speeds, it was found rather more convenient to keep the tunnel inlet reference dynamic pressure, instead of speed, fixed at constant value. A value of 57.5 mm of water was chosen for the reference inlet dynamic pressure throughout the present investigation. The tunnel inlet flow velocity ranged between 30.4 and 30.82 $m.sec^{-1}$ through the experiments (air density varied between 1.22 and 1.188 kg m^{-3}). This corresponds to a maximum change of 1.37% of the nominal 30.5 $m.sec^{-1}$ speed. Three barometric pressure readings, at least, were taken every test day and the flow temperature was measured, frequently during the experiments, using a thermometer placed in the free stream near the

working section exit. Any changes in the tunnel inlet speed could, thus, be recorded for future use.

The following precautions were taken to make sure the flow conditions remained unchanged throughout the experiments:-

(i) The wing model was kept always fitted in its place in the tunnel rear working section. Other workers who used the tunnel in the intervals of the present experiments carried their work out in the front test section or with their own special test sections.

(ii) Every time the tunnel was re-assembled, the following steps were taken before collecting a new set of measurements:-

(a) All the junctions and tunnel side gaps were sealed against leakage using masking tape.

(b) Leakage checks were carried out.

(c) The streamwise (x-direction) distribution of tunnel floor static pressure along the tunnel centreline was checked.

(d) Crosswise (z-direction) wall static pressure distributions were measured at some selected axial stations in the corner as well as ahead of the wing.

(e) The "body" boundary layer thickness was checked, using a Pitot tube, at three x-stations: the first upstream, and the second and ninth downstream of the wing leading edge. The checks were performed on the tunnel centreline at the upstream station and at z = 60 mm at the downstream ones.

These checks showed excellent repeatability and the main results, taken over a period of three years, can thus confidently be stated to be self-consistent.

(iii) Each day, before taking any measurements, the tunnel was left running at nearly the reference speed for about an hour.

(iv) Some of the laboratory windows were kept open during experiments ensuring enough ventilation to avoid warming up of air in the room (tunnel sucks from, and delivers into, the room).

2.4.2 Flow Visualization

As mentioned before in Sub-section 2.2.7, the oil flow visualization technique described in detail by de Brederode (1975) was used in the present investigation. The preparation of the oil mixture is also described in Sub-section 2.2.7. In fact, some trials were made before deciding upon the mixture proportions suitable for the tunnel surface in the present range of flow speeds. The oil was brushed on the tunnel floor surface as economically as possible to avoid accumulation in regions of low velocity. From 20 to 30 minutes of running time were needed to arrive at a constant flow pattern along the corner. The tunnel roof was then removed and the pattern was photographed from the top.

2.4.3 Static Pressure Measurements

2.4.3.1 Surface Static Pressure Measurements

The ordinary technique of measuring surface pressure through

tappings was applied in the present investigation. The arrangement described in Sub-section 2.2.3.1 allowed "body" surface pressure to be surveyed in both the streamwise (x) and crosswise (z) directions.

Measurements in an aerofoil-wing-body junction done by Sepri (1973) has shown constant wall static pressure distribution on the wing surface along its span despite any changes in the body wall pressure with the distance away from the corner. Sepri's findings have shown that this applies starting from very near to the wing leading edge and downstream to more than half the wing chord (i.e. far downstream of the maximum wing thickness). The present wall static pressure measurements on the tunnel floor, showed very slight changes in the pressure coefficient C_p as one proceeds away from the corner except very close to the leading edge (i.e. except at station No. 1). On the basis of Sepri's results and the preliminary tests of the present work, it was found unnecessary to measure wall static pressure distribution over the wing surface.

2.4.3.2 Static Pressure Across the Boundary Layers

Static pressure profiles across corner boundary layers were measured by some previous workers. Leutheusser (1963), Bragg (1965) and Mojola (1972) took their measurements in streamwise corners of symmetrical boundary layers with uniform free-stream pressure. Their findings have agreed on a value of about $0.01 \sim 0.03 \cdot \rho U_e^2/2$ for the maximum change in static pressure across the layers. On the other hand, Bradshaw and Goodman (1966) imply that the uncertainty of static pressure measurements, due to the unknown effect of turbulence on the static tube, is likely to be as large as the above-mentioned differences. It was thus thought that a uniform static pressure across the boundary layer would be an adequate assumption, being at the worst, in the same

level of uncertainty as static tube measurements and implying an uncertainty of only about 1% in U-component velocity.

Static pressure was thus measured only on the "body" surface beneath the thicker boundary layer and the gradient $\partial p/\partial y$ was assumed equal to zero in the corner region.

2.4.4 Skin Friction Measurements

The small-diameter Preston tube described in Sub-section 2.2.3.2 was used, fitted to the traverse gear arrangement described in Sub-section 2.2.4 and connected to the multi-tube inclined manometer, to measure the local skin friction. Traverses were carried out on both surfaces of the wing and the body (tunnel floor) at axial stations number 2, 3, 4, 5, 7 and 9, and on the tunnel floor at axial stations number - 7, - 5, - 4, - 3, - 2, - 1 and 1*. At each station, a z-wise traverse was made, taking care to keep the tip of the tube in contact with the body surface. This was followed, at stations 2, 3, 5, 7 and 9, by a y-wise traverse with the tube touching the wing surface. Wall static pressure distributions, measured as explained in the previous sections, were used with the Preston tube readings to compute the skin friction coefficient C_f using the modified "PRESTON" program. The values of wall static pressure at the tube mouth were deduced by a parabolic interpolation in the x-direction.

2.4.5 Mean Flow Measurements Using Pitot Tube

The Pitot tube of Sub-section 2.2.3.2 was used connected to

---

* The corresponding x-distance (mm) measured from the wing leading edge is given by the relation: $x = 25.4 \left(6n - \frac{3|n|}{n}\right) + 53$ where n is the station number. Alternatively, see Table (3.1).

the data-logging system described in Sub-section 2.2.5 to measure the total-pressure profiles in the corner region. Stations 1, 2, 3, 4, 5, 7 and 9* were traversed. Some more traverses were carried out at station 9 in which pressures were read off a Betz manometer and recorded by hand. These were done in the first stage of experiments and as a preliminary check on the logged data. The checks made every time the tunnel was re-assembled for the collection of a new set of data were also recorded by hand.

Usually vertical traverses (in the y-direction) at different distances from the wing (each at constant z) were taken, but some five z-wise profiles at each surveyed axial station were also measured. The number of points on each traverse and their distribution depended on the total pressure gradient as monitored, at the time of the experiment, on the DVM (or the Betz manometer). More points were taken in regions of high gradients near the solid walls.

At the end of every traverse, three points, at least, were taken in the free stream for the purpose of defining the free stream value of velocity, U_e, used in the data-analysis program. Similar number of dummy points, again taken in the free stream, were added to those traverses that did not end outside the corner boundary layers (in other words, on vertical traverses close to the wing and horizontal traverses close to the tunnel floor).

2.4.6 Measurements of Turbulence Fluctuating Quantities

Constant temperature hot wires were used throughout the present investigation. Measurement of the longitudinal turbulence component (u) and the mean streamwise velocity (U) was performed using

---

* $x = 25.4\left(6n - \frac{3\ln l}{n}\right) + 41.54$ (mm)

the single- (U-) wire, while the cross- (X-) wire was used for measuring all the three fluctuating components, their higher products, and the secondary-flow components of mean velocity.

2.4.6.1 Measurements of the Longitudinal Turbulence Intensity

The single wire arrangement described in Sub-section 2.2.6.2 was used for analogue measurements of $\overline{u^2}$ and U. A full survey of stations 1, 2, 3, 5, 7 and 9 was done in which both quantities were measured. Mainly vertical traverses were carried out and checked by some lateral traverses. Reduction of the U-wire data was performed on the College Computer, as explained in Sub-section 2.5.3, using the "AXTURB" program.

2.4.6.2 Measurement of Other Turbulence Quantities and the Secondary Flow Components

Cross-wires were used for measuring turbulence quantities $\overline{v^2}$, $\overline{w^2}$, $\overline{uv}$, $\overline{uw}$, $\overline{vw}$, and their higher products (e.g. $\overline{u^3}$, $\overline{v^3}$, $\overline{u^2v}$, $\overline{v^2u}$, ...), and the secondary flow components v and w. For measuring $\overline{v^2}$, $\overline{uv}$, $\overline{u^2v}$, $\overline{v^3}$, ... etc., the plane of the wires was aligned to the vertical (x-y) plane, while they were placed horizontally (i.e. parallel to the x-z plane) for measuring $\overline{w^2}$, $\overline{uw}$, ... etc. For measuring the secondary shear stress $\overline{vw}$, two readings of the cross-wire (one with the wires inclined + 45^o to the horizontal and the second with them inclined - 45^o) were required at the same point (see Appendix B for details). The probe itself was carefully adjusted to the horizontal in the (x-y) plane by rotating its vertical stem and bending its overhanging support slightly. Alignment was checked by obtaining the same voltage from each wire at any angle to the vertical plane (x-y).

Setting the wires' plane to 0, + 45, - 45 and 90^o to the x-y

plane was done manually. A special arrangement was made to ease the accurate setting of the wires. The probe support was supplied with a very thin needle glued along its generator, to act as a pointer, and the probe holder itself was scratched at four positions corresponding to the four settings. A quick analysis of the involved error is given in Appendix C.

(a) Analogue Measurements

The linearized cross-wire signals were processed by analogue electronics using the sum-and-difference module connected as shown in Fig. (2.6b). Instructions given by Weir, in Bradshaw (1977), were carefully followed. Twenty seconds of integrating time were allowed for each measured quantity. Due to the rapid drift in linearizer electronics, the linearizer constants had to be reset and, consequently, the sum-and-difference module coefficients had to be altered, about every twelve readings.

(b) Digital Measurements

Detailed traverses at stations 2, 5 and 9 were carried out in which the hot wire signals were recorded on analogue tapes.

A speed of 30 ips (76.2 cm.sec^{-1}) was used throughout all the recording process giving about 10 kHz bandwidth. At least thirteen points were recorded on each traverse, most of them taken inside the boundary layers. Not less than sixteen traverses were made at each section, mainly in the vertical direction (at constant z's); some three cross traverses were always performed as checks. Thirty seconds of signal were recorded at each point. Hot wire signals were amplified, using PHI System Data Amplifiers, but care was taken not to exceed 50% of the maximum permissible input to the tape recorder, which

is 2 V peak-to-peak (1 V peak-to-peak recommended for minimum distortion). After ~~every~~ few traverses, a calibration sine wave of known amplitude (strictly speaking rms) and frequency was recorded.

The complete survey at one axial station was executed according to the following sequence:-

1. Yaw calibration of the probe in the horizontal (u-w) plane.
2. Velocity calibration of the probe in the vertical (u-v) plane.
3. Full traverse of the station measuring u-v components with brief velocity re-calibration every ten points at most.
4. Final velocity calibration in the vertical plane.
5. Yaw calibration in the horizontal plane.
6. Velocity calibration of the probe in the horizontal (u-w) plane.
7. Full traverse of the station to measure u-w components with velocity re-calibration at most every ten points.
8. Final velocity calibration in the horizontal plane.
9. Yaw calibration.
10. Velocity calibration of the wires in the planes - 45 and + 45^{o}.
11. One traverse with the wires in the + 45^{o} plane.
12. The same traverse with the wires in the - 45^{o} plane.
13. Repeat of steps (10 - 12) for all the traverses at the station.
14. Final velocity calibration in the - 45 and + 45^{o} planes.
15. Final yaw calibration.

The recorded data was then sampled and reduced as explained in the following section.

2.5 Data Processing and Reduction

The experimental data collected using the aforementioned

techniques were processed and reduced mainly using the Imperial College computing facilities (CDC 6400 computer). A number of the standard programs available in the Aeronautics Department were used, after some slight modifications, applied by the present author, for plotting the results and/or storing them on files for future use. In addition, some special programs were written to serve the present case.

2.5.1 Processing of Preston Tube Data

The skin friction coefficient (C_f) was deduced from the Preston tube and the wall static pressure data with the "PRESTON" program (originally written by S. T. B. Young) which uses the Patel (1965) calibration.

2.5.2 Processing of Pitot Tube Data

The Pitot tube data produced, on paper tapes, by the data-logging system, described in Sub-section 2.2.5, was analysed using the modified CDC version of the "VELPROF" boundary layer data analysis program. The original version of this program, written for the Aeronautics Department Honeywell H21 computer, is described by de Brederode (1973). Another version of the CDC program given the name "VELPRF1" has been written by the author to read Pitot tube data (originally taken by hand) from punched cards instead of paper tapes. "VELPRF1" was used in reduction of data collected in the preliminary experiments and during the checking tests carried out before every collection of a new set of data (see Sub-section 2.4.1).

2.5.3 Processing of U-Wire Data

Differentiating the King's law adopted for the hot wires' calibration and response (Equation (2.2)), we get:-

$$2E\ U\ dE = n(E^2 - A)\ dU \tag{2.4}$$

If e is the fluctuation in the wire voltage around the mean E produced as a result of the fluctuation u in the flow velocity around its mean U, then writing dE = e and dU = u, we get:-

$$2E\ Ue = n(E^2 - A)\ u \tag{2.5}$$

and taking the mean square of both sides:-

$$\frac{\overline{u^2}}{U^2} = \left[\frac{2E}{n(E^2 - A)}\right]^2 \overline{e^2} \tag{2.6}$$

Equation (2.6), together with the wire calibration (2.2), were used in the "AXTURB" program written by the author to work out $\overline{u^2}$ and U from the U-wire readings. The program produces tables and plots of $\overline{u^2}/U_e^2$ and U/U_e vs. y (or z).

2.5.4 Processing of Cross-Wire Data

(a) Data Sampling Technique

The cross-wire data recorded on analogue tapes as explained in Sub-section 2.2.6.3b was later sampled on the Departmental Data-Logging System described in the second part (ii) of the same sub-section. Digitization was carried out with the analogue tape recorder running at a replay speed equal to one quarter of the recording speed, i.e. 7.5 ips (19.05 $cm.sec^{-1}$). A sampling rate of 10,000 samples per second per channel was used resulting in an equivalent real-time rate of 40,000 sample/sec per channel (spatial resolution at 30 $m.sec^{-1}$ is, therefore, 30/10,000/4 or 0.75 mm).

When processing the data, it was found that well-converged averages could be obtained by processing 150 records* (about 3 seconds of real-time data) in most locations. For points near the boundary layer edges, 220 records (about 4.3 seconds) were needed. In order to allow the input filters of the digital system to settle down, 20 replay seconds (5 seconds real-time) of the analogue recording were digitized.

For calculating the overall gain of the system, the voltage output of the replayed analogue calibration signal (the sine wave) was measured, for each channel, after passing through the input operational amplifiers of the digital system, i.e. before passing to the sample-and-hold unit. This allows for the variation of gain of various plug-in modules of the tape recorder, the gain of amplifiers used in the recording process, and gains in the input amplifiers of the digital system.

(b) Data Reduction

The standard two channel "DIG2U" program (see Weir and Bradshaw, 1974), was used after slight modification to allow it to store its output on permanent disc files. "DIG2U" program input comprises the digitally recorded data of the cross-wire and its calibration constants. The program also accepts an intermittency threshold factor whose value was chosen according to Weir (1976). "DIG2U" prints the accumulated averages every few records, whose number is selected via an output control parameter. After running long enough to obtain convergence of mean squares to 2%, the program produces the final averages which comprise: the mean values of axial and secondary flow velocities, the mean squares of the two fluctuating

---

* One record corresponds to one buffer of size 1536 words (points).

components, the shear stress components, the fluctuating components' mean triple products, and their fourth powers. It also prints out the computed skewness and flatness factors for both velocity components, and the intermittency factor γ. Two programs written during the present work dealt afterwards with "DIG2U" final averages. "NORMD", which is a simple program, used with the data of cross-wires in the vertical (x-y) and the horizontal (x-z) planes, normalizes the final averages by a suitable power of the free stream velocity U_e. The second program, "VWTURB", reads the final averages of the data collected with the cross-wires in the + 45 and - 45^{o} to the horizontal. It then works out $\overline{vw}$, and other turbulence quantities and normalizes them by U_e raised to a suitable power. The different relations that "VWTURB" uses are given in Appendix B.

FIG. (2·1) a: THE 30 × 5" BOUNDARY LAYER TUNNEL

(The "second half of the roof" is removed for clarity , to show the Wing-Model)

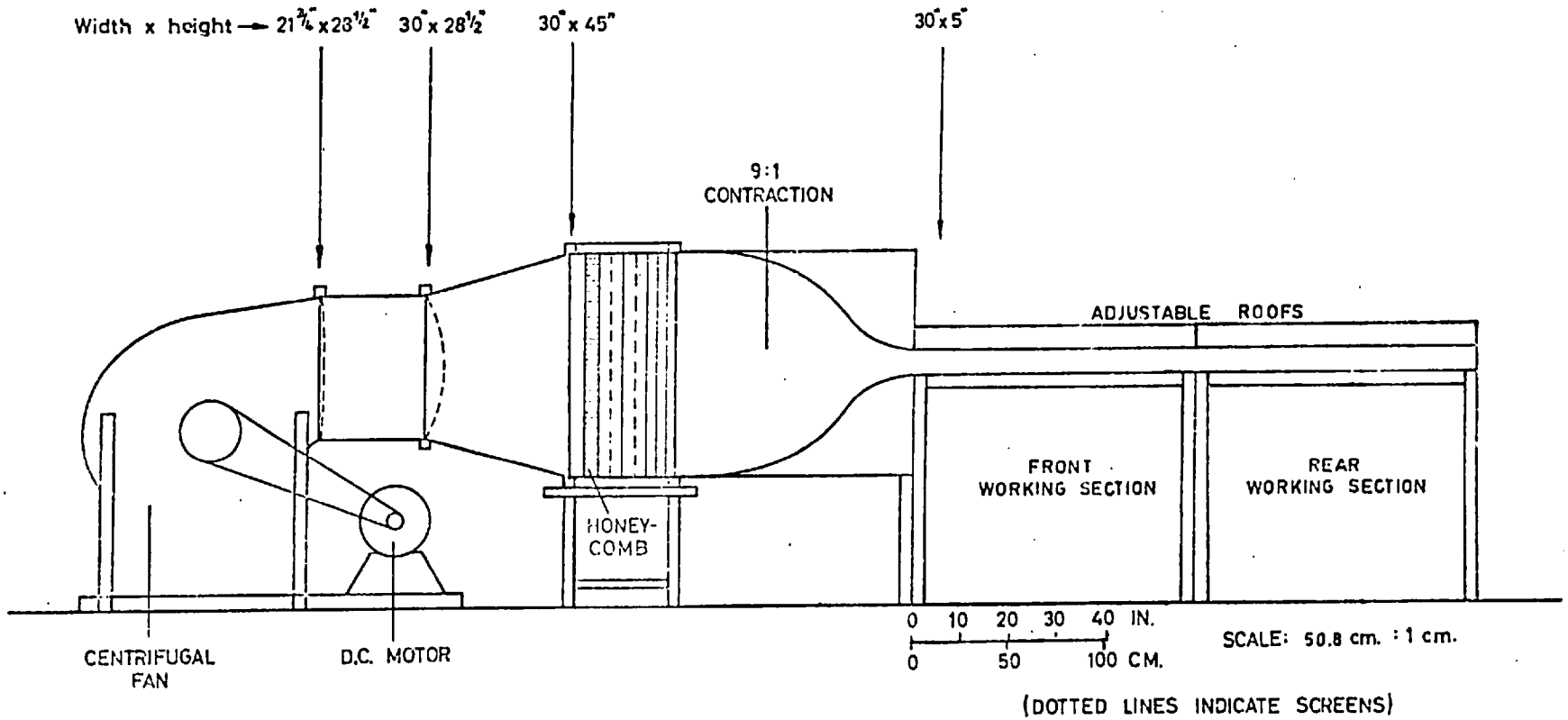

FIG.(2.1) b: SIDE VIEW OF THE 30" x 5" TUNNEL

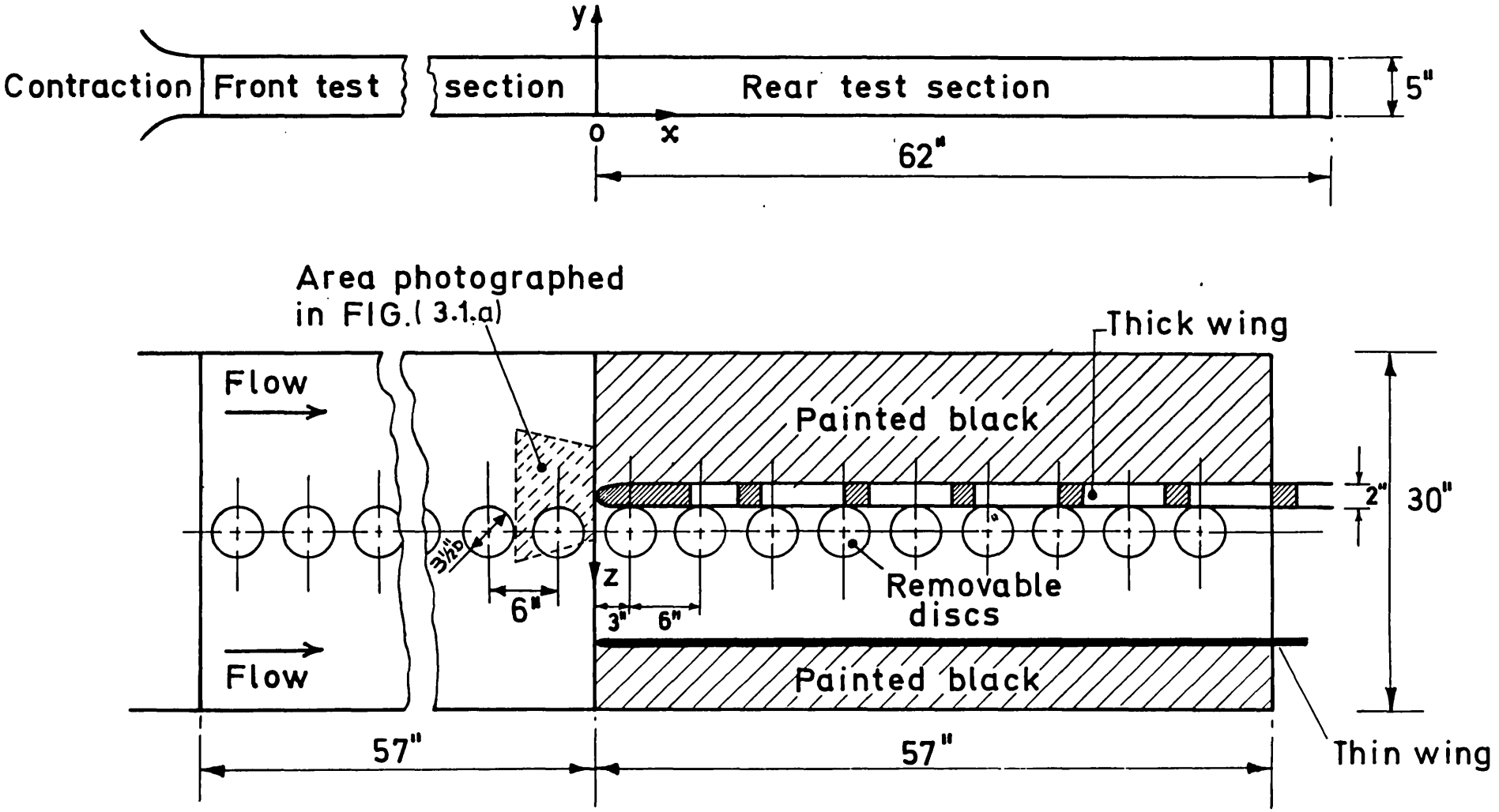

FIG.(2.2) Schematic of tunnel test-sections with models inside

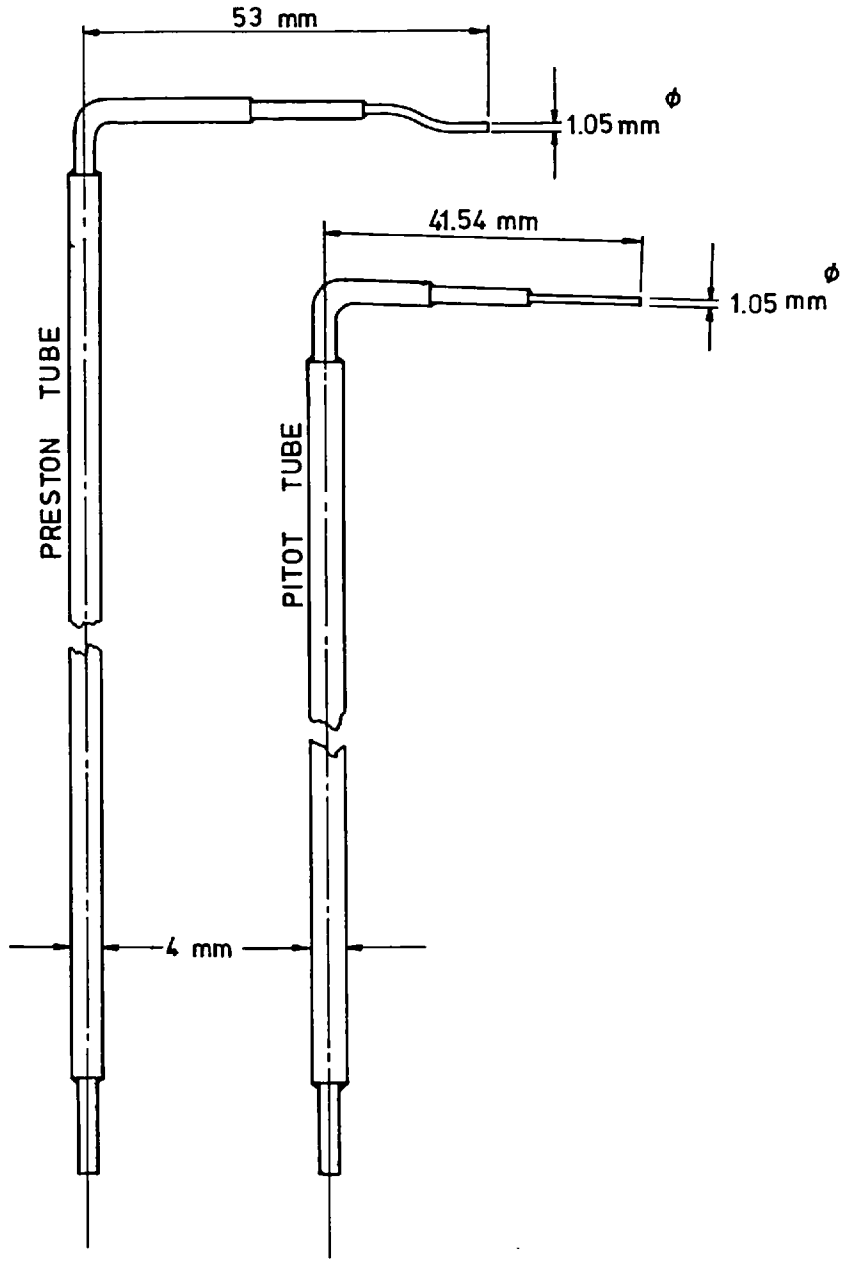

FIG.(2.3) PITOT AND PRESTON TUBES

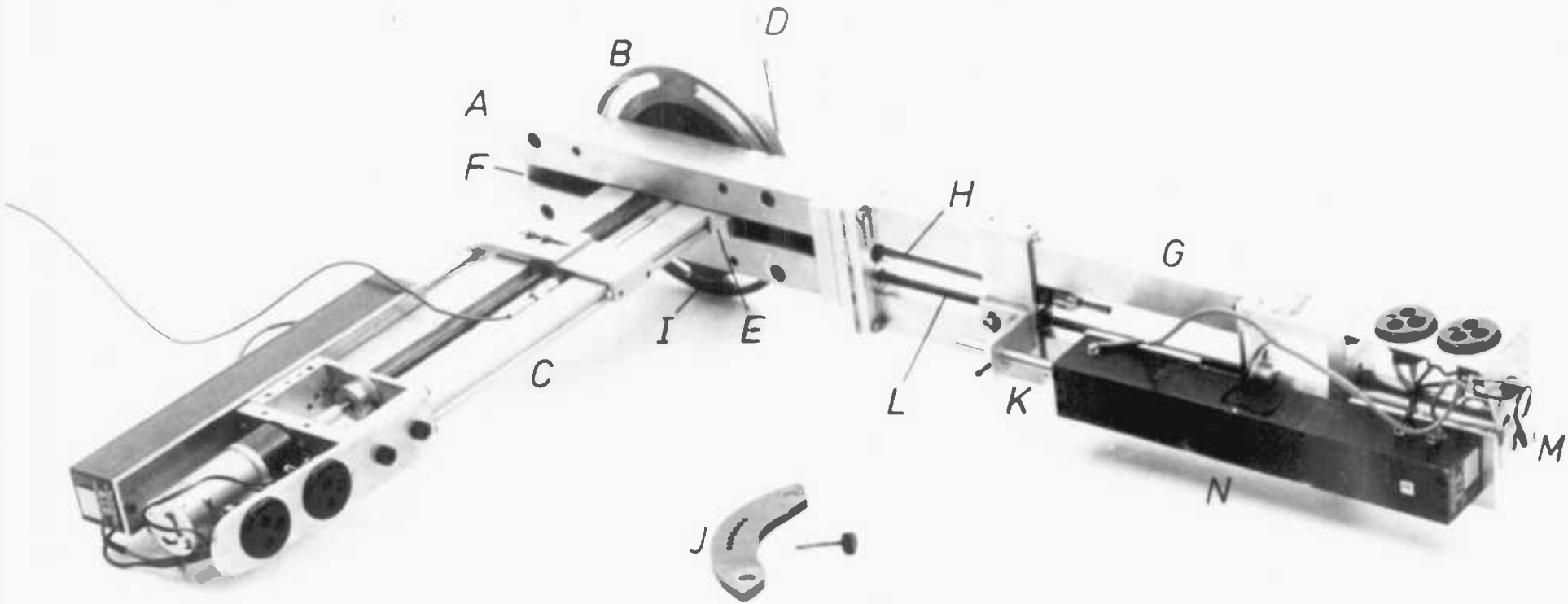

FIG.(2.4) THE TRAVERSE GEAR ARRANGEMENT

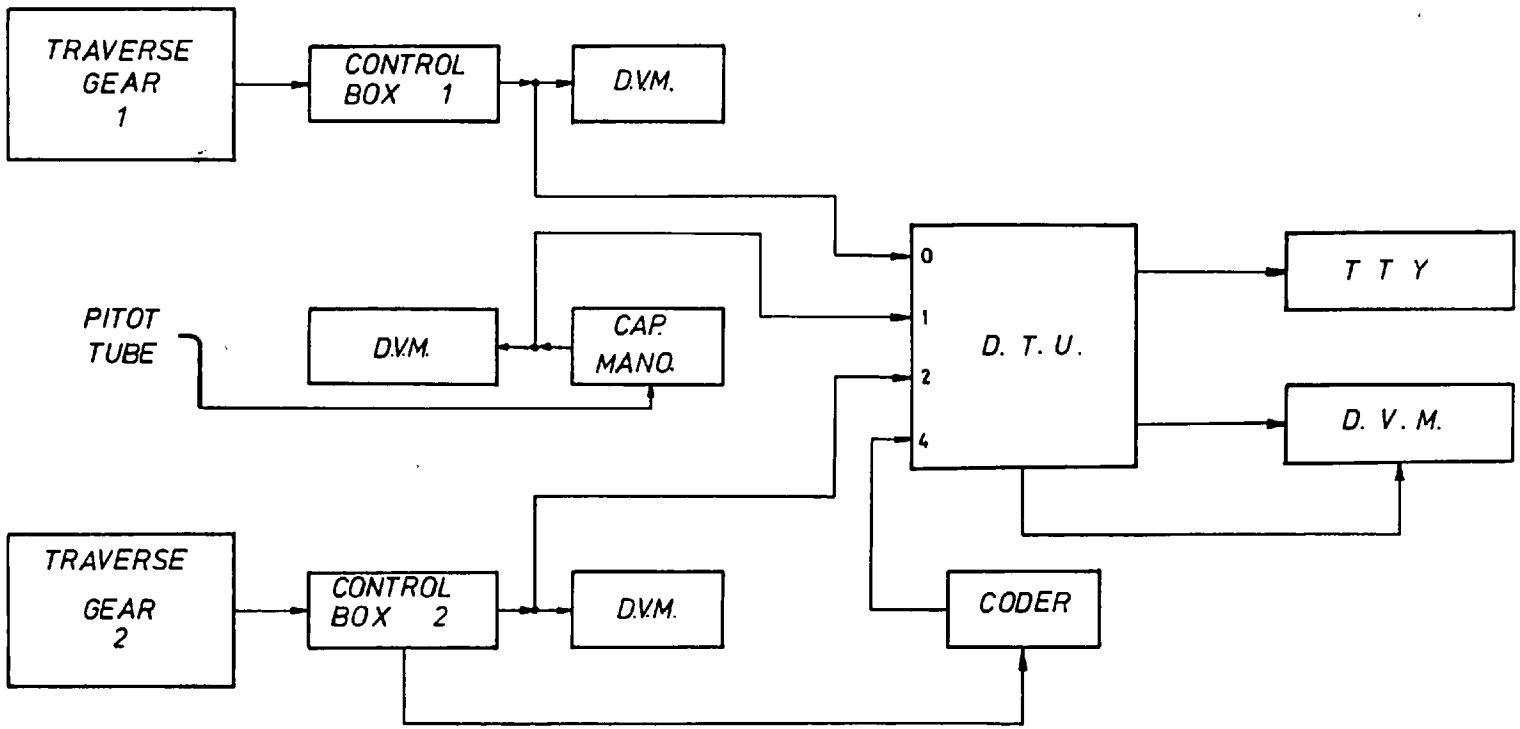

FIG.(2.5) BLOCK DIAGRAM OF THE DATA LOGGING SET-UP

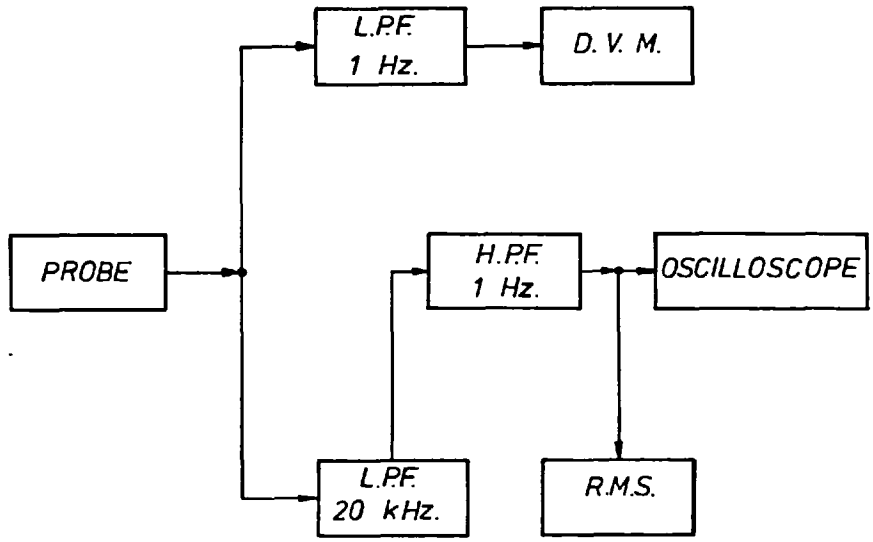

FIG.(2.6) a: BLOCK DIAGRAM OF THE U-WIRE SET-UP

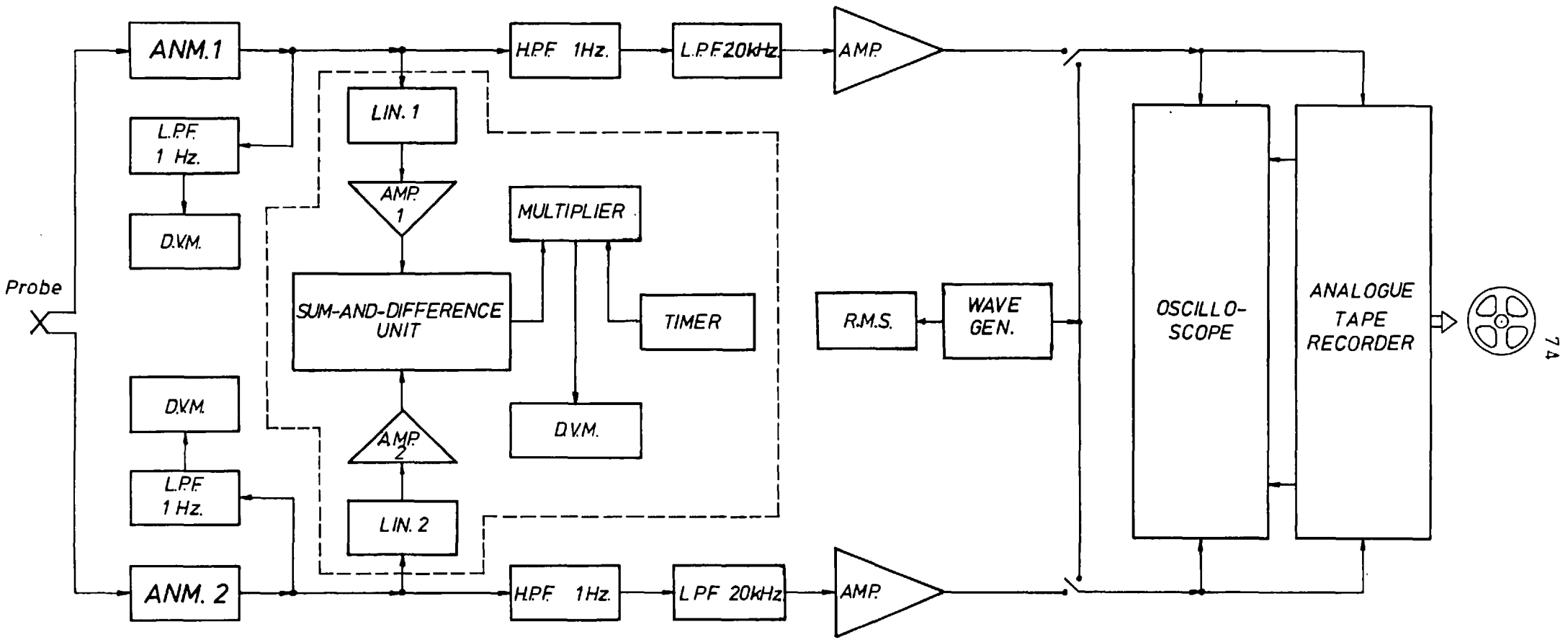

FIG.(2.6) b: BLOCK DIAGRAM OF THE X-WIRE SET-UP

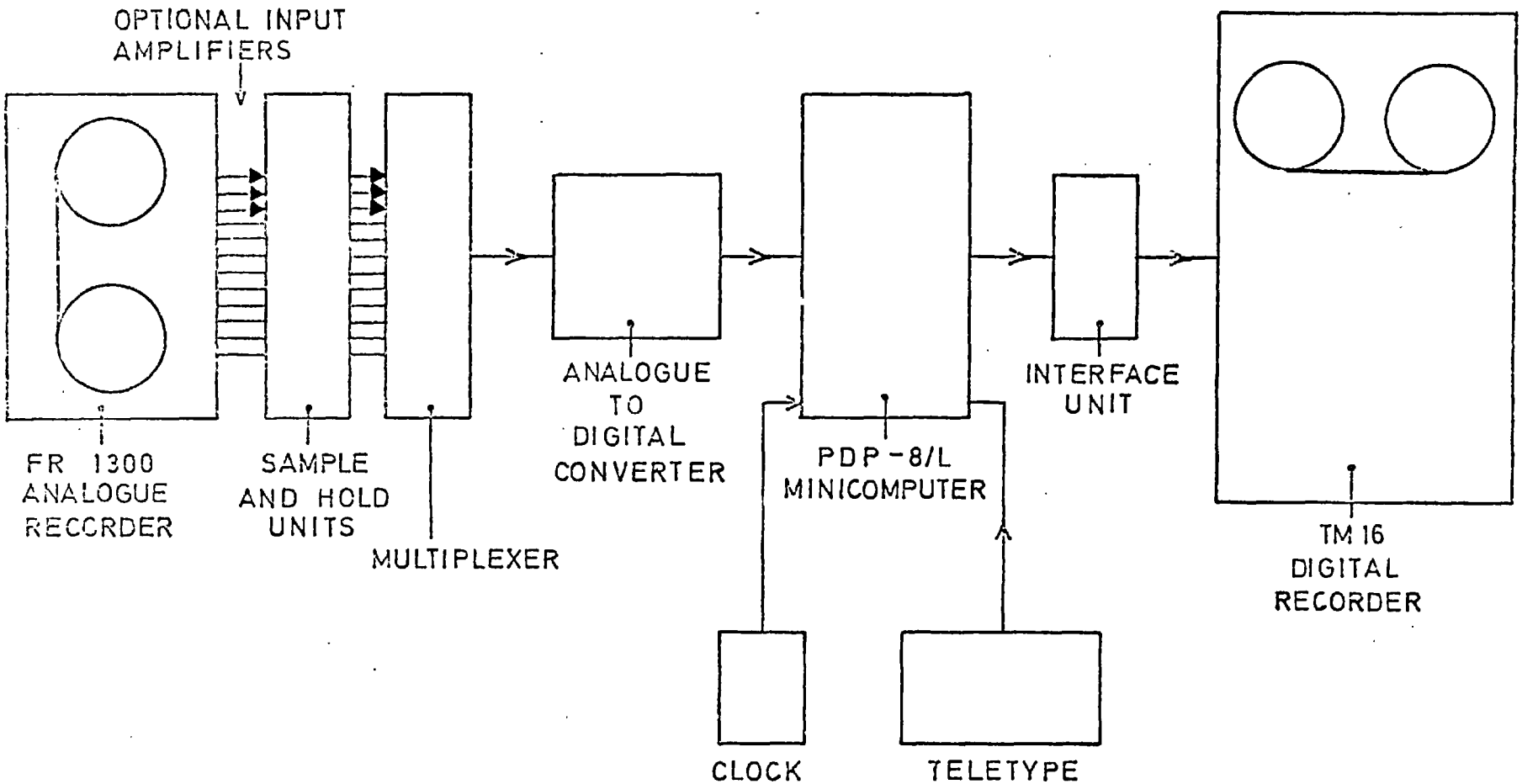

FIG.(2.7) Block diagram of A-D system (hardware).

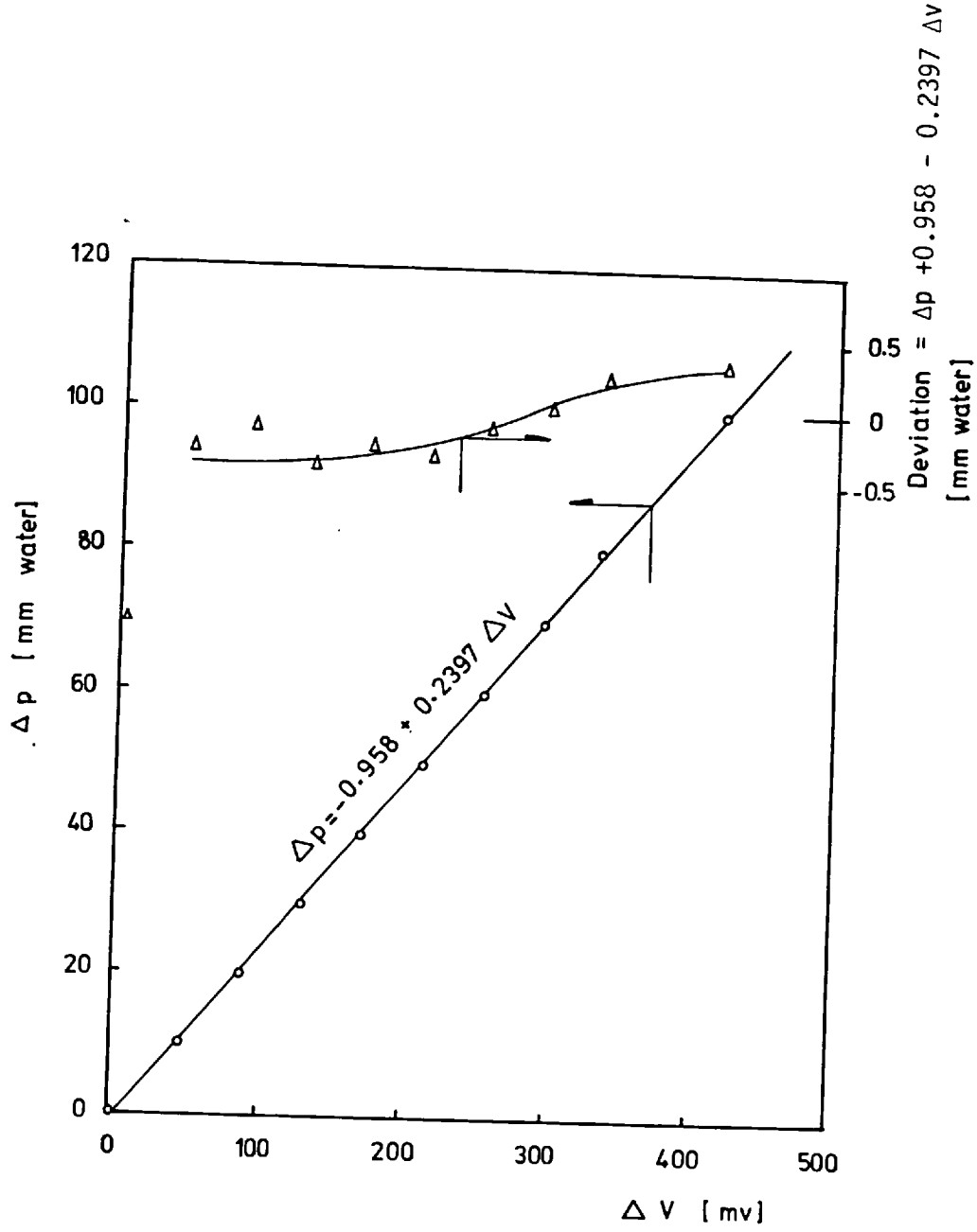

FIG.(2.8) TYPICAL CALIBRATION OF
CAPACITOR MICROMANOMETER

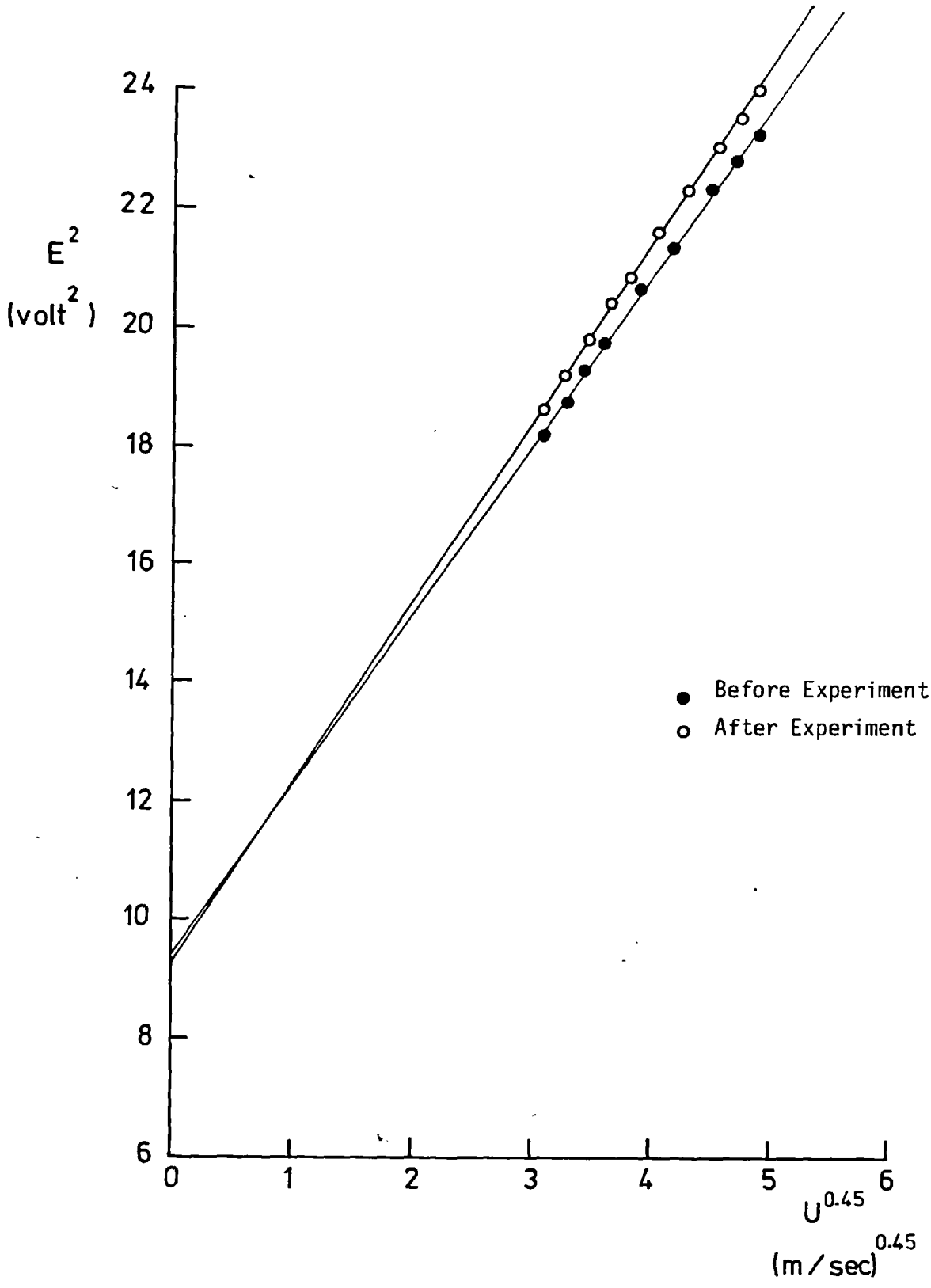

FIG.(2.9) TYPICAL U-WIRE CALIBRATION

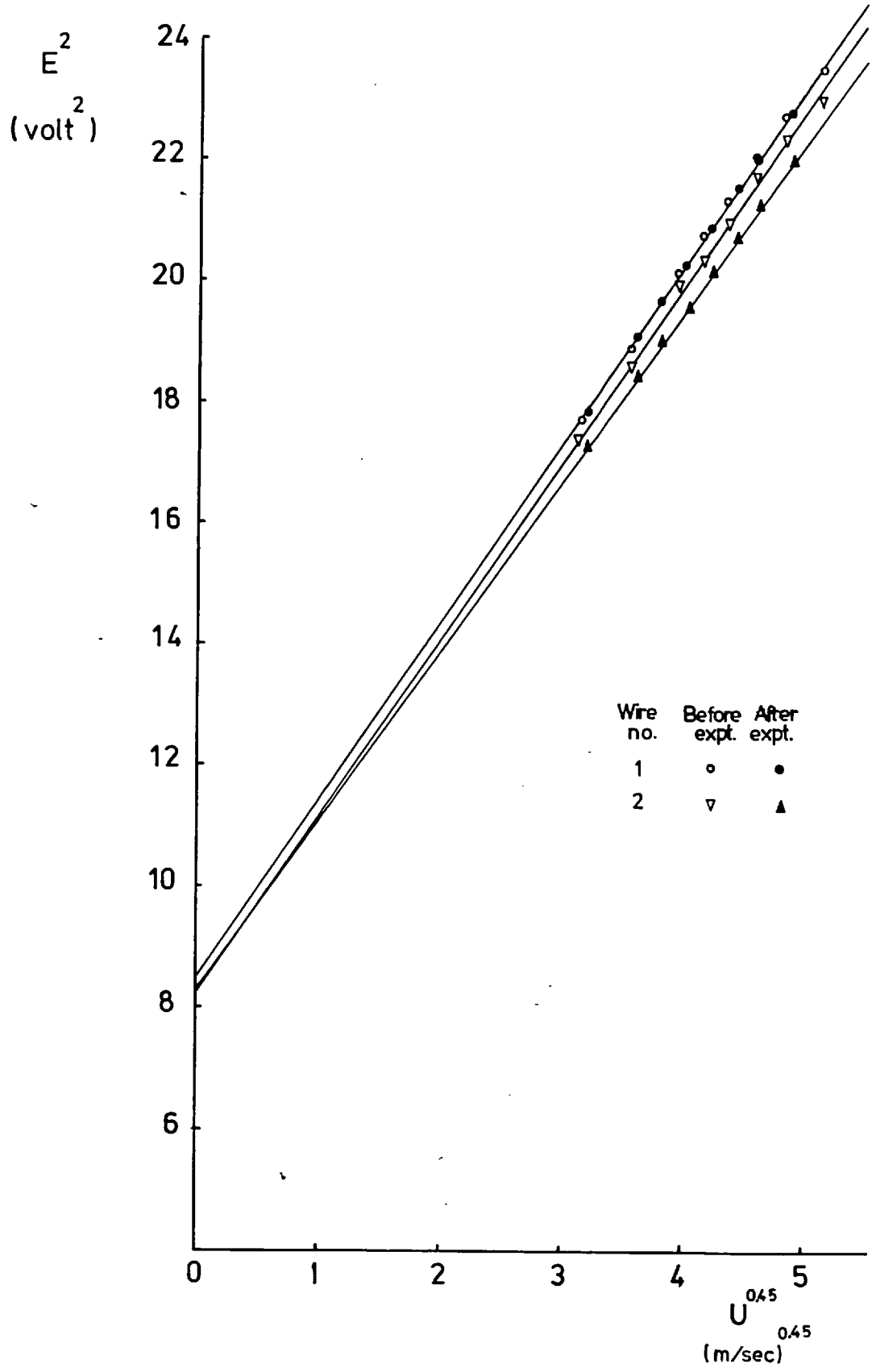

FIG.(2.10) TYPICAL CROSS-WIRE VELOCITY CALIBRATION

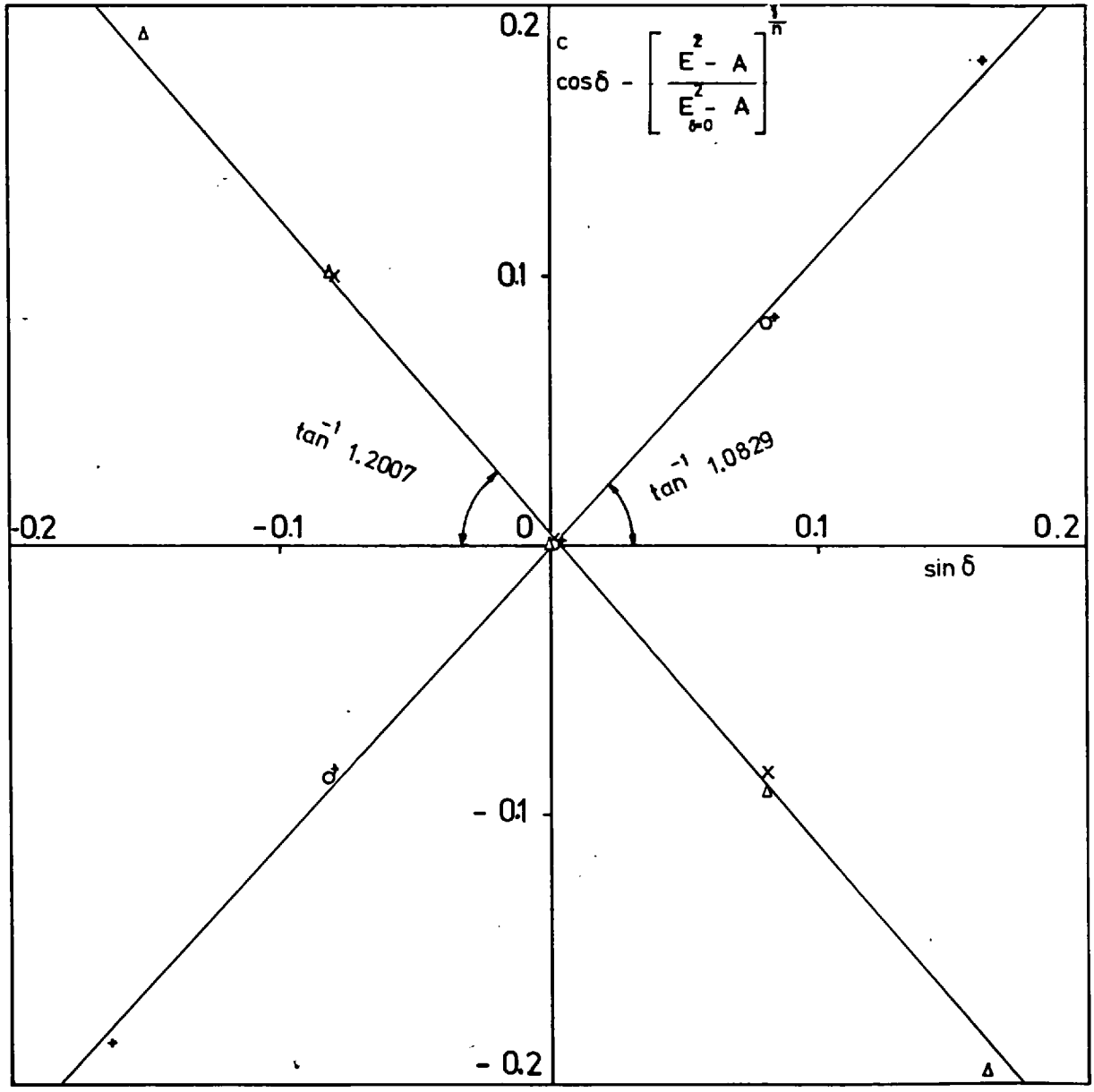

FIG.(2.11) TYPICAL CROSS-WIRE YAW CALIBRATION

CHAPTER 3

EXPERIMENTAL RESULTS

The main experimental results are presented and discussed in this chapter together with some comparisons between measurements obtained by different instruments. Further detailed discussions are given in the following chapter, which also deals with higher order quantities derived from the measurements.

3.1 Flow Visualization Results

Photographs of the surface flow pattern on the tunnel floor obtained by the oil flow visualization technique described in Subsection 2.2.7 are shown in Figs. (3.1a) - (3.1c). Fig. (3.1a) shows the flow pattern just upstream of the leading edge in the area shown in Fig. (2.2) bounded with a dotted line. It should be noted, as indicated by the trapezoid dotted boundary of Fig. (2.2), that the view in Fig. (3.1a) is distorted as a result of setting the camera at approximately 45^{o} to the tunnel floor. Putting the camera at this position resulted also in the blank strip at the downstream end of the figure. This blank strip, in fact, shows the downstream edge of the first working section floor. The flow pattern in the leading half of the corner up to 73 cm from the wing leading edge is shown in Fig. (3.1b); and Fig. (3.1c) shows the rear part from $x \cong 63$ cm to $x \cong 135$ cm.

It is clear from Fig. (3.1a) that a nodal point of separation occurs at about 13 mm upstream of the leading edge. A curved separation line is also clear, along which the "body" boundary layer separates from the surface and rolls up to form a strong horseshoe vortex which wraps around the nose due to the skew of the mean flow there (secondary flow of the "first kind"; see Section 1.1). Once formed, the horseshoe

vortex continues to stretch in the axial direction as the flow accelerates round the wing leading edge, forming two legs, each extending along one of the wing sides. This mechanism of horseshoe vortex formation has been postulated and demonstrated by many previous investigators, e.g. Stanbrook (1957), East and Hoxey (1968), Sepri (1973) and Chu and Young (1975). Figs. (3.1b) and (3.1c) show clearly the diffusive effects of Reynolds stresses on the vortex. In the case of all real wing-body corners, Reynolds stresses act to reduce skew-induced secondary flows all the way to the trailing edge, rather than generating secondary flows of the second kind as found in developed flow along streamwise corners, reported by many workers, e.g. Brundrett and Baines (1964), Perkins (1970), Mojola (1972), among others: the latter type of flow would eventually occur in a long wing-body junction flow but only at very large distances downstream.

Oil-flow visualization was carried out also in the corner of a thin wing (6.4 mm thick) but the results, which were not photographed, showed nothing of interest. The mean flow skew being very small, no appreciable horseshoe vortex was produced.

3.2 Distribution of Experimental Points

The number and distribution of experimental points over the measurement domain varied from one axial station to the other and also according to the measuring instrument. Generally, more points were taken in areas of high gradient close to walls and smaller numbers of measurements were taken when the gradients, as monitored at the time of experiment, were small. The number of points depended also on the measuring instrument's spatial resolution and on the time needed for taking a reading, and the associated effect on calibration drift and change in flow conditions (temperature and pressure). The relatively

large number of observations made by the Pitot tube and single hot wire probe helped in roughly determining suitable locations of the smaller number of measurements made by the cross-wire probe, these being the most time-consuming and the most sensitive to calibration drift.

Surface static pressure was measured at the first five upstream stations (station - 5 to - 1) and at all the nine stations (1 to 9) in the corner region. Pitot tube traverses were performed at stations 1 to 5 and stations 7 and 9. Stations 1, 2, 3, 5, 7 and 9 and the first upstream station (- 1) were traversed using the single hot wire, while the cross-wire was used to probe the flow at stations 2, 5 and 9 only. The location of planes of measurements relative to the wing leading edge is set out in Table (3.1). The cross-wire measurement points at a given station were actually 30.5 mm ahead, and the single wire points 20 mm ahead of the Pitot tube tip position. The discrepancies in this slowly-changing flow are negligible for most purposes.

3.3 Presentation of Results

Two forms of presentation are believed to be suitable for showing clearly the behaviour of a three-dimensional flow parameter in the plane of measurements. The first is an isometric plot in which the quantity is plotted vertically against the two coordinates in the plane of measurements (e.g. Fig. (3.5)), and the second is a contour map for the variable in the measurement planes (e.g. Fig. (3.13)). Both methods have been used in presenting most of the results. Generally, the reader who needs only a qualitative picture is better served by contour plots, while the isometric views are more convenient for reading off quantitative values. The less intelligible isometric plots have been relegated to the Appendices. Due to the great amount of data to be displayed, the plotting facilities of the Imperial College Computer

Centre were utilized for producing most figures.

For isometric plotting of data, the program "PLT3D" was written by the author. PLT3D produces plots which comprise only the experimental points and leaves the connecting curves to be traced later by hand. The quantity measured is plotted vertically, while the distances from the body and wing surfaces (y and z respectively) are represented in the horizontal and the inclined (depth) directions respectively. In the case of C_p and C_f only, the horizontal and depth directions represent z and x (the streamwise distance) respectively. To minimize interference on the plots, only the data of y-(spanwise) traverses were plotted. The z-traverse data were used for checking the y-traverses and, as a rule, are not presented in the thesis. However, few cross-planes are produced from the y-traverses and traced on the graphs to give a three-dimensional impression. The true axes are left unlabelled in the figures, for less interference. Three labelled exploded axes are then added to each figure. As indicated by the small arrows in the figures, the latter system of axes is moved away from the plots; the vertical ( ) and the inclined (z) axes are moved in the true y-axis direction and the y-axis itself is moved in the z-axis direction. The true origin of the figure is marked with a black blob. In spite of the complication associated with each figure, accurate reading from the graphs is made easy by means of the transparent reading sheet supplied with each copy of the thesis. Locating any of the node points on the line OO_1 of this sheet at the origin of a certain traverse with the appropriate inclined line aa' (or any of its parallels) on top of the true z-axis isolates the desired curve from the rest of the plot so that accurate reading from it is possible. In Fig. (3.6), it was necessary to replot some of the traverses on a set of shifted axes as their curves are over-written

by each other. In this case, the shifted axes plot was added as an inset to one corner of the figure.

Contour maps were also, in most cases, produced on the College Computer plotter using the "CONTPLT" program written by the author. The program has some weak points compared to manual plotting. "CONTPLT" program uses the standard routine "ARKIST" to fit smooth curves between linearly interpolated points of equal values. This routine, which tried to pass the best smooth curve through most of the points, produced some non-realistic wiggles near the end of the contours (at large z or y); at low gradients (small $\partial/\partial z$ or ∂y), the interpolated location is subjected to higher error. For the same reasons, the routine produced some intersections between contours of different values in a very few number of maps. These intersections were removed by hand. It is, thus, not advisable to try to read accurate values from the contour plots, but only to use them as descriptive maps. Also, it was necessary, in some cases, to relabel some contours by hand when the computer-generated labels were overwritten or unclear.

The system of cartesian coordinates used is shown in the corner of Fig. (3.2). The streamwise distance x is measured in the main flow direction starting from the wing leading edge. The distance y is measured from the tunnel floor vertically upwards. z is measured from the dividing streamline, but half the thickness of the "wing" has been subtracted from all z ordinates, at all the stations downstream of the leading edge, so that the z = 0 line in the main part of Fig. (3.2) is actually the bold line in the inset. As far as possible, the fact that the wing span was vertical, contrary to normal aeronautical practice, is concealed from the reader in the presentation below.

3.4 Wall Static Pressure

Wall static pressure is represented by the static pressure coefficient C_p, defined as:-

$$C_p = \frac{p - p_{ref}}{\frac{1}{2}\rho U^2_{ref}} \tag{3.1}$$

where: p = static pressure

p_{ref} = reference static pressure, taken equal to atmospheric pressure (i.e. pressure at trailing edge)

$\frac{1}{2}\rho U^2_{ref}$ = tunnel reference dynamic pressure at inlet to the working section, where $C_p = 0.355$

and is presented in Figs. (3.2 - 3.4). Fig. (3.2) gives $C_p = f(x, z)$ in an isometric form and Fig. (3.3) as a contour map. In Fig. (3.4), three curves are displayed: (i) the variation of C_p with the streamwise distance, x, along the tunnel centreline; (ii) the variation in C_p with x close to the corner line ($z \simeq 2$ mm), and, (iii) the inviscid-flow calculated C_p on the wing. The latter was computed by applying the A. M. O. Smith method of calculation using the "AMOS" program (see Mahgoub, 1978); "off-body" points upstream of the leading edge were not computed.

Far upstream of the wing leading edge ($x < -37$ cm), the static pressure decreases at a constant rate due to the boundary layer growth on the tunnel walls and the resulting acceleration of the potential core. As the flow approaches the leading edge, the static pressure rises markedly (to $C_p \simeq 0.4$) due to the rapid deceleration as the flow gets closer to the stagnation saddle point. The flow then accelerates around the curved sides of the wing nose and, accordingly,

the pressure drops sharply below the reference value, (p_{ref}), close to the wing where C_p drops to - 0.06. Static pressure recovers back downstream of the leading edge reaching its maximum at x ≃ 50 cm. Beyond this point, the static pressure starts to fall again, at a constant rate, as a result of the boundary layers' growth. This latter rate of decrease in C_p is higher than the upstream rate of decrease because of the additional boundary layers growing on the wing surfaces. Fig. (3.4) also shows a generally good agreement between C_p measured close to the wing surface and the calculated values based on the potential flow assumptions. The difference between the two is attributable to the effect of the displacement thickness on the wing surfaces which was not included in the calculation.

3.5 Mean Flow Velocities

3.5.1 Main Streamwise Velocity Component (U)

The average streamwise flow velocity U was measured in the corner region of the "wing-body" junction from the wing leading to the trailing edge. A few measurements were also performed in the flow upstream of the corner. Measurements were made mainly using the Pitot tube, and the U component was also produced as a by-product of single and cross-wire measurements. Pitot tube data were reduced using the two programs "VELPROF" (de Brederode, 1973) for reduction of paper tape data, obtained from stations 1, 2, 3, 4, 5 and 7, and "VELPRF1" for punched card data from station 9. The standard "VELPROF" program uses the data taken in the free stream in evaluating U_e, the free stream axial component of velocity, and does not store them as points on the velocity profile. Pitot tube velocity profiles were, thus, extended asymptotically in the free stream after consulting the hot wire data

of the same profiles.

Velocity profiles are shown in Figs. (3.5 - 3.12) followed by manually produced contour maps in Figs. (3.13 - 3.19). All these figures, except Fig. (3.5), present the results of the Pitot tube measurements. The only hot wire data displayed in Fig. (3.5) are the measurements at the first upstream station (station - 1) where no Pitot measurements were made. At other stations, where both measurements were available, the different instruments' data were compared against each other. Agreement between the measurements of the Pitot tube and the hot-wire data is excellent, except very close to the wing surface where the hot wire reads higher by up to 0.05 U_e.

It is clear from Figs. (3.6 - 3.12) that the velocity profiles in the corner of the wing-body junction are distorted with comparison to the two-dimensional boundary layer velocity profile. The bulges in the velocity profiles are, in fact, a result of the streamwise vortex generated at the wing leading edge and embedded in the body boundary layer. Velocity profile bulges are familiar features in flows that comprise strong vortical motion; velocity profile distortion has been reported to exist in the corners of rectangular ducts where the anisotropy in Reynolds stress components in the normal plane create a double vortex pattern in the corner (e.g. Brundrett and Baines, 1964; Perkins, 1970 and Mojola, 1972). The small undulations that appear in Fig. (3.5) in the crosswise profiles (i.e. U/U_e vs. z) at the first upstream station are probably due to the tunnel screens. The existence of an embedded vortex in the corner region of the wing-body junction is evidently indicated by the shapes the isovels (contours of constant U/U_e) take as shown in Figs. (3.13 - 3.19). Looking in the downstream direction into any of these figures, one can infer the anticlockwise rotary motion of secondary flow currents (V and W components of mean

velocity) in the corner region. Near the wing, the vortex secondary flow is moving towards the corner line, carrying the outer-layer fluid of the body boundary layer and reducing the thickness of the body boundary layer there. Far from the wing, the other side of the vortex is moving upwards, pushing fluid from the body boundary layer outwards and thickening it. At further distances from the wing outside the vortex, the body boundary layer relaxes back to its asymptotic two-dimensional thickness and the isovels become parallel to the body surface. The development in the vortex strength and the rate of its growth (increase in diameter) can also be detected from the degree of its effect and the extent of the region over which both velocity profiles and contours are affected by its existence. Figs. (3.6 - 3.19) show an increase in the degree of distortion of the profiles and contours from the two-dimensional case up to a maximum at $x \simeq 33$ cm and a reduction in the severity of distortion with further streamwise distance. Hence, an increase in the strength of the vortex formed at the "wing" leading edge is believed to occur up to $x \simeq 33$ cm followed by attenuation in the strength with further downstream distance. The region of flow affected by the vortex expands from up to $z \simeq 20$ mm at station 1 ($x \simeq 3.5$ cm) to $z \simeq 50$ mm at station 9 ($x \simeq 125$ cm).

3.5.2 Secondary Flows (V and W)

The mean secondary velocity components V and W were deduced from the cross-wire measurements in the normal planes at stations 2, 5 and 9; $x = 15.66$, 61.38 and 122.34 cm respectively. Figs. (3.20) - (3.22) show the resultant secondary velocity, $V_s = \sqrt{V^2 + W^2}$, plotted as vectors emerging from the corresponding points of measurements in the y-z planes at these stations respectively. The length of each

vector is proportional to V_s and is inclined at $\tan^{-1}$ (W/V) to the z-axis.

Secondary flow vectors show clearly the existence of an anti-clockwise vortical motion as postulated previously from the U-velocity profiles and contours. Fig. (3.20) shows how strong the vortex is at about 15.7 cm from the leading edge, where it is originally formed as a horseshoe vortex. A slightly weaker vorticity is indicated in Fig. (3.21) of station 5 ($x \simeq 61.4$ cm). Further downstream, at station 9 ($x \simeq 122.3$ cm), the shorter secondary flow vectors indicate a much weaker vortex there. This attenuation of the vortex strength with streamwise distance, which agrees with both the flow visualization observation and velocity profiles and contours, supports the argument that, unlike the flow in corners of rectangular ducts and open channels, the Reynolds stresses act to <u>diffuse</u> the skew induced secondary flow rather than <u>create</u> secondary flows of the second kind.

The estimated location of the vortex centre is indicated in each of Figs. (3.20 - 3.22). As the vortex moves downstream in the growing "boundary region" along the corner, its centre moves slightly away from the walls. The location of the centre relative to the wing surface increases from $\sim$ 19 mm at $x \simeq 15.7$ cm to $\sim$ 21.5 mm at $x \simeq 61.4$ cm and finally to $\sim$ 24.5 mm at $x \simeq 122.3$ cm, while its distance from the body surface varies from 13 mm to 17 mm at $x \simeq 15.7$ cm and $\sim$ 61.7 cm respectively, but it then gets closer to the body surface at $x \simeq 122.3$ cm where it lies approximately at $y = 15$ mm.

3.6 Skin Friction

Preston tube measurements of the wall shear stress are given in Figs. (3.23 - 3.25) in three different forms. In the isometric plot of Fig. (3.23), the wing is rotated 90° so that the two surfaces of the body and the wing lie in the same horizontal plane of the figure.

Fig. (3.24) shows the contours of constant values of wall shear stress and Fig. (3.25) is given for accurate reading of C_f, because the x-axis in Fig. (3.22) is inclined at a different angle from the supplied reading sheet. The measurements are presented as variation in the coefficient of wall shear stress C_f, defined as:-

$$C_f = \frac{\tau_w}{\frac{1}{2}\rho U_e^2} \tag{3.2}$$

where: τ_w = shear stress at the wall

$\frac{1}{2}\rho U_e^2$ = the local dynamic pressure in the free stream.

Figs. (3.23 - 3.25) show that C_f rises suddenly (from the upstream value of 0.0027 which is not shown in the figures) to a value of 0.007 very near to the wing leading edge at station 1. A general trend is evident at all the streamwise stations: approaching the corner line normally along any of the two walls, the wing or the body, C_f rises from its asymptotic value far from the corner to a maximum. This rise is then followed by a rapid fall on both walls in the close vicinity of the corner. Proceeding downstream, the peak value of C_f drops from 0.007 at station 1 on the body surface and from 0.0043 at station 2 on the wing to about 0.0029 on the "wing" and 0.0025 on the "body" at the last downstream station (no. 9). The location of the peak moves away from the corner with increasing streamwise distance: on the body, from z = 4 mm at station 1 to z ≃ 18 mm at station 9 and on the wing from y ≃ 15 mm at station 2 to y ≃ 28 at station 9. The change of the z and y ordinates of the peaks of C_f from one station to another is an indication of the movement of the vortex relative to the corner walls with the downstream distance, while the drop in the

peak value is itself an indication of the attenuation in the vortex strength.

Figs. (3.23 and 3.25) show that C_f asymptotes to about 0.0029 on the wing and to a slightly lower value of 0.0025 on the body at all the stations starting from the third. At station 2, the "asymptotic" values are 0.00275 on the "body" and 0.00383 on the "wing". These two last values were tested against Coles' values and the result is as follows: $R_\theta \approx 1858$ and 5450 on the wing and the body respectively; correspondingly, Coles' chart (Fig. 11, Page 43 of Coles and Hirst, 1968, Part II) gives 0.00384 and 0.00291 for C_f. The ratio between the two values obtained in the present work is 1.39 and 1.32 with C_f from Coles' chart, compared to 1.33 ratio between $R_\theta^{-1/4}$ on the wing and the body. The disagreement between Coles' results in zero-pressure gradient and the present results at station 2, is probably due to the relatively high streamwise adverse pressure gradient at station 2 (see Fig. (3.2)). Moreover, the flow over the wing is subjected to a different pressure gradient from that on the flow away from the wing.

3.7 The Reynolds Stresses

All of the six components of the Reynolds stress tensor $(\overline{u_i u_j})$* were measured at the second, fifth and the ninth downstream stations using the cross-wire. The axial turbulence intensity $\overline{u^2}$ was measured in more detail using the single hot wire at stations - 1, 1, 2, 3, 5, 7 and 9. The results of all the measurements are displayed in Figs. (3.26 - 3.75). Plotted values are always normalized by U_e^2, where U_e is the local free stream value of U.

---

* Strictly speaking, the Reynolds stress tensor is $-\rho\,\overline{u_i u_j}$, but for an incompressible flow, it is a convention to omit the (constant) density, ρ.

(a) Normal Stresses ($\overline{u^2}$, $\overline{v^2}$, $\overline{w^2}$)

Single wire measurements of $\overline{u^2}$ at stations -1, 1, 2, 3, 5, 7 and 9 are shown in Figs. (3.26 - 3.32) in an isometric form and are presented in Figs. (3.33 - 3.39) as contour maps. Comparing the single wire results at stations 2, 5 and 9 with those obtained by the cross-wire at the same stations (cross-wire data are not displayed here) showed a very good agreement between the two instruments except in the close vicinity of the corner walls.

The measurements of $\overline{v^2}$ and $\overline{w^2}$ obtained by the cross-wire at stations 2, 5 and 9 are presented in Figs. (3.40 - 3.45) and Figs. (3.46 - 3.51) respectively. Again here, it should be noticed that the wiggles in the contours at large distances, z, from the wing are not realistic and are produced by the Computer plotting routine as mentioned before in Section 3.3. The general trend of variation in the three components, as can be seen from the isometric plots, is similar. Away from the wing, the turbulent intensities decrease with distance from the body. The rate of their decrease reduces with distance from the body surface, then increases again to drop the intensity to zero in the free stream. $\overline{v^2}$ and $\overline{w^2}$ have plateaus of constant values at a small distance from the body which extend up to near the edge of the body boundary layer. Generally speaking, the profiles of $\overline{u^2}$, $\overline{v^2}$, $\overline{w^2}$ far from the wing are almost similar to those obtained in a two-dimensional boundary layer. Near the wing, the profiles are much distorted from the two-dimensional one: the profiles comprise troughs close to the body surface and peaks at a distance from the surface. The form that the contours of $\overline{u^2}$, $\overline{v^2}$ and $\overline{w^2}$ take in the corner as shown in the figures, again indicate the existence of the anticlockwise vortex in the corner region. Close to the wing, the vortex is pulling the outer part of the body boundary layer, in which

it is embedded, bringing down low turbulent energy air. At a distance from the wing, the opposite occurs; layers of higher turbulent energy are carried away from the body surface. The effect of the vortex motion in the corner on the profiles and contours of the fluctuating components is larger than on the mean velocity. This larger effect on turbulent quantities was noticed by other workers when studying the flow in corners of ducts and between two flat plates at 90^{o}. Mojola (1972) has explained this to be a result of the higher ability of secondary flow to act upon turbulent velocities of their own order of magnitude, compared to their ability to affect the higher order mean components. In fact, it should be taken into account that the effect is squared since $\overline{u^2}$, ... etc. are considered rather than $\sqrt{\overline{u^2}}$, ... etc.

Examining the values that both $\overline{v^2}$ and $\overline{w^2}$ have in the corner region (e.g. in Figs. (3.40 and 3.46)), one finds that $\overline{v^2}$ is always slightly lower than $\overline{w^2}$, close to the body surface at large distances from the wing. On the other hand, near the wing surface and away from the body, $\overline{v^2}$ has higher values compared to $\overline{w^2}$. Hence, in the zones close to one of the corner walls and away from the other, the turbulent intensity normal to the first wall is always smaller than that normal to the second wall. The proximity of a wall, of course, tends to reduce the velocity normal to it. In a two-dimensional boundary layer flowing at zero pressure gradient, $\overline{w^2} \simeq 2.2\ \overline{v^2}$ close to the surface (v being normal to the surface). Examining the relative values of $\overline{w^2}$ and $\overline{v^2}$ in the present wing-body junction, say at large distances from the wing and close to the body, we find that the ratio $\overline{w^2}/\overline{v^2}$ is only ~ 1.2 at station 2 near the leading edge, but this ratio rises with downstream distance to about 2.0. This indicates that, when strong, the streamwise vortex embedded in the body boundary layer is stirring the flow in the boundary layer, pushing it towards isotropy. This

thought may be emphasized when examining Fig. (3.28) for $\overline{u^2}$ at station 2. The figure shows that away from the wing, $\overline{u^2}$ drops very quickly, with y, to reach a comparable value to $\overline{v^2}$ and $\overline{w^2}$ at a small distance from the body (y ≃ 4 mm). Far downstream at station 9, the vortex is weaker than upstream and is no more able to stir the flow in the much thicker boundary region.

The turbulent kinetic energy represented by $\overline{q^2} = \overline{u^2} + \overline{v^2} + \overline{w^2}$, (which is, in fact, twice the turbulent kinetic energy per unit mass), is plotted in Figs. (3.52 - 3.54) and in a contour form in Figs. (3.55 - 3.57).

(b) Turbulent Shear Stresses ($-\overline{uv}$, $-\overline{uw}$, $-\overline{vw}$)

Figs. (3.58 - 3.66) present isometric plots of the shear stress components $-\overline{uv}$, $-\overline{uw}$, $-\overline{vw}$ measured by the cross-wire at stations 2, 5 and 9. Contour maps of them are shown in Figs. (3.67) - (3.75). Secondary flows associated with the vortex reduce the body shear stress components $-\overline{uv}$ and $-\overline{vw}$ at the corner to the extent that they create zones of negative shear (i.e. positive $\overline{uv}$ and $\overline{vw}$) near the wing. The areas of negative "body" main shear stress ($-\overline{uv}$) shrinks as the flow moves from station 2 to 5 (from x = 15.7 to 61.4 cm), but gets wider again at further distances downstream (at station 9, x = 122.3 cm). As seen in Fig. (3.68), a zone of positive ($-\overline{uv}$) separates the negative areas from the wing surface at station 5, while Fig. (3.69) shows a wide area of negative "body" main shear near the wing surface. As a check, $-\overline{uv}$ was computed from the measurements of the cross-wire in the ± 45° inclined positions, made mainly to measure $-\overline{vw}$. The result was a qualitative agreement on the distribution of positive and negative areas of ($-\overline{uv}$) in the corner region of stations 2, 5 and 9. Figs. (3.67 - 3.69) show that the average slope of the ($\overline{uv} = 0$)

contour, in the z-y plane, decreases from $\sim 70^{o}$ at station 2 to $\sim 60^{o}$ at station 5 and then to $\sim 40^{o}$ at station 9. For the contour $\overline{vw} = 0$, Figs. (3.73 - 3.75) show a change in the angle from $\sim 45^{o}$ to $\sim 35^{o}$ and finally to $\sim 20^{o}$. Closed areas of negative ($-\overline{uw}$) component, the "wing" main shear stress component, are found near the body surface in Figs. (3.70 - 3.72). The negative ($-\overline{uw}$) zone moves away from the wing with the downstream distance, with its approximate centre changing location from $z \simeq 20$ mm, $y \simeq 10$ mm at station 2 to (~ 30, ~ 9) at station 5, and to (~ 40, ~ 5) at station 9. It is clear from Figs. (3.58) - (3.66) that the secondary shear stress component ($-\overline{vw}$) is generally very small compared to the corresponding main components ($-\overline{uv}$) and ($-\overline{uw}$).

The skin friction velocity (u_τ) was calculated from the Preston tube measurements of Figs. (3.23 - 3.25) on both walls of the corner at stations 2, 5 and 9. u_τ^2 found from the measurements on the body was plotted, as chain-dotted lines, on the plane $y = 0$ in Figs. (ɔ.58 - ɔ.60) and similarly the values of u_τ^2 on the wing were added to Figs. (ɔ.61 - ɔ.63) on the plane $z = 0$. Figs. (ɔ.58 - ɔ.63) show that the cross-wire measurements of the body main shear stress ($-\overline{uv}$) and the wing main shear stress ($-\overline{uw}$) asymptote reasonably well to the Preston tube data on the body and wing surfaces except near the corner at station 2. We will return again to this point in the following chapter when discussing the existence of a log-law region in the corner flow.

TABLE 3.1

AXIAL POSITIONS OF MEASUREMENT STATIONS

(Distances are measured in mms relative to the wing leading edge)

Station No.	Disc centre and static pressure tappings	Pitot tube measurement planes	Preston tube measurement planes	Single wire (U-wire) measurement planes	Cross-wire (X-wire) measurement planes
- 9	- 1,295.4				
- 8	- 1,143.0				
- 7	- 990.6		- 1,043.6		
- 6	- 838.2				
- 5	- 685.8		- 738.8		
- 4	- 533.4		- 586.0		
- 3	- 381.0		- 434.0		
- 2	- 228.6		- 281.6		
- 1	- 76.2		- 129.2	- 137.2	
1	76.2	34.66	23.2	15.2	
2	228.6	187.06	175.6	167.6	156.6
3	381.0	339.46	328.0	320.0	
4	533.4	491.86	480.4		
5	685.8	644.26	632.8	624.8	613.8
6	838.2				
7	990.6	949.06	937.6	929.6	
8	1,143.0				
9	1,295.4	1,253.86	1,242.4	1,234.3	1,223.4

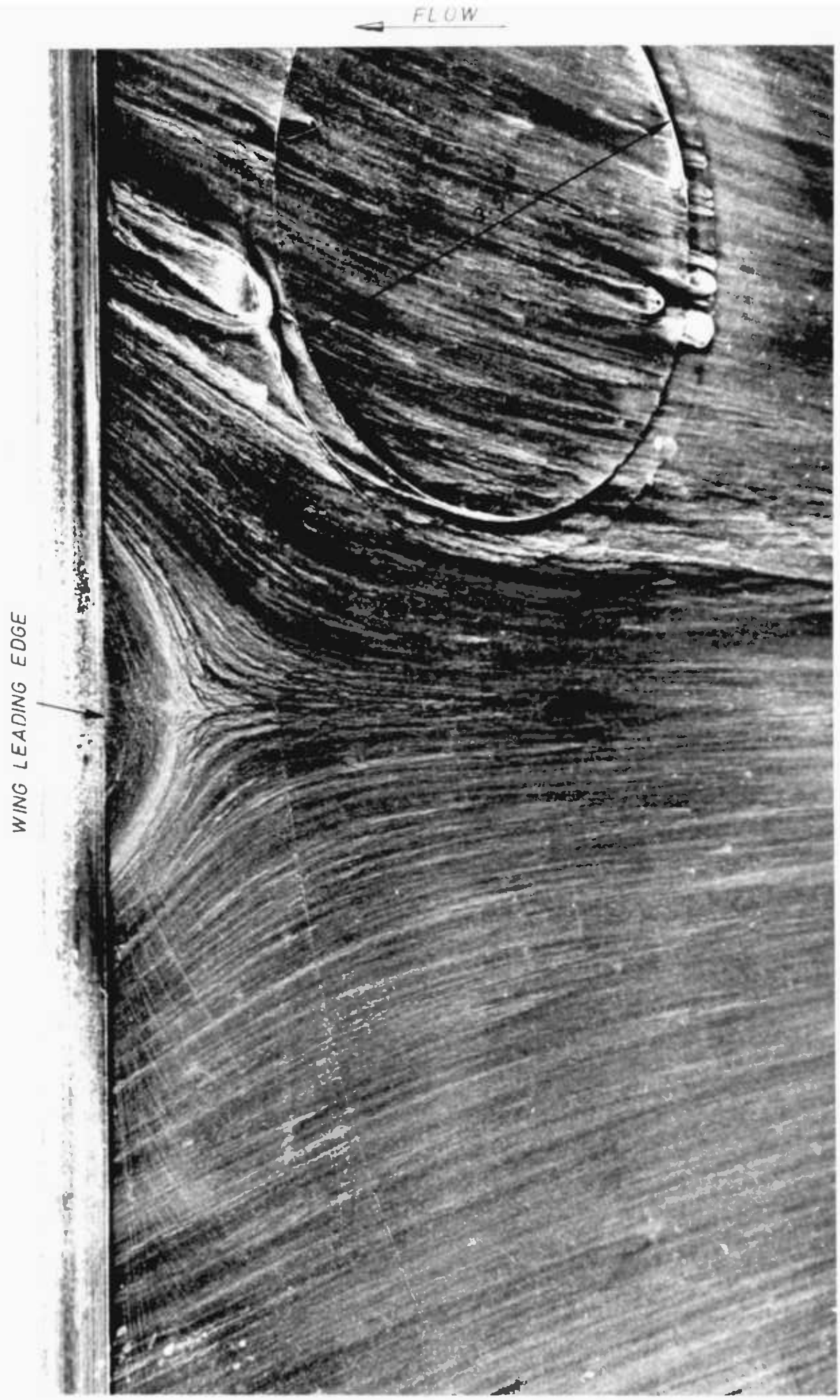

FIG. (3.1) OIL-FILM FLOW VISUALIZATION PATTERN

A SURFACE STREAMLINES NEAR THE WING LEADING EDGE

(Leading Edge just outside picture to the left, Camera looking upstream at 45°)

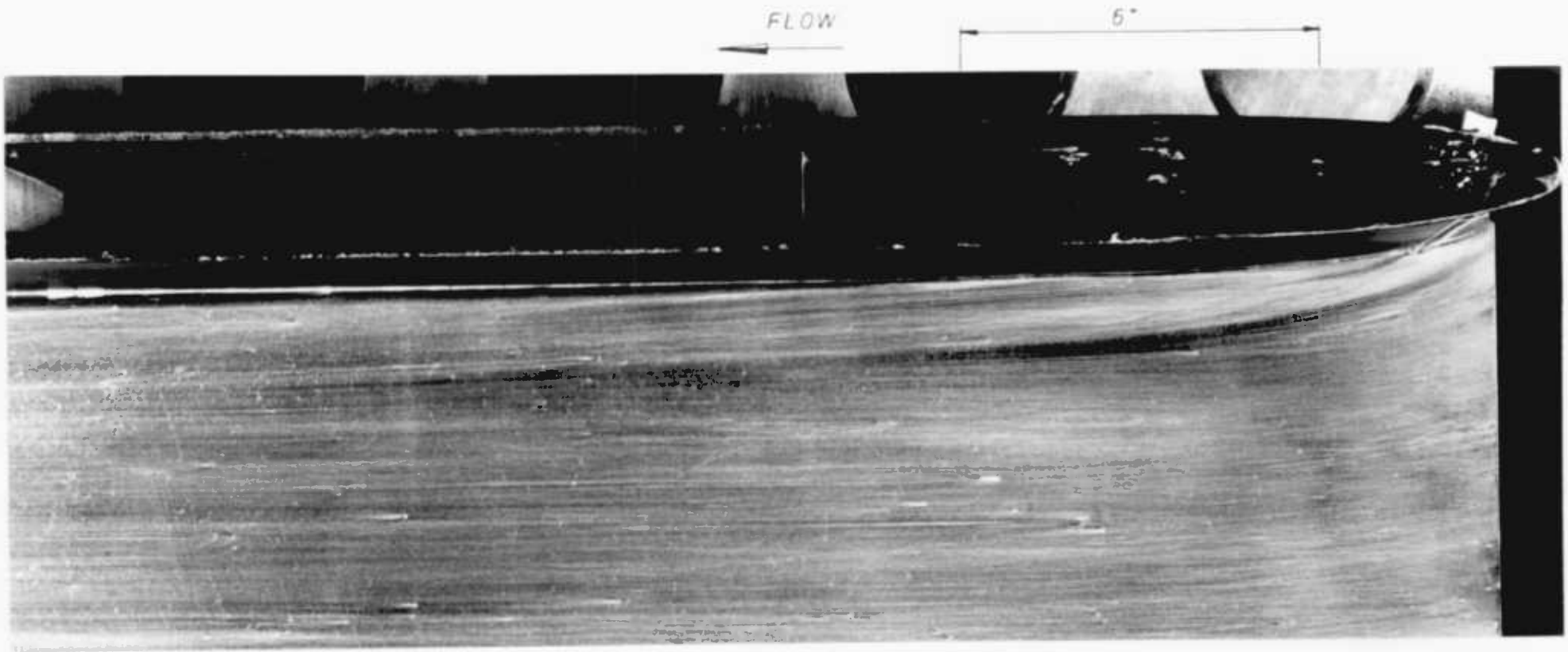

FIG. (3.1) OIL-FILM FLOW VISUALIZATION PATTERN

B: FRONT HALF OF FLOW

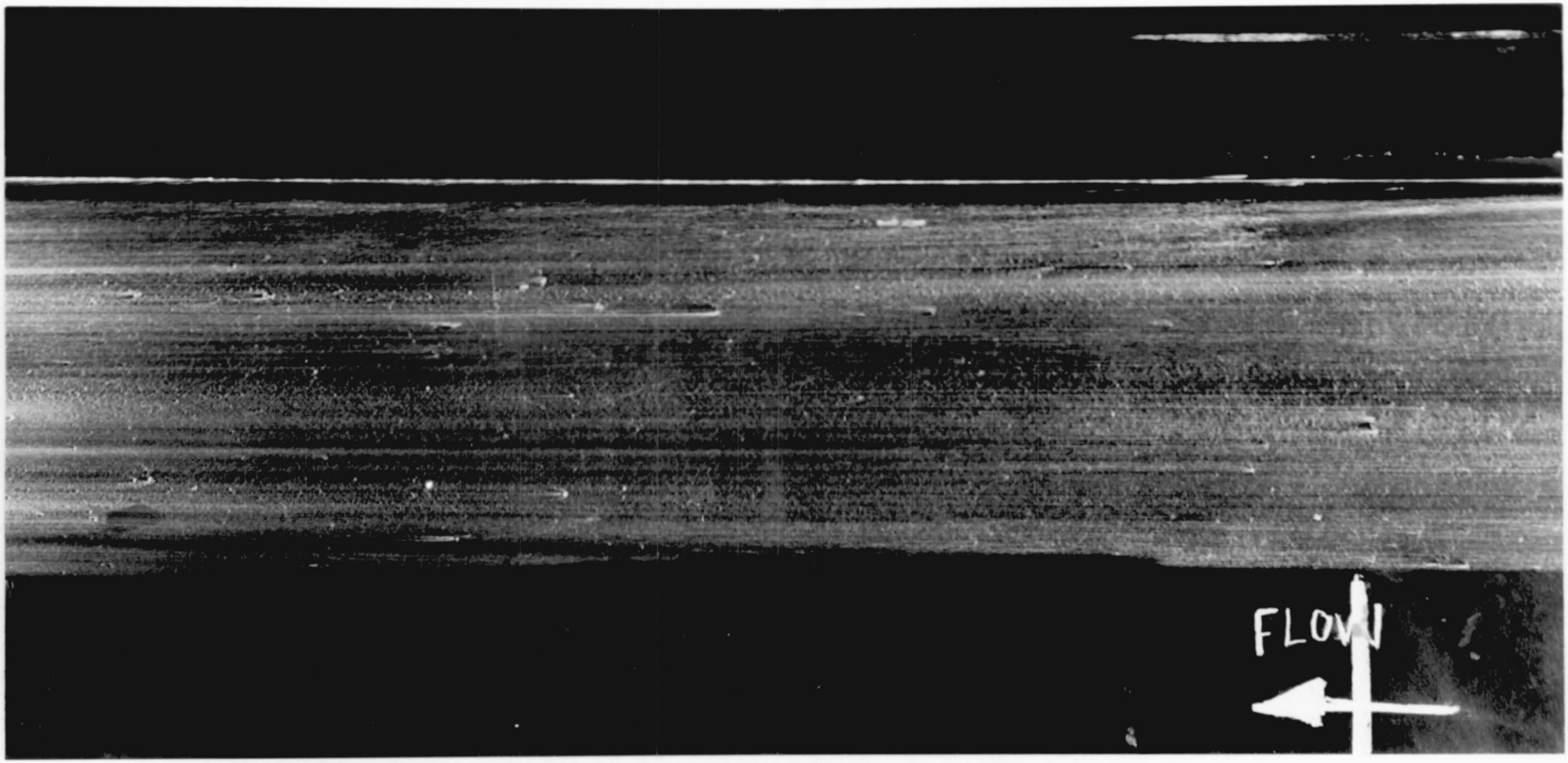

FIG.(3.1) OIL-FILM FLOW VISUALIZATION PATTERN

C: REAR HALF OF FLOW

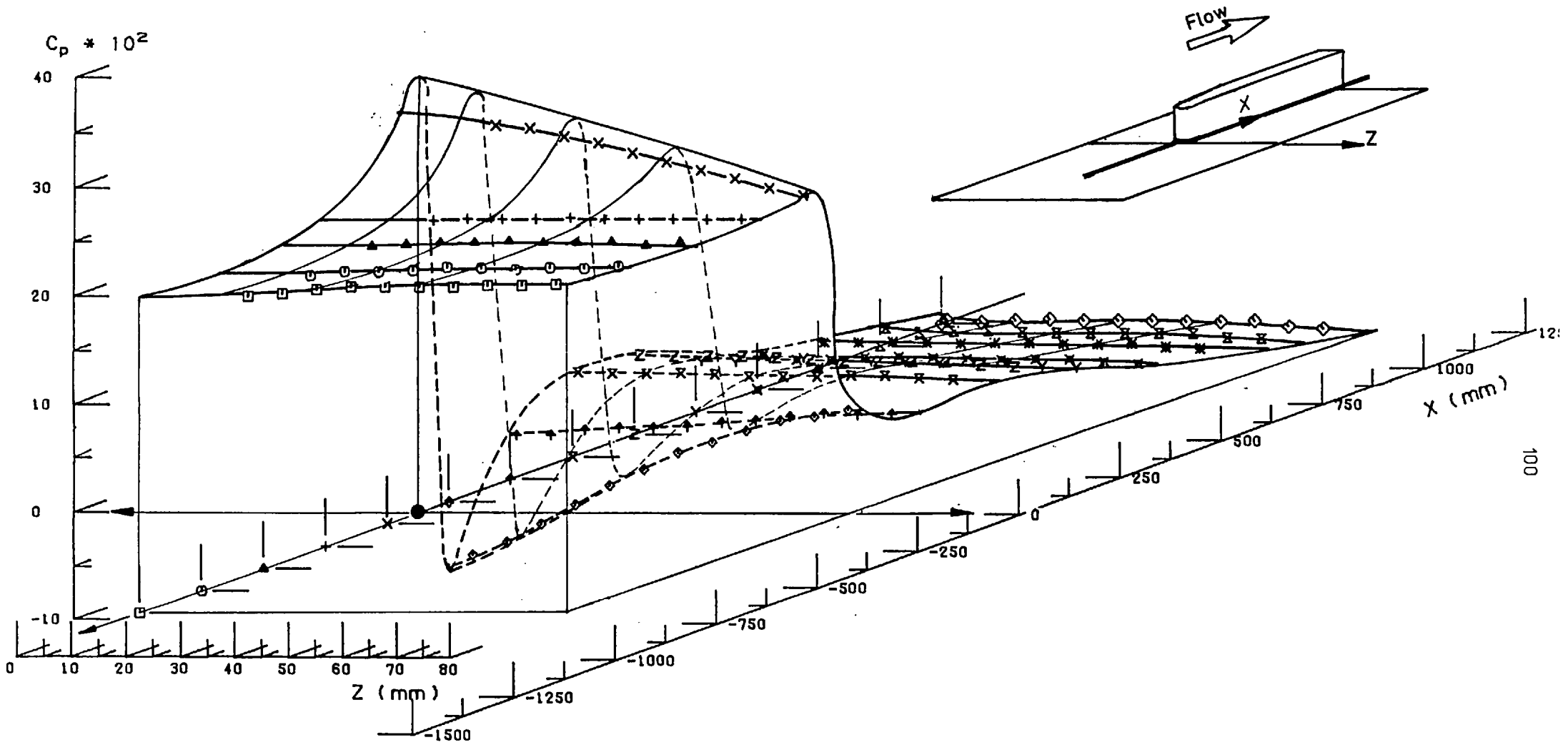

FIG.(3.2) WALL STATIC PRESSURE COEFFICIENT C_p

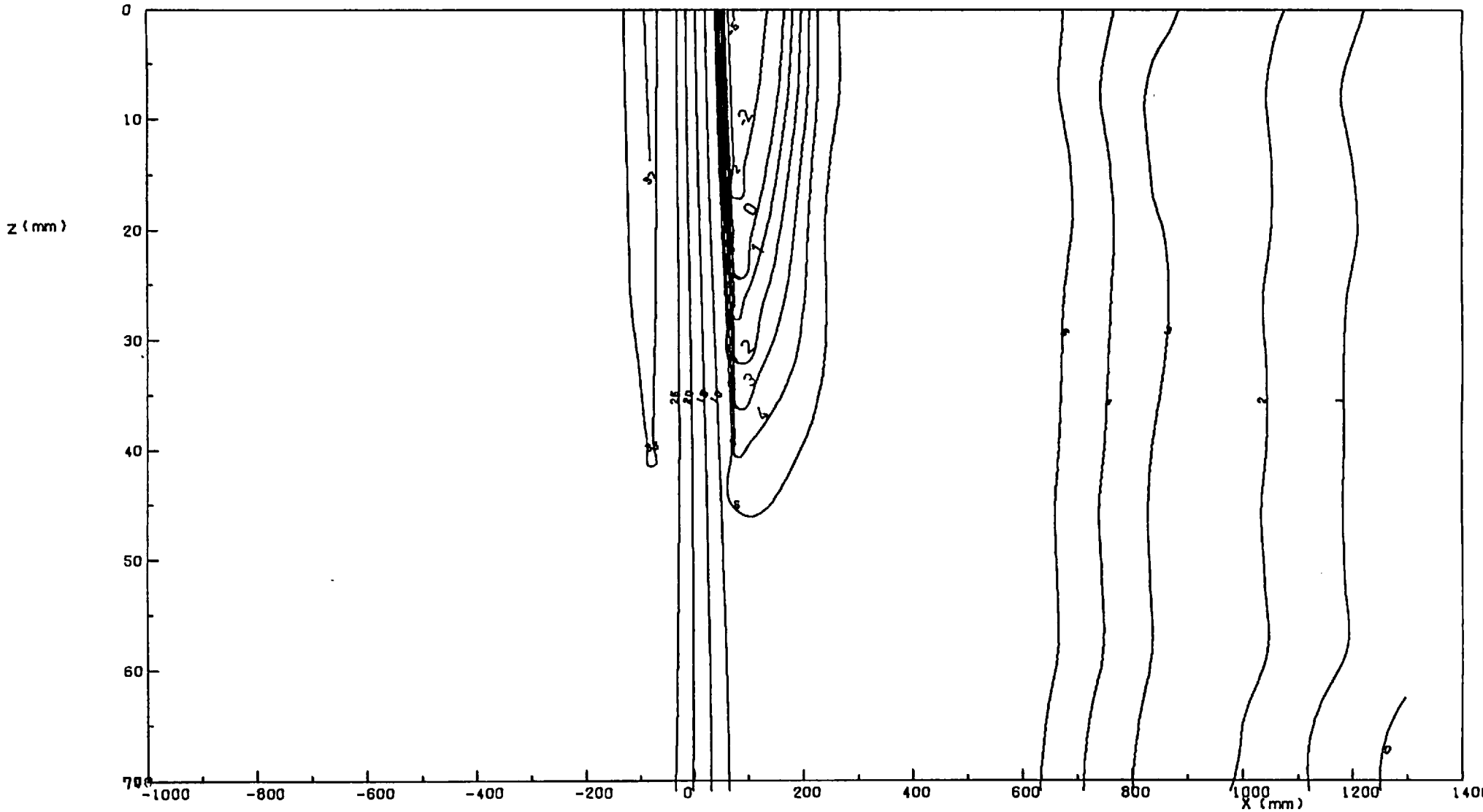

FIG.(3.3) CONTOUR MAP OF WALL STATIC PRESSURE COEFFICIENT (C_p)*100

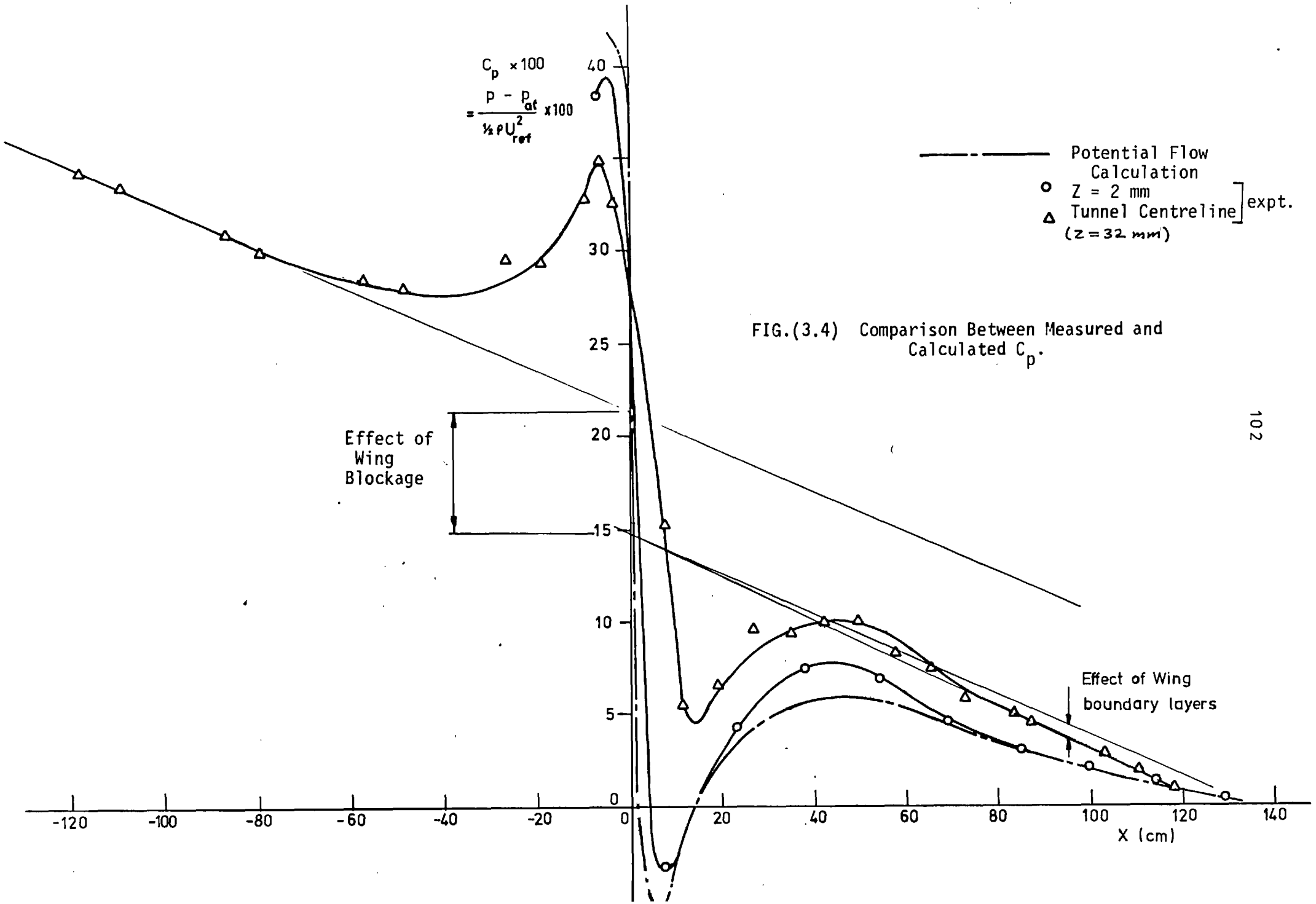

FIG.(3.4) Comparison Between Measured and Calculated C_p.

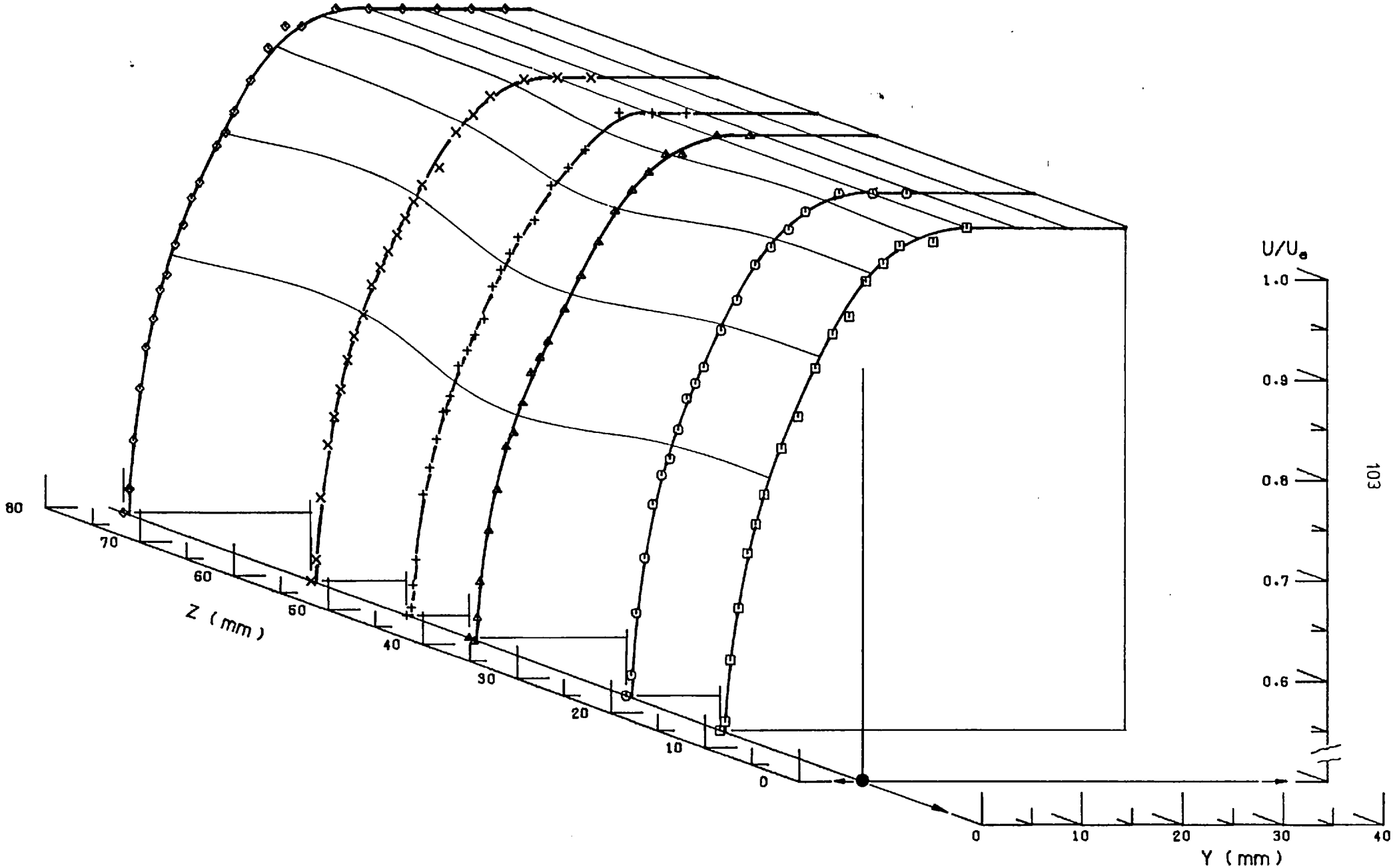

FIG.(3.5) STREAMWISE VELOCITY PROFILES AT STATION -1 (X=-137.2mm)

Results of U-Wire

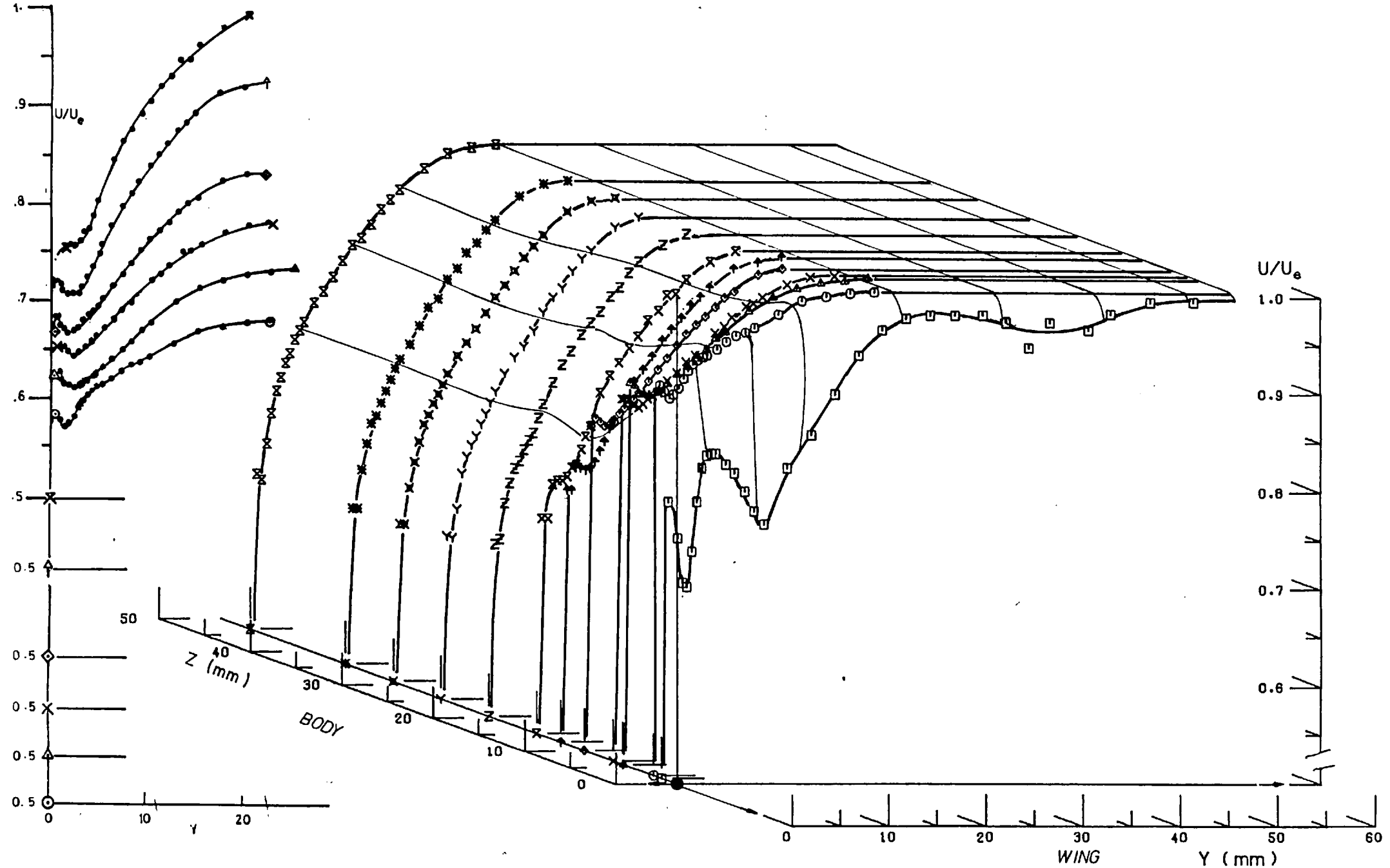

FIG.(3.6) STREAMWISE VELOCITY PROFILES AT STATION 1 (X= 34.66 mm)

Pitot Tube Measurements

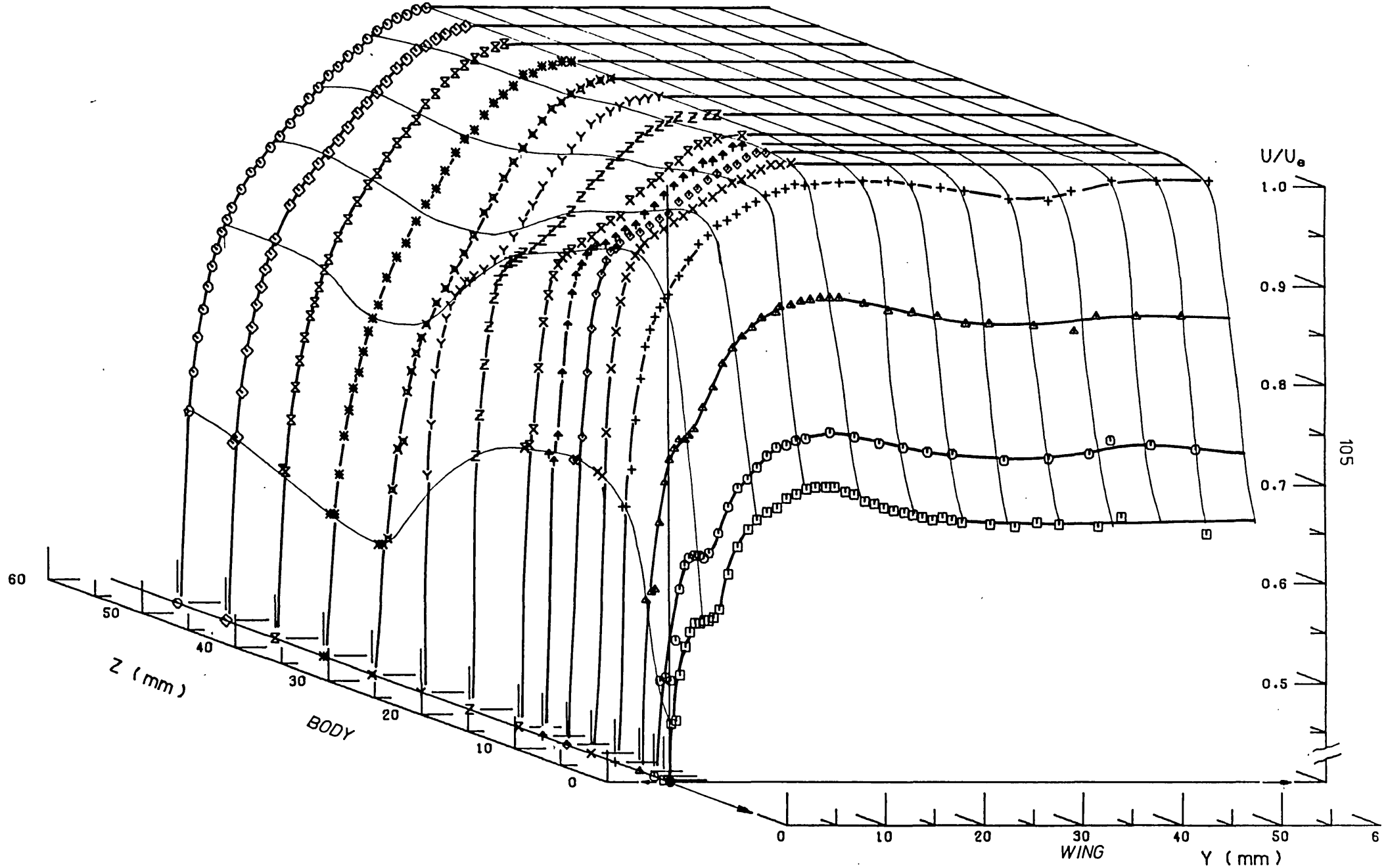

FIG.(3.7) STREAMWISE VELOCITY PROFILES AT STATION 2 (X= 187.06 mm)

Pitot Tube Measurements

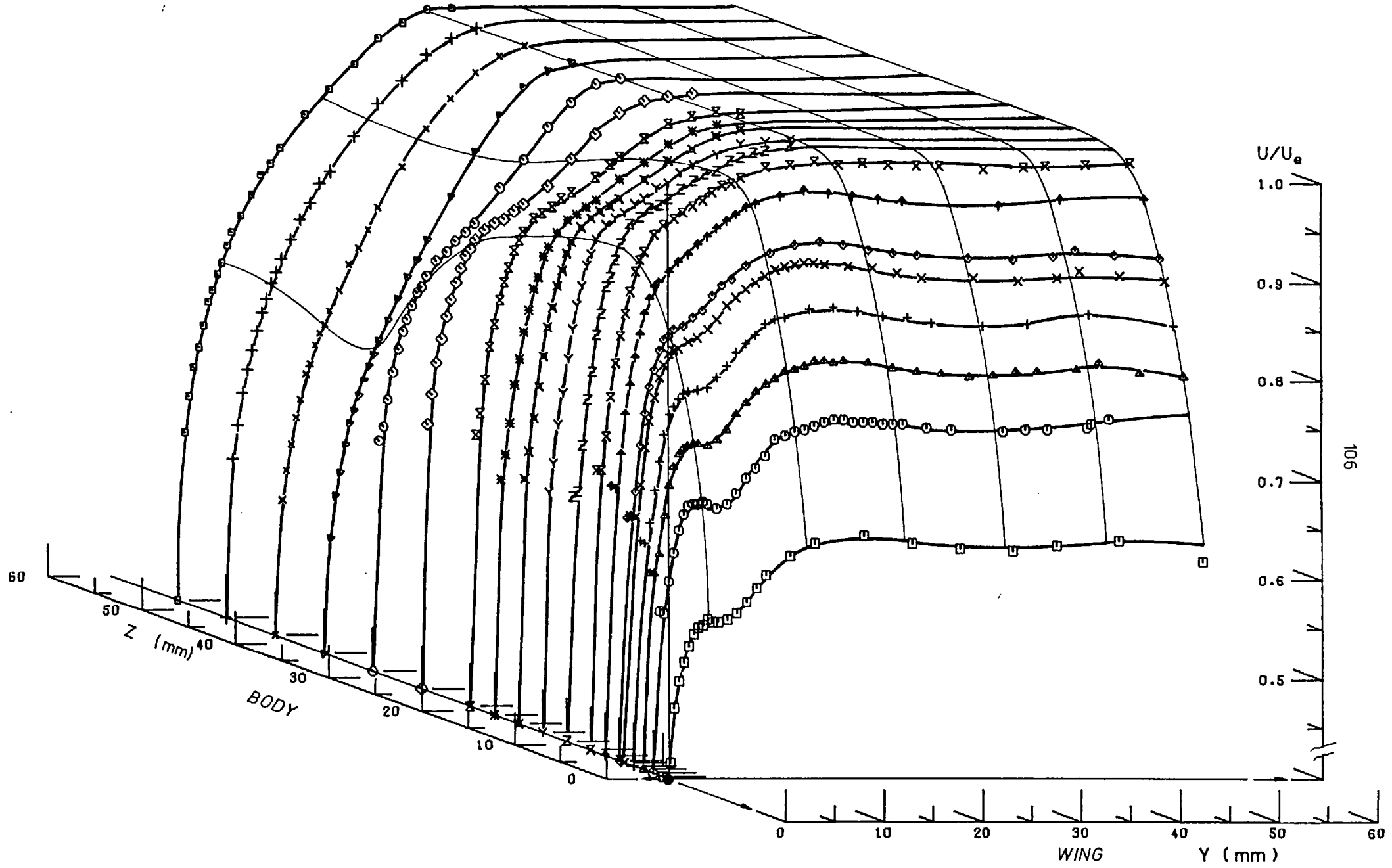

FIG.(3.8) STREAMWISE VELOCITY PROFILES AT STATION 3 (X= 339.46 mm)

Pitot Tube Measurements

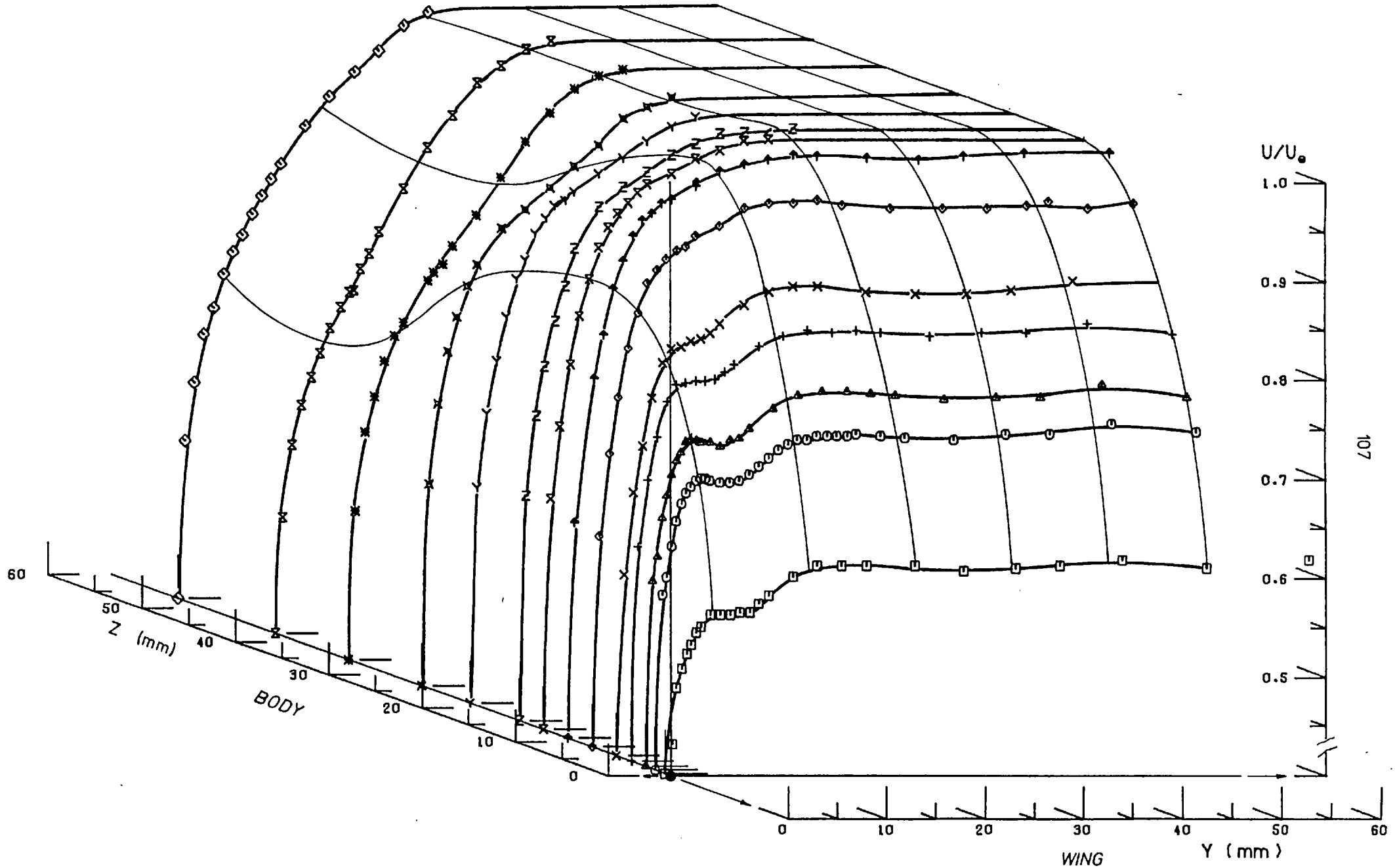

FIG.(3.9) STREAMWISE VELOCITY PROFILES AT STATION 4 (X= 491.86 mm)

Pitot Tube Measurements

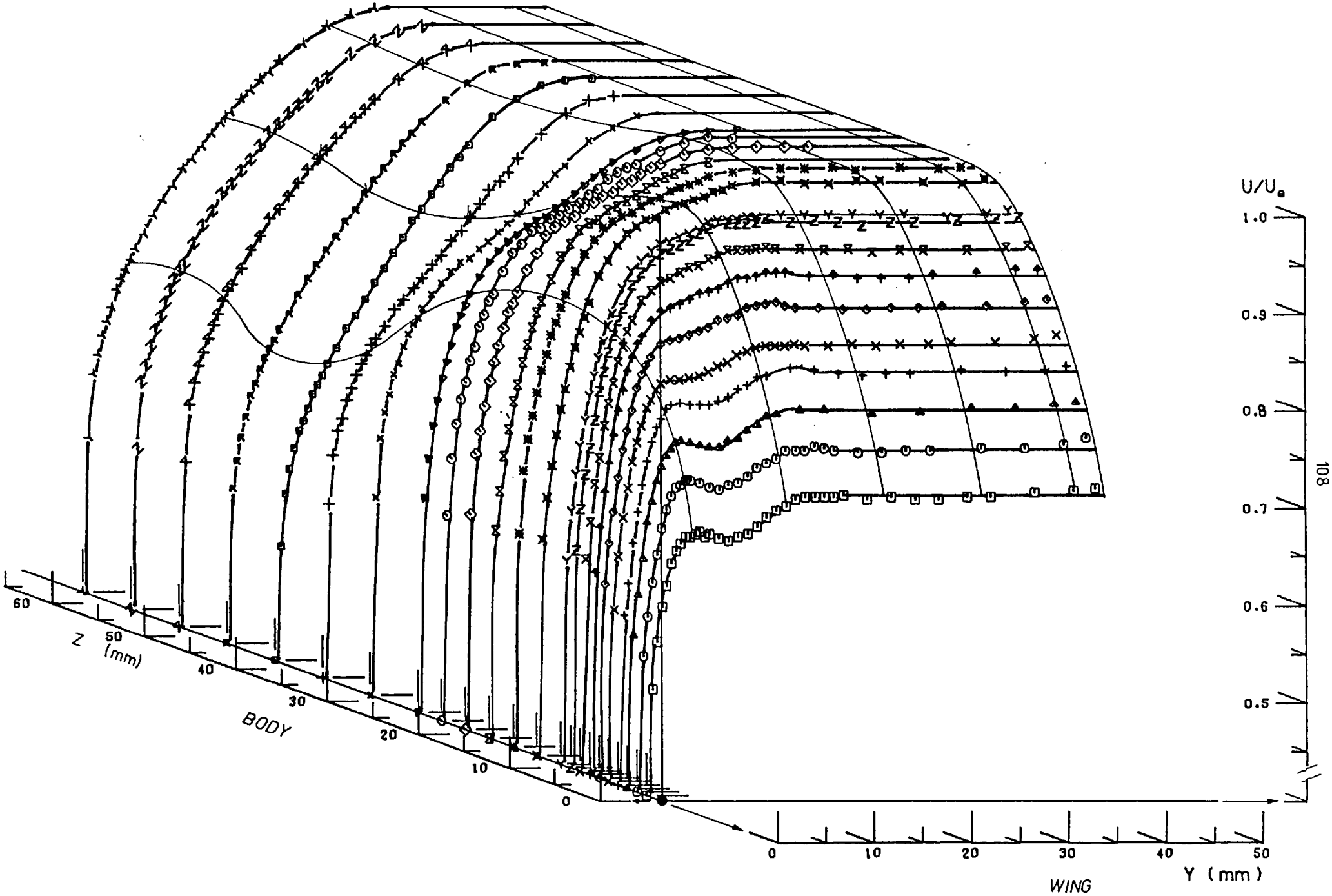

FIG.(3.10) STREAMWISE VELOCITY PROFILES AT STATION 5 (X= 644.26 mm)

Pitot Tube Measurements

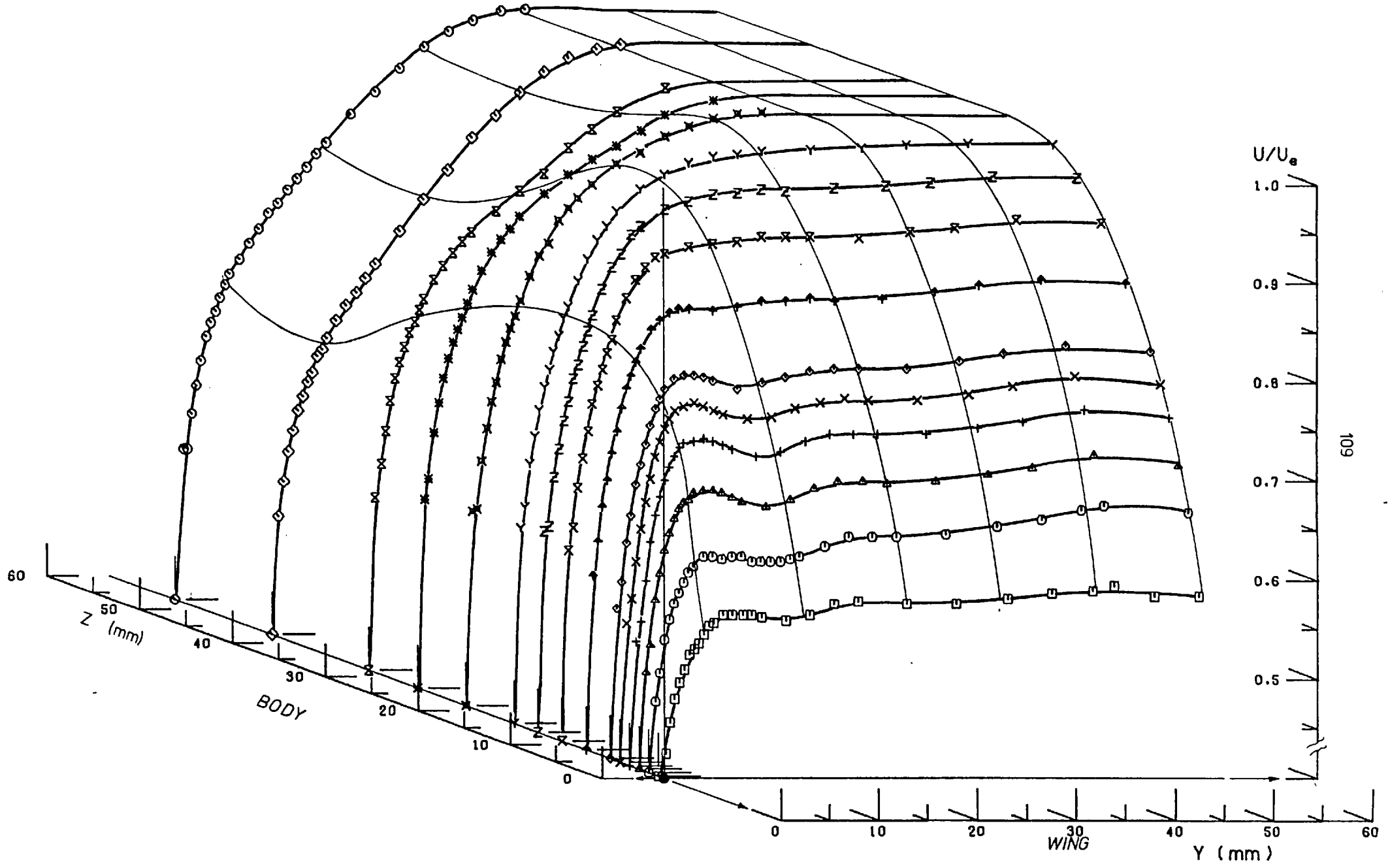

FIG.(3·11) STREAMWISE VELOCITY PROFILES AT STATION 7 (X= 949.06 mm)

Pitot Tube Measurements

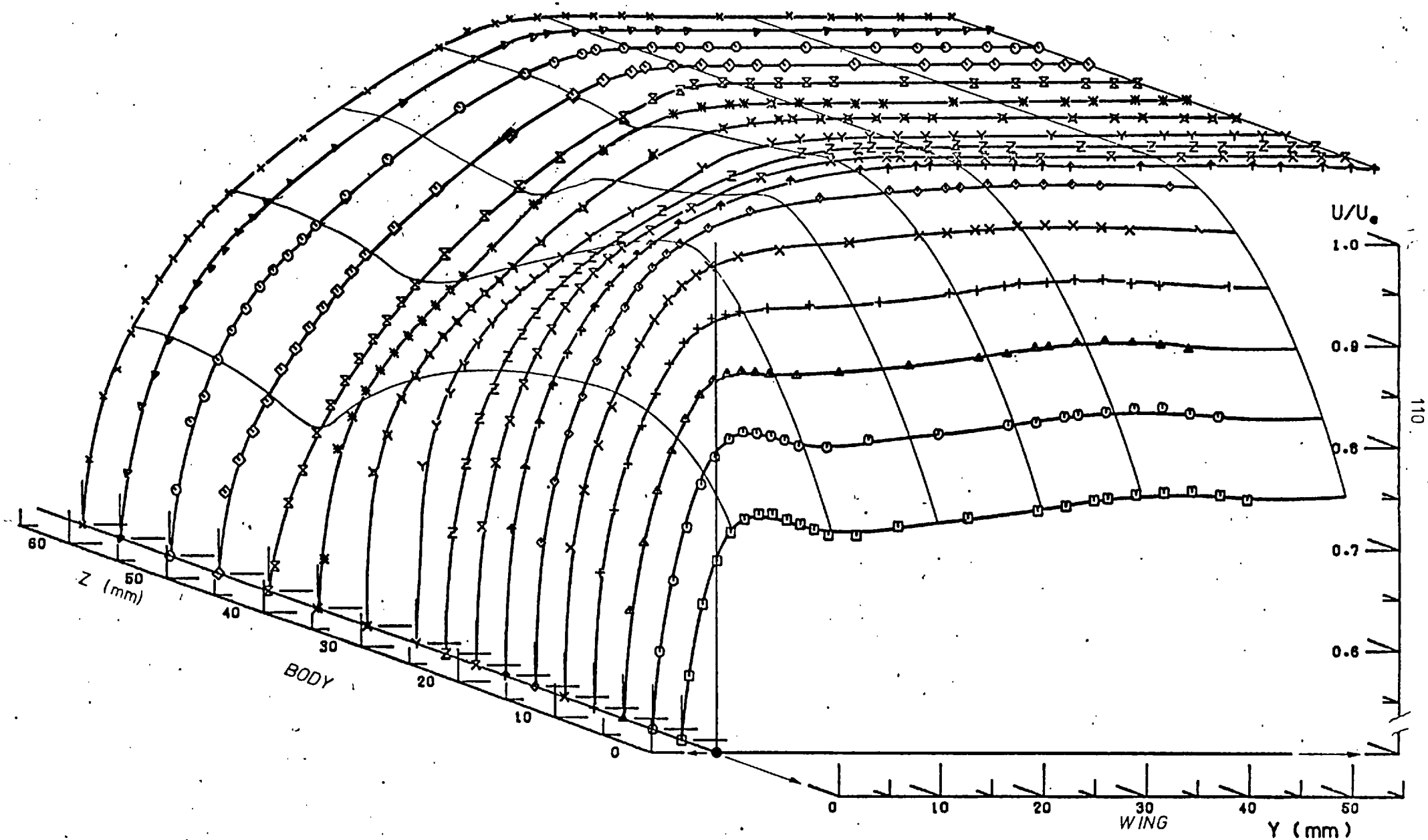

FIG.(3.12) STREAMWISE VELOCITY PROFILES AT STATION 9 (X=1253.86 mm)

Pitot Tube Measurements

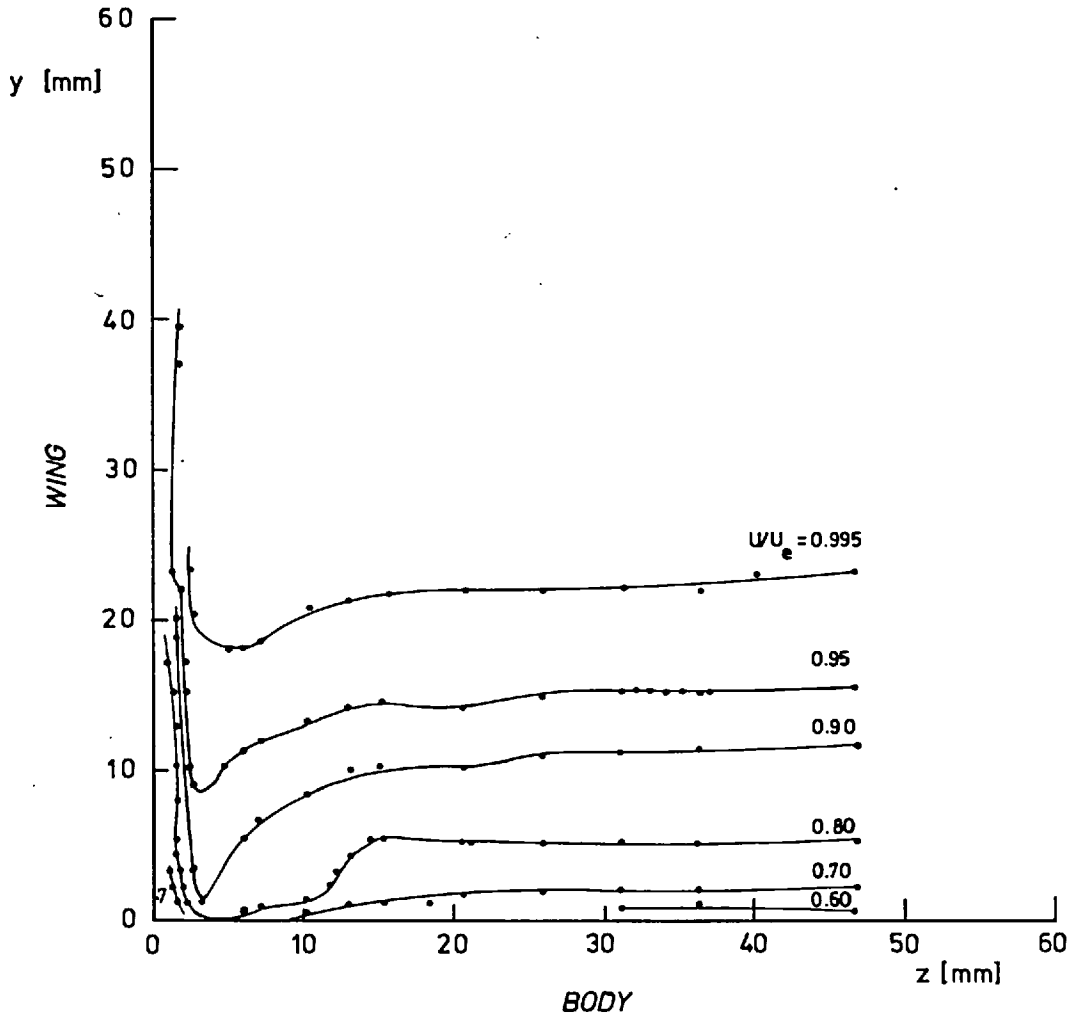

FIG.(3.13) STREAMWISE VELOCITY CONTOURS AT STATION 1 (X = 34.7 mm)

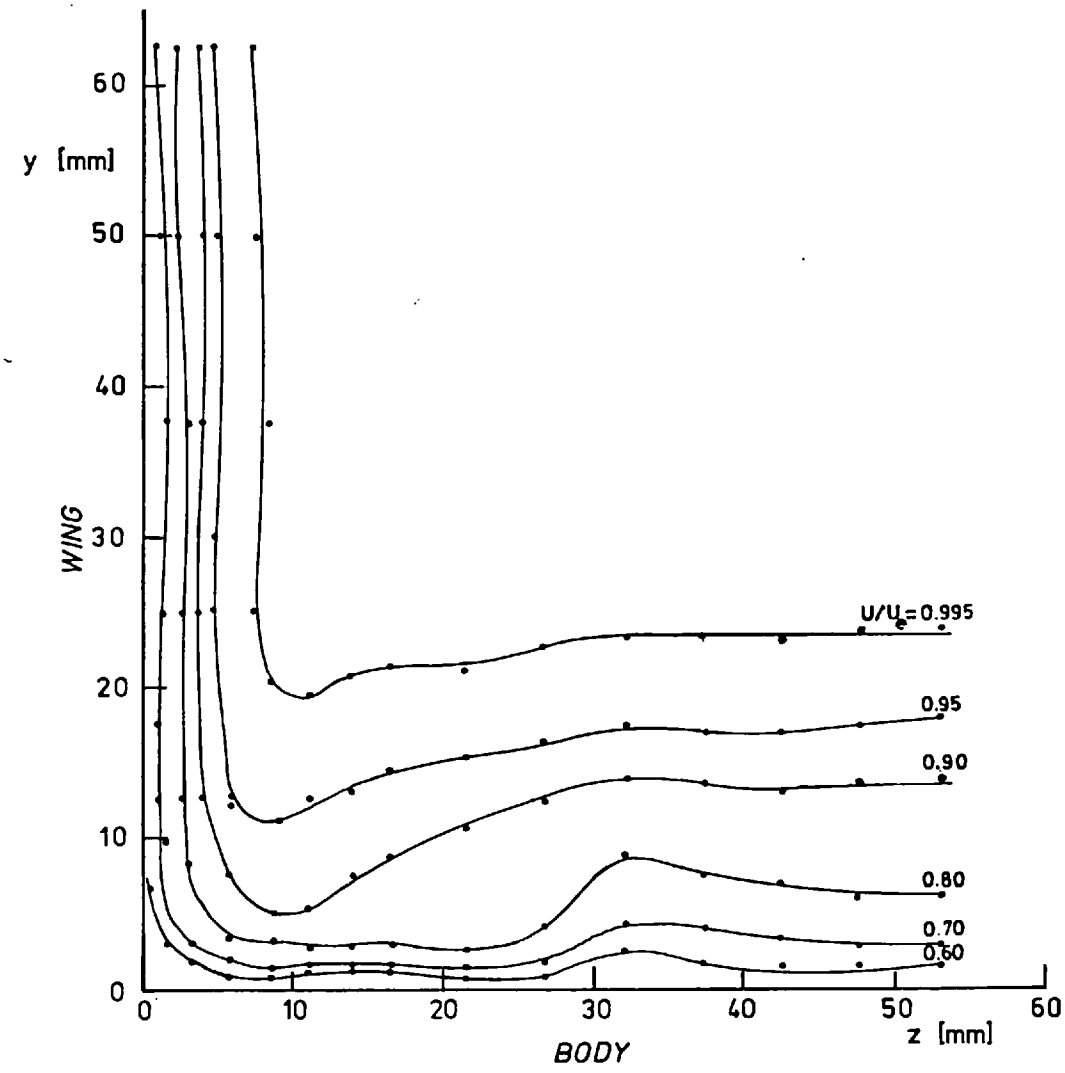

FIG. (3.14) STREAMWISE VELOCITY CONTOURS
AT STATION 2 (X = 187.1 mm)

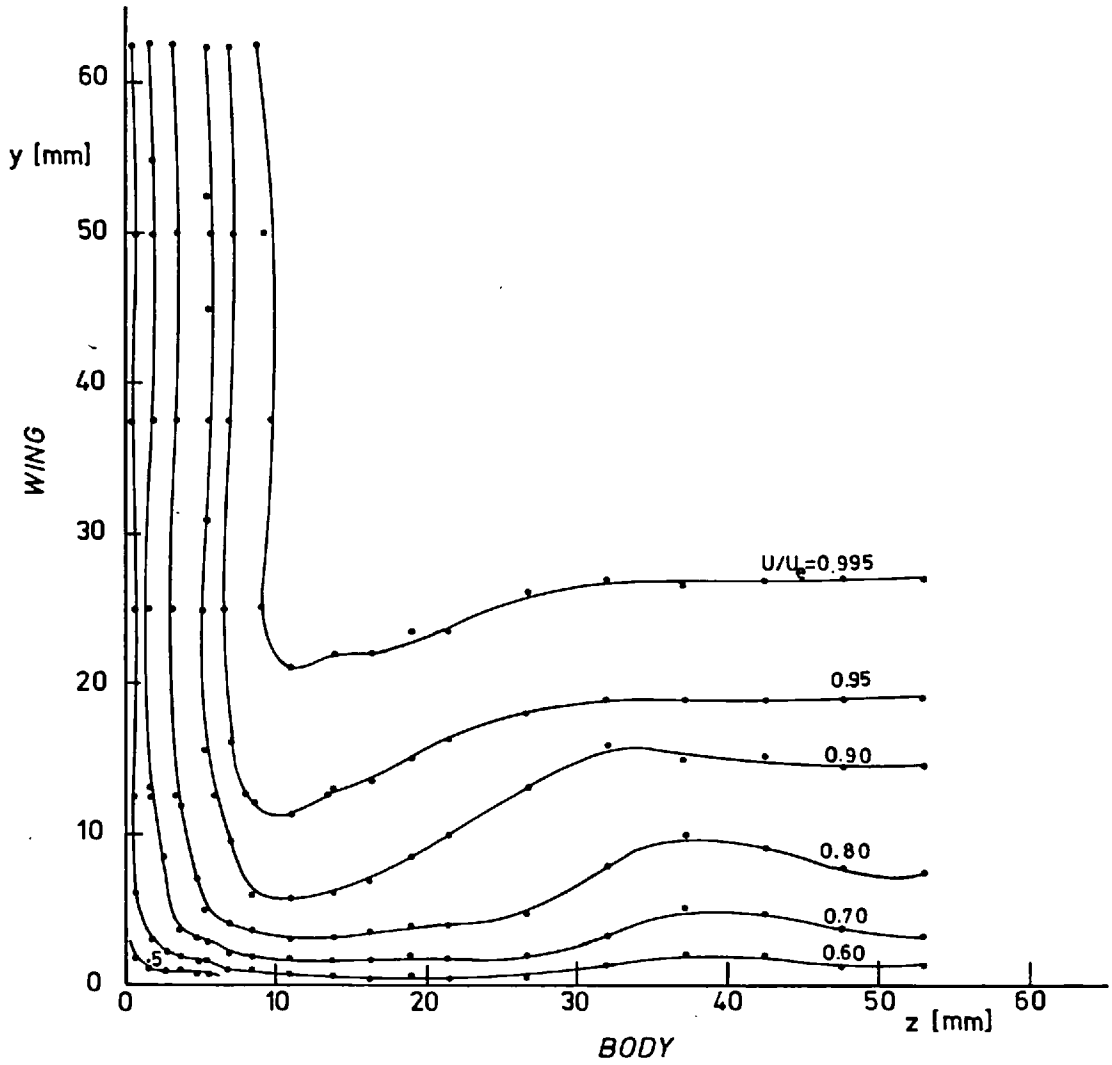

FIG.(3.15) STREAMWISE VELOCITY CONTOURS
AT STATION 3 (X = 339.5 mm)

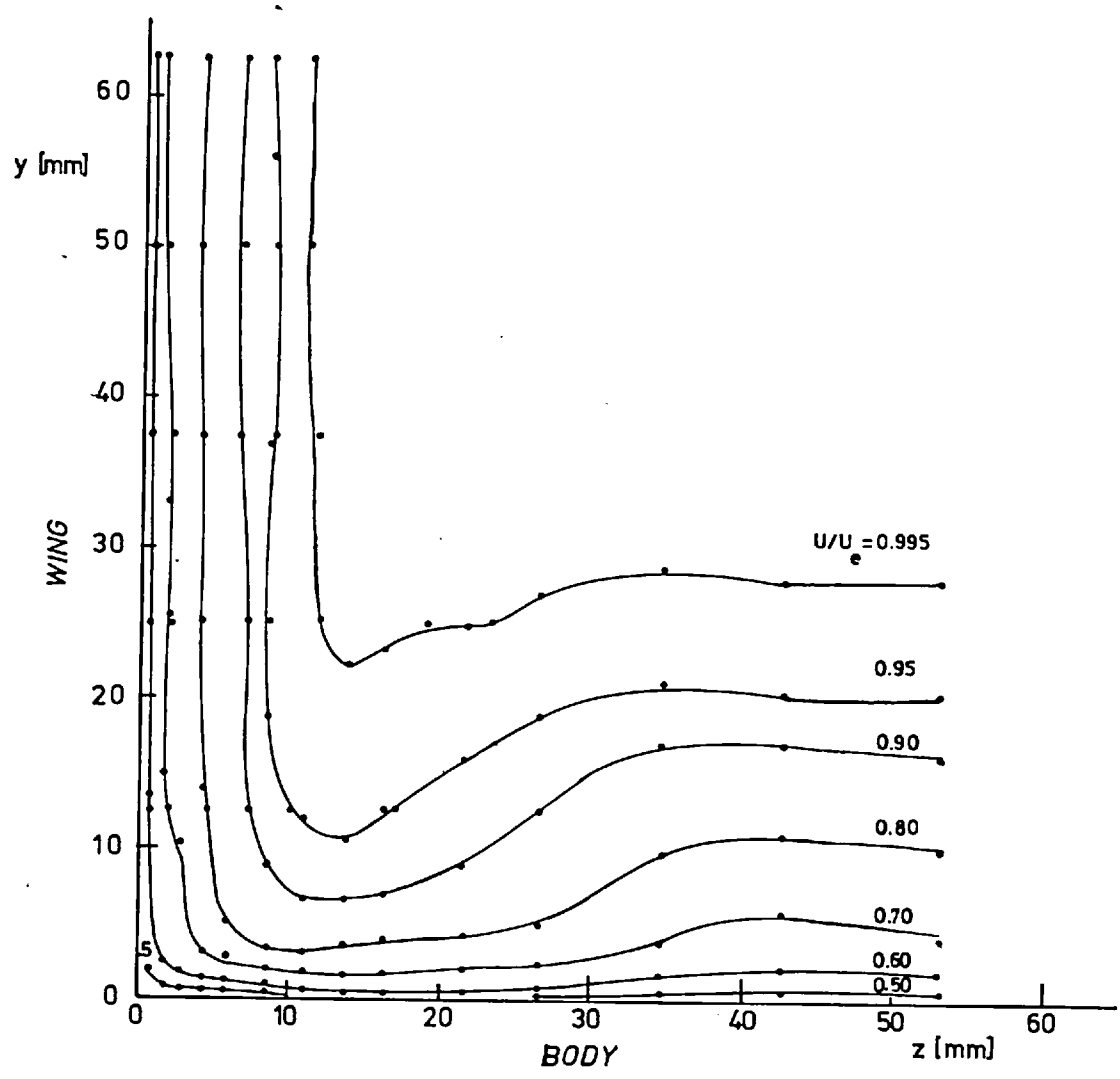

FIG.(3.16) STREAMWISE VELOCITY CONTOURS AT STATION 4
(X = 491.9 mm)

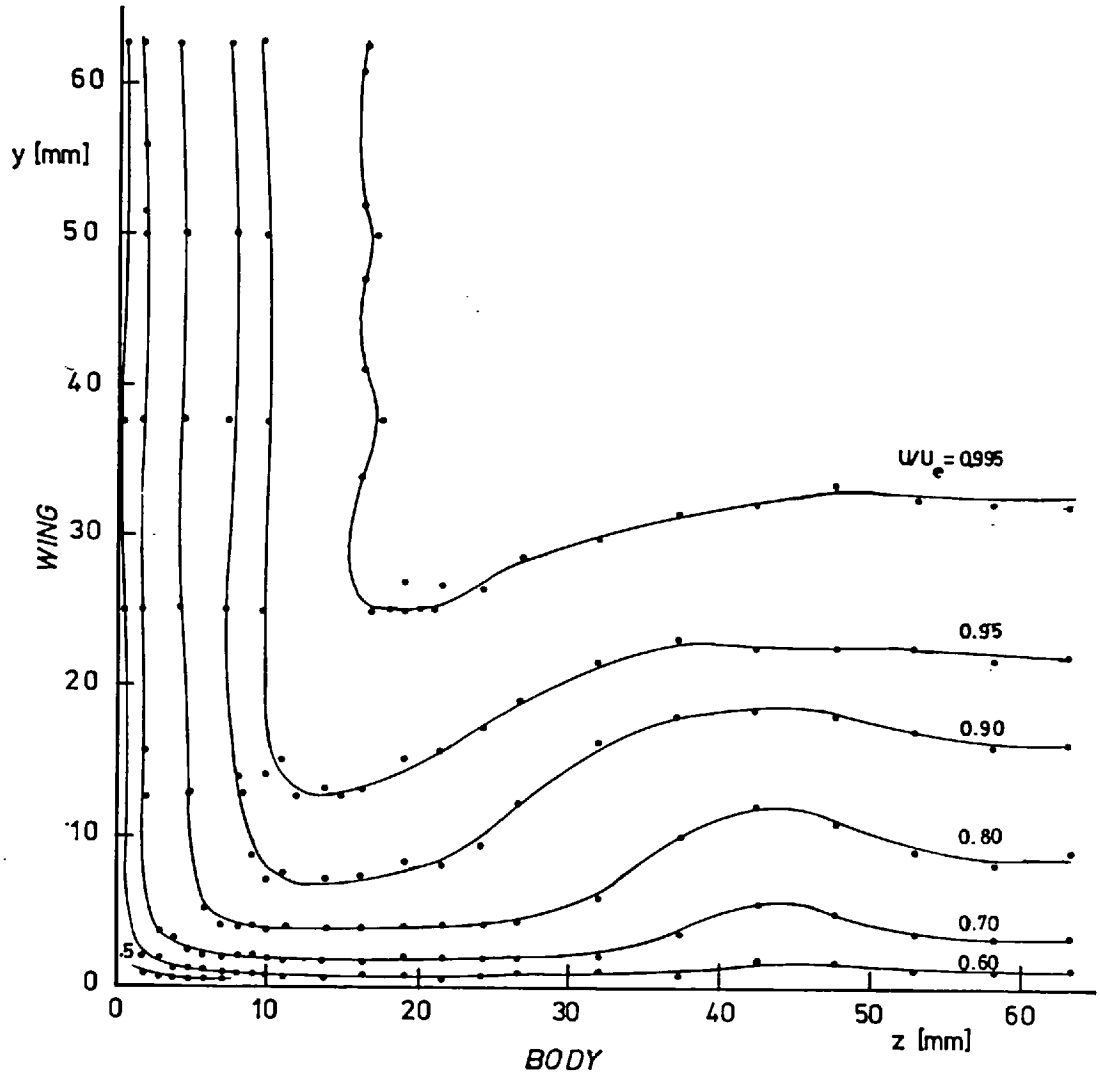

FIG.(3.17) STREAMWISE VELOCITY CONTOURS AT STATION 5
(X = 644.3 mm)

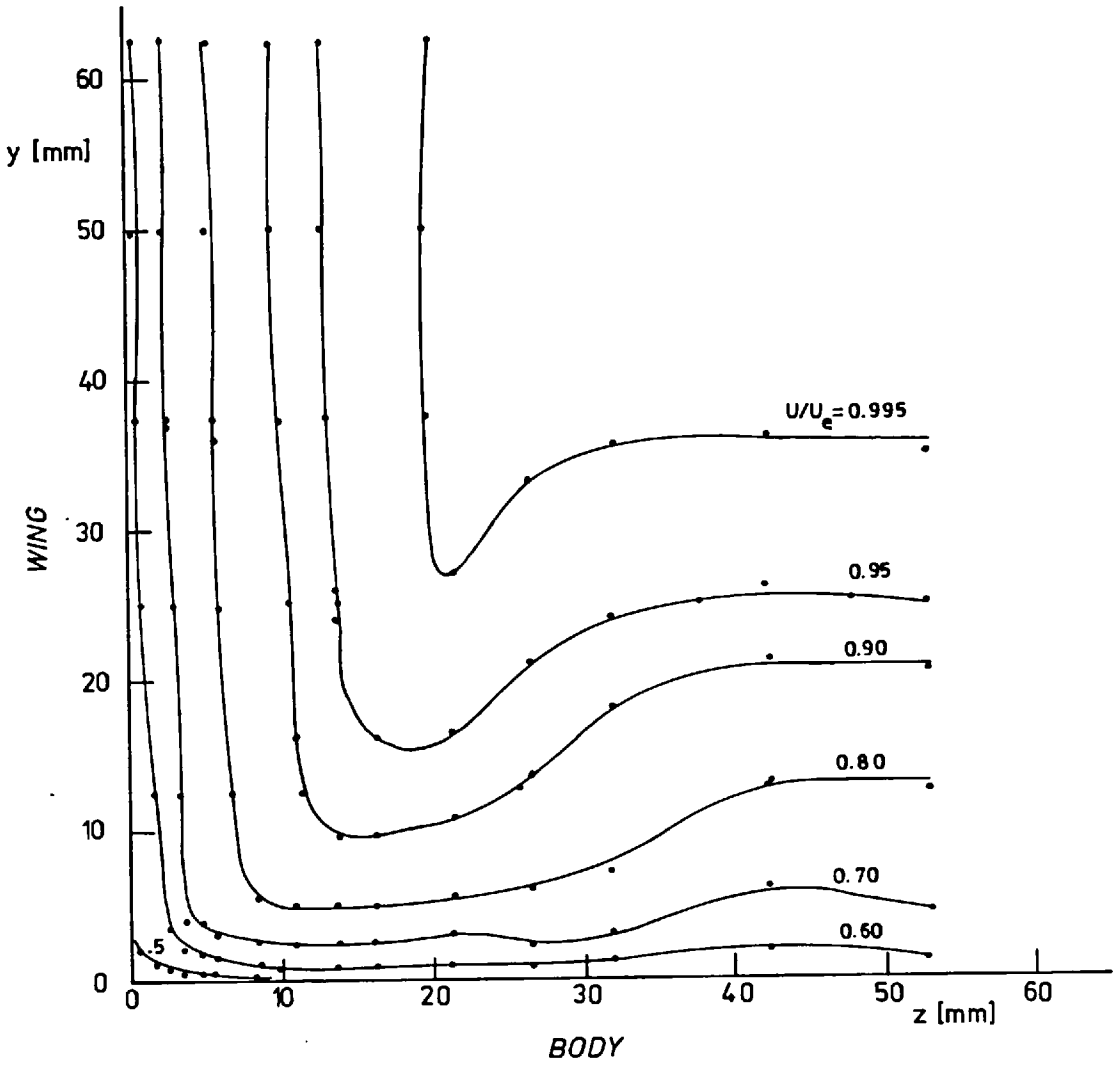

FIG.(3.18) STREAMWISE VELOCITY CONTOURS AT STATION 7
(X = 949.1 mm)

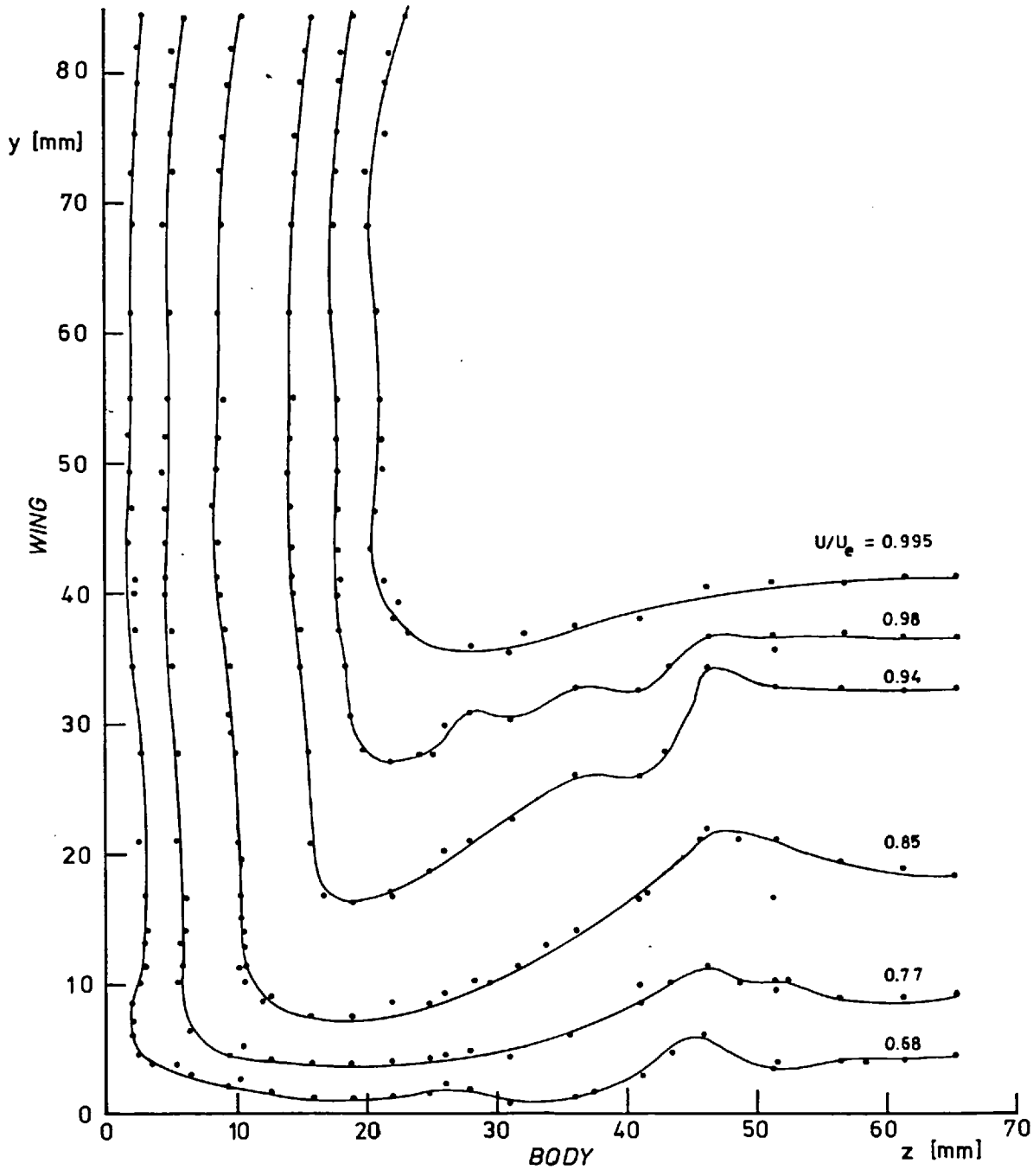

FIG.(3.19) STREAMWISE VELOCITY CONTOURS AT STATION 9
(X = 1253.9 mm)

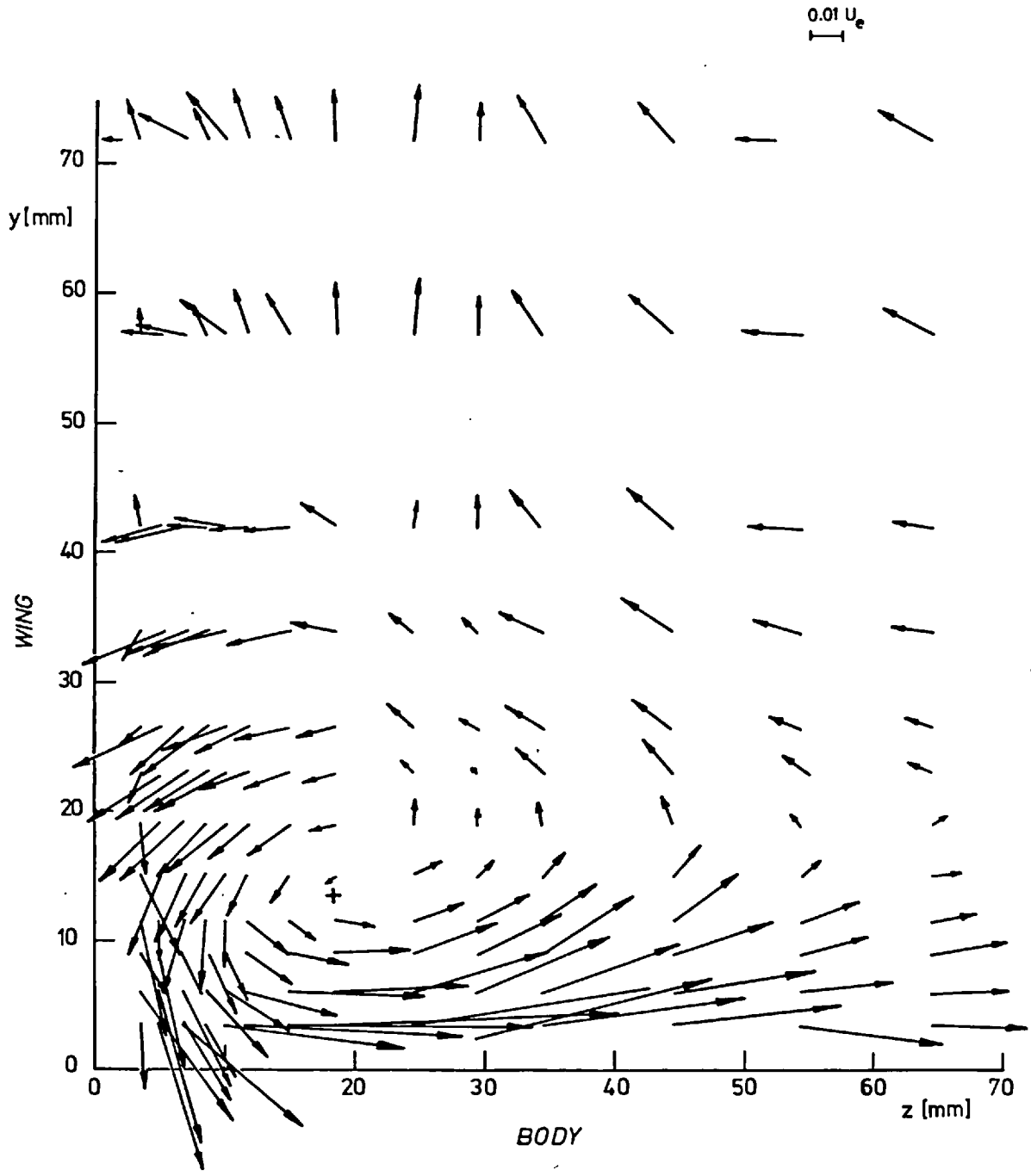

FIG.(3.20) SECONDARY FLOW VECTORS AT STATION 2 (X = 156.6 mm)

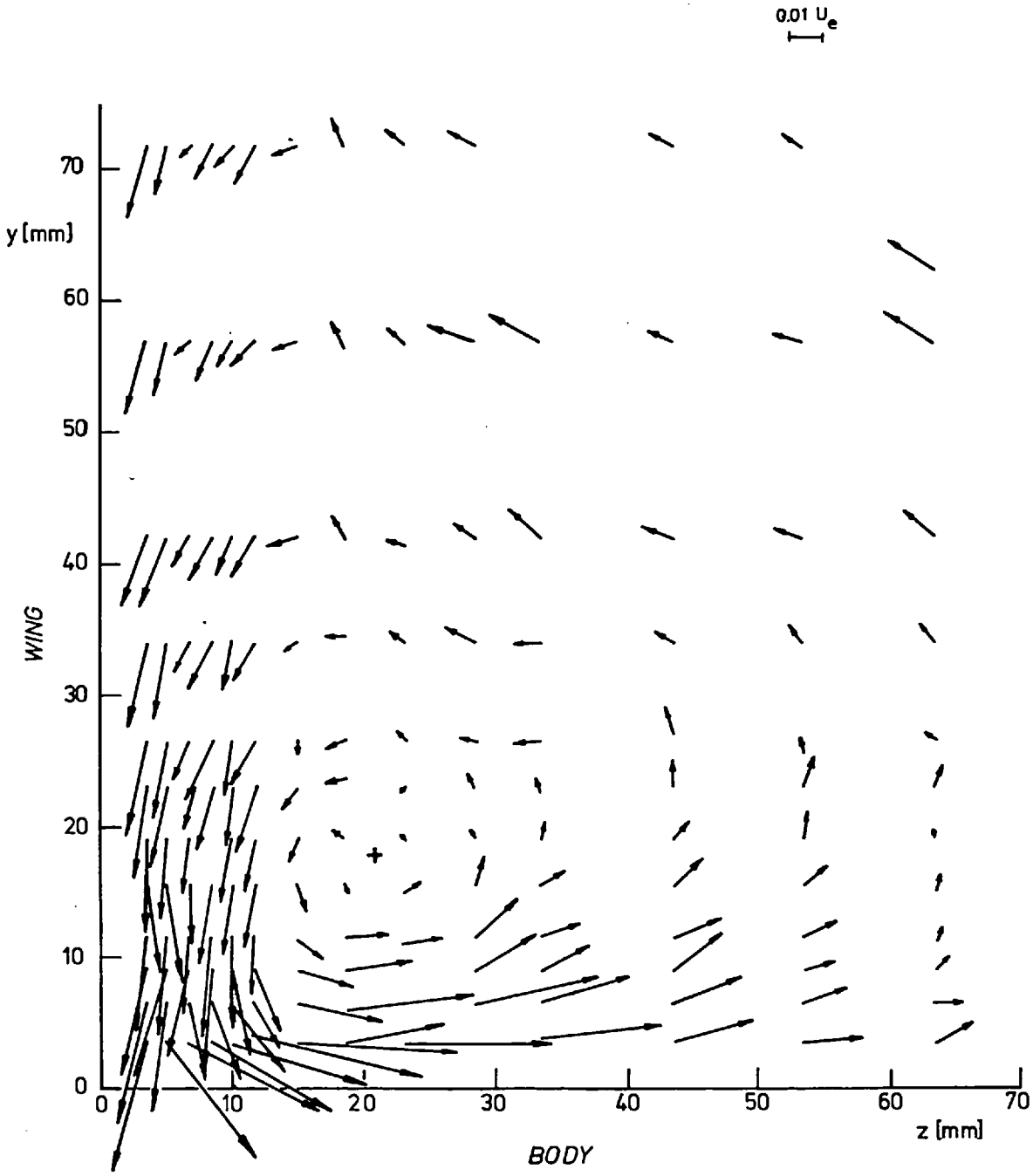

FIG.(3.21) SECONDARY FLOW VECTORS AT STATION 5 (X = 613.8 mm)

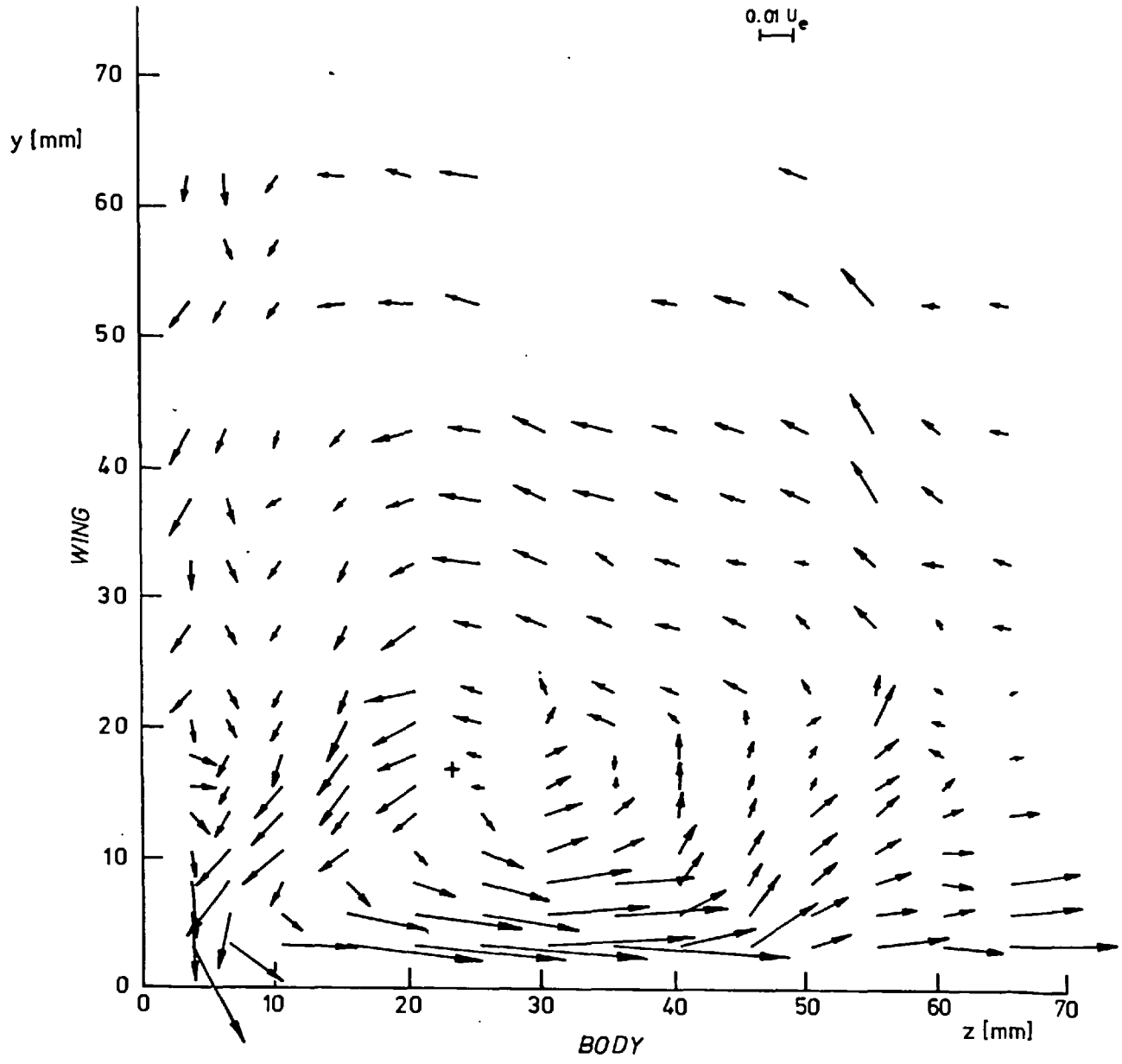

FIG.(3.22) SECONDARY FLOW VECTORS AT STATION 9
(X = 1223.4 mm)

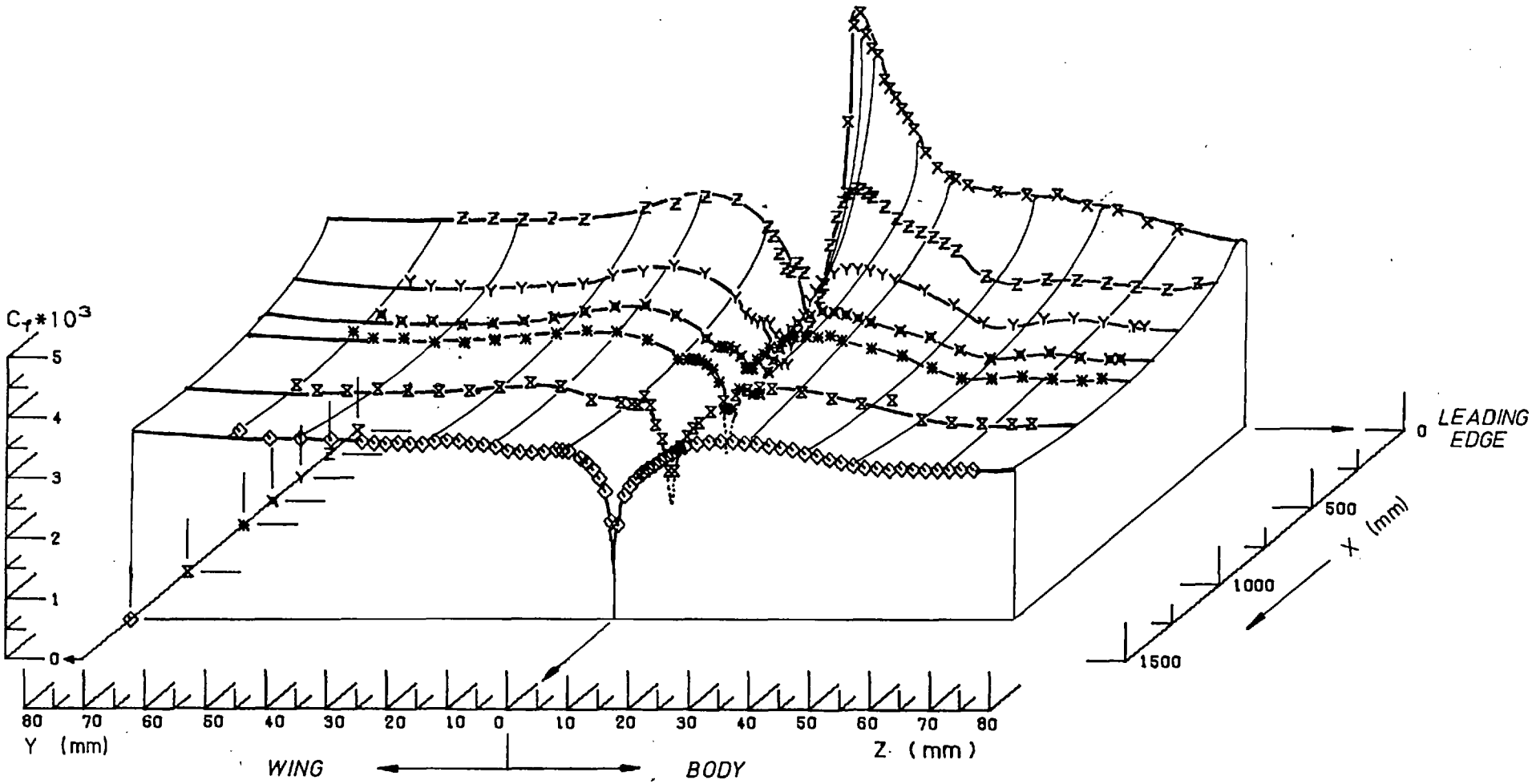

FIG. (3.23) WALL SHEAR STRESS COEFFICIENT C_f
Preston Tube Measurements

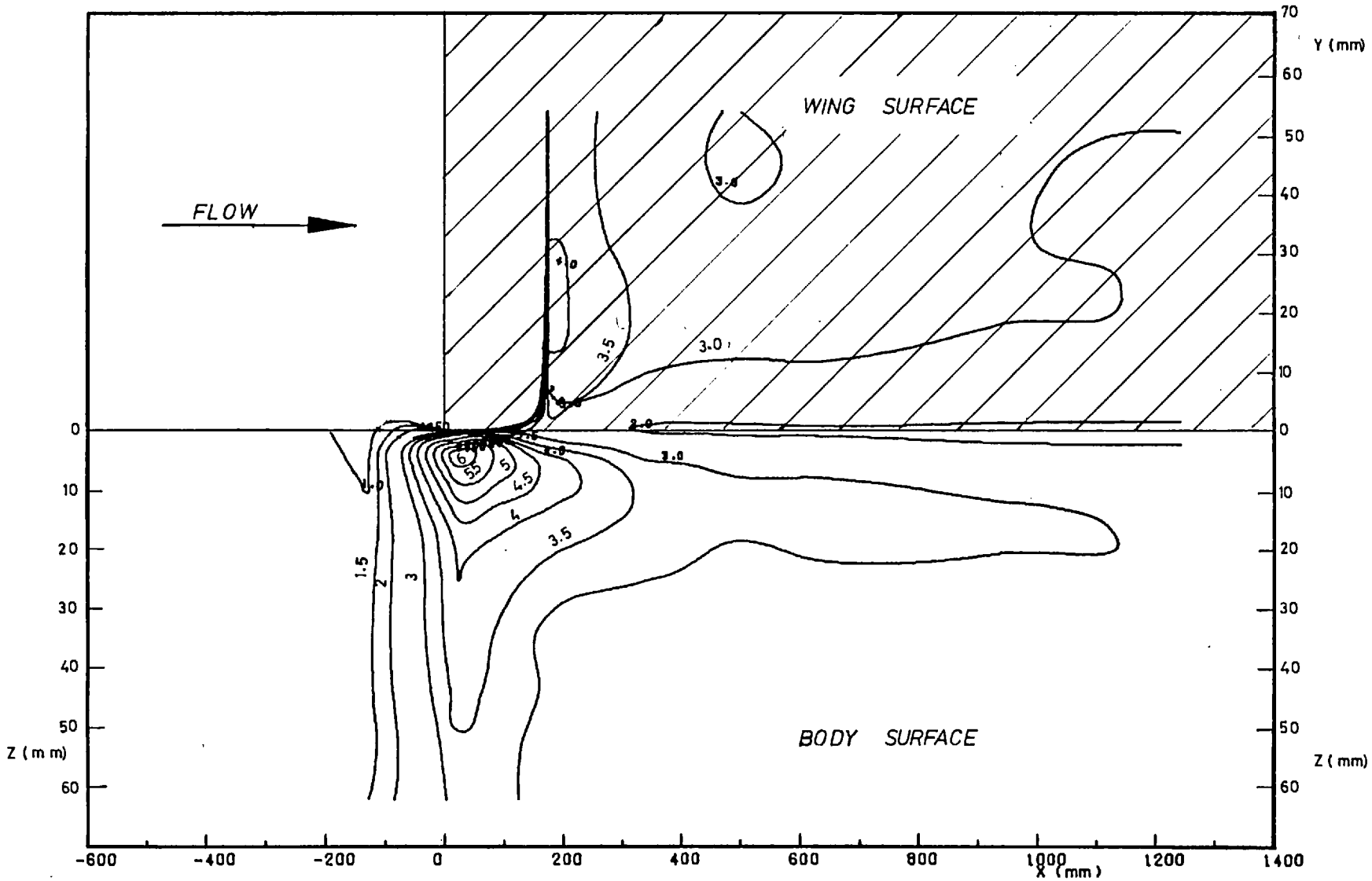

FIG.(3.24) WALL SHEAR STRESS COEFFICIENT (C_f)*1000

Preston Tube Measurements

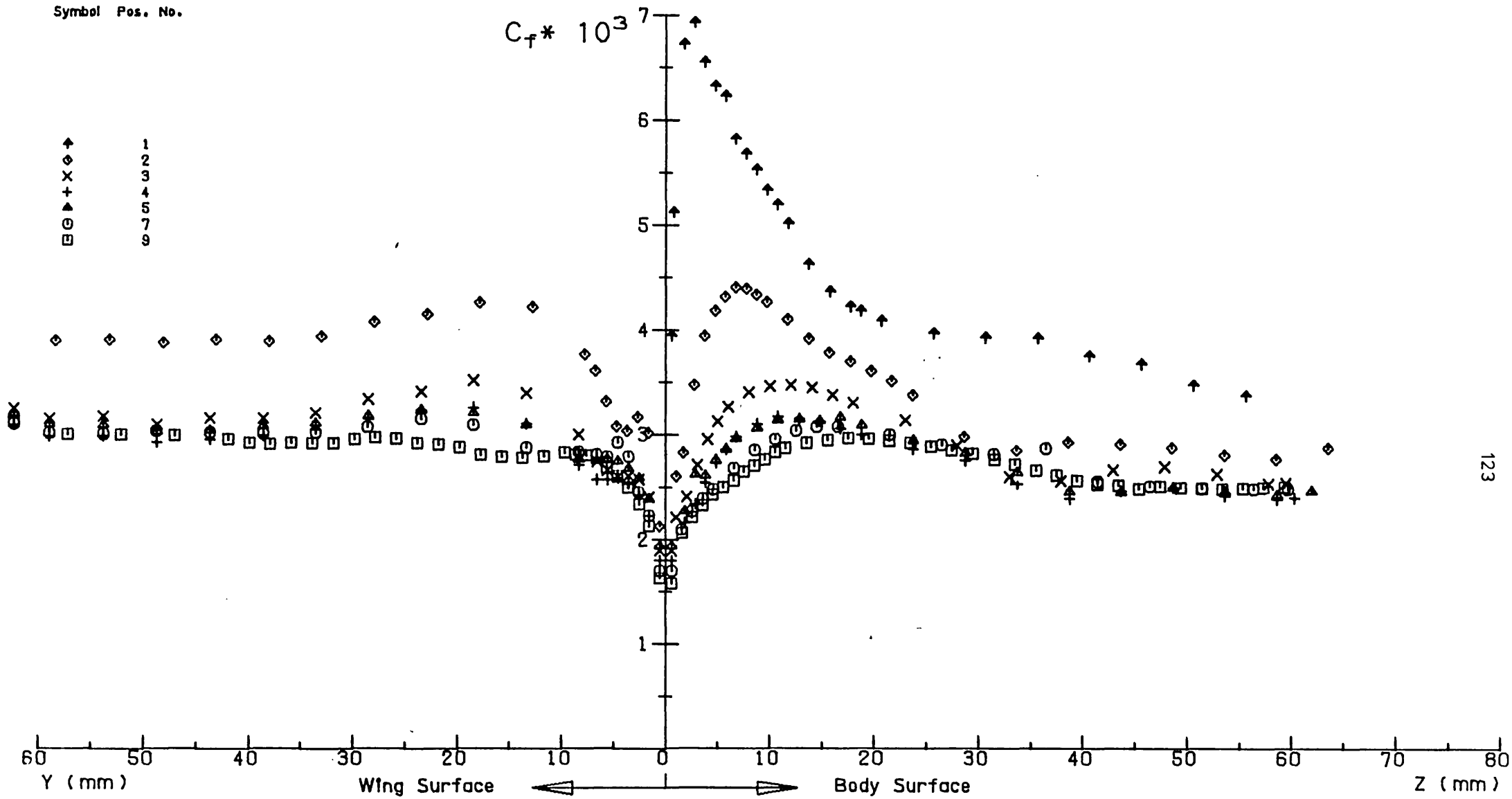

FIG.(3·25) WALL SHEAR STRESS COEFFICIENT C_f

Preston Tube Measurements

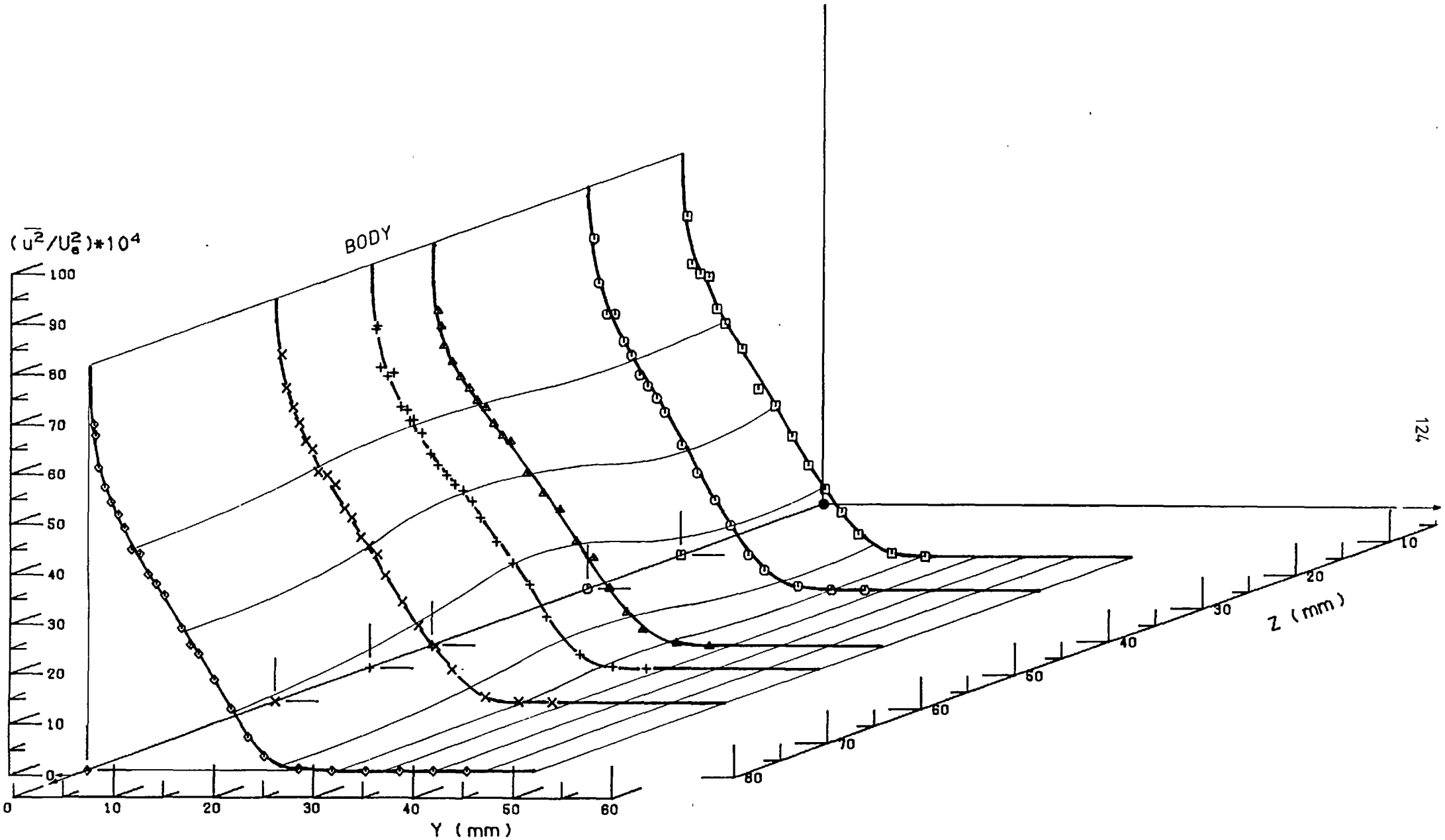

FIG.(3·26) PLOTS OF $(\overline{u^2}/U_e^2)*10^4$ AT STATION -1 (X=-137.2mm)
Results of U-Wire

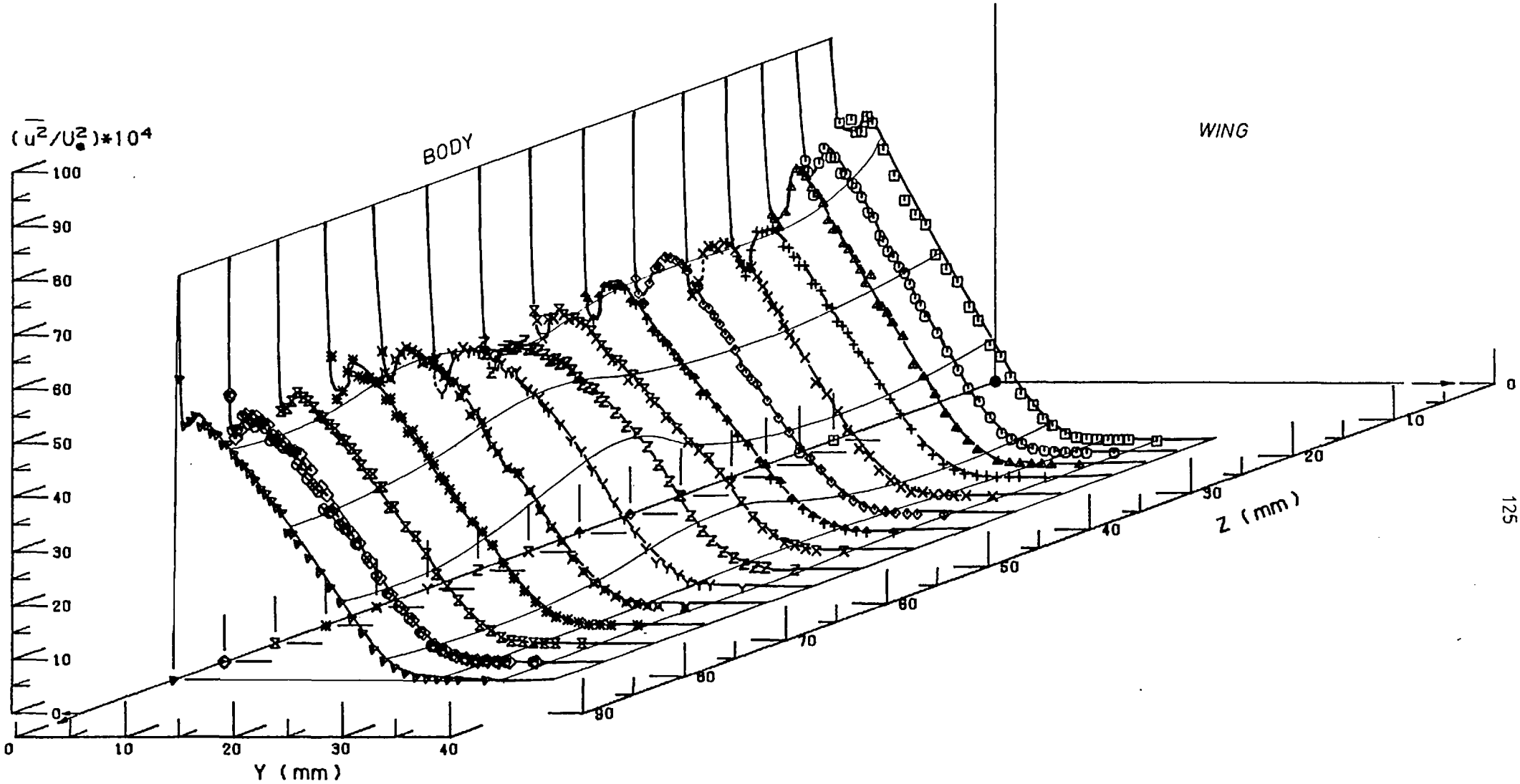

FIG.(3·27) PLOTS OF $(\overline{u^2}/U_e^2)*10^4$ AT STATION 1 (X= 15.2 mm)

Results of U-Wire

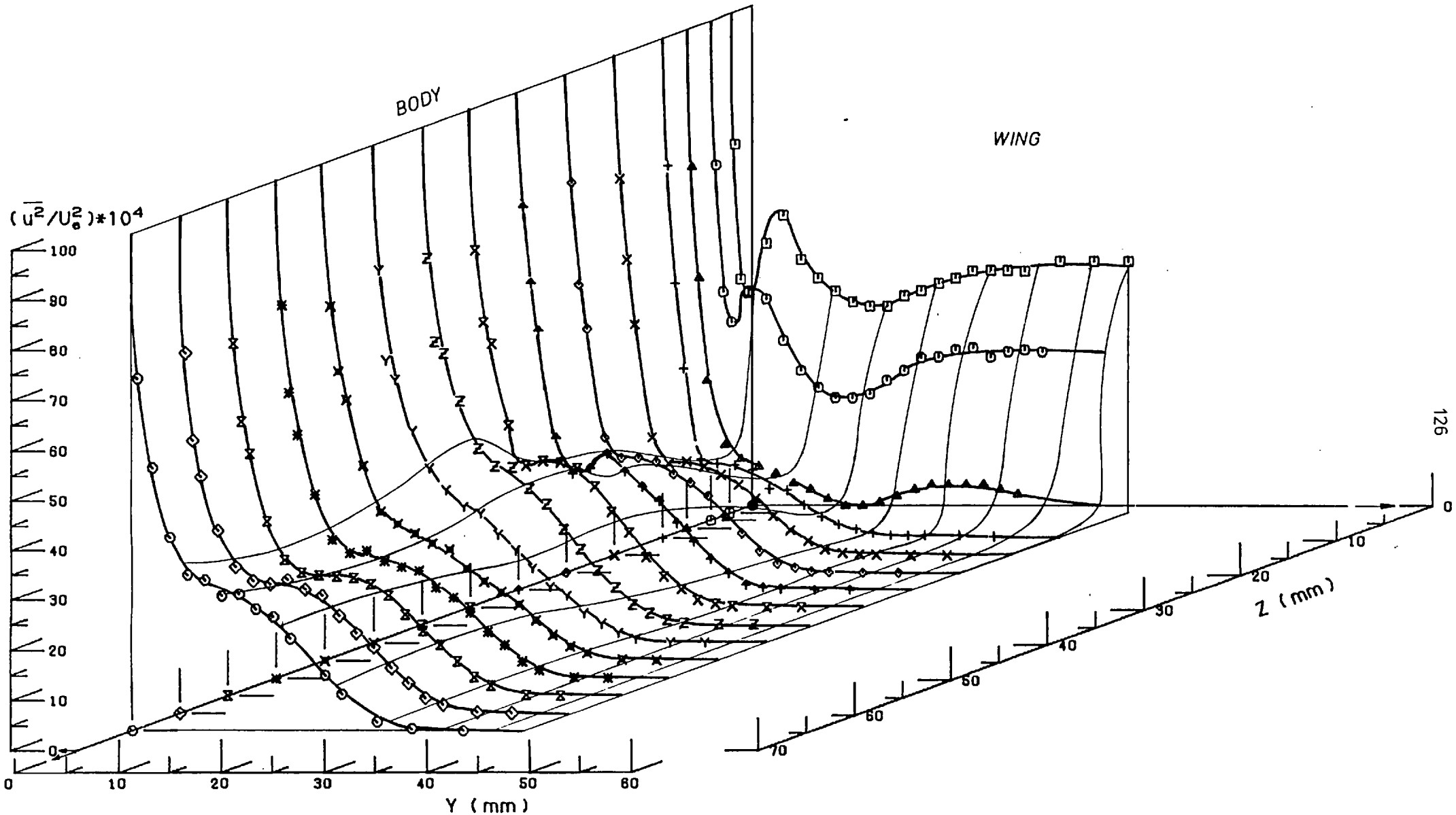

FIG.(3·28) PLOTS OF $(\overline{u^2}/U_e^2)*10^4$ AT STATION 2 (X= 167·6 mm)

Results of U-Wire

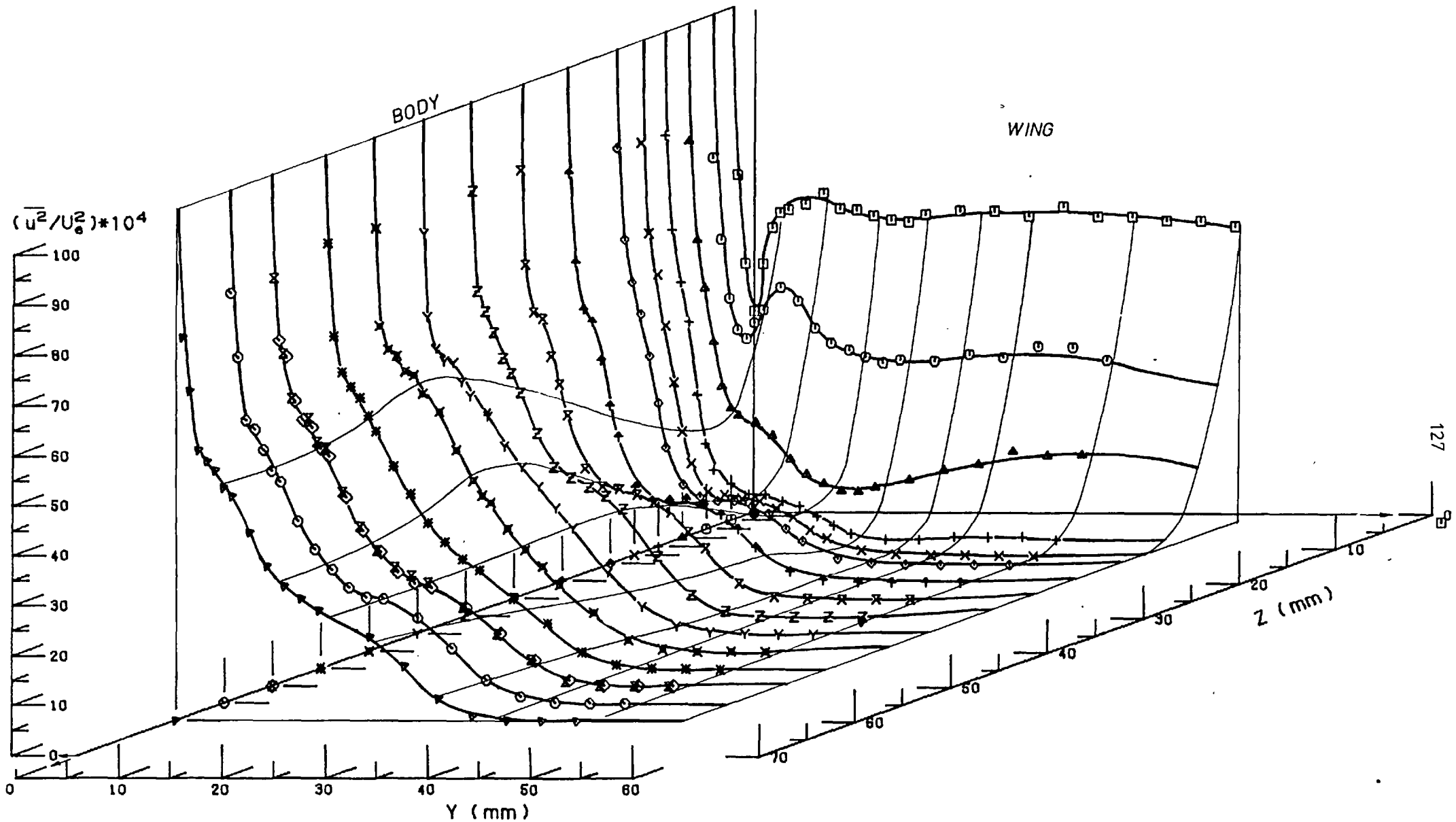

FIG.(3·29) PLOTS OF $(\overline{u^2}/U_e^2)*10^4$ AT STATION 3 (X= 320 mm)

Results of U-Wire

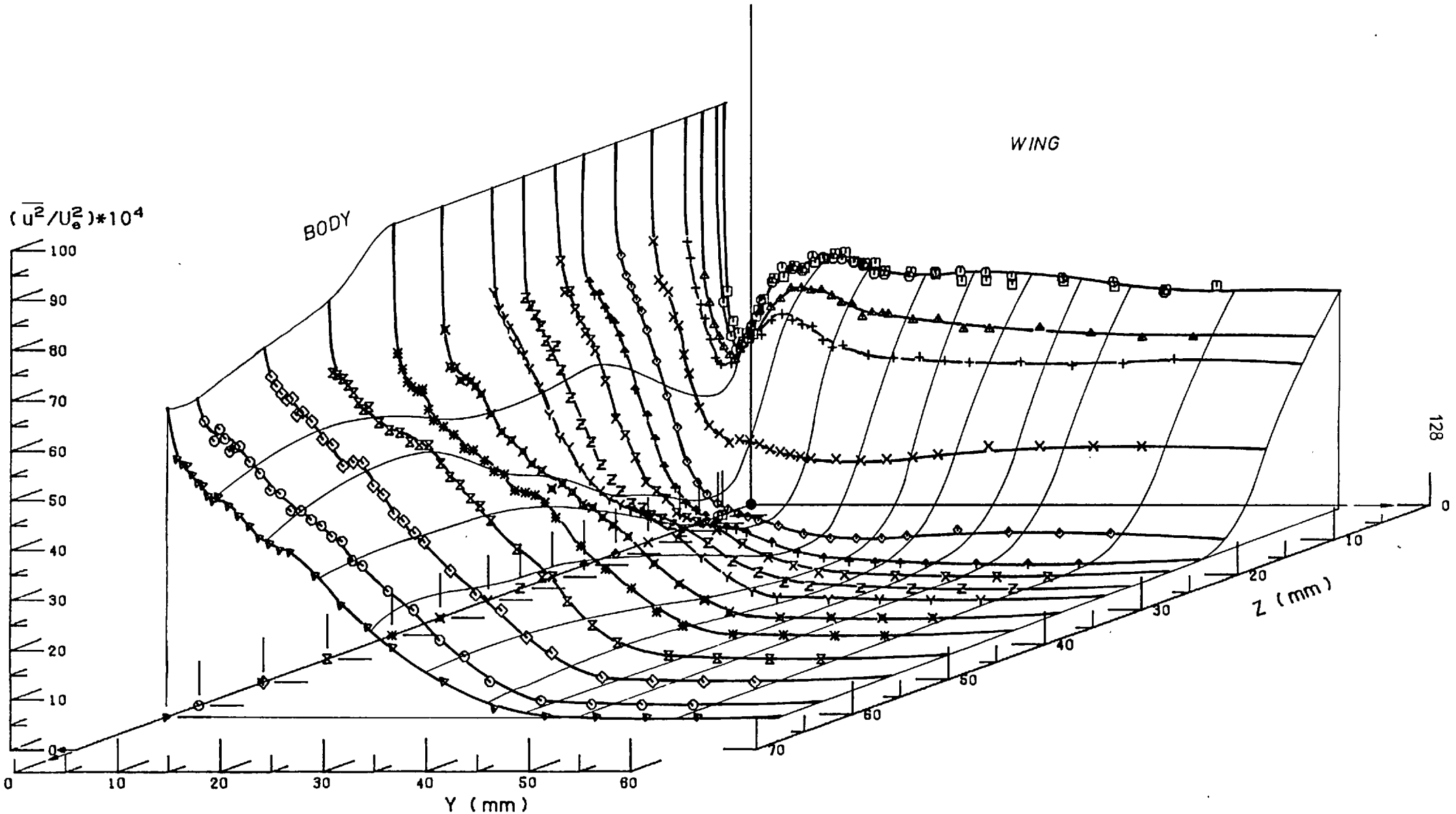

FIG.(3·30) PLOTS OF $(\overline{u^2}/U_e^2)*10^4$ AT STATION 5 (X=624·8 mm)

Results of U-Wire

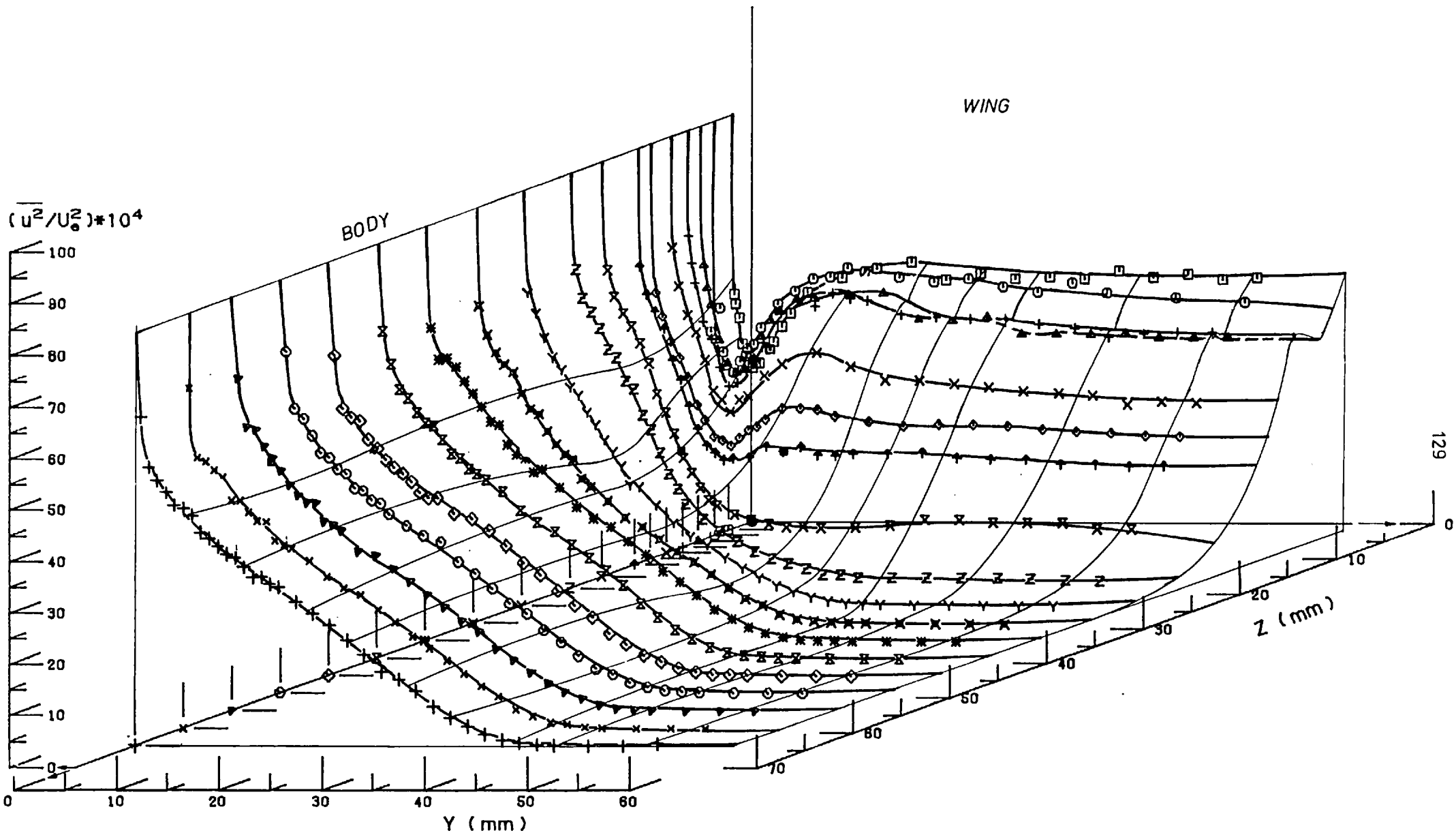

FIG.(3·31) PLOTS OF $(\overline{u^2}/U_e^2)*10^4$ AT STATION 7 (X= 929.6mm)

Results of U-Wire

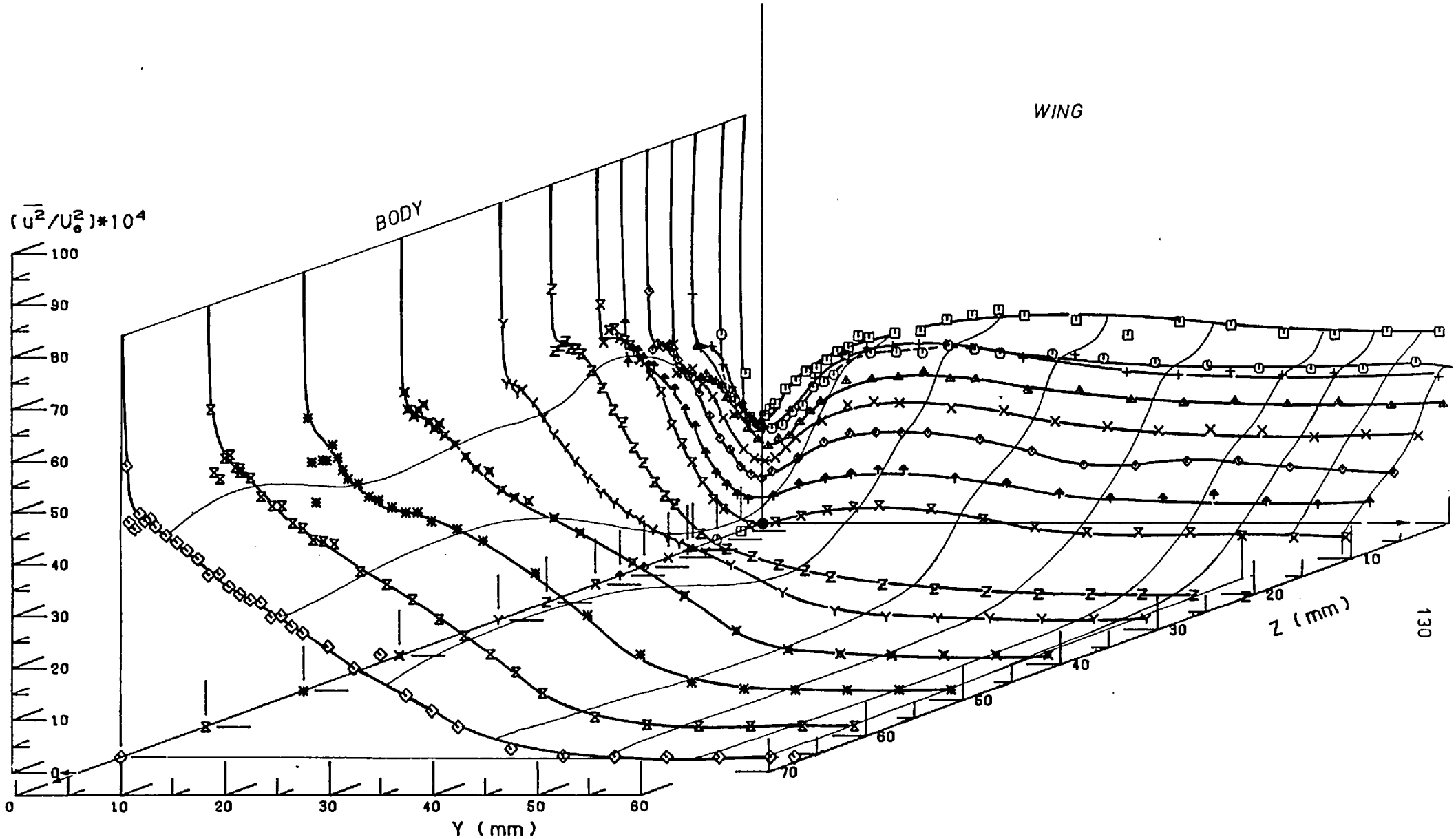

FIG.(3·32) PLOTS OF $(\overline{u^2}/U_e^2)*10^4$ AT STATION 9 (X=1234.3mm)
Results of U-Wire

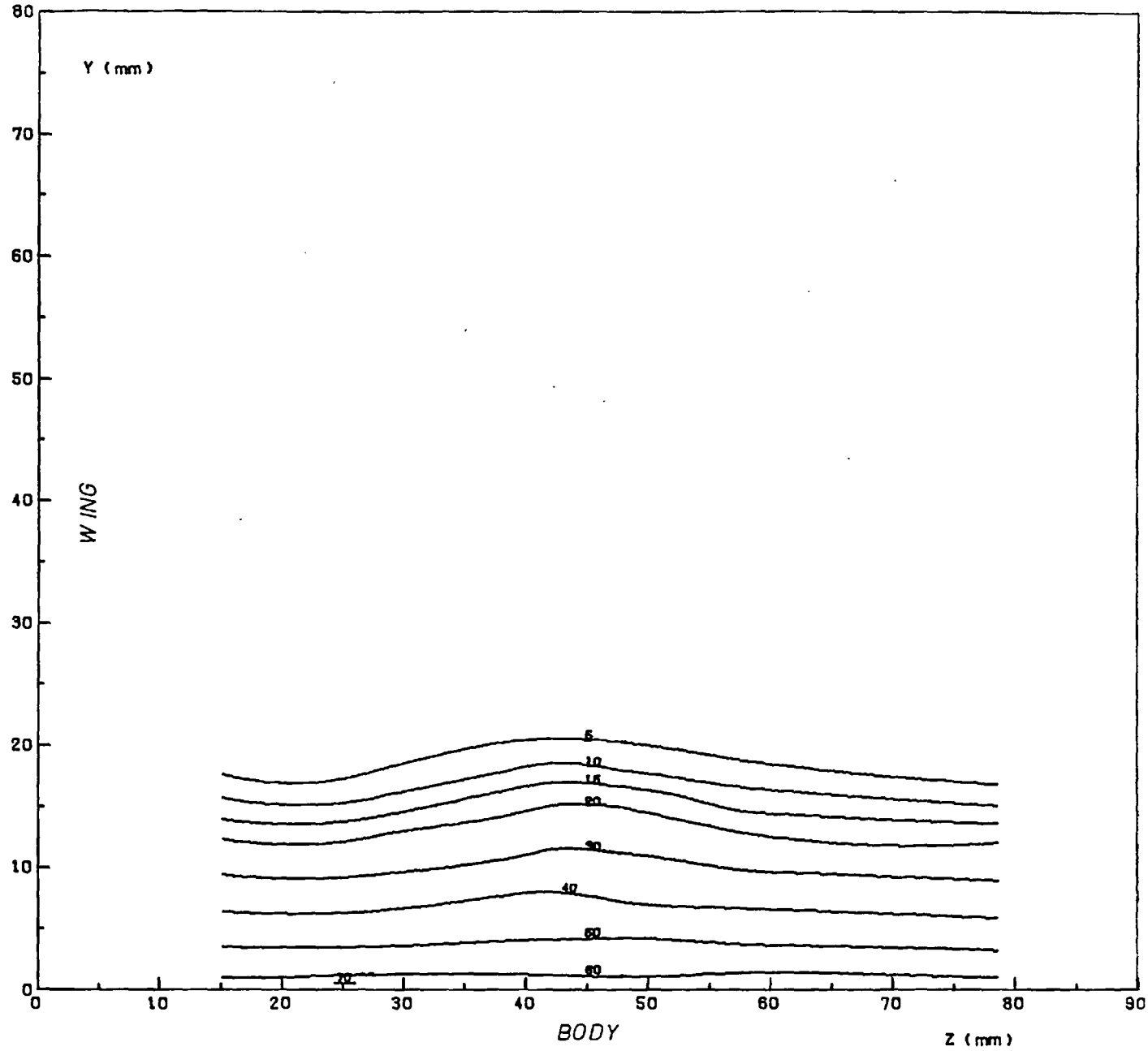

FIG.(3·33) CONTOUR MAP OF $(\overline{u^2}/U_e^2)*10^4$
AT AXIAL STATION NO. -1 (X =-137.2 mm)
Results of U-Wire

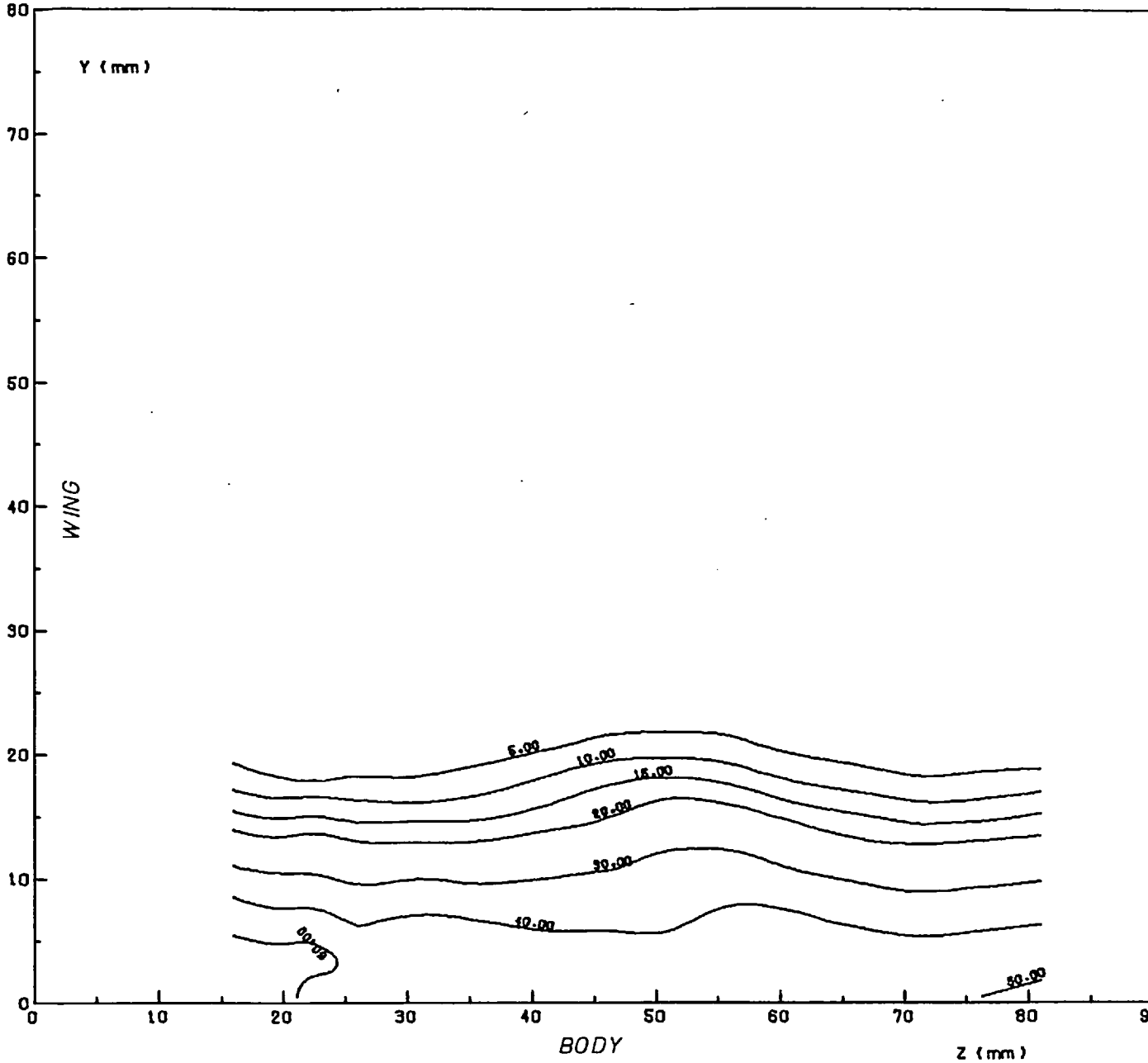

FIG.(3.34) CONTOUR MAP OF $(\overline{u^2}/U_e^2)*10^4$
AT AXIAL STATION NO. 1 (X = 15.2 mm)
Results of U-Wire

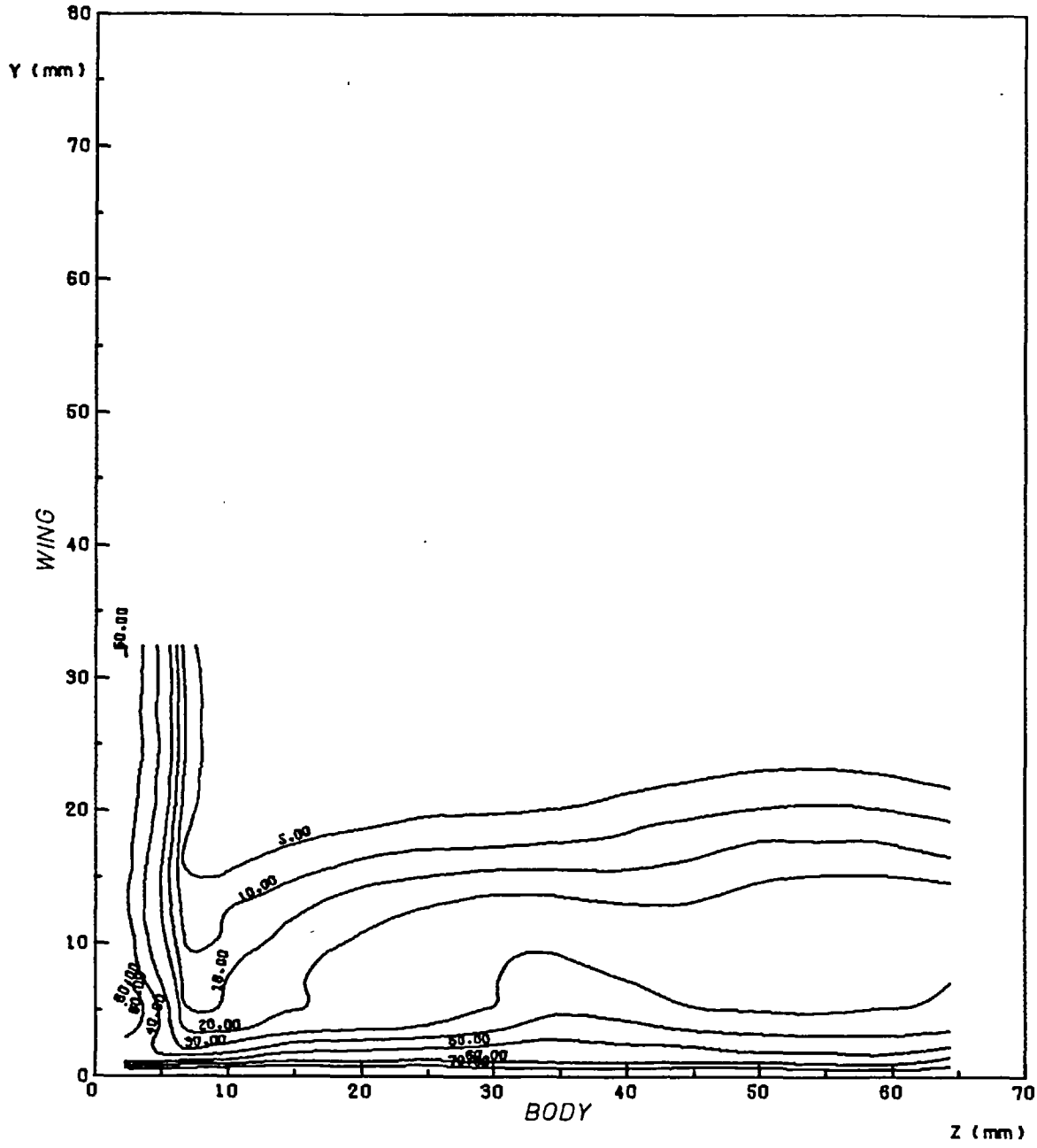

FIG. [3.35] CONTOUR MAP OF $(\overline{u^2}/U_e^2)*10^4$
AT AXIAL LOCATION NO. 2 (X = 167.6 mm)
Results of U-Wire

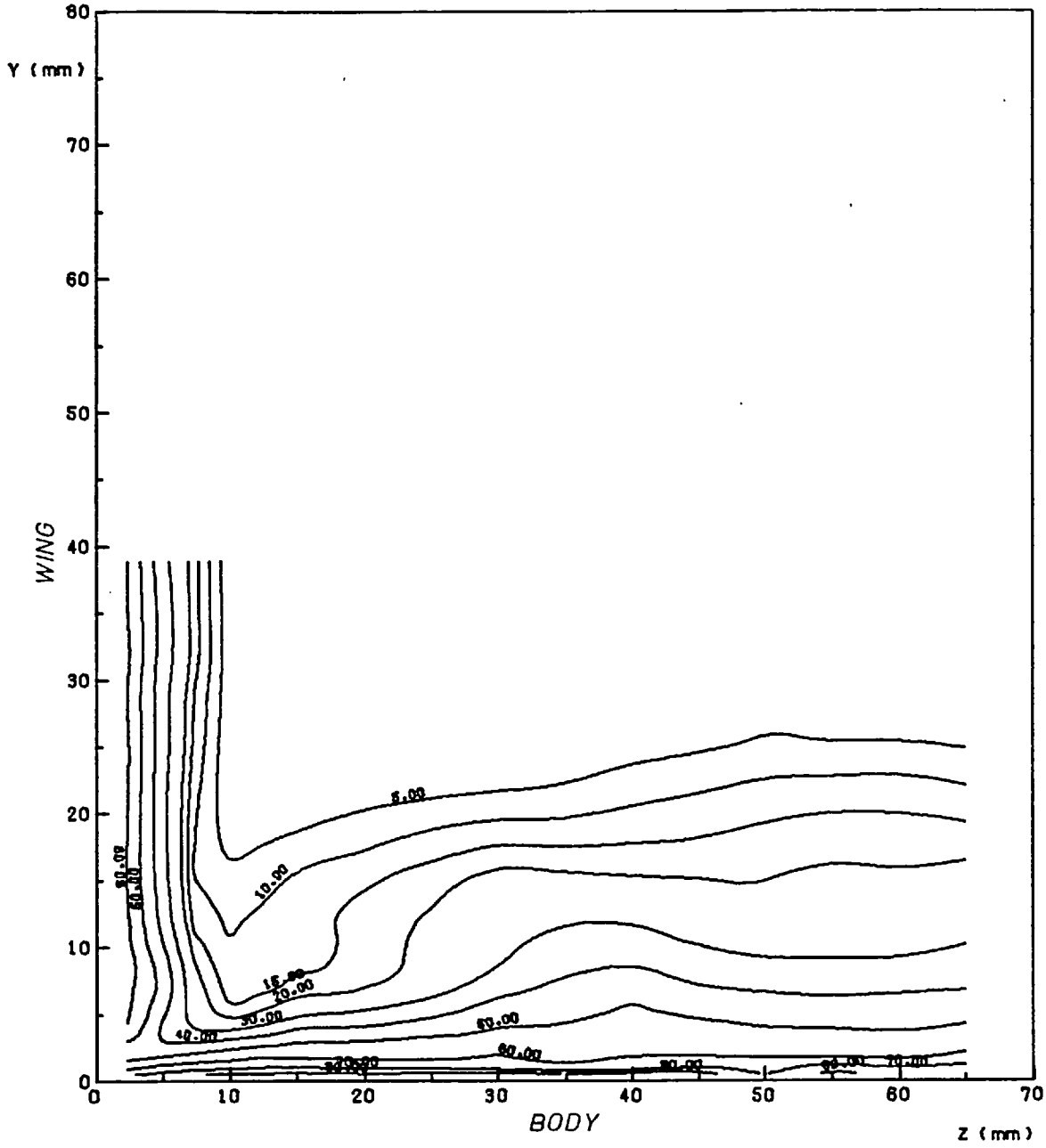

FIG.(3.36) CONTOUR MAP OF $(\overline{u^2}/U_e^2)*10^4$
AT AXIAL STATION NO. 3 (X = 320.0 mm)

Results of U-Wire

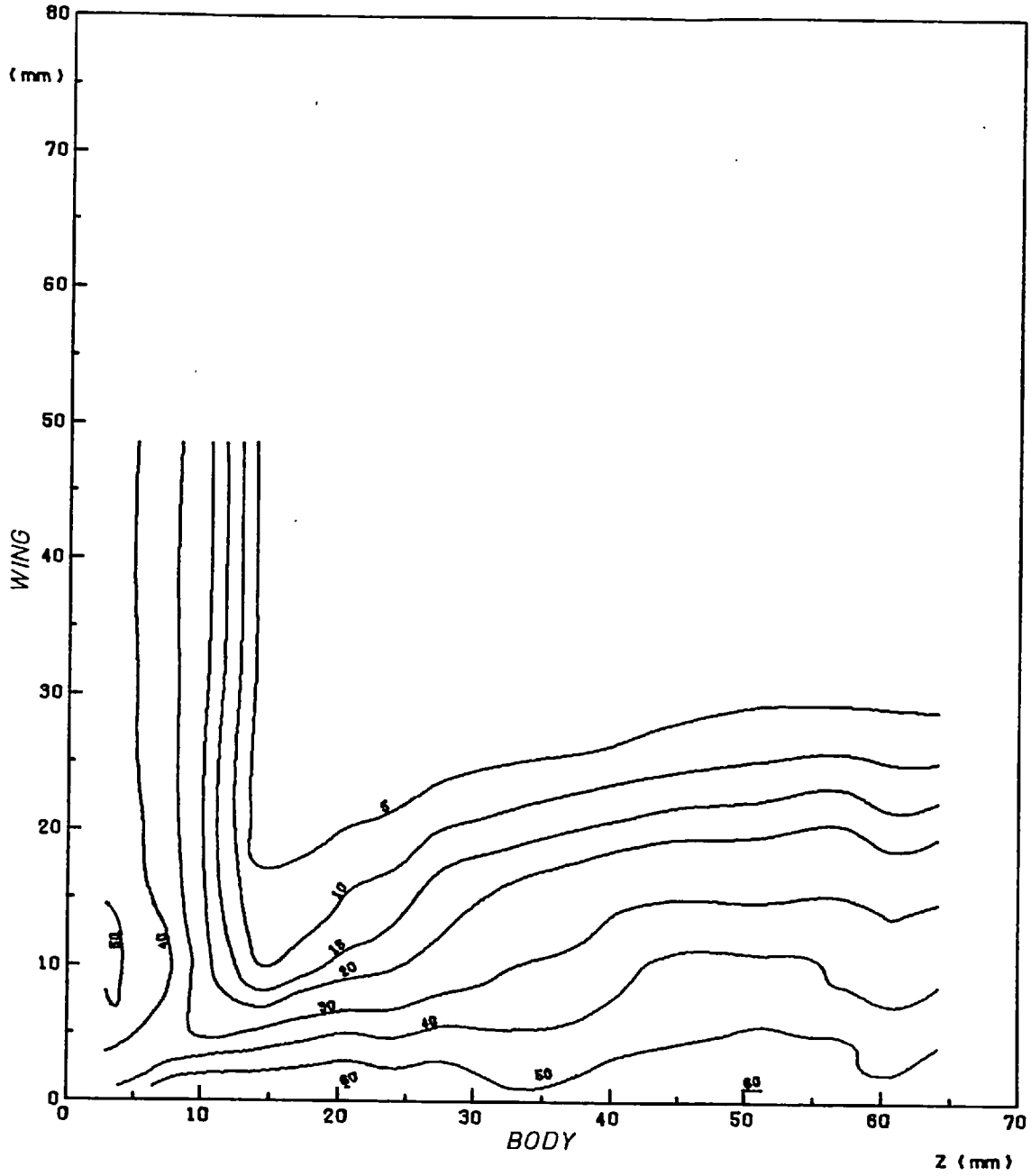

FIG.(3.37) CONTOUR MAP OF $(\overline{u^2}/U_e^2)*10^4$
AT AXIAL STATION NO. 5 (X = 624.8 mm)
Results of U-Wire

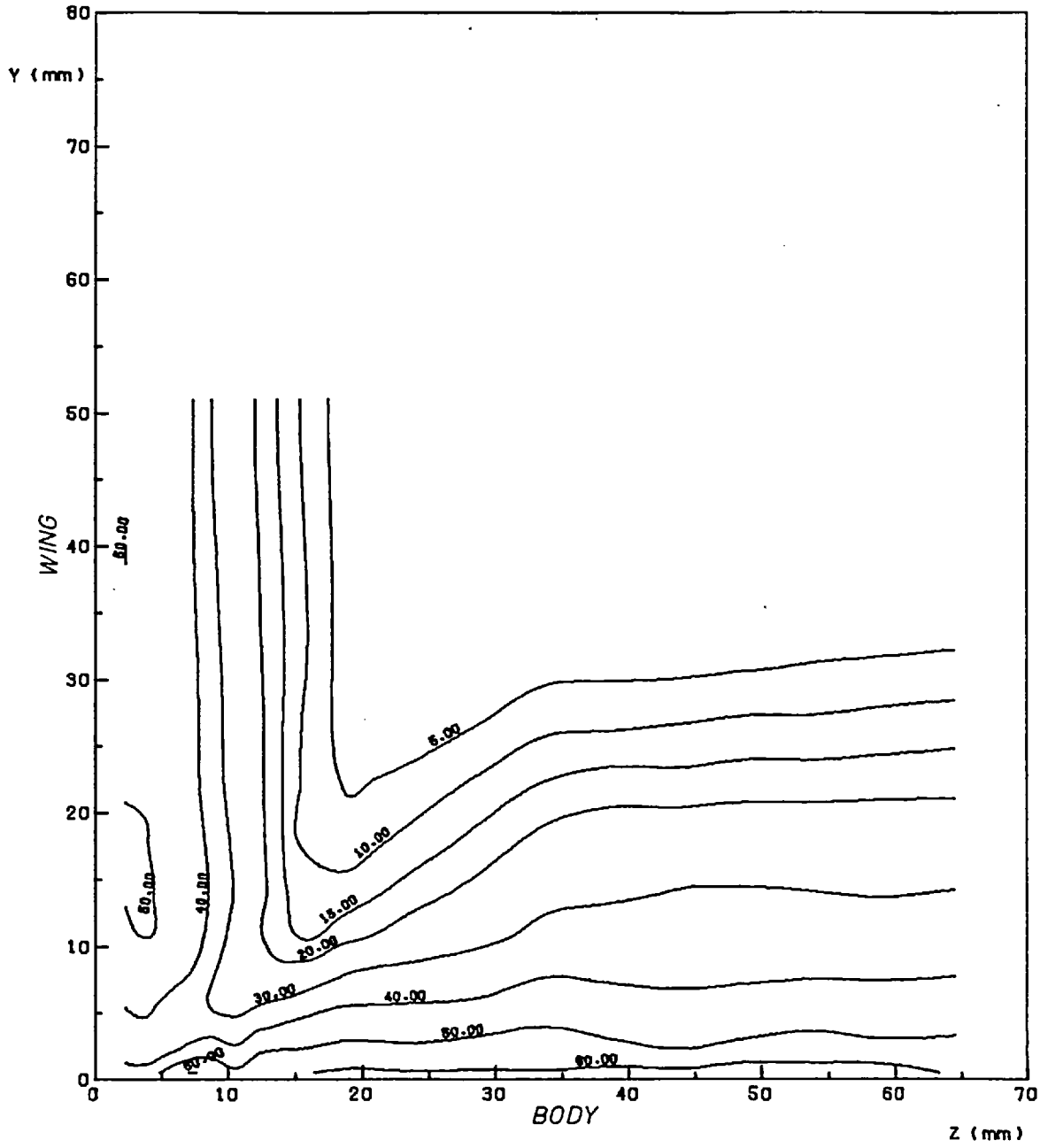

FIG.(3·38) CONTOUR MAP OF $(\overline{u^2}/U_e^2)*10^4$
AT AXIAL STATION NO. 7 (X = 929.6 mm)
Results of U-Wire

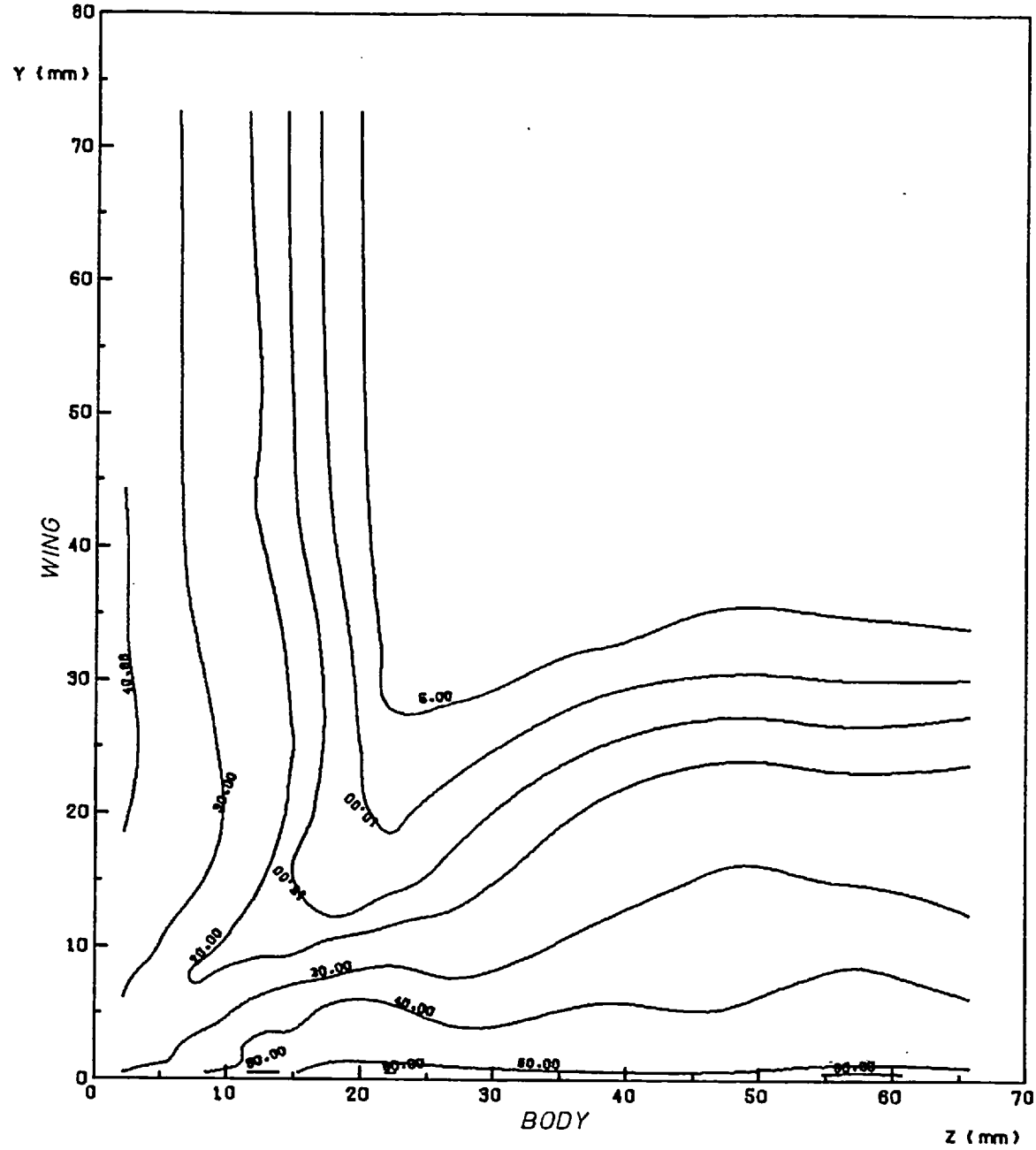

FIG.(3·39) CONTOUR MAP OF $(\overline{u^2}/U_e^2)*10^4$
AT AXIAL STATION NO. 9 (X =1234.3 mm)
Results of U-Wire

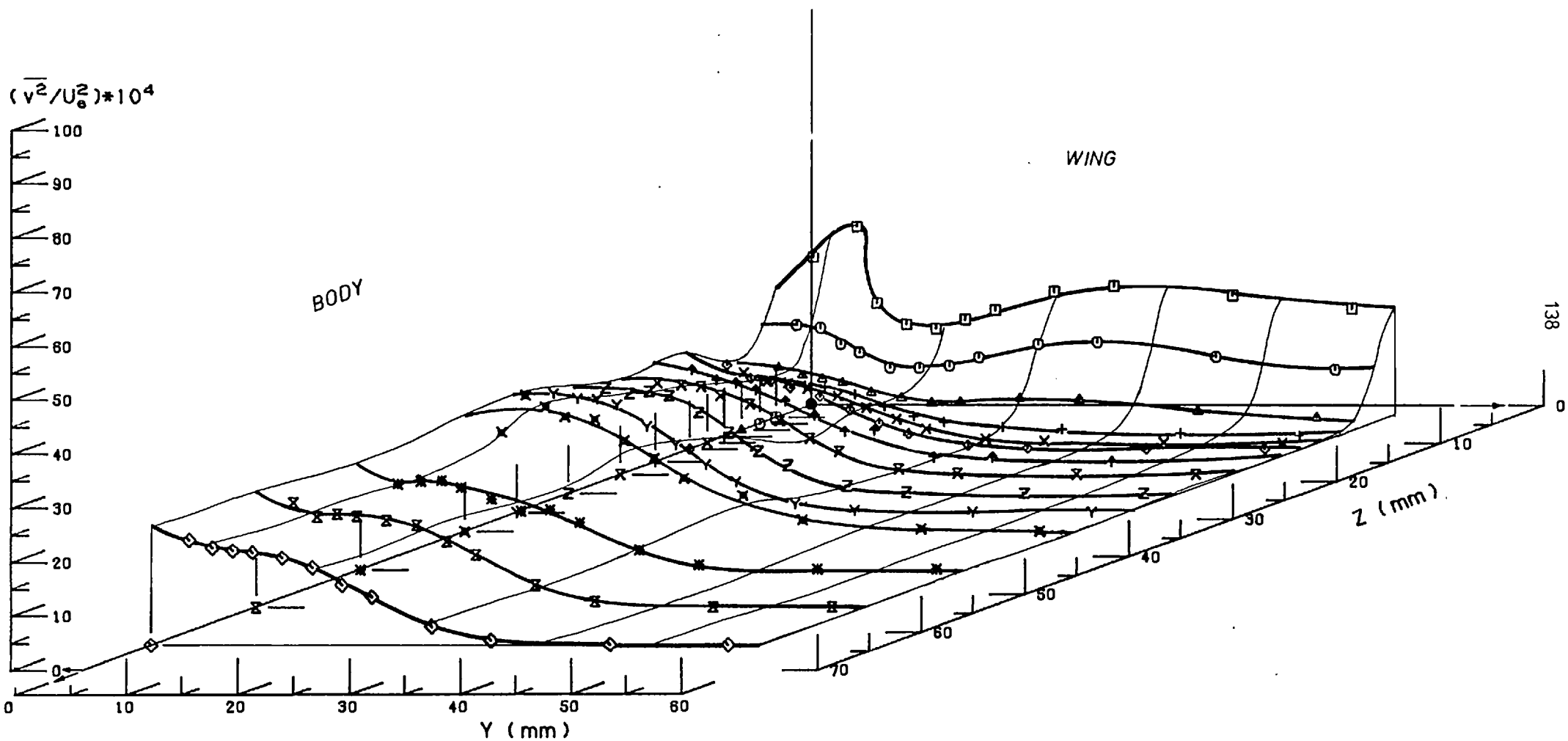

FIG.(3.40) PLOTS OF $(\overline{v^2}/U_e^2)*10^4$ AT STATION 2 (X=156.6 mm)

Results of Cross Wire in Vertical (U-V) Position

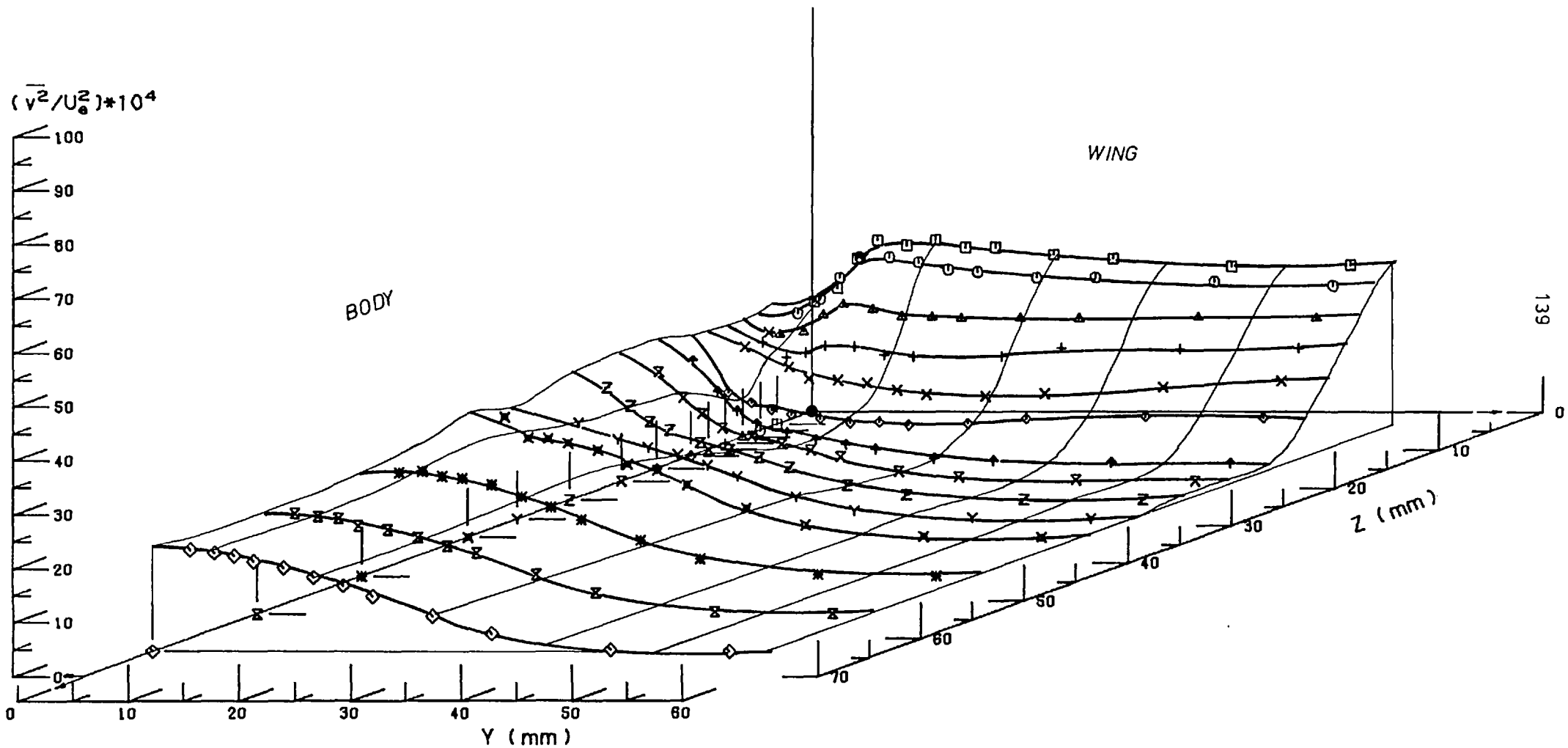

FIG.(3.41) PLOTS OF $(\overline{v^2}/U_e^2)*10^4$ AT STATION 5 (X=613.6 mm)

Results of Cross Wire in Vertical (U-V) Position

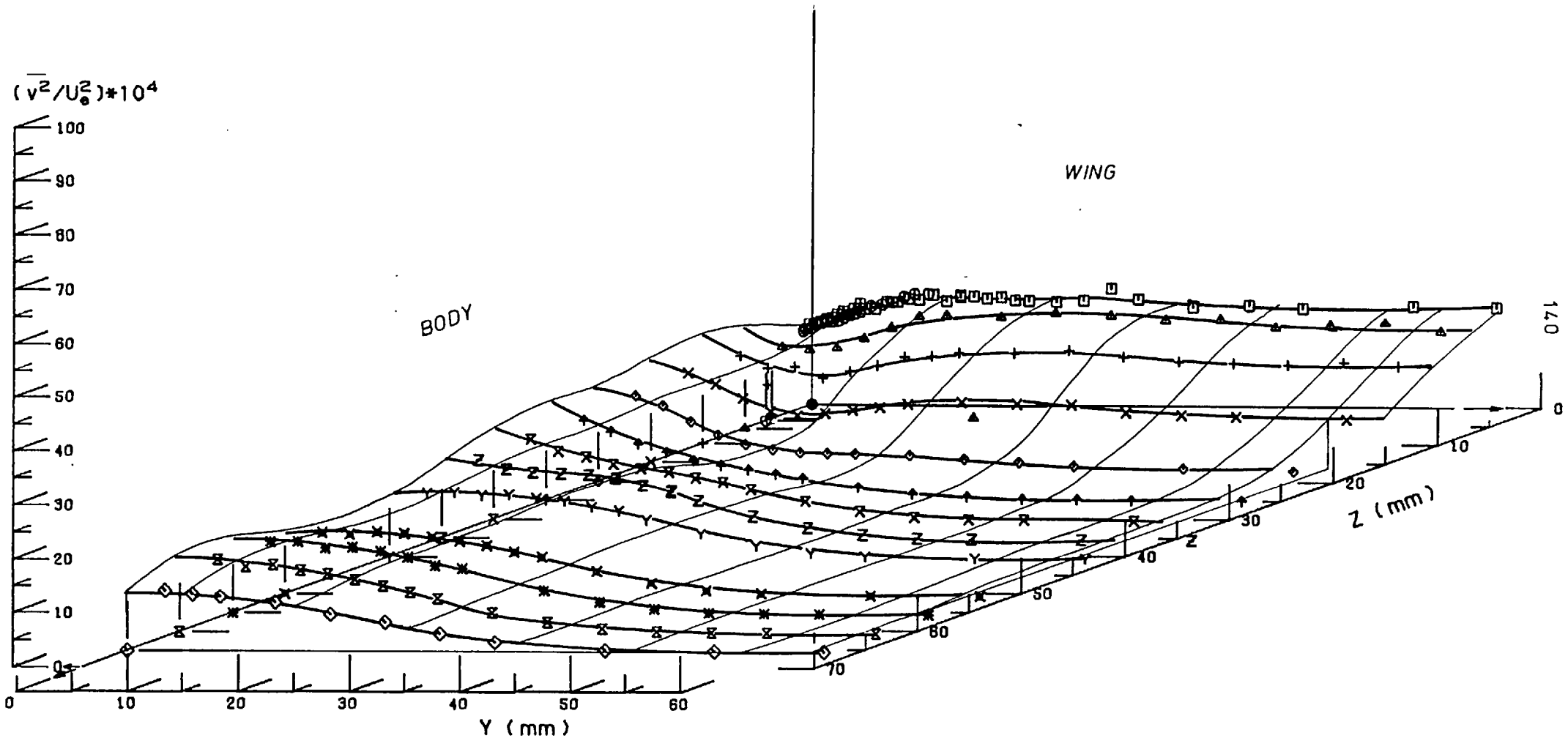

FIG.(3.42) PLOTS OF $(\overline{v^2}/U_e^2)*10^4$ AT STATION 9 (X=1223.4 mm)

Results of Cross Wire in Vertical (U-V) Position

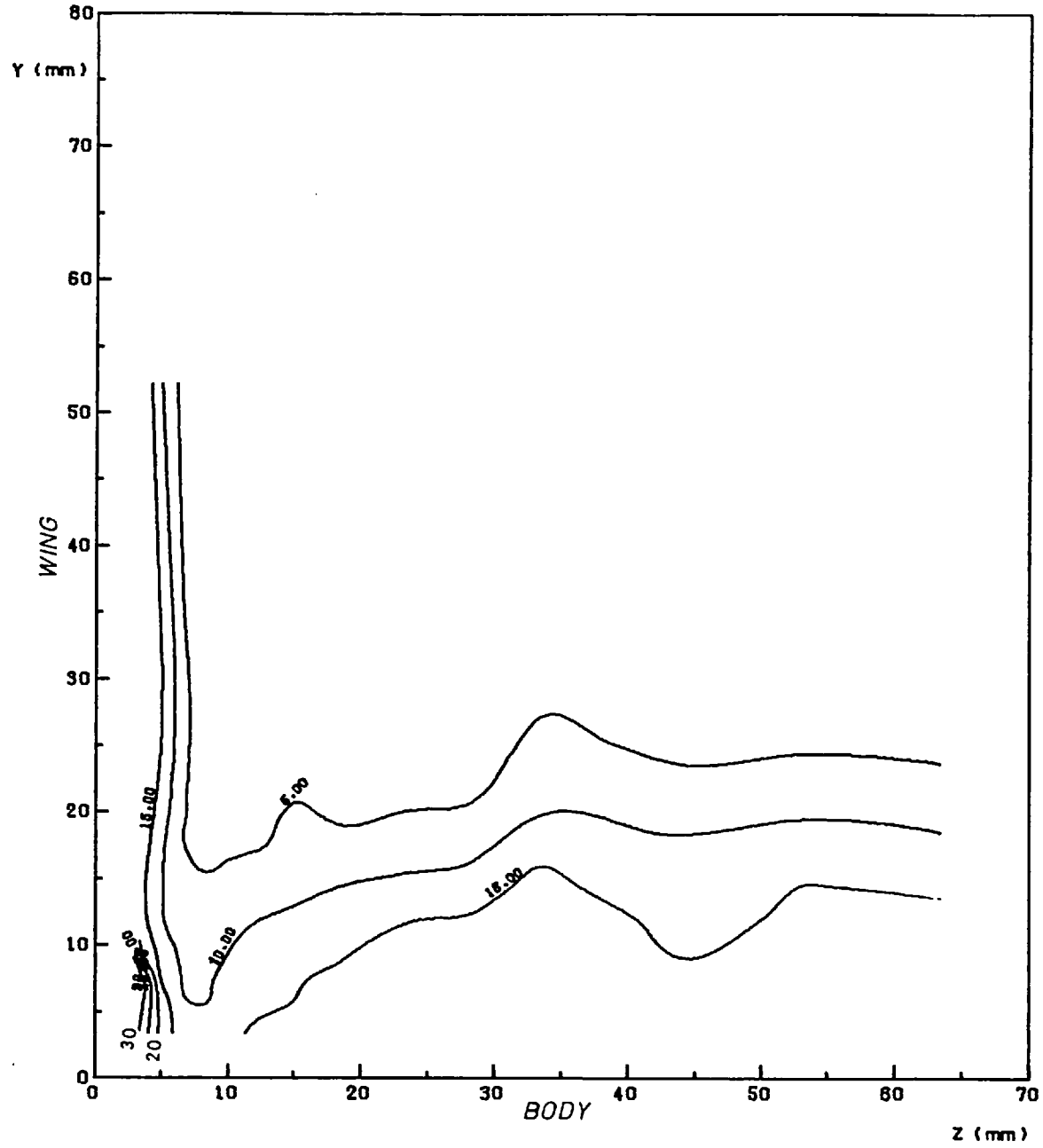

FIG.(3.43) CONTOUR MAP OF $(\overline{v^2}/U_e^2)*10^4$
AT AXIAL STATION NO. 2 (X = 156.6 mm)
Results of Cross Wire in Vertical (U-V) Position

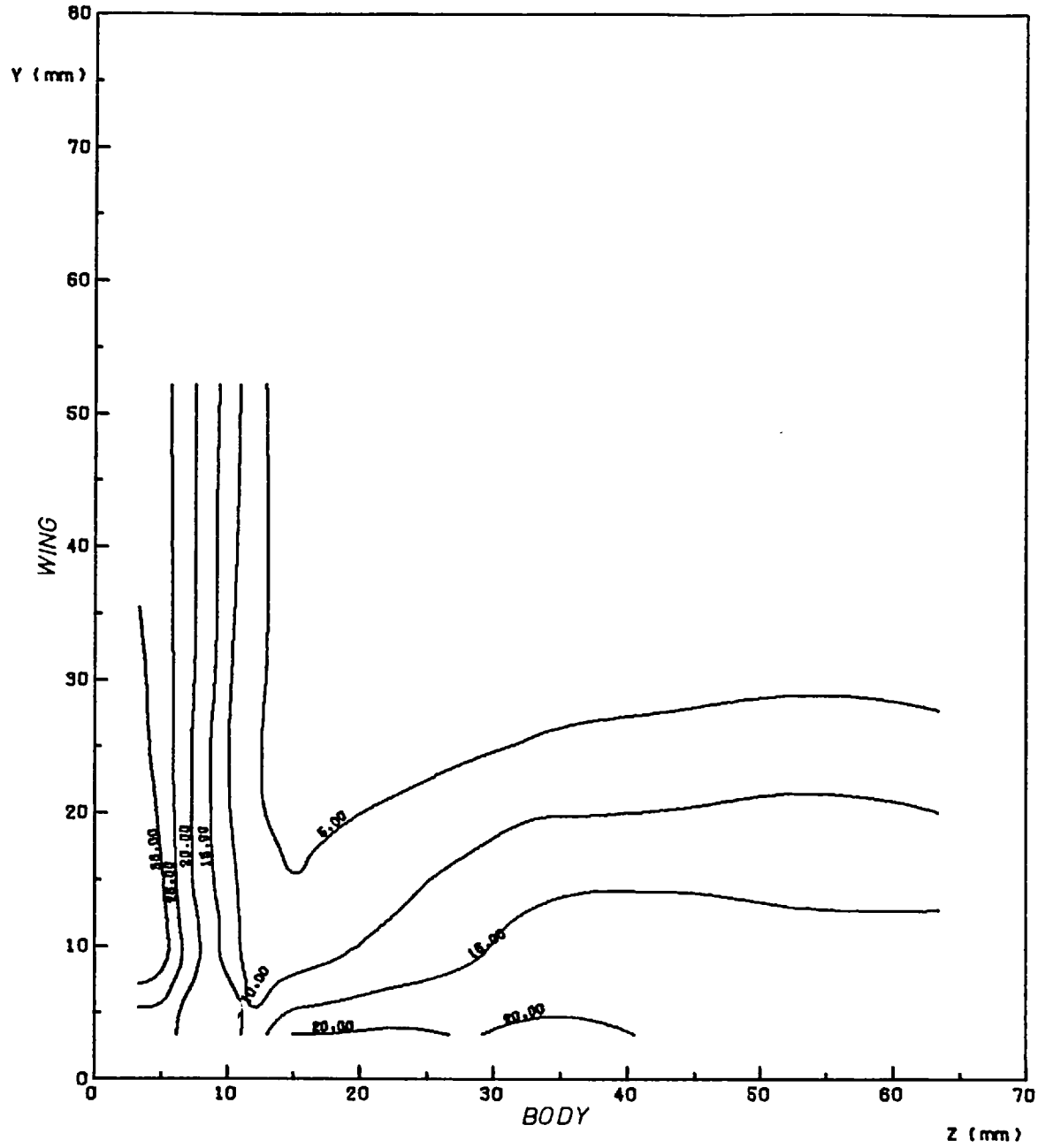

FIG.(3.44) CONTOUR MAP OF $(\overline{v^2}/U_e^2)*10^4$
AT AXIAL STATION NO. 5 (X = 613.8 mm)
Results of Cross Wire in Vertical (U-V) Position

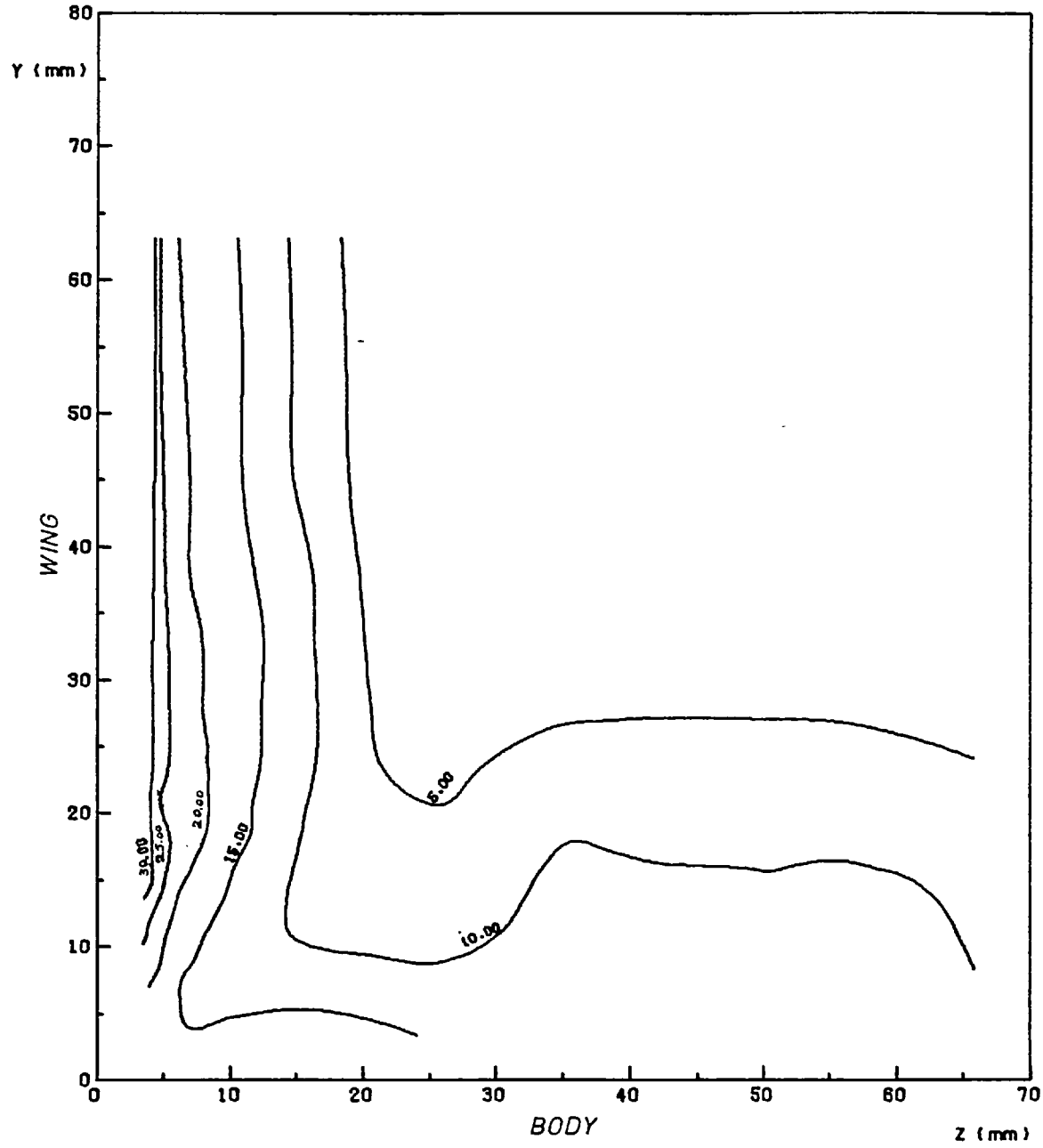

FIG.(3.45) CONTOUR MAP OF $(\overline{v^2}/U_e^2)*10^4$
AT AXIAL STATION NO. 9 (X = 1223.4 mm)
Results of Cross Wire in Vertical (U-V) Position

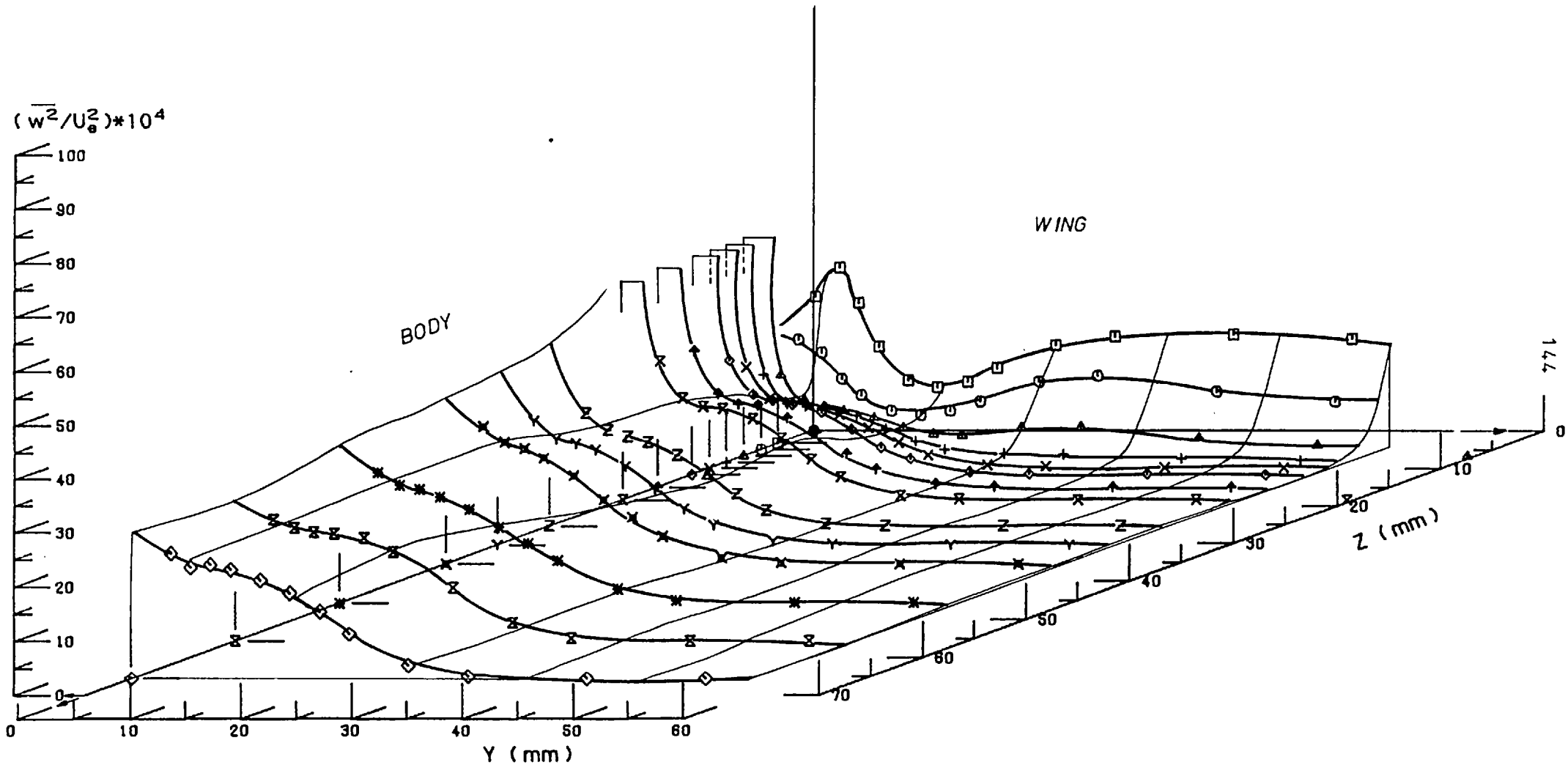

FIG.(3·46) PLOTS OF $(\overline{w^2}/U_e^2)*10^4$ AT STATION 2 (X=156.6 mm)

Results of Cross Wire in Horizontal (U-W) Position

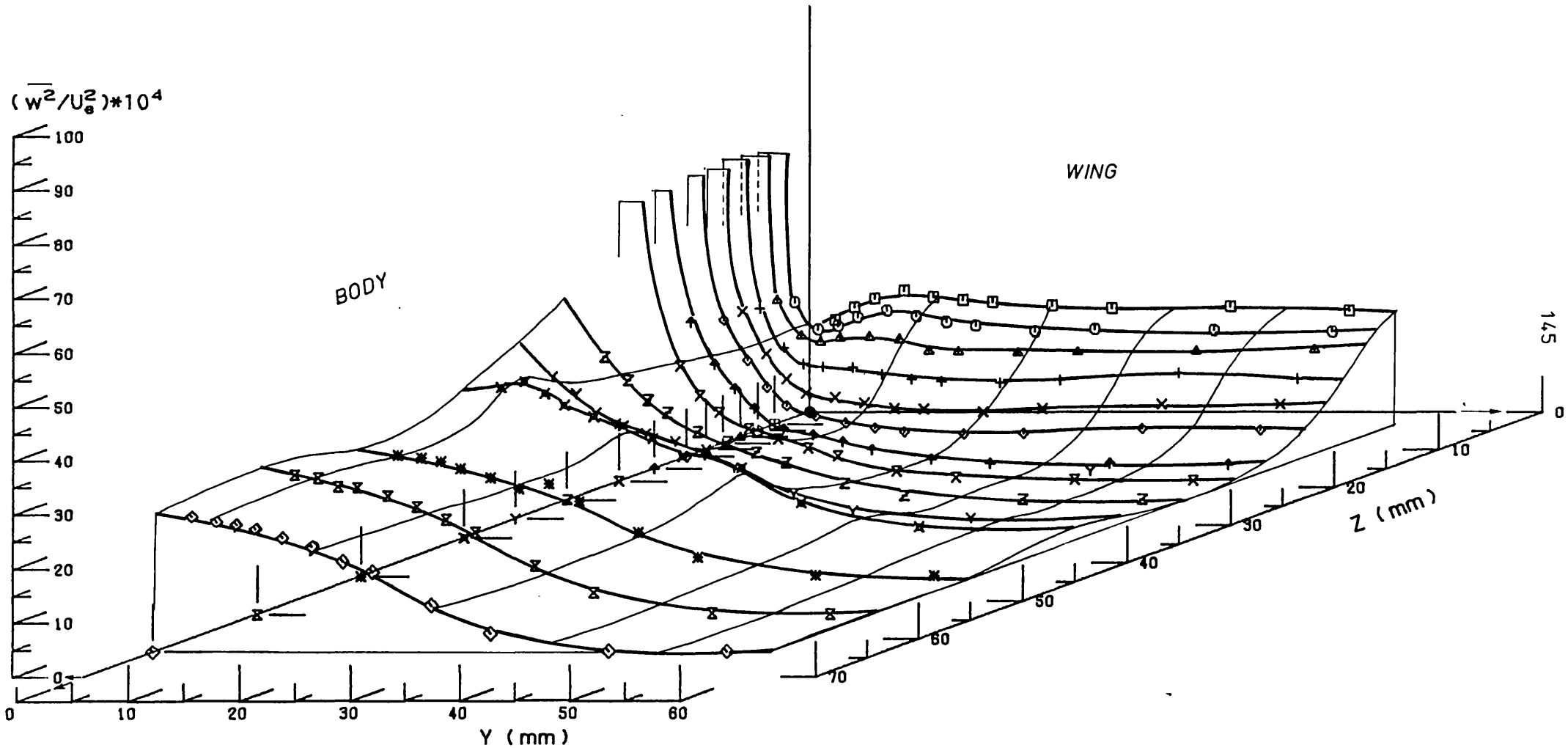

FIG.(3.47) PLOTS OF $(\overline{w^2}/U_e^2)*10^4$ AT STATION 5 (X=613.8 mm)

Results of Cross Wire in Horizontal (U-W) Position

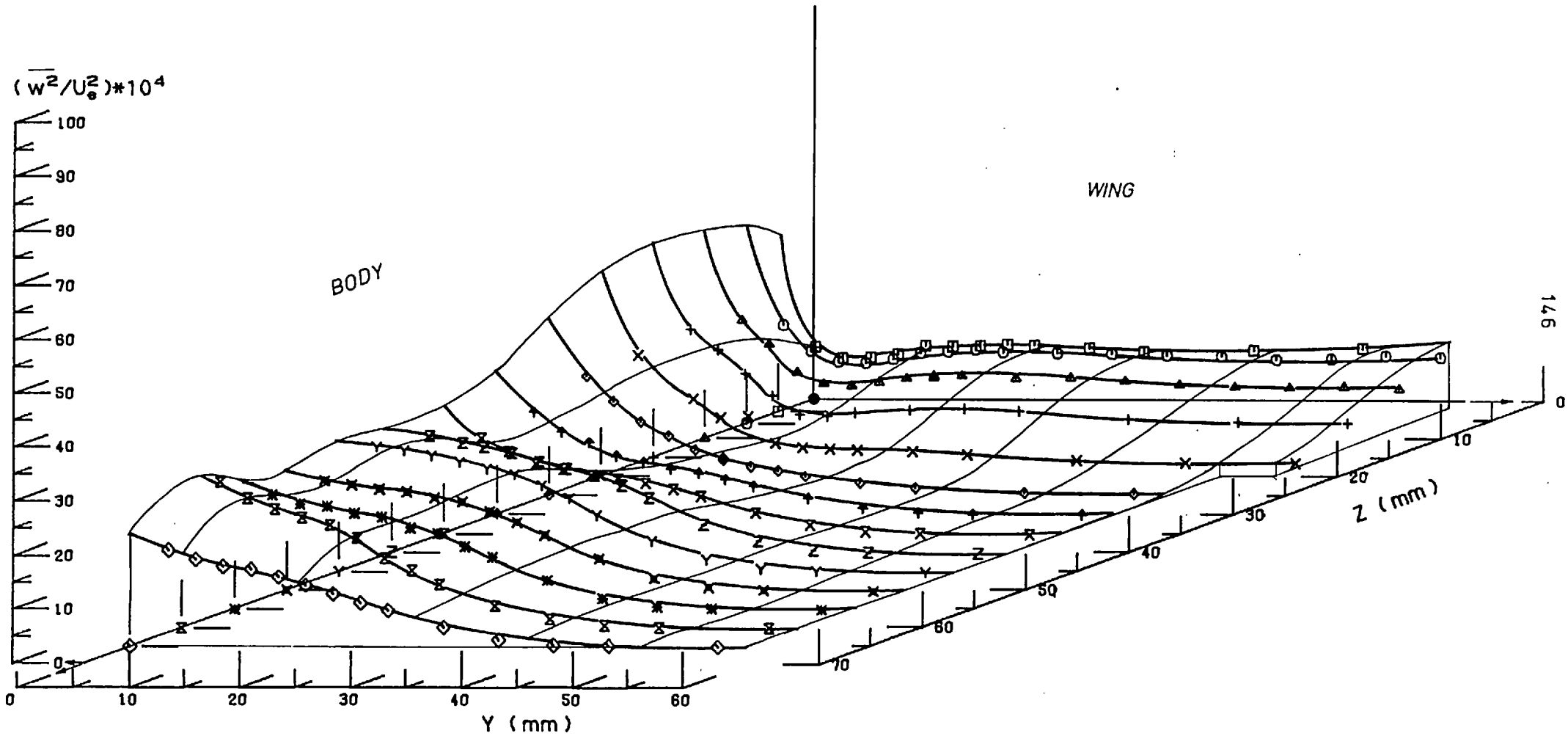

FIG.(3.48) PLOTS OF $(\overline{w^2}/U_e^2)*10^4$ AT STATION 9 (X=1223.4 mm)

Results of Cross Wire in Horizontal (U-W) Position

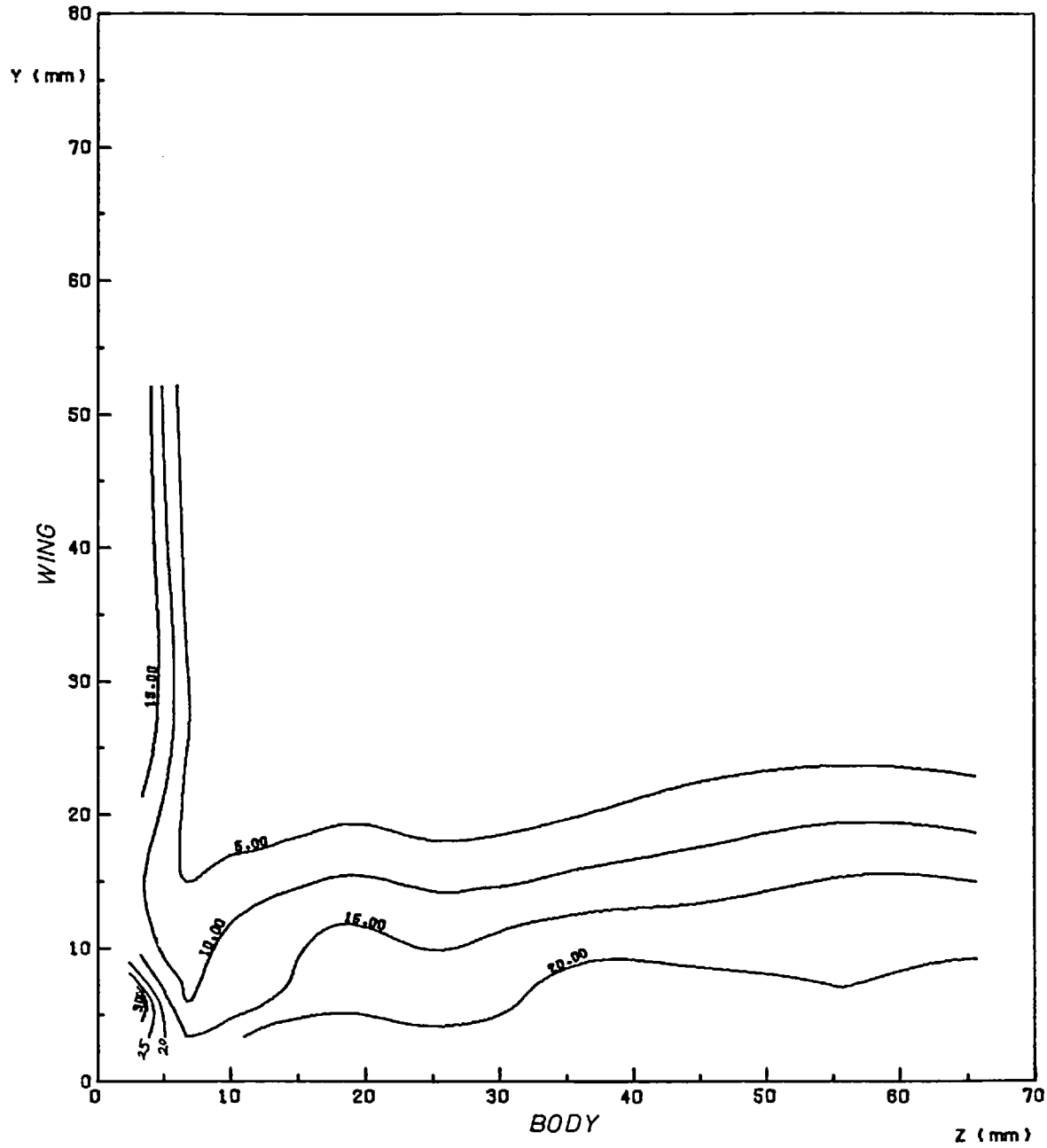

FIG.(3.49) CONTOUR MAP OF $(\overline{w^2}/U_e^2)*10^4$
AT AXIAL STATION NO. 2 (X = 156.6 mm)
Results of Cross Wire in Horizontal (U-W) Position

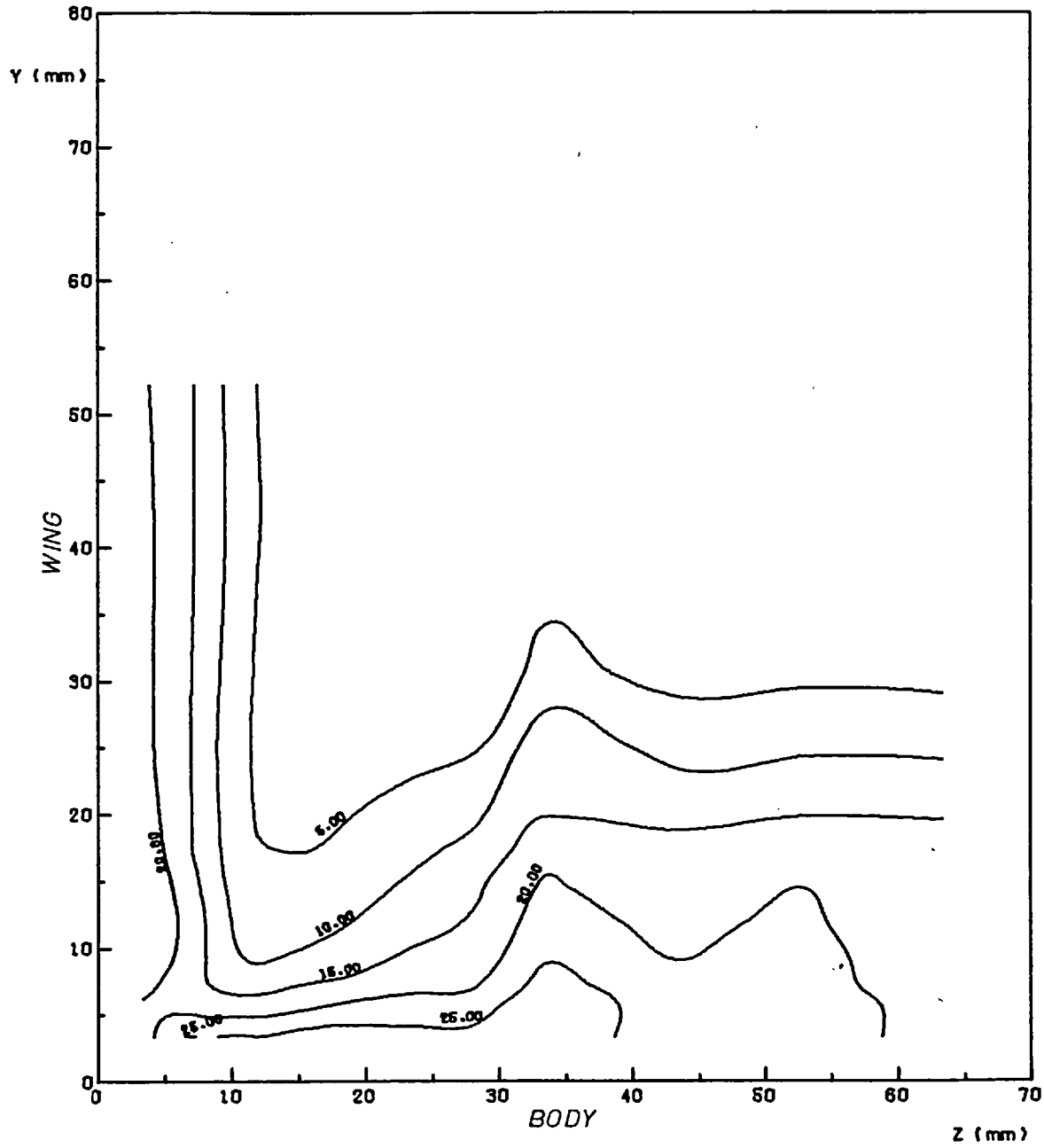

FIG.(3.50) CONTOUR MAP OF $(\overline{w^2}/U_0^2)*10^4$
AT AXIAL STATION NO. 5 (X = 613.8 mm)
Results of Cross Wire in Horizontal (U-W) Position

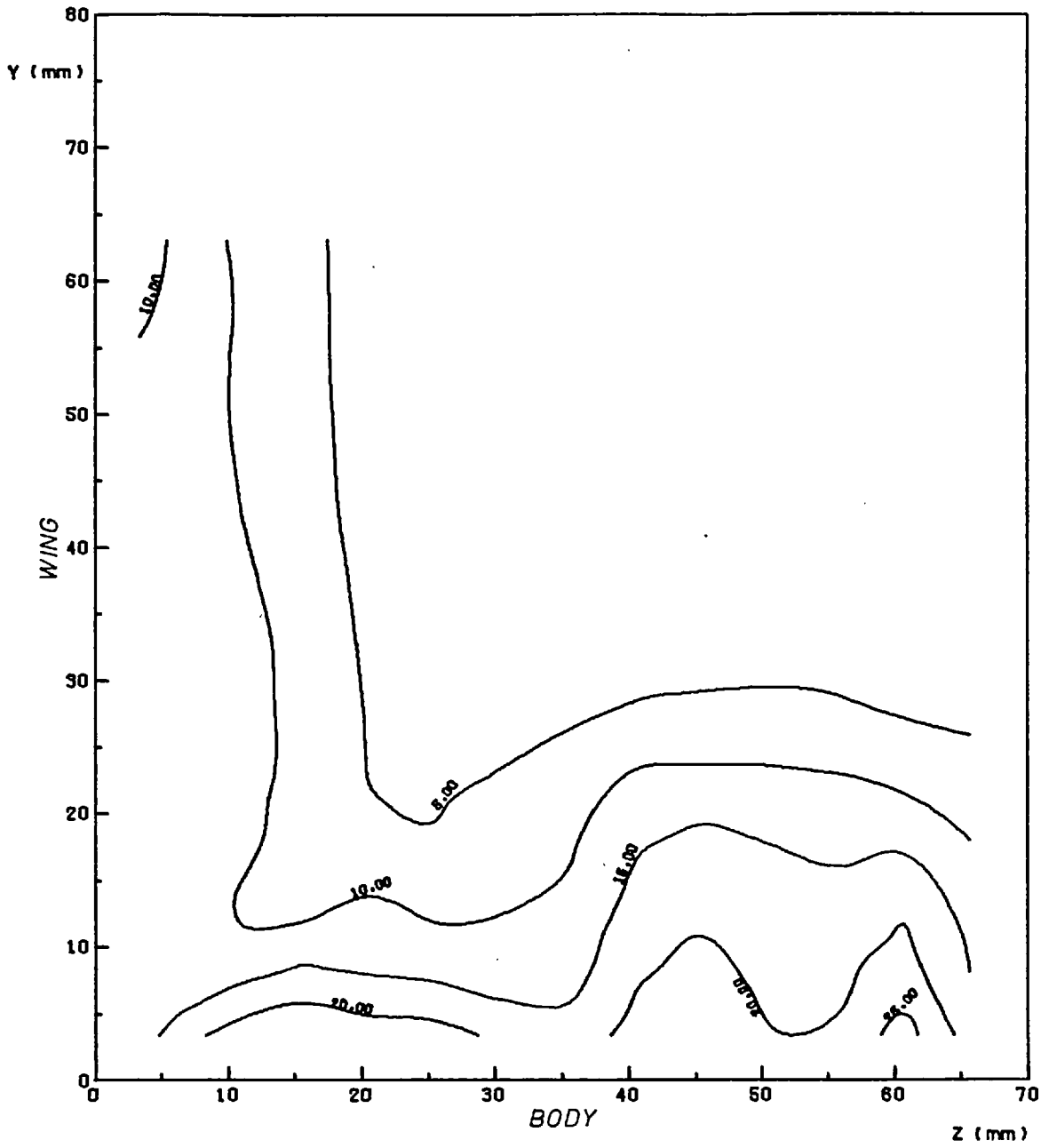

FIG.(3·51) CONTOUR MAP OF $(\overline{w^2}/U_e^2)*10^4$
AT AXIAL STATION NO. 9 (X = 1223.4 mm)
Results of Cross Wire in Horizontal (U-W) Position

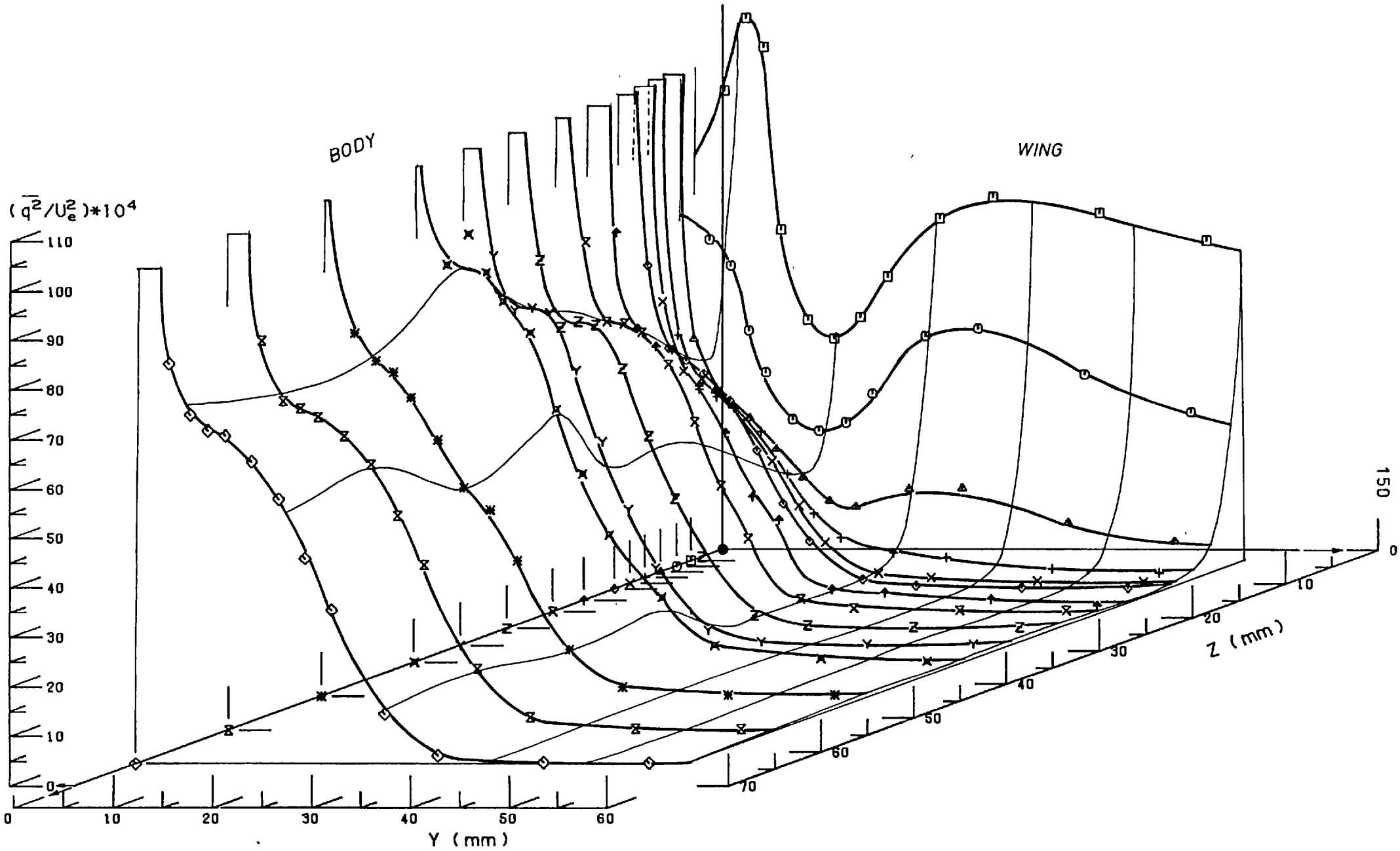

FIG.(3.52) PLOTS OF TURBULENT KINETIC ENERGY $(\overline{q^2}/U_e^2)*10^4$ AT STATION 2 (X= 156.6mm)

Results of Cross Wire

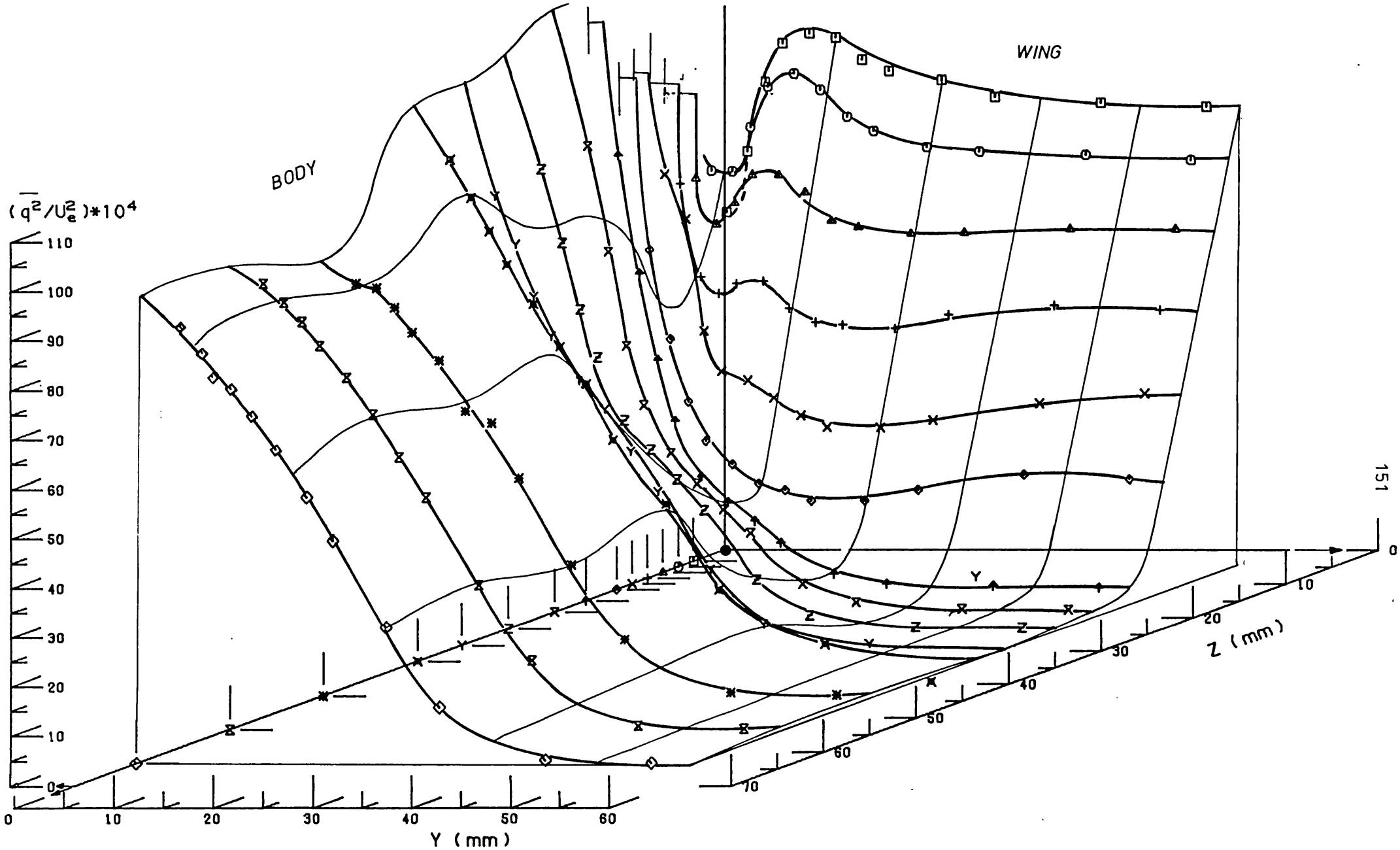

FIG.(3·53) PLOTS OF TURBULENT KINETIC ENERGY $(\overline{q^2}/U_e^2)*10^4$ AT STATION 5 (X= 613.8mm)

Results of Cross Wire

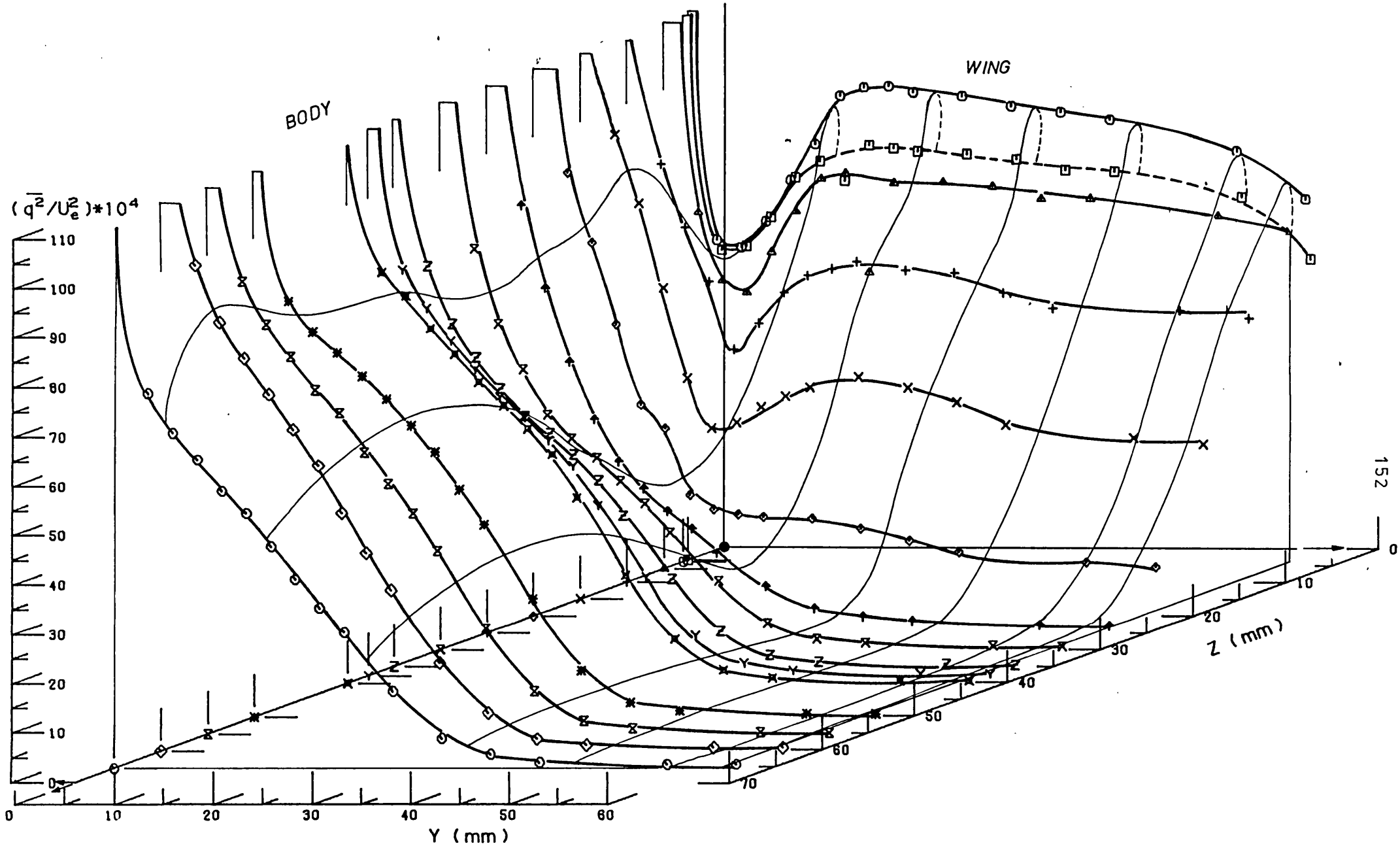

FIG.(3.54) PLOTS OF TURBULENT KINETIC ENERGY $(\overline{q^2}/U_e^2)*10^4$ AT STATION 9 (X=1223.4mm)

Results of Cross Wire

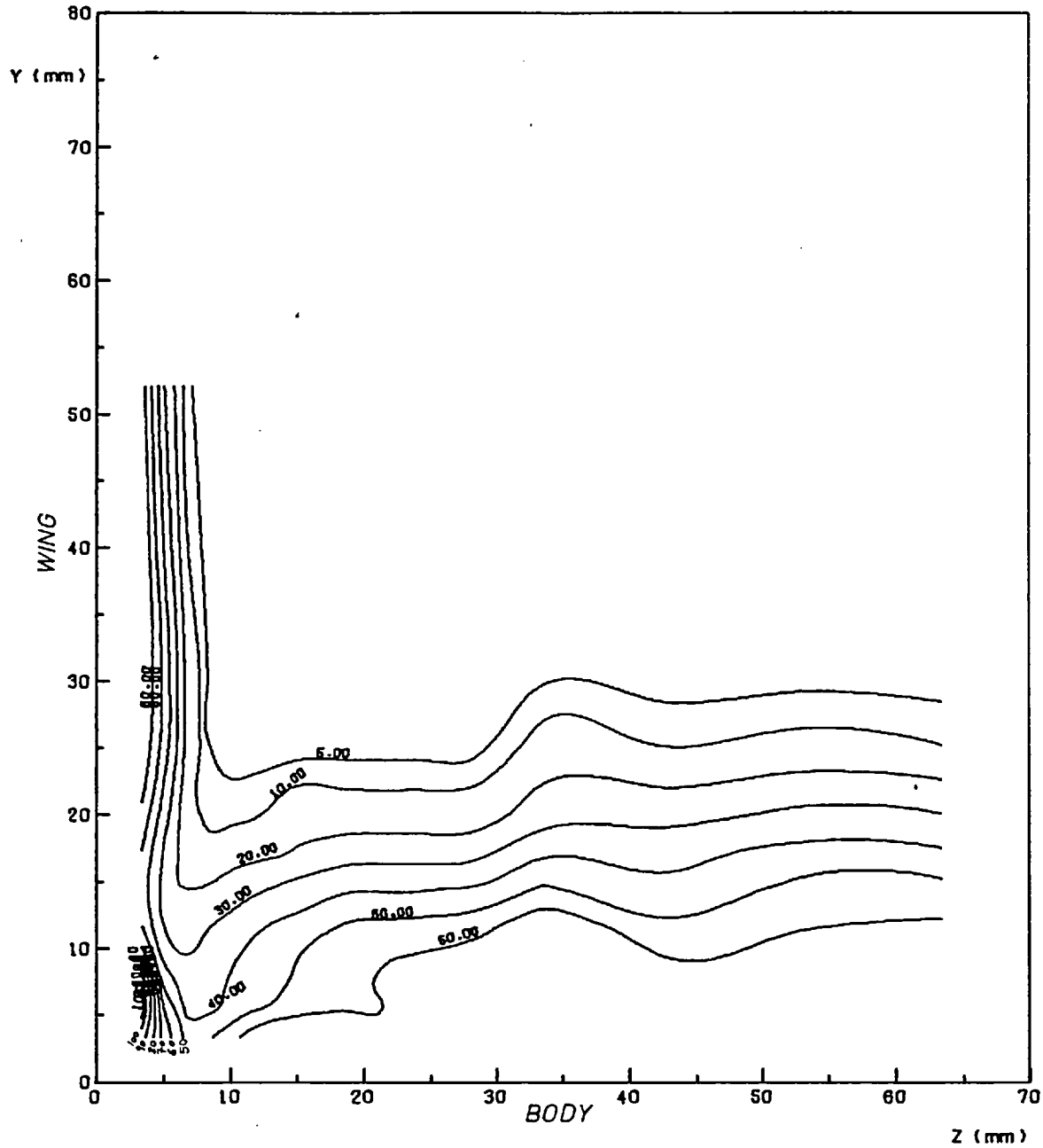

FIG.(3.55) CONTOUR MAP OF $(\overline{q^2}/U_e^2)*10^4$
AT AXIAL STATION NO. 2 (X = 156.6 mm)
Results of Cross Wire

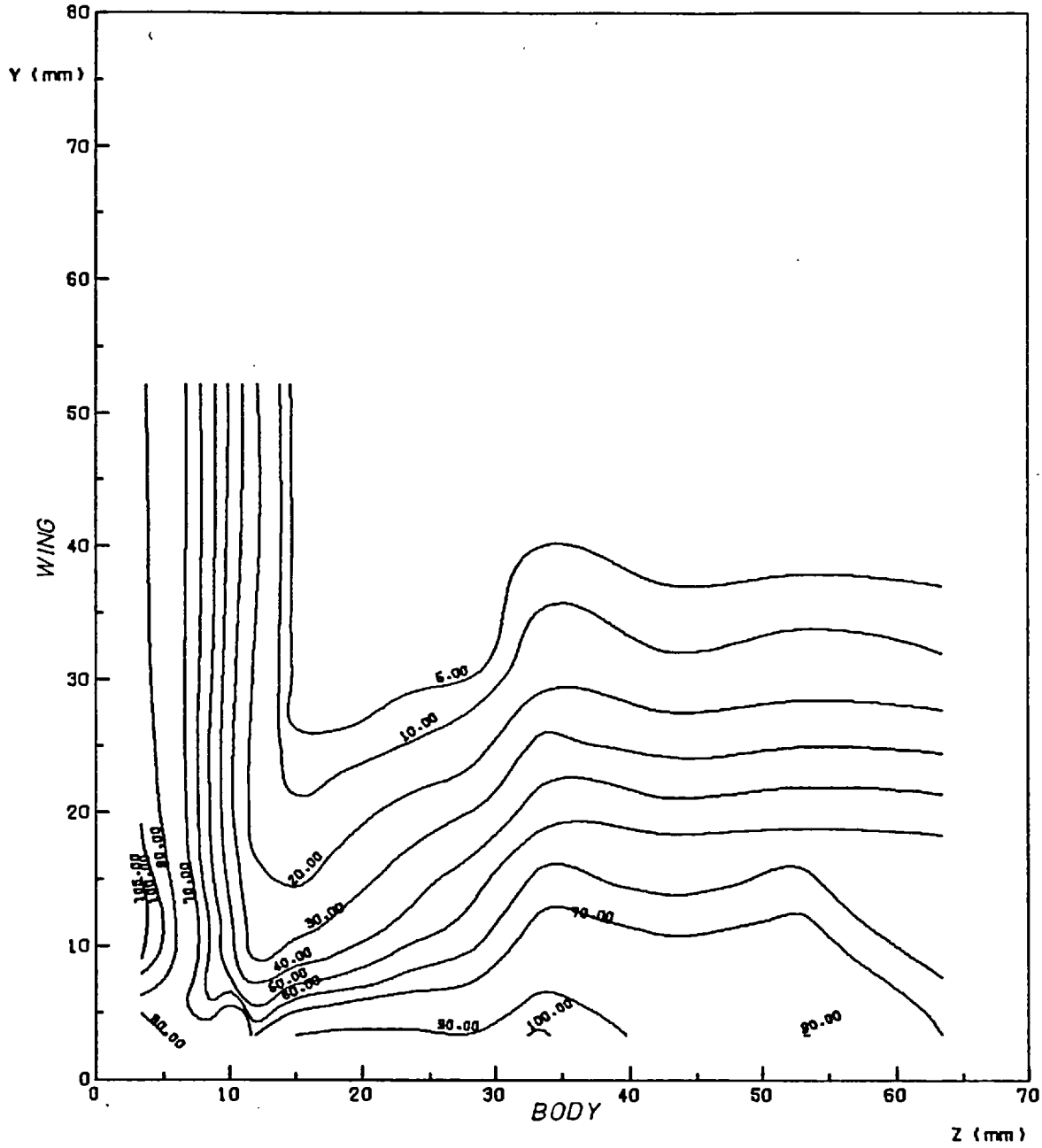

FIG.(3 . 56) CONTOUR MAP OF $(\overline{q^2}/U_e^2)*10^4$
AT AXIAL STATION NO. 5 (X = 6'3.8 mm)
Results of Cross Wire

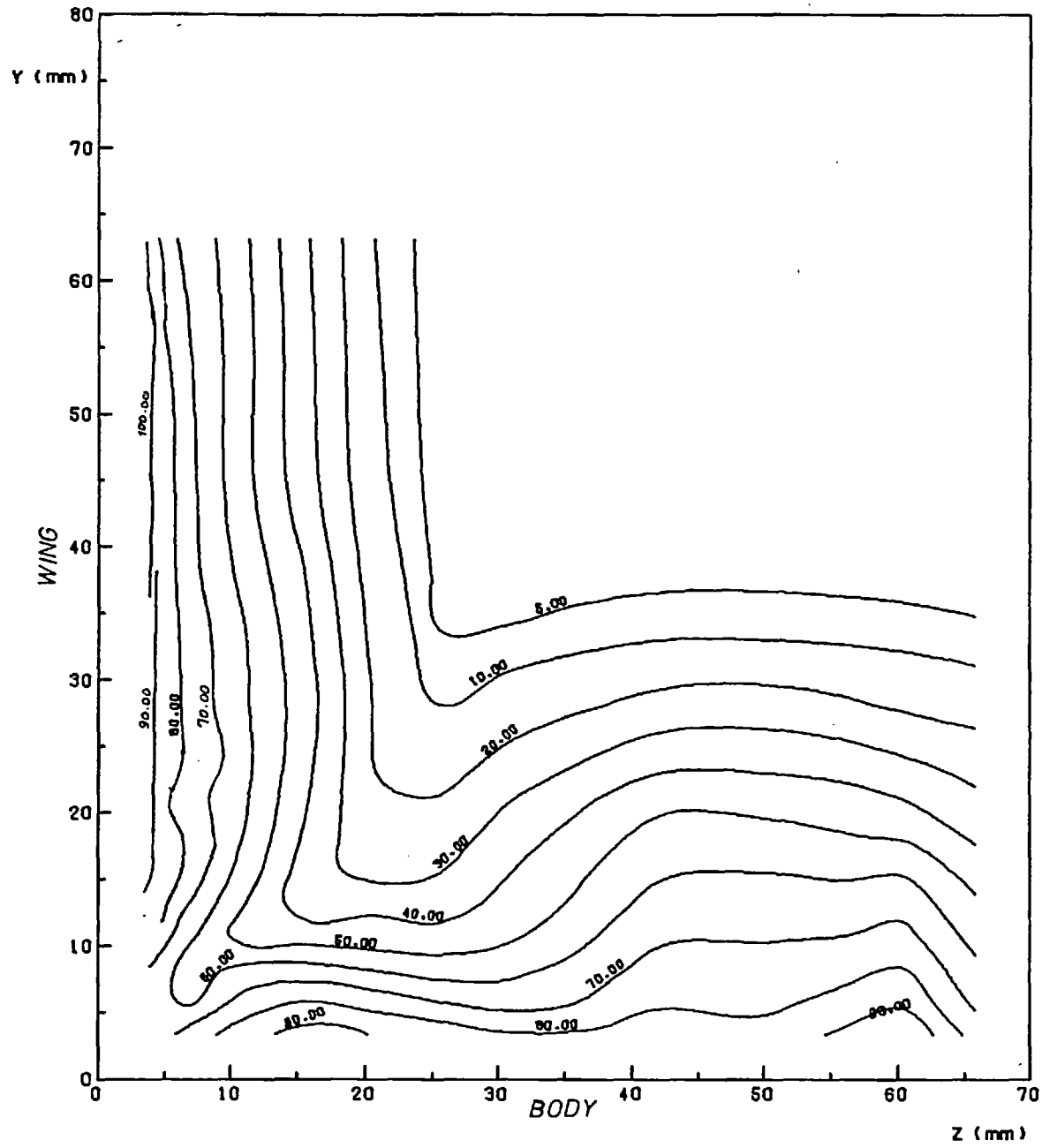

FIG.(3.57) CONTOUR MAP OF $(\overline{q^2}/U_e^2)*10^4$
AT AXIAL STATION NO. 9 (X = 1223.4 mm)
Results of Cross Wire

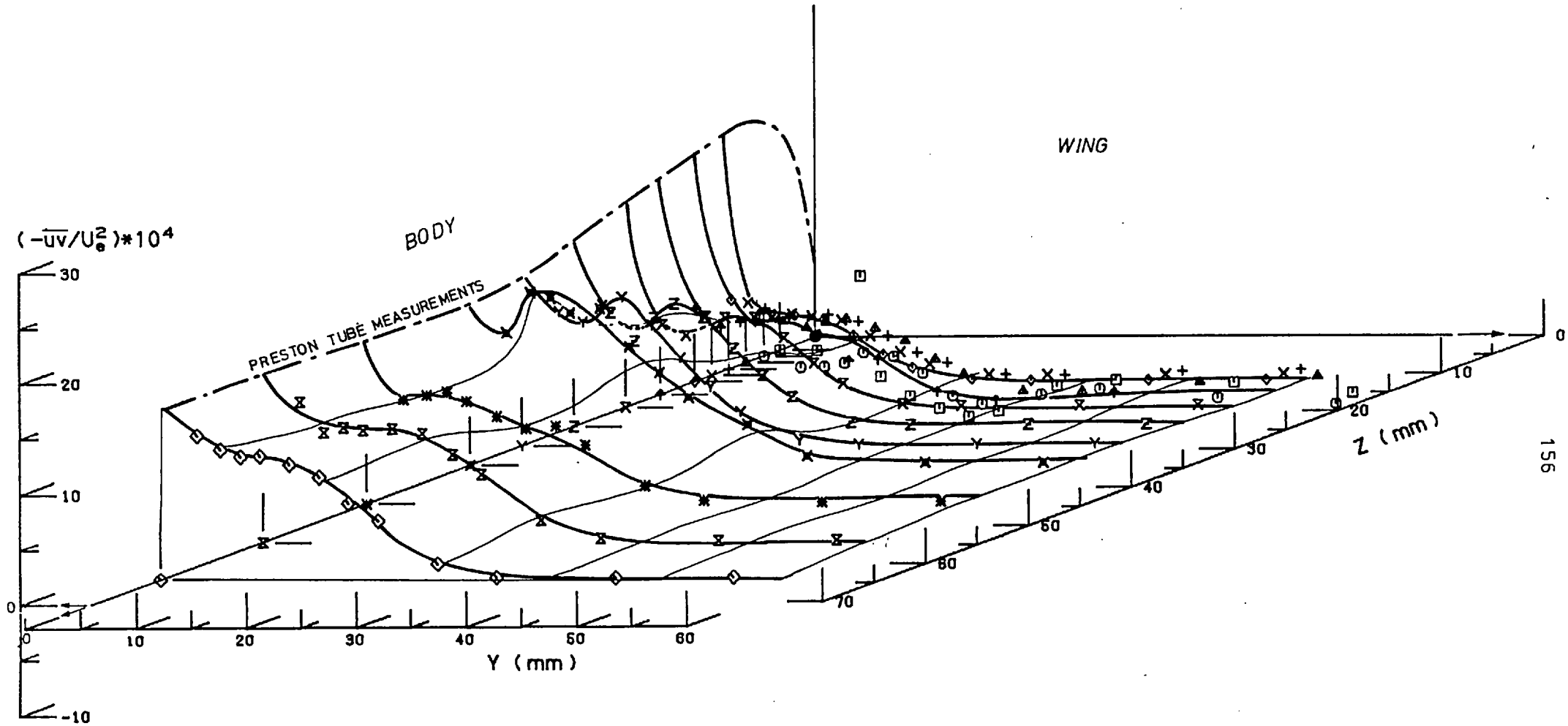

FIG.(3.58) PLOTS OF REYNOLDS SHEAR STRESS ($-\overline{uv}$) AT STATION 2 (X=156.6 mm)
Results of Cross Wire in Vertical (U-V) Position

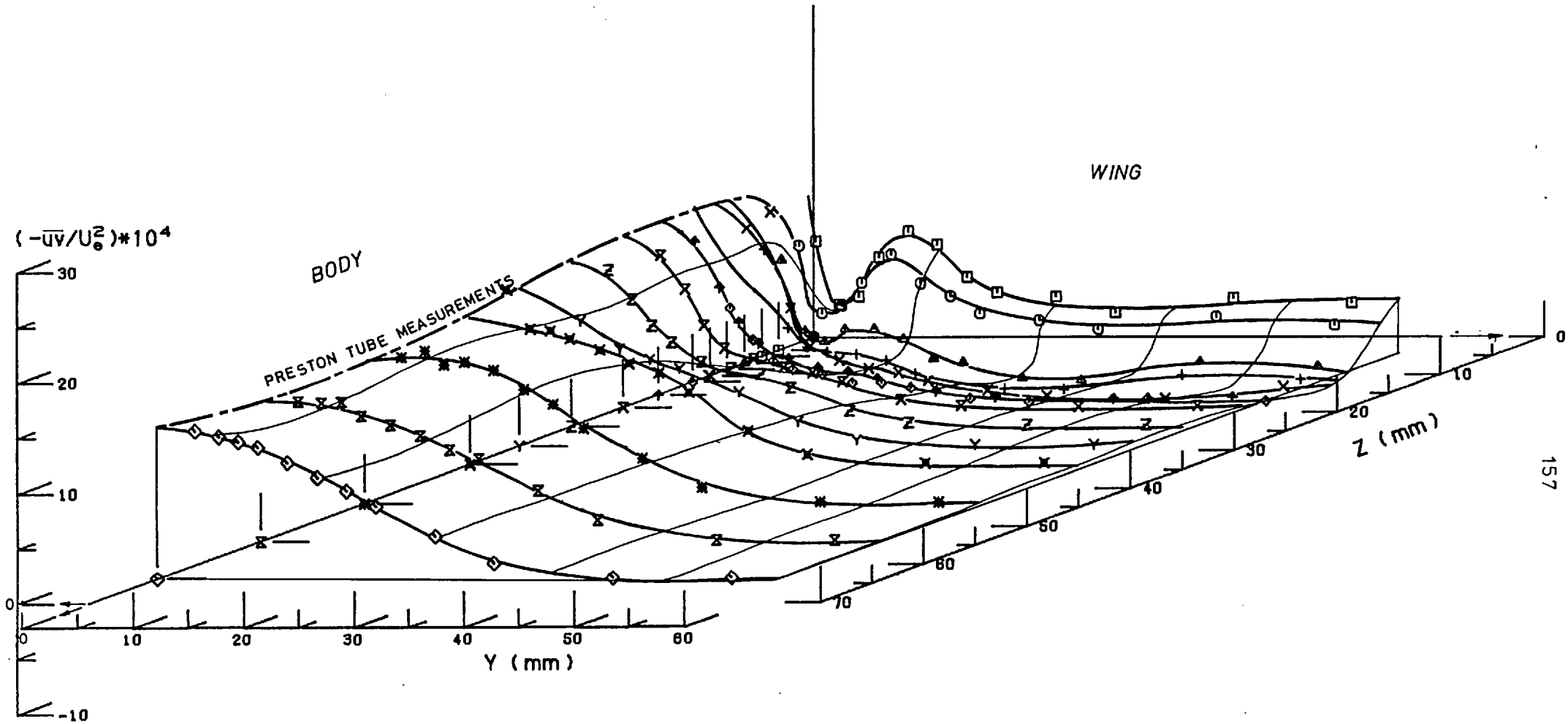

FIG.(3.59) PLOTS OF REYNOLDS SHEAR STRESS ($-\overline{uv}$) AT STATION 5 (X=613.8 mm)
Results of Cross Wire in Vertical (U-V) Position

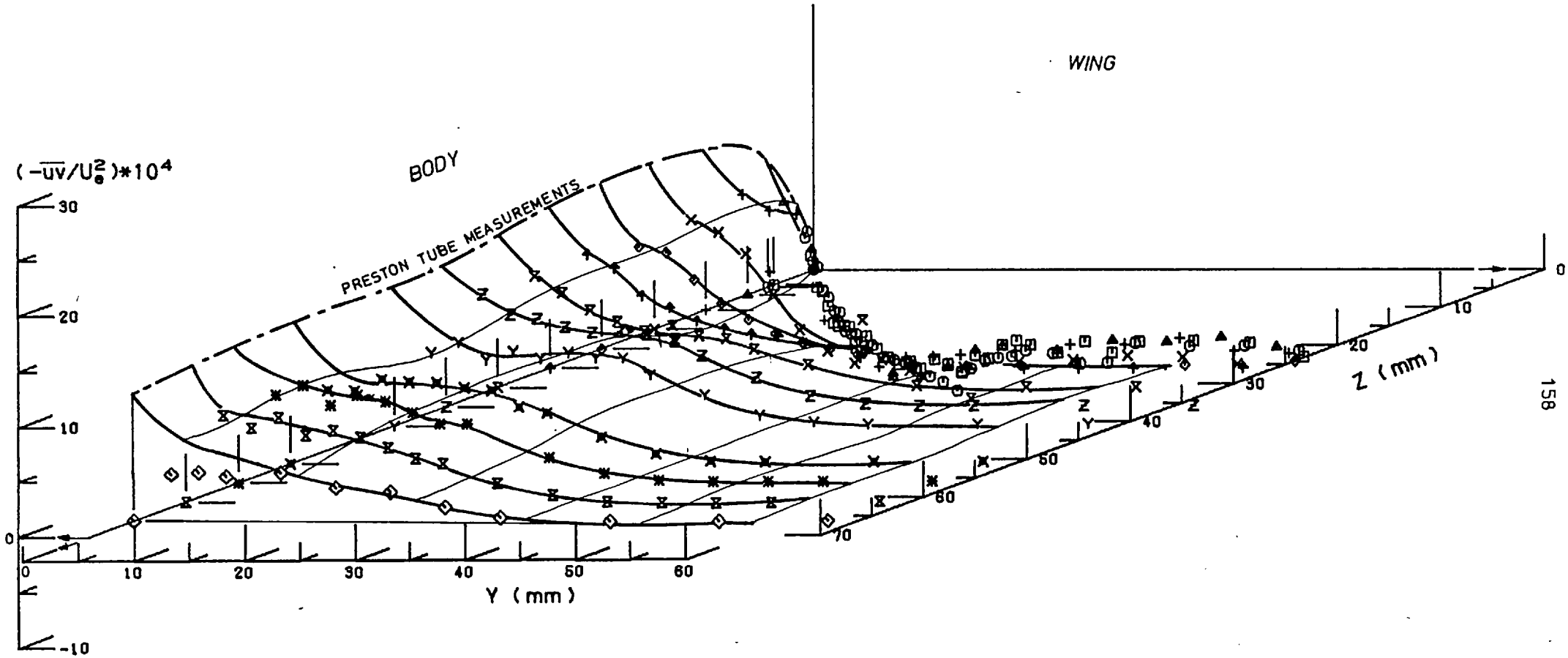

FIG.(3.60) PLOTS OF REYNOLDS SHEAR STRESS ($-\overline{uv}$) AT STATION 9 (X=1223.4 mm)

Results of Cross Wire in Vertical (U-V) Position

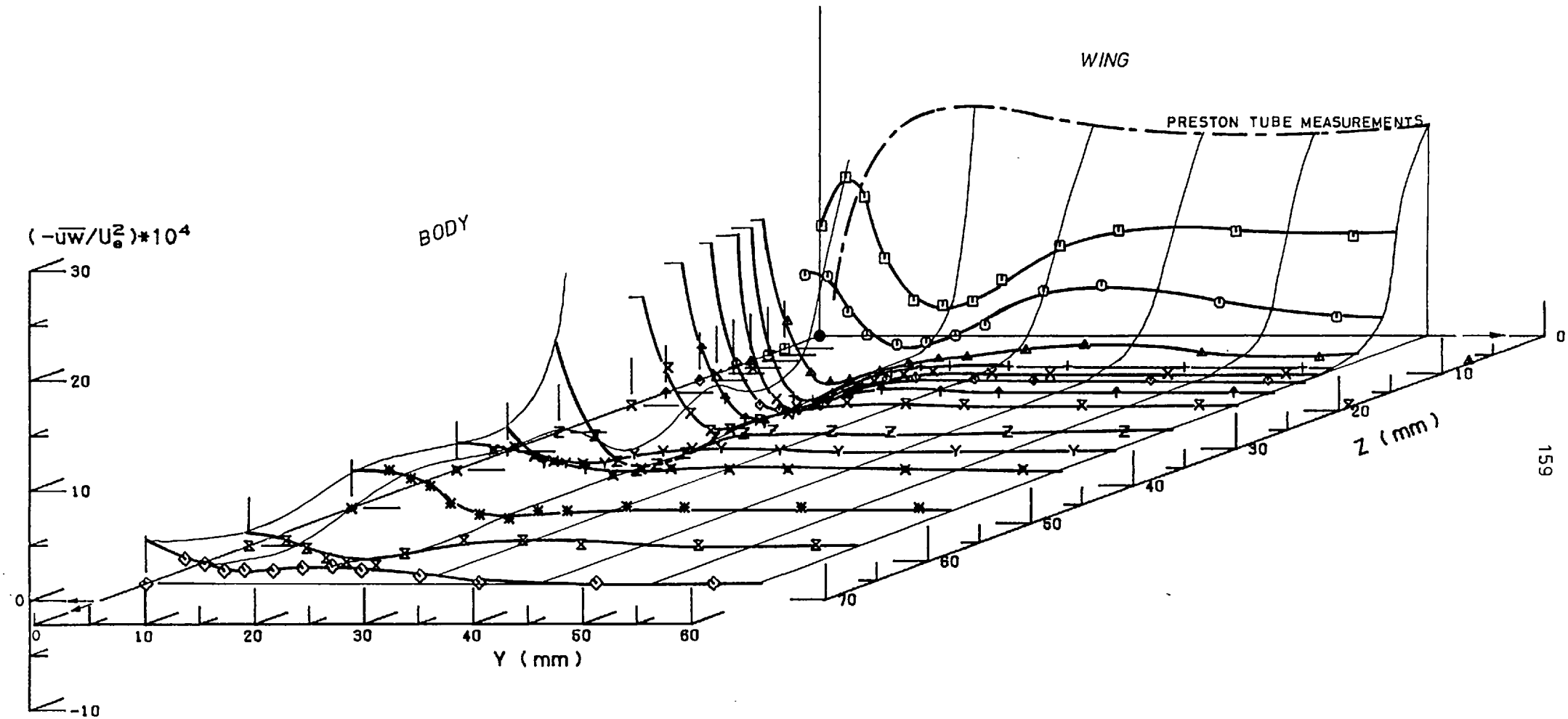

FIG.(3.61) PLOTS OF REYNOLDS SHEAR STRESS ($-\overline{uw}$) AT STATION 2 (X=156.6 mm)
Results of Cross Wire in Horizontal (U-W) Position

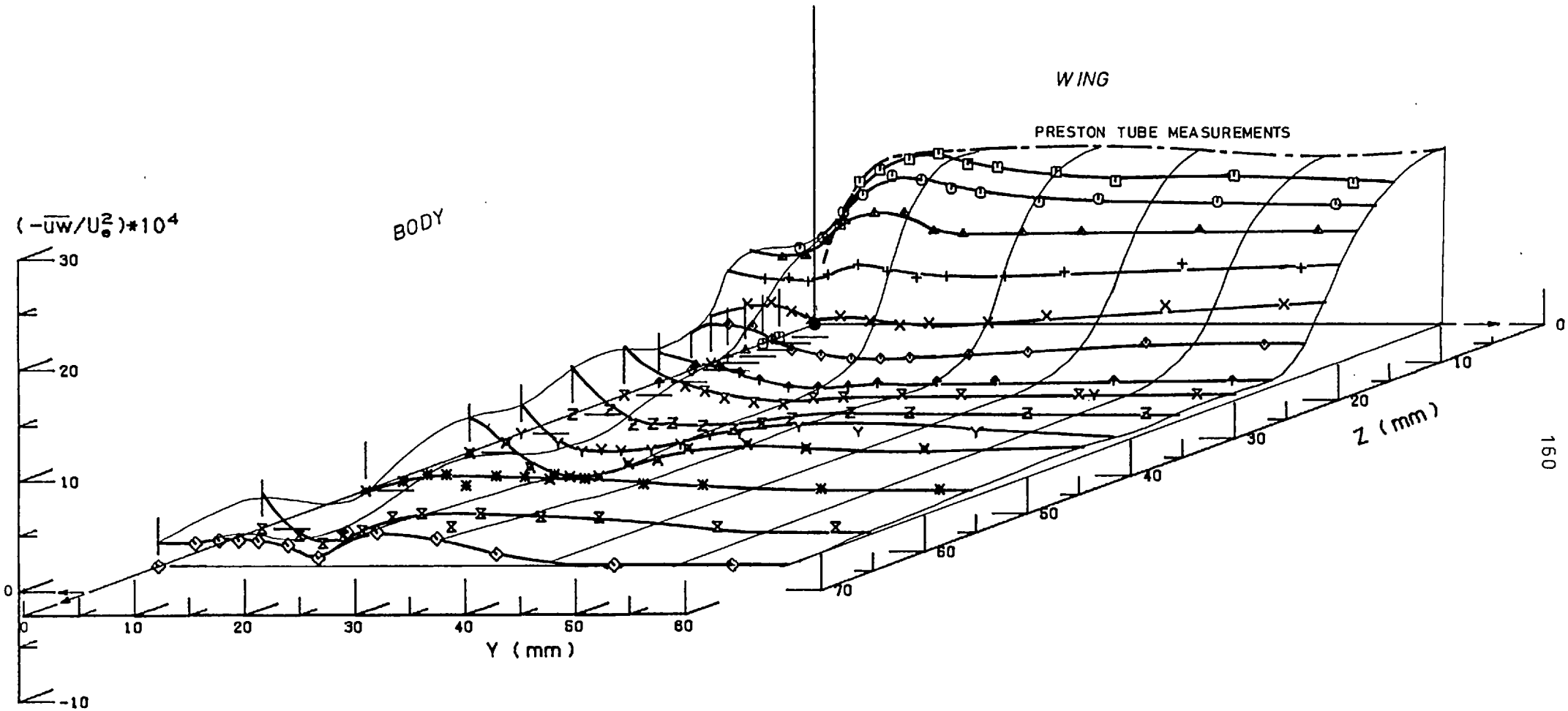

FIG.(3·62) PLOTS OF REYNOLDS SHEAR STRESS ($-\overline{uw}$) AT STATION 5 (X=613.6 mm)

Results of Cross Wire in Horizontal (U-W) Position

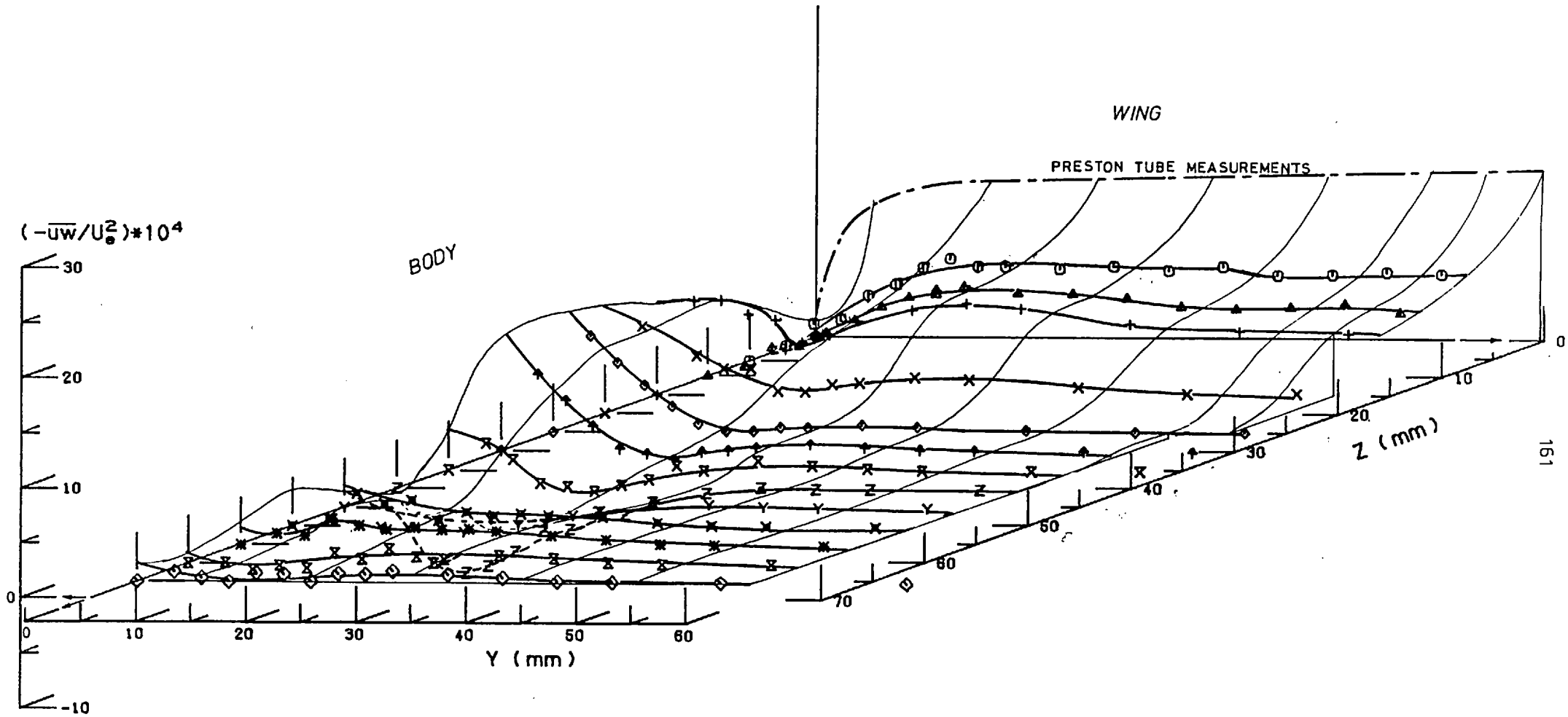

FIG.(3.63) PLOTS OF REYNOLDS SHEAR STRESS ($-\overline{uw}$) AT STATION 9 (X=1223.4 mm)

Results of Cross Wire in Horizontal (U-W) Position

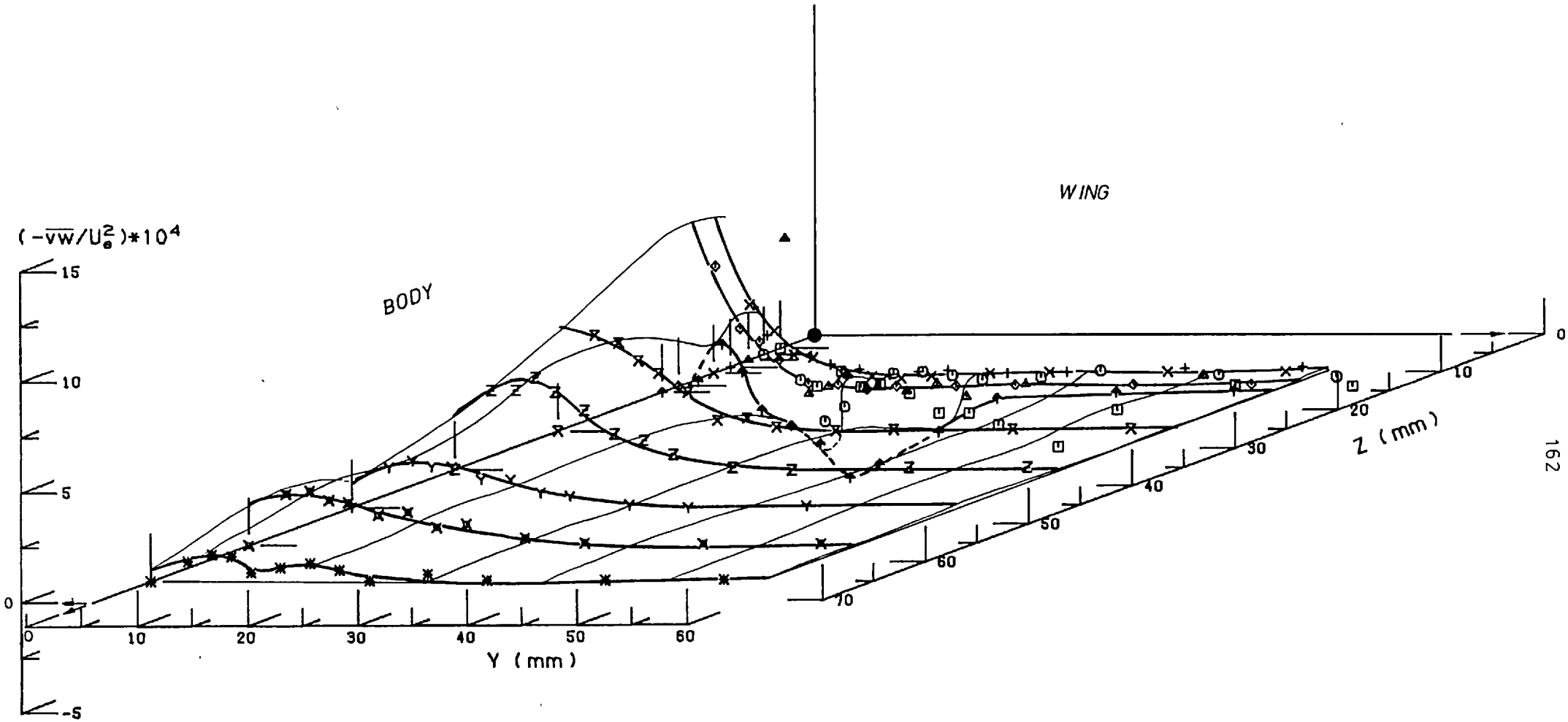

FIG.(3.64) PLOTS OF REYNOLDS SHEAR STRESS $(-\overline{vw})$ AT STATION 2 (X=156.6 mm)

Results of Cross Wire in Inclined ±45° (V-W) Position

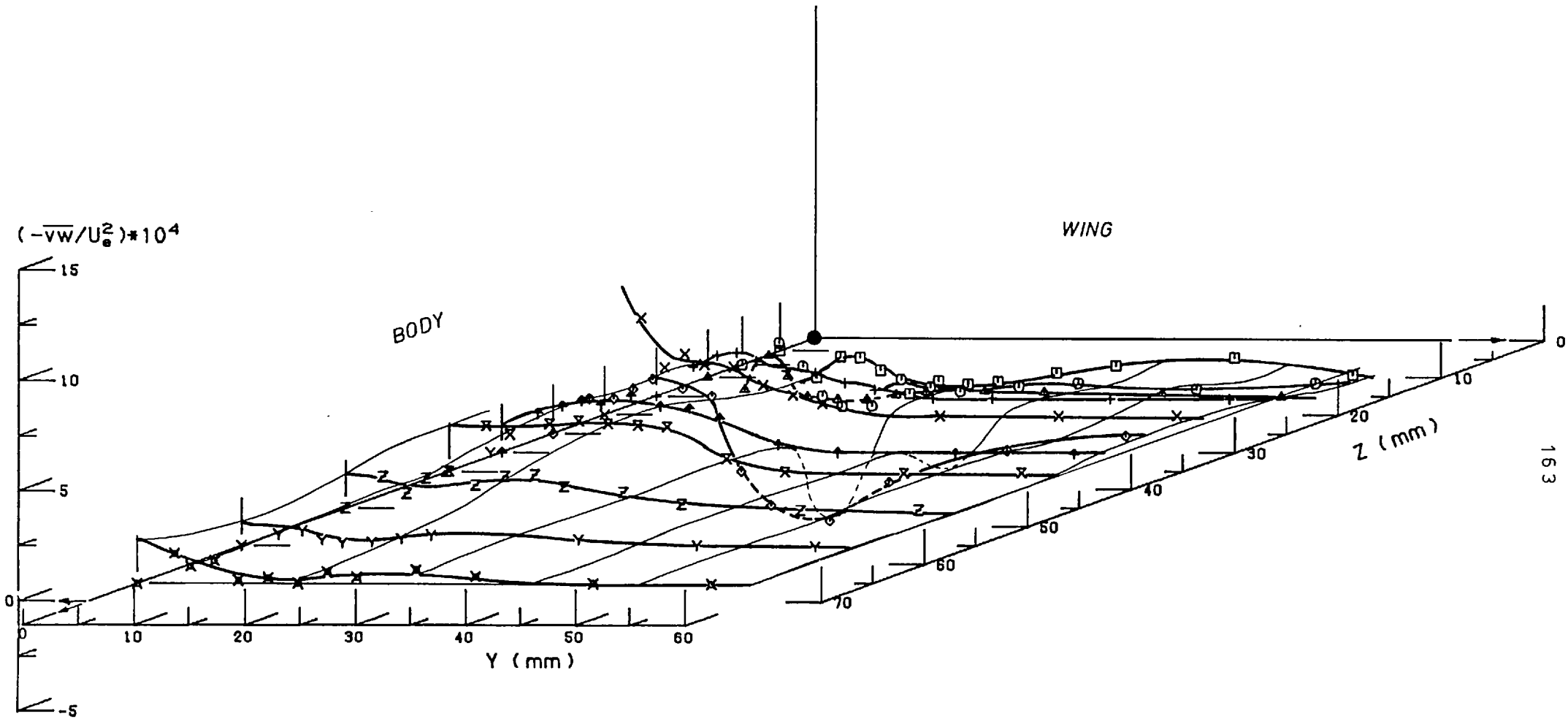

FIG.(3·65) PLOTS OF REYNOLDS SHEAR STRESS ($-\overline{vw}$) AT STATION 5 (X=613.6 mm)

Results of Cross Wire in Inclined ±45° (V-W) Position

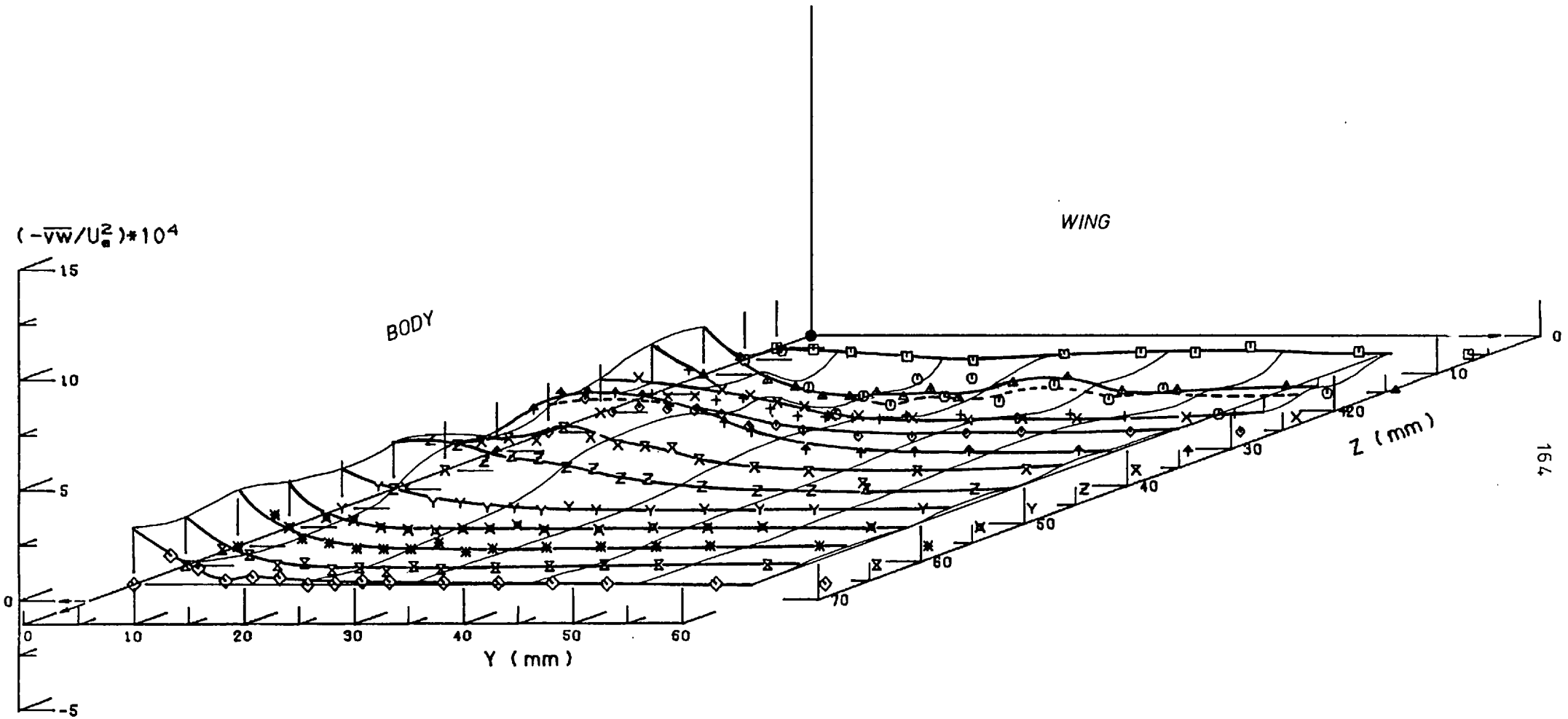

FIG.(3.66) PLOTS OF REYNOLDS SHEAR STRESS ($-\overline{vw}$) AT STATION 9 (X=1223.4 mm)

Results of Cross Wire in Inclined ±45° (V-W) Position

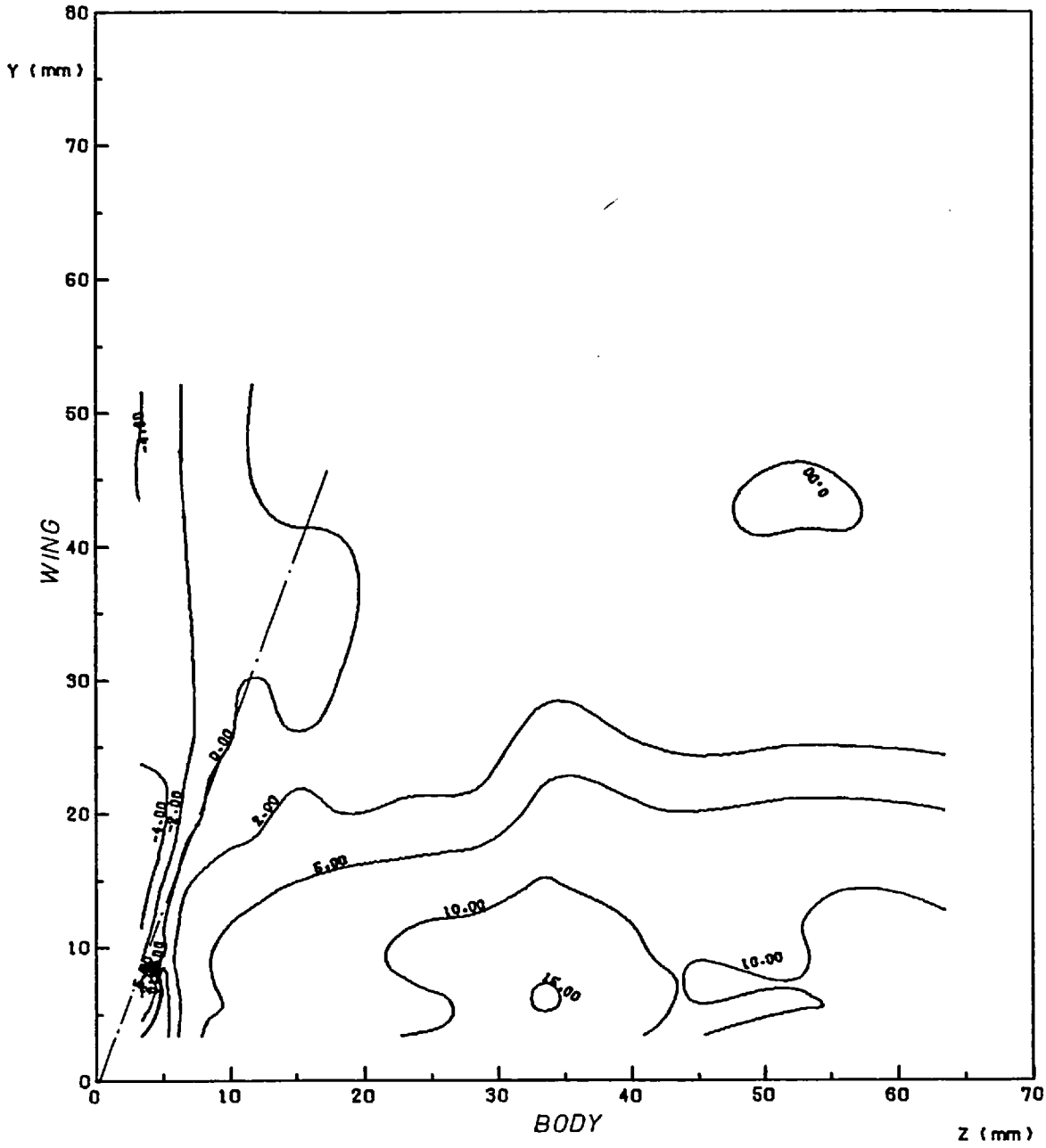

FIG.(3 · 67) CONTOUR MAP OF $(-\overline{uv}/U_e^2)*10^4$
AT AXIAL STATION NO. 2 (X = 156.6 mm)
Results of Cross Wire in Vertical (U-V) Position

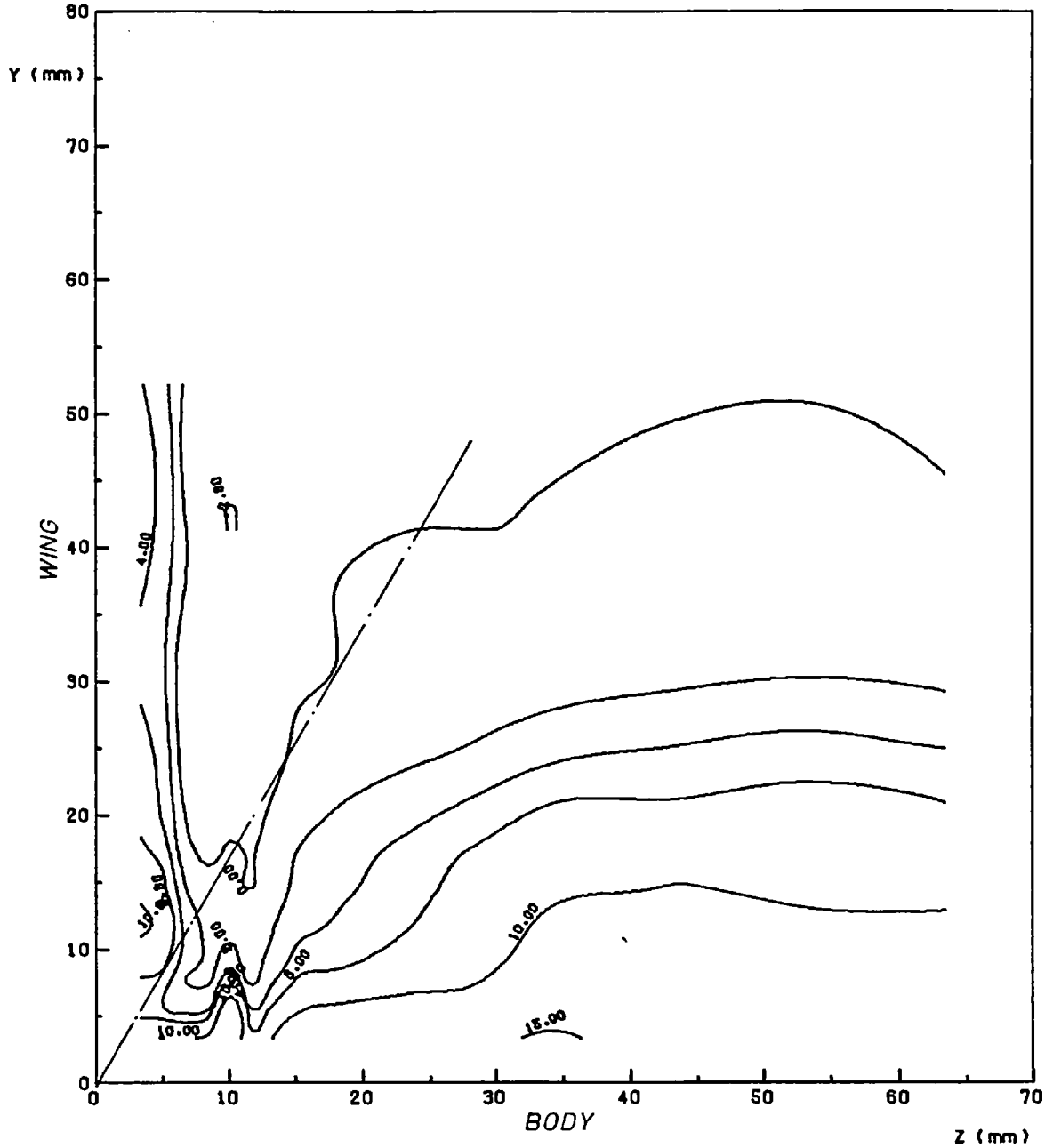

FIG.(3·68) CONTOUR MAP OF $(-\overline{uv}/U_e^2)*10^4$

AT AXIAL STATION NO. 5 (X = 613.8 mm)

Results of Cross Wire In Vertical (U-V) Position

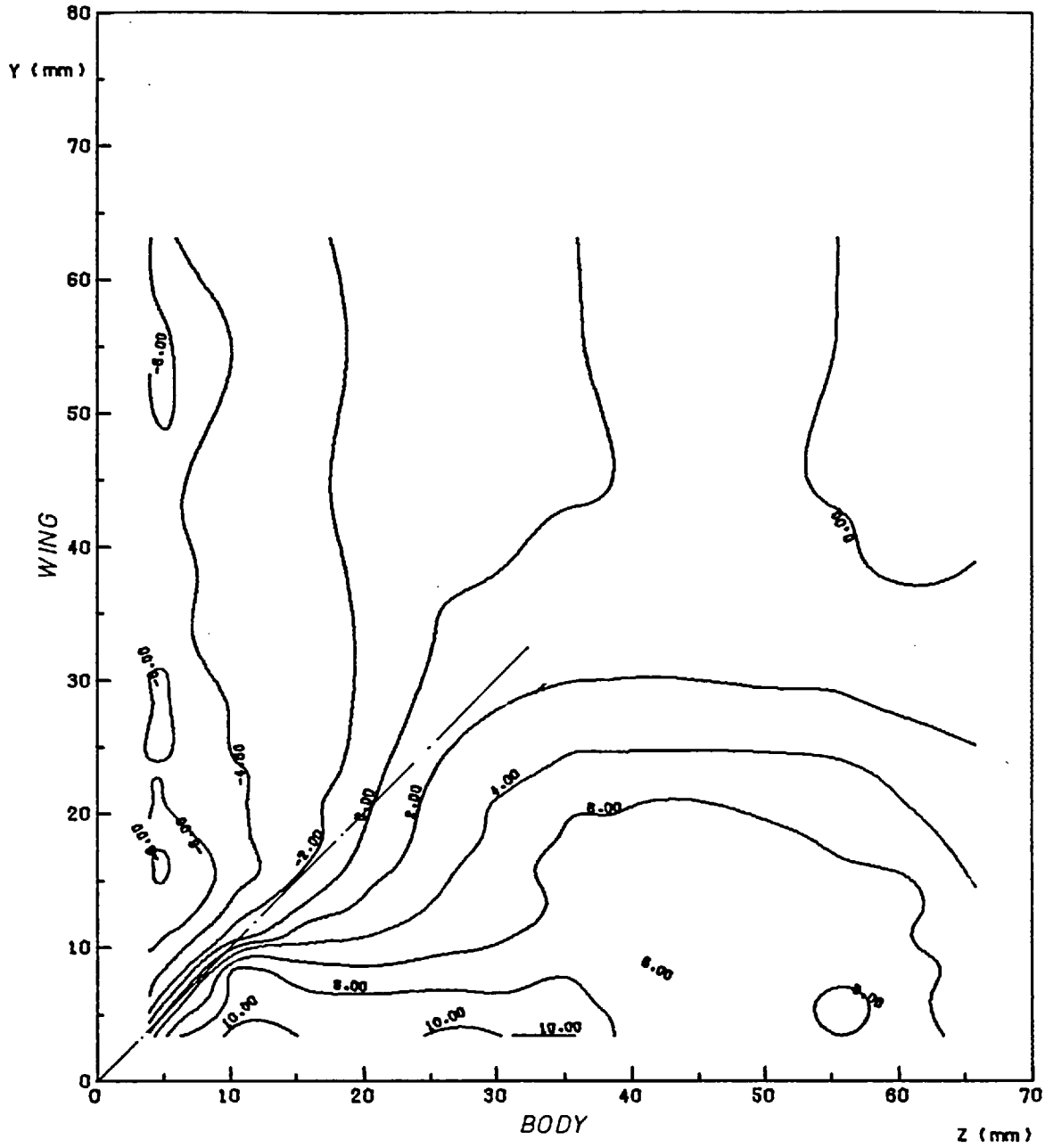

FIG.(3.69) CONTOUR MAP OF $(-\overline{uv}/U_e^2)*10^4$
AT AXIAL STATION NO. 9 (X = 1223.4 mm)
Results of Cross Wire in Vertical (U-V) Position

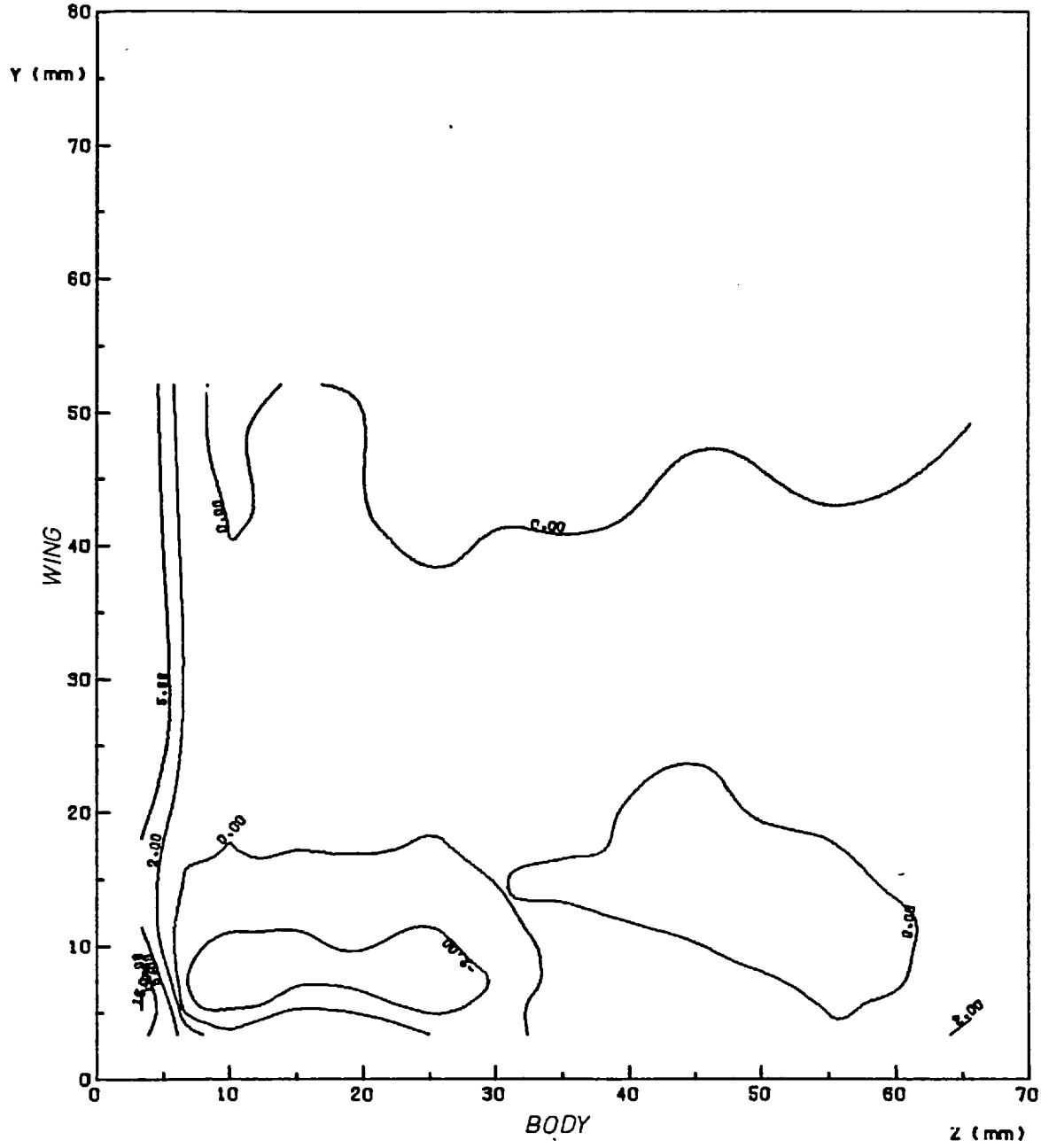

FIG.(3·70) CONTOUR MAP OF $(-\overline{uw}/U_e^2)*10^4$
AT AXIAL STATION NO. 2 (X = 156.6 mm)
Results of Cross Wire in Horizontal (U-W) Position

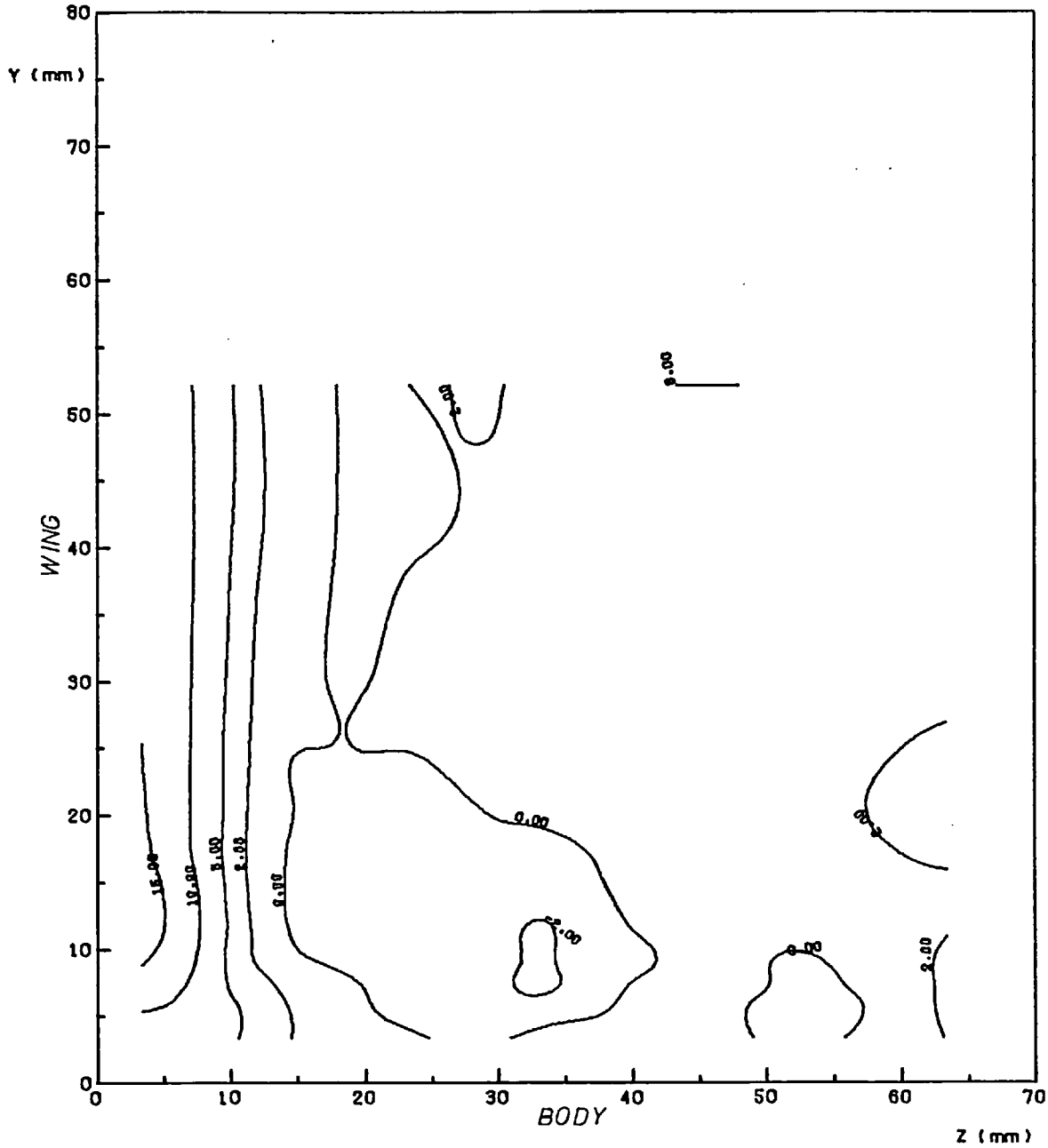

FIG.(3·71) CONTOUR MAP OF $(-\overline{uw}/U_e^2)*10^4$
AT AXIAL STATION NO. 5 (X = 613.8 mm)
Results of Cross Wire in Horizontal (U-W) Position

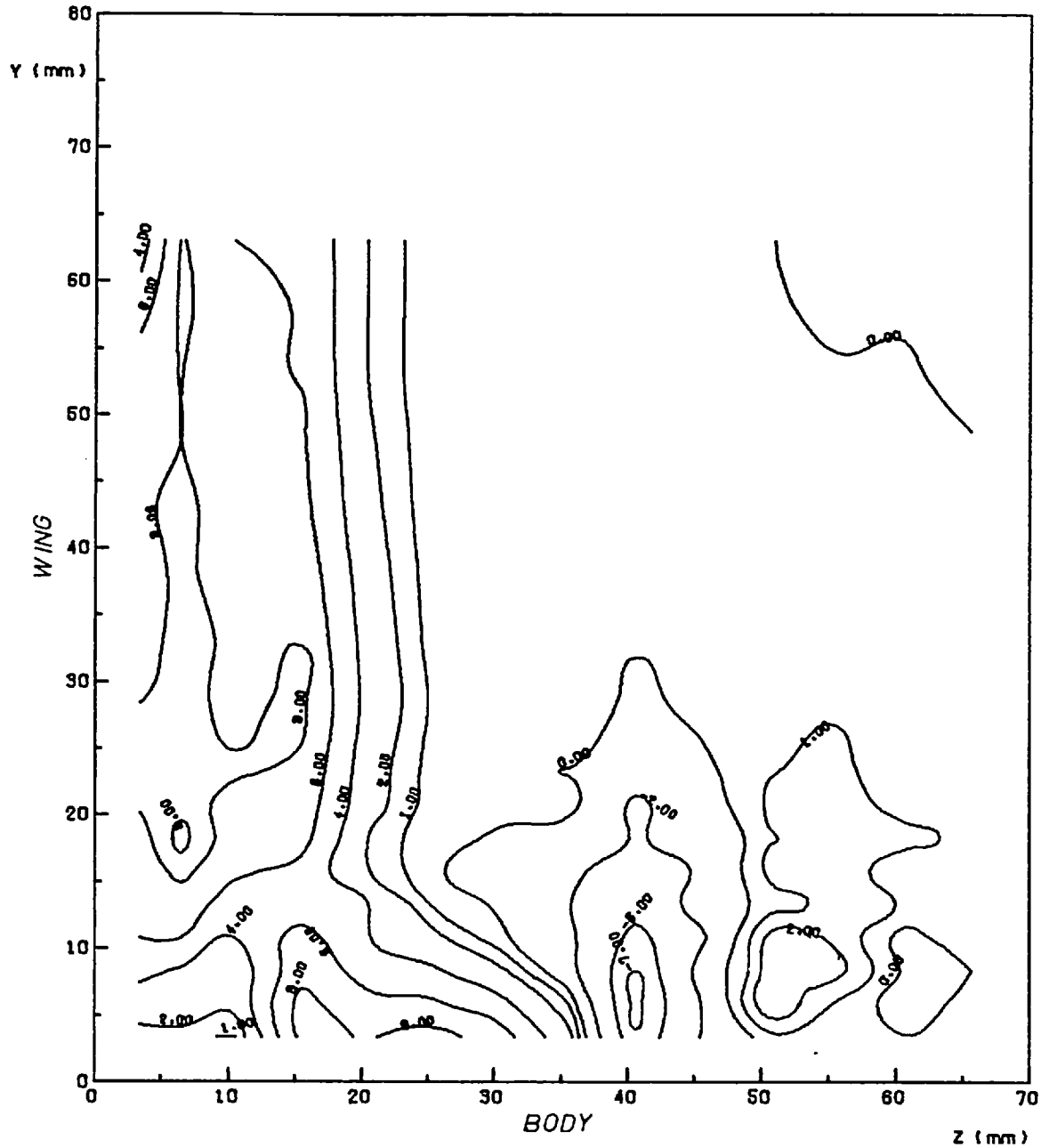

FIG.(3·72) CONTOUR MAP OF $(-\overline{uw}/U_e^2)*10^4$
AT AXIAL STATION NO. 9 (X = 1223.4 mm)
Results of Cross Wire in Horizontal (U-W) Position

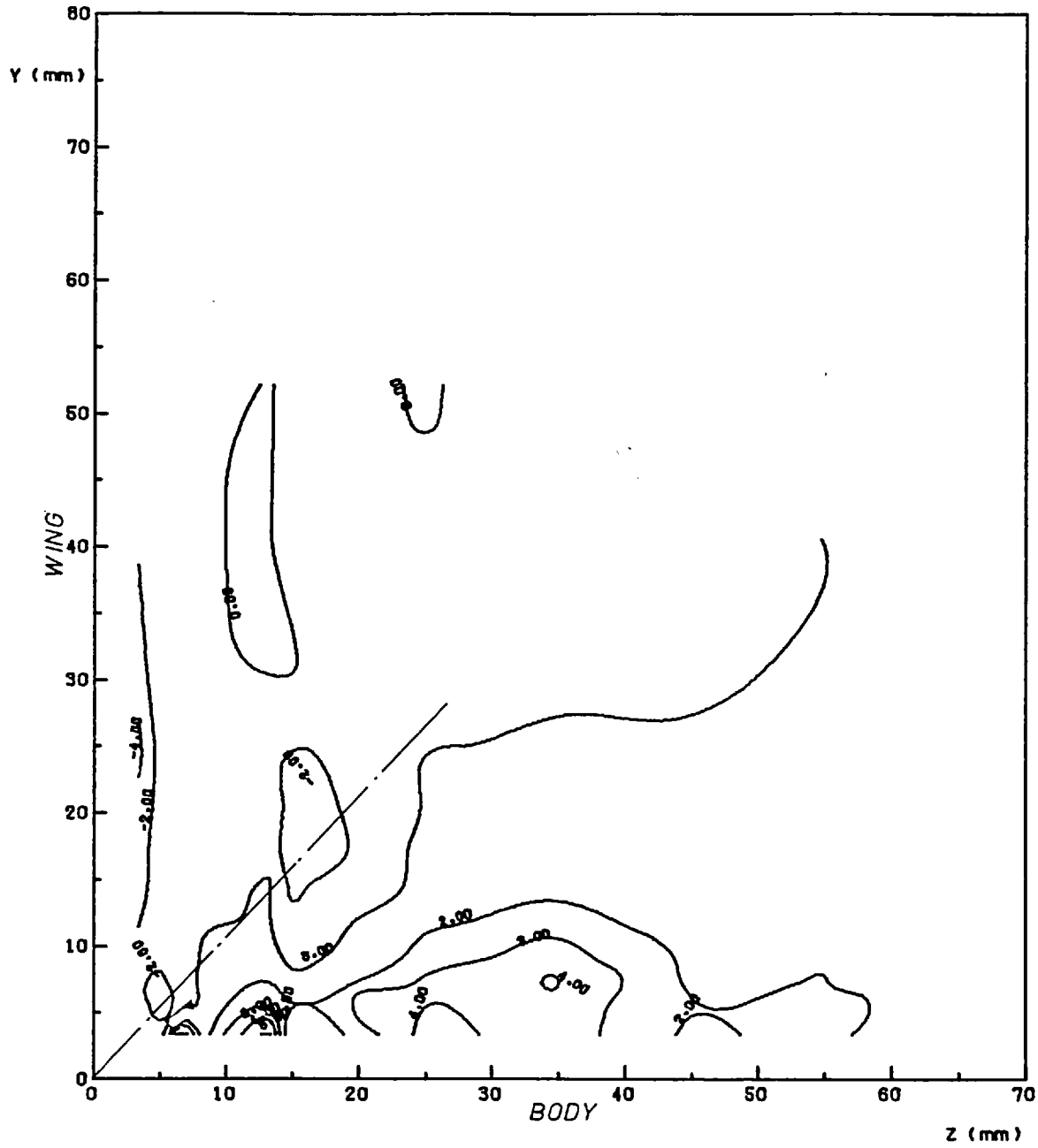

FIG.(3·73) CONTOUR MAP OF $(-\overline{vw}/U_e^2)*10^4$
AT AXIAL STATION NO. 2 (X = 156.6 mm)
Results of Cross Wire Inclined 45°((V-W) Position)

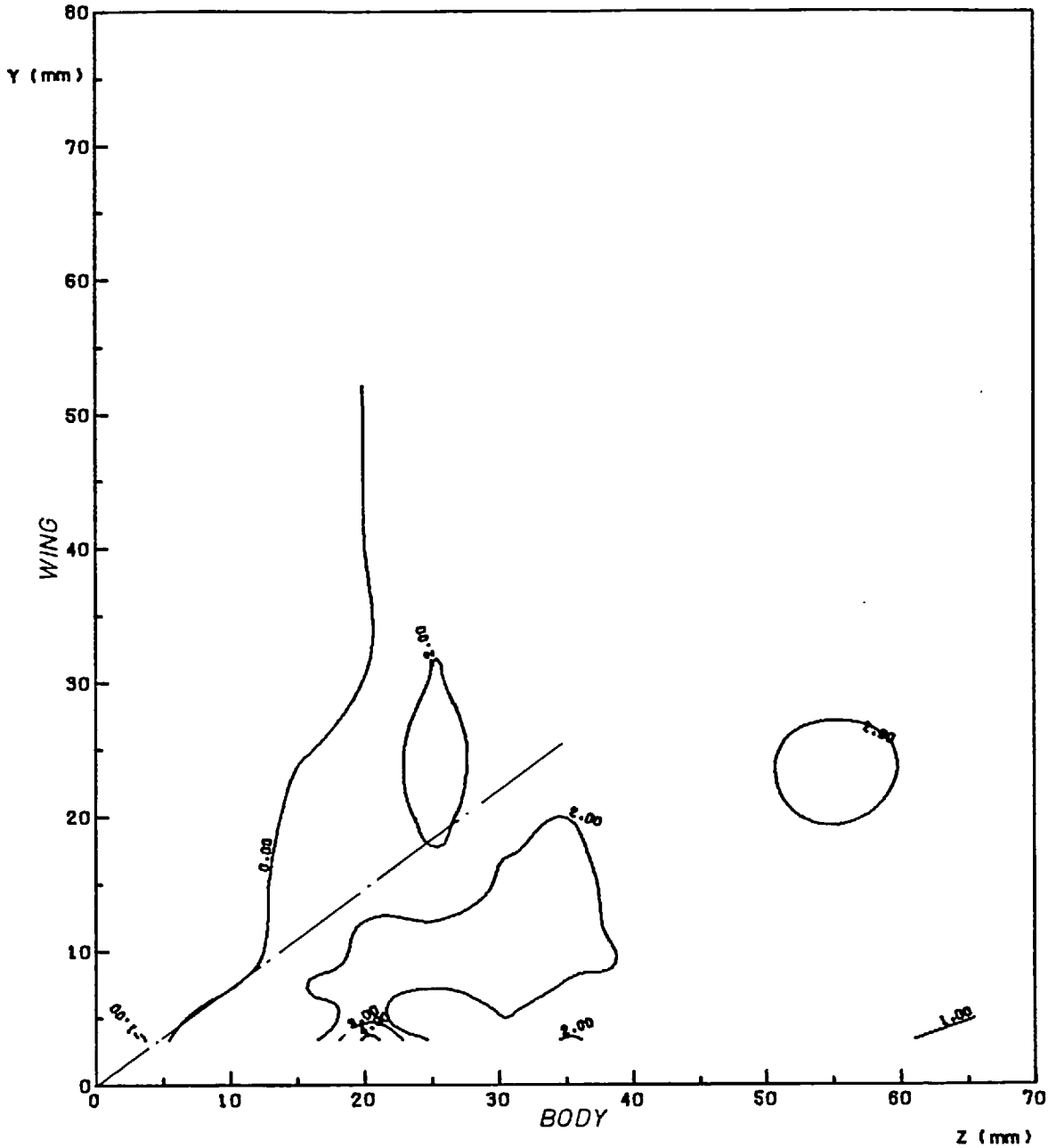

FIG.(3·74) CONTOUR MAP OF $(-\overline{vw}/U_e^2)*10^4$
AT AXIAL STATION NO. 5 (X = 613.8 mm)
Results of Cross Wire Inclined 45°((V-W) Position)

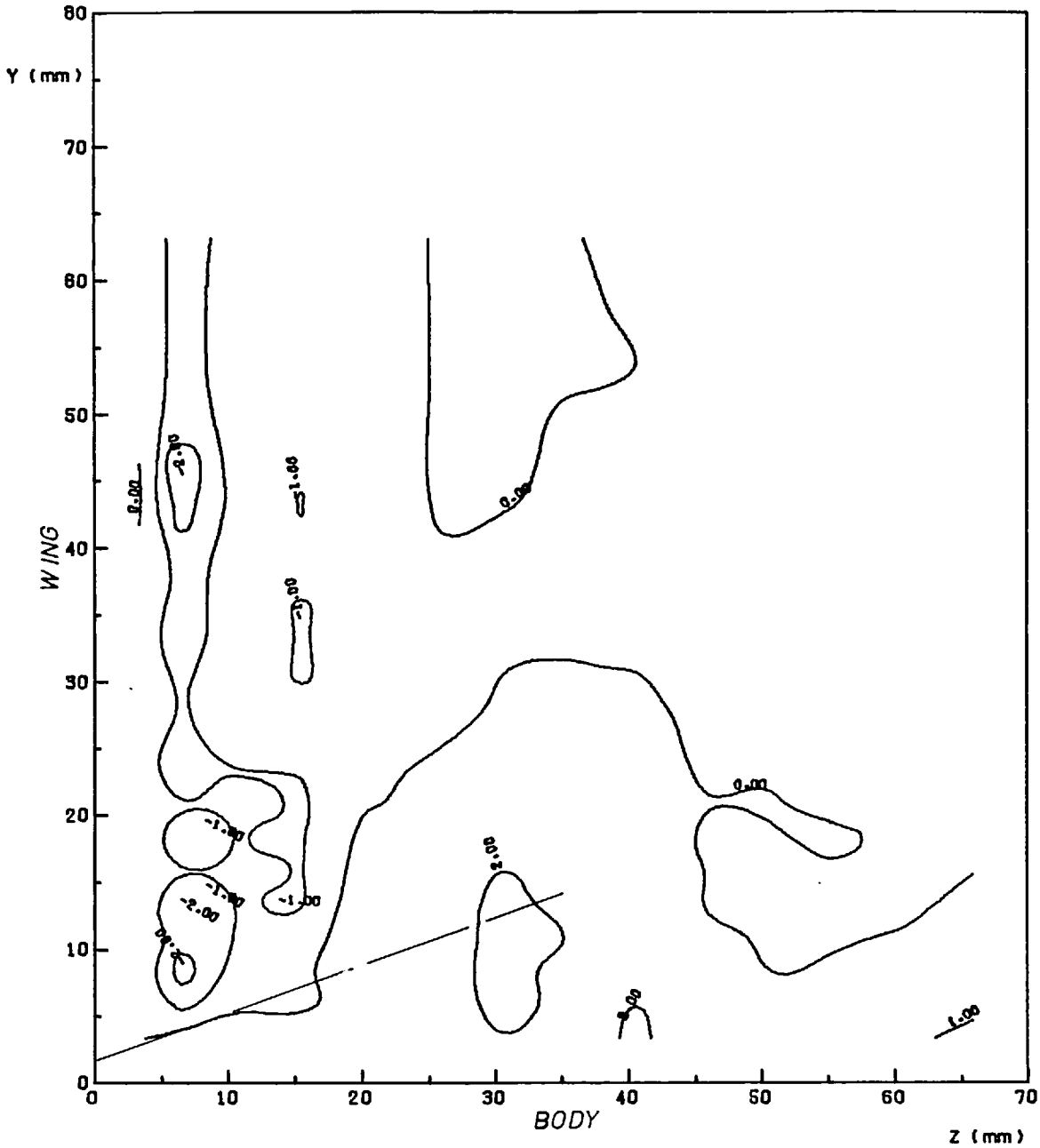

FIG.(3·75) CONTOUR MAP OF $(-\overline{vw}/U_e^2)*10^4$
AT AXIAL STATION NO. 9 (X = 1223.4 mm)
Results of Cross Wire Inclined 45°((V-W) Position)

CHAPTER 4

FURTHER RESULTS AND DISCUSSION

Most of the present experimental results have already been presented in the preceding chapter. This chapter deals with indirect results deduced from the experimental data and with the higher order results (e.g. the triple products). All the calculations were performed on the College CDC computers and Computer Centre plotting software was used in plotting some of the graphs. No smoothing was done on the real experimental points and this resulted in scatter in some derived values.

4.1 Mean Flow and the Logarithmic Profile

The mean streamwise velocity U in the corner region of the "wing-body" junction has already been plotted in Figs. (3.5 to 3.19) and was discussed in the last chapter. Now, the validity of the two-dimensional boundary layer law of the wall is tested in the inner layers of the "body" and the "wing" boundary layers. The log-law is expressed in the form:-

$$\frac{U}{u_\tau} = A \log_{10} y^+ + B \qquad (4.1)$$

where: u_τ = the friction velocity at the wall = $\sqrt{C_f/2}\ .\ U_e$

U_e = free stream streamwise velocity

$y^+ = u_\tau\, y/\nu$

y = distance from the body surface

ν = kinematic viscosity of the air

A = constant = 5.616 in a two-dimensional boundary layer (corresponding to von Karman constant K = 0.41)

B = constant $\simeq$ 5.2 in a two-dimensional boundary layer

z^+ and z replaces y^+ and y in the above Equation (4.1) when discussing the "wing" boundary layer.

Semi-logarithmic velocity profiles were produced from Pitot and Preston tube measurements, of U and u_τ respectively, at stations 1, 2, 3, 5, 7 and 9 (x = 3.47, 18.71, 33.95, 64.4, 94.91 and 125.4 cm). Plots across the body boundary layer are given in Figs. (4.1 , 4.2a ....) while those of the wing boundary layer are presented in Figs. (4.2b, 4.3b ....). The logarithmic law was checked in the inner layers, for which 0.1 δ_b was taken as the outer edge in the body boundary layer and 0.15 δ_w as an outer edge in the relatively thin wing boundary layer. δ_b and δ_w are the body and wing boundary layer thicknesses far from the wing and the body respectively. Straight lines of slope A = 5.616, corresponding to the universal constant K = 0.41, were fitted to the experimental points in the inner layers and the intercept B was found graphically.

The law seems to fit the measurements except near the wing leading edge where it fails completely to agree with experiment (no agreement was found for z $\lesssim$ 40 mm at stations 1 and 2). In regions of agreement, the constant B ranges between 4.88 and 6.2, excluding the few odd values. This range lies inside the limits between which opinions about the value of the constant B vary*. However, it is thought

---

* Townsend (1956) remarked that many of the observed data tend to give a value of B nearer to 7, while Clauser (1956) suggested 4.9. Patel (1965) used 5.45, Huffman and Bradshaw (1972) give 5.0 and Brederode (1973) used 5.2. Values between 5.2 and 5.5 are also found depending on the constant A (Hinze, 1975).

that a probable small error in determining the Pitot tube position relative to the body and the wing surfaces, especially close to the corner where the wall shear stress gradients ($\partial u_\tau/\partial y$ and $\partial u_\tau/\partial z$) are high, is the real reason for the obtained difference in B (B = 5.2 in the used Preston tube calibration). Preston tube measurements should lie on the corresponding profiles of the streamwise velocity U obtained from the Pitot tube of its size (both tubes integrate the total pressure over the same area in the flow). The validity of the log-law thus implies that the streamwise vortex embedded in the body boundary layer seems to have a negligible effect on the turbulence structure of the eddies and the local equilibrium of the flow in the inner region of the body and wing boundary layers except when the vortex is very strong in its early stages (secondary flow $\simeq$ 6% of the main flow component). In these regions of high secondary flow, the direction of the shear stress ($-\overline{uv}\,\underline{i} + -\overline{vw}\,\underline{k}$) is no longer in the direction of the mean velocity gradient $\left(\frac{\partial U}{\partial y}\,\underline{i} + \frac{\partial W}{\partial y}\,\underline{k}\right)$ (see Bradshaw, 1968). On the other hand, the effect of the vortex on the large eddies in the outer layers is evident. The wake component (see Coles, 1956) reduces in size with decrease in distance from both surfaces. Similarity to the law of the wake for the two-dimensional boundary layer, appears only where the velocity profiles (U vs. y or z) are negligibly distorted by the axial mean vorticity, i.e. where the isovels in the (z - y) planes, Figs. (3.13 - 3.19), are nearly parallel to the body or the wing surfaces. The invalidity of the log-law at the upstream stations near the wing leading edge explains the inconsistency between the Preston tube measurements of τ_w and the hot wire results near the corner walls at station 2 (Figs. (3.58), (3.61)). In this region, the cross wire is expected to be more reliable than the Preston tube.

In fact, the validity of the log-law has been found by previous

workers in the 90^{o} corners of square and rectangular ducts. The corner secondary flow was found by Leutheusser (1963) not to affect the two-dimensionality of the inner regions of the boundary layers except in the vicinity of the corner where the log-law region shrinks quickly. Also, the wake region was examined in square ducts by Mauer (1961), Bragg (1965) and Perkins (1970a); each of them suggested an empirical wake function. It is expected that the wing-body corner flow, which is a slender flow (away from the leading edge) should also follow the wall- and wake-laws. However, it is also expected that their formulae will be more complicated as a result of the non-negligible gradient $\partial/\partial z$ in addition to $\partial/\partial y$, the only gradient in two-dimensional boundary layers.

4.2 Shear Stresses and the Turbulent Kinetic Energy

The distribution of the six Reynolds stresses was given in the last chapter (Figs. (3.26 - 3.75)) where they were discussed. Here, we shall examine the direction of the primary shear stress resultant, and the relation between the shear stresses $-\overline{uv}$, $-\overline{uw}$ and $-\overline{vw}$ and the turbulent kinetic energy as expressed by $\overline{q^2}(= \overline{u^2} + \overline{v^2} + \overline{w^2})$ in the z-y plane.

4.2.1 The Primary Shear Stress Direction

The direction in which the resultant primary shear stress $\sqrt{\overline{uv}^2 + \overline{uw}^2}$ acts in the second, fifth and ninth y-z planes (x = 15.7, 61.4 and 122.3 cm from the leading edge) is shown in Figs. (4.7 - 4.9). The resultant direction $\left[\tan^{-1}\frac{\overline{uw}}{\overline{uv}}\right]$ is represented by a short arrow centred at the measurement point and drawn on a background of velocity contours. Figs. (4.7 - 4.9) show that the primary shear stress acts almost in a normal direction to the local isovel, i.e. in the direction of maximum gradient of velocity (U) in the z-y plane, over a great portion of the corner region. However, as seen in the figures, this

proved not to be true in the regions where $-\overline{uv}$ is negative (see Figs. (3.67 - 3.69)) near the wing surface. In zones of negative $-\overline{uw}$ (see Figs. (3.70 - 3.72)), the deviation of the primary shear stress direction from the normal to the isovels is much smaller; this may be because $|-\overline{uw}|$ and $\partial U/\partial z$ are relatively small in these regions.

In a fully-developed flow along duct corners where symmetry exists about the duct corner bisector, Perkins (1970a) has found that the resultant primary shear stress acts "almost always" in the direction perpendicular to the local isovel, i.e. along the resultant mean-velocity gradient. In duct flows, both shear stress components $-\overline{uv}$ and $-\overline{uw}$ change their signs together from one side of the corner bisector to the other in a way that keeps the resultant "always" normal to the isovels. Perkins' results thus indicate that the use of an isotropic eddy viscosity assumption might be a suitable one for fully-developed duct corners. In the wing-body junction, the present measurements showed that $-\overline{uv}$ goes negative although $\partial U/\partial y$ is still positive, which makes an isotropic eddy viscosity - or mixing length - model unsuitable for describing the flow in the corner region.

4.2.2 The Relation Between Shear Stress and Turbulent Kinetic Energy

Dryden (1947) showed that the shear stress $-\overline{uv}$, in a two-dimensional flow, is closely related to the turbulent kinetic energy. Bradshaw, Ferriss and Atwell (1967) obtained good results by assuming a constant proportionality between the local turbulent intensity and the shear stress in their method of calculation of boundary layer development. As a test of the hypothesis in the three-dimensional flow in the wing-body corner, the ratios between each of the shear stress components and the turbulent kinetic energy were computed and

are presented in Figs. (4.10 - 4.18) on shifted-origin graphs. The short horizontal lines on the right of each curve correspond to zero ratio.

Profiles of the ratio $-\overline{uv}/\overline{q^2}$ are shown in Figs. (4.10) - (4.12) for axial stations 2, 5 and 9 (x = 15.7, 61.4 and 122.3 cm) respectively. Far from the corner region (outside the wing boundary layer), the profile of $-\overline{uv}/\overline{q^2}$ across the body boundary layer, at stations 2 and 5, is similar to that in a two-dimensional boundary layer under zero pressure gradient, e.g. Klebanoff (1955), presented in Fig. (3) of Bradshaw (1965). The rather low values, of about 0.10, obtained at station 9 may be due to an experimental error. The favourable pressure gradient to which the flow is subjected at station 9 (see Fig. (3.4)) is too weak to be a cause. $-\overline{uv}/\overline{q^2}$ is constant over most of the body boundary layer except very near to the layer edge where it drops sharply. The constant ratio between $-\overline{uv}$ and $\overline{q^2}$ in the body boundary layer decreases insignificantly with downstream distance from the leading edge. It reduces from about 0.16 at station 2 to about 0.15 at station 5 compared to 0.155 in Klebanoff's boundary layer and 0.15 used by Bradshaw et al (1967). The y-distance over which $-\overline{uv}/\overline{q^2}$ has a constant value shrinks as the wing is approached. Considering the streamwise velocity contours of Figs. (3.14), (3.17) and (3.19) when examining the profiles in Figs. (4.10 - 4.12) we find that $-\overline{uv}/\overline{q^2}$ has a nearly constant value over the y-distance where the velocity contours are nearly parallel to the body surface, i.e. when $\partial U/\partial y$ is finite, and drops quickly as the contours turn to the vertical, i.e. when $\partial U/\partial y$ becomes small. A similar conclusion could be drawn from Figs. (4.13) and (4.14). In the wing boundary layer (at $z < 7$ mm at station 2, $z \leq 15$ mm at station 5) the ratio $-\overline{uw}/\overline{q^2}$ almost attains a constant value of 0.145.

The results at station 9 (see Fig. (4.15)), however, show a low constant value of about 0.1 in the wing boundary layer up to $z \cong 5$ mm only, and then indicate a rise in the ratio up to 0.16 at $z \simeq 18.4$ mm. At all the three stations, the ratio $-\overline{uw}/\overline{q^2}$ drops sharply in the corner regions of almost-vanishing $\partial U/\partial z$, i.e. the regions where the isovels are parallel to the body surface. At a distance from the wing, where the isovels are no longer parallel to the body surface, i.e. in the body-boundary layer zones of finite gradient $(\partial U/\partial z)$, the ratio $(-\overline{uw}/\overline{q^2})$ is greater than zero.

The ratio of the secondary shear stress $-\overline{vw}$ to the turbulent kinetic energy represented by $\overline{q^2}$ is given in Figs. (4.16 - 4.18) for stations 2, 5 and 9 respectively. $-\overline{vw}/\overline{q^2}$ is, generally, very small compared to $-\overline{uv}/\overline{q^2}$ or $-\overline{uw}/\overline{q^2}$ (notice the change in the scale of the figures), except at station 2. Its absolute value diminishes with the downstream distance as a result of the decay of the secondary flows and their associated gradients $\partial V/\partial z$ and $\partial W/\partial y$. The average value of $|-\overline{vw}/\overline{q^2}|$ reduces from about 0.07 at station 2 to $\sim$ 0.05 at 5 and to 0.02 at 9.

We may expect the ratio of the resultant shear stress in the normal plane $\sqrt{\overline{uv}^2 + \overline{uw}^2}$ to be better behaved than the individual stress ratios. The results are given in Figs. (4.19 - 4.21). The ratio is also presented in contour form in Figs. (4.22 - 4.24). Figs. (4.19 - 4.21) indicate that this ratio is constant over the flow cross-section ($\simeq$ 0.165 at station 2, 0.155 at 5, and 0.125 at station 9) except very close to the corner itself in the zones bounded by the corner walls and the planes $z \simeq 9$ mm and $y \simeq 20$ mm at station 2, $z \simeq 13$ and $y \simeq 20$ at station 5, and $z \simeq 15$ and $y \simeq 20$ at station 9. In other words, the zone of inconstancy of the ratio expands in the z-direction only, as the vortex grows, with the downstream distance. The

drop in the ratio of the primary shear stress to the turbulent kinetic energy close to the corner may indicate the weakness of the active part of the turbulent motion that contributes to the shear stress production (see Bradshaw, 1965). Low ratio ($\sqrt{\overline{uv}^2 + \overline{uw}^2}/\overline{q^2}$) was expected at station 9 as a result of the small values obtained for $-\overline{uv}/\overline{q^2}$ there.

Mojola (1972) plotted $\sqrt{\overline{uv}^2 + \overline{uw}^2}/\overline{q^2}$ using the data of Brundrett and Baines (1964) obtained in fully-developed flow in a square duct. The ratio rises slowly with distance along the duct corner bisector from 0.07 close to the corner to 0.10 over most of the boundary region. It then rises to 0.12 near the duct centre before it drops rapidly to zero at the centre.

The above study indicates that assuming a unique relation between the local shear stress and the turbulence intensity seems promising. However, one needs more than just constant $|\tau|/\overline{q^2}$ (e.g. the direction at which the shear stress acts) for a calculation method. Successful trials have already been made recently by Gessner and Emery (1976) in symmetrical corners between two flat plates using a unique relation between $|\tau|$ and $\overline{q^2}$.

4.3 Triple Products and Turbulent Transport of Kinetic Energy and Shear Stresses

The ten elements of the triple product tensor, $\overline{u_i u_j u_k}$, namely, $\overline{u^3}$, $\overline{v^3}$, $\overline{w^3}$, $\overline{u^2v}$, $\overline{u^2w}$, $\overline{v^2u}$, $\overline{v^2w}$, $\overline{w^2u}$, $\overline{w^2v}$ and $\overline{uvw}$, were deduced from the cross-wire measurements at stations 2, 5 and 9 (x = 15.7, 61.4, 122.3 cm). Triple products appear in the turbulent transport terms of the transport equations for turbulent kinetic energy and shear stresses (Equations (4.6) and (4.9)). Figs. (4.25 - 4.34) show the triple products at station 5 (x = 61.4 cm) only, to reduce reader confusion by a massive amount of figures. These graphs were reproduced from the

isometric plots originally produced by the College computer. In Appendix D , the complete set of graphs (at the three stations 2, 5 and 9) are displayed in their original form. Accurate values of the triple products can be read from the latter set of graphs using the read-out sheet supplied with the thesis. Presenting the triple products in the form of turbulent transport velocities of Reynolds stresses and turbulent kinetic energy is more convenient. The transport velocity $u_{i\overline{u_j u_k}}$ of the Reynolds stress $\overline{u_j u_k}$ in the x_i direction is defined as:-

$$\frac{\overline{u_i u_j u_k}}{\overline{u_j u_k}} \qquad \left(\text{e.g. } u_{\overline{vw}} = \frac{\overline{uvw}}{\overline{vw}} \ , \ u_{\overline{uv}} = \frac{\overline{u^2 v}}{\overline{uv}} \ , \ \ldots . \right).$$

In Figs. (4.35 - 4.40), the transport velocities of the main shear stresses, $-\overline{uv}$ and $-\overline{uw}$ in the x-, y- and z-directions, at station 5, are presented. The corresponding graphs for stations 2 and 9, together with the transport velocities of the secondary shear stress-$\overline{vw}$, are given in Appendix D. Triple products and turbulent transport velocities shown in the figures are normalized by U_e^3 and U_e respectively, where U_e is the free stream value of U.

The profiles of $\overline{u^3}$ are given in Fig. (4.25). Far from the wing surface ($z \gtrsim 28$ mm), the profiles show positive values over a short distance from the body and negative $\overline{u^3}$ over the rest of the body boundary layer as expected in a plane boundary layer. $\overline{u^3}$ is always negative for $z \lesssim 28$ mm. In the close vicinity of the wing, the profiles have a"zigzag"shape whose middle portion is negative. Such a profile could not be measured at station 2 where the wing boundary layer is very thin ($\simeq$ 8 mm) and the closest possible traverse lies at a relatively large distance (z/δ_w) in the wing boundary layer. $\overline{u^3}$ is transported in short positive bursts near the body surface and in negative bursts at a

distance from the body.

Turbulent kinetic energy transport in the streamwise direction (x) is represented by the triple products $\overline{u^3}$, $\overline{v^2u}$ and $\overline{w^2u}$ displayed in Figs. (4.25 - 4.27). For $z \gtrsim 33$ mm at stations 2 and 5 and for $z \gtrsim$ 15 mm at station 9, the turbulent kinetic energy transport velocity is negative (relative to the mean flow) except very close to the body ($y \lesssim 7$ mm). In the vicinity of the wing ($z \lesssim 4.5$ mm), the transport velocity is mostly negative.

Profiles of $\overline{u^2v}$, $\overline{v^3}$ and $\overline{w^2v}$, which contribute to the kinetic energy transport in the spanwise (y) direction, are shown in Figs. (4.28) - (4.30). Outside the wing boundary layer ($z \gtrsim 8$, 11, 20 mm at stations 2, 5 and 9 respectively) the kinetic energy is transported away from the body by the turbulence fluctuations throughout the body boundary layer. Inside the wing boundary layer, the transport is away from the body at small y and towards the body at large y.

Figs. (4.31 - 4.33) show the profiles of the products $\overline{u^2w}$, $\overline{v^2w}$ and $\overline{w^3}$. Inside the wing boundary layer, the turbulent transport of the kinetic energy is away from the wing (positive $\overline{u^2w} + \overline{w^3}$ > negative $\overline{v^2w}$ there). At $z > 30$, 33 and 45 mm in planes 2, 5 and 9 respectively, the transport of turbulent kinetic energy in the z-direction is very small due to the cancellation of the positive transport of $\overline{w^2}$ and the negative transport of $\overline{u^2} + \overline{v^2}$*. In fact, all the triple products $\overline{u^2w}$,

---

* An artificial example of v and w signals that result in positive $\overline{w^3}$ and negative $\overline{v^2w}$ is shown in this sketch.

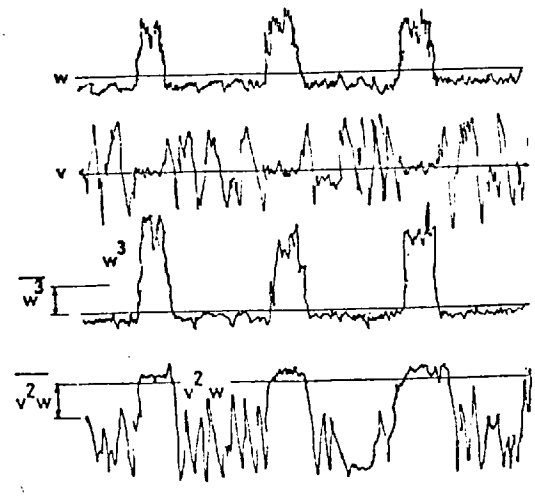

$\overline{v^2w}$ and $\overline{w^3}$ should vanish in the body boundary layer at large distances from the wing, i.e. outside the three-dimensional region. Excluding the one or two odd values near the body surface (where probe blockage may result in relatively large errors), we find that within the inevitable hot wire measurements scatter they do.

Fig. (4.34) shows the triple product $\overline{uvw}$. Discussion of this quantity which represents the transport of the shear stresses ($-\overline{uv}$ in the z-direction, $-\overline{uw}$ in the y-direction and $-\overline{vw}$ in the x-direction) is given below.

The shear stress transport velocities defined as:-

$$u_{\overline{uv}} = \frac{\overline{u^2v}}{\overline{uv}} \quad , \quad v_{\overline{uv}} = \frac{\overline{v^2u}}{\overline{uv}} \quad , \ldots . \text{ etc}$$

are shown in Figs. (4.35) - (4.40) for the main shear stresses at station 5 (x = 61.4 cm). As mentioned before, the corresponding graphs at stations 2 and 9 (x = 15.6 and 122.3 cm) are given in Appendix D. We now discuss the general trends of the transport velocities of the main shear stress components, $-\overline{uv}$ and $-\overline{uw}$, in the three directions, x, y and z. Since the shear stresses change their sign over the measurement domain (see Figs. (3.67 - 3.75)), infinite values of transport velocities appear at isolated points.

The transport velocities of $-\overline{uv}$ in the x-direction (i.e. $u_{\overline{uv}} = \overline{u^2v}/\overline{uv}$) are given in Fig. (4.35). At large distances from the wing surface (i.e. outside the wing boundary layer), $u_{\overline{uv}}$ is always positive close to the body and negative at a distance from the body surface, i.e. $\overline{uv}$ is transported downstream, relative to the mean flow, in the body boundary layer close to the surface and upstream in the outer part of the body boundary layer. The transport velocity increases with y. As the wing is approached, the zone of "downstream" transport diminishes.

In the close vicinity of the wing $\overline{uv}$ is always transported upstream. Fig. (4.36) shows the transport of $\overline{uv}$ in the y-direction. Away from the wing, the general trend is a decrease in the positive transport velocity as the body is approached within its boundary layer. At $z < \delta_w$ (δ_w = wing boundary layer thickness) the inwards transport velocities increase rapidly as the border between negative and positive $\overline{uv}$ is approached. The results show that away from the wing, the transport velocities of $\overline{uv}$ in the streamwise direction and relative to the body surface are similar to those in a two-dimensional boundary layer (e.g. Andreopoulos, 1978). It can be seen from Fig. (4.37a) and (4.37b) that the crosswise (z-wise) transport of $\overline{uv}$ is generally lower than those in the x- and y-directions (notice the change in figures' scales). $\overline{uv}$ is always transported away from the wing except near the body boundary layer edge and very close to the wing surface.

The transport velocities of the wing main shear stress - $\overline{uw}$ are given in Figs. (4.38 - 4.40). Fig. (4.38) of $\overline{u^2w}/\overline{uw}$ shows that $\overline{uw}$ is transported in the upstream direction (relative to the mean flow) close to the wing. As the distance from the wing increases, a growing region of downstream transport of $\overline{uw}$ appears at small y. Outside the body boundary layer, upstream transport increases with distance z from the wing. The wing main shear stress is transported relative to the body surface at velocity $v_{\overline{uw}} = \overline{uvw}/\overline{uw}$ displayed in Fig. (4.39). Inside the wing boundary layer, $\overline{uw}$ is transported towards the body at a low velocity decreasing with z. Crosswise transport of $\overline{uw}$ relative to the wing surface is given in Fig. (4.40). Near the wing (at $z < \delta_w$), $\overline{uw}$ is transported away from the wing at velocity increasing with z.

It is thus concluded that:-

(a) Far from the corner region the transport velocities of the

main body and wing shear stresses (- $\overline{uv}$ and - $\overline{uw}$) are similar to those in a two-dimensional boundary layer. The streamwise transport, relative to the mean flow, is always upstream except very close to the corresponding surface. Across the boundary layers, shear stresses are transported away from the corresponding surface except in the inner layers.

(b) Near the borders between shear stresses of different signs, infinite values of the transport velocities are found.

(c) At the edge of the boundary region and where the triple products, and the shear stresses, approach zero, a great scatter is noticed in the computed transport velocities.

4.4 Statistics of Turbulence in the Corner

The statistics of turbulence is described in the following sections using the statistical quantities computed, in the DIG2U program (Weir and Bradshaw, 1974), from the cross-wire measurements in the corner region of the wing-body junction. Three statistical factors are computed in the program: the flatness factor, the skewness factor and the intermittency factor.

4.4.1 The Flatness Factor

The flatness (kurtosis) factor, F_{u_i}, of the turbulent velocity component u_i, is the ratio of its fourth moment to the square of its variance, i.e.:-

$$F_{u_i} = \frac{\overline{u_i^4}}{\sigma_i^4} = \frac{\overline{u_i^4}}{\overline{u_i^2}^2} \qquad (4.2)$$

(notice that $\overline{u_i^2}^2$ is not summed).

It is a measure of the inhomogeneity in the turbulent intensity in the i^{th} direction (Townsend, 1956). The flatness factors of the three components F_u, F_v and F_w are shown in Figs. (4.41 - 4.49).

The general behaviour of the flatness factor of the three turbulent components of velocity in the corner is similar. Away from one of the surfaces, e.g. the wing, the flatness factor increases quickly with distance from the second surface, y in this case. Close to the walls, F_u and F_w have flat minima, except in the region influenced by the corner vortex. As the wing boundary layer grows, and because of the slight departure of the vortex centre relative to the wing surface with downstream distance, the width of the layer of constant minimum flatness spreads from a very narrow zone at station 2 to 7 mm from the wing surface at station 5 and to 10 mm at station 9. Areas of minimum flatness also spread in the body boundary layer from $y \cong 10$ mm at station 2 to ~ 12.5 mm at 5 and to $\simeq 14$ mm at 9. The minimum values close to the walls are: 2.8 for F_u, 3.0 for F_v and 3.1 for F_w compared to 3 in signals with Gaussian probability distributions. Measurements carreid out in the Department in a two-dimensional boundary layer (e.g. Andreopoulos, 1978) showed $F_u \cong 2.7$ and $F_v \simeq 3.0$ near the wall. The v-component flatness factor F_v, Figs. (4.44 - 4.46), increases from its minimum in the close vicinity of the body. Clear evidence of this behaviour appears in Fig. (4.44) at station 2. In the regions of distorted velocity contours in the corner (see Figs. (3.14), (3.17) and (3.19)), the flatness factor of the three components rise from their minimum. The absolute rise reduces with downstream distance, i.e. with attenuation in the vortex strength.

Large flatness factor near the corner may result from the transport of intermittent fluid towards the corner by the vortex. This

could lead to higher flatness factor, though the flow was not truly intermittent, as a result of the occasional large eddies swept towards the corner.

It is thus concluded that close to the wing-body corner walls, but outside the regions influenced by the presence of the vortex, the three turbulence velocity components, u, v and w, are non-intermittent and the flow is nearly fully turbulent with well-ordered structure similar to that in a two-dimensional boundary layer. Non-intermittent turbulent flow in the vicinity of the corner walls spreads with the growth and attenuation of the corner vortex. As the boundary region shrinks in the corner by the action of the vortex, the turbulence velocity components become more intermittent. Hence, the structure is, as usual, roughly Gaussian in the fully-turbulent region except for the rise in the flatness factor near the corner, due either to large eddies swept in by the vortex or to the extra damping in the corner region due to the presence of two walls.

4.4.2 The Skewness Factor

The skewness factor, S_{u_i}, of the velocity component u_i is a measure of asymmetry of its probability density function. It is defined as:-

$$S_{u_i} = \overline{u_i^3}/\sigma_{u_i}^3 = \overline{u_i^3}/(\overline{u_i^2})^{3/2} \qquad (4.3)$$

($\overline{u_i^2}$ is not summed)

The skewness factors of u, v and w are plotted in Figs. (4.50) - (4.58). Close to the body or the wing surface at stations 5 and 9, the skewness factor of the three components is nearly zero (i.e. the probability of having high positive and high negative values of each of

$\overline{u^3}$, $\overline{v^3}$ and $\overline{w^3}$ is almost equal. S_u changes sign with distance from either surface, from a very small positive value near the walls to a relatively high negative value away from them, while S_v and S_w increase with distance monotonically in the positive direction. The region of zero skewness widens with downstream distance, while the level of skewness reduces, in general. Approaching the body surface in the zone influenced by the vortex at station 2, the skewness factors (absolute values) decrease to zero (S_u from the negative and S_v and S_w from the positive side) at a distance $y \simeq 7$ mm. With further decrease in y, S_u goes negative while S_v and S_w go positive again. Away from the wing (outside the zone influenced by the vortex), S_u, S_v and S_w behave similarly as they do away from the wing at stations 5 and 9. In a two-dimensional flow (e.g. Andreopoulos, 1978), both u and v almost always have equal negative skewness that reduces nearly to zero near the wall.

Hence, it is concluded that turbulence velocity components u, v and w are nearly symmetrical close to the corner surfaces, except in the region of high vorticity, and are less symmetrical away from the walls. The degree of lack of symmetry in the outer part of the boundary region gets smaller, i.e. the flow becomes more symmetrical as the vortex attenuates, with downstream distance (x). The u-component is skewed to the negative side, except very close to the body at large distances from the wing, and v- and w-components are skewed to the positive side. In other words, negative $\overline{u^3}$ is more frequent while positive $\overline{v^3}$ and $\overline{w^3}$ are more frequent in regions of non-symmetry.

4.4.3 The Intermittency Factor

The definition of the flow intermittency factor is given by:-

$$\gamma = \frac{\text{the time spent in turbulent flow}}{\text{the total time}} \qquad (4.4)$$

Figs. (4.59 - 4.61) contain the plots of γ worked out from the cross-wire measurements using the "DIG2U" program. The "DIG2U" discrimination between turbulent and non-turbulent flow is based on the local time derivatives, $\partial\overline{uv}/\partial t$ and $\partial^2\overline{uv}/\partial t^2$. The intermittency threshold values on these derivatives are read in to the program only for the first five records of the digital data. Threshold values of 0.3 and 0.35 were used on $\partial\overline{uv}/\partial t$ and $\partial^2\overline{uv}/\partial t^2$ respectively (Murlis, 1975). For the rest of the data, the threshold is based on the mean value of the local derivatives at the same point. This results in high values of γ near boundary region edges, or in the free stream, where very small non-intermittent fluctuations, or even instrument noise, are seen by the program as long turbulent bursts of low amplitude. Computed intermittency factor, hence, rises suddenly outside the boundary layer. In Figs. (4.59) - (4.61), such non-realistic points were removed from the graphs.

The profiles of γ are flat, at a maximum value of nearly 0.9, close to the body and at nearly 0.92 close to the wing surface. The average position of the interface between the turbulent and irrotational flow is, by definition, where $\gamma = 0.5$. The locus $\gamma = 0.5$ is indicated in the figures by chain-dotted lines. Away from the wing, the interface between the body boundary layer and the irrotational flow occurs at $y = 0.88\ \delta_b$ and moves to $y \simeq 0.85\ \delta_b$ with decrease in z, δ_b being the local body boundary layer thickness, compared to $y/\delta \simeq 0.88$ obtained from temperature signals in two-dimensional boundary layers (e.g. Andreopoulos, 1978). Outside the corner region, Figs. (4.59 - 4.61) indicate that the interface between turbulence in the wing boundary layer and the potential core occurs at $z/\delta_w \simeq 0.62$ at station 2, 0.74 at station 5 and 0.8 at station 9, where δ_w is the local thickness of the wing boundary layer. However, the interface between the wing turbulence and the irrotational core as defined above should not be

trusted all the way. Figs. (4.59 - 4.61) are for γ computed on the bases of the $-\overline{uv}$ time derivatives, while the wing shear stress component is, in fact, $-\overline{uw}$. The present results, thus, call for a new algorithm to define the intermittency in a three-dimensional flow, probably based on the three shear stress components.

4.5 The Turbulent Kinetic Energy Balance

The turbulent kinetic energy conservation equation in tensor form is:-

$$\frac{\partial}{\partial t}\frac{1}{2}\overline{u_i^2} + U_\ell \frac{\partial}{\partial x_\ell}\frac{1}{2}\overline{u_i^2} = -\overline{u_i u_\ell}\frac{\partial U_i}{\partial x_\ell} - \frac{\partial}{\partial x_\ell}\frac{1}{2}\overline{u_i^2 u_\ell} - \frac{\partial}{\partial x_i}\overline{p' u_i} - \nu\overline{u_i \frac{\partial^2 u_i}{\partial x_\ell^2}}$$

(Bradshaw, 1975) (4.5)

For a steady three-dimensional shear flow, the equation takes the following form in cartesian coordinates:-

TERM	PHYSICAL MEANING	
$\left(U\frac{\partial}{\partial x} + V\frac{\partial}{\partial y} + W\frac{\partial}{\partial z}\right)\frac{1}{2}\overline{q^2} =$	ADVECTION	
$-\left[\overline{u^2}\frac{\partial U}{\partial x} + \overline{uv}\frac{\partial U}{\partial y} + \overline{uw}\frac{\partial U}{\partial z}\right.$		
$+ \overline{uv}\frac{\partial V}{\partial x} + \overline{v^2}\frac{\partial V}{\partial y} + \overline{vw}\frac{\partial V}{\partial z}$	PRODUCTION	(4.6)
$\left. + \overline{uw}\frac{\partial W}{\partial x} + \overline{vw}\frac{\partial W}{\partial y} + \overline{w^2}\frac{\partial W}{\partial z}\right]$		

(to be continued)

TERM	PHYSICAL MEANING
$-\left[\frac{\partial}{\partial x}\frac{1}{2}\overline{q^2u}+\frac{\partial}{\partial y}\frac{1}{2}\overline{q^2v}+\frac{\partial}{\partial z}\frac{1}{2}\overline{q^2w}\right]$	DIFFUSION
$-\left[\frac{\partial}{\partial x}\frac{\overline{p'u}}{\rho}+\frac{\partial}{\partial y}\frac{\overline{p'v}}{\rho}+\frac{\partial}{\partial z}\frac{\overline{p'w}}{\rho}\right]$	
$-\nu\left[\overline{u\frac{\partial^2u}{\partial x^2}}+\overline{u\frac{\partial^2u}{\partial y^2}}+\overline{u\frac{\partial^2u}{\partial z^2}}\right.$	DISSIPATION AND VISCOUS DIFFUSION
$+\overline{v\frac{\partial^2v}{\partial x^2}}+\overline{v\frac{\partial^2v}{\partial y^2}}+\overline{v\frac{\partial^2v}{\partial z^2}}$	
$\left.+\overline{w\frac{\partial^2w}{\partial x^2}}+\overline{w\frac{\partial^2w}{\partial y^2}}+\overline{w\frac{\partial^2w}{\partial z^2}}\right]$	

(4.6) (Continued)

An order of magnitude analysis showed that all production terms are negligible except $\overline{uv}\frac{\partial U}{\partial y}$ and $\overline{uw}\frac{\partial U}{\partial z}$, as in this slender flow the streamwise gradient $\partial/\partial x$ and the secondary flow gradients are comparatively small.

The present measurements were used for the evaluation of all terms in the equation except the diffusion by pressure fluctuation $\left[\frac{\partial}{\partial x}\frac{\overline{p'u}}{\rho}+\frac{\partial}{\partial y}\frac{\overline{p'v}}{\rho}+\frac{\partial}{\partial z}\frac{\overline{p'w}}{\rho}\right]$; which includes the unmeasurable pressure fluctuation p' and was ignored. Near the edge of a two-dimensional boundary layer, both production and dissipation of the turbulent kinetic energy are negligible. Several workers' measurements showed that the advection and the turbulent transport $\frac{\partial}{\partial y}\overline{q^2v}$ are almost in balance. Accordingly, it is concluded that the pressure diffusion term $\frac{\partial}{\partial y}\overline{p'v}$ is negligible (i.e. $\overline{p'v} << \overline{q^2v}$) near the boundary layer edge, and, it is to be hoped, negligible everywhere in the layer! If this is really so,

then ignoring the pressure diffusion terms does not involve a considerable error. (Very close to the wall, in the buffer layer, Moin, Reynolds and Ferziger's large eddy simulation of channel flow (1978) shows that the pressure terms are not negligible where they redistribute v-fluctuations (damped by the wall) into u and w. Close to a wall combination, e.g. in the wing-body corner, it is difficult to say what $\partial\overline{p'v'}/\partial y$ or $\partial\overline{p'w'}/\partial z$ do). The last term in the equation (the dissipation and viscous diffusion) was found by difference and thus includes the neglected pressure fluctuation term. Evaluation was performed on the computer using the program "ENGBNC" written by the author. Only the cross-wire measurements were used in the computation without any data smoothing. The three-point Lagrange formula* (see Appendix E) was used in computing all the differentiations, and linear interpolation was performed, when necessary, to evaluate the variables at unified mesh points in the (y-z) planes. Terms in the equation were evaluated only at station 5 where the differentiations w.r.t.x are expected to be relatively accurate.

The turbulent energy balance for the corner boundary region of station 5 is plotted in Figs. (4.62 - 4.72). Each figure shows the balance in the y-direction at a fixed distance, z, from the wing. Figs. (4.65 - 4.72) were plotted in the same way as Fig. (10.2) of Townsend (1956), i.e. with a ten times magnified scale in the outer part of the body boundary layer. The dotted line in each figure

---

* The best one can do with three points only (at stations 2, 5 and 9) is to fit a parabola through them from which the derivative is deduced.

represents* the function u_τ^3/Ky. All the terms have been divided by (U_e^3), and have the units of (mm^{-1}).

Close to the wing (at z = 5.03 mm), Fig. (4.62) indicates an increase in both production and dissipation with y to maximum values of $\simeq 60 \times 10^{-6}$ and 50×10^{-6} mm^{-1} respectively at y ≃ 12 mm ($u_\tau^3/Ky = 11.2 \times 10^{-6}$ mm^{-1} at y ≃ 12 mm). Production and dissipation then drop slightly and asymptote approximately to 44×10^{-6} and 40×10^{-6} mm^{-1}. The figure also indicates constant advection and diffusion for $y \gtrsim 20$ mm. The explanation is evident from Fig. (3.17). A section in the flow at z ≃ 5 mm coincides with a contour of constant relative distance z/δ_w in the wing boundary layer (hence $\partial/\partial y|_{z < \delta_w} = 0$). Similarly, all terms in the energy equation have constant values for all vertical sections (z = const.) taken within the wing boundary layer (i.e. for $z < \delta_w$) as seen from Figs. (4.63) - (4.65).

As shown in Figs. (4.69) - (4.72), the turbulent kinetic energy balance across the body boundary layer at relatively large distance from the wing (z > 33 mm), is nearly similar to that for an ordinary two-dimensional boundary layer. The main contributions are due to the production and dissipation except in the outer regions of the body boundary layer. The near-equality of production and dissipation near the wall in a two-dimensional boundary layer suggests that pressure diffusion ($\partial\overline{p'v'}/\partial y$ is a transport term) is small compared to the production or dissipation. The reason is that the measured dissipation =

---

*. In the inner layer of a two-dimensional boundary layer $\partial U/\partial y = u_\tau/Ky$ and assuming $-\overline{uv} \simeq u_\tau^2$, hence the production $-\overline{uv}\,\partial U/\partial y \simeq u_\tau^3/Ky \simeq \varepsilon$, the dissipation; the advection and diffusion are negligibly small.

$= \varepsilon + \partial\overline{p'v'}/\partial y$ behaves the same way as $-\overline{uv}\frac{\partial U}{\partial y}$. Since dissipation and production are both local quantities, the similarity suggests that the non-local quantity $\partial\overline{p'v'}/\partial y$ is small. Near the body, advection is negligible but the striking result is that in contrast to measurements in two-dimensional boundary layers, the term is mostly negative indicating a gain of energy by advection. This is, of course, due to the existence of secondary flow in the present case, i.e. due to the contribution of $\left(V\frac{\partial}{\partial y} + W\frac{\partial}{\partial z}\right)\frac{1}{2}\overline{q^2}$, to the advection term. The inspection of the different components of the advection term (computed but not presented) showed that $U\frac{\partial}{\partial x}\left(\frac{1}{2}\overline{q^2}\right)$ has generally a positive value of the order of 0.5×10^{-6} (mm^{-1}) near the body increasing to 1.0×10^{-6} at the edge of the body boundary layer and dropping outside the layer to the order of 0.03×10^{-6}. $V\frac{\partial}{\partial y}\frac{1}{2}\overline{q^2}$ is always negative but changes from the order of -1.7×10^{-6} for $33 > z > 28$ and -0.3×10^{-6} for $z > 33$ near the body to $\sim -1.2 \times 10^{-6}$ at $y \sim 14$ mm and to $\sim -0.2 \times 10^{-6}$ near the body boundary layer edge. $W\frac{\partial}{\partial z}\frac{1}{2}\overline{q^2}$ has a positive value of the order of 0.2×10^{-6} close to the body for $z < 43$ changing to negative value of about -0.5×10^{-6} at larger z-values, in the outer parts of the body boundary layer $W\frac{\partial}{\partial z}\frac{1}{2}\overline{q^2}$ attains a negative value of the order of -0.5×10^{-6} for $43 > z > 28$ and a very small negative value at larger z-distances. Closer to the wing (at $z < 23$ mm), the advection is positive, i.e. loss. At $z < 18$ mm, computations indicate positive contributions of all the three components of advection at all distances except for $y < 10$ mm and $z \lesssim 5$ mm. The three advection terms are of the average order of 1.5×10^{-6} mm^{-1} except for $z \lesssim 3.5$ mm where $\frac{1}{2}V\frac{\partial q^2}{\partial y}$ is roughly one order of magnitude higher than each of the other two terms $\frac{1}{2}W\frac{\partial q^2}{\partial z}$ and $\frac{1}{2}U\frac{\partial q^2}{\partial x}$. The above results show that the advection associated with the secondary flow is comparable to the primary advection. Moreover, it exceeds the primary advection in the region very

close to the wing. As can be seen in Figs. (4.62 - 4.65), for $z < 15$ mm, the advection term is not negligible.

The diffusion term almost integrates (w.r.t.y) to zero far from the wing (at $z \gtrsim 23$ mm) as it does in two-dimensional flows. This is not true at shorter distances relative to the wing. In a three-dimensional flow, the integral over the whole y-z plane is zero but individual y integration (say) may have either sign. Also, the pressure diffusion term was neglected but it may not be important except very close to the wall.

Production and dissipation close to the body decrease with distance from the wing to a minimum of $\sim 30 \times 10^{-6}\,\text{mm}^{-1}$ at $z \simeq 28$ mm and then increase with further distance from the wing. This is attributed to the changes in the levels of secondary flows, their signs and gradients, and to the changes in the signs of the different shear stress components around the vortex core. Production by the two primary shear stresses, $-\overline{uv}$ and $-\overline{uw}$, acting respectively on the primary flow gradients $\partial U/\partial y$ and $\partial U/\partial z$ were compared but not separately plotted. Close to the wing ($z < 10$ mm), the largest contribution to the production was from $-\overline{uw}\,\frac{\partial U}{\partial z}$ which is about 40×10^{-6} mm^{-1} close to the wing and reduces to 10×10^{-6} mm^{-1} at $z \simeq 10$ mm. Closer to the wing, $z < 7$ mm, the contribution of $-\overline{uv}\,\frac{\partial U}{\partial y} \simeq 2 \times 10^{-6}$ mm^{-1} only. At $z > 10$ mm, the production is mainly due to $-\overline{uv}\,\frac{\partial U}{\partial y}$ which $\simeq 25 \times 10^{-6}$ mm^{-1} close to the body and reduces rapidly with y. Small negative production terms, i.e. loss in kinetic energy, is noticed at $z \simeq 15.03$ mm due to negative shear (positive $\overline{uw}$) and positive $\frac{\partial U}{\partial z}$ there, even though $-\overline{uv}\,\frac{\partial U}{\partial y}$ is still positive.

4.6 Shear Stress Balance

The transport equation of the shear stress $-\overline{u_i u_j}$ takes the

following general tensor form:-

$$U_\ell \frac{\partial \overline{u_i u_j}}{\partial x_\ell} = - \left(\overline{u_i u_\ell} \frac{\partial U_j}{\partial x_\ell} + \overline{u_j u_\ell} \frac{\partial U_i}{\partial x_\ell} \right) + \overline{\frac{p'}{\rho} \left(\frac{\partial u_i}{\partial x_j} + \frac{\partial u_j}{\partial x_i} \right)} -$$

MEAN TRANSPORT — GENERATION — PRESSURE STRAIN

$$- \frac{\partial}{\partial x_i} \left(\overline{\frac{p' u_j}{\rho}} \right) - \frac{\partial}{\partial x_j} \left(\overline{\frac{p' u_i}{\rho}} \right) - \frac{\partial}{\partial x_\ell} \overline{u_i u_j u_\ell} +$$

TURBULENT TRANSPORT

$$+ \nu \overline{\left(u_i \frac{\partial^2 u_j}{\partial x_\ell^2} + u_j \frac{\partial^2 u_i}{\partial x_\ell^2} \right)} \qquad (4.7)$$

DESTRUCTION

The destruction term:-

$$\nu \overline{\left(u_i \frac{\partial^2 u_j}{\partial x_\ell^2} + u_j \frac{\partial^2 u_i}{\partial x_\ell^2} \right)}$$

is negligibly small outside the viscous sublayer except for very low Reynolds numbers. Turbulent transport by pressure fluctuations, i.e:-

$$\frac{\partial}{\partial x_i} \left(\overline{\frac{p' u_j}{\rho}} \right) - \frac{\partial}{\partial x_j} \left(\overline{\frac{p' u_i}{\rho}} \right)$$

is also believed to be small with comparison to other terms and will be neglected (it is impossible to evaluate experimentally because of the unmeasurable p'). Equation (4.7), hence, reduces to:-

$$U_\ell \frac{\partial \overline{u_i u_j}}{\partial x_\ell} = - \left(\overline{u_i u_\ell} \frac{\partial U_j}{\partial x_\ell} + \overline{u_j u_\ell} \frac{\partial U}{\partial x_\ell} \right) + \overline{\frac{p'}{\rho} \left(\frac{\partial u_i}{\partial x_j} + \frac{\partial u_j}{\partial x_i} \right)} - \frac{\partial}{\partial x_\ell} \overline{u_i u_j u_\ell} \qquad (4.8)$$

For the three components of shear stress, $-\overline{uv}$, $-\overline{uw}$ and $-\overline{vw}$, Equation (4.8) takes the following cartesian forms:-

$$\left(U \frac{\partial}{\partial x} + V \frac{\partial}{\partial y} + W \frac{\partial}{\partial z} \right) \overline{uv} = - \left(\overline{u^2} \frac{\partial V}{\partial x} + \overline{uv} \frac{\partial V}{\partial y} + \overline{uw} \frac{\partial V}{\partial z} + \right.$$

MEAN TRANSPORT

$$\left. + \overline{uv} \frac{\partial U}{\partial x} + \overline{v^2} \frac{\partial U}{\partial y} + \overline{wv} \frac{\partial U}{\partial z} \right) -$$

GENERATION

$$- \left(\frac{\partial}{\partial x} \overline{u^2 v} + \frac{\partial}{\partial y} \overline{uv^2} + \frac{\partial}{\partial z} \overline{uvw} \right) +$$

TURBULENT TRANSPORT

$$+ \overline{\frac{p'}{\rho} \left(\frac{\partial u}{\partial y} + \frac{\partial v}{\partial x} \right)} \quad ; \qquad (4.9a)$$

PRESSURE STRAIN

$$\left(U \frac{\partial}{\partial x} + V \frac{\partial}{\partial y} + W \frac{\partial}{\partial z} \right) \overline{uw} = - \left(\overline{u^2} \frac{\partial W}{\partial x} + \overline{uv} \frac{\partial W}{\partial y} + \overline{uw} \frac{\partial W}{\partial z} + \right.$$

$$\left. + \overline{uw} \frac{\partial U}{\partial x} + \overline{wv} \frac{\partial U}{\partial y} + \overline{w^2} \frac{\partial U}{\partial z} \right) -$$

$$- \left(\frac{\partial}{\partial x} \overline{u^2 w} + \frac{\partial}{\partial y} \overline{uvw} + \frac{\partial}{\partial z} \overline{uw^2} \right) +$$

$$+ \overline{\frac{p'}{\rho} \left(\frac{\partial u}{\partial z} + \frac{\partial w}{\partial x} \right)} \quad ; \text{ and} \qquad (4.9b)$$

$$\left(U\frac{\partial}{\partial x}+V\frac{\partial}{\partial y}+W\frac{\partial}{\partial z}\right)\overline{vw}=-\left(\overline{uv}\frac{\partial W}{\partial x}+\overline{v^2}\frac{\partial W}{\partial y}+\overline{vw}\frac{\partial W}{\partial z}+\right.$$

$$\left.+\overline{uw}\frac{\partial V}{\partial x}+\overline{vw}\frac{\partial V}{\partial y}+\overline{w^2}\frac{\partial V}{\partial z}\right)-$$

$$-\left(\frac{\partial}{\partial x}\overline{uvw}+\frac{\partial}{\partial y}\overline{v^2w}+\frac{\partial}{\partial z}\overline{vw^2}\right)+$$

$$+\overline{\frac{p'}{\rho}\left(\frac{\partial v}{\partial z}+\frac{\partial w}{\partial y}\right)}\quad\cdot \qquad (4.9c)$$

The different terms in the above shear stress transport equations were computed and plotted in Figs. (4.73 - 4.84) at the fifth downstream station of the wing-body junction. The mean transport terms, the generation terms and the turbulent transport terms, as expressed in the above Equation (4.9), were evaluated directly, while the pressure strain terms (the redistribution by pressure fluctuations) were found by difference. Similar to what was done with the energy balance, linear interpolation was used to transform the measurements to a unified mesh and the Lagrangian three-point formula (Appendix D) was used in computing the necessary differentiation. Also, all the terms are divided by $10^{-6}\ U_e^3$.

Figs. (4.73 - 4.76) present the body main shear stress ($-\overline{uv}$) balance in the body boundary layer. Close to the body surface, the dominant terms in the balance are the generation and the pressure strain terms, except close to the wing ($z \lesssim 5$ mm) where all the four terms are comparable. Referring to Fig. (3.68) which shows contours of constant $-\overline{uv}$ at the fifth z-y plane together with Figs. (4.73 - 4.76), it is clear that both generation and pressure strain terms change signs with the change in the shear stress sign. In zones of negative shear stress, i.e. positive $\overline{uv}$, these terms respectively represent loss and gain of

$-\overline{uv}$. We are not aware of any other measurements in which the pressure strain term represents a gain of shear stress; however, there is nothing to forbid this. Near the wing surface ($z \lesssim 15$ mm), both mean and turbulent transport are considerable and opposite in direction at small distances from the body surface. Both of the terms increase in magnitude with decrease in z within this range. At larger distances from the wing ($z > 15$ mm), the two transport terms are neglected compared to the generation and the pressure strain terms, except near the edge of the body boundary layer where the latter two terms are small.

The balance of the wing main shear stress ($-\overline{uw}$) is shown in Figs. (4.77 - 4.80). At $z = 5.03$ mm, the generation and pressure strain terms dominate the balance while both the mean and turbulent transport terms are very small. At $z = 5.03$ and $z = 15.03$ mm, where the flow sections lie at constant height inside the wing boundary layer, all the terms in the shear stress balance asymptote to constant values with y. Generation and pressure strain terms which have their maxima close to the wing (see Fig. (4.77)) decrease rapidly with $-\overline{uw}$ to a lower level at $z = 15.03$ mm (notice the change in scales between figures) where $-\overline{uw}$ is very small (see Fig. (3.71)). At $z = 28.4$ mm, the wing shear stress $-\overline{uw}$ is negative, as seen in Fig. (3.71) and Fig. (4.79) shows a change in the signs of both generation and strain terms. Similar to the case of body shear, the generation and pressure strain represents loss and gain of $-\overline{uw}$ when $\overline{uw}$ is positive. The scatter in the profiles at $z = 63.4$ mm (Fig. (4.80)), is due to a probable error in the numerical evaluation of the terms, especially the derivatives w.r.t.z because $z = 63.4$ mm is the furthest traverse from the wing.

From the study of the balance of both body and wing main shear stresses, $-\overline{uv}$ and $-\overline{uw}$, it is evident that:-

(i) the dominant terms in the balance, close to the corresponding wall, are the generation and the pressure strain terms;

(ii) both terms drop quickly with distance from the body and the wing respectively, and,

(iii) in regions of negative shear stress, they change signs so that the "generation" becomes a loss and the pressure strain becomes a gain in the shear stresses - $\overline{uv}$ and - $\overline{uw}$.

The balance of the secondary shear stress - $\overline{vw}$ at station 5 is given in Figs. (4.81 - 4.84) for completeness. Opposite to - $\overline{uv}$ and - $\overline{uw}$, the generation term represents a loss of - $\overline{vw}$ and the pressure strain represents a gain of - $\overline{vw}$ when the latter is positive and vice versa. Close to the body, all the four terms drop quickly with z. Turbulent transport is always larger than, and generally opposite to, the mean transport.

4.7 Streamwise Vorticity and Streamwise Vorticity Equation

4.7.1 The Streamwise Vorticity

Contours of the streamwise component of vorticity $\xi = \frac{\partial W}{\partial y} - \frac{\partial V}{\partial z}$ at x = 15.6, 61.4 and 122.3 cm from the leading edge are shown in Figs. (4.85 - 4.87). The inset in each figure shows the change of ξ across a section in the body boundary layer passing through the apparent vortex centre. The streamwise vorticity level drops with downstream distance. Its maximum value (ξ_{max}) decreases from about 30 U_e sec^{-1} at x = 15.6 cm to 21 U_e sec^{-1} at x = 61.4 cm and to about 15 U_e sec^{-1} at x = 122.3 cm, compared to a decrease in U_e/δ_b from 43.5 U_e sec^{-1} to 31.3 U_e then to 24.4 U_e and in U_e/δ_w from 125 U_e to 62.5 U_e to 47.6 U_e at the same streamwise distances x. δ_b and δ_w are the body boundary

layer thickness away from the wing and the wing boundary layer thickness away from the body respectively. Reduction in ξ_{max} is accompanied by a spread in the vortex cross-sectional area. Taking the contour $\xi = 0.5\ \xi_{max}$ as a measure of the relative size of the vortex, we find that the vortex cross section increases from z x y ≅ 27 x 5.5 mm to 33 x 6.25 and finally to 37.5 x 6.25 with increase in x from 15.6 cm to 61.4 cm and to 122.3 cm. The location of the vortex centre (where $\xi = \xi_{max}$) relative to the wing surface as seen in Figs. (4.85 - 4.87) agrees with Figs. (3.20 - 3.22) of the secondary flow vectors in the normal planes, while no such agreement is noticed for the distance of the centre from the body surface.

The vortex strength expressed by the streamwise circulation, Γ_x, was also roughly deduced using the present measurements. Circulation around a closed contour, C, in the y-z plane is given by:-

$$\Gamma_x = \oint_C V_s \, ds \qquad (4.10)$$

where V_s is the secondary velocity component along the infinitesimal arc length ds. Γ_x is related to the streamwise vorticity ξ in the form:-

$$\Gamma_x = \int\int_{A_c} \xi \cdot dA_c \qquad (4.11)$$

where ξ is the streamwise vorticity component over the cross-section area dA_c, and A_c = area enclosed by the contour C. In the present study, we considered $\Gamma_x = \xi_{max} \cdot A_{\xi_{max/2}}$ as a rough estimate proportional to vortex strength, where $A_{\xi_{max/2}}$ is the cross-sectional area enclosed by the contour $\xi = 0.5\ \xi_{max}$. Γ_x drops slightly from $4.5 \times 10^{-3}\ U_e$ ($m^2\ sec^{-1}$) at x = 15.6 cm to $4.12 \times 10^{-3}\ U_e$ at x ≅ 61.4 cm and then to $3.52 \times 10^{-3}\ U_e$

at x ≃ 122.3 cm. This reduction in the vortex strength with x agrees with the attenuation in the secondary flow strength apparent in Figs. (3.20 - 3.22).

Figs. (4.85 - 4.87) indicate the existence of a narrow zone of opposite vorticity (relative to the main vortex) in the wing boundary layer. This region of relatively weak opposite vorticity spreads, and its vorticity increases with downstream distance. It is the natural result of the surface shear stress in the y-z plane.

4.7.2 Streamwise Vorticity Equation

The absence of the unmeasurable pressure field from the streamwise vorticity equation (Equation (1.3)) makes all of its terms, in theory, computable. However, the accuracy of computation is expected to be very low. Evaluation of terms in the equation involve computing partial derivatives of at least the second order for scattered experimental data. The probability of obtaining accurate results can be improved with the increase in the number of measurements at the same point. Perkins (1970a) tried to derive an equation for the streamwise circulation, Γ_x, by integrating the streamwise Equation (1.3) as a method for reducing the scatter but his trial was not successful. But on the basis of symmetry of his flow field about the corner bisector, he was able to increase the number of samples, in some of the terms, by regarding the data on each side of the bisector independently. However, he did not check the balance of the equation due to the expected errors in terms like $U \frac{\partial \xi}{\partial x}$ and $\xi \frac{\partial U}{\partial x}$, deduced from one trial.

Unfortunately, and due to the lack of symmetry in the corner of a "wing-body" junction, only one trial is available at each point for all terms in the equation. A poor accuracy is thus expected in the present evaluation. The best evaluated terms are P_3 and P_4 which contain

no derivatives w.r.t.x; only three points are available in the streamwise direction (x).

Some of the terms in the equation were evaluated at station 5 (x = 61.4 cm) and are presented separately in Figs. (4.88 - 4.91). The contribution of the vortex stretching (flow acceleration) to the production of ξ, given by $P_1 = \xi \frac{\partial U}{\partial x}$, is shown in Fig. (4.88). P_1 almost always represents a loss in the streamwise vorticity, as the flow in the growing boundary region, where the vortex exists, is decelerating ($\partial U/\partial x < 0$). P_1 drops sharply in value with distance from any of the walls, the wing or the body, due to the reduction in $|\partial U/\partial x|$.

The effect of the skewing of the other two vorticity components η and ζ is presented in Fig. (4.89). $P_2 = \eta \frac{\partial U}{\partial y} + \zeta \frac{\partial U}{\partial z} = \frac{\partial U}{\partial z}\frac{\partial V}{\partial x} - \frac{\partial U}{\partial y}\frac{\partial W}{\partial x}$ which is an order of magnitude lower than P_1 reduces sharply with distance from the body as a result of the reduction in both the velocity gradient $\frac{\partial U}{\partial y}$ and the vorticity component η. The decrease in P_2 with z is much slower than with y. Close to the body (at $y \lesssim 15$ mm), P_2 represents a loss in ξ. At $y \gtrsim 15$ mm and $z \lesssim 23$ mm in the zones of distorted isovels, under the influence of the secondary flows, P_2 represents a gain of ξ as a result of the changes in the directions of the velocity gradients. In fact, the skew $\partial W/\partial x$ at station 5 is very weak compared to that near the leading edge which initiates the secondary vorticity in the wing-body corner. The former is generally in opposite direction to the latter, which explains its dissipating action to the leading edge vortex. The very small gain noticed at $z \simeq 53$ mm in the region $14 \lesssim y \lesssim 40$ mm is mainly due to $\eta \frac{\partial U}{\partial y}$.

The contributions of the Reynolds stress components in the cross planes, represented by P_3 and P_4, are shown in Figs. (4.90) and (4.91). P_3 and P_4 are the largest two terms in the equation (at station 5). They are an order of magnitude greater than P_1 and P_4 is much greater than P_3.

P_3, which expresses the effect of the inhomogeneity of the secondary shear stress - $\overline{vw}$, causes a gain in ξ inside the wing boundary layer ($z \lesssim 23$ mm) close to the body surface $y \lesssim 10$ mm and a loss for $y \gtrsim 10$ mm. Outside the wing boundary layer, P_3 represents a loss at $y \lesssim 10$ mm and a gain in the outer parts of the body boundary layer. Away from the wing, P_3 again causes loss in ξ in the outer parts of the body boundary layer and a gain near the body. In fact, P_3 is diffusing ξ from the regions of high vorticity near the body surface and just outside the wing boundary layer in both z-directions and also to the outer layers of the body boundary layer above the vortex centre.

The diffusion of ξ due to the anisotropy of the normal Reynolds stresses $\overline{v^2}$ and $\overline{w^2}$, expressed as P_4, is presented in Fig. (4.91). At $z \lesssim 23$ mm, a big loss in ξ occurs at $y \lesssim 10$ mm, and a very small gain occurs in the region $10 \lesssim y \lesssim 20$ mm. P_4 becomes two orders of magnitude lower at $z \gtrsim 23$ mm and is subjected to some scatter. In this region, P_4 represents a diffusion of ξ from the inner part of the body boundary layer to the outer part.

Viscous diffusion of streamwise vorticity (term D in Equation (1.3)) proved to be, as expected, negligible; the measurements did not extend into the viscous sublayer where viscous diffusion might be important.

The overall result is a big reduction in ξ close to the body surface and a relatively small addition to ξ in the regions where it is low. The net outcome, as has already been seen in the previous section and in Figs. (3.20 - 3.22), is an attenuation in the vorticity (reduction in ξ_{max}), formed originally near the wing leading edge and a growth in the vortex cross-section with x.

The main contribution to the diffusion of streamwise vorticity is due to the Reynolds stresses in the cross plane. Hence, Reynolds

stresses act to diffuse the streamwise vorticity of the first kind rather than induce secondary flows of the second kind as in corners of rectangular ducts.

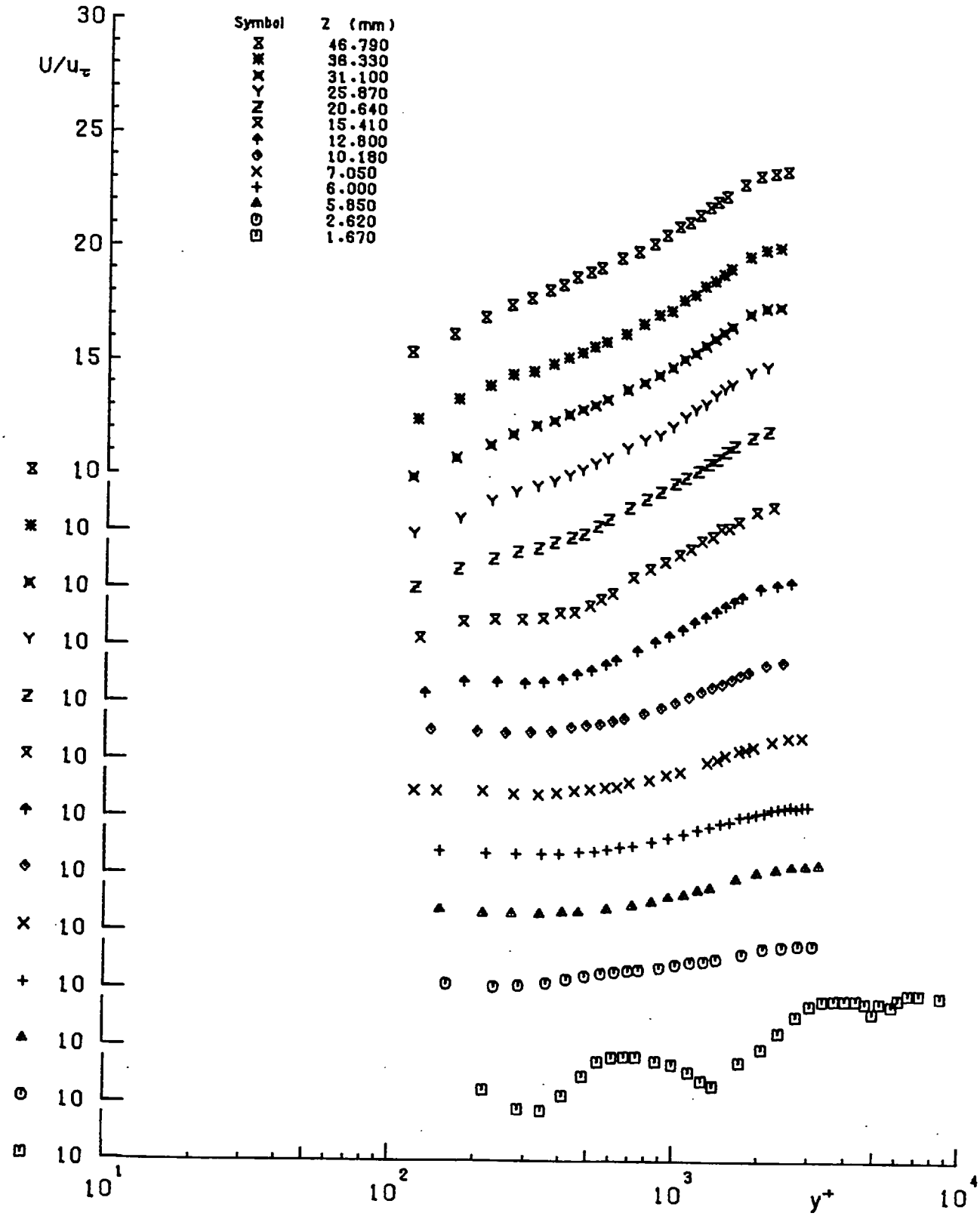

FIG.(4.1) SEMI LOGARITHMIC PLOTS OF STREAMWISE VELOCITY PROFILES AT STATION 1 (X= 34.66 mm)

Pitot Tube Measurements
C_f From Preston Tube Measurements

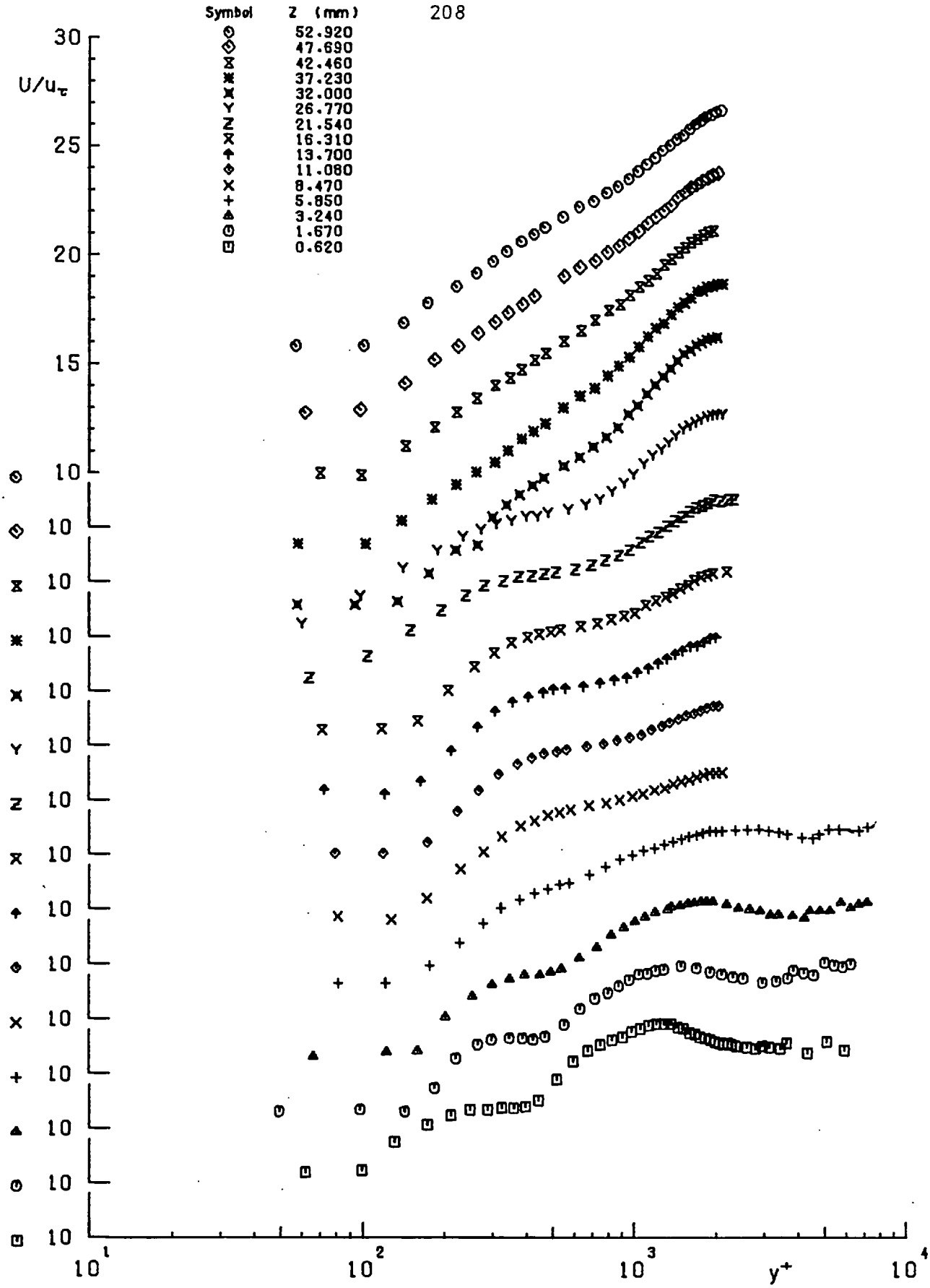

FIG.(4.2:a) SEMI LOGARITHMIC PLOTS OF STREAMWISE VELOCITY PROFILES AT STATION 2 (X= 187.06 mm)

Pitot Tube Measurements
C_f From Preston Tube Measurements

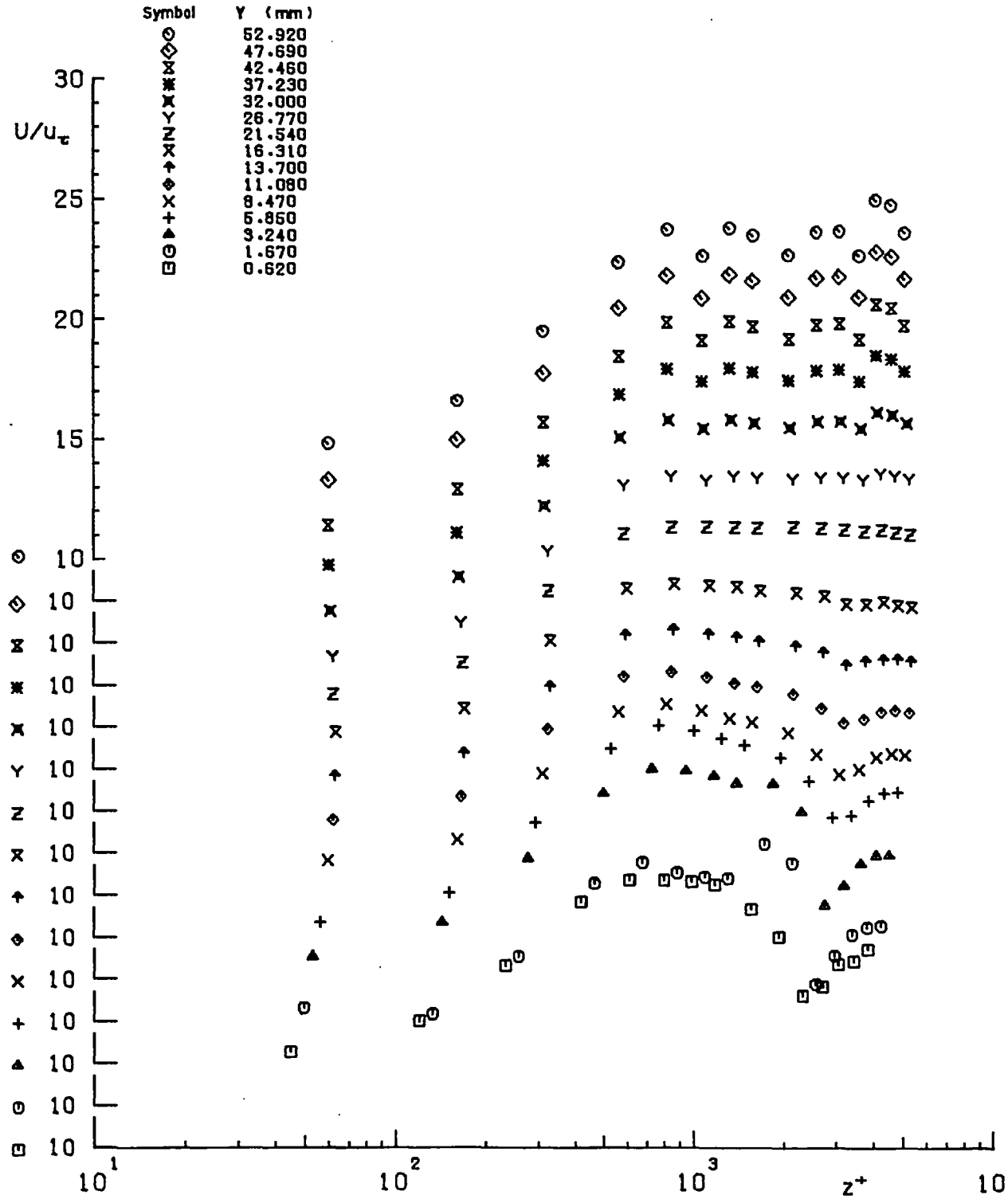

FIG.(4.2: b) SEMI LOGARITHMIC PLOTS OF STREAMWISE VELOCITY PROFILES AT STATION 2 (X= 187.06 mm)

Pitot Tube Measurements
C_f From Preston Tube Measurements

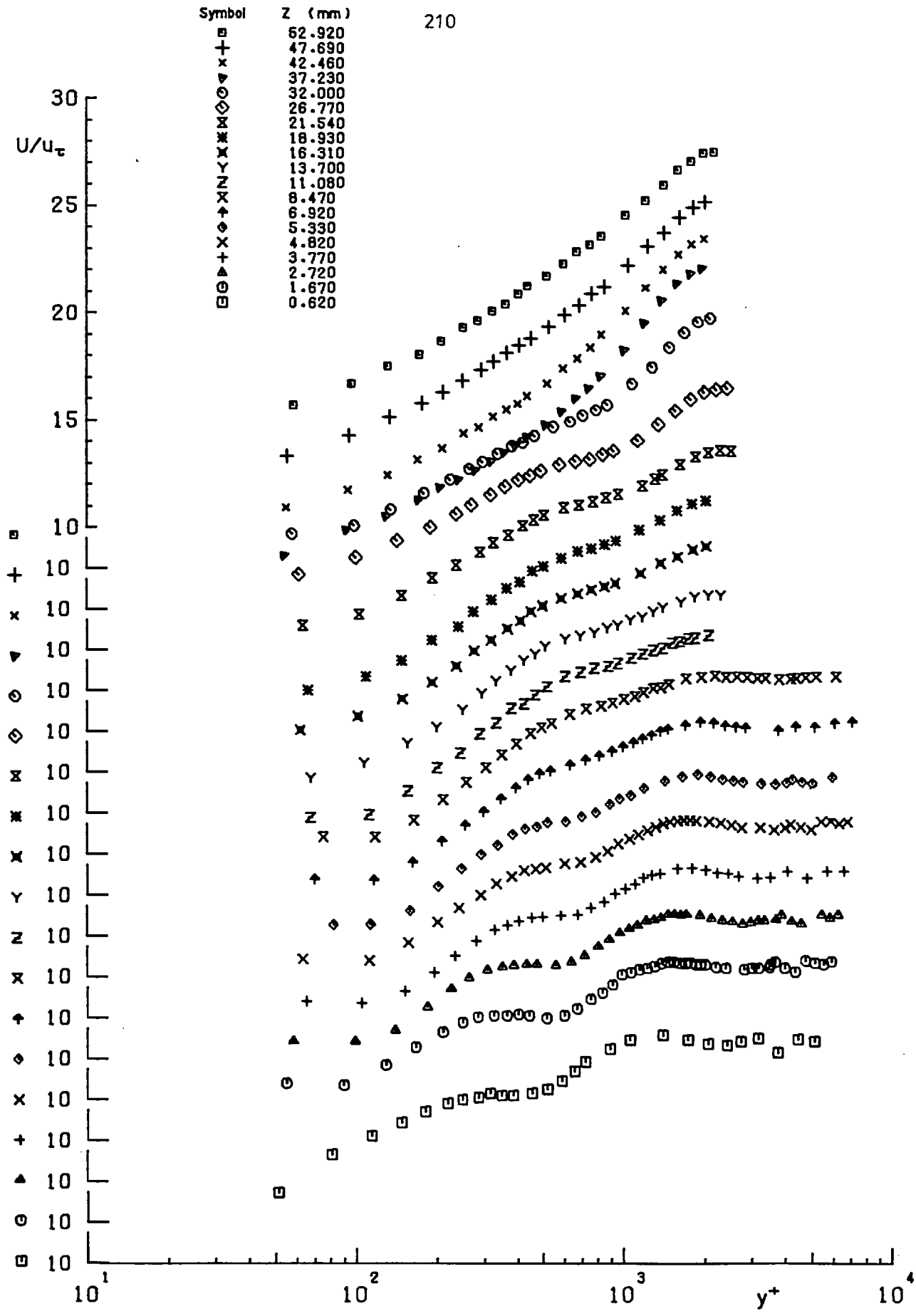

FIG.(4.3:a) SEMI LOGARITHMIC PLOTS OF STREAMWISE VELOCITY PROFILES AT STATION 3 (X= 339.46 mm)

Pitot Tube Measurements
C_f From Preston Tube Measurements

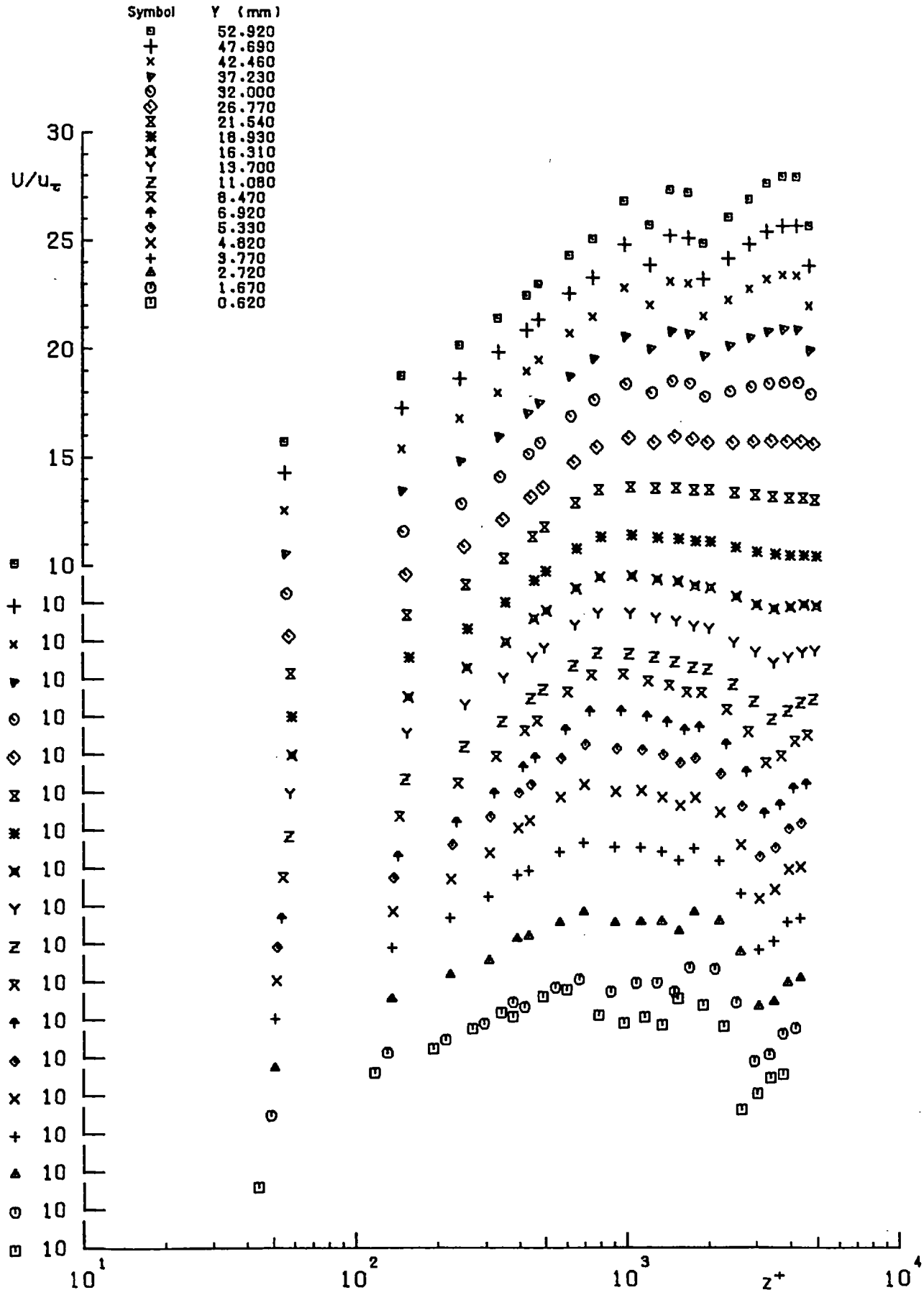

FIG.(4.3:b) SEMI LOGARITHMIC PLOTS OF STREAMWISE VELOCITY PROFILES AT STATION 3 (X= 339.46 mm)

Pitot Tube Measurements
C_f From Preston Tube Measurements

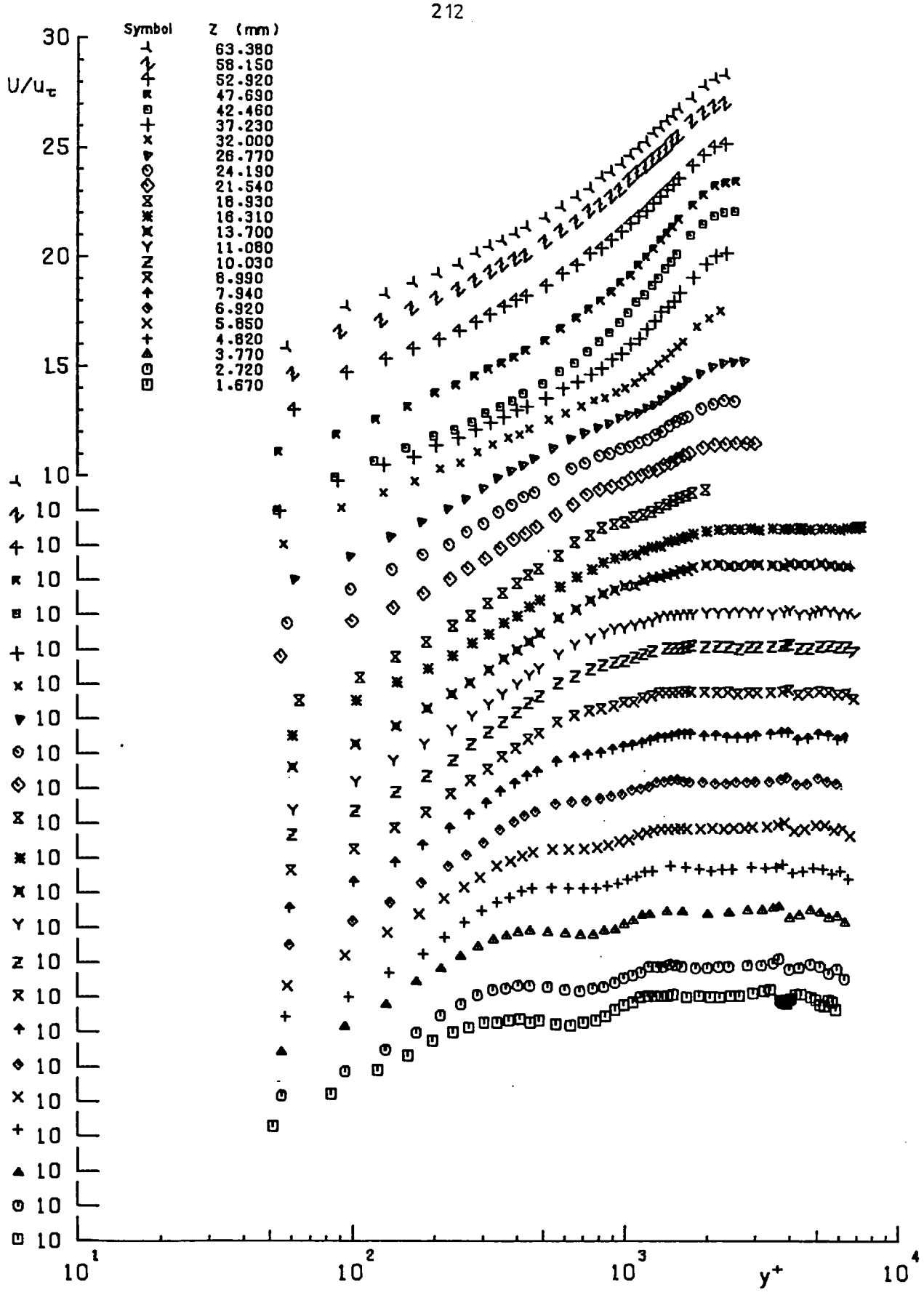

FIG.(4.4:a) SEMI LOGARITHMIC PLOTS OF STREAMWISE VELOCITY PROFILES AT STATION 5 (X= 644.26 mm)

Pitot Tube Measurements
C_f From Preston Tube Measurements

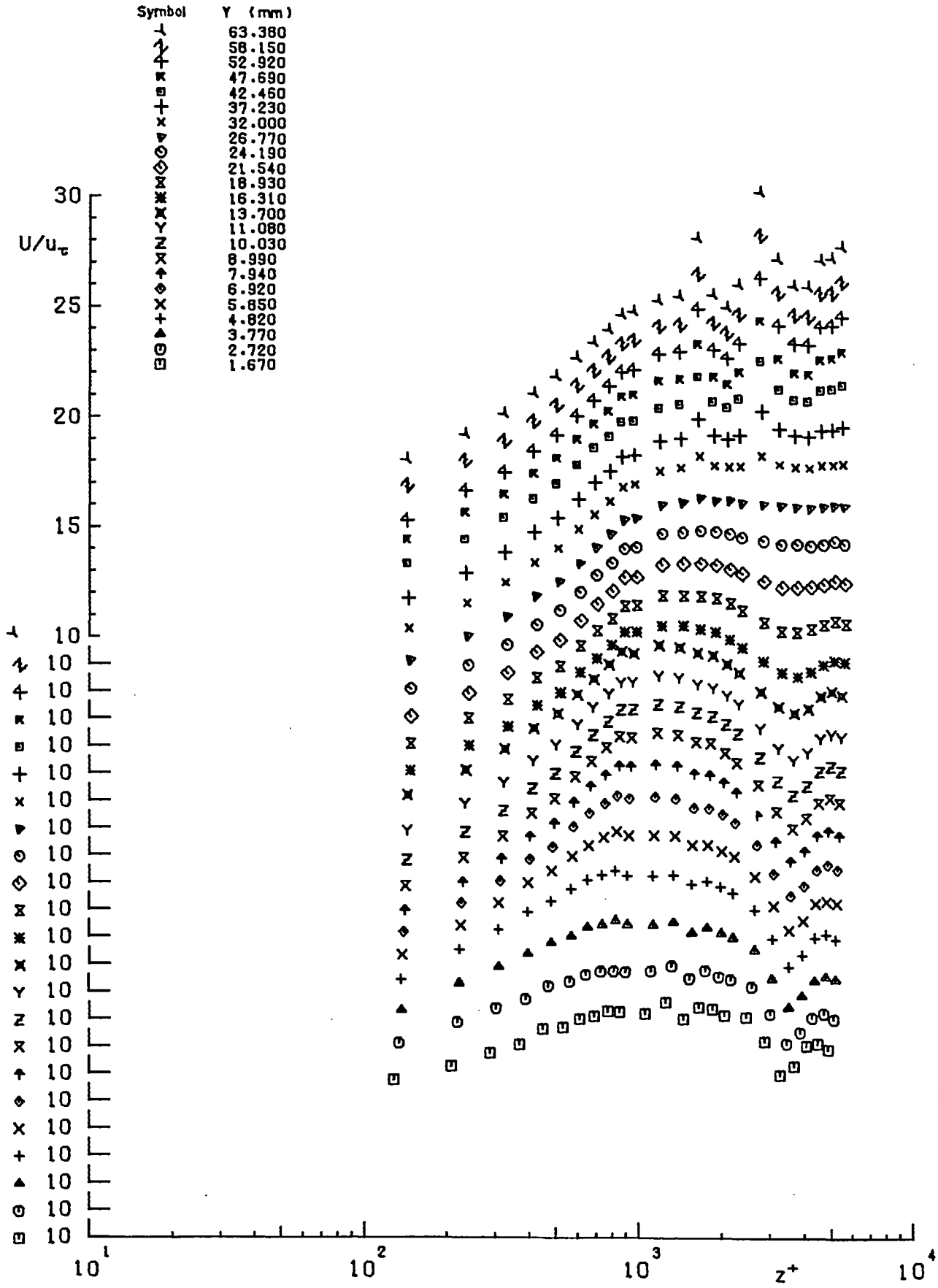

FIG.(4.4:b) SEMI LOGARITHMIC PLOTS OF STREAMWISE VELOCITY PROFILES AT STATION 5 (X= 644.26 mm)

Pitot Tube Measurements
C_f From Preston Tube Measurements

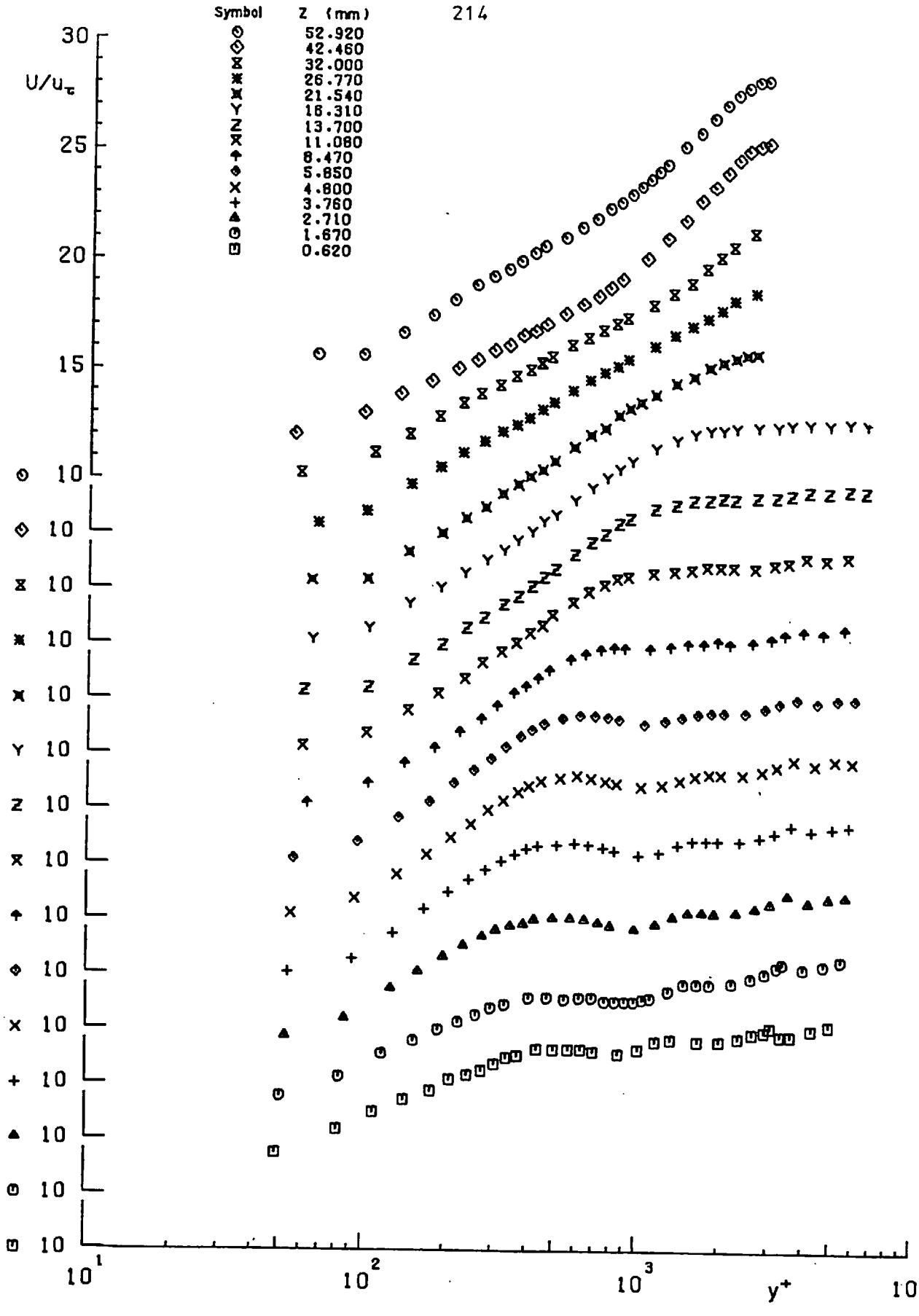

FIG.(4.5:a) SEMI LOGARITHMIC PLOTS OF STREAMWISE VELOCITY PROFILES AT STATION 7 (X= 949.06 mm)

Pitot Tube Measurements
C_f From Preston Tube Measurements

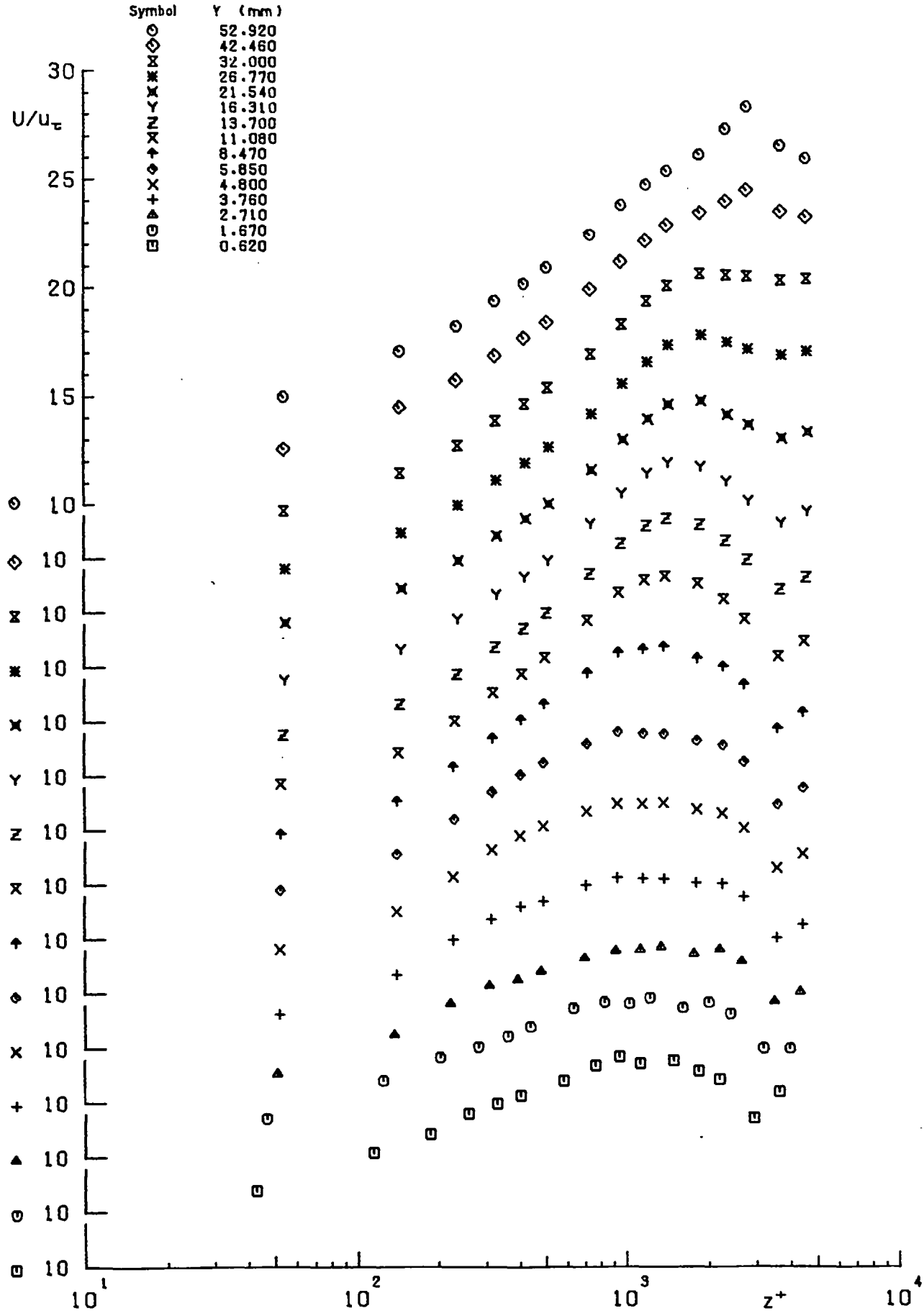

FIG.(4·5:b) SEMI LOGARITHMIC PLOTS OF STREAMWISE VELOCITY PROFILES AT STATION 7 (X= 949.06 m.m)

Pitot Tube Measurements
C_f From Preston Tube Measurements

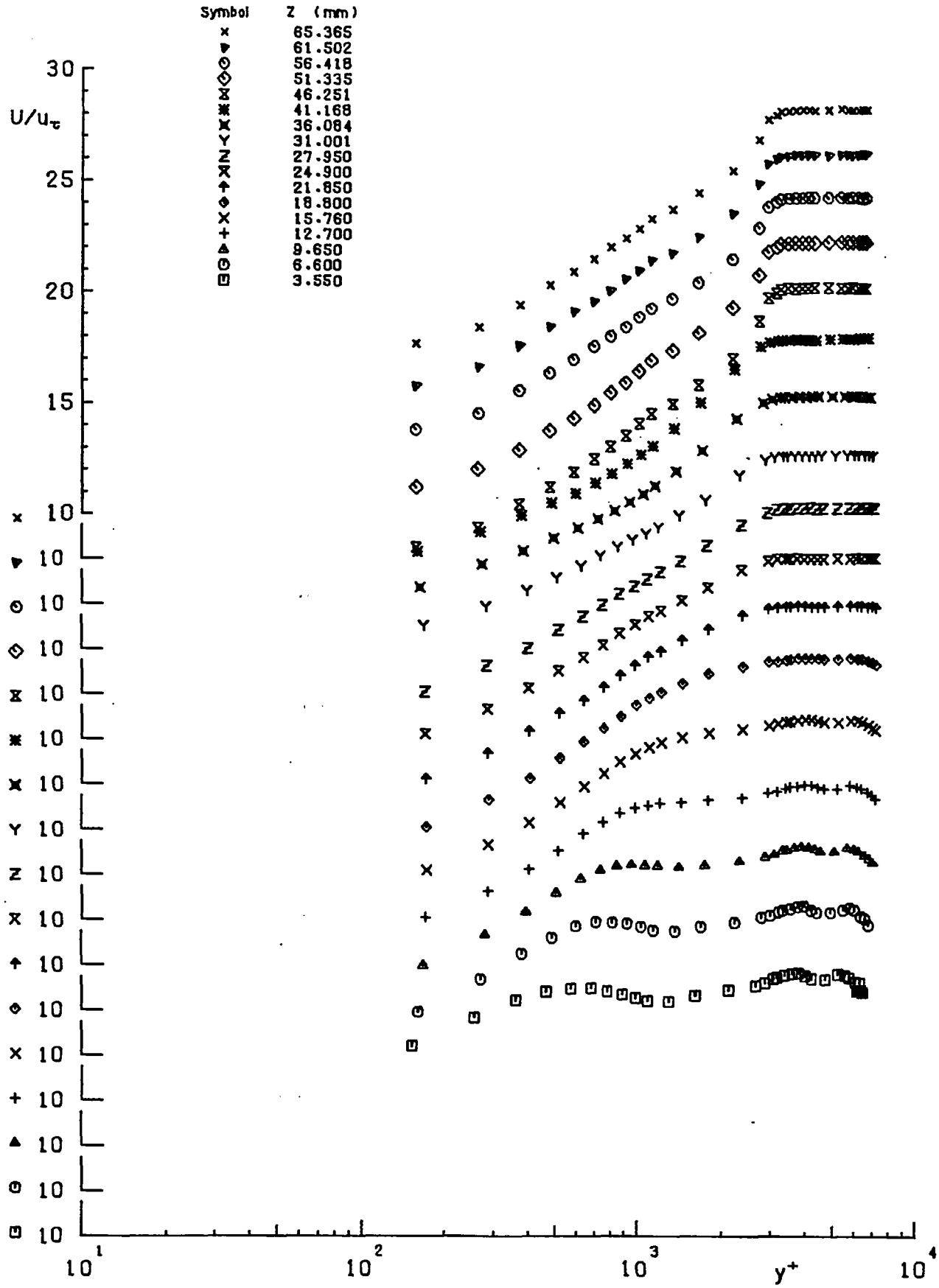

FIG.(4.6:a) SEMI LOGARITHMIC PLOTS OF STREAMWISE VELOCITY PROFILES AT STATION 9 (X=1253.86 mm)

Pitot Tube Measurements
C_f From Preston Tube Measurements

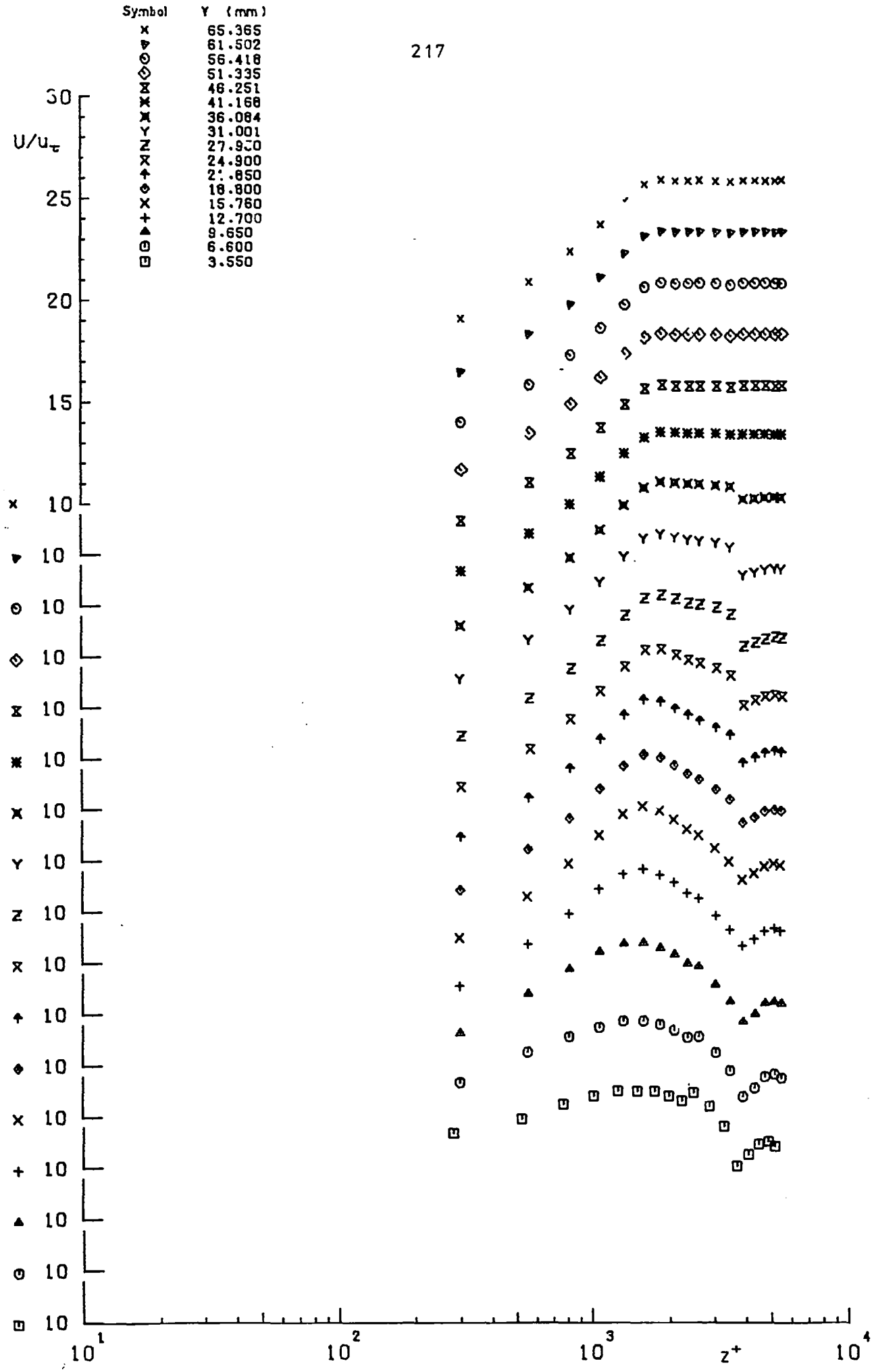

FIG.(4.6 : b) SEMI LOGARITHMIC PLOTS OF STREAMWISE VELOCITY PROFILES AT STATION 9 (X=1253.86 mm)

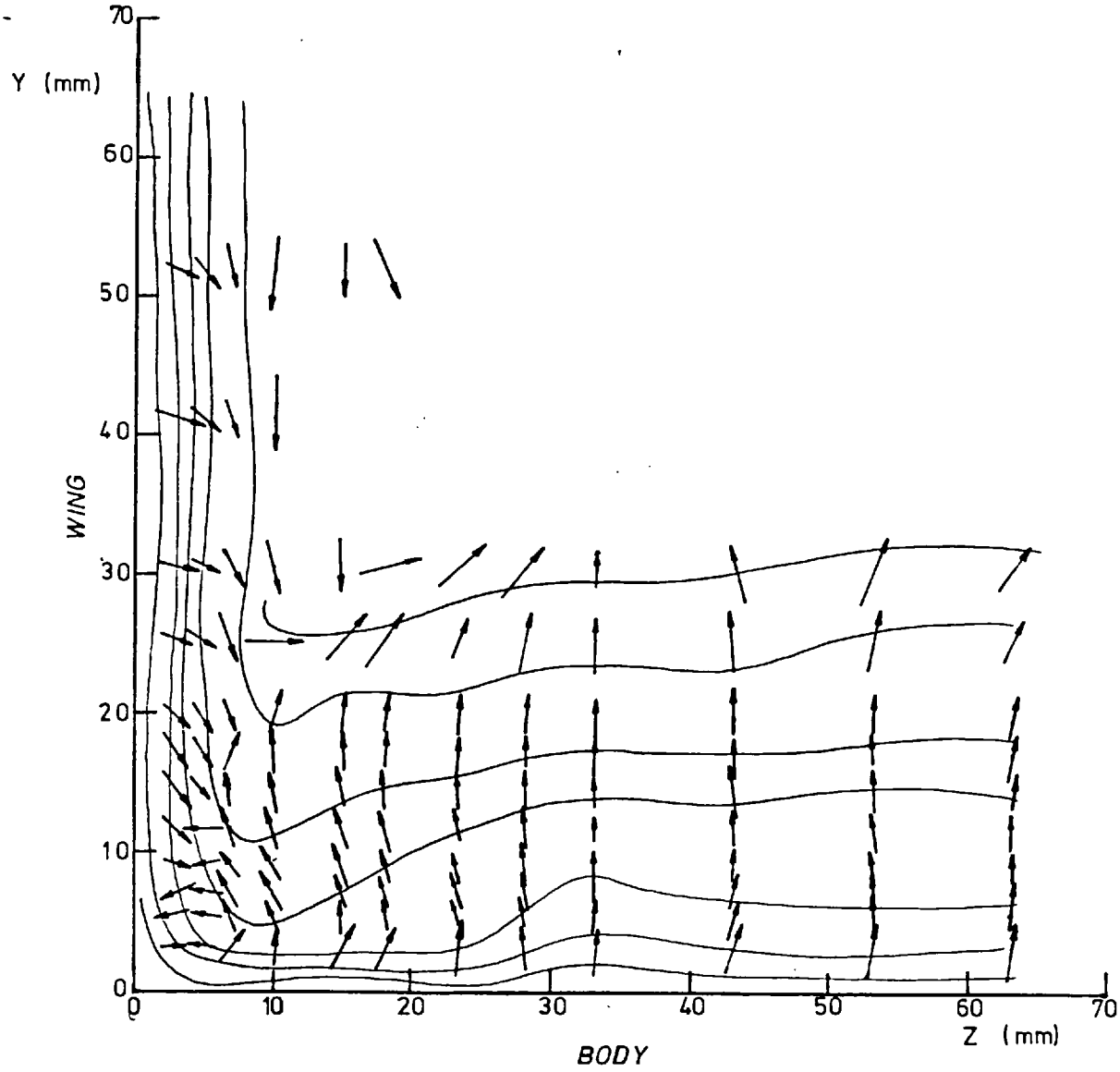

FIG.(4.7) THE MAIN SHEAR STRESS DIRECTION AT STATION 2
(X = 156.6 mm)

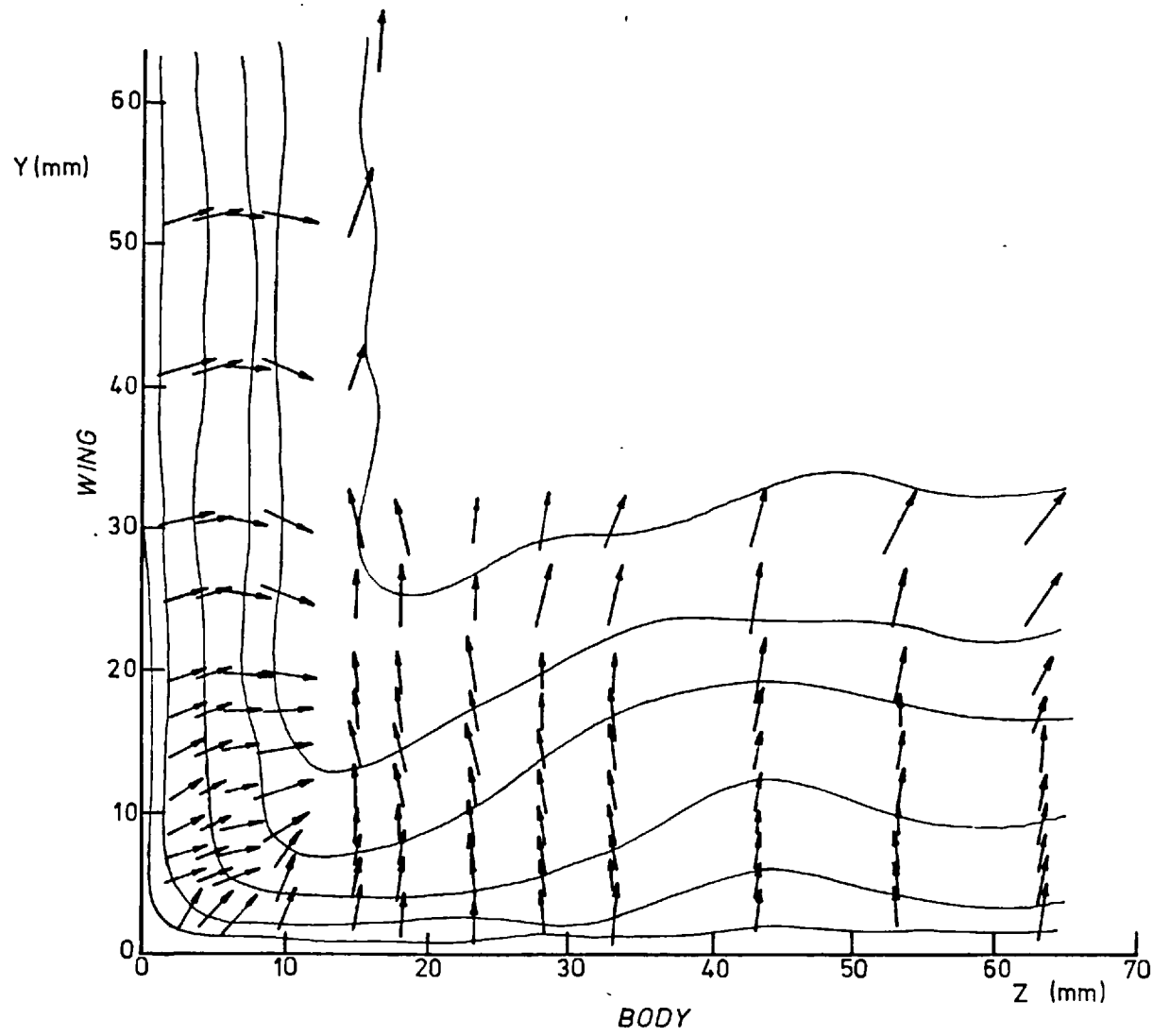

FIG.(4.8) THE MAIN SHEAR STRESS DIRECTION AT STATION 5 (X = 613.8 mm)

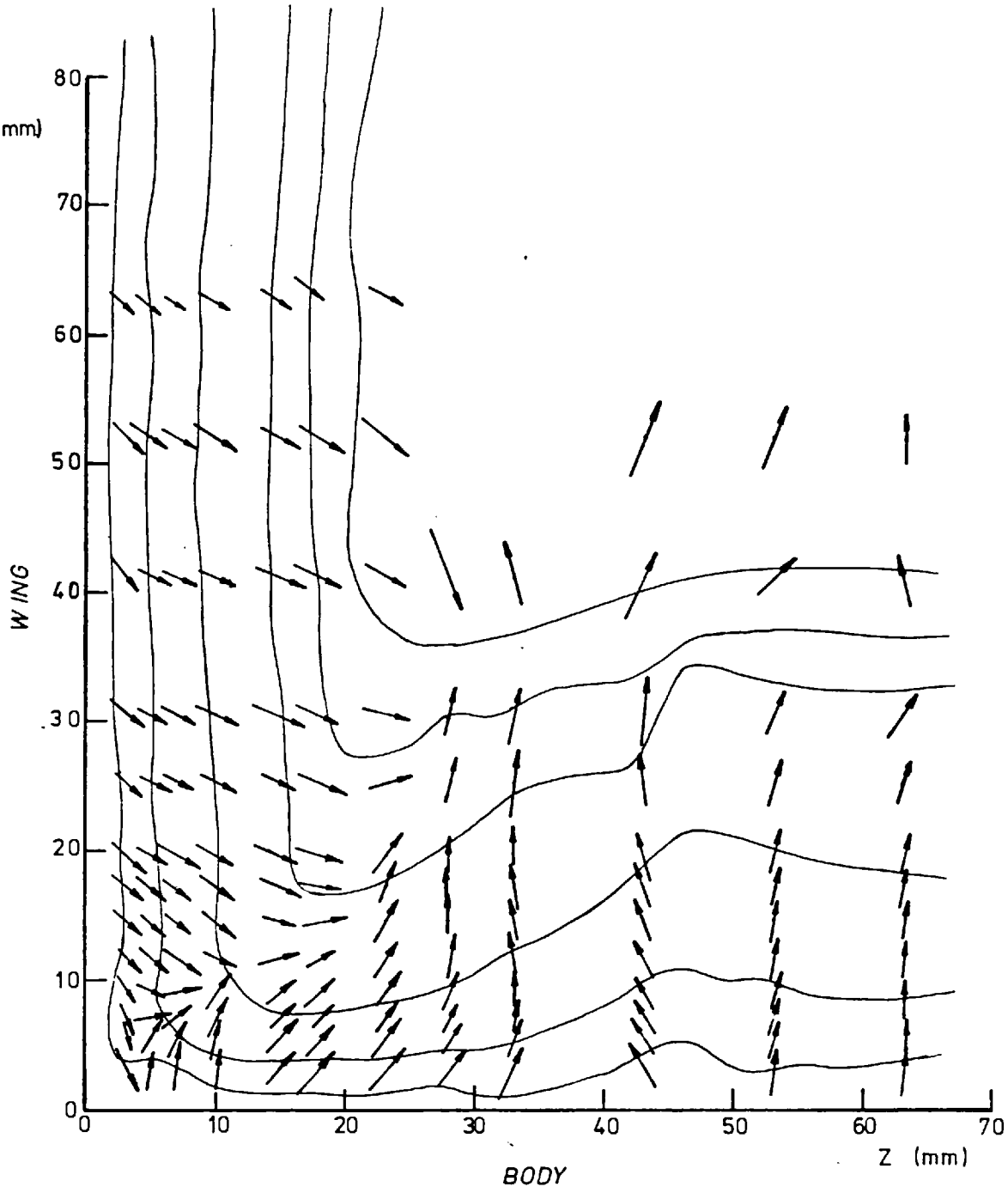

FIG.(4.9) THE MAIN SHEAR STRESS DIRECTION AT STATION 9 (X = 1223.4 mm)

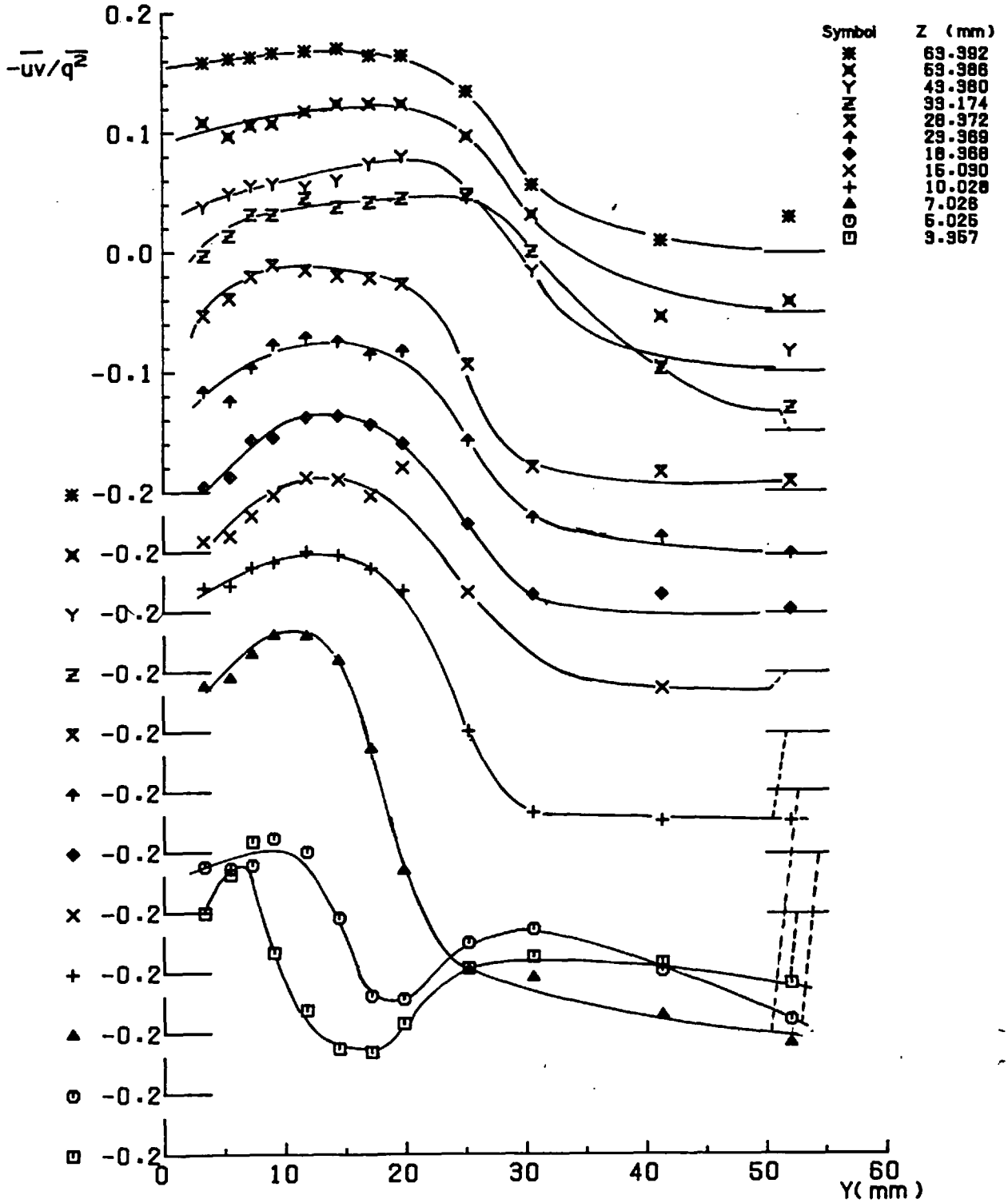

FIG.(4.10) $-\overline{uv}/\overline{q^2}$ AT STATION 2 (X= 156.6 mm)

Cross Wire Measurements

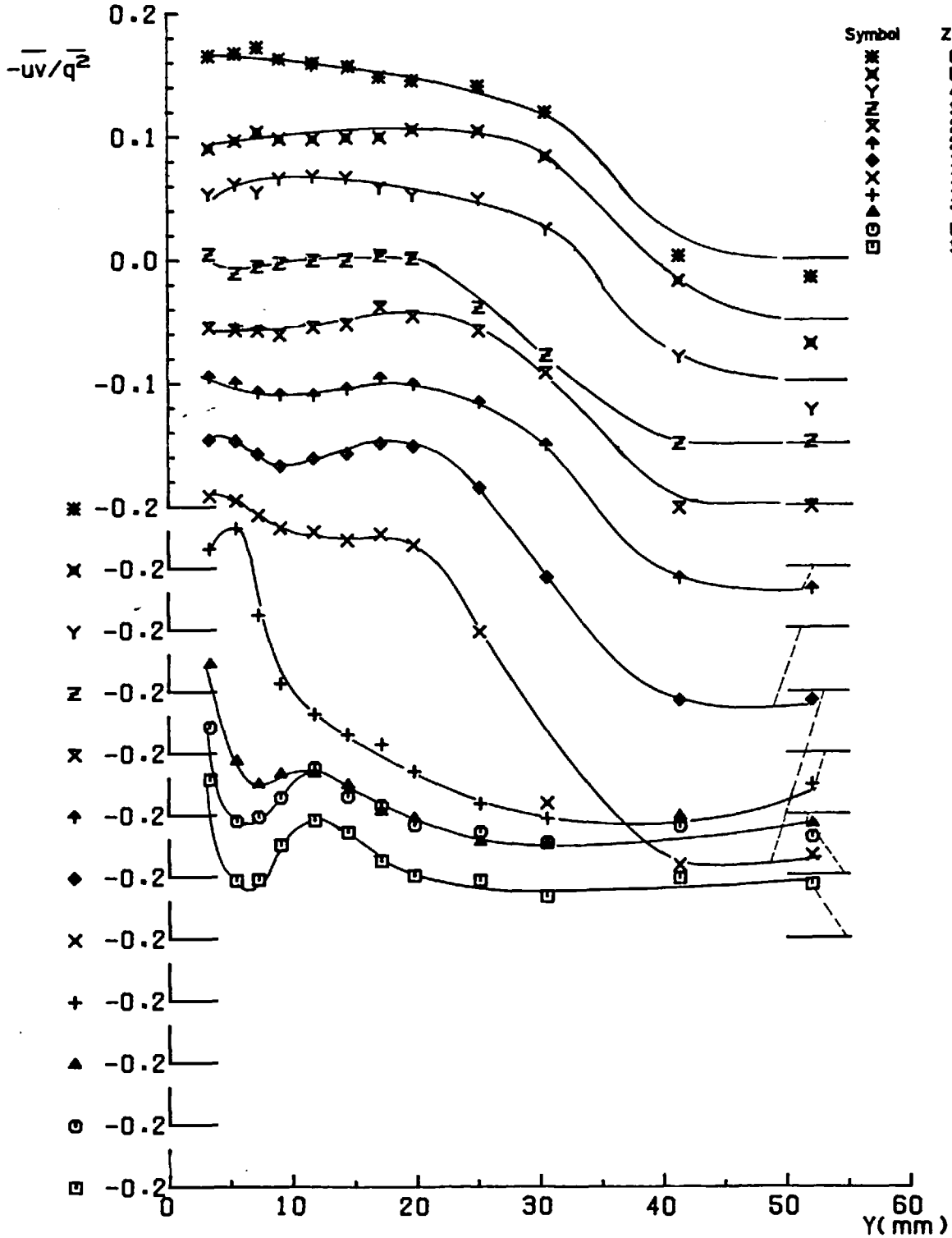

FIG.(4·11) $-\overline{uv}/\overline{q^2}$ AT STATION 5 (X= 613.8 mm)

Cross Wire Measurements

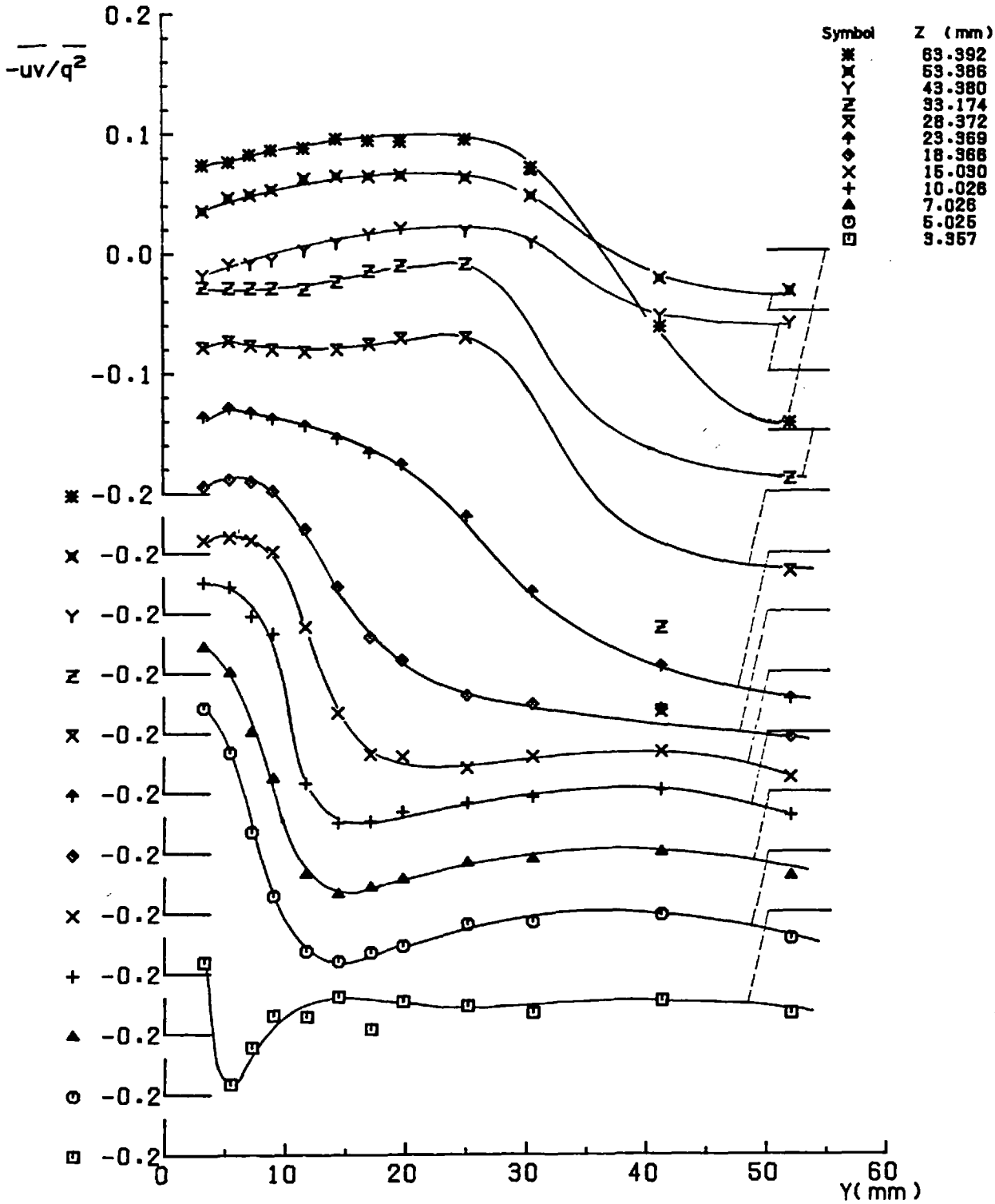

FIG.(4.12) $-\overline{uv}/\overline{q^2}$ AT STATION 9 (X=1223.4 mm)

Cross Wire Measurements

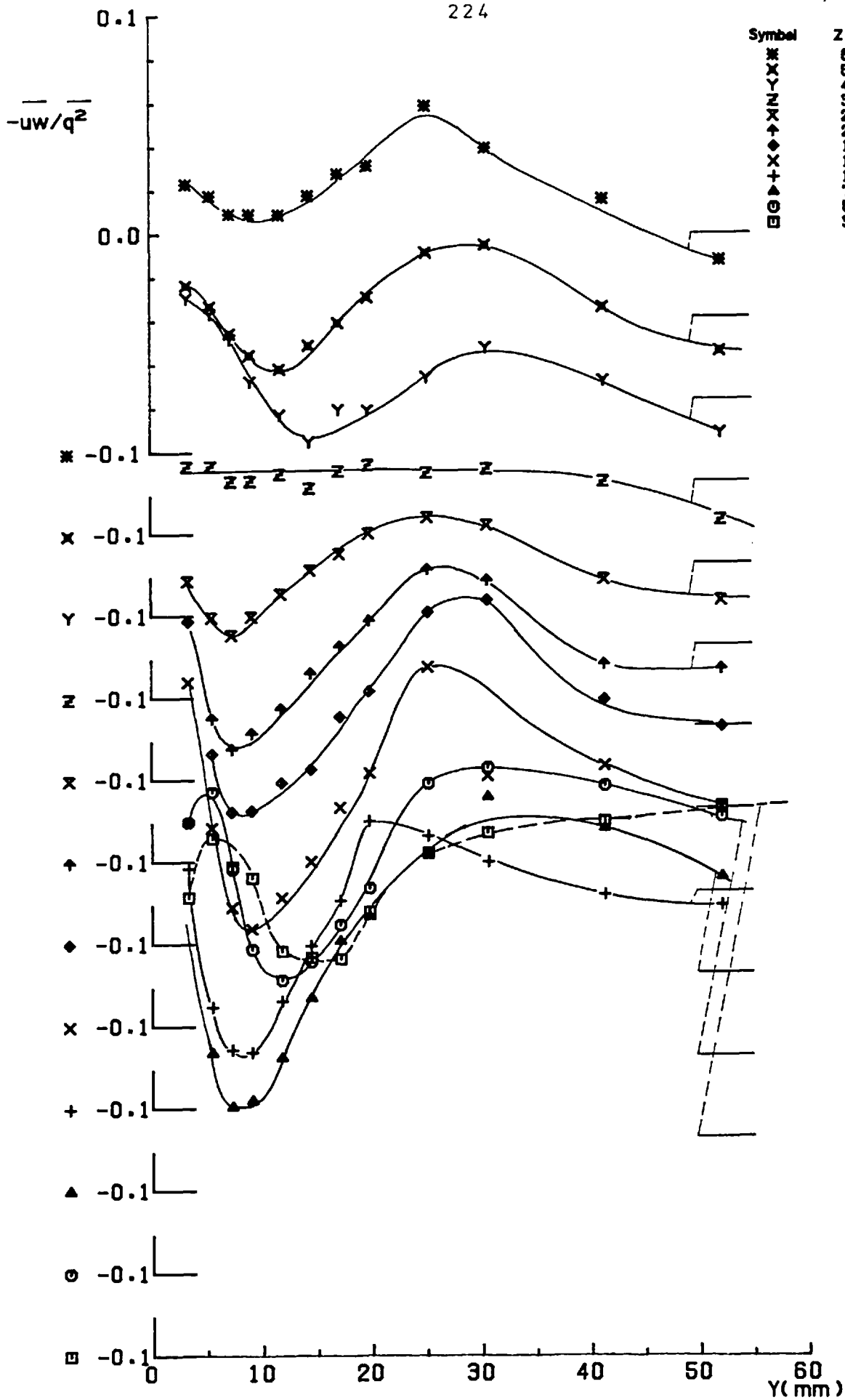

FIG.(4.13) $-\overline{uw}/\overline{q^2}$ AT STATION 2 (X= 156.6 mm)

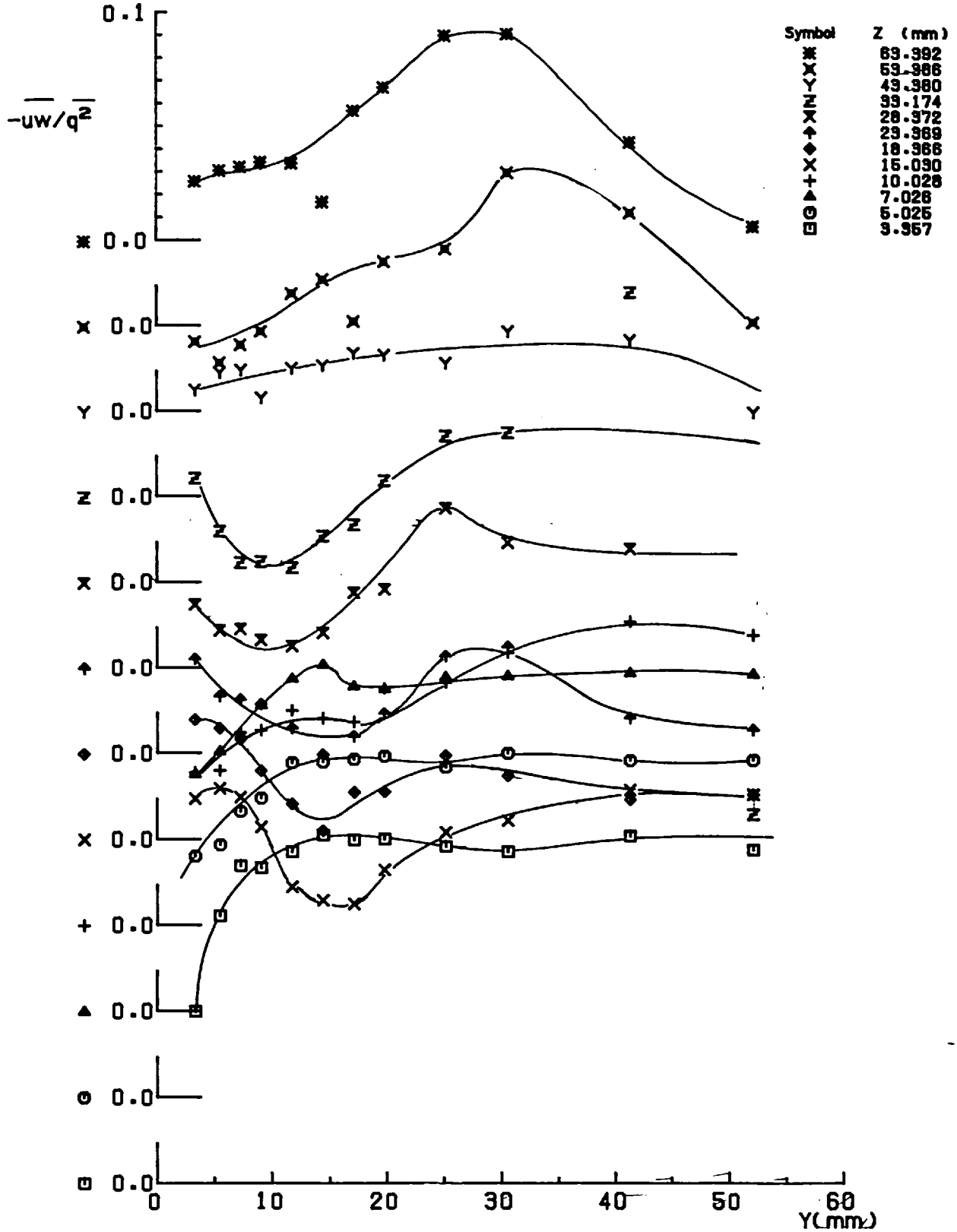

FIG.(4.14) $-\overline{uw}/\overline{q^2}$ AT STATION 5 (X= 613.8 mm)

Cross Wire Measurements

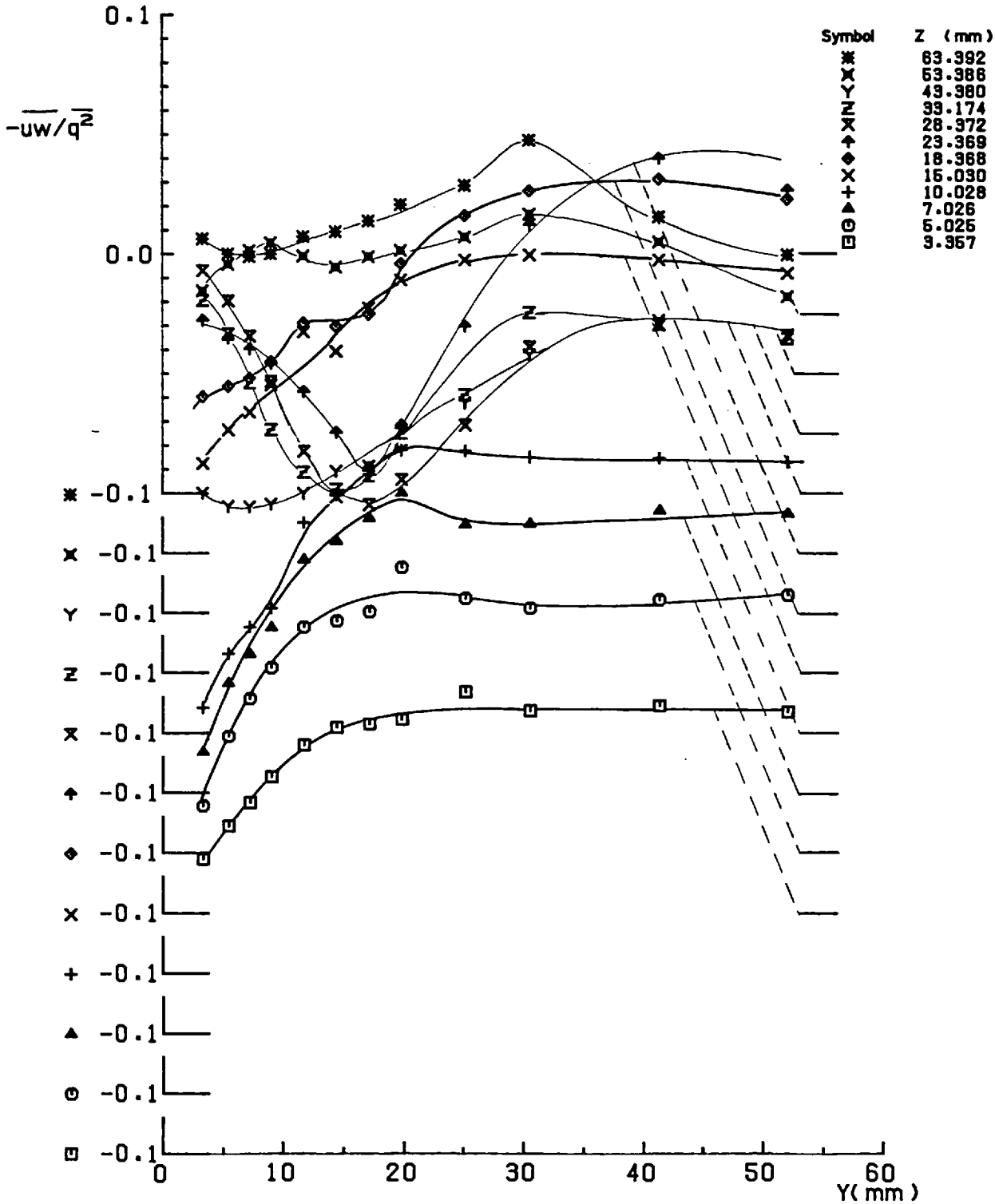

FIG.(4.15) $-\overline{uw}/\overline{q^2}$ AT STATION 9 (X=1223.4 mm)

Cross Wire Measurements

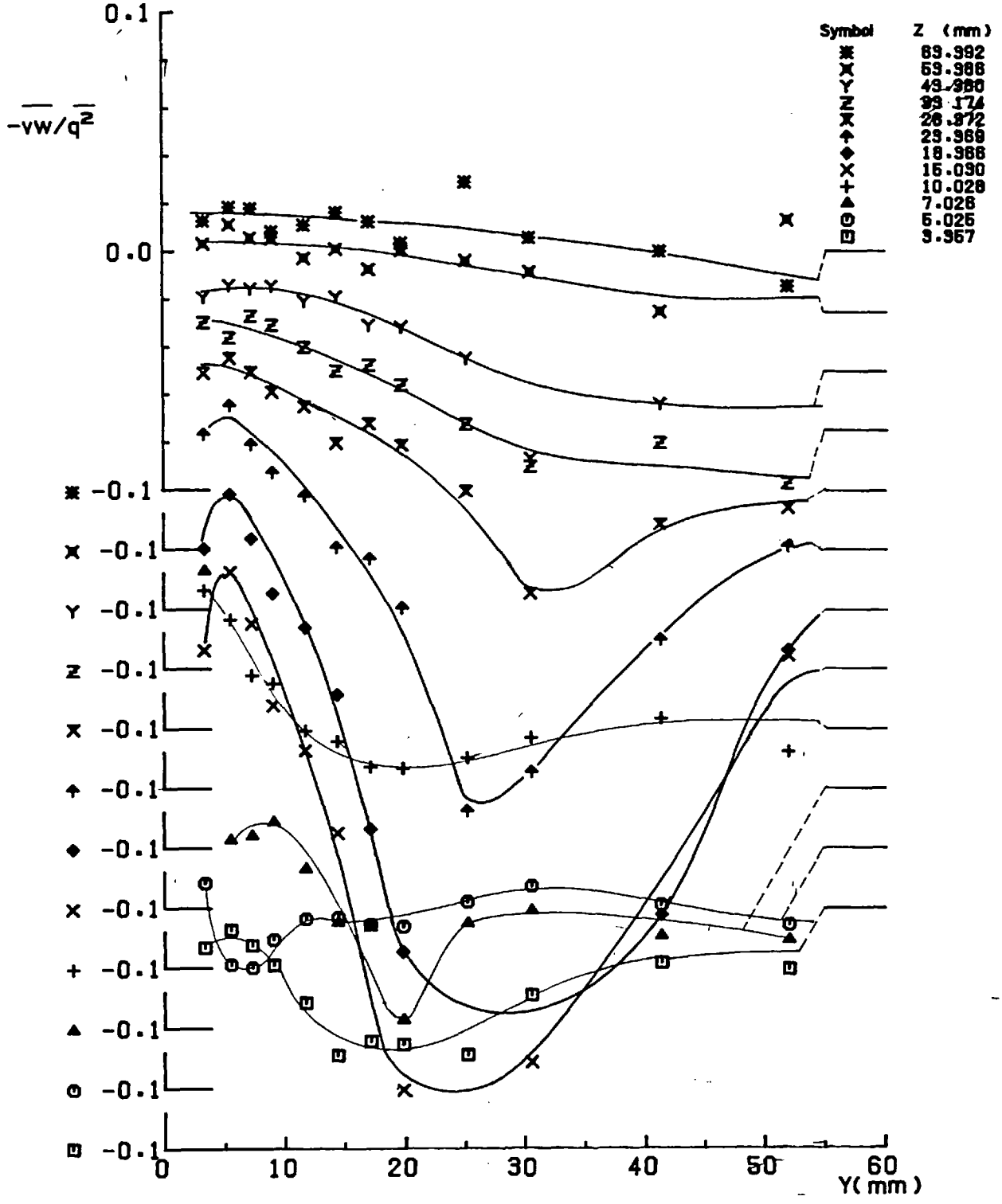

FIG.(4.16) $-\overline{vw}/\overline{q^2}$ AT STATION 2 (X= 156.6 mm)

Cross Wire Measurements

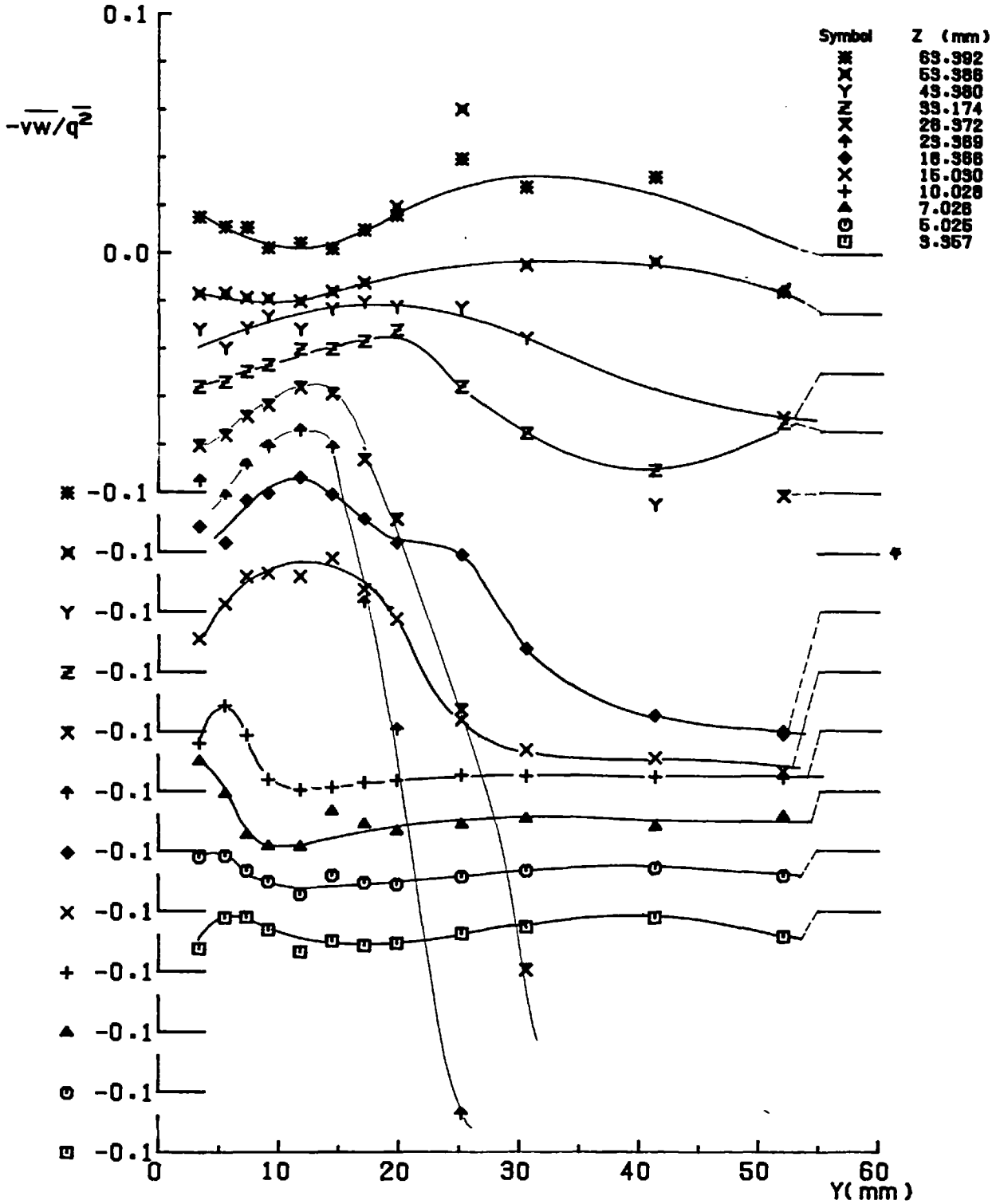

FIG.(4.17) $-\overline{vw}/\overline{q^2}$ AT STATION 5 (X=-613.8 mm)

Cross Wire Measurements

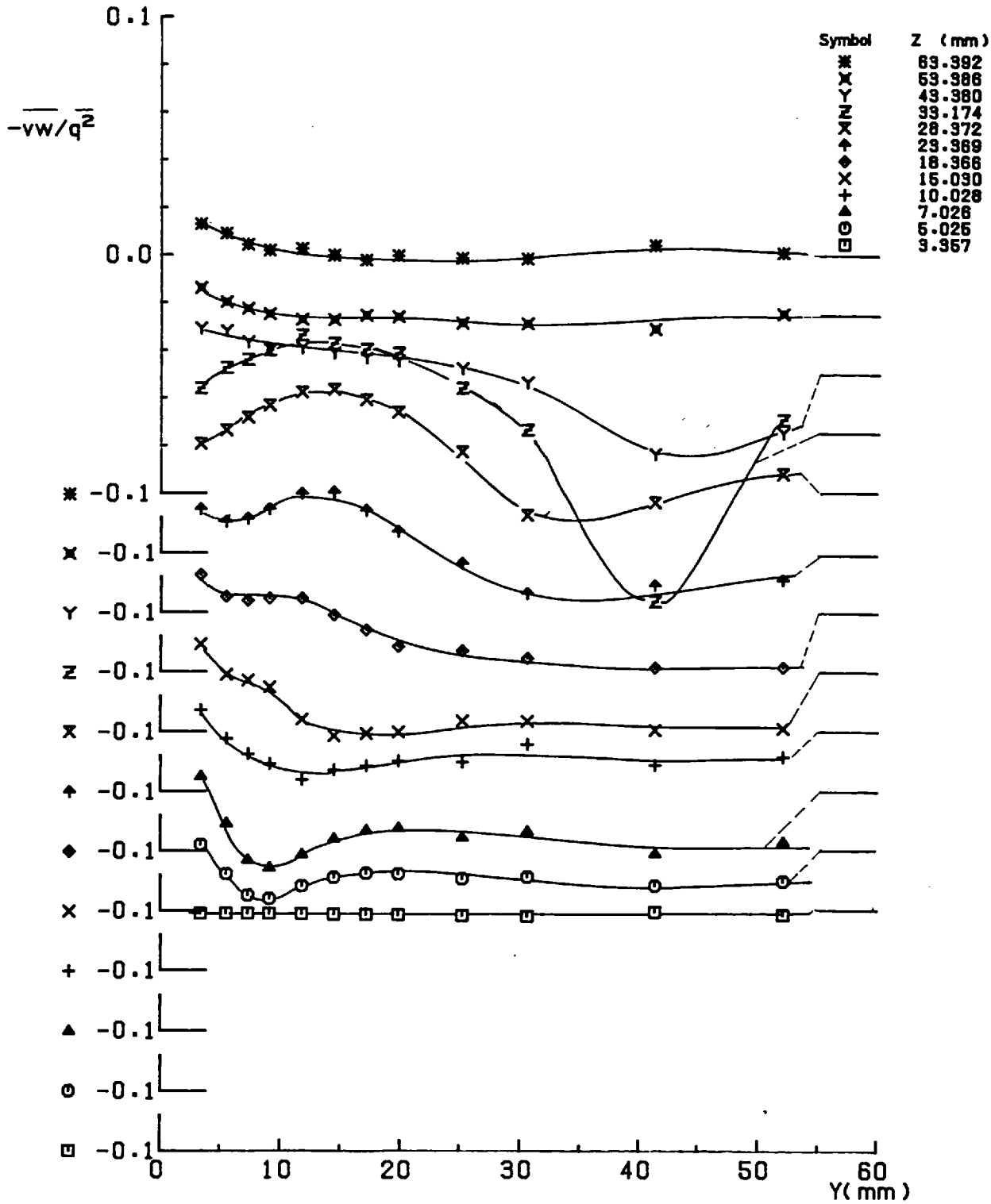

FIG.(4.18) $-\overline{vw}/\overline{q^2}$ AT STATION 9 (X=1223.4 mm)

Cross Wire Measurements

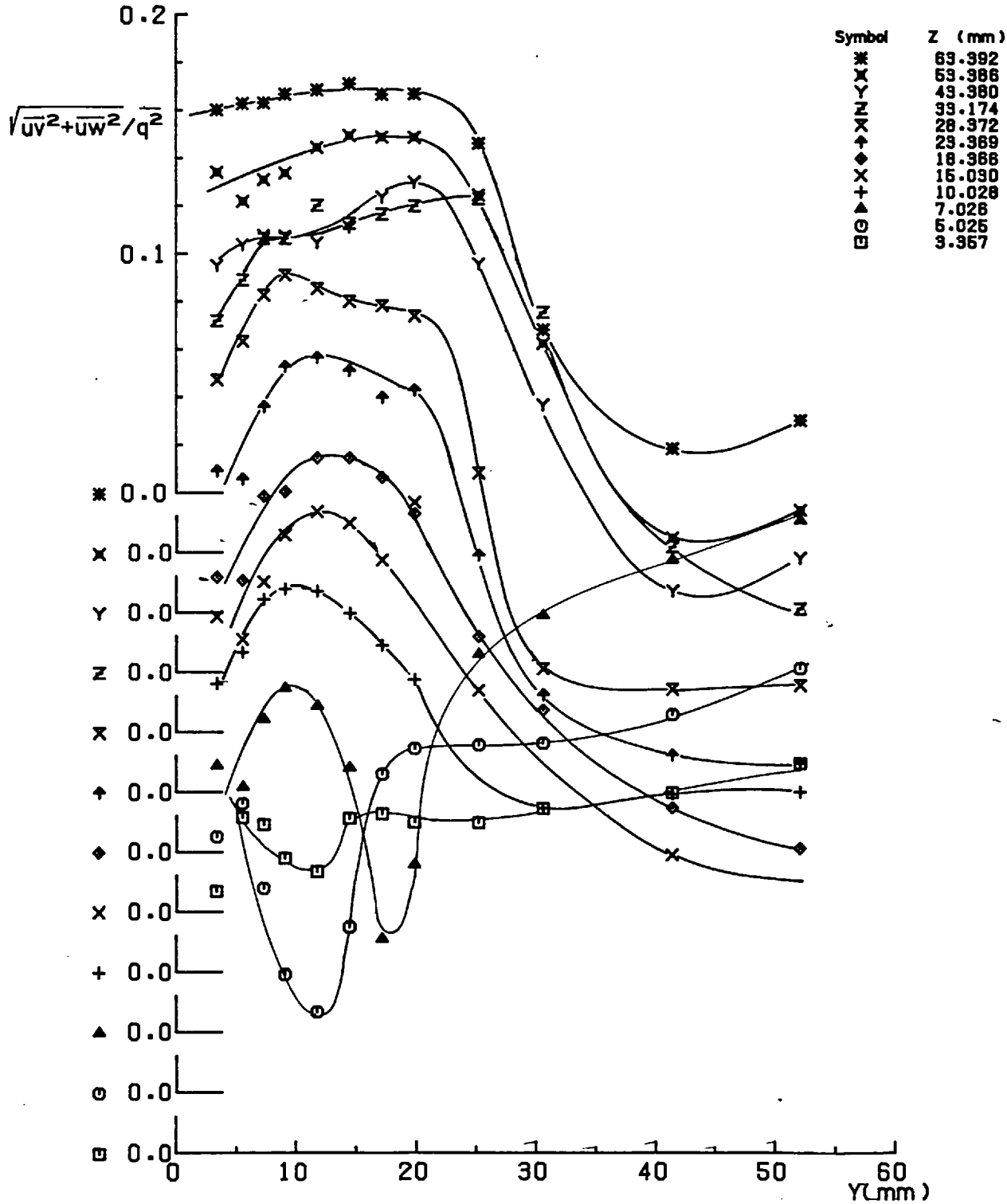

FIG.(4.19) $\sqrt{\overline{uv}^2+\overline{uw}^2}/\overline{q^2}$ AT STATION 2 (X= 156.6 mm)

Cross Wire Measurements

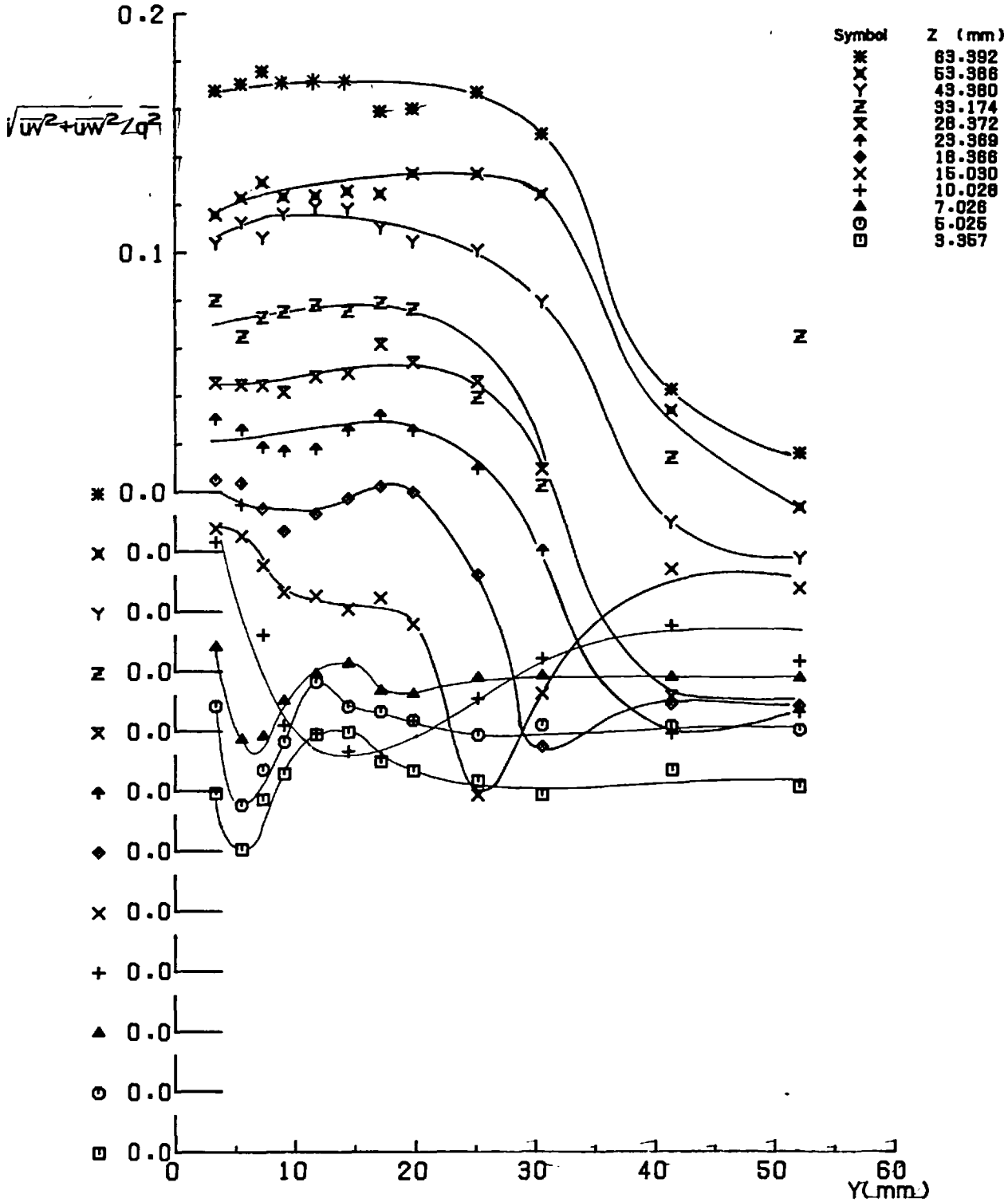

FIG.(4.20) $\sqrt{\overline{uv}^2+\overline{uw}^2}/\overline{q}^2$ AT STATION 5 (X= 613.8 mm)

Cross Wire Measurements

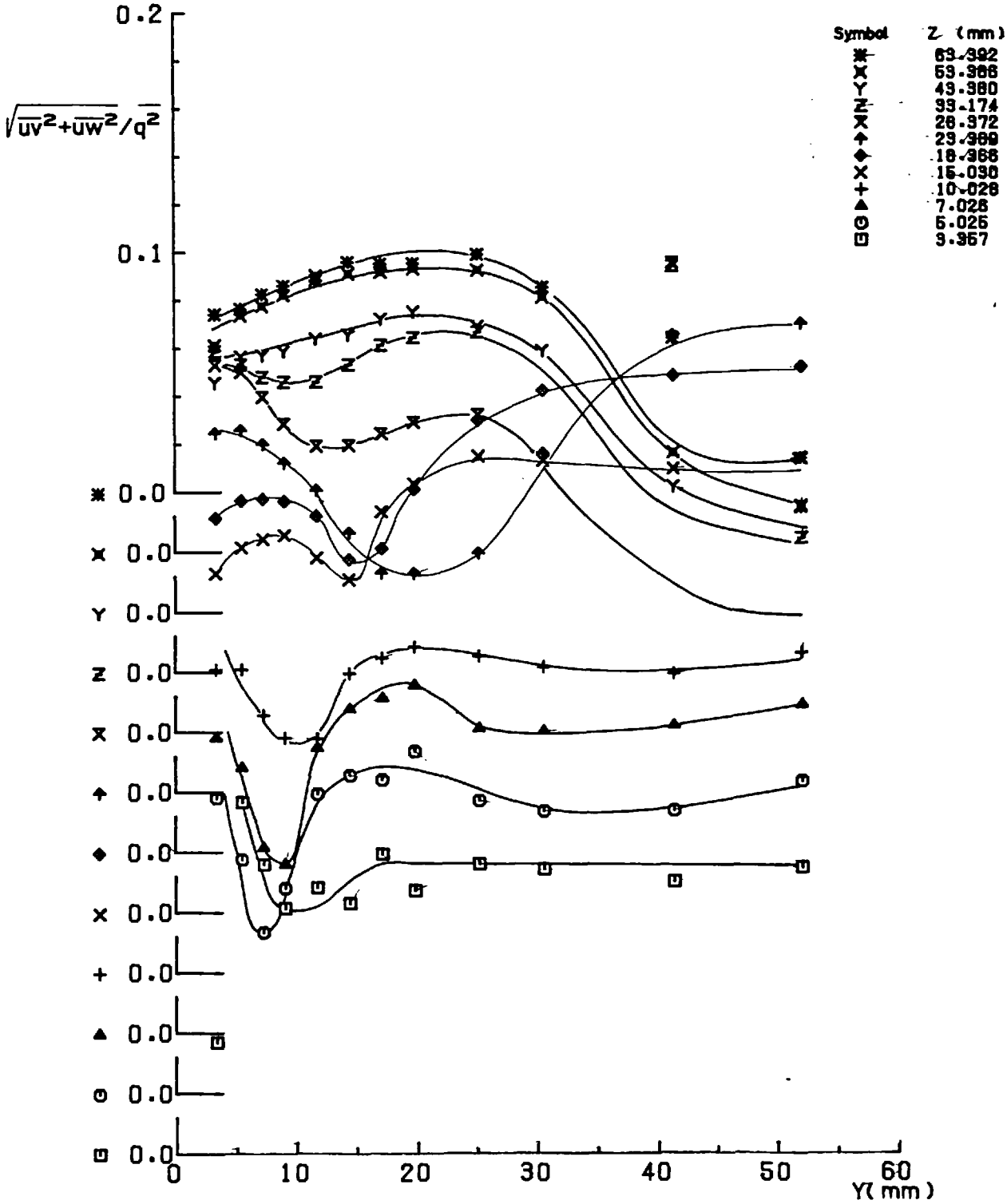

FIG.(4.21) $\sqrt{\overline{uv}^2+\overline{uw}^2}/\overline{q}^2$ AT STATION 9 (X=1223.4 mm)

Cross Wire Measurements

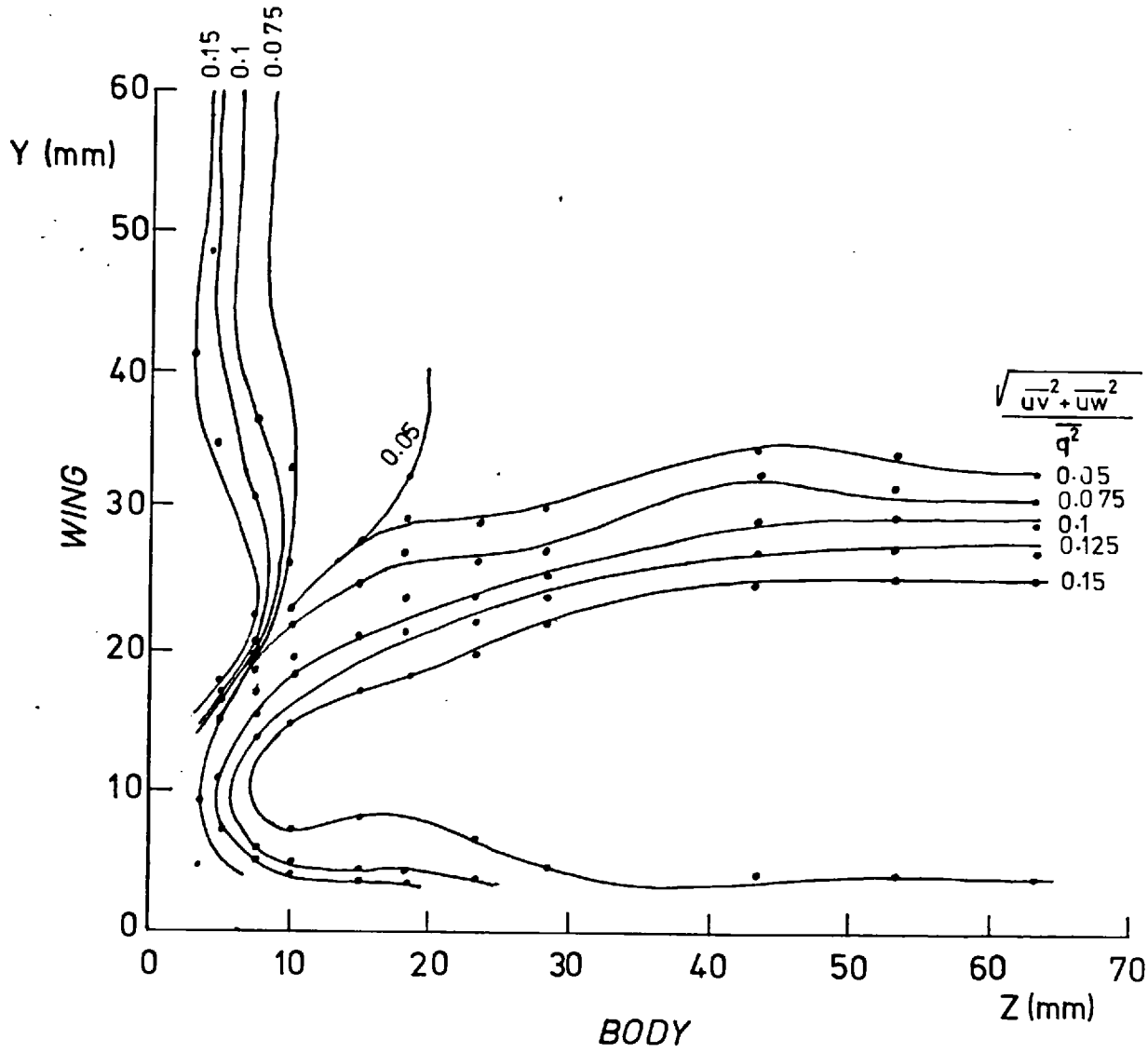

FIG.(4.22) CONTOUR MAP OF $(\sqrt{\overline{uv}^2 + \overline{uw}^2}/\overline{q}^2)$
AT STATION 2 (X = 156.6 mm)

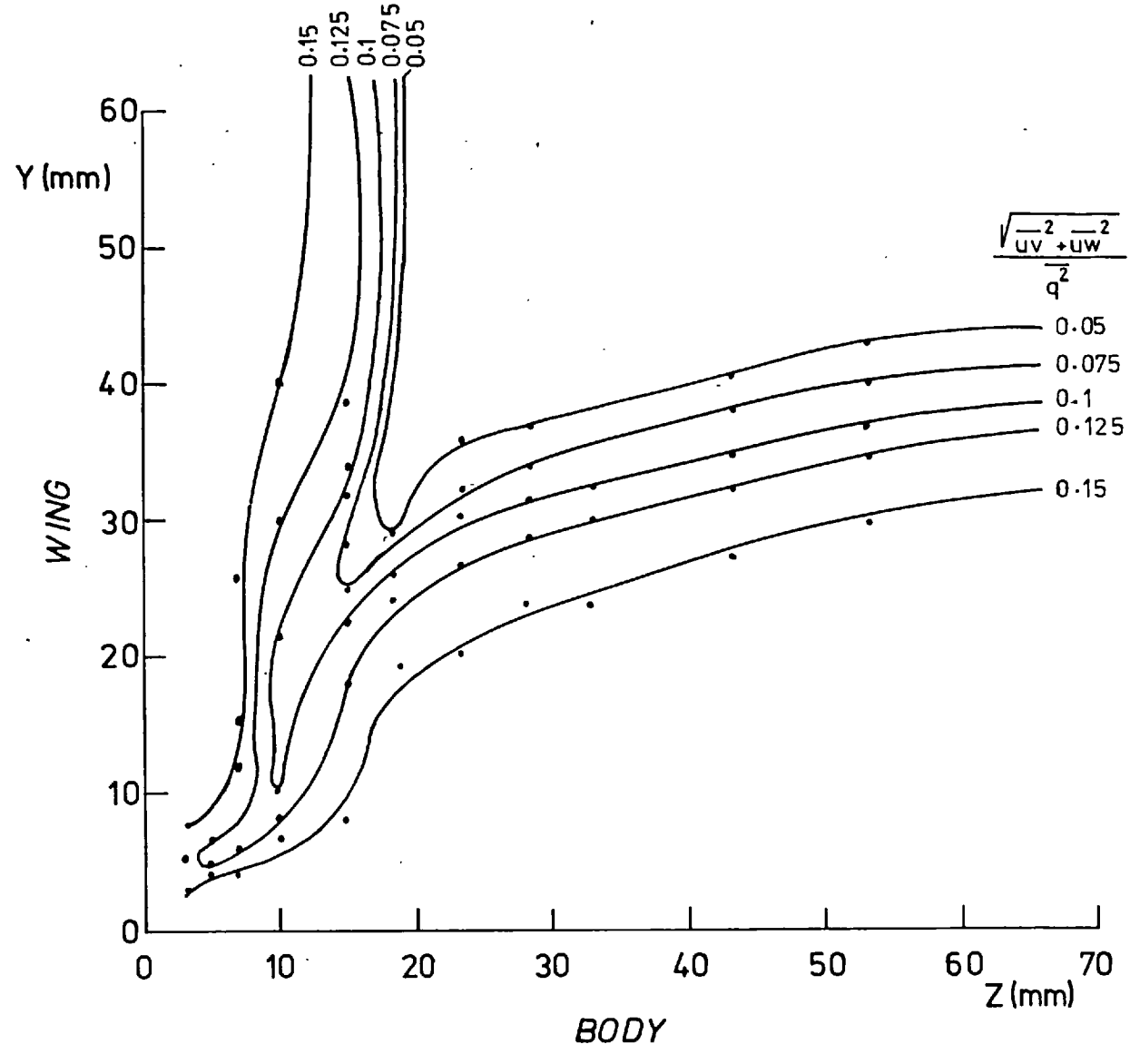

FIG.(4.23) CONTOUR MAP OF $(\sqrt{\overline{uv}^2 + \overline{uw}^2}/\overline{q^2})$
AT STATION 5 (X = 613.8 mm)

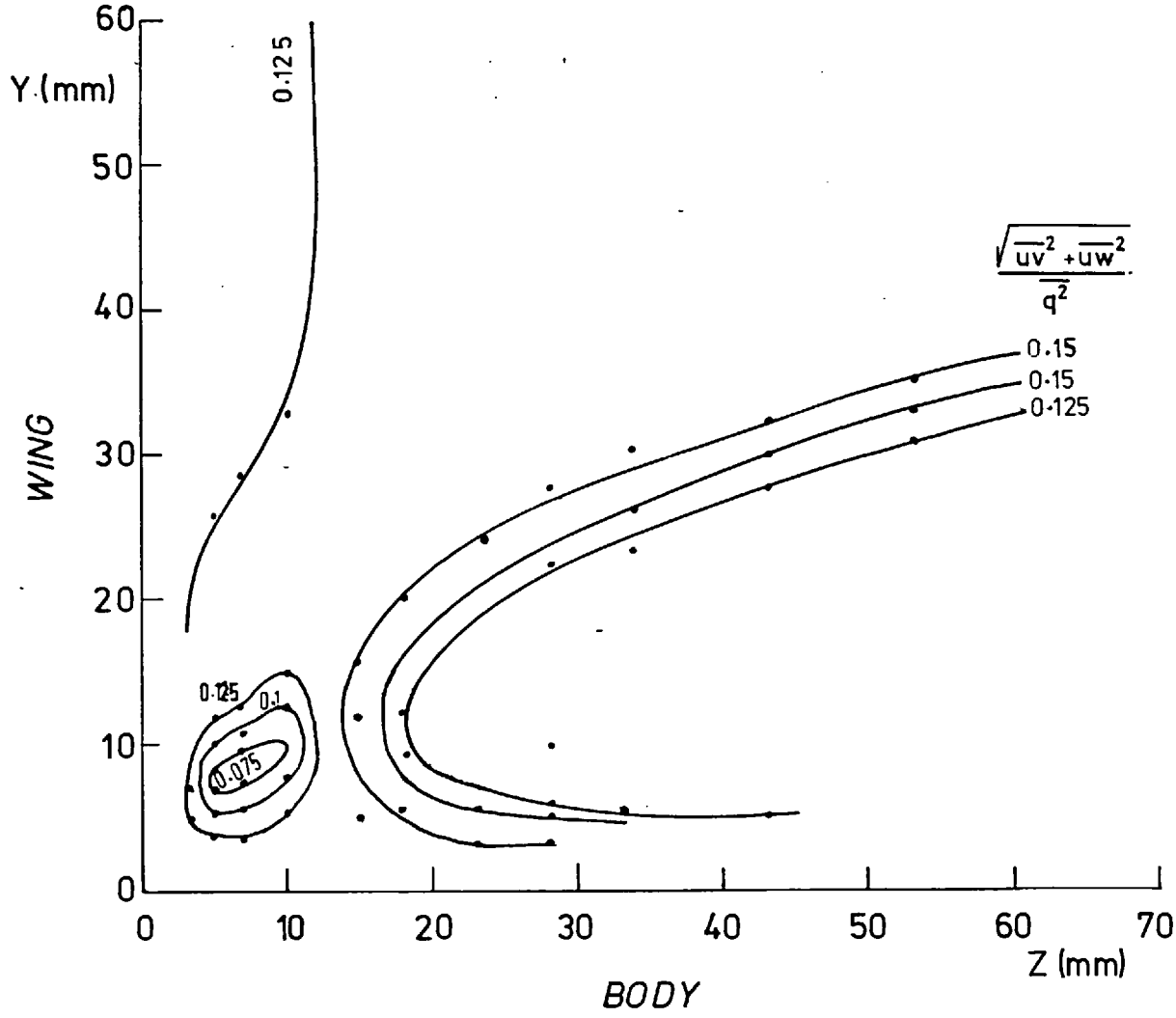

FIG.(4.24) CONTOUR MAP OF $(\sqrt{\overline{uv}^2 + \overline{uw}^2}/\overline{q^2})$
AT STATION 9 (X = 1223.4 mm)

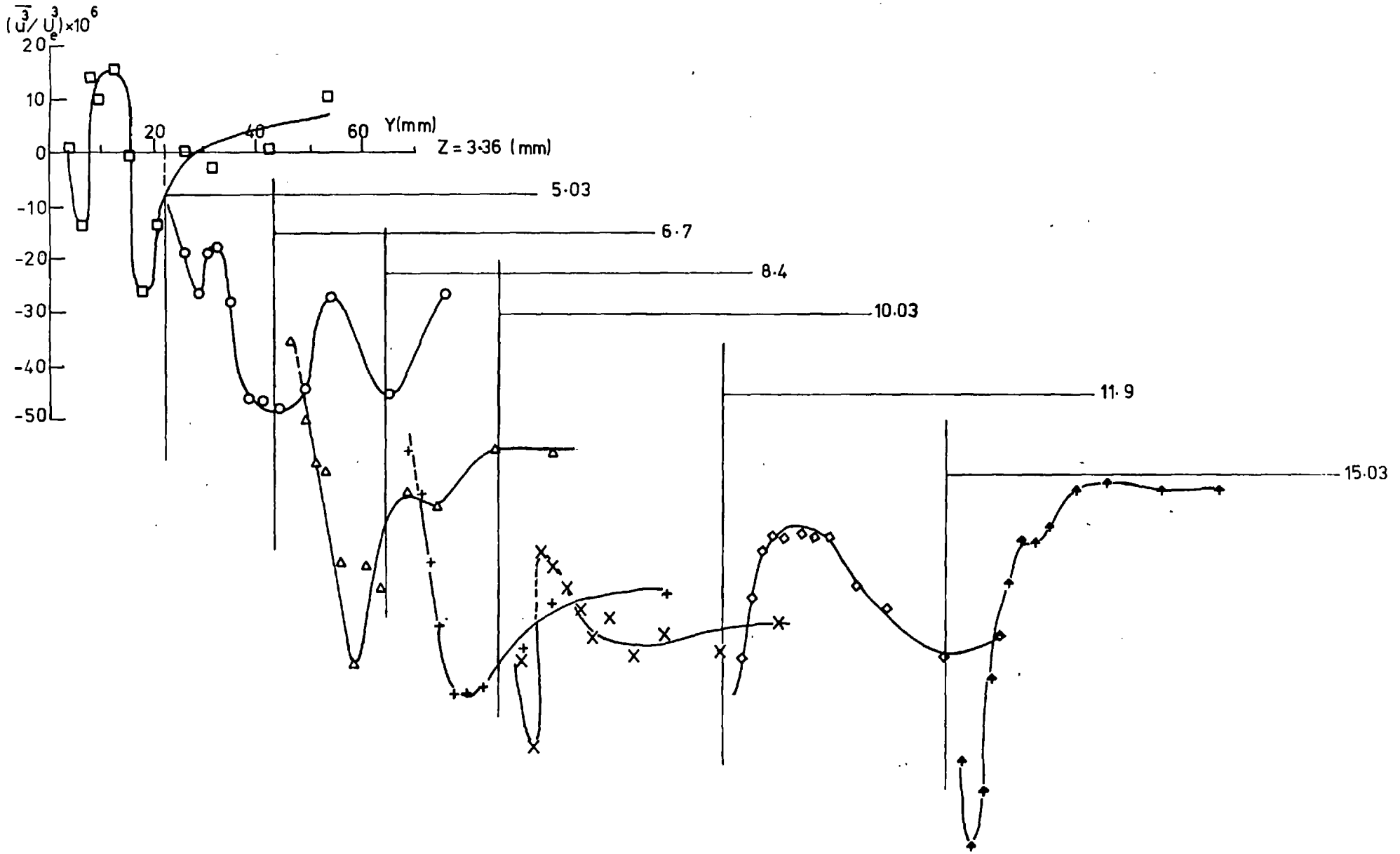

FIG.(4.25) $\overline{u^3}$ AT STATION 5 (X = 613.8 mm)

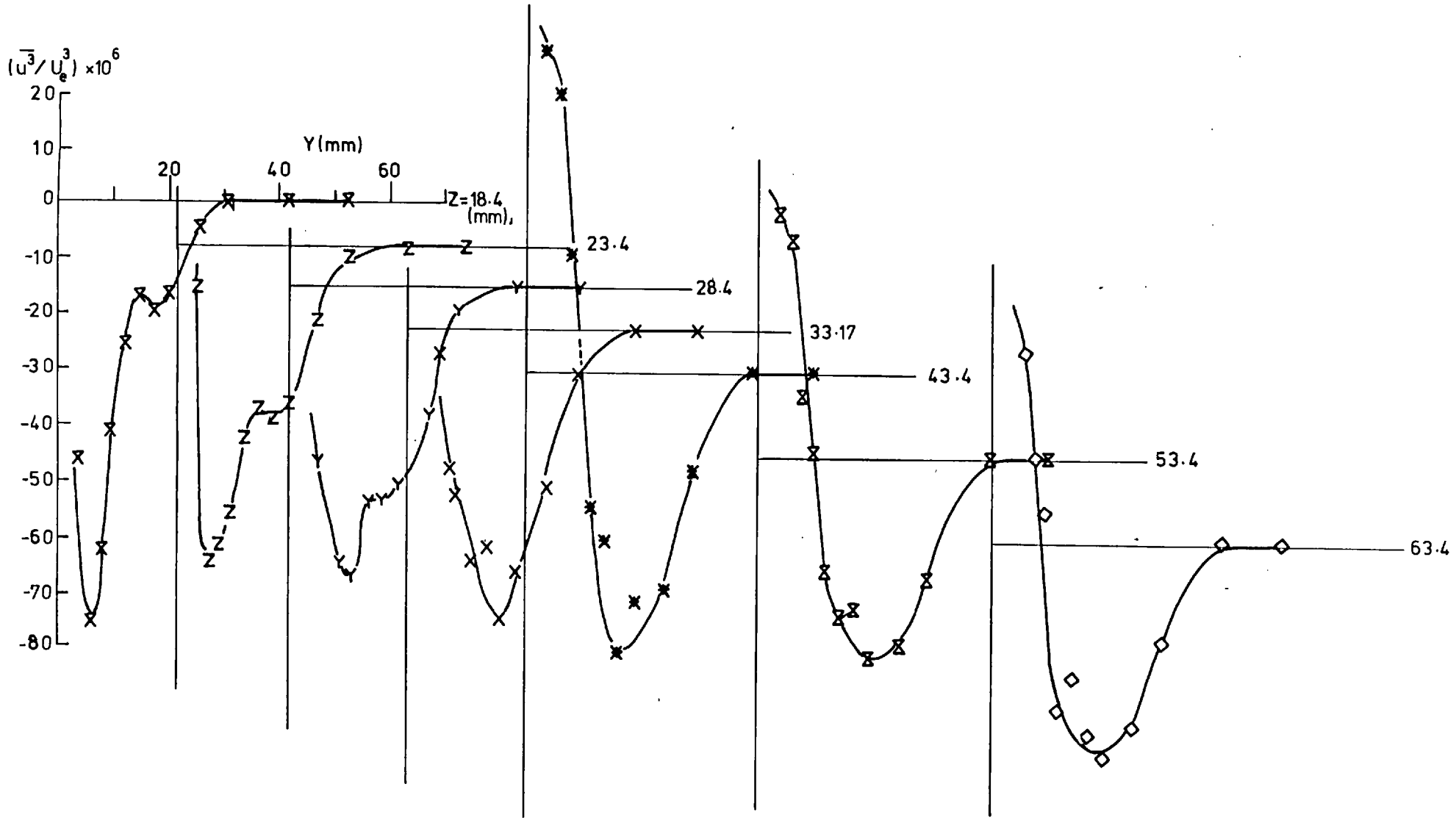

FIG.(4.25 cont.) $\overline{u^3}$ AT STATION 5 (X = 613.8 mm)

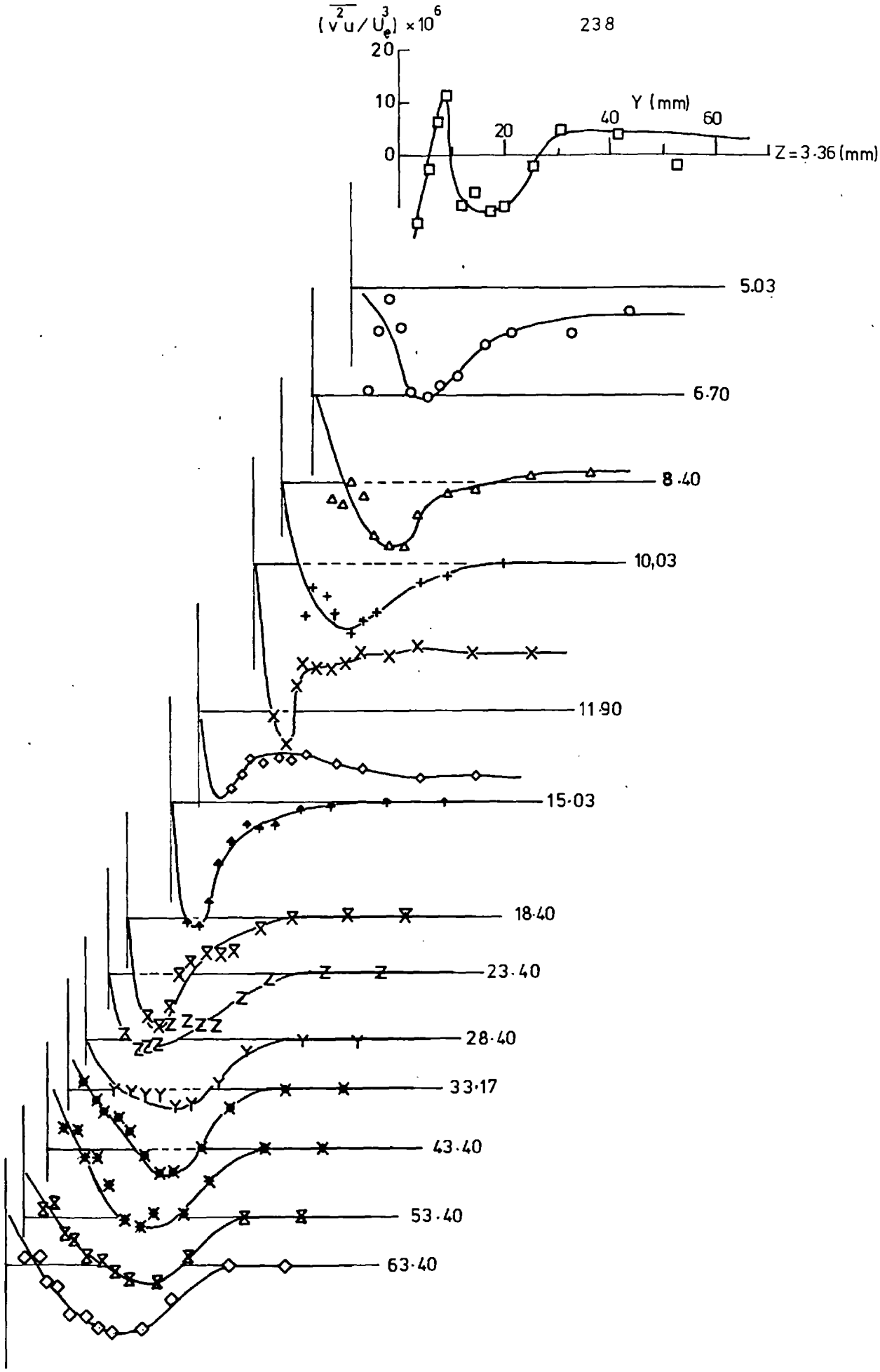

FIG.(4.26) $\overline{v^2u}$ AT STATION 5 (X = 613.8 mm)

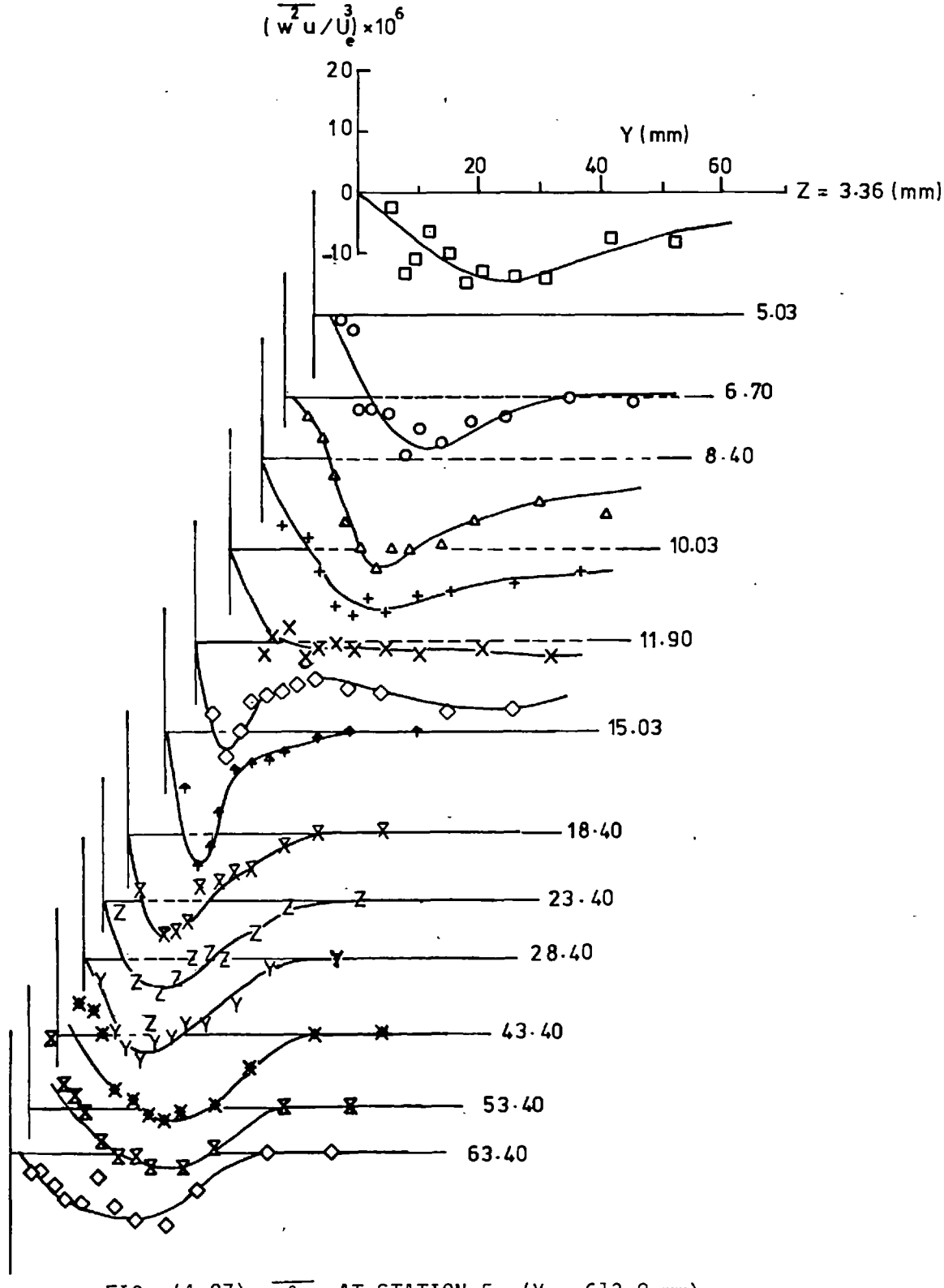

FIG. (4.27) $\overline{w^2u}$ AT STATION 5 (X = 613.8 mm)

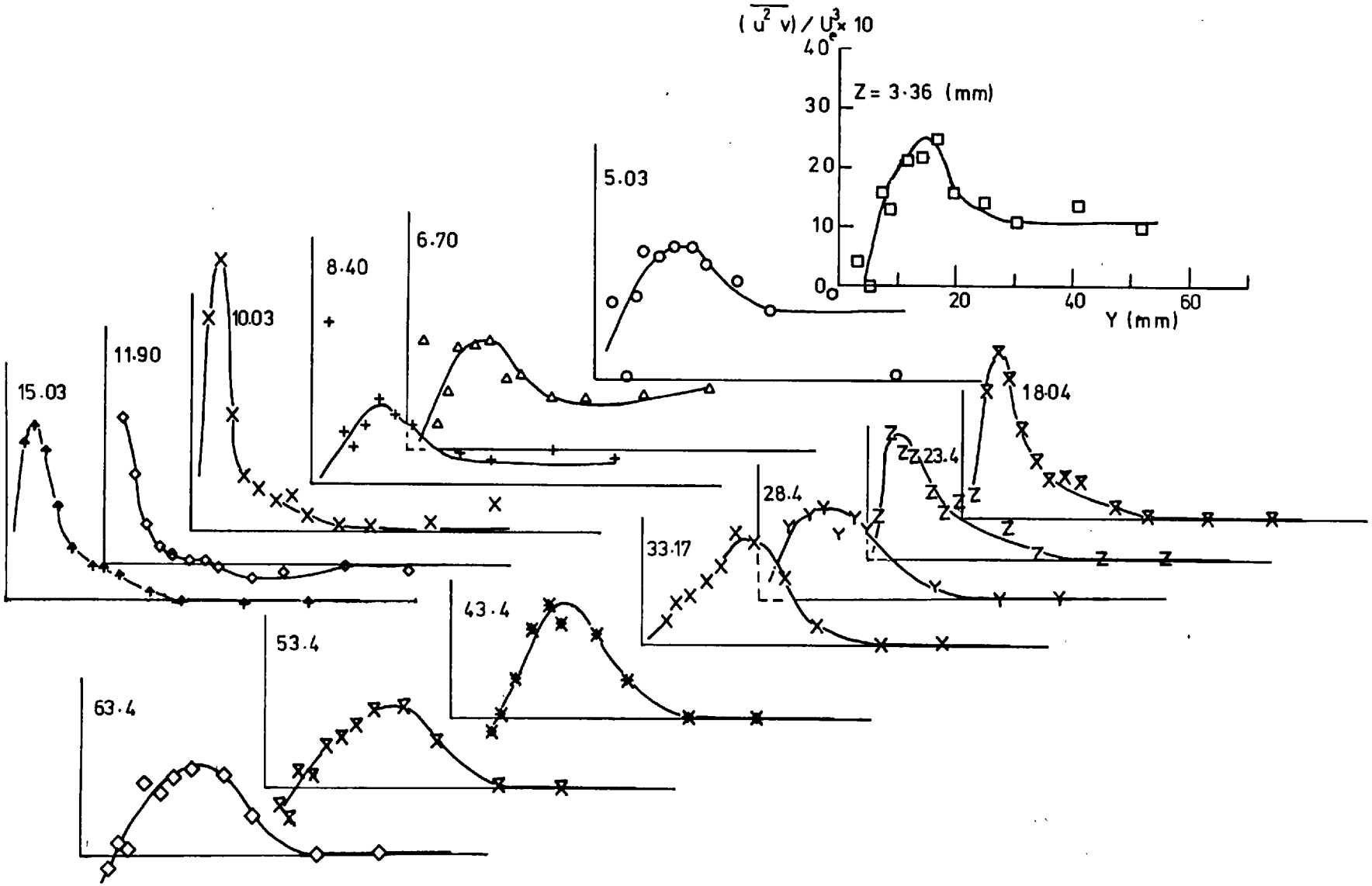

FIG.(4.28) $\overline{u^2v}$ AT STATION 5 (X = 613.8 mm)

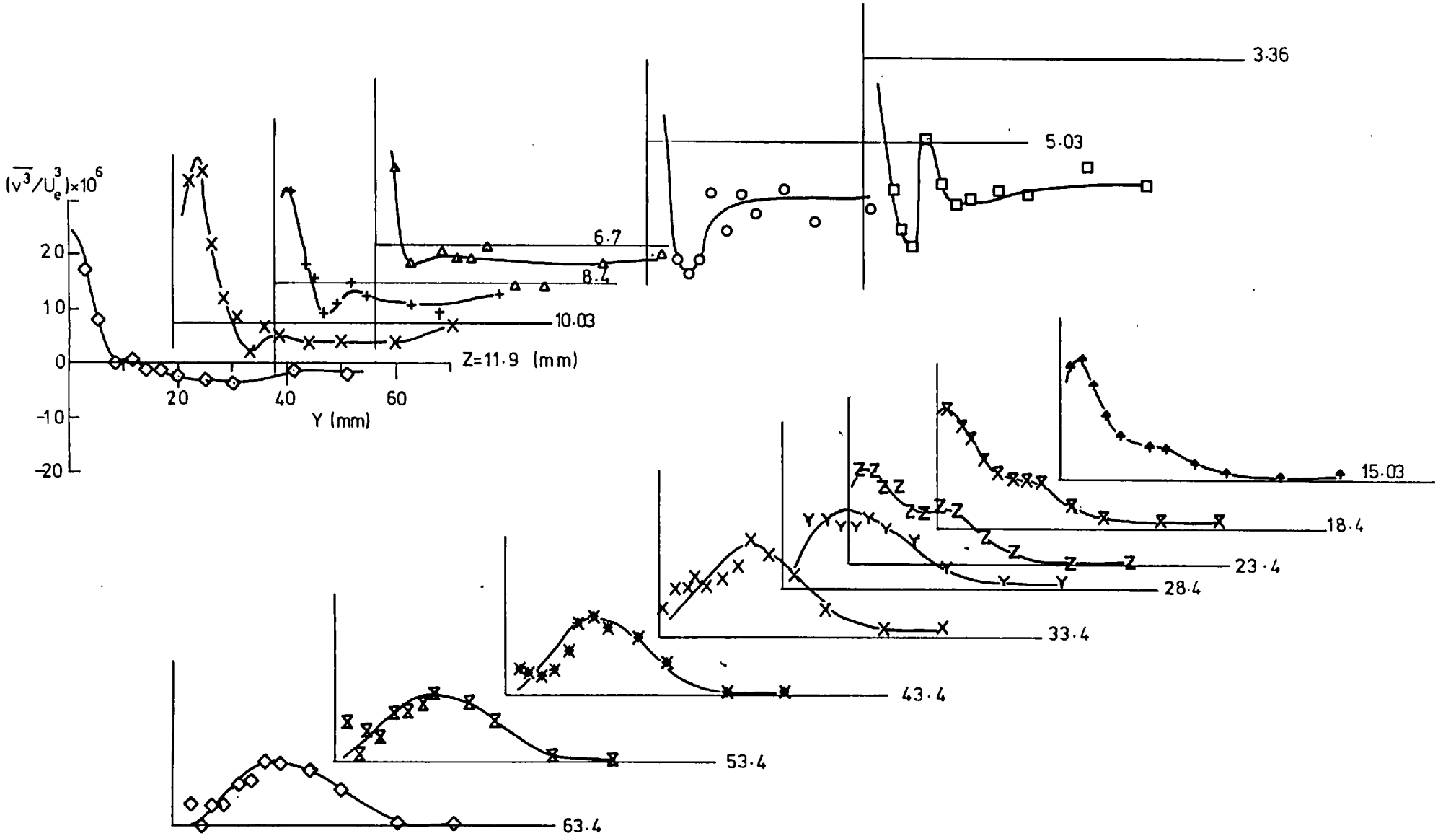

FIG.(4.29) $\overline{v^3}$ AT STATION 5 (X = 613.8 mm)

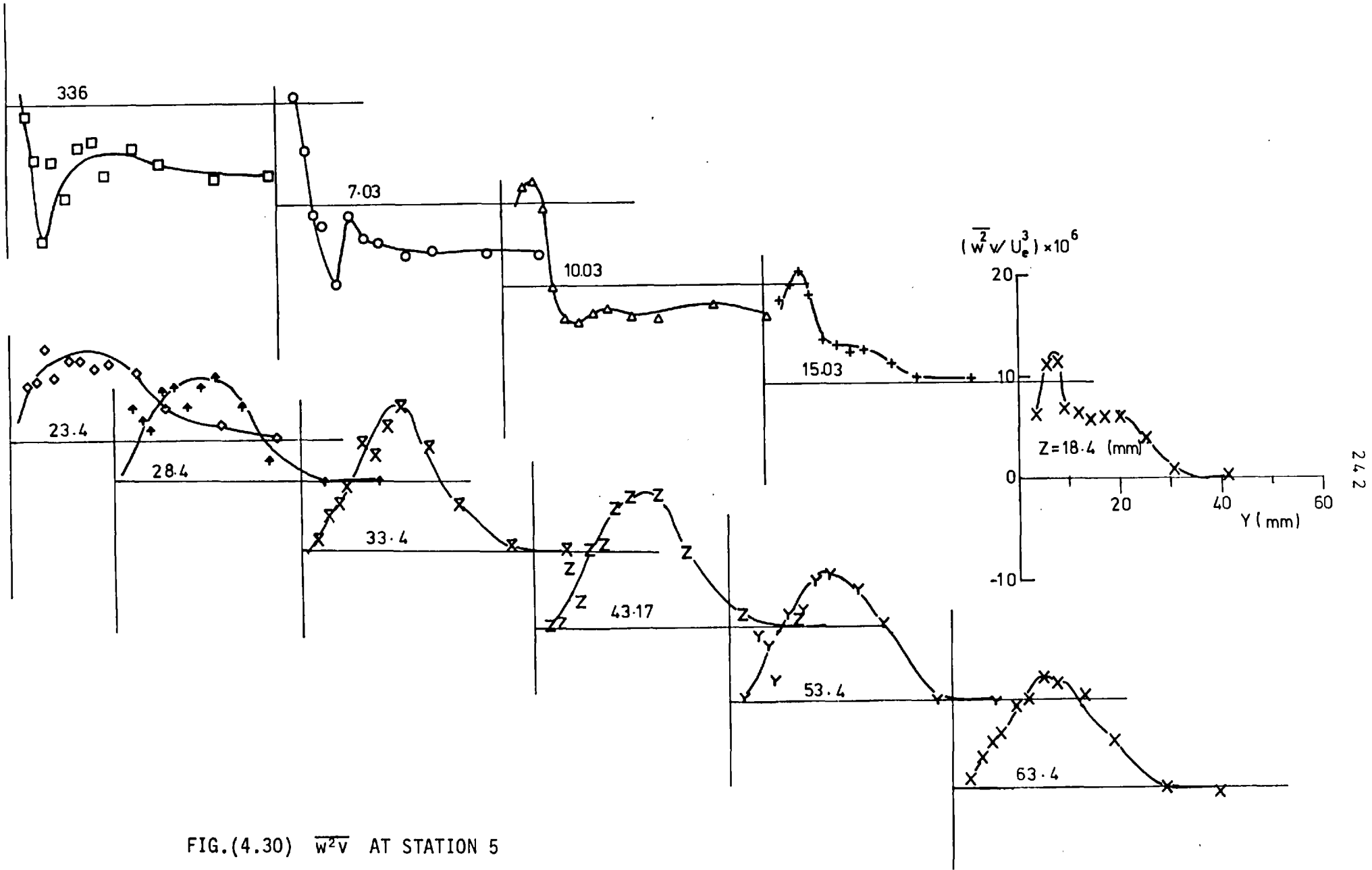

FIG.(4.30) $\overline{w^2v}$ AT STATION 5
(X = 613.8 mm)

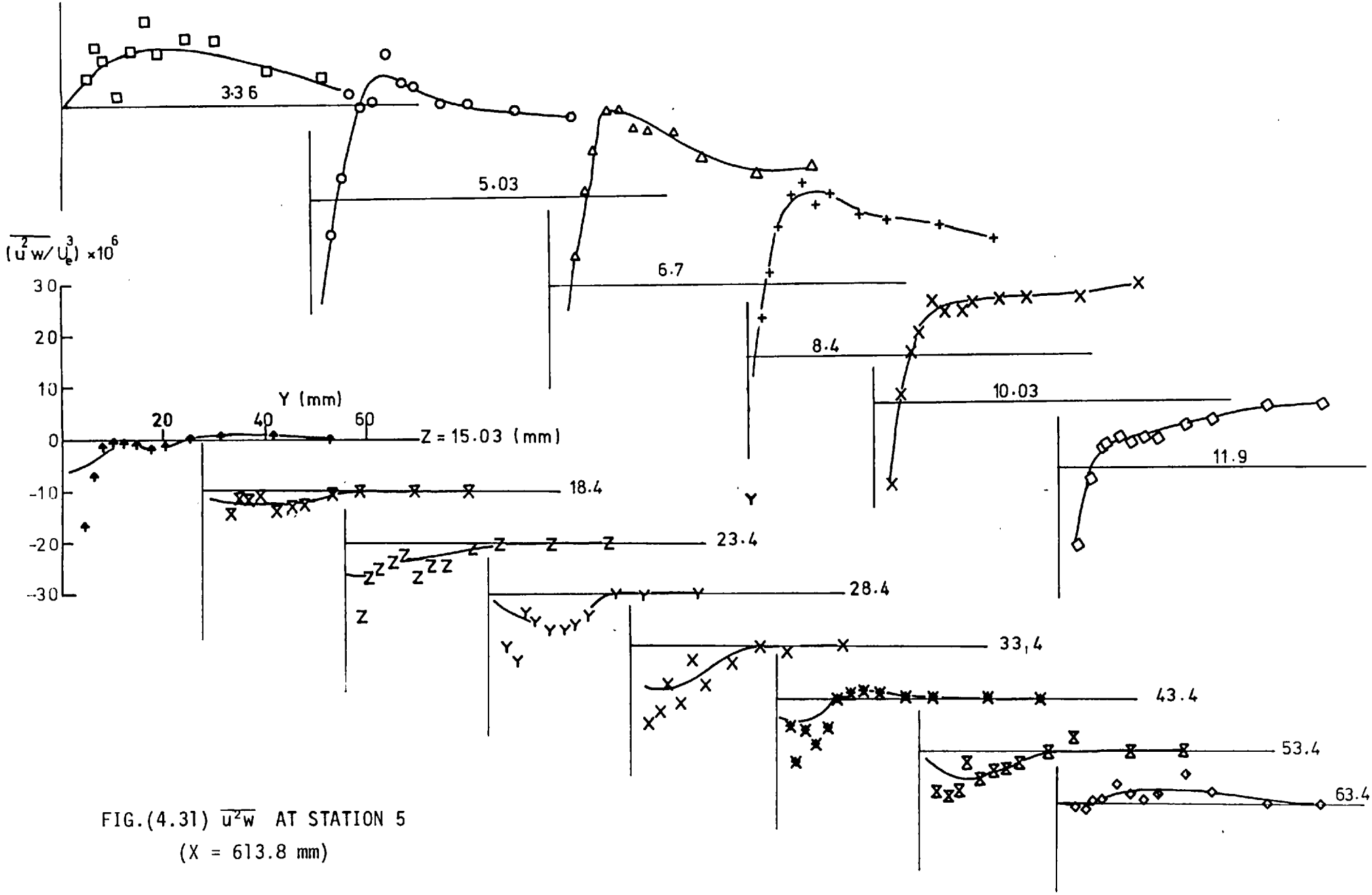

FIG.(4.31) $\overline{u^2w}$ AT STATION 5
(X = 613.8 mm)

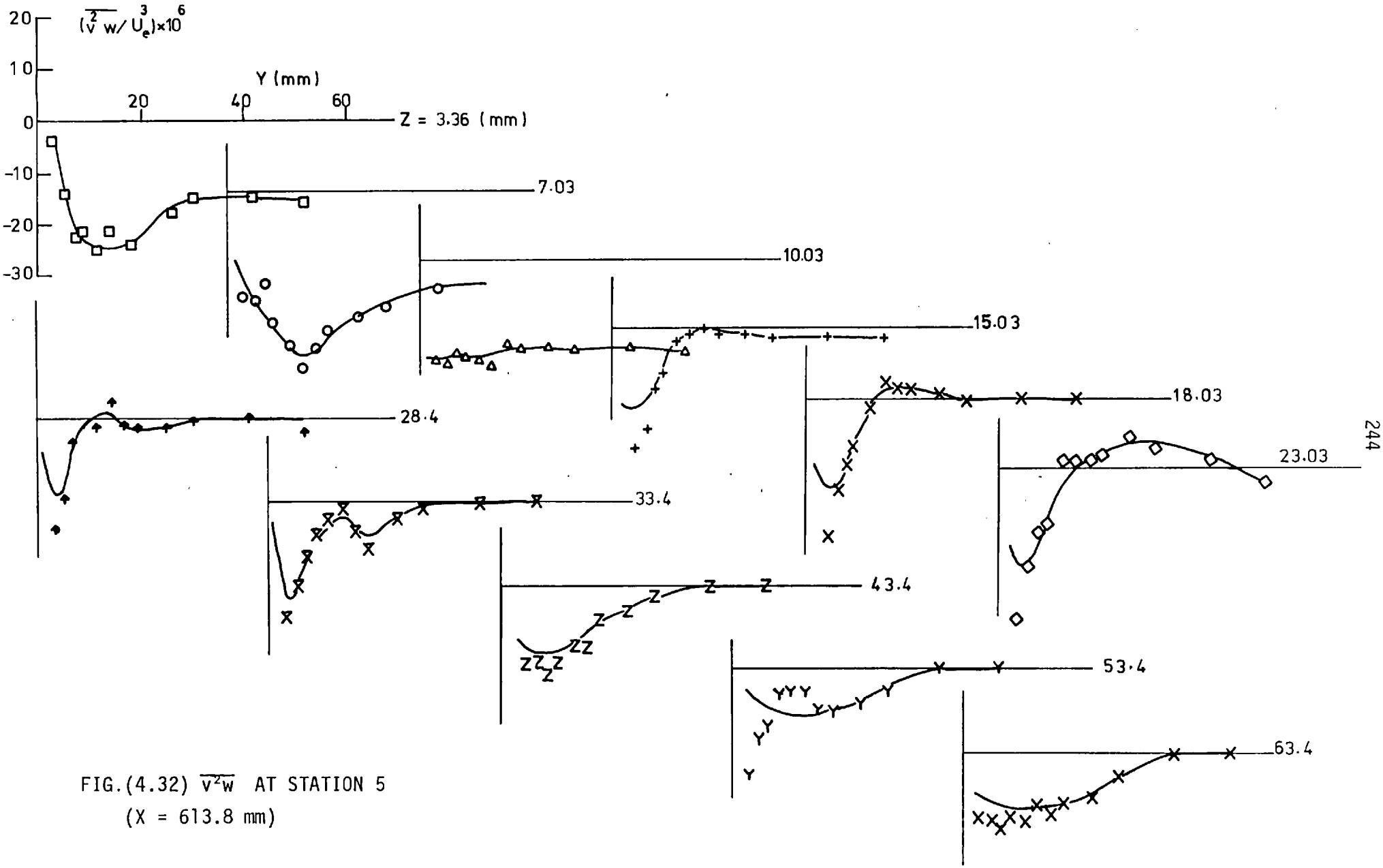

FIG.(4.32) $\overline{v^2w}$ AT STATION 5
(X = 613.8 mm)

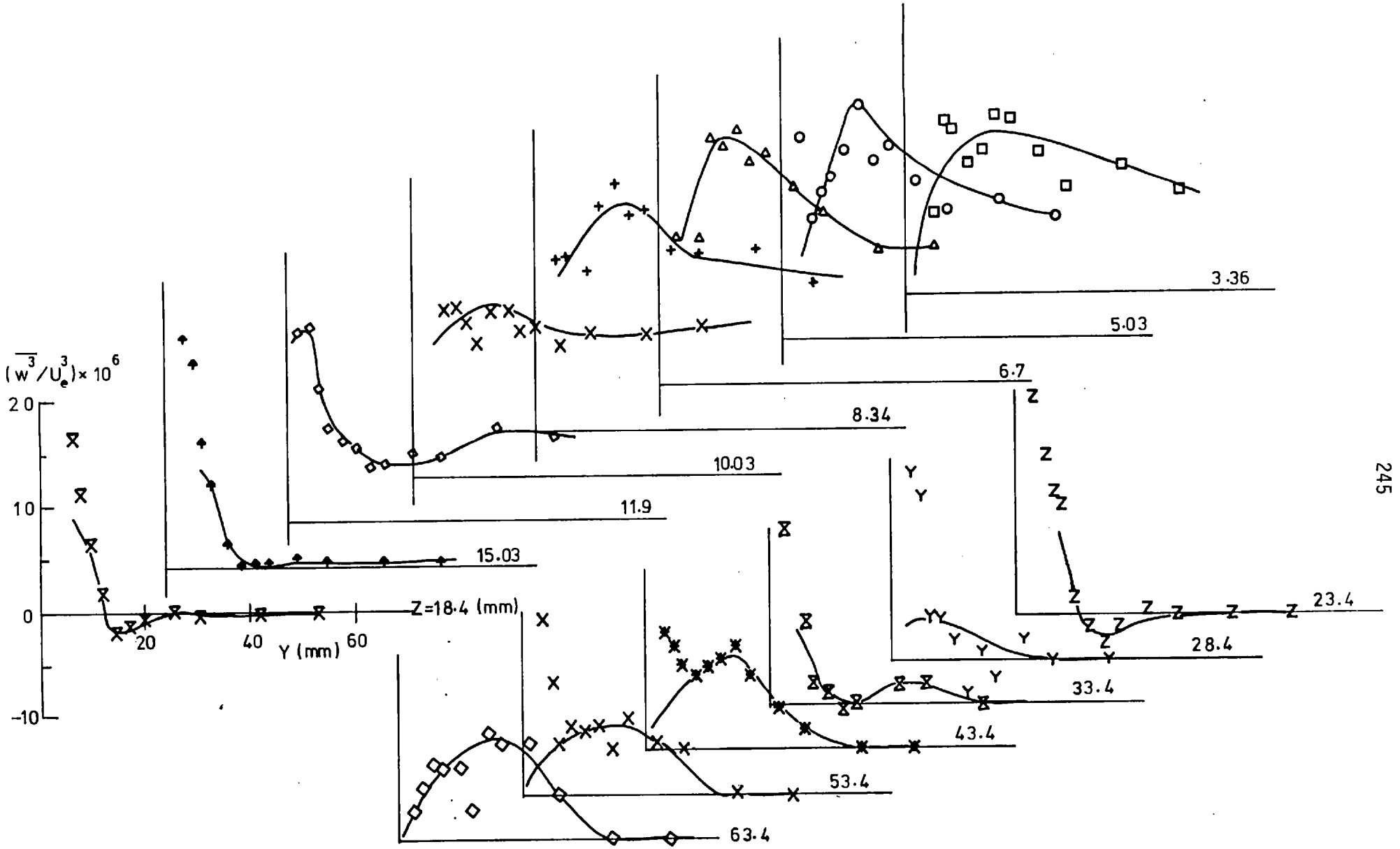

FIG.(4.33) $\overline{w^3}$ AT STATION 5
(X = 613.8mm)

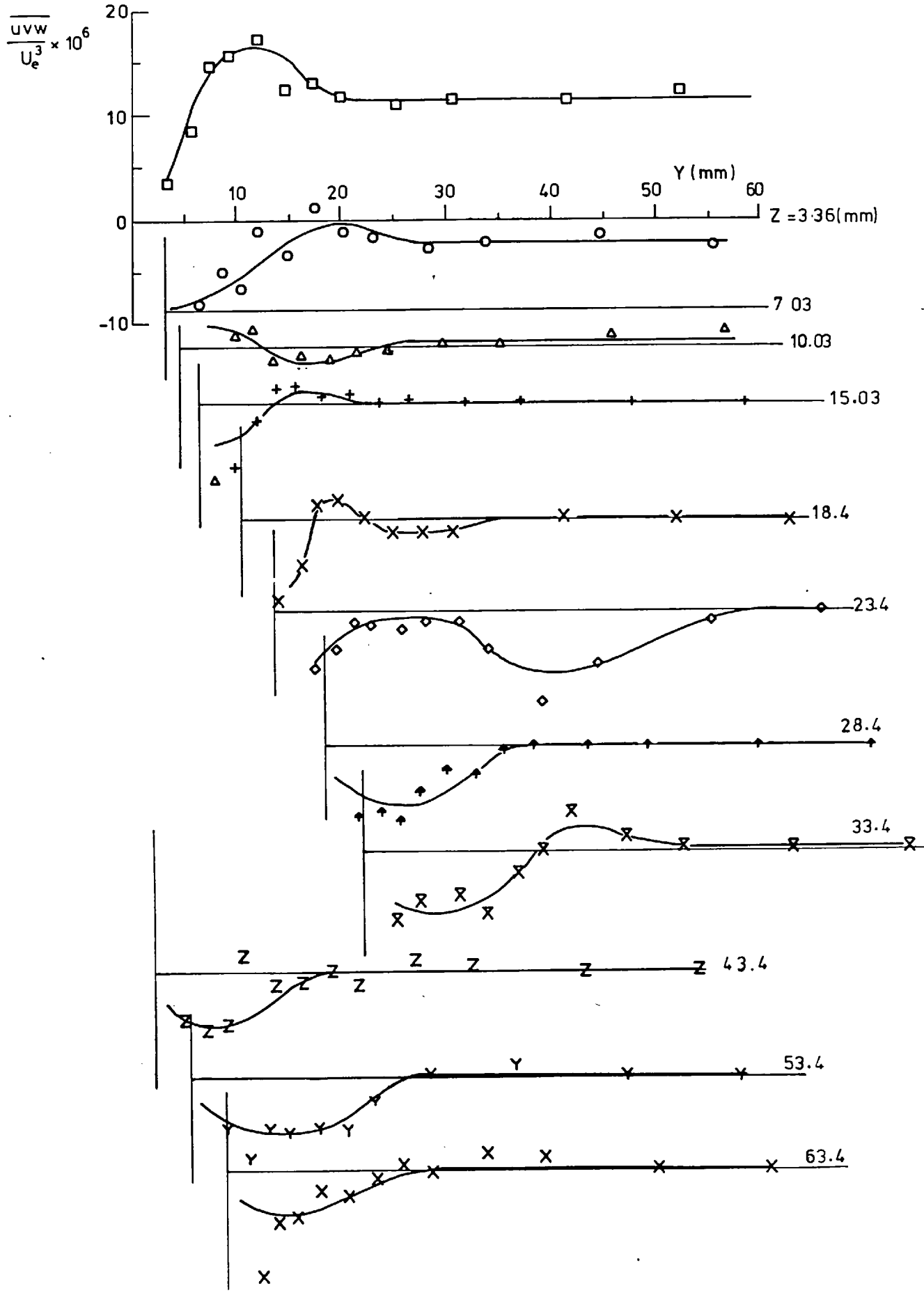

FIG.(4.34) $\overline{uvw}$ AT STATION 5
(X = 613.8 mm)

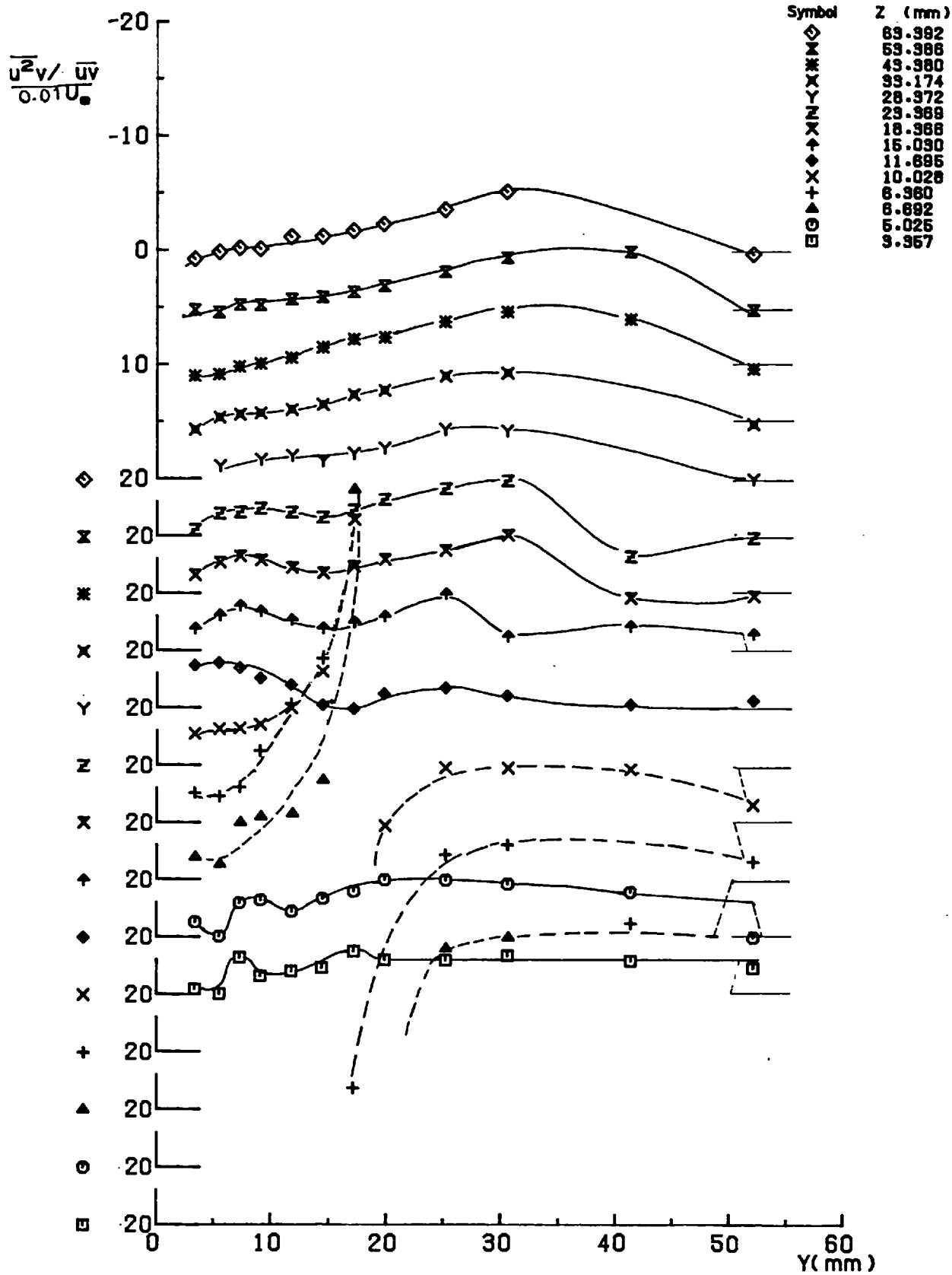

FIG.(4.35) $\overline{u^2v}/\ \overline{uv}$ AT STATION 5 (X= 613.8 mm)

Cross Wire Measurements

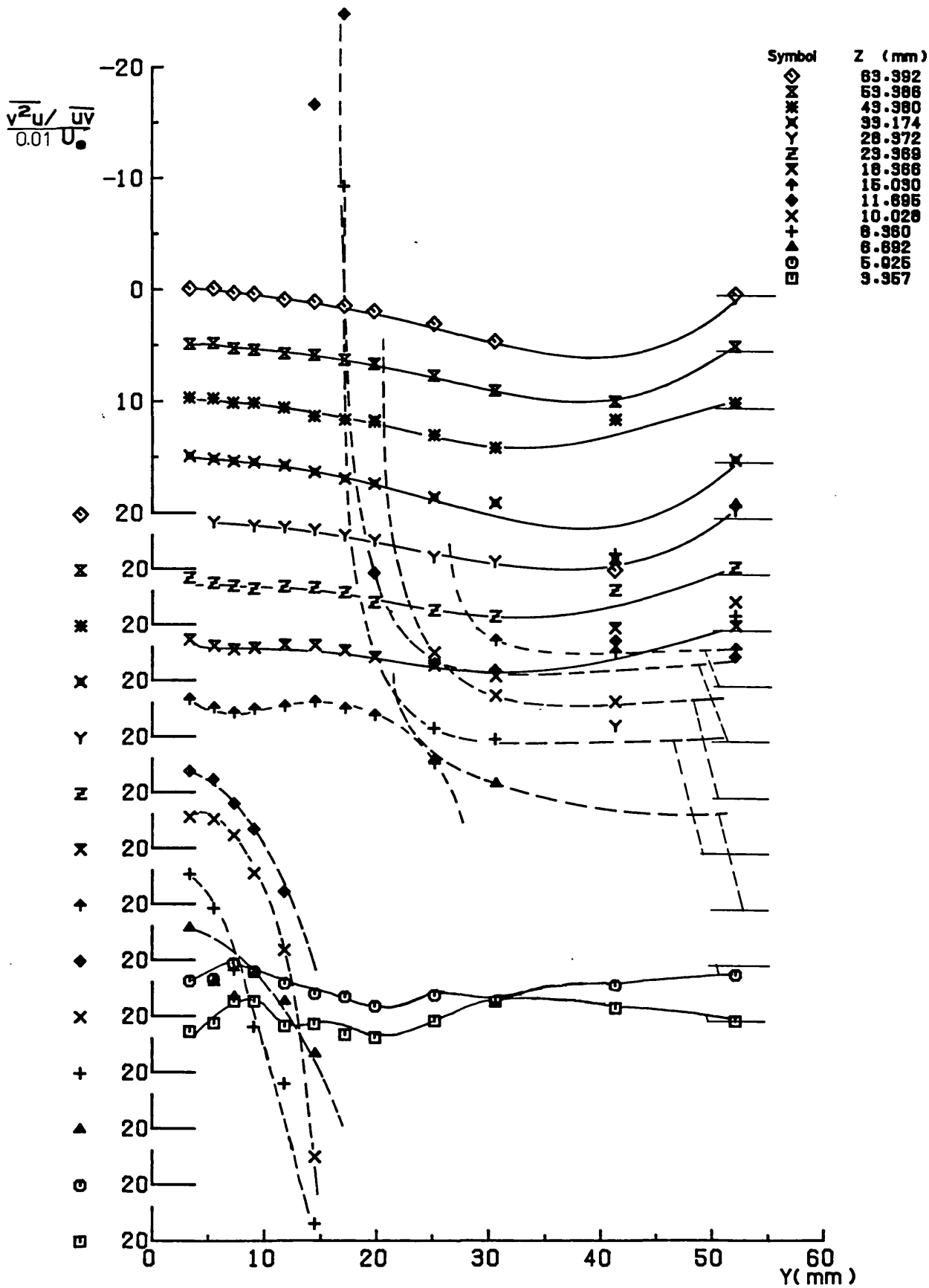

FIG.(4.36) $\overline{v^2u}/\ \overline{uv}$ AT STATION 5 (X= 613.8 mm)

Cross Wire Measurements

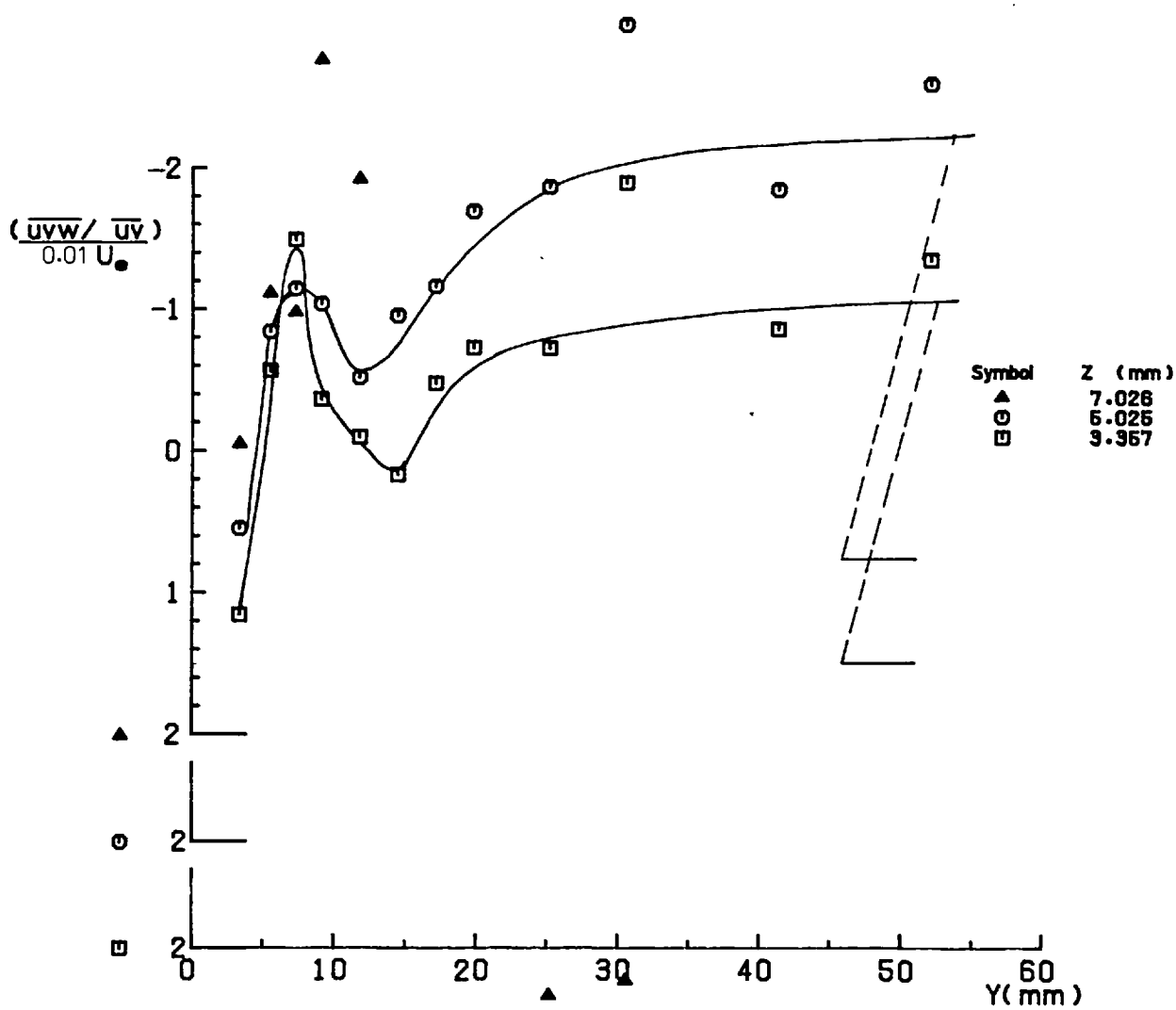

FIG.(4.37) $\overline{uvw}/\ \overline{uv}$ AT STATION 5 (X= 613.8 mm)

Cross Wire Measurements

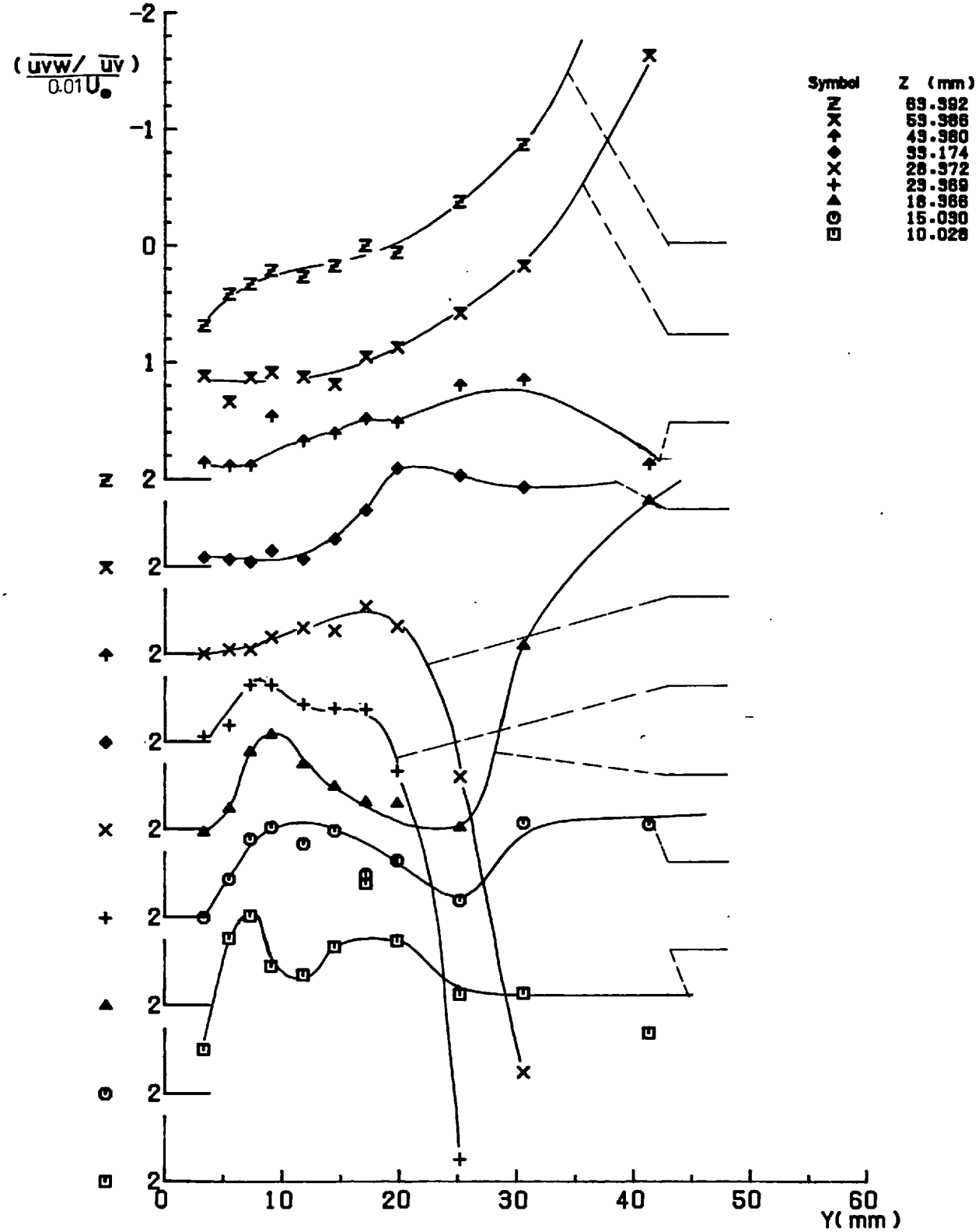

FIG.(4·37 cont.) $\overline{uvw}/\overline{uv}$ AT STATION 5 (X= 613.8 mm)

Cross Wire Measurements

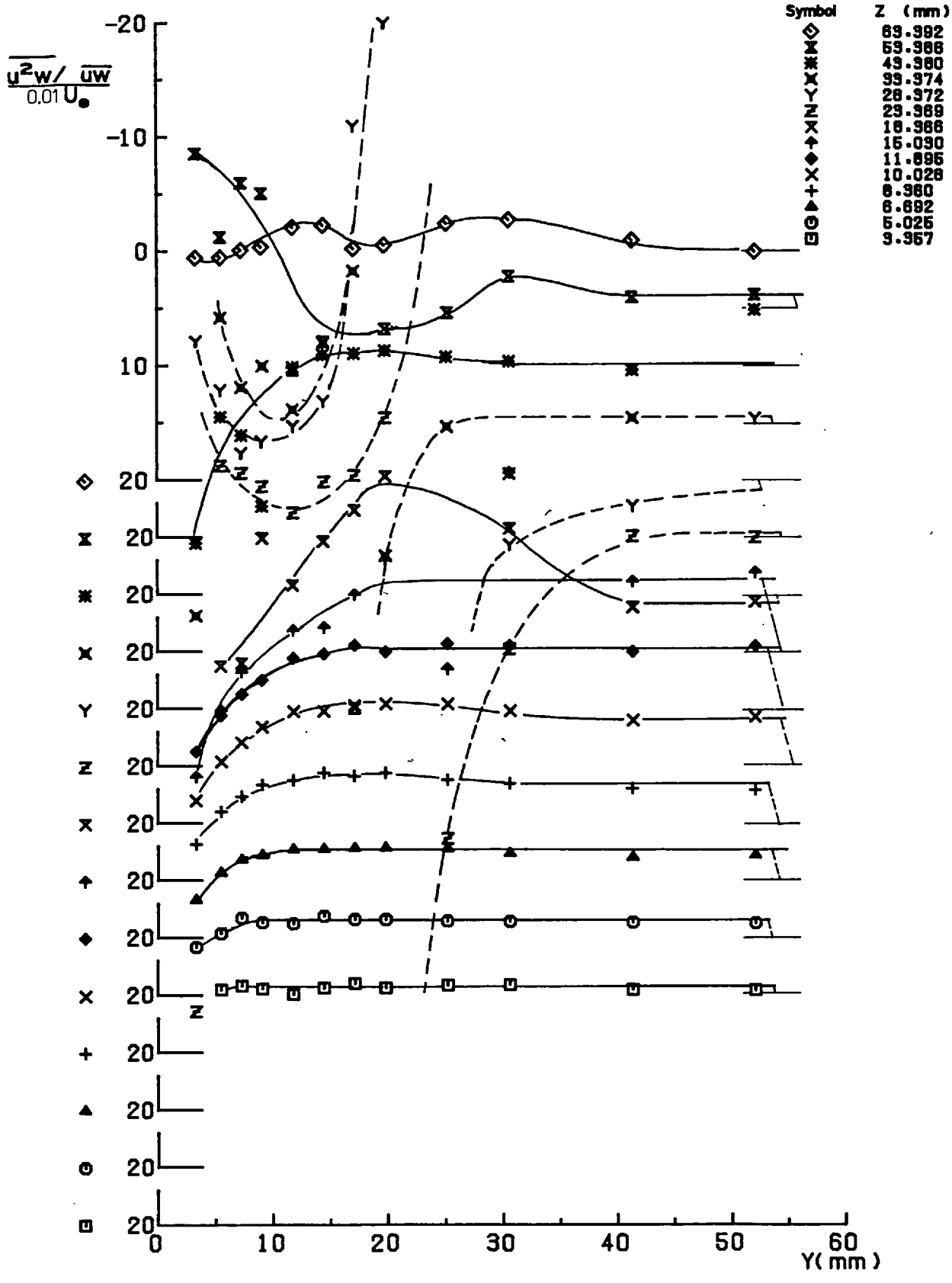

FIG.(4.38) $\overline{u^2w}/\overline{uw}$ AT STATION 5 (X= 613.8 mm)

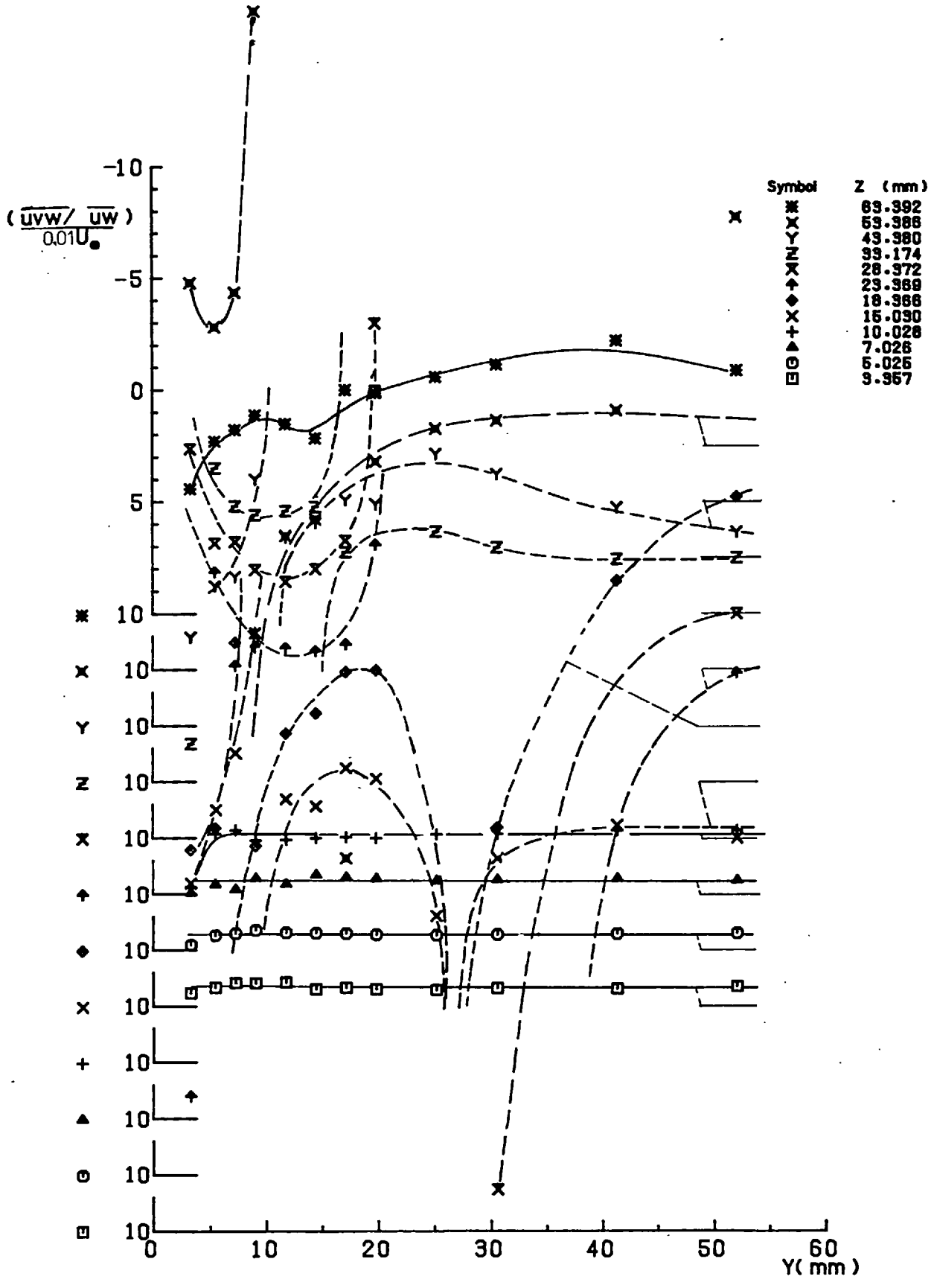

FIG.(4.39) $\overline{uvw}/\overline{uw}$ AT STATION 5 (X= 613.8 mm)

Cross Wire Measurements

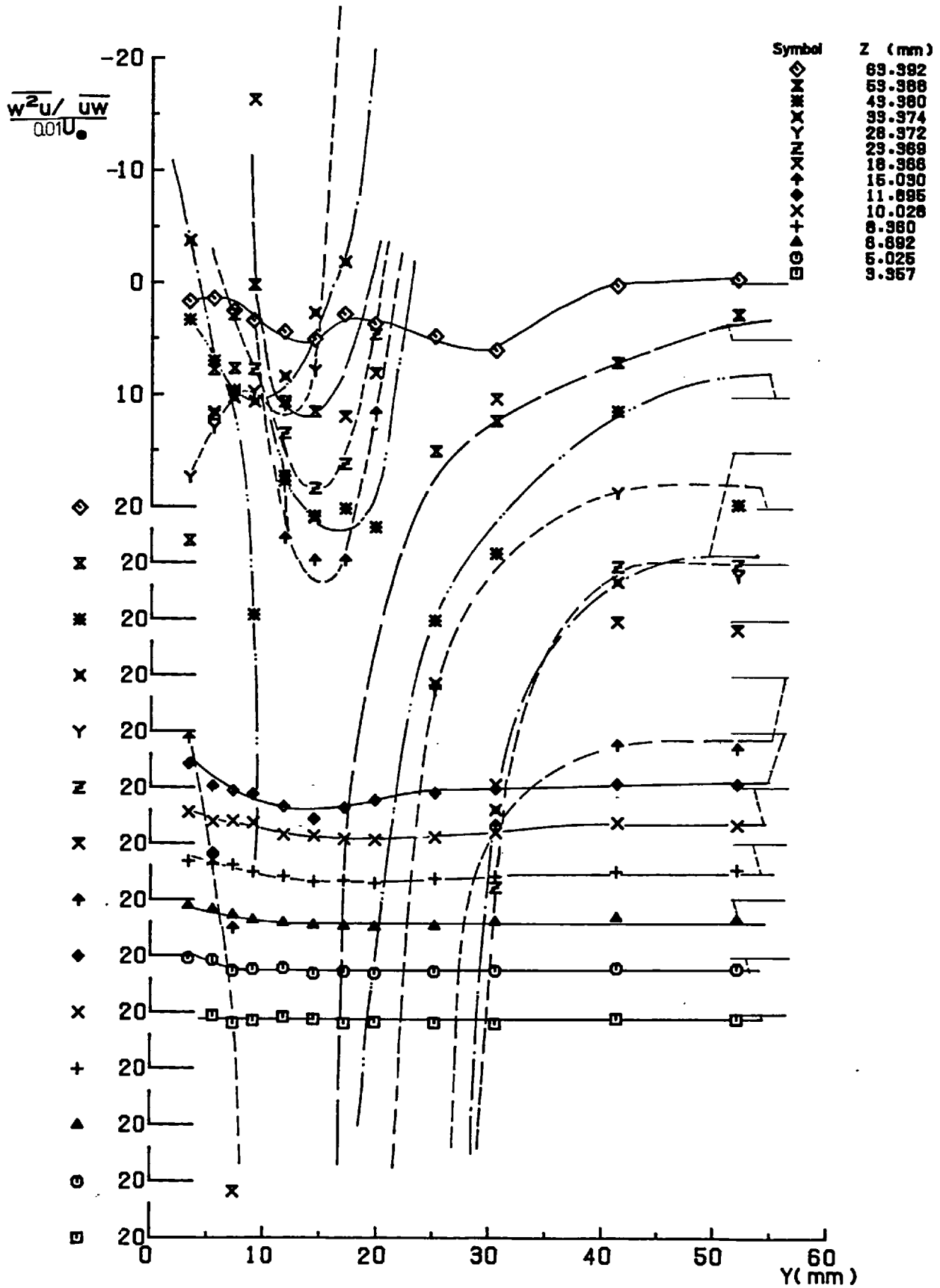

FIG.(4.40) $\overline{w^2u}/\ \overline{uw}$ AT STATION 5 (X= 613.8 mm)

Cross Wire Measurements

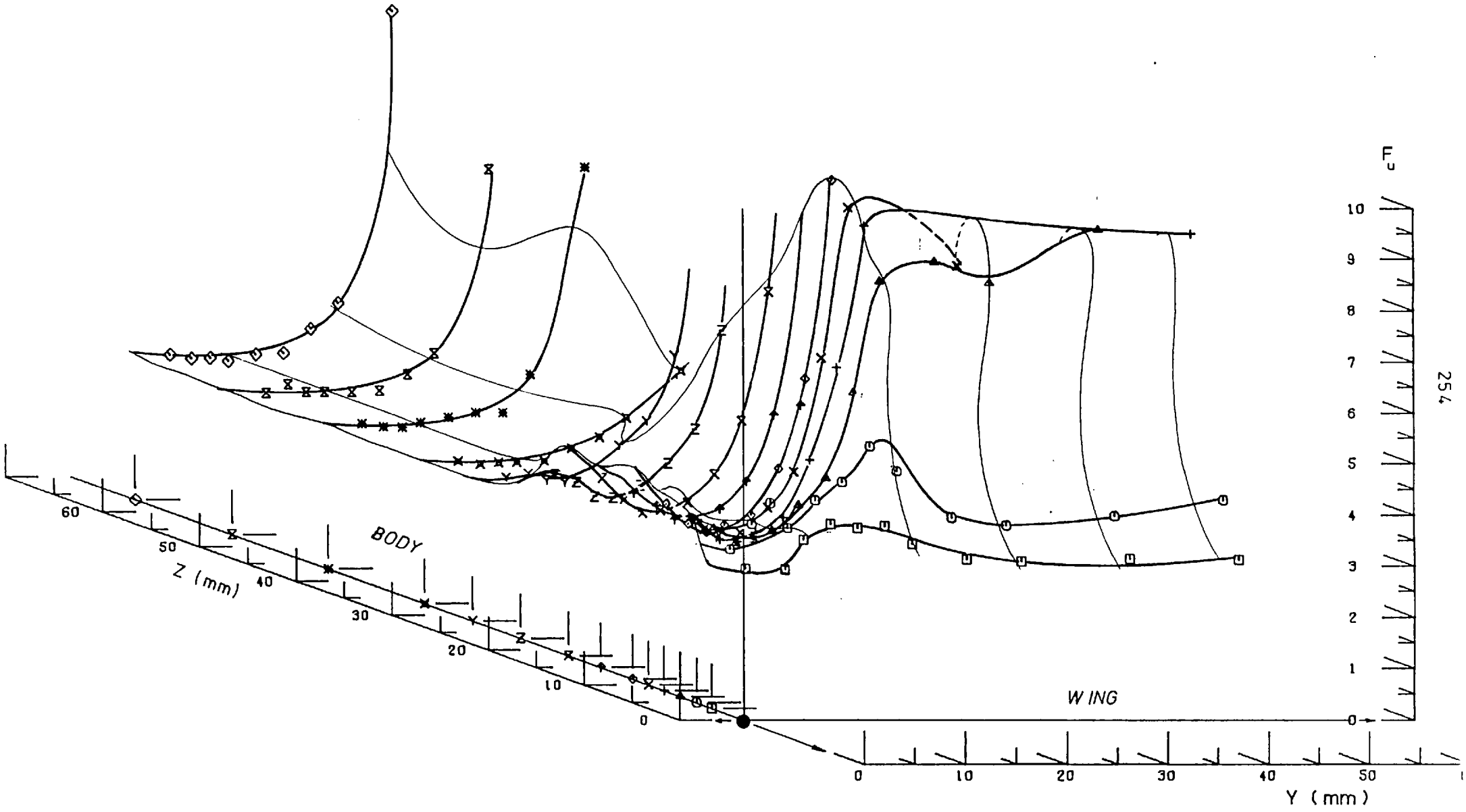

FIG.(4 . 41) u-COMPONENT FLATNESS FACTOR (F_u) AT STATION 2 (X= 156.6mm)

Results of Cross Wire in Vertical (U-V) Position

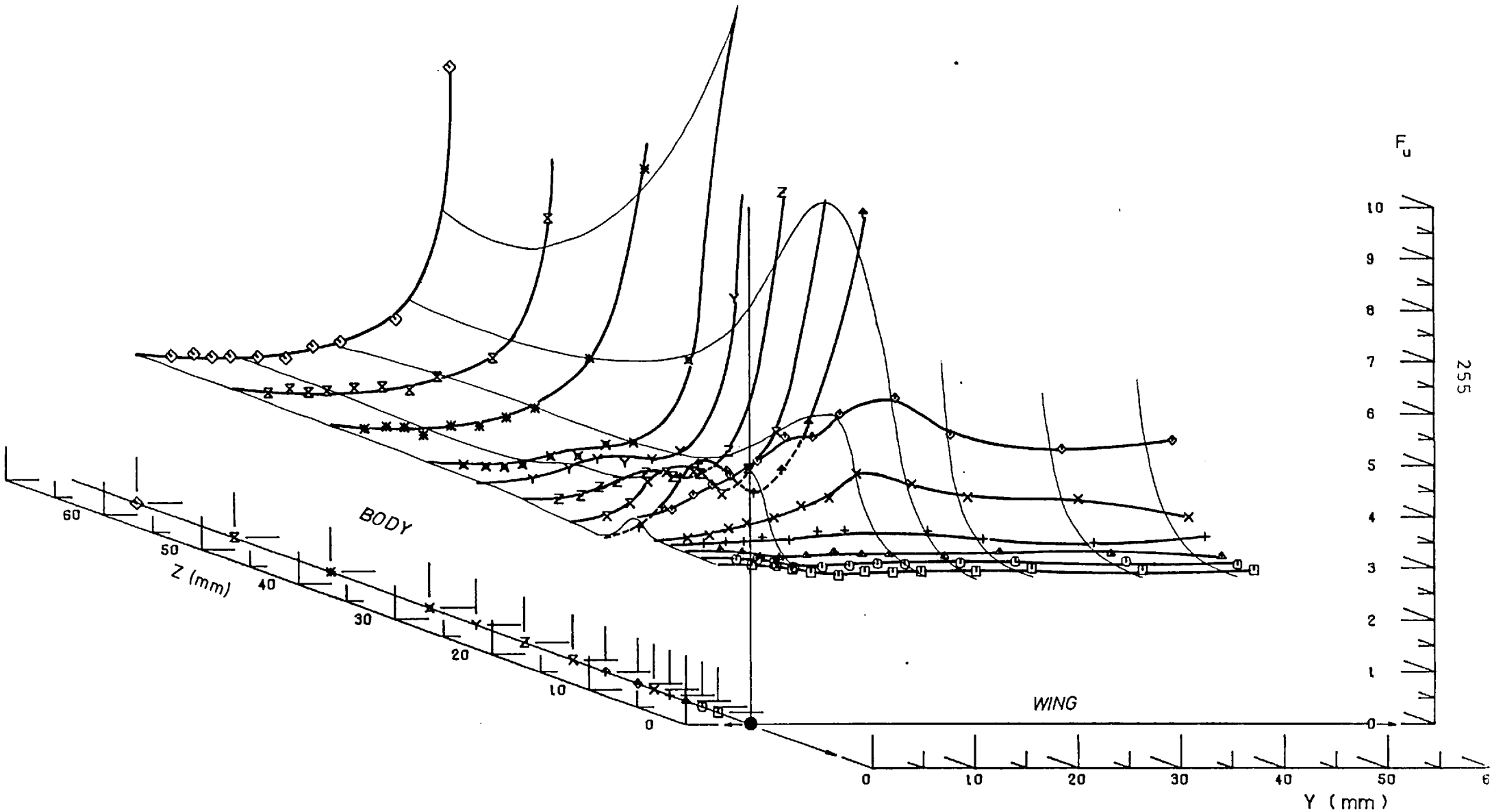

FIG.(4.42) u-COMPONENT FLATNESS FACTOR (F_u) AT STATION 5 (X= 613.8mm)

Results of Cross Wire in Vertical (U-V) Position

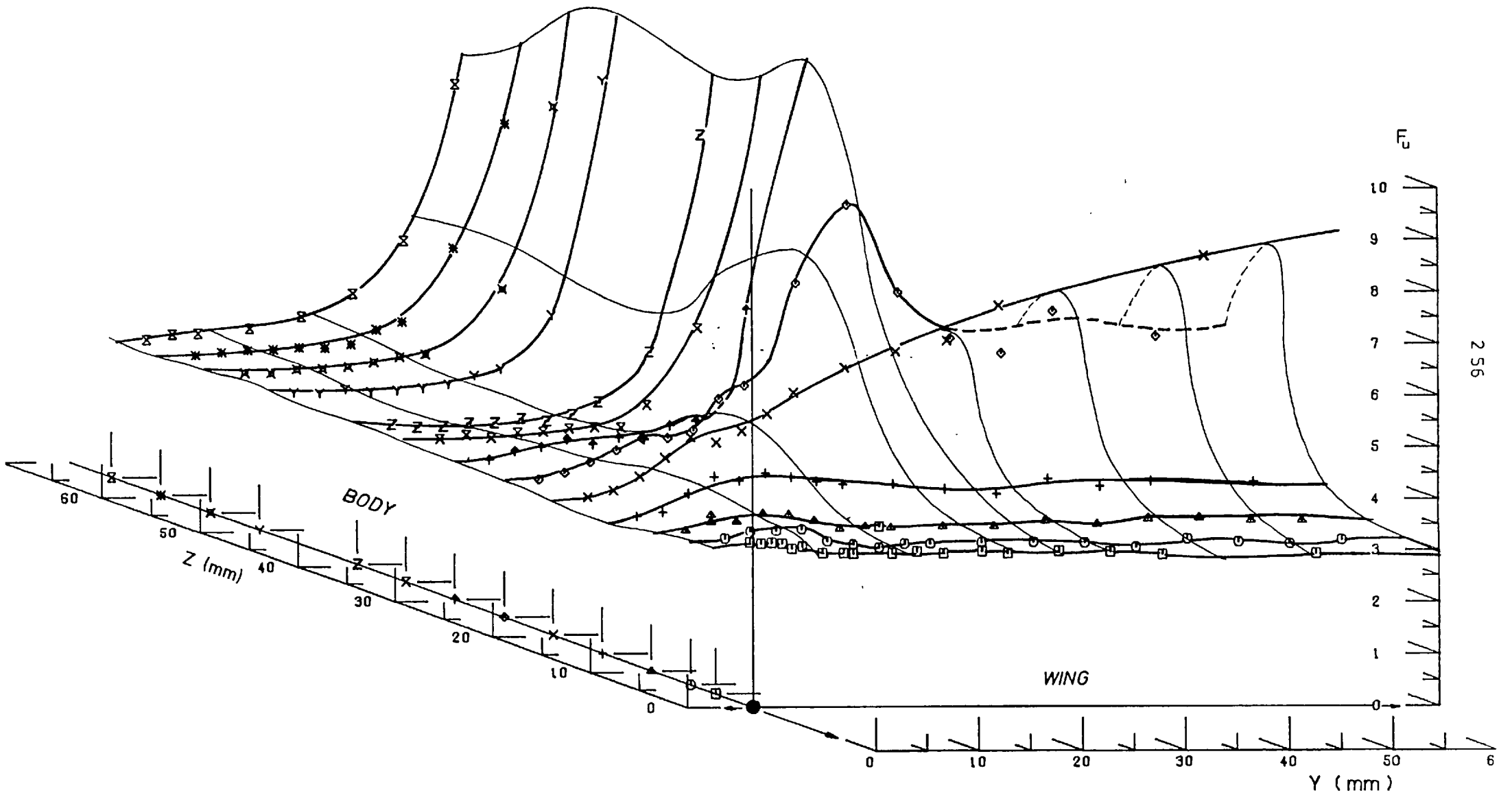

FIG.(4.43) u-COMPONENT FLATNESS FACTOR (F_u) AT STATION 9 (X=1223.4mm)

Results of Cross Wire in Vertical (U-V) Position

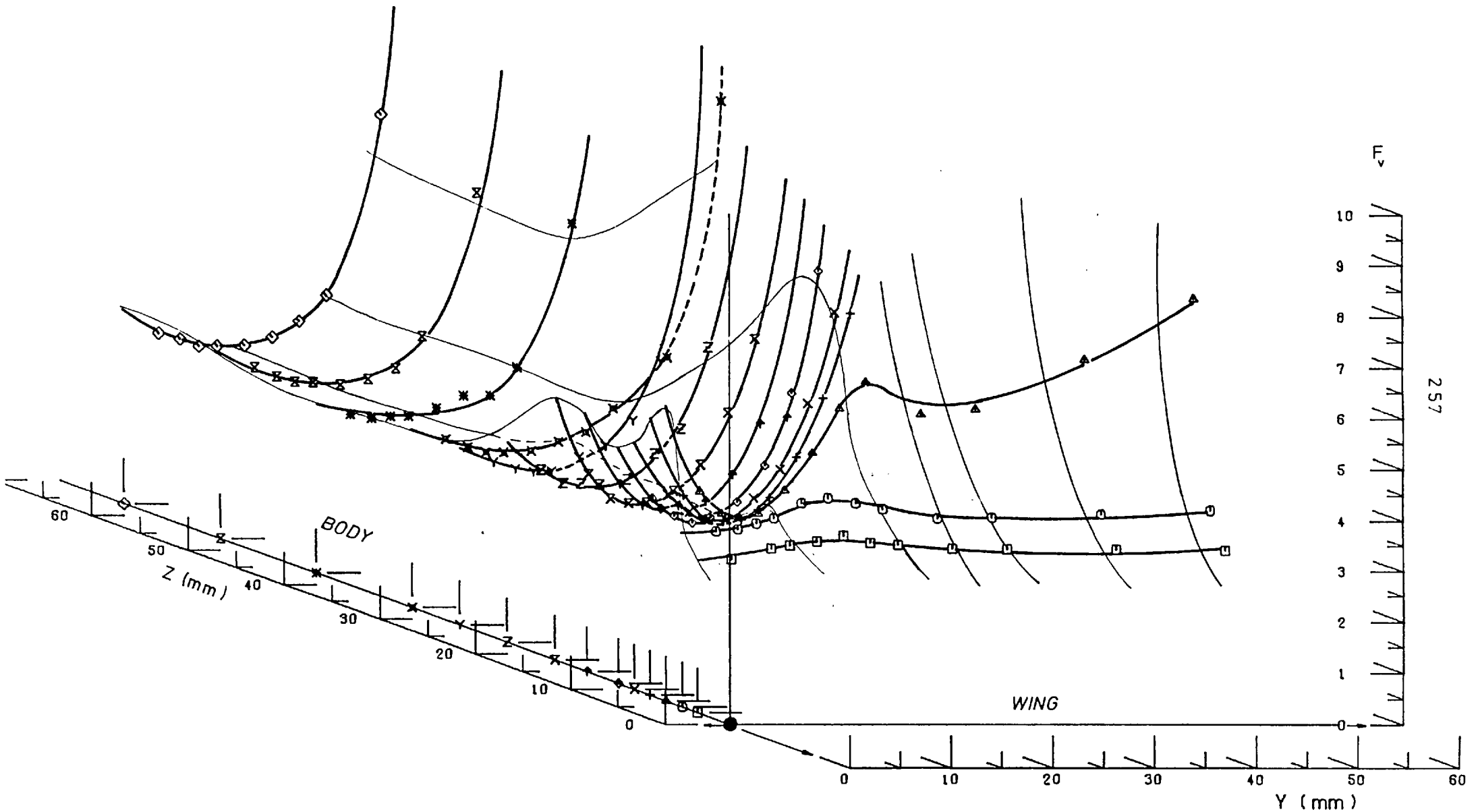

FIG.(4.44) v-COMPONENT FLATNESS FACTOR (F_v) AT STATION 2 (X= 156.6mm)

Results of Cross Wire in Vertical (U-V) Position

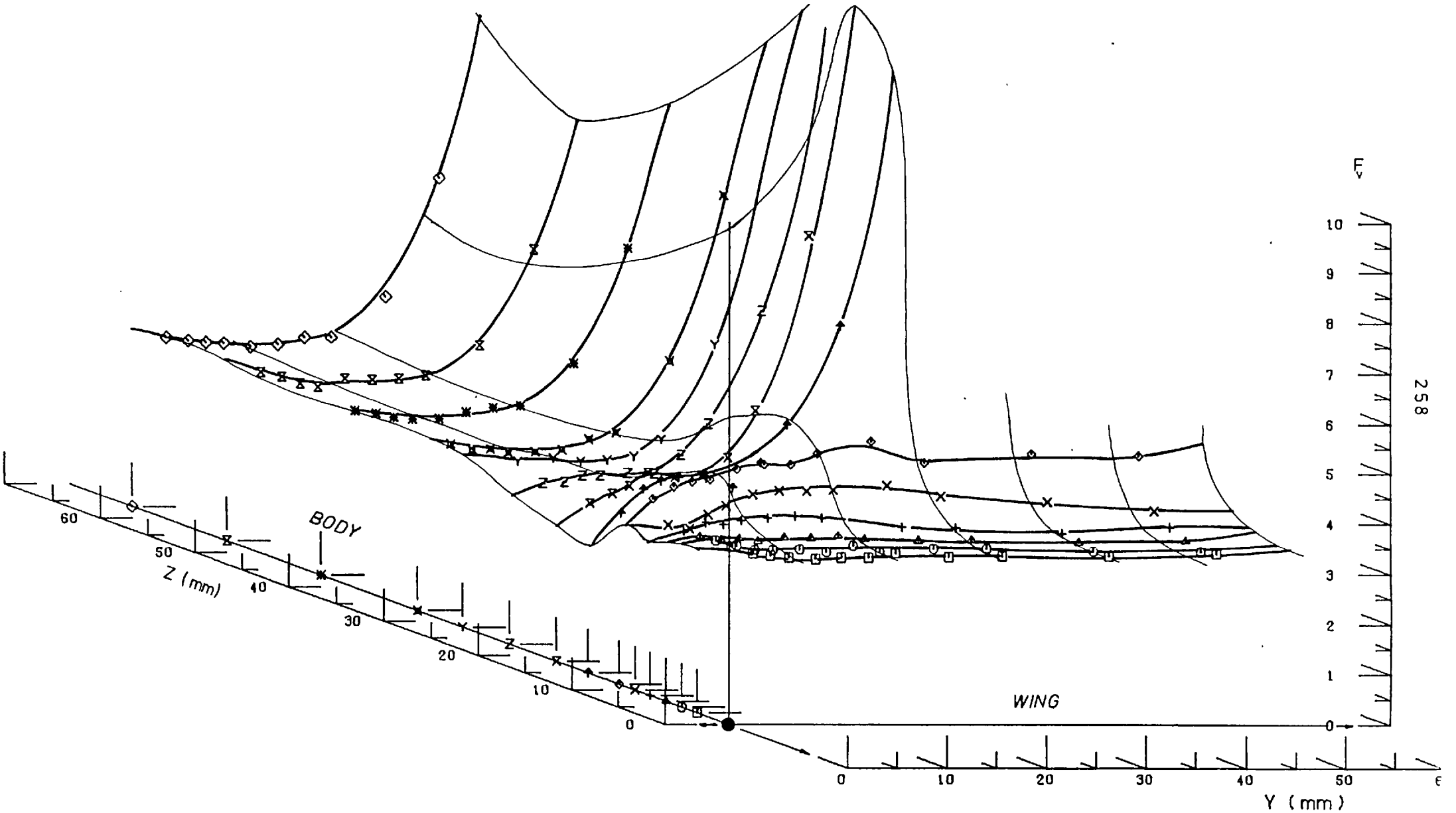

FIG.(4.45) v-COMPONENT FLATNESS FACTOR (F_v) AT STATION 5 (X= 613.8mm)

Results of Cross Wire In Vertical (U-V) Position

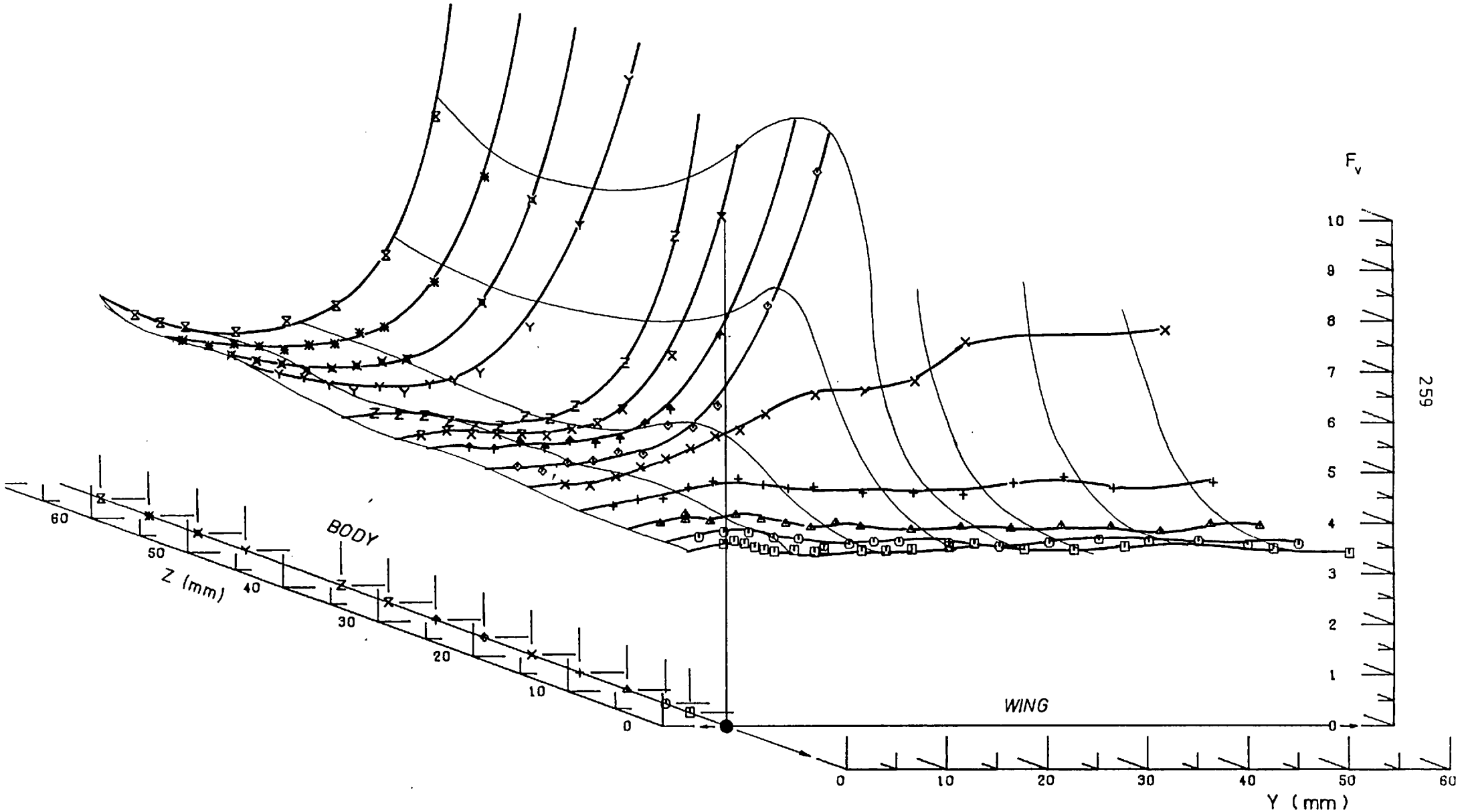

FIG.(4.46) v-COMPONENT FLATNESS FACTOR (F_v) AT STATION 9 (X=1223.4mm)

Results of Cross Wire in Vertical (U-V) Position

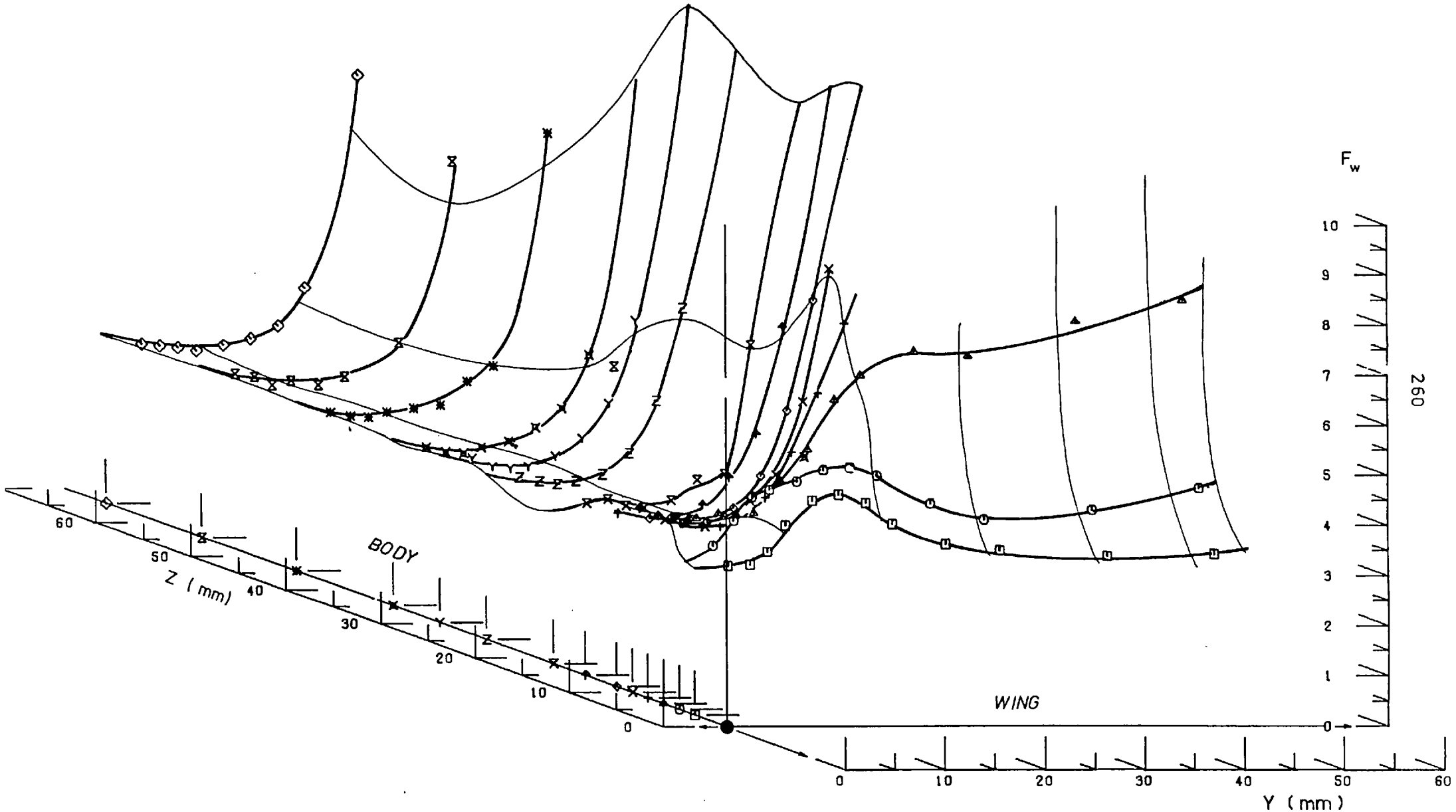

FIG.(4.47) w-COMPONENT FLATNESS FACTOR (F_w) AT STATION 2 (X= 156.6mm)

Results of Cross Wire in Horizontal (U-W) Position

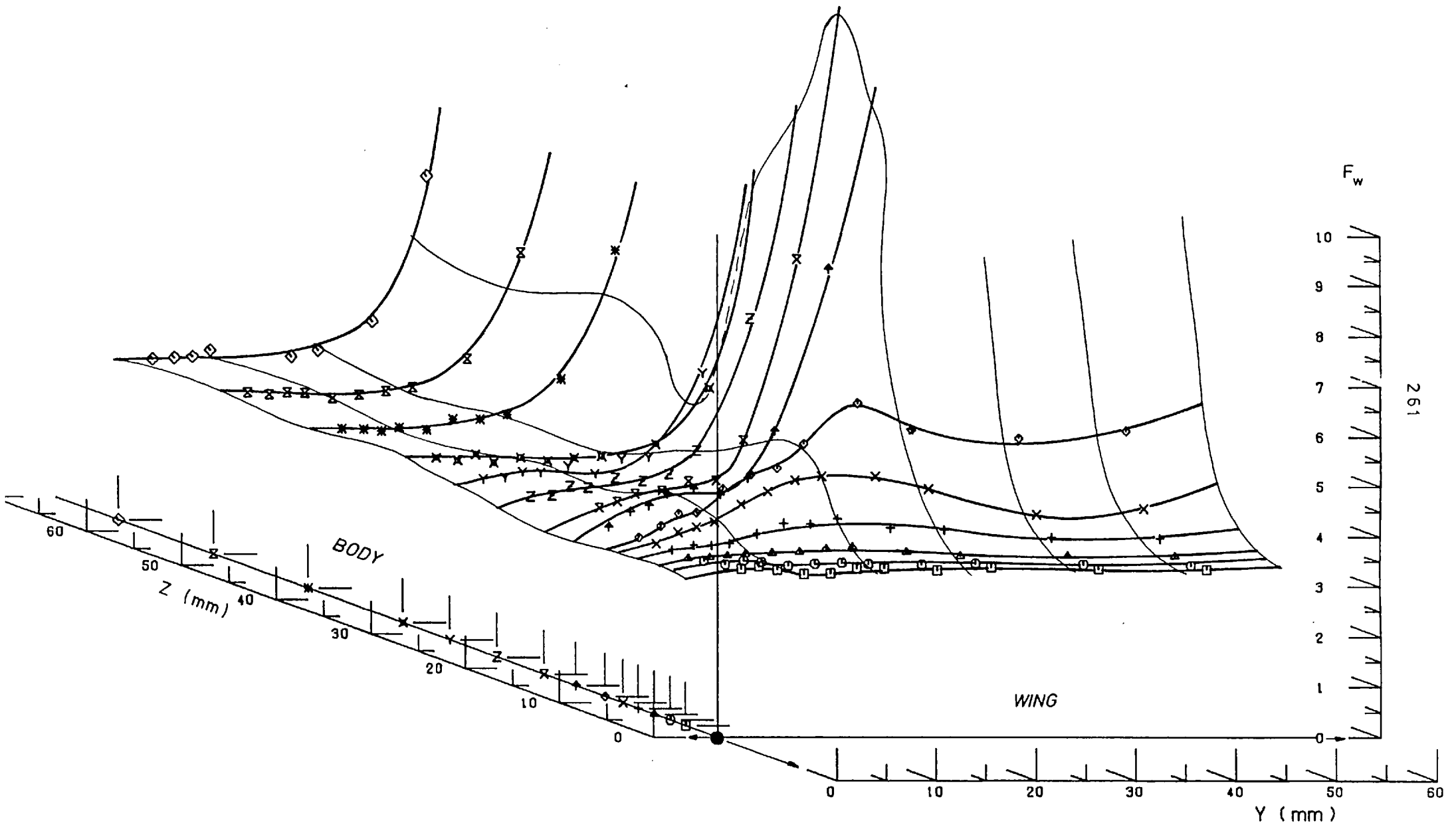

FIG.(4.48) w-COMPONENT FLATNESS FACTOR (F_w) AT STATION 5 (X= 613.8mm)

Results of Cross Wire in Horizontal (U-W) Position

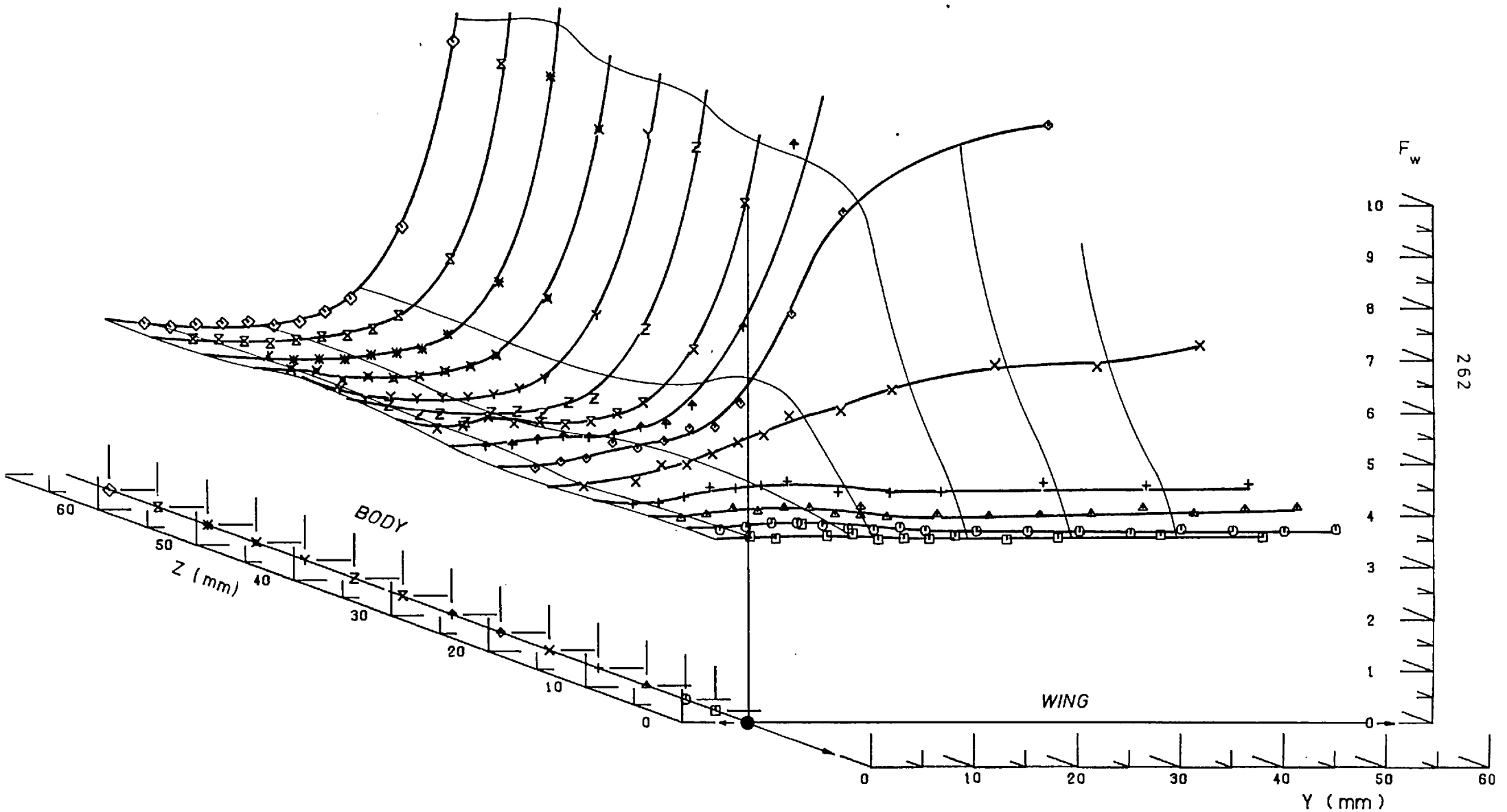

FIG.(4.49) w-COMPONENT FLATNESS FACTOR (F_w) AT STATION 9 (X=1223.4mm)

Results of Cross Wire in Horizontal (U-W) Position

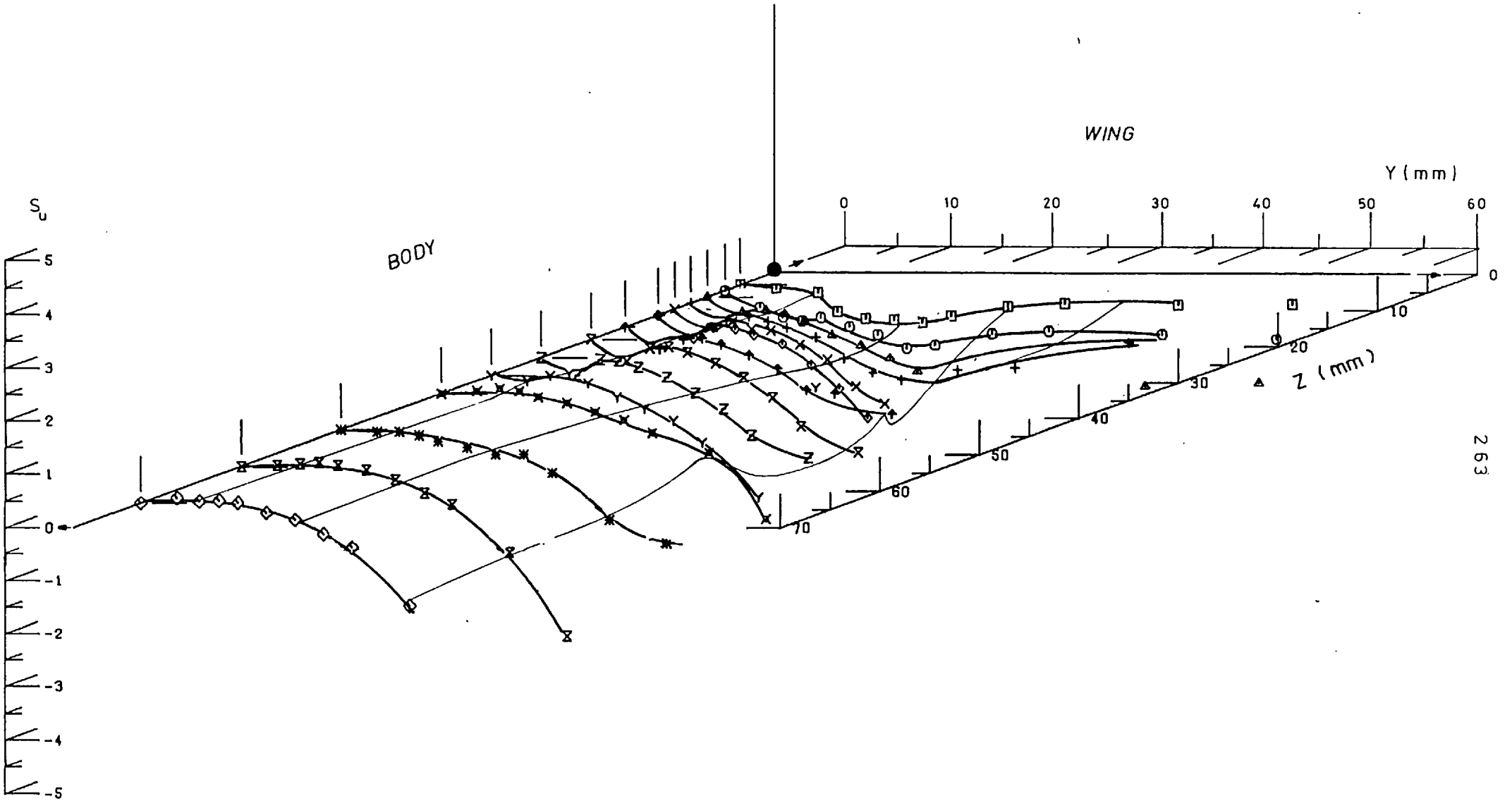

FIG.(4 . 50) u-COMPONENT SKEWNESS FACTOR (S_u) AT STATION 2 (X= 156.6mm)
Results of Cross Wire in Vertical (U-V) Position

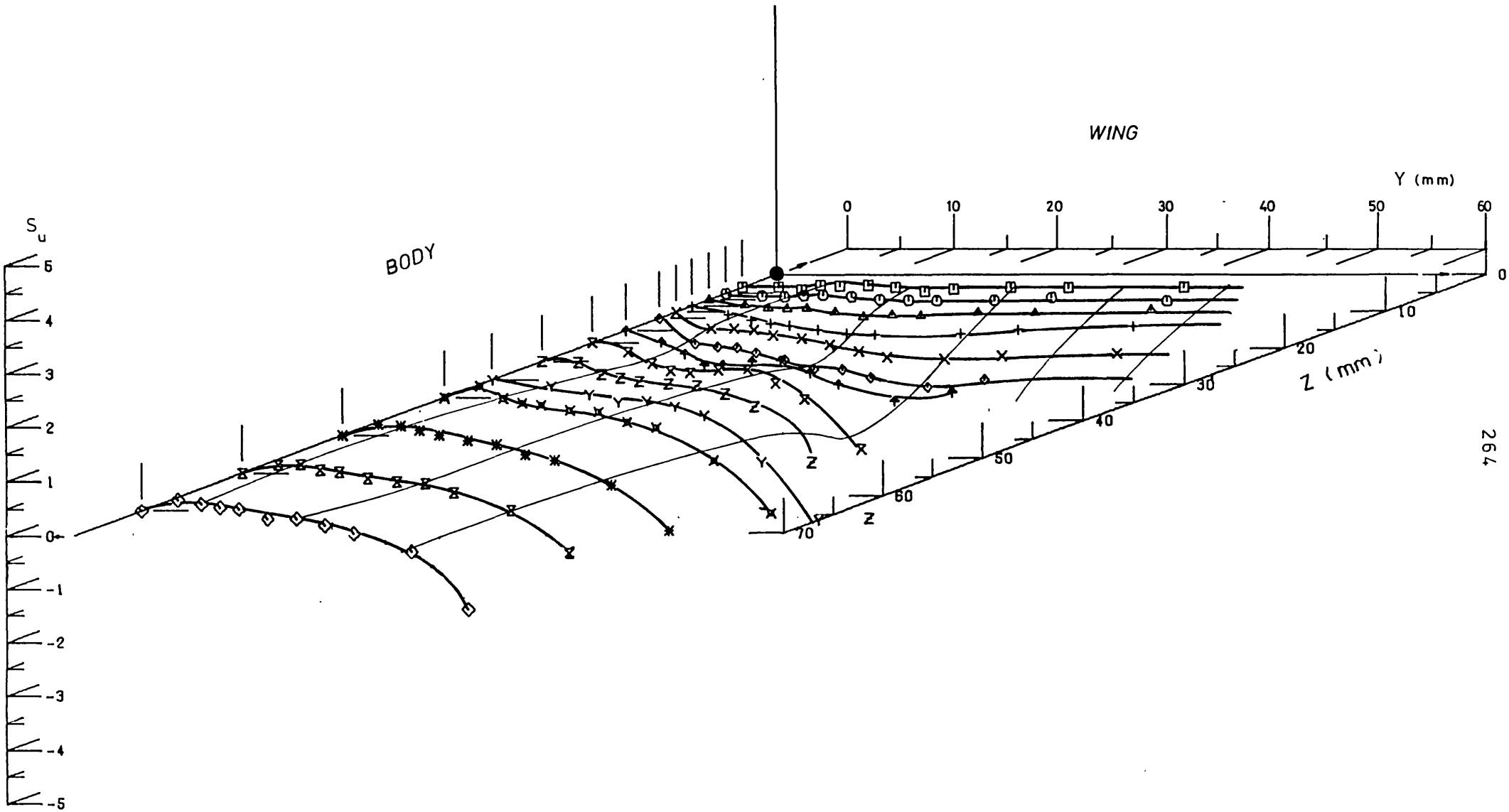

FIG.(4.51) u-COMPONENT SKEWNESS FACTOR (S_u) AT STATION 5 (X= 613.8mm)

Results of Cross Wire in Vertical (U-V) Position

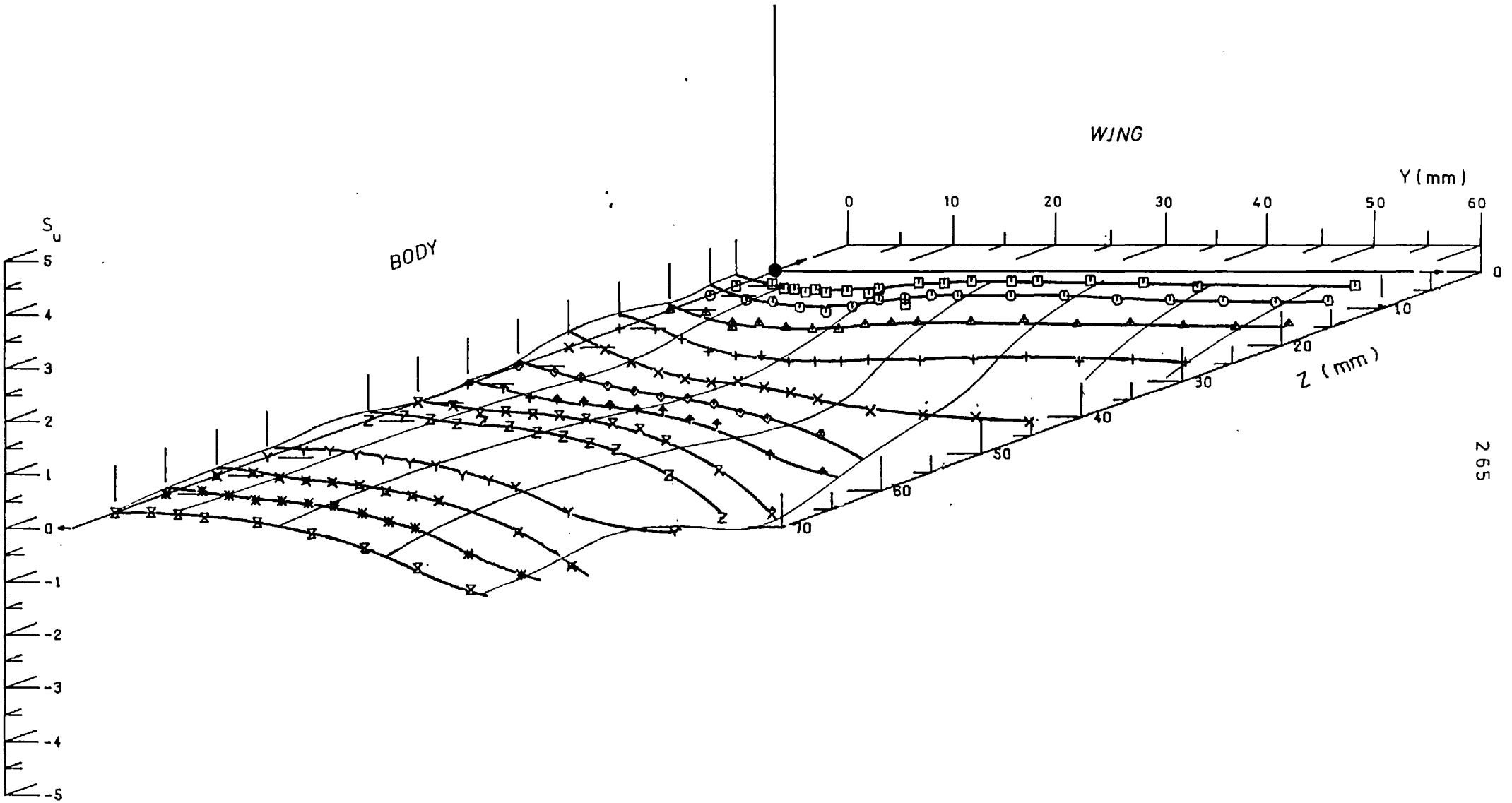

FIG.(4.52) u-COMPONENT SKEWNESS FACTOR (S_u) AT STATION 9 (X=1223.4mm)
Results of Cross Wire in Vertical (U-V) Position

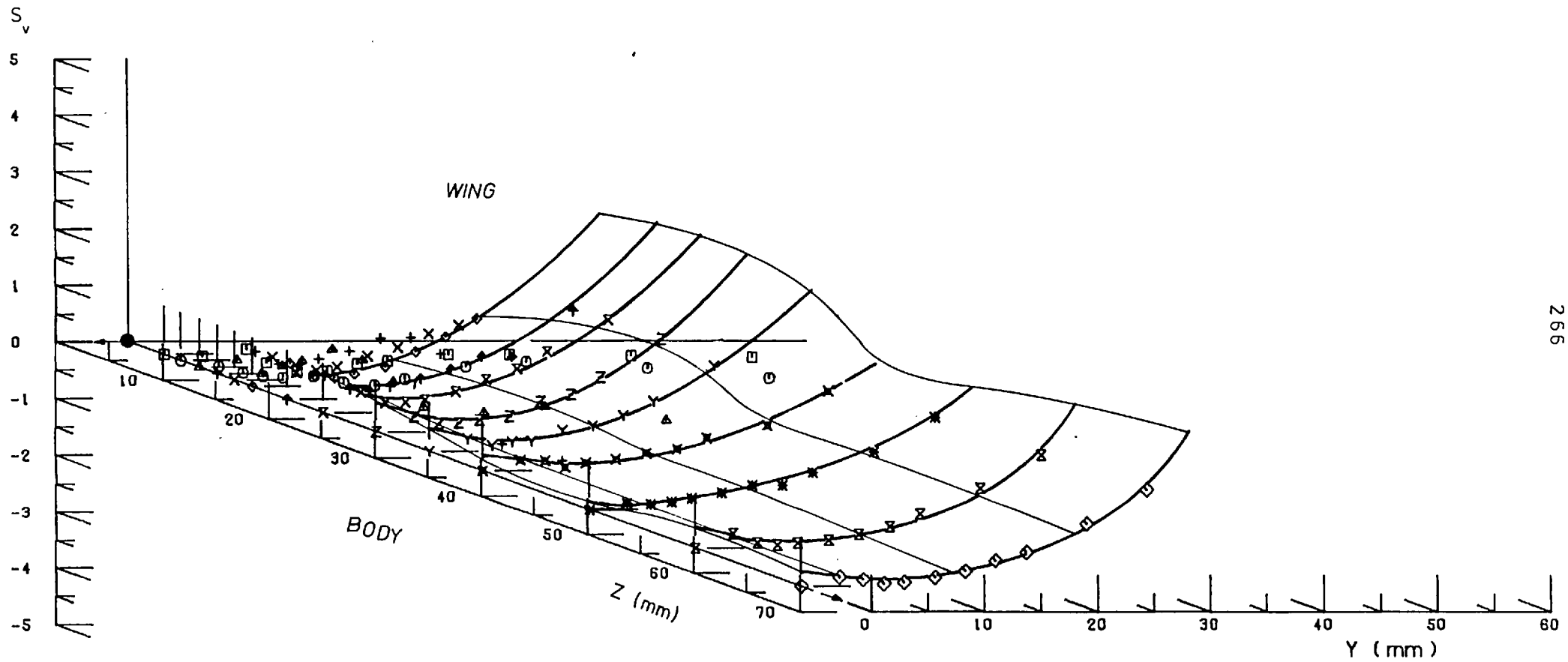

FIG.(4.53) v-COMPONENT SKEWNESS FACTOR (S_v) AT STATION 2 (X= 156.6mm)
Results of Cross Wire in Vertical (U-V) Position

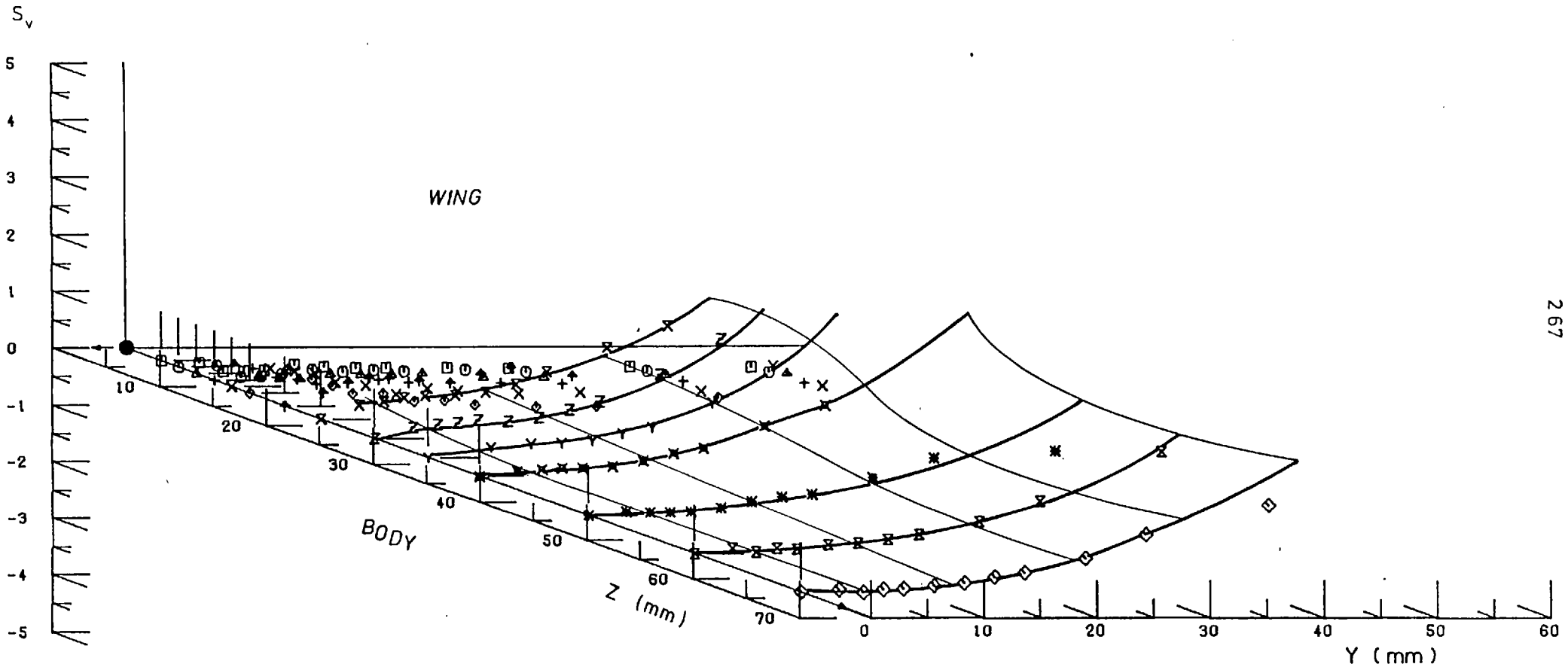

FIG.(4 . 54) v-COMPONENT SKEWNESS FACTOR (S_v) AT STATION 5 (X= 613.8mm)

Results of Cross Wire In Vertical (U-V) Position

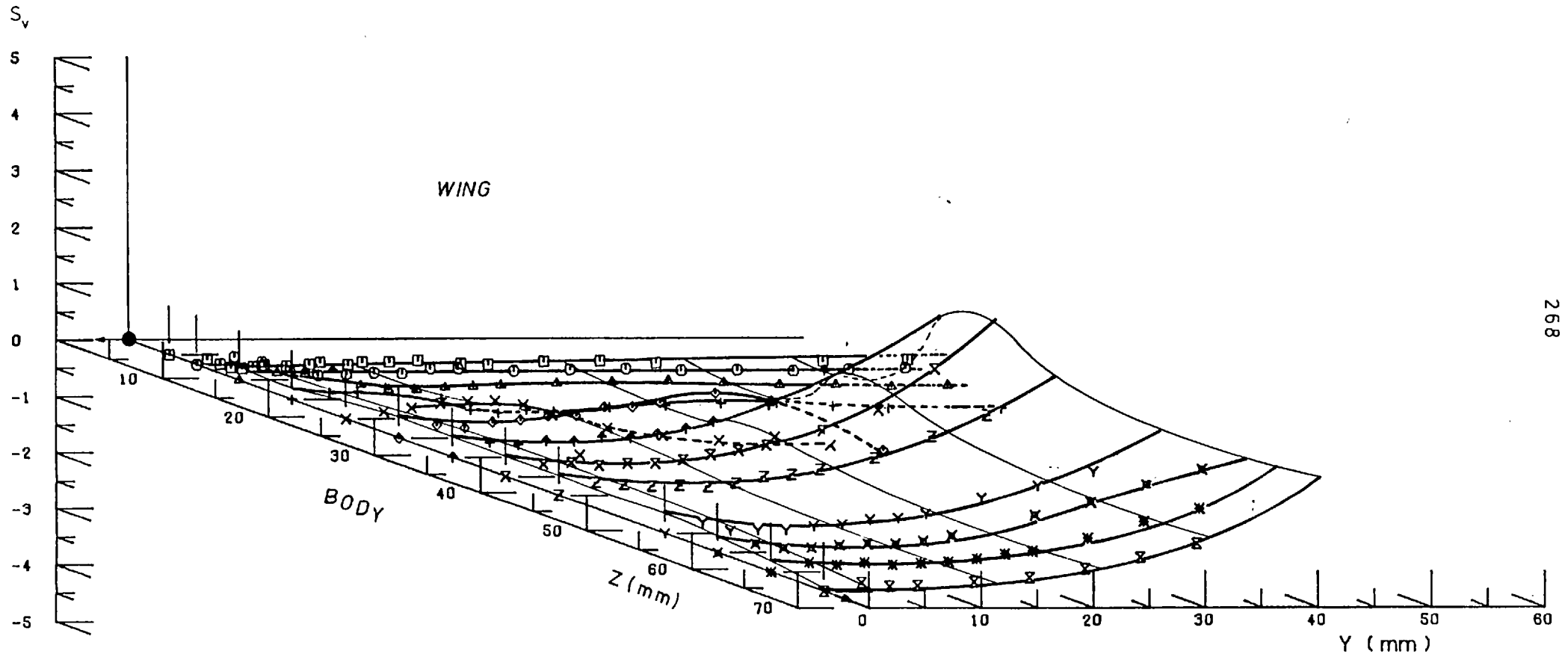

FIG.(4.55) v-COMPONENT SKEWNESS FACTOR (S_v) AT STATION 9 (X=1223.4mm)
Results of Cross Wire in Vertical (U-V) Position

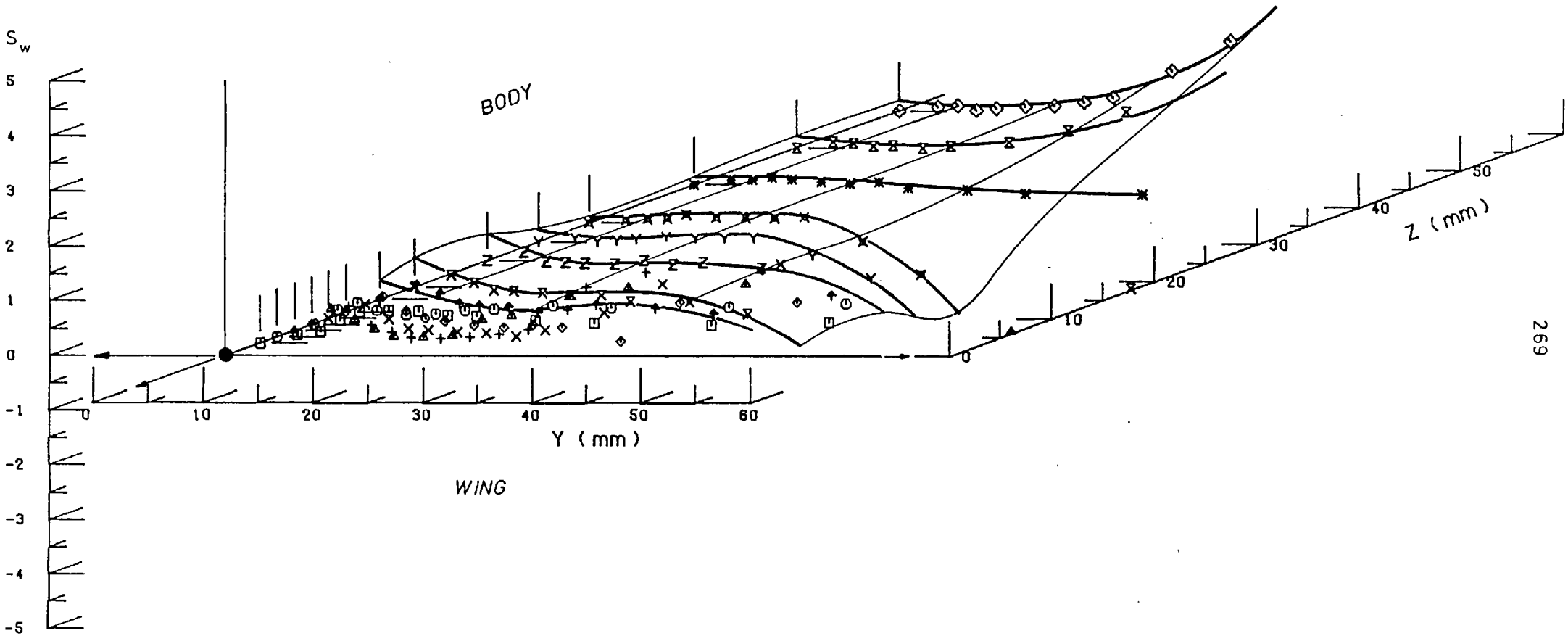

FIG.(4.56) w-COMPONENT SKEWNESS FACTOR (S_w) AT STATION 2 (X= 156.6mm)

Results of Cross Wire In Horizontal (U-W) Position

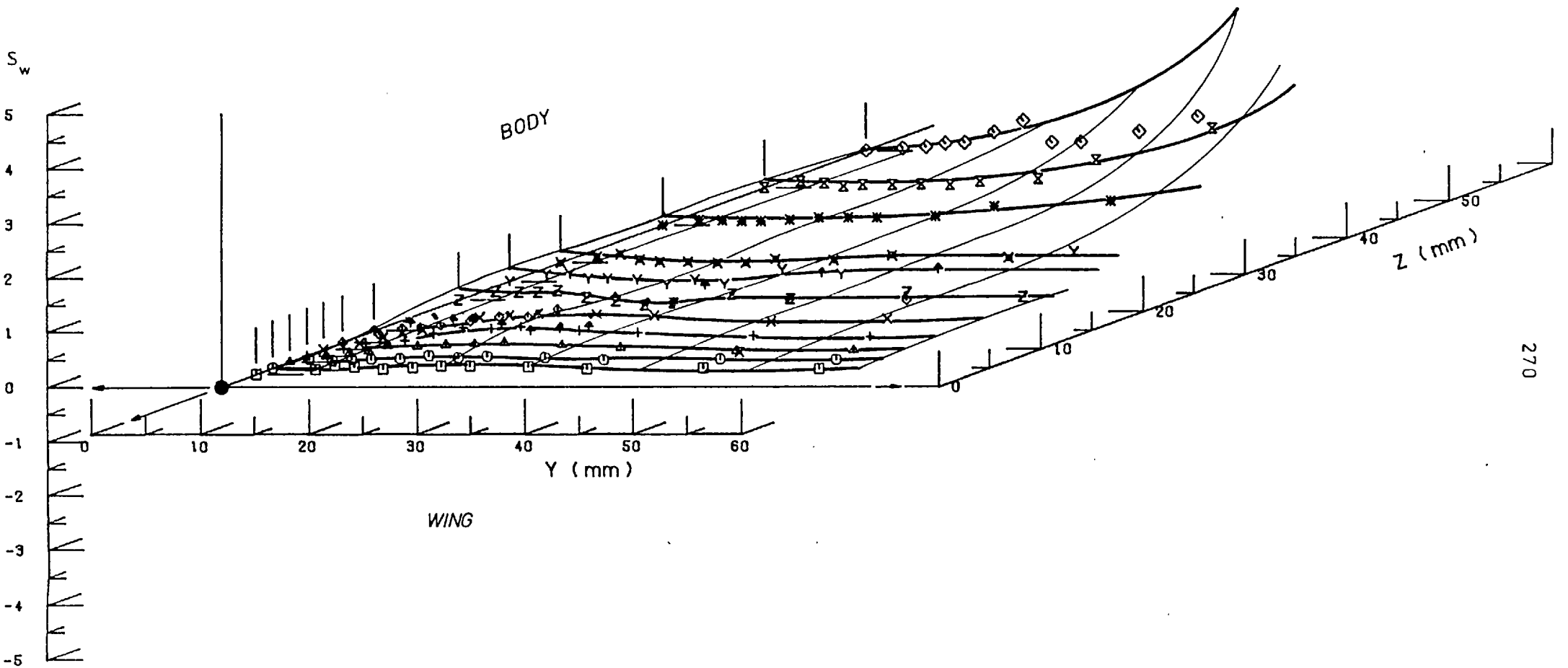

FIG.(4.57) w-COMPONENT SKEWNESS FACTOR (S_w) AT STATION 5 (X= 613.8mm)

Results of Cross Wire in Horizontal (U-W) Position

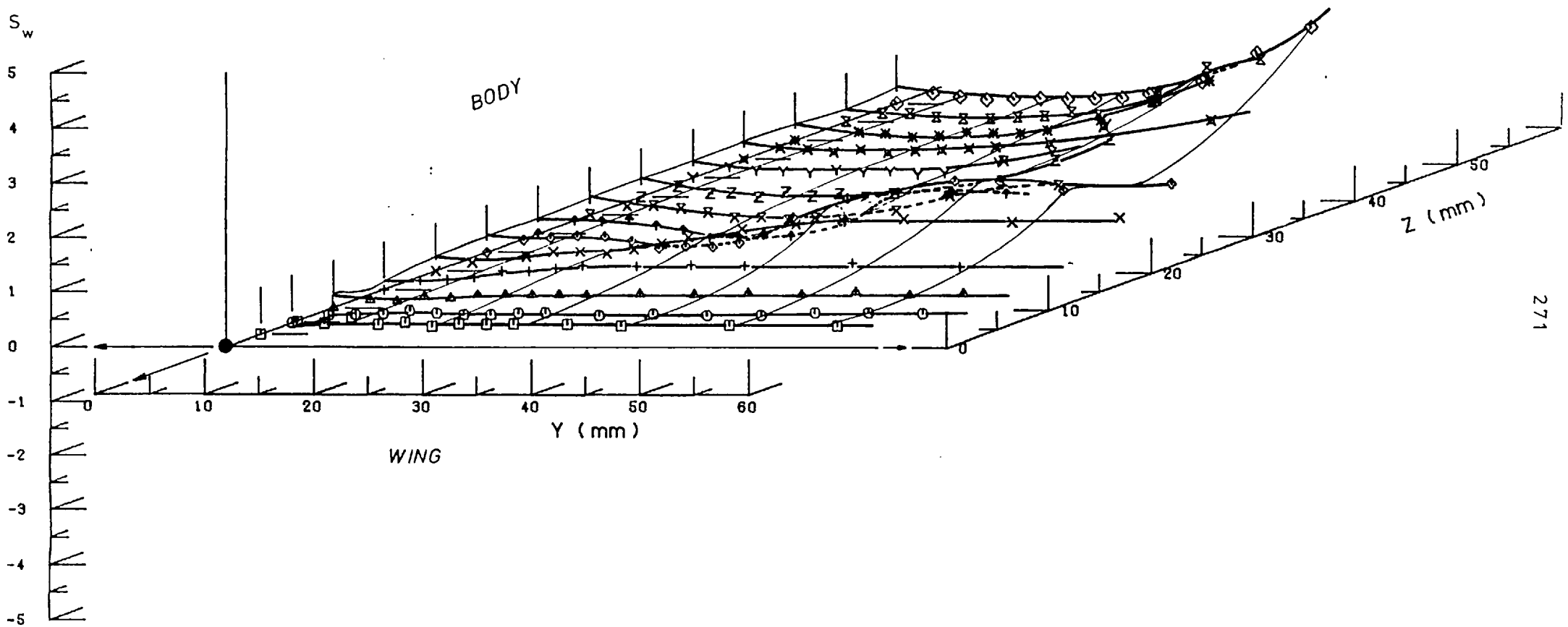

FIG.(4.58) w-COMPONENT SKEWNESS FACTOR (S_w) AT STATION 9 (X=1223.4mm)

Results of Cross Wire in Horizontal (U-W) Position

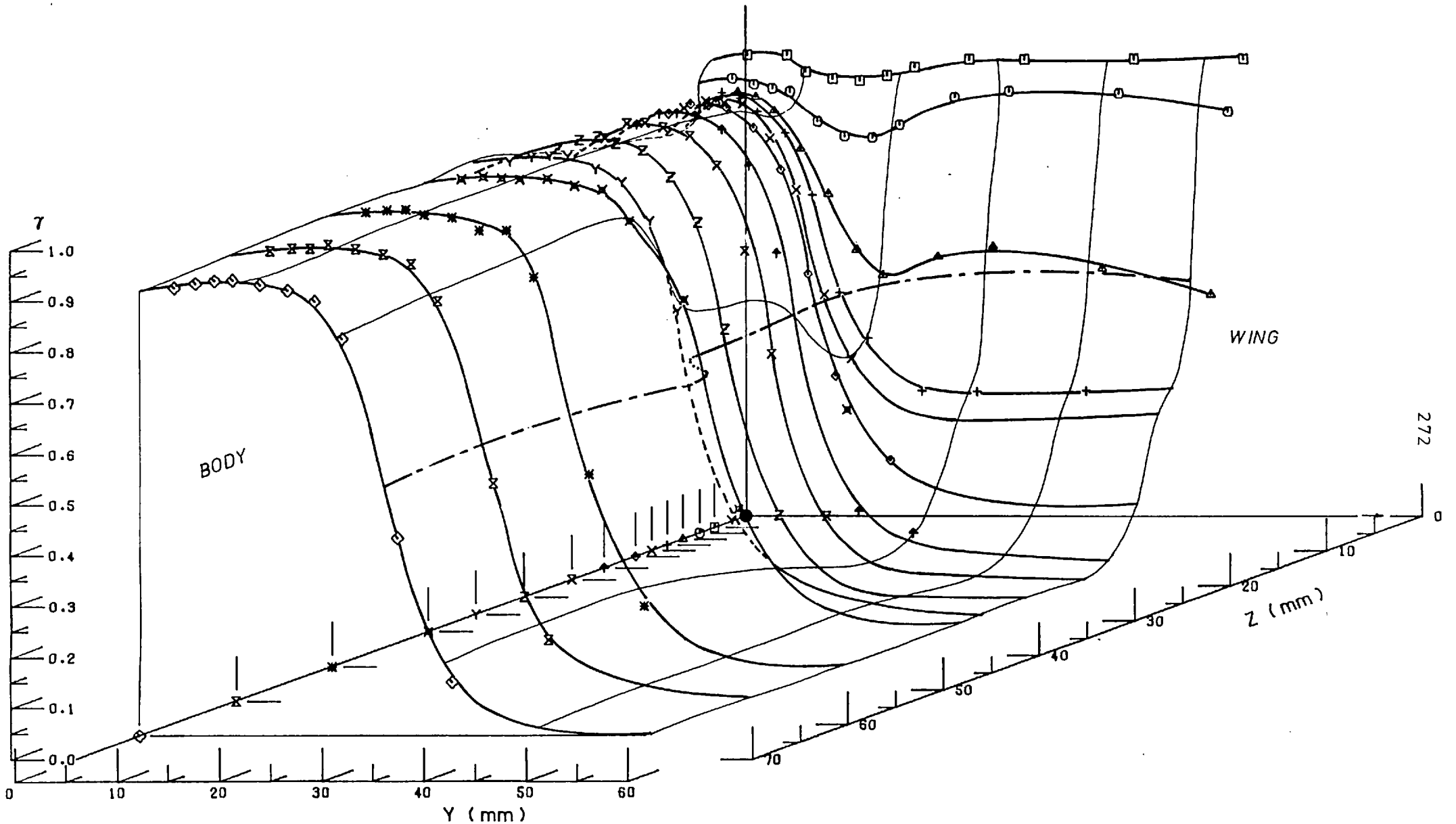

FIG.(4 . 59) INTERMITTENCY FACTOR γ AT STATION 2 (X= 156.6mm) (DIG2U Output)

Results of Cross Wire in Vertical (U-V) Position

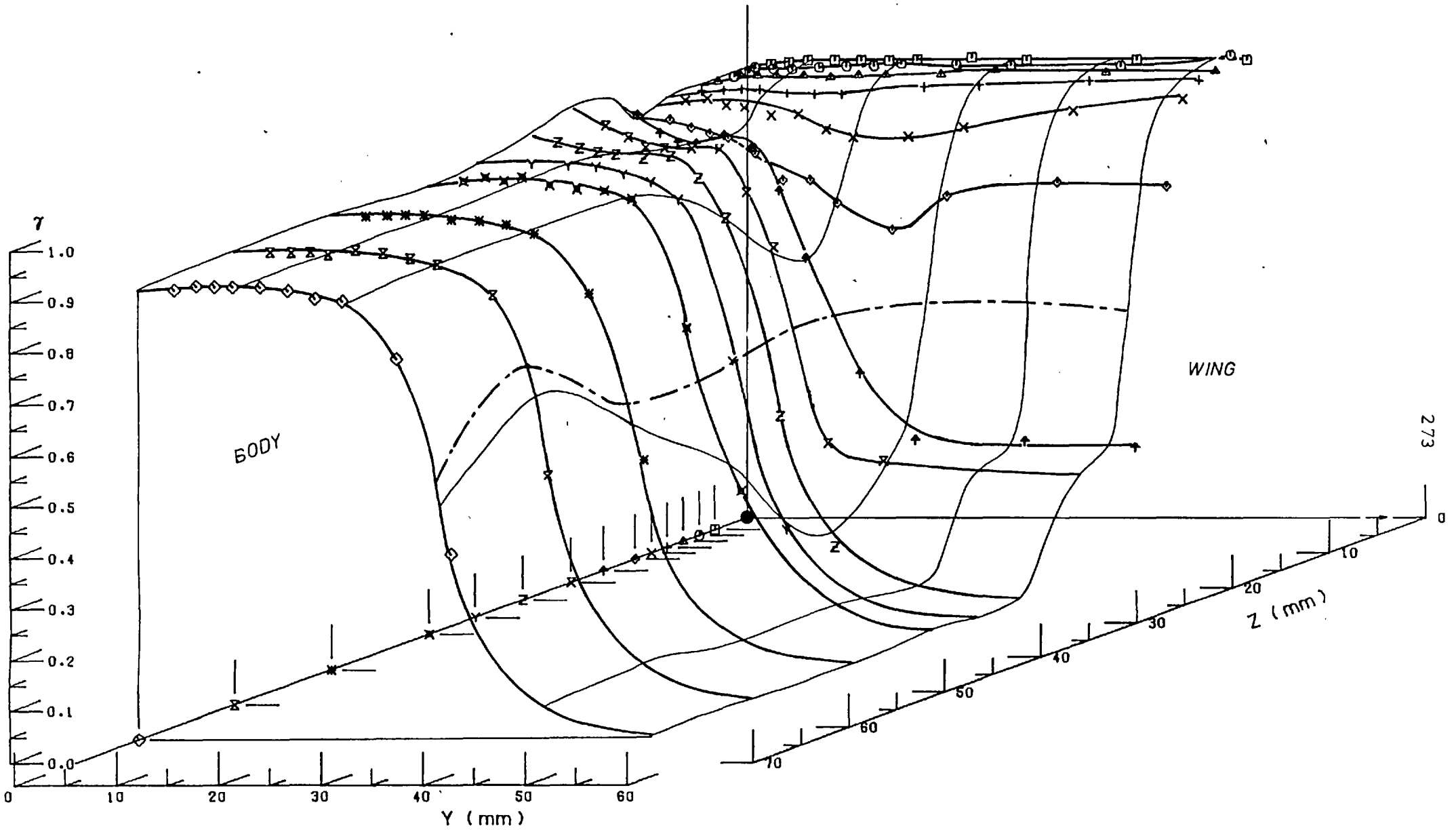

FIG.(4 . 60) INTERMITTENCY FACTOR γ AT STATION 5 (X= 613.8mm) (DIG2U Output)

Results of Cross Wire in Vertical (U-V) Position

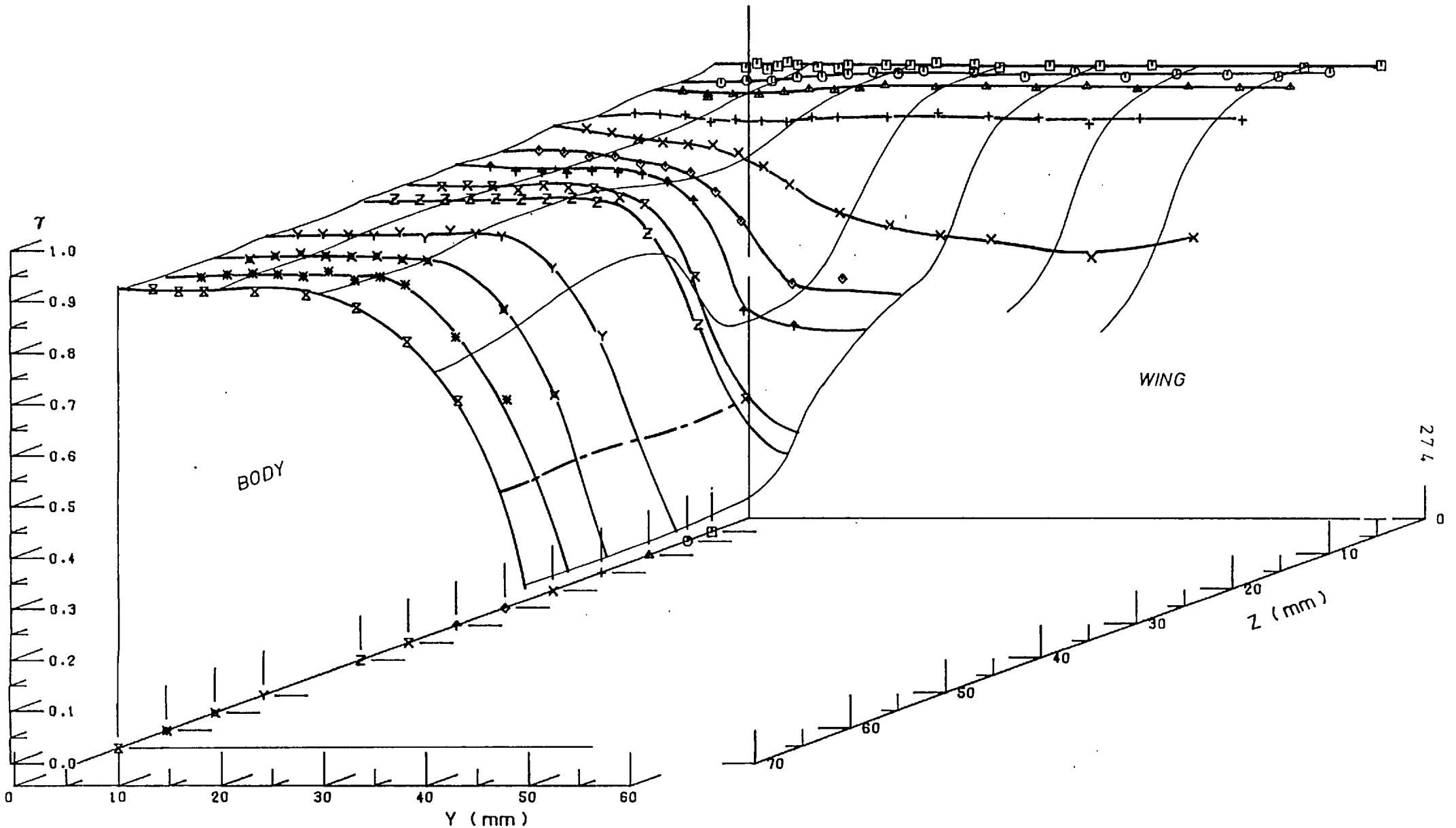

FIG.(4.61) INTERMITTENCY FACTOR γ AT STATION 9 (X=1223.4mm) (DIG2U Output)

Results of Cross Wire in Vertical (U-V) Position

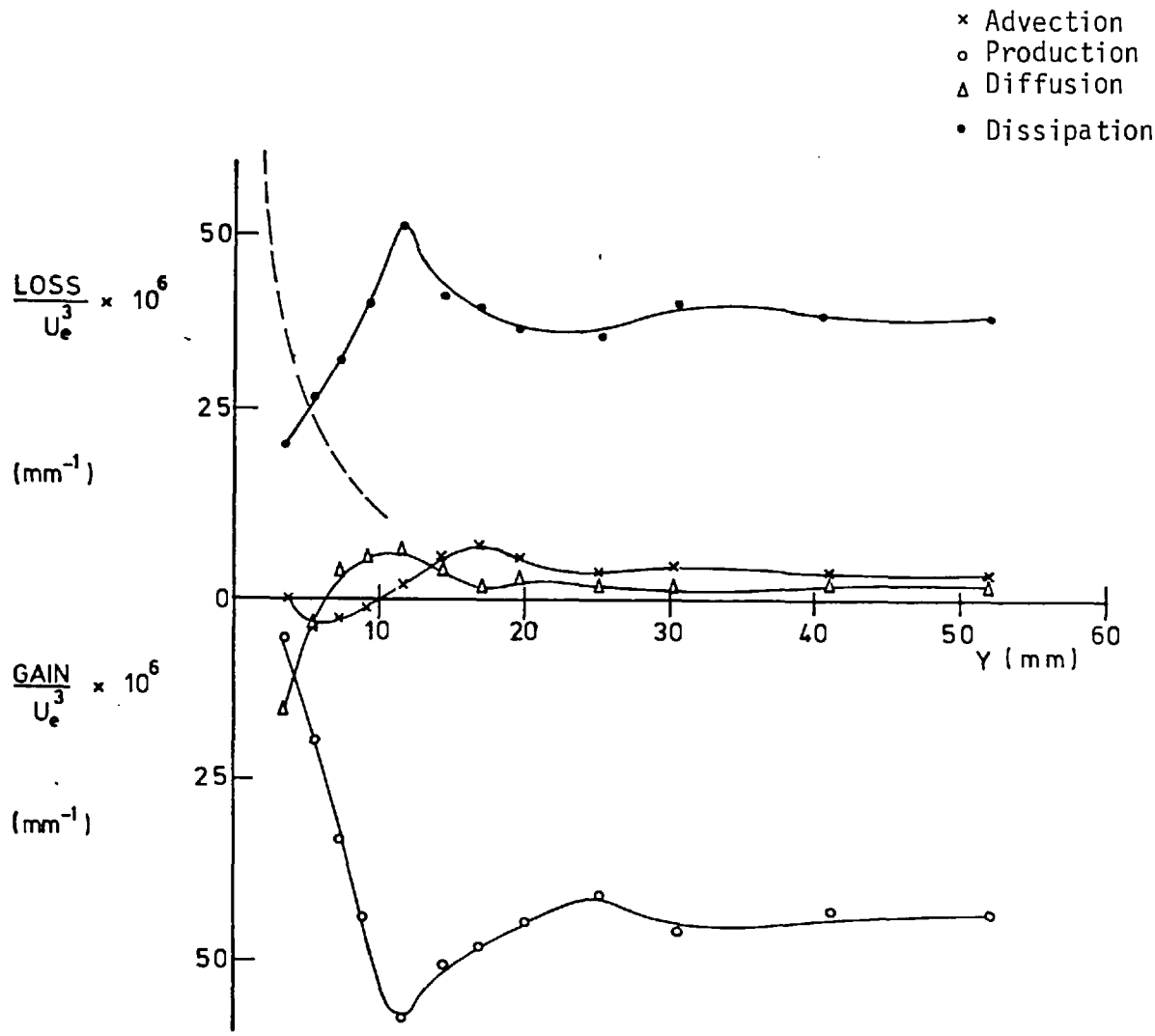

FIG.(4.62) TURBULENT KINETIC ENERGY BALANCE AT Z = 5.03 mm

STATION 5 (X = 613.8 mm)

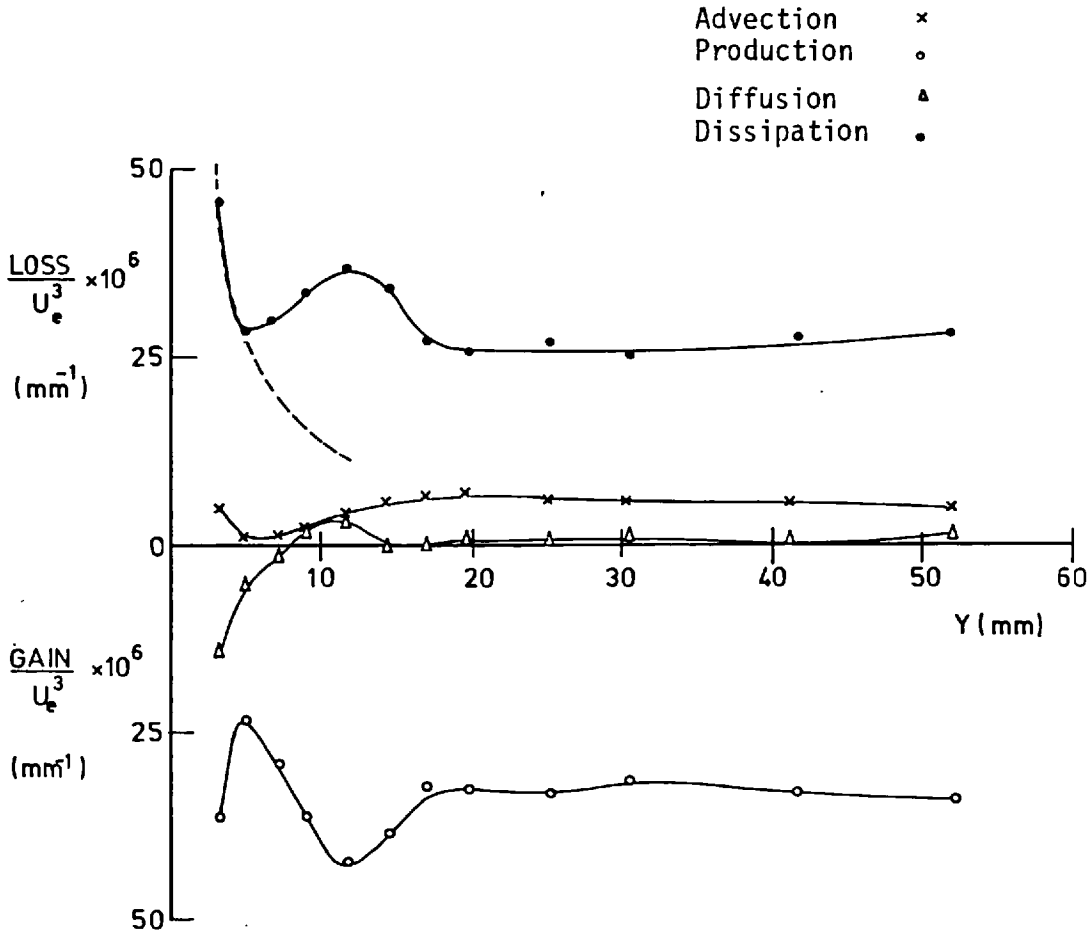

FIG.(4.63) TURBULENT ENERGY BALANCE AT Z = 7.03 mm

STATION 5 (X = 613.8 mm)

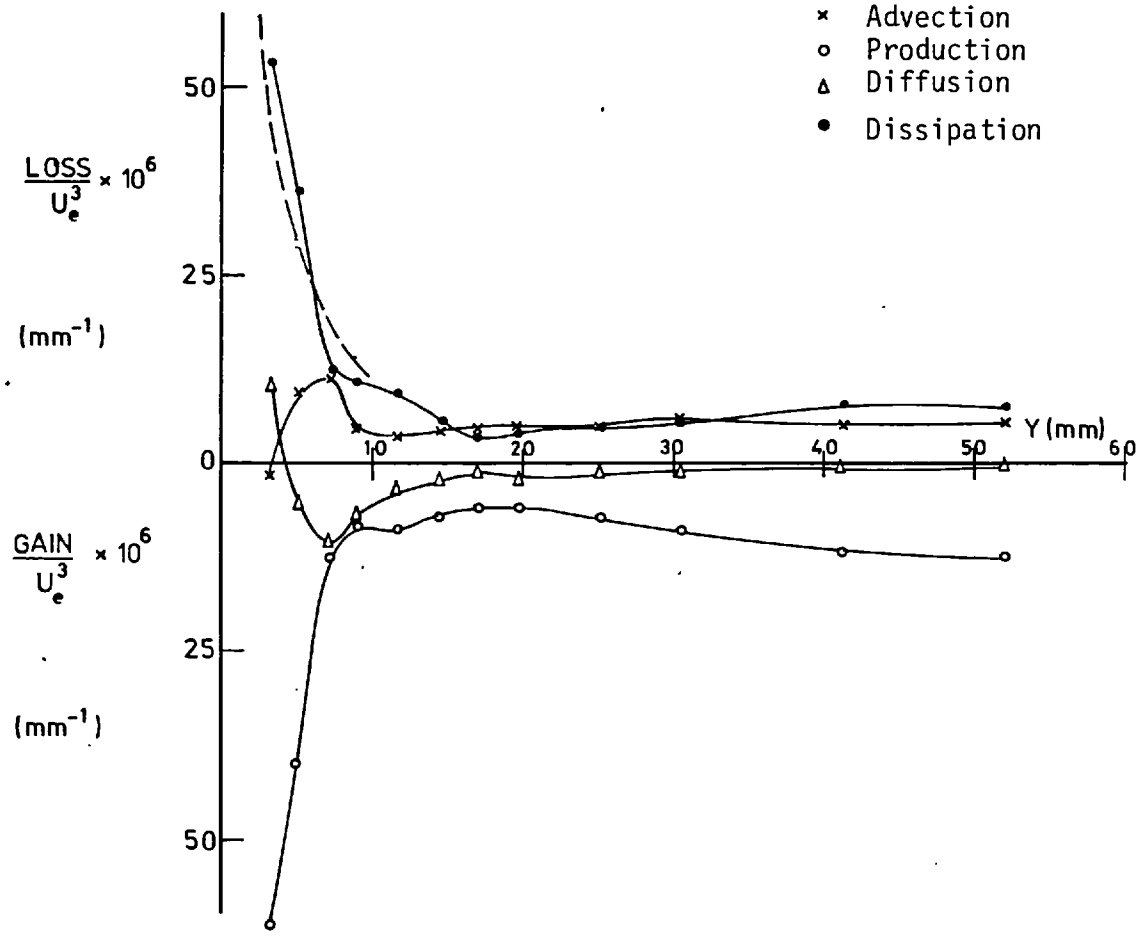

FIG.(4.64) TURBULENT KINETIC ENERGY BALANCE AT Z = 10.03 mm

STATION 5 (X = 613.8 mm)

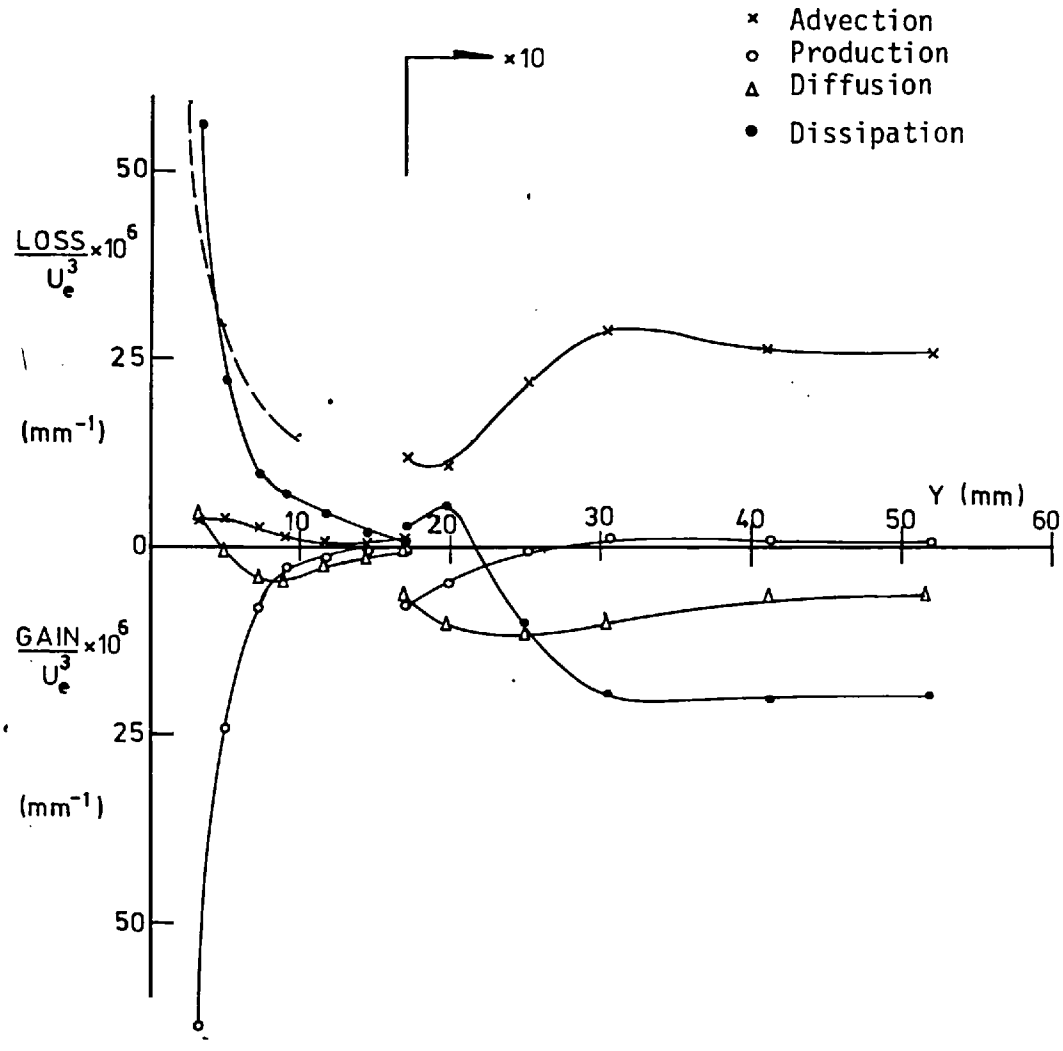

FIG.(4.65) TURBULENT KINETIC ENERGY BALANCE AT Z = 15.03 mm

STATION 5 (X = 613.8 mm)

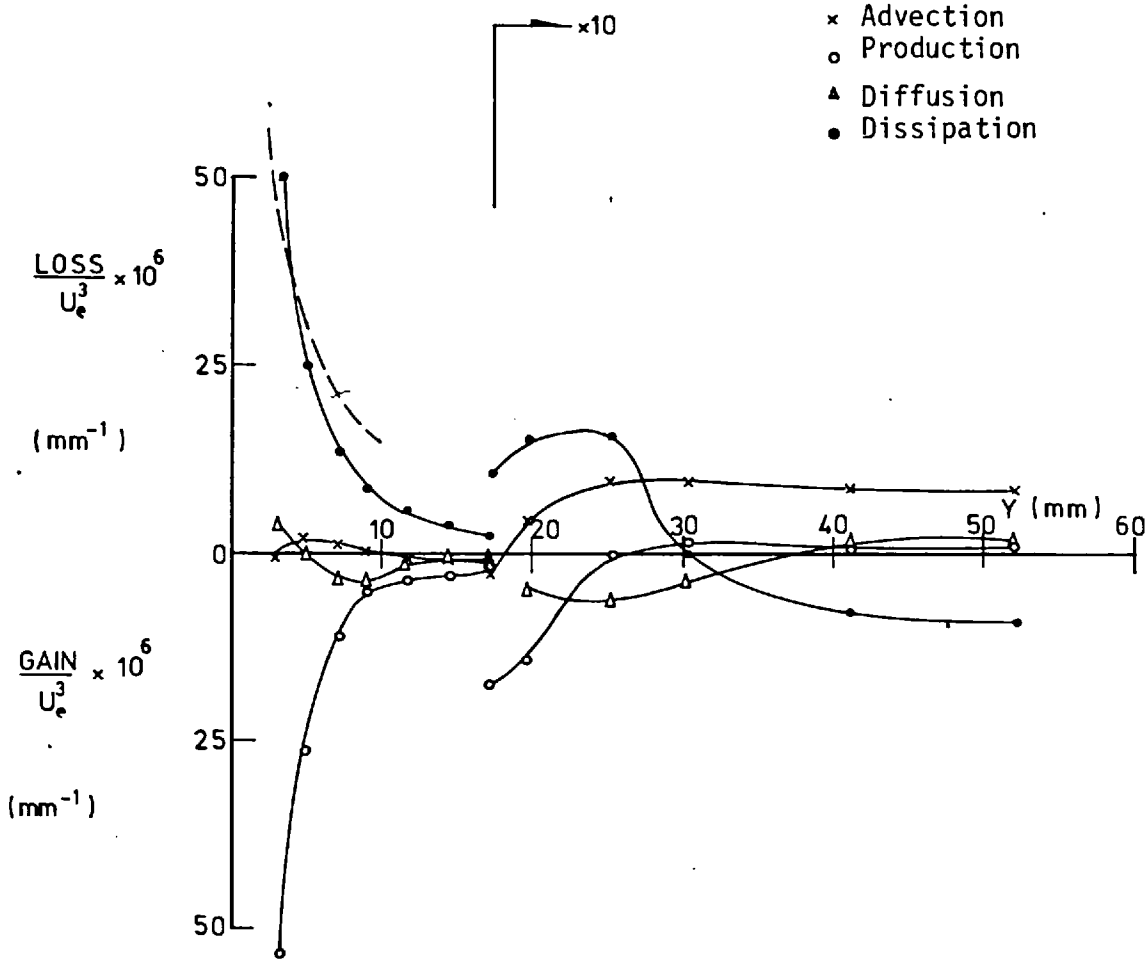

FIG.(4.66) TURBULENT KINETIC ENERGY BALANCE AT Z = 18.40 mm

STATION 5 (X = 613.8 mm)

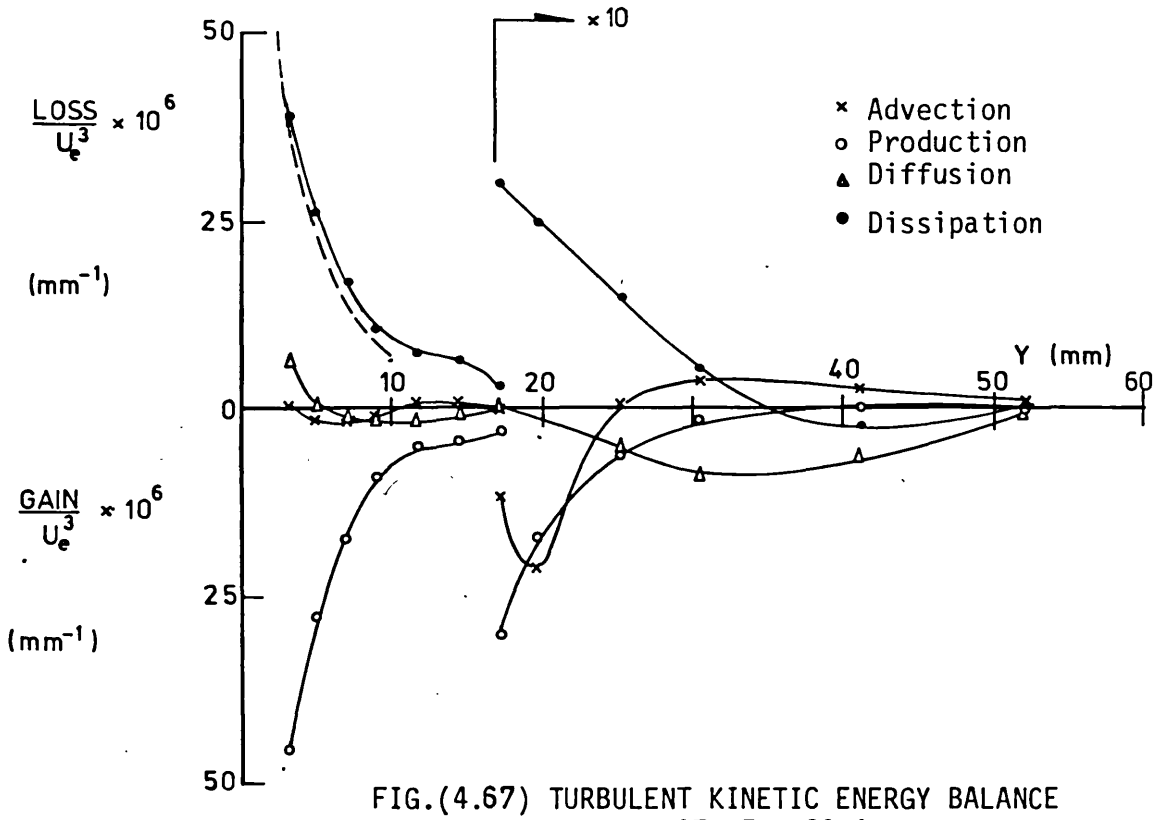

FIG.(4.67) TURBULENT KINETIC ENERGY BALANCE
AT Z = 23.4 mm

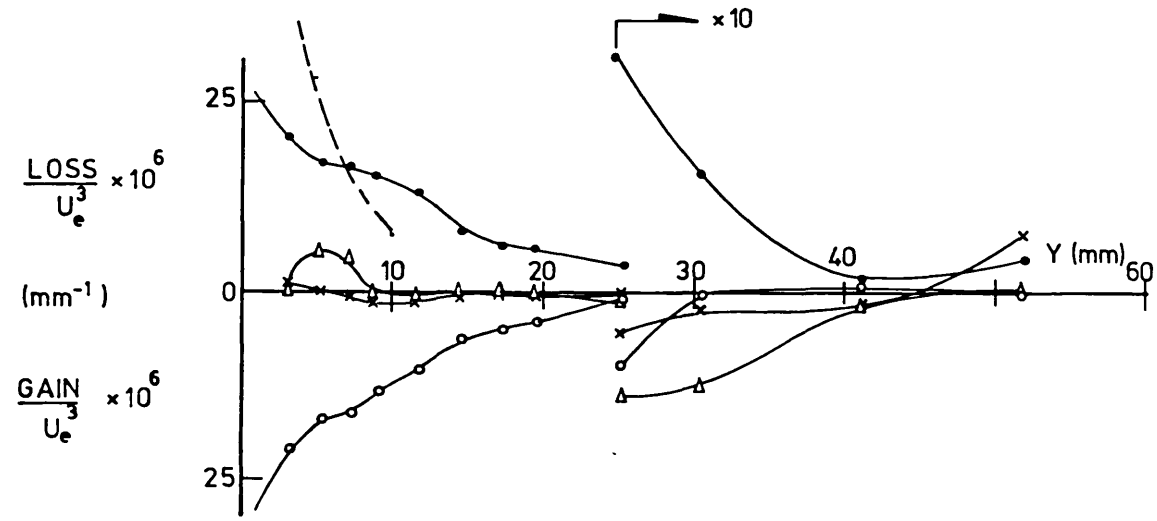

FIG.(4.68) TURBULENT KINETIC ENERGY BALANCE
AT Z = 28.4 mm

STATION 5 (X = 613.8 mm)

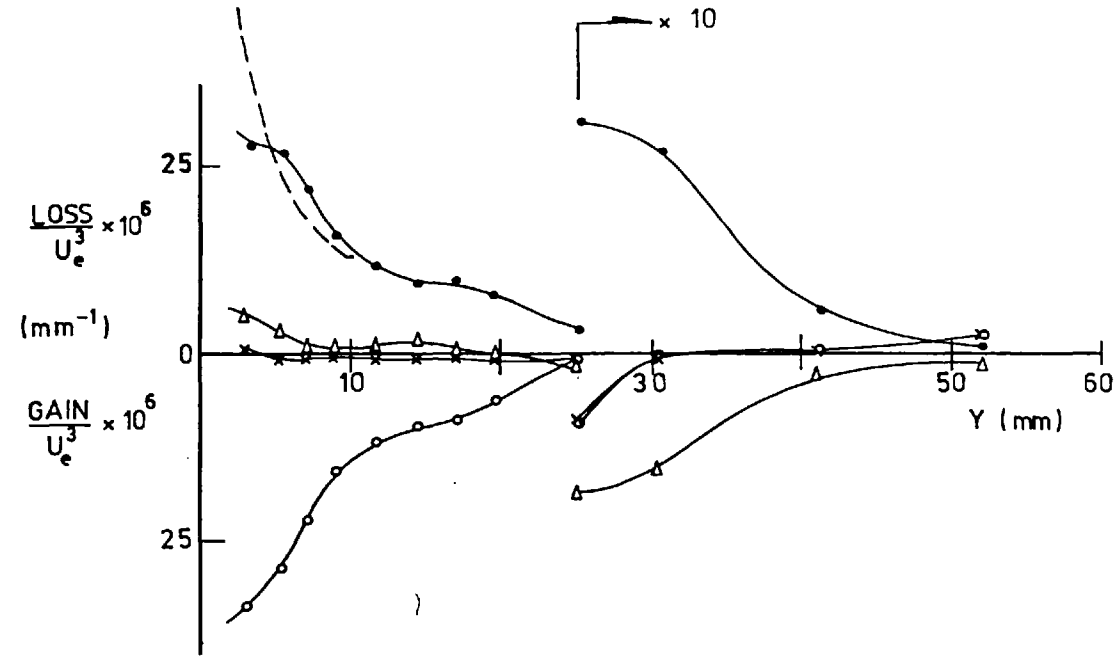

FIG.(4.69) TURBULENT ENERGY BALANCE AT Z = 33.17 mm

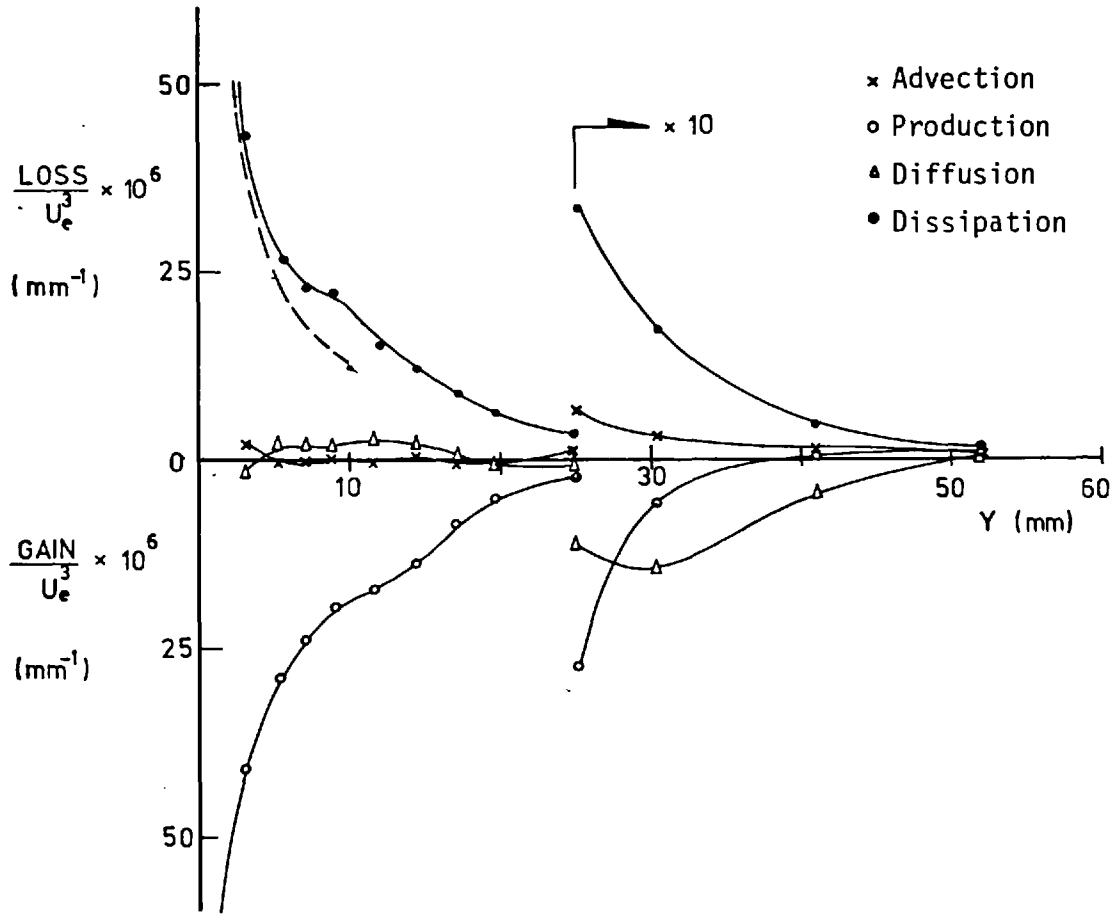

FIG.(4.70) TURBULENT ENERGY BALANCE AT Z = 43.4 mm

STATION 5 (X = 613.8 mm)

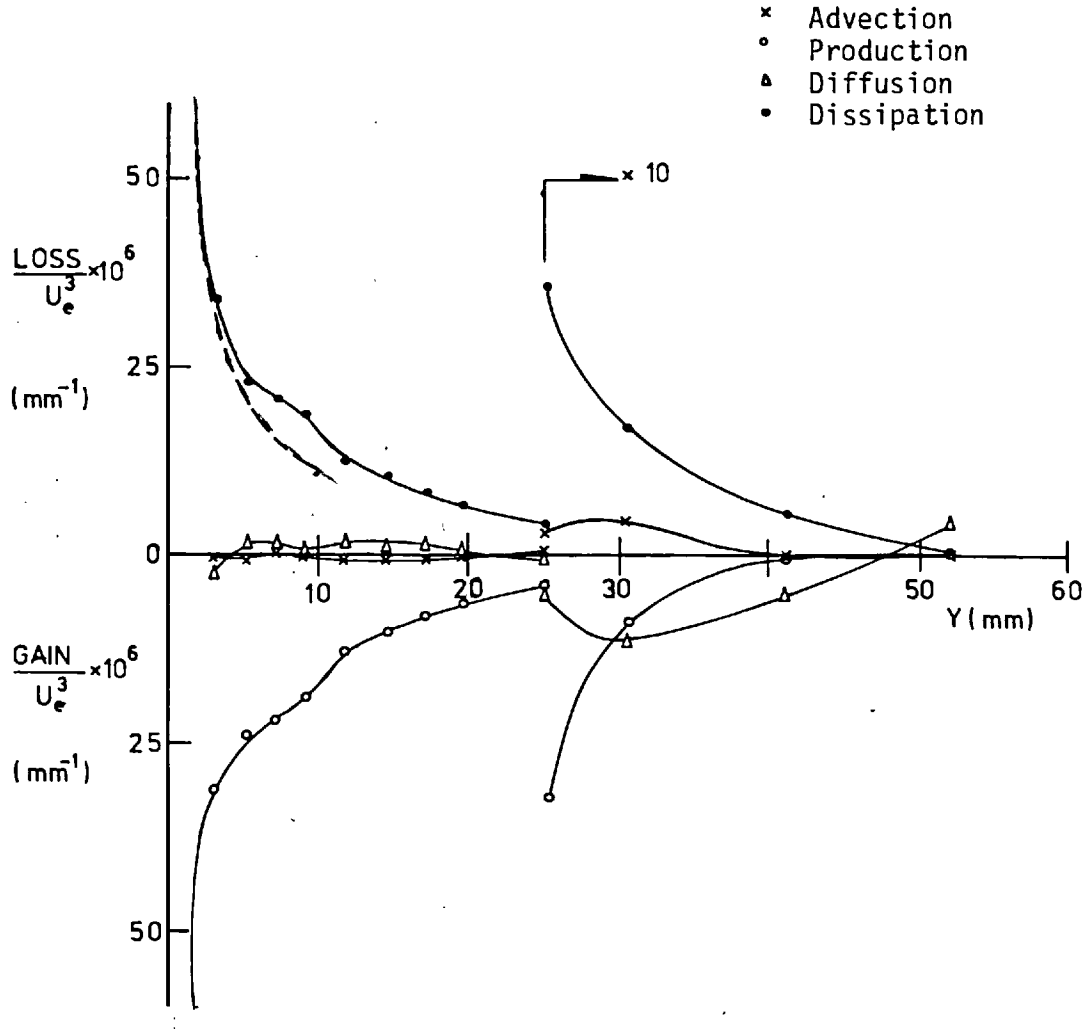

FIG.(4.71) TURBULENT ENERGY BALANCE AT Z = 53.4 mm

STATION 5 (X = 613.8 mm)

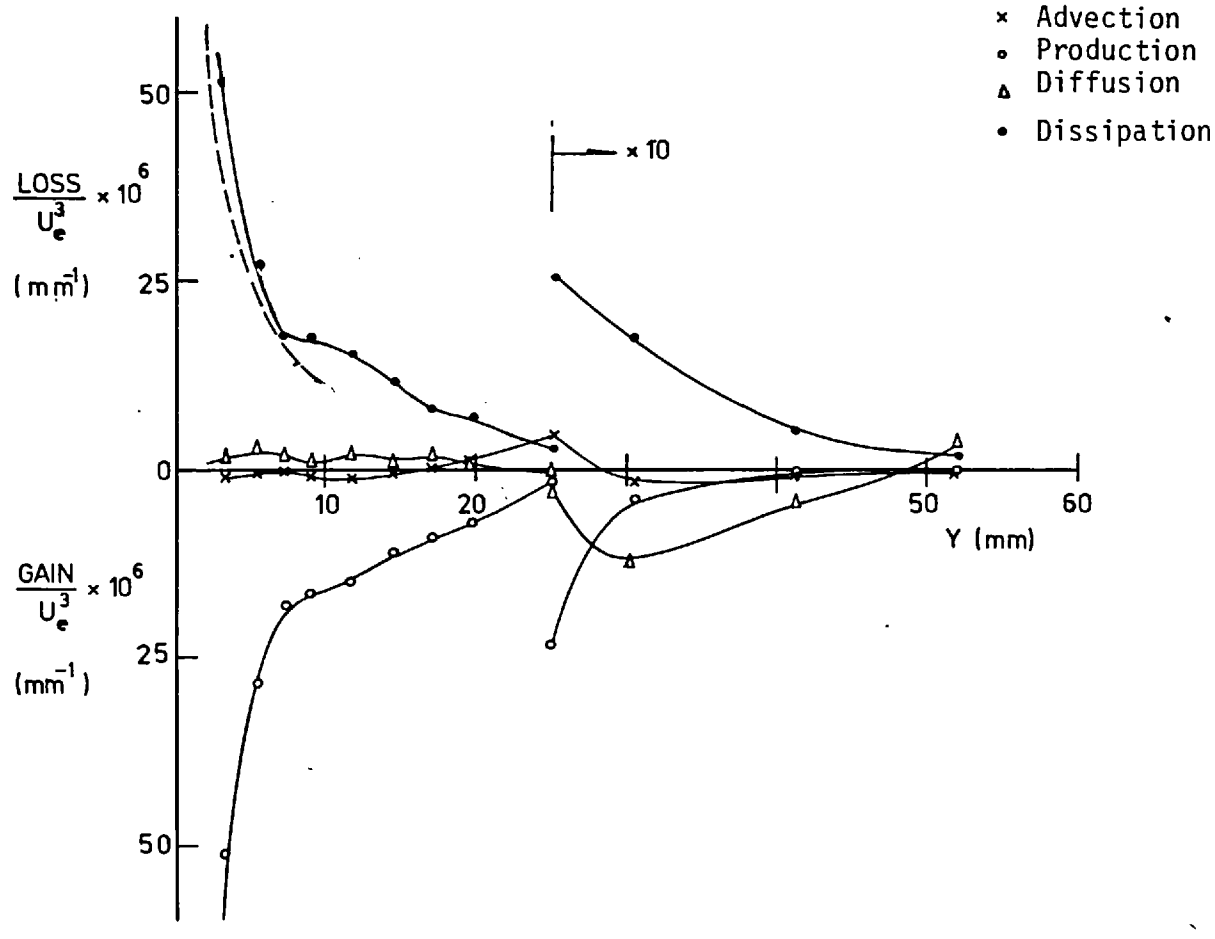

FIG.(4.72) TURBULENT ENERGY BALANCE AT Z = 63.4 mm

STATION 5 (X = 613.8 mm)

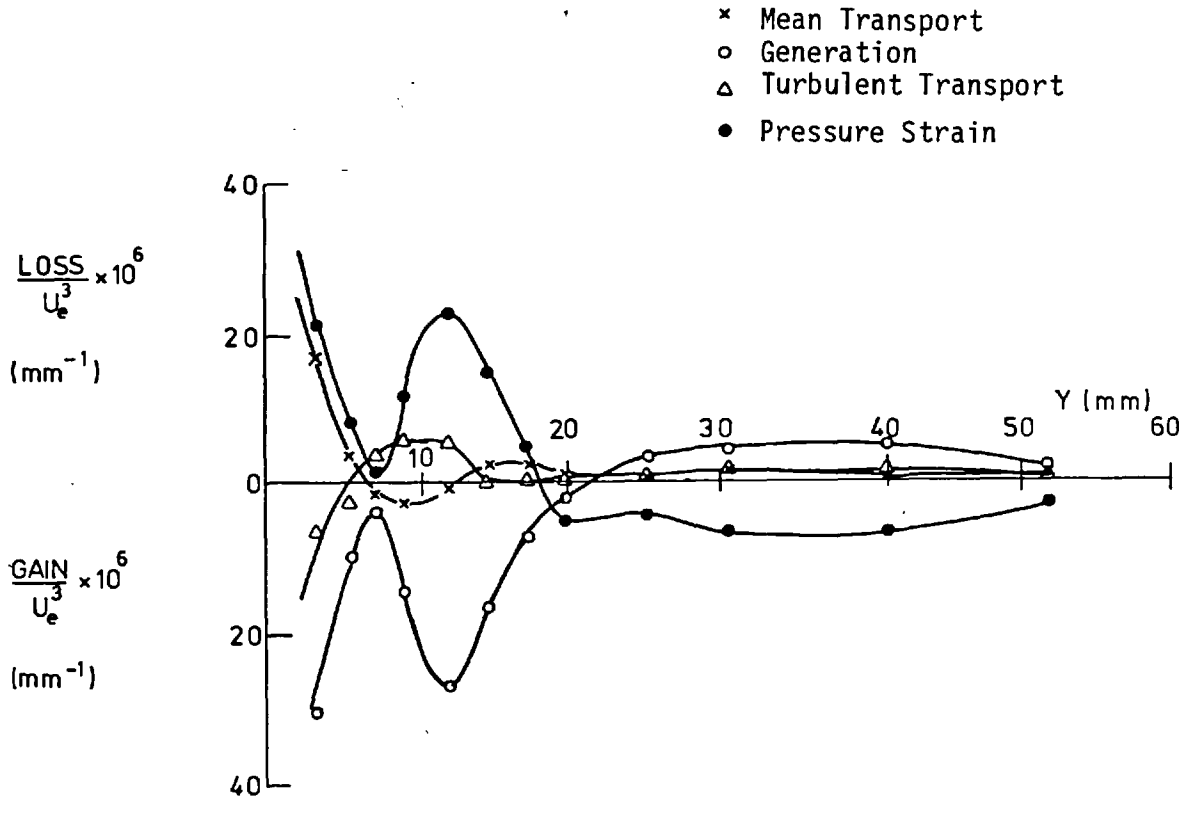

FIG.(4.73) $-\overline{uv}$ BALANCE AT Z = 5.03 mm

STATION 5 (X = 613.8 mm)

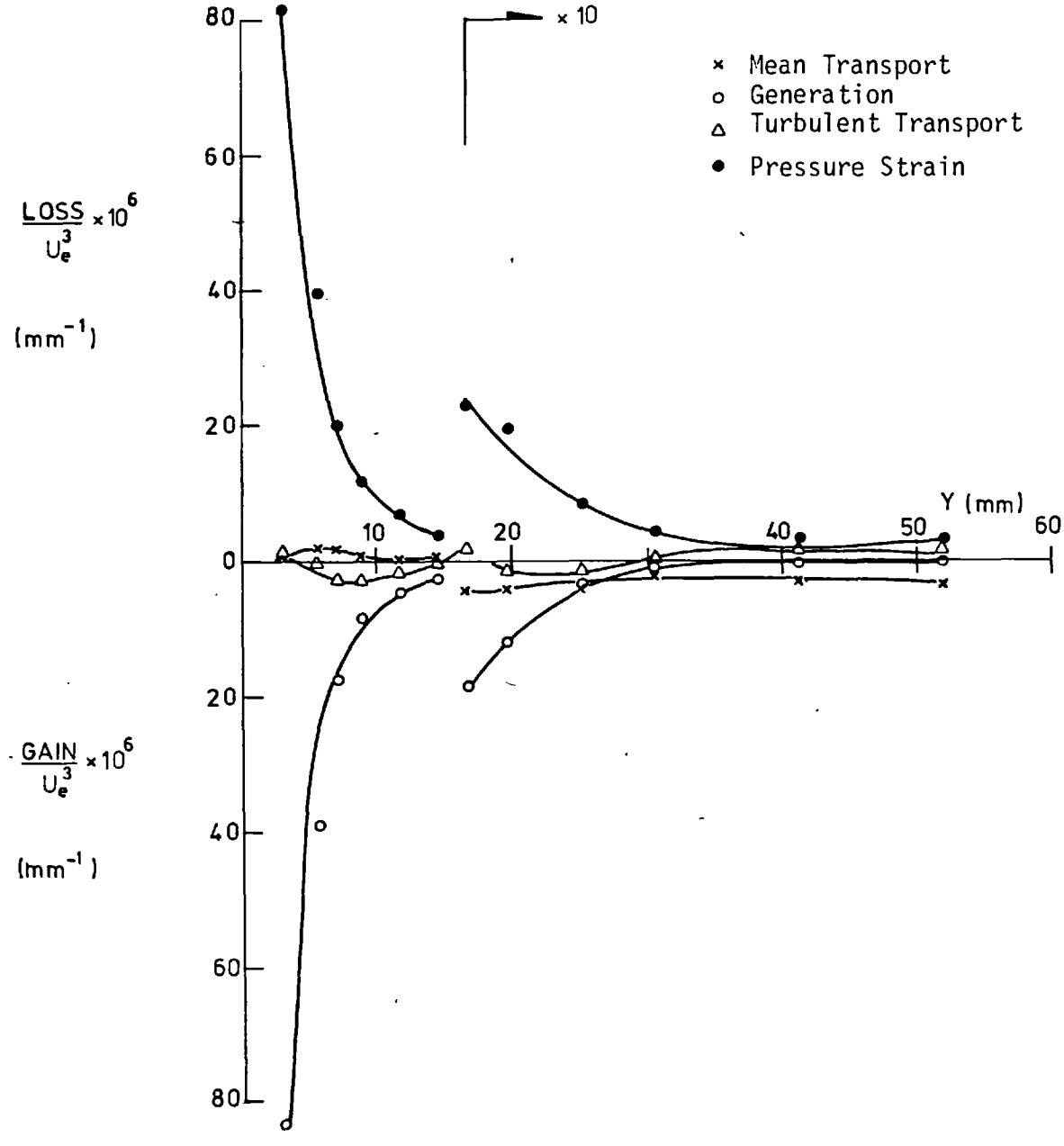

FIG.(4.74) $-\overline{uv}$ BALANCE AT Z = 15.03 mm

STATION 5 (X = 613.8 mm)

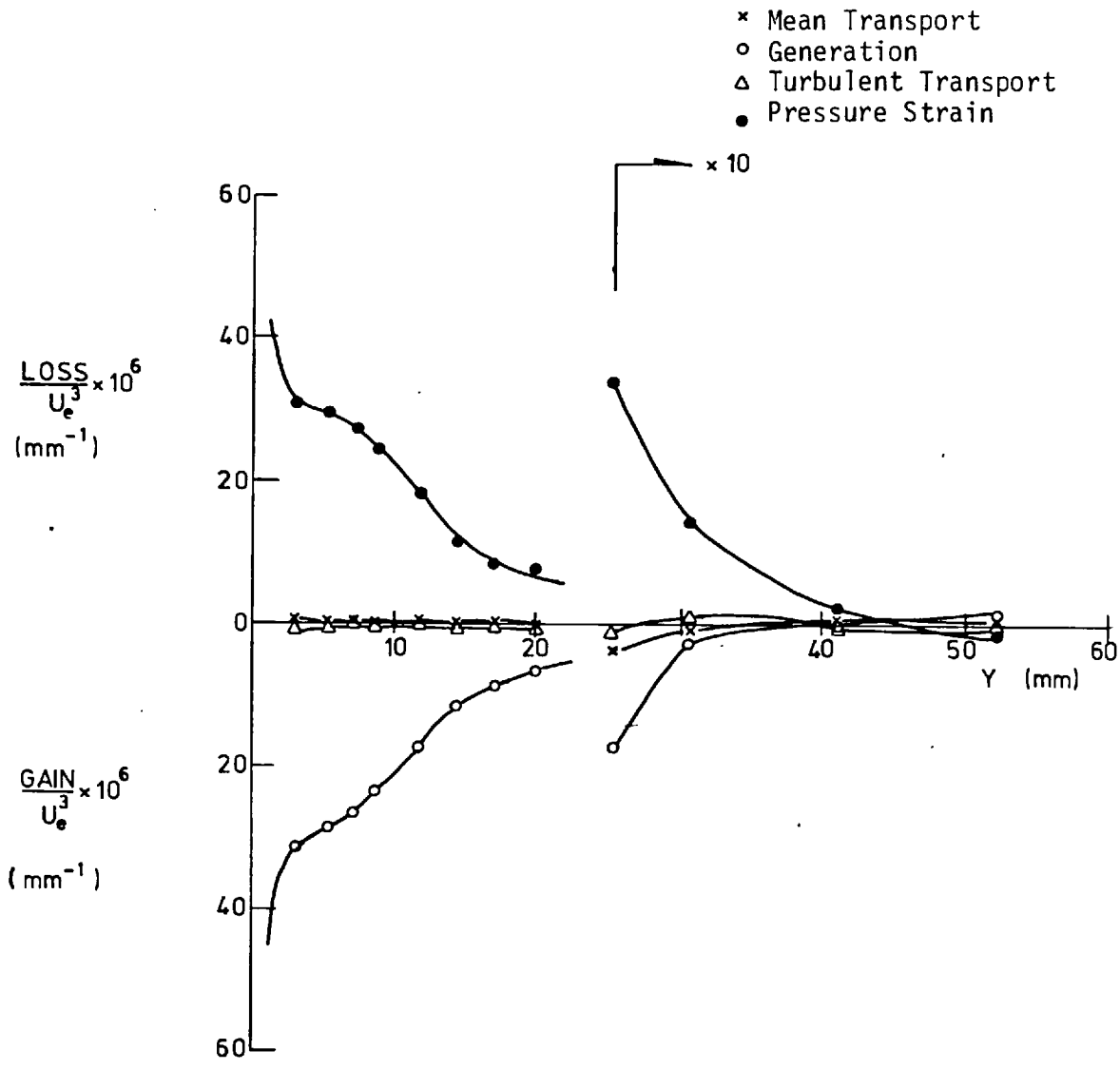

FIG.(4.75) $-\overline{uv}$ BALANCE AT Z = 28.4 mm

STATION 5 (X = 613.8 mm)

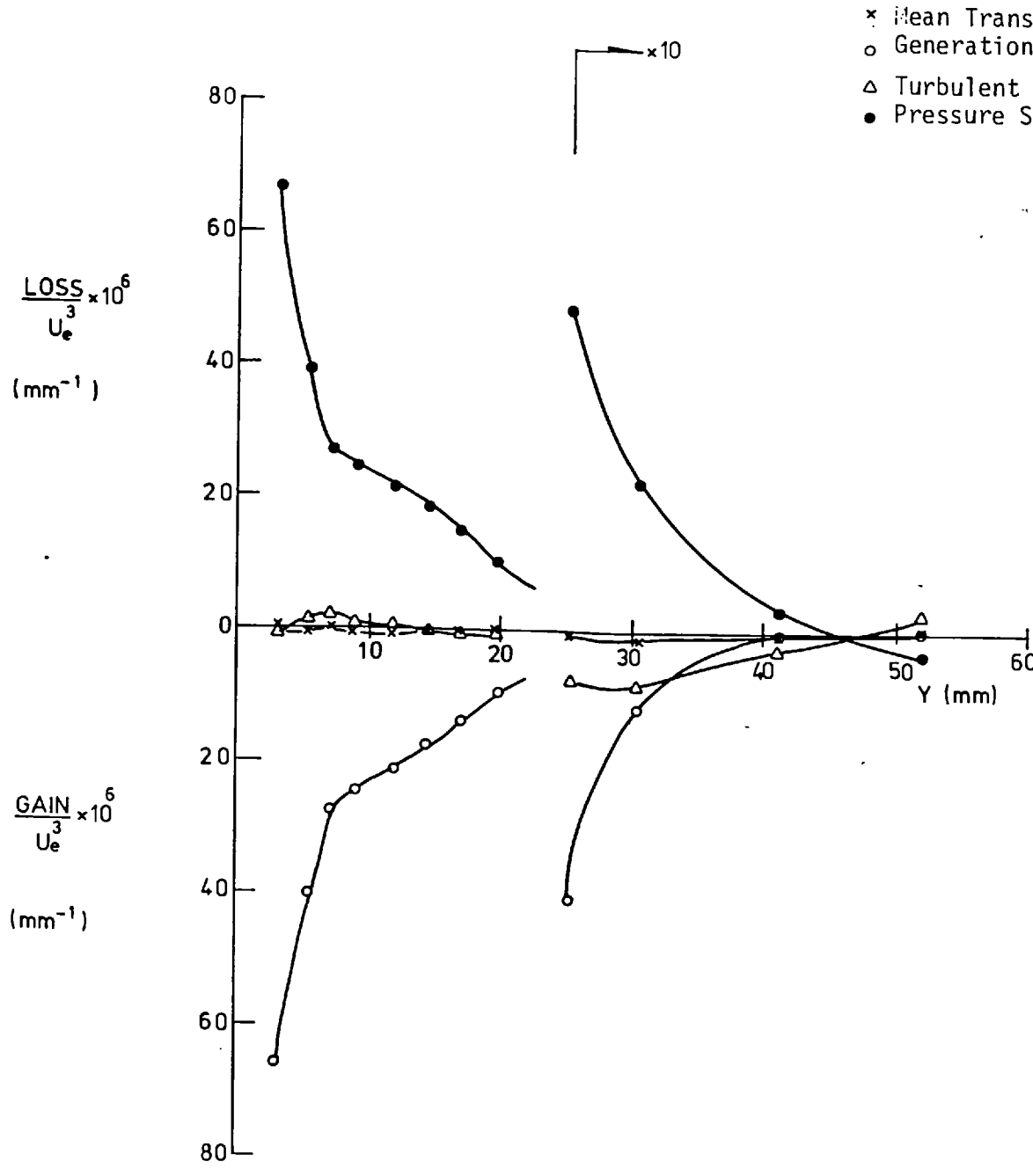

FIG.(4.76) $-\overline{uv}$ BALANCE AT Z = 63.4 mm

STATION 5 (X = 613.8 mm)

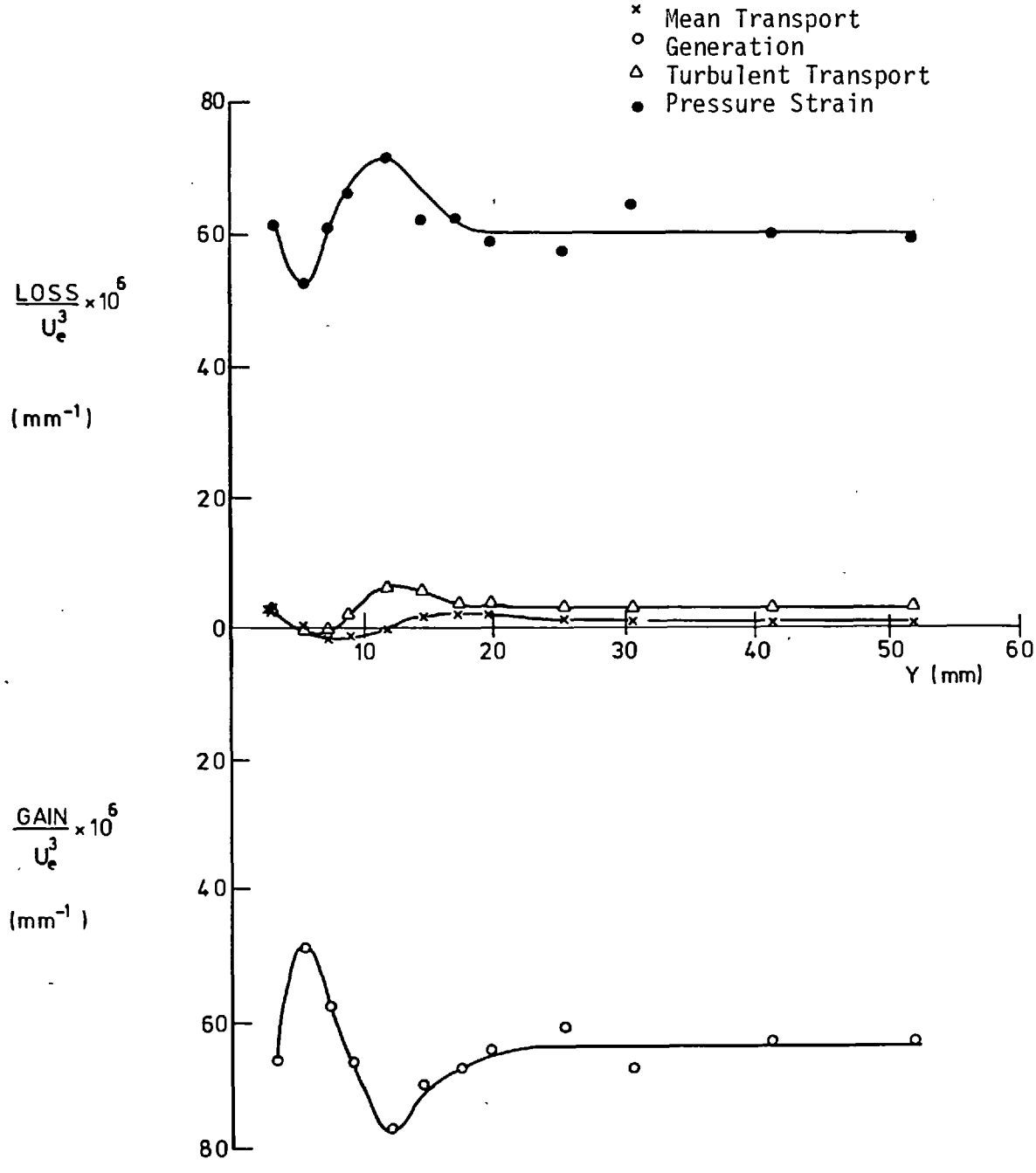

FIG.(4.77) $-\overline{uw}$ BALANCE AT Z = 5.03 mm

STATION 5 (X = 613.8 mm)

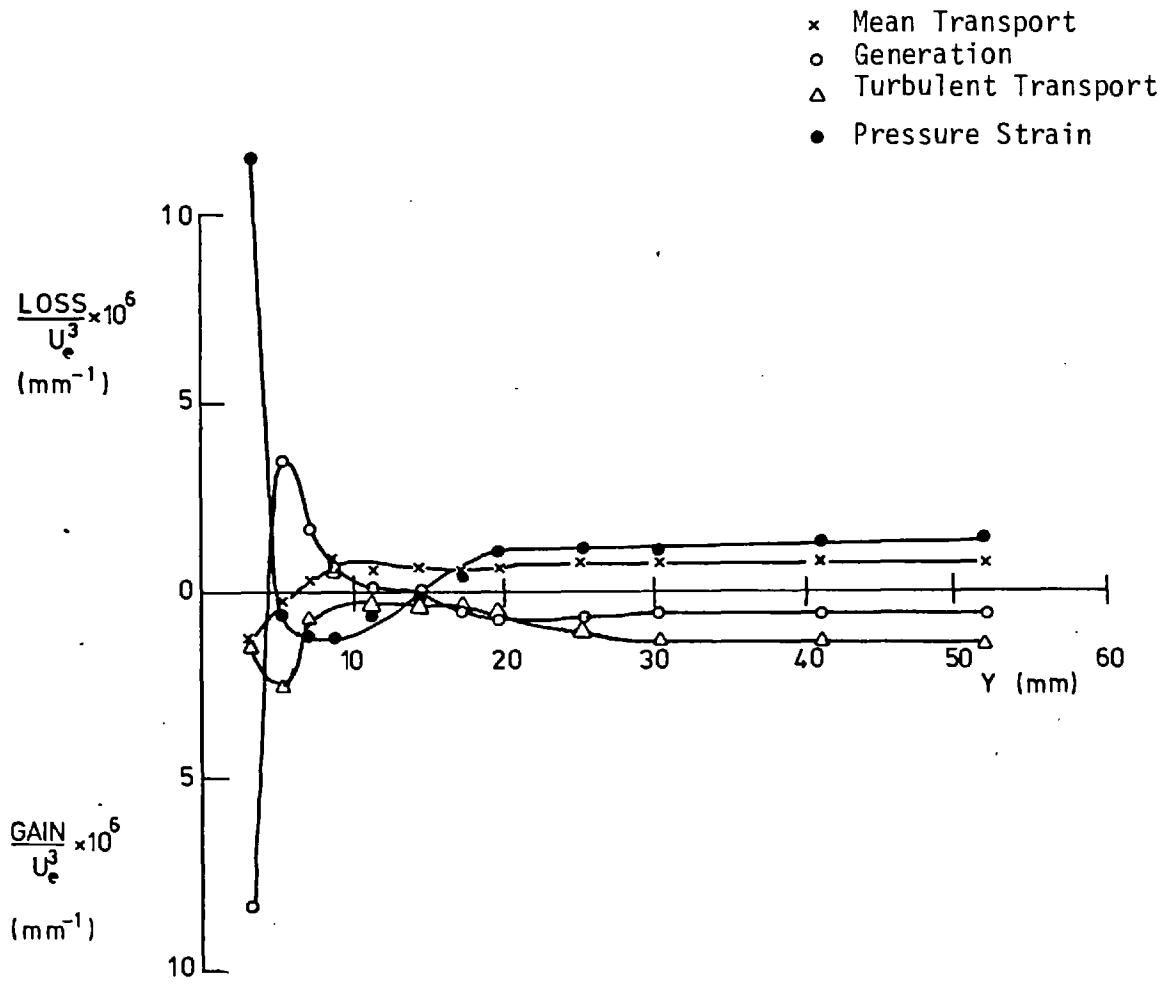

FIG.(4.78) $-\overline{uw}$ BALANCE AT Z = 15.03 mm

STATION 5 (X = 613.8 mm)

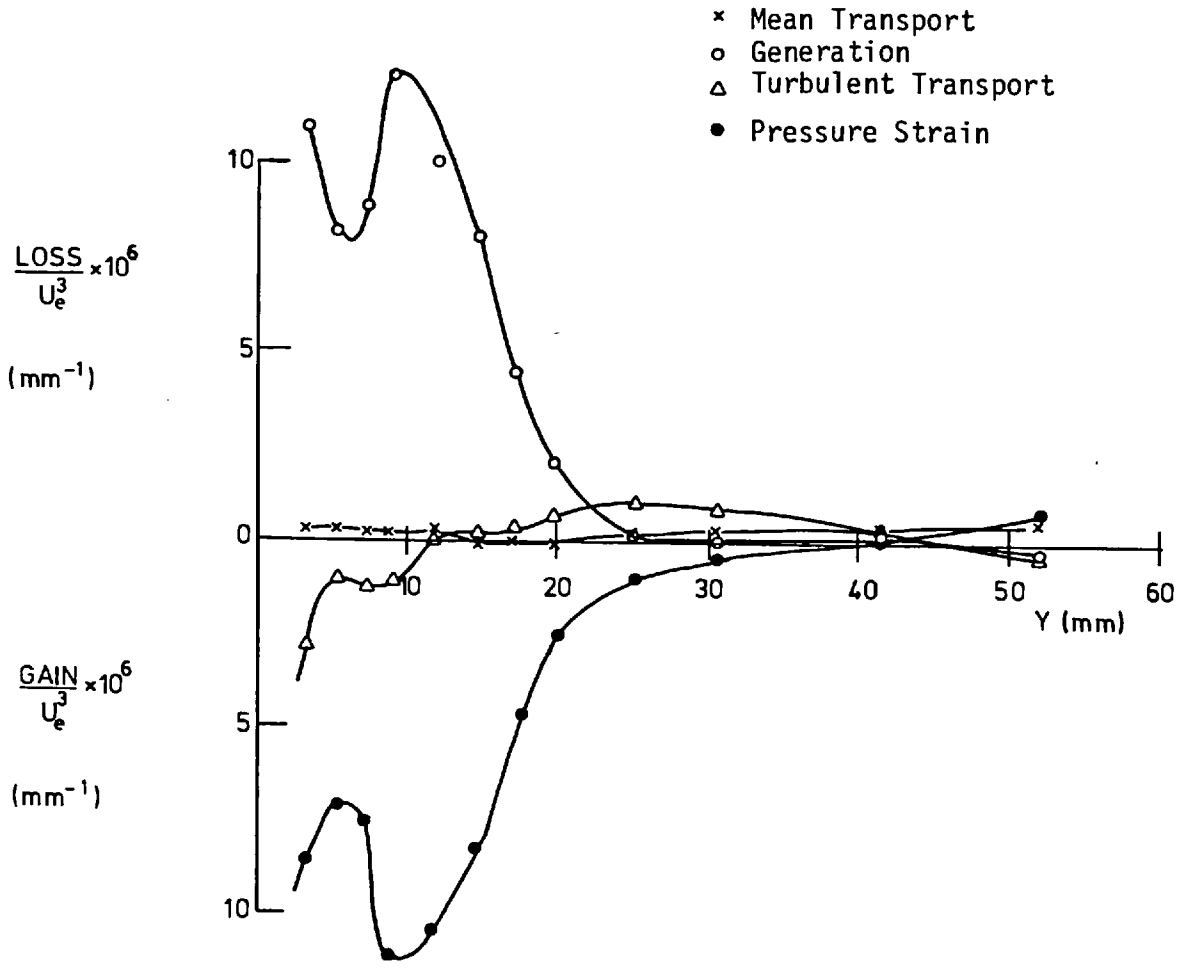

FIG.(4.79) $-\overline{uw}$ BALANCE AT Z = 28.40 mm

STATION 5 (X = 613.8 mm)

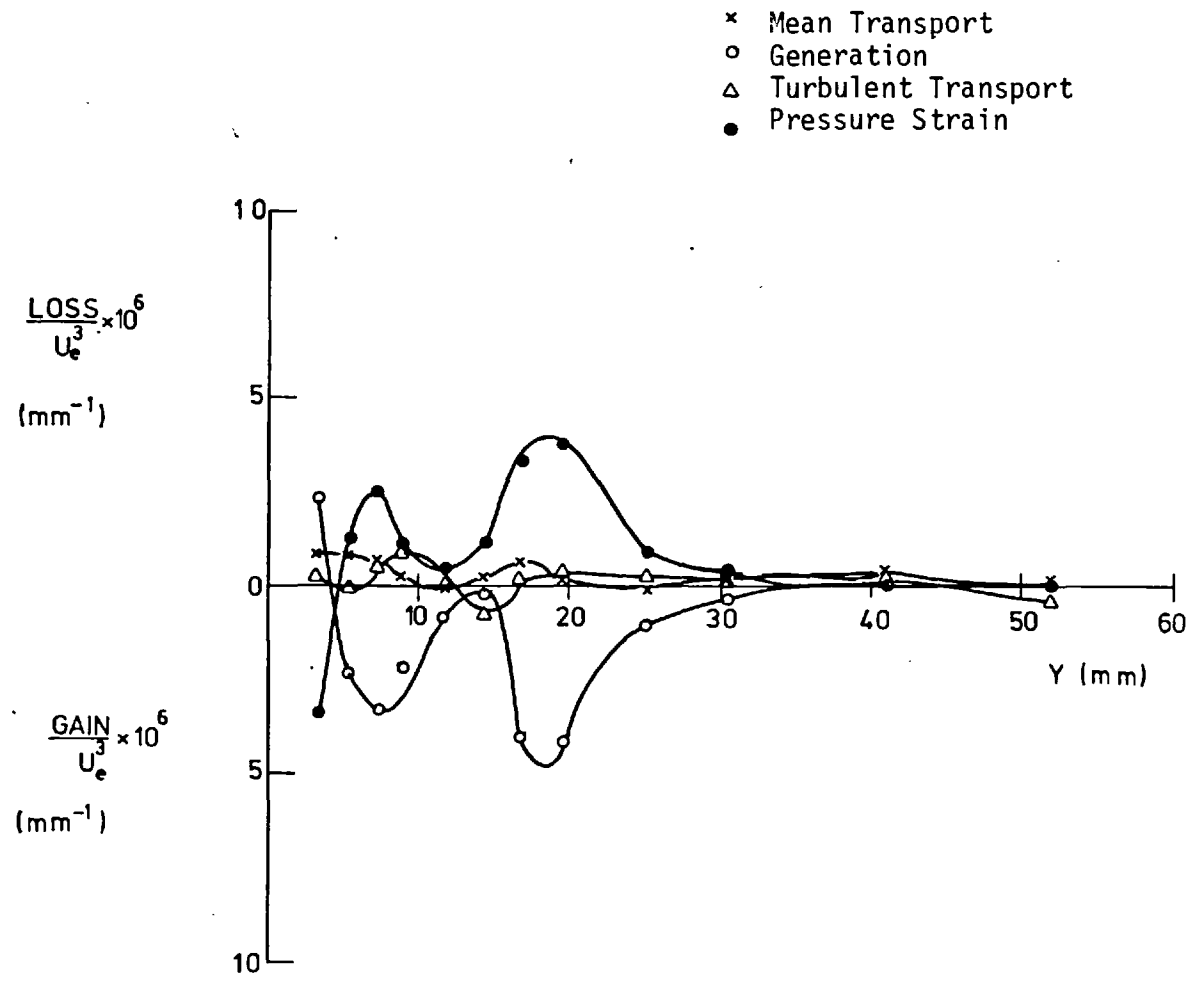

FIG.(4.80) $-\overline{uw}$ BALANCE AT Z = 63.40 mm

STATION 5 (X = 613.8 mm)

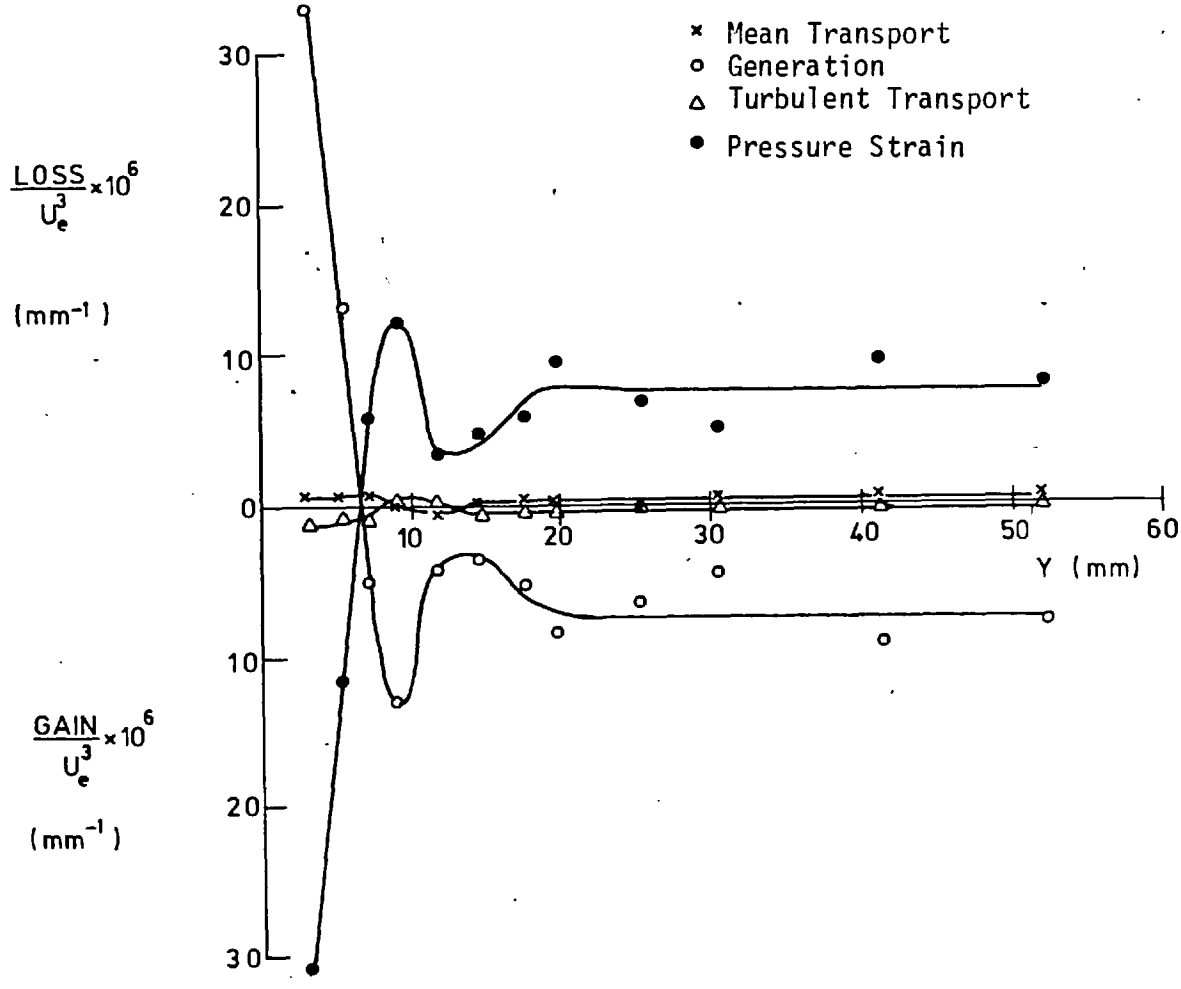

FIG.(4.81) $-\overline{vw}$ BALANCE AT Z = 5.03 mm

STATION 5 (X = 613.8 mm)

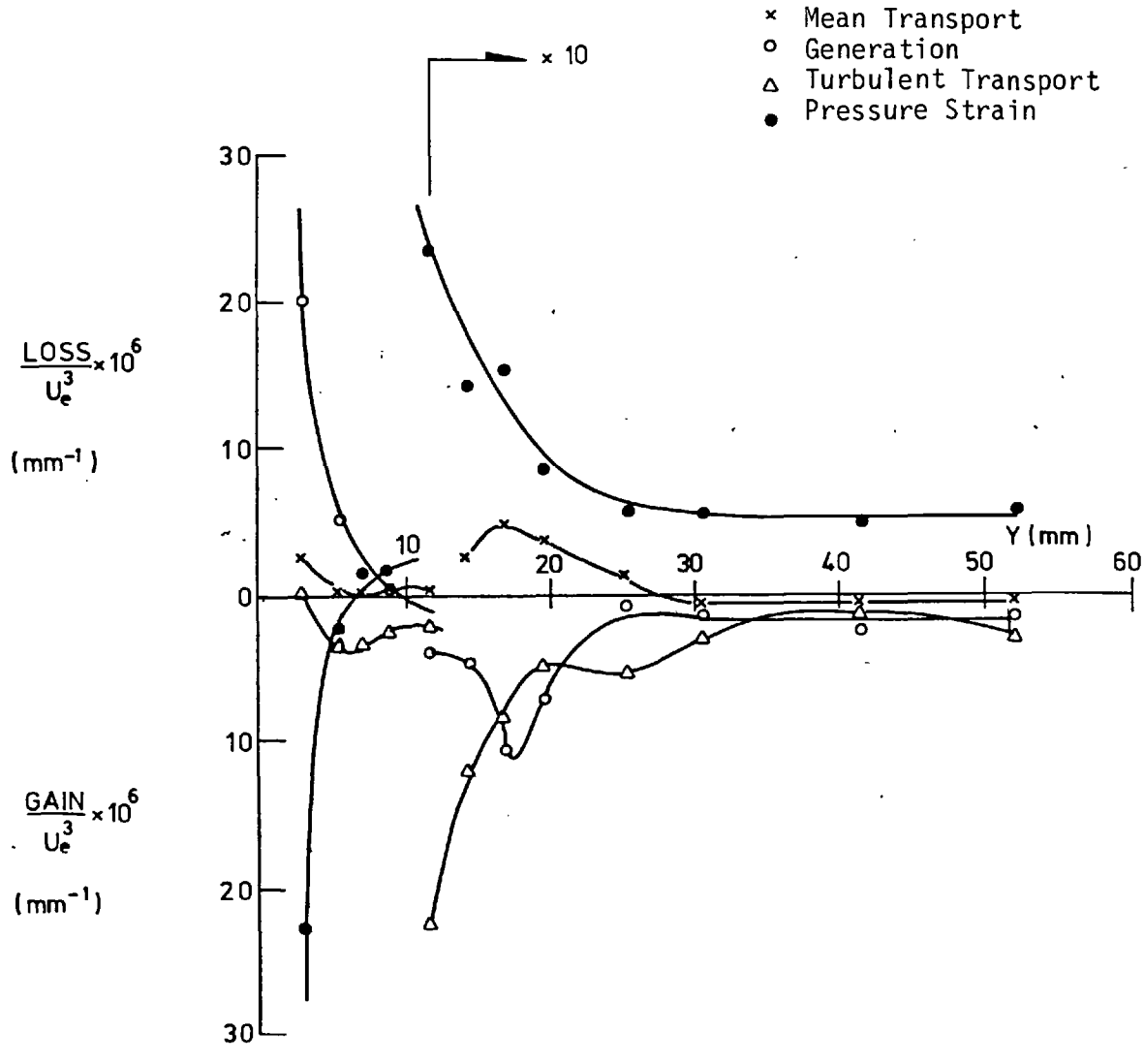

FIG.(4.82) $-\overline{vw}$ BALANCE AT Z = 15.03 mm

STATION 5 (X = 613.8 mm)

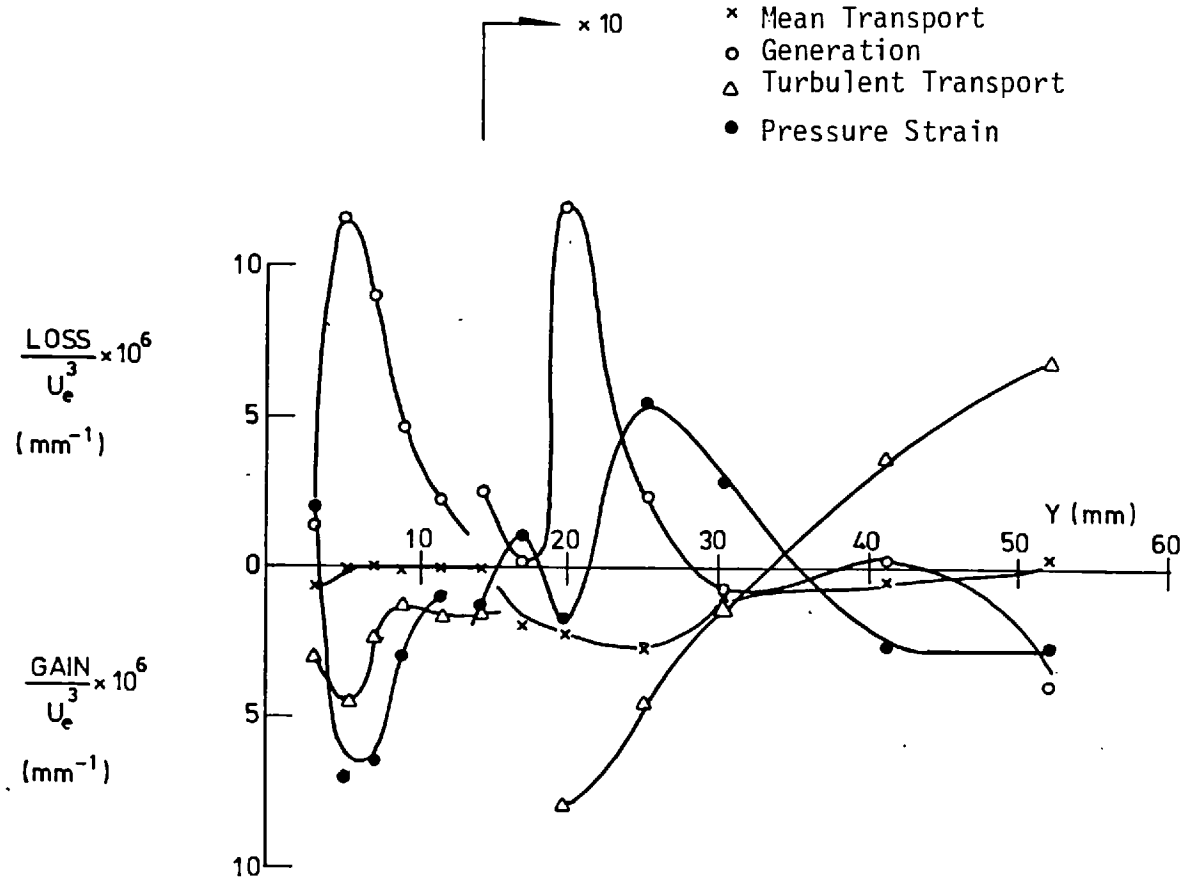

FIG.(4.83) $-\overline{vw}$ BALANCE AT Z = 28.4 mm

STATION 5 (X = 613.8 mm)

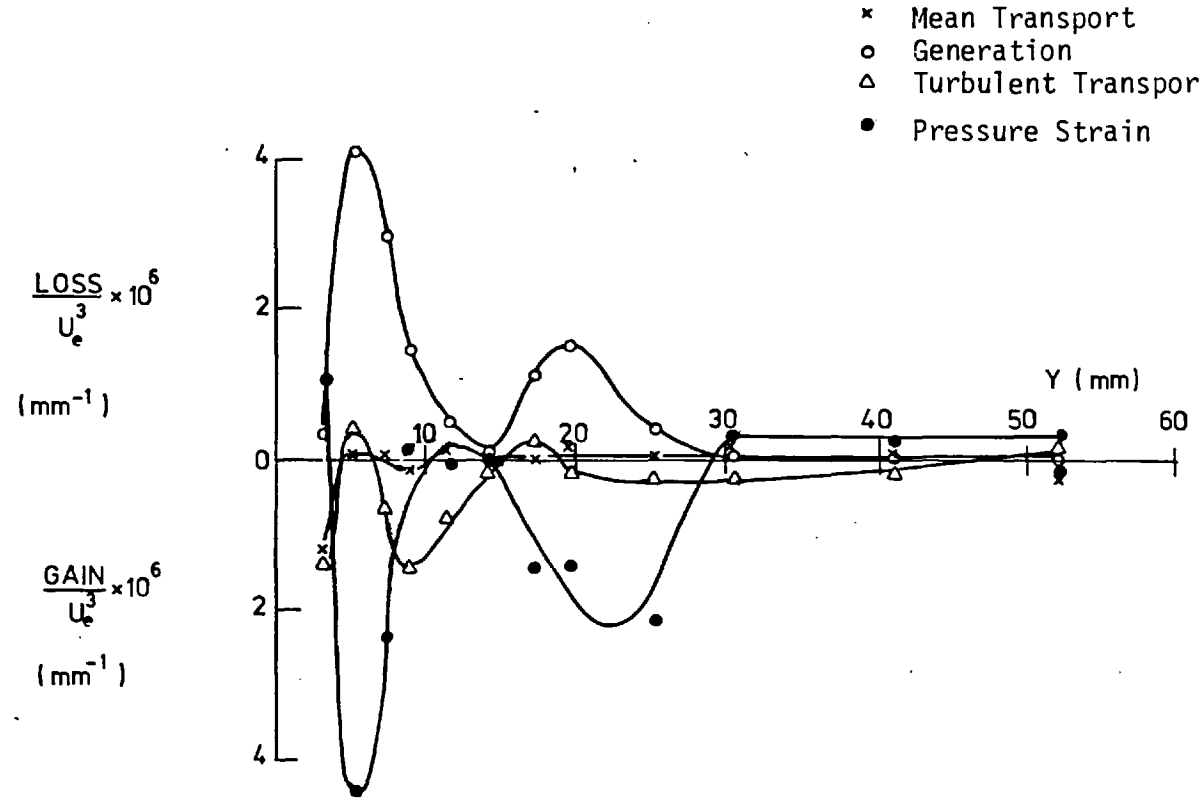

FIG.(4.84) $-\overline{vw}$ BALANCE AT Z = 63.4 mm

STATION 5 (X = 613.8 mm)

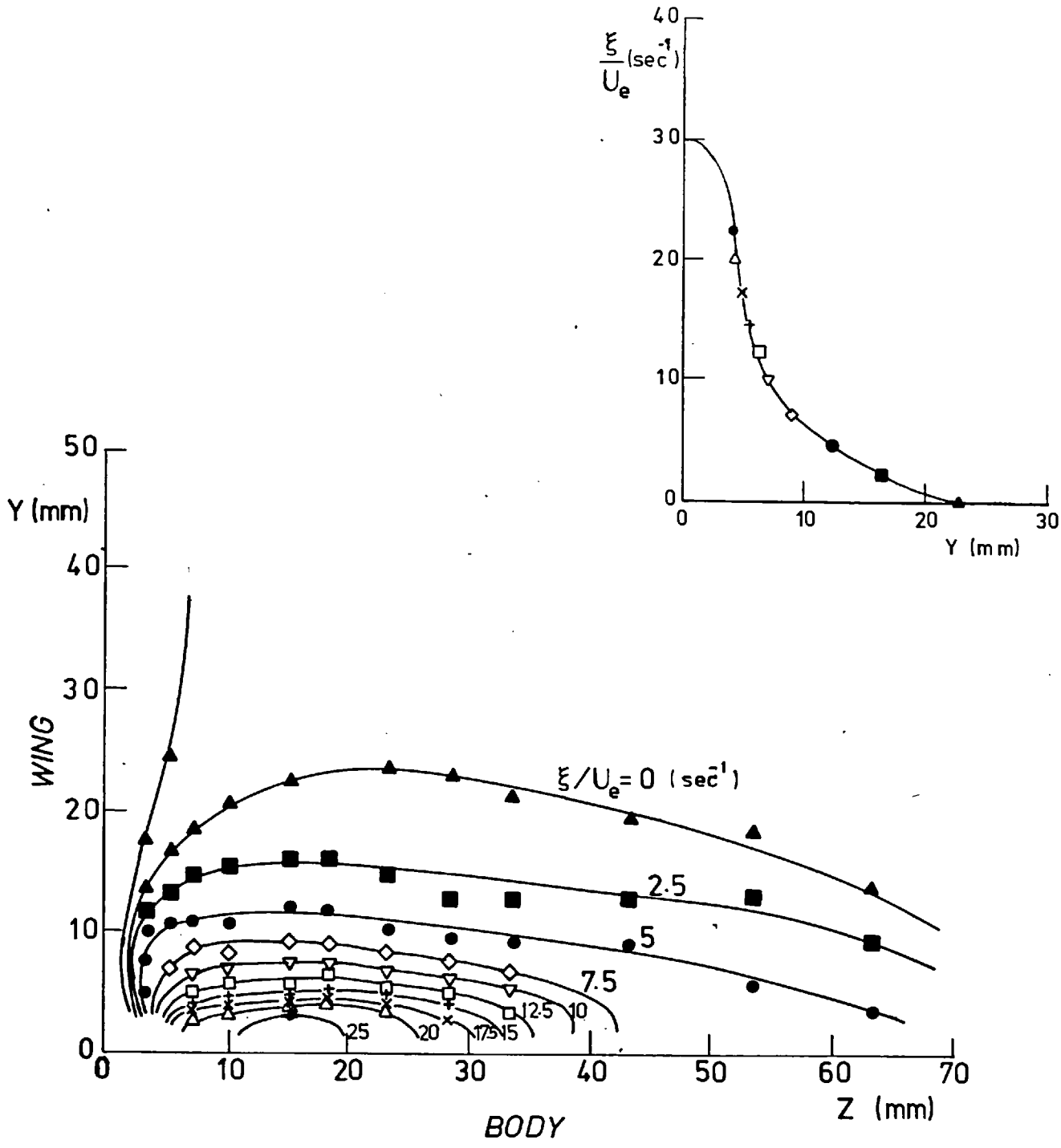

FIG.(4.85) CONTOUR MAP OF THE STREAMWISE VORTICITY AT STATION 2 (X = 156.6 mm)

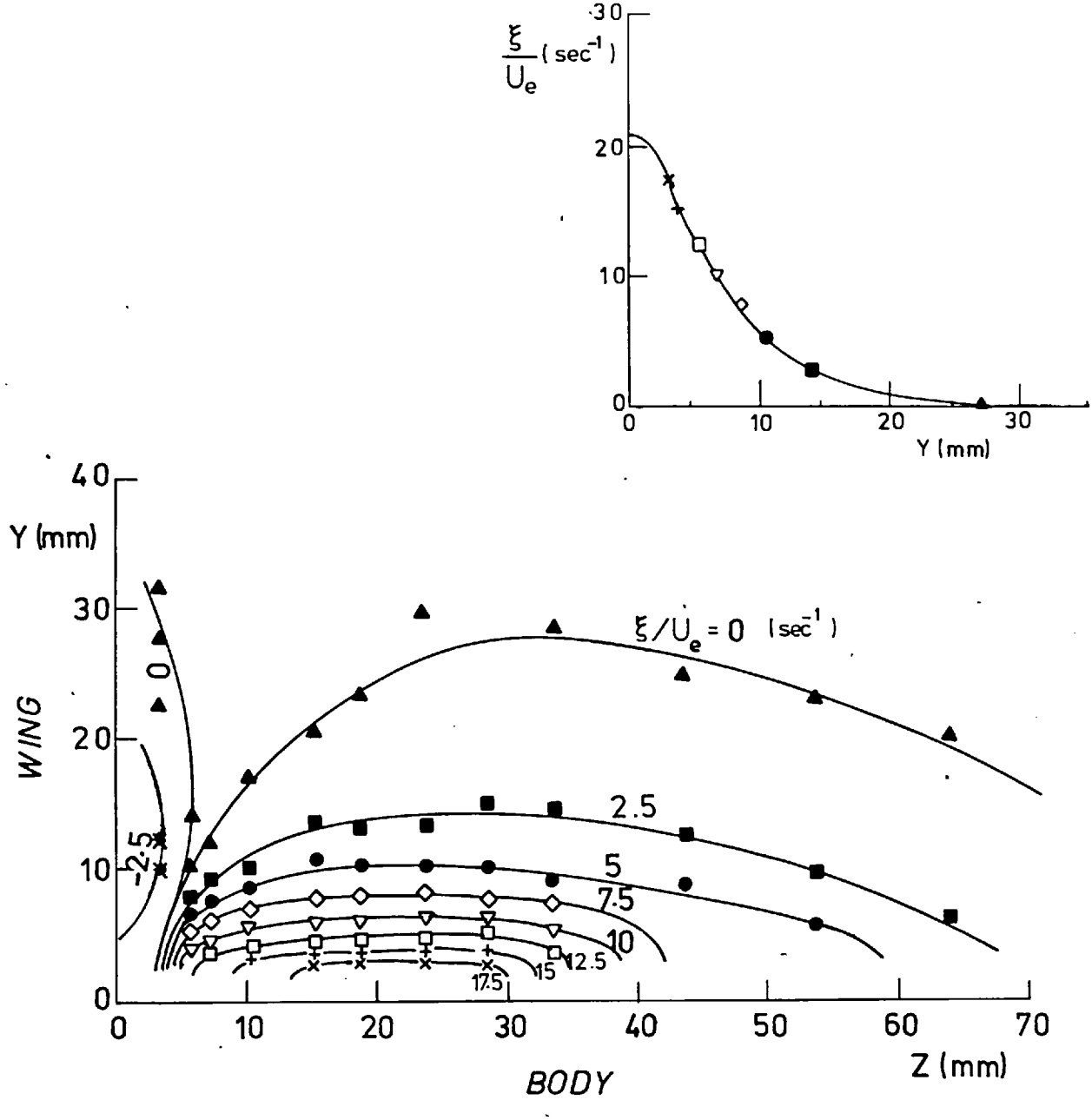

FIG.(4.86) CONTOUR MAP OF THE STREAMWISE VORTICITY AT STATION 5 (X = 613.8 mm)

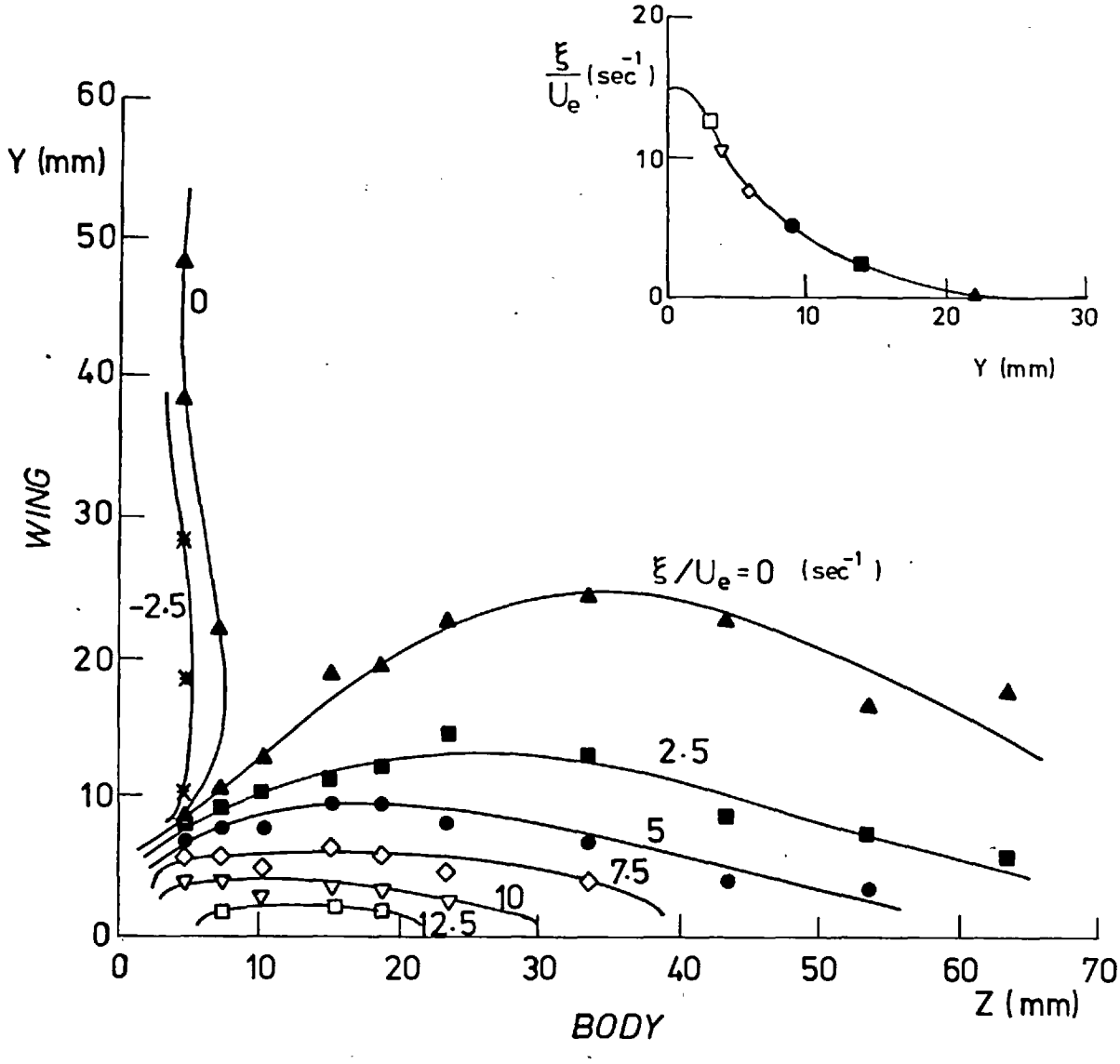

FIG.(4.87) CONTOUR MAP OF THE STREAMWISE VORTICITY AT STATION 9 (X = 1223.4 mm)

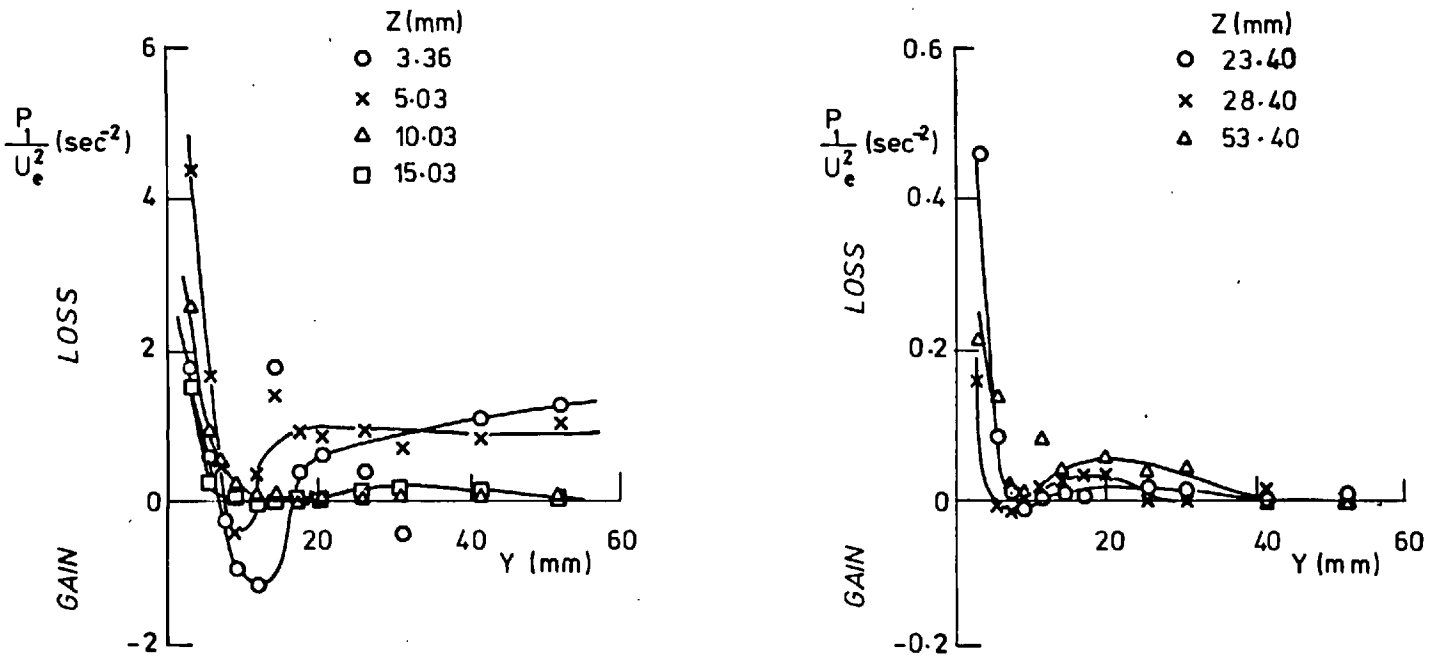

FIG.(4.88) THE TERM P_1 IN THE STREAMWISE VORTICITY EQUATION AT STATION 5 (X = 613.8 mm)

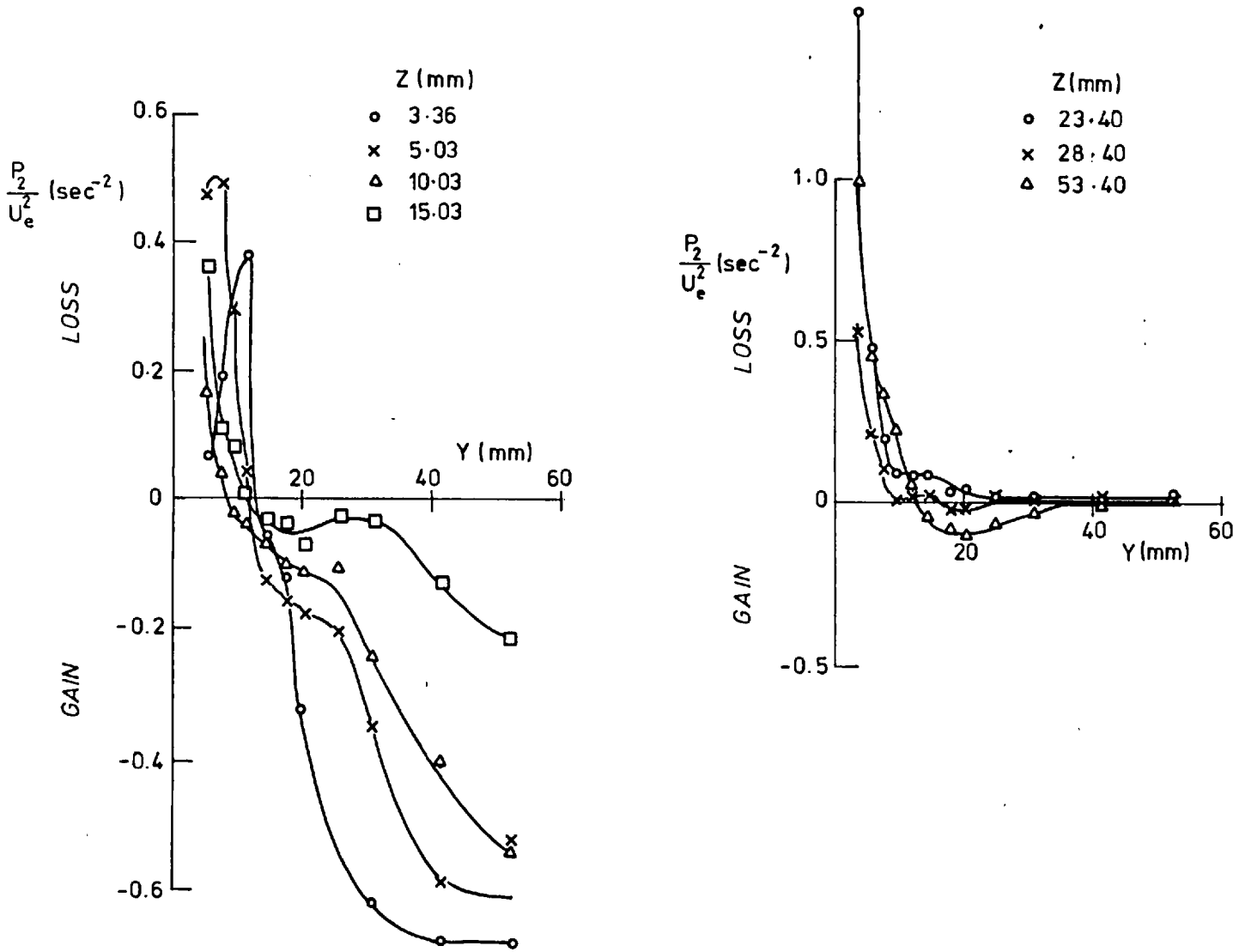

FIG.(4.89) THE TERM P_2 IN THE STREAMWISE VORTICITY EQUATION AT STATION 5 (X = 613.8 mm)

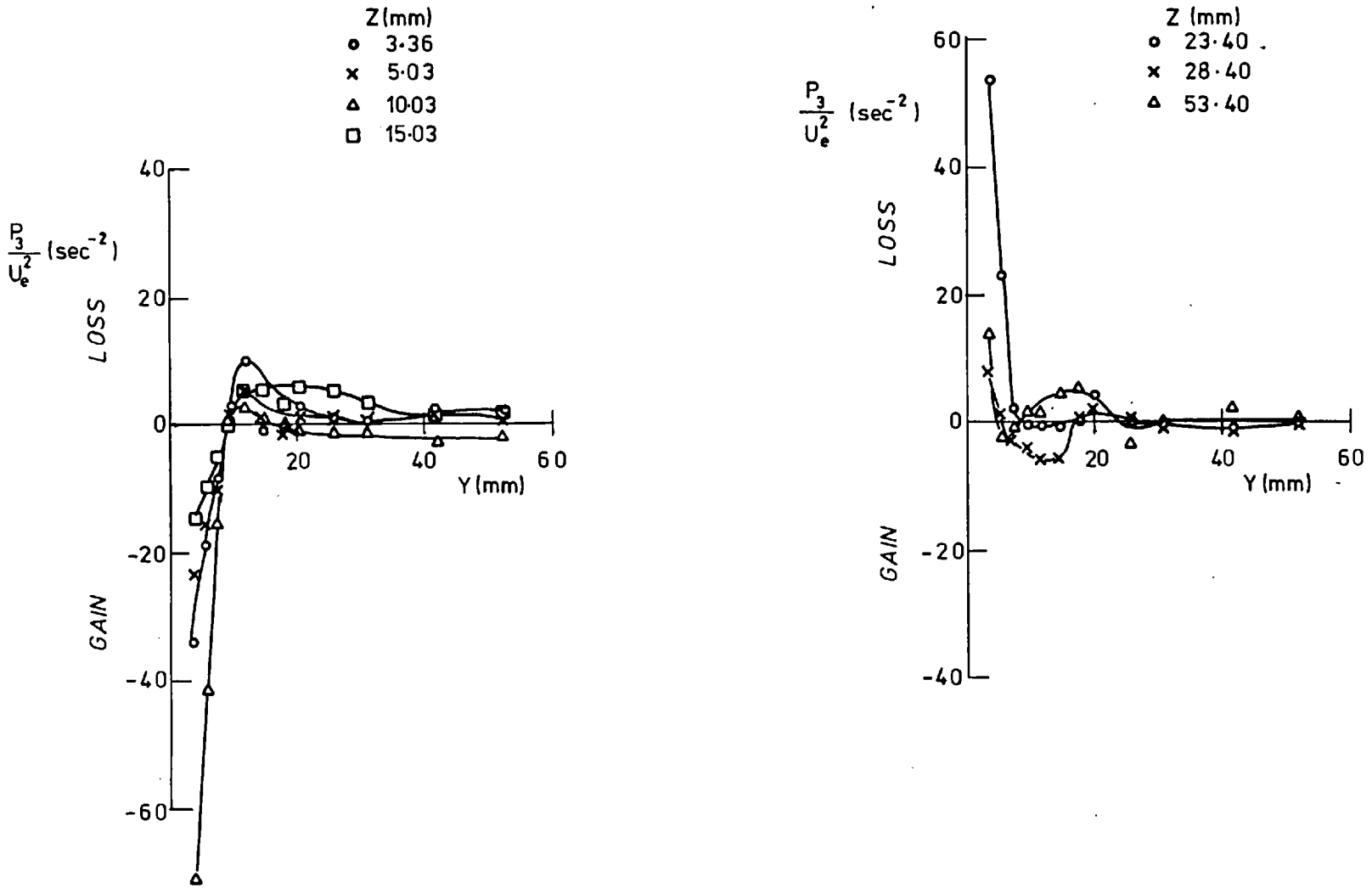

FIG.(4.90) THE TERM P_3 IN THE STREAMWISE VORTICITY EQUATION AT STATION 5 (X = 613.8 mm)

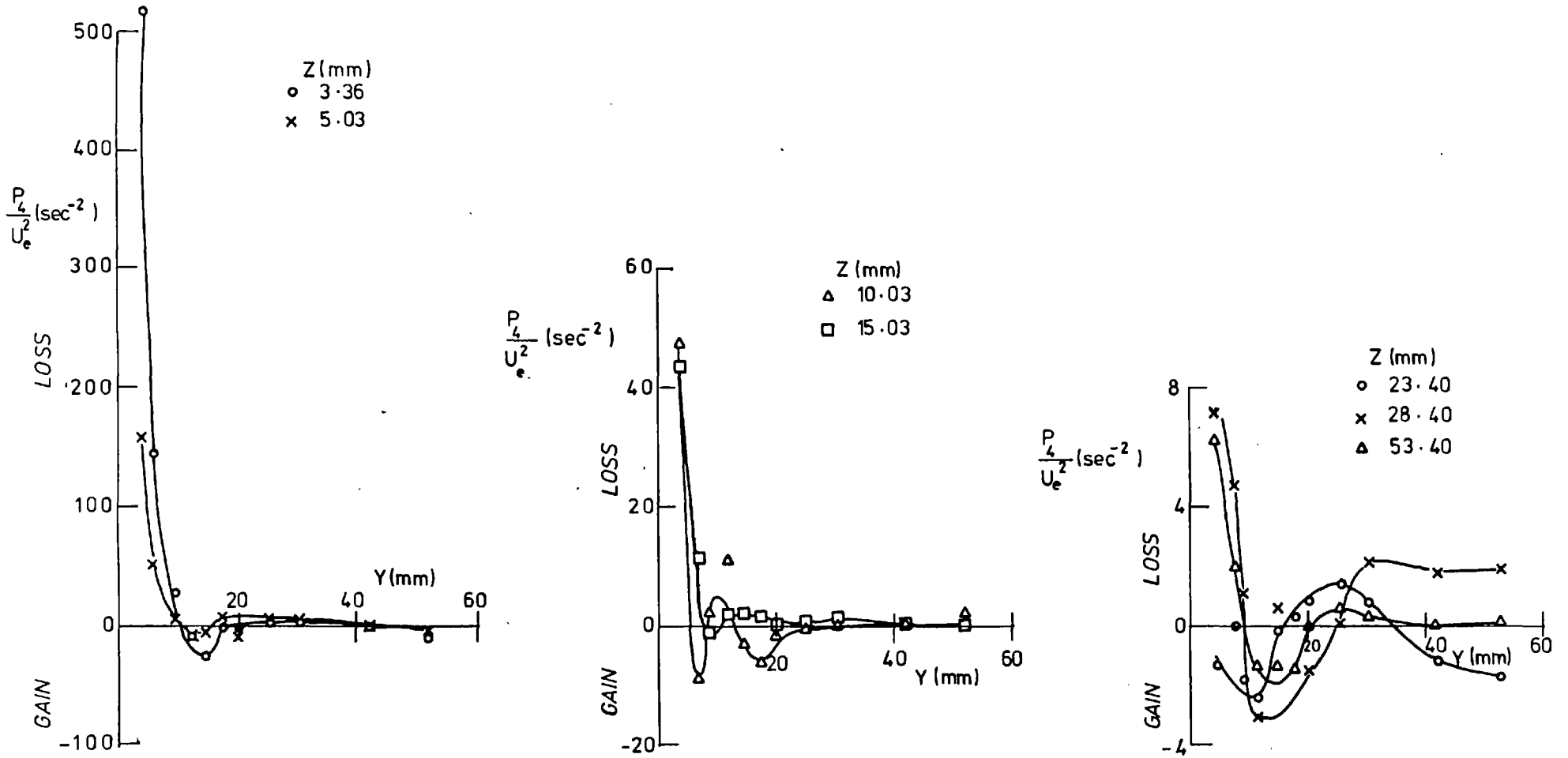

FIG.(4.91) THE TERM P_4 IN THE STREAMWISE VORTICITY EQUATION AT STATION 5 (X = 613.8 mm)

CHAPTER 5

CONCLUSIONS

5.1 The Present Work

The flow along the streamwise corner of an "idealized wing-body" junction in a near-zero pressure gradient has been studied in detail. Measurements of the three mean and three fluctuating velocity components, yielding the six Reynolds stresses and the ten triple products of the turbulence fluctuating velocities, have been obtained. The validity of some two-dimensional-turbulent flow laws and hypotheses was examined, and the turbulent kinetic energy and shear-stress budget were evaluated.

General conclusions are as follows:-

(a) As a result of separation of the body boundary layer ahead of the wing leading edge and the streamline skew there, a horse-shoe vortex is formed or wrapped around the leading edge and extends downstream along the corners between the wing surfaces and the body. The secondary flow found in the corner of the wing-body junction is thus of the "FIRST KIND".

(b) The vortex strength reduces and its cross-sectional area grows with downstream distance, mainly due to the diffusive action of the Reynolds stresses in the wing-body corner. (In the corners of rectangular ducts and between flat plates, the Reynolds stresses create a pair of contra-rotating vortices, i.e. they generate secondary flow of the "SECOND KIND").

(c) Flow in the wing-body junction is predominantly affected by

the presence of the streamwise vortex. Large effects on the velocity and Reynolds stress profiles in the outer part of the boundary layer are evident from the present measurements.

(d) However, the vortex has a small effect on the local equilibrium of the inner layers of the corner boundary region, except near the wing leading edge where the vortex is strong. The invalidity of the log-law in the inner layers very close to the corner-line is attributed to the vanishing wall shear stress there.

(e) The present study showed that eddy viscosity and mixing length models are not suitable for modelling the flow in the wing-body corners, where asymmetrical boundary layers interact, contrary to the symmetrical flow in duct corners to which the models seem applicable.

(f) A strong correlation between the resultant local shear stress and the turbulent kinetic energy exists over a large section of the flow.

(g) The corner secondary flows contribute greatly to the turbulent kinetic energy advection. Their contribution is comparable to the primary flow advection and they even exceed the primary advection close to the corner walls.

(h) Regions of negative shear stresses were found in the corner, where the "generation" term in the shear stress equation causes "destruction" of the mair stresses - $\overline{uv}$ and $\overline{uw}$ and the pressure-strain term (measured by difference of the other terms) contributes positively to their generation.

It is, in fact, very difficult to summarize all the detailed conclusions drawn from the discussion of the complicated turbulence quantities measured in the present experiment. For instance, no simple general conclusion can be drawn from the discussion of the measurements of the ten triple products of the fluctuating turbulence velocities u, v, w.

5.2 Future Work

It is hoped that the detailed investigation of the idealized wing-body corner flow, given in the present work, will contribute to a better understanding of this complex type of turbulent flow. The collected data can be used for testing and improving future calculation methods of wing-body corner flows. It seems that a unique relation between the resultant shear stress and the turbulent kinetic energy, found in both symmetrical and asymmetrical corner flows, is a first clue towards the right path. However, there is still much to be done, both experimentally and theoretically, before a full understanding of the wing-body corner flow is claimed:-

(a) The interaction between isolated vortices embedded in two-dimensional boundary layers and the turbulent flow in the layers is a problem that should be studied to throw more light on the major factor affecting the corner flow.

(b) The effect of streamwise pressure gradient on the corner flow needs to be studied. In most practical applications, e.g. turbo-machines, corner flows are subjected to pressure gradients. Pressure fields have great effect on the intensification (or attenuation) of vortex strength as the streamwise vorticity Equation (1.3) shows; $\frac{D\xi}{Dt} = \xi \frac{\partial U}{\partial x} + \ldots$, and if $dp/dx > 0$, i.e. $\partial U/\partial x < 0$, then ξ decreases.

(c) Corners between practical aerofoil-section wings and curved bodies, should be an ultimate case to be studied in detail.

(d) It is hoped that the present data can serve in developing general forms of the law of the wall and the law of the wake in wing-body corner flow specifically, and in slender flows in general.

REFERENCES

AHMED, S. and BRUNDRETT, E. (1971)
"Turbulent Flow in Non-Circular Ducts. Mean Flow Properties in the Developing Region of a Square Duct".
Int. J. Heat and Mass Transfer, Vol. 14, p. 365.

AINLEY, D. G. and MATHEIESON, G. C. R. (1951)
"An Examination of the Flow and Pressure Losses in Blade Rows of Axial Flow Turbines".
ARC Reports & Memoranda No. 2891.

ANDREOPOULOS, J. (1978)
"Symmetric and Asymmetric Near Wake of a Flat Plate".
Ph.D. Thesis, University of London.

ARMSTRONG, W. D. (1955)
"The Secondary Flow in a Cascade of Turbine Blades".
ARC Reports & Memoranda No. 2979.

ARMSTRONG, W. D. (1957)
"An Experimental Investigation of the Secondary Flow Occurring in a Compressor Cascade".
Aero. Quart., Vol. 8, p. 240.

BANSOD, P. and BRADSHAW, P. (1972)
"The Flow in S-Shaped Ducts".
Aero. Quart., Vol. 23, p. 131.

BARCLAY, W. H. (1971)
"Laminar Flow in a Streamwise Corner".
Ph. D. Thesis, University of London.

BARCLAY, W. H. (1973)
"Experimental Investigation of the Laminar Flow Along a Straight 135^{0} Corner".
Aero. Quart., Vol. 24, p. 147.

BEARMAN, P. W. (1971)
"Correction for the Effect of Ambient Temperature Drift on Hot-Wire Measurements in Incompressible Flows".
DISA Information, No. 11.

BĚLIK, L. (1972)
"Secondary Flow in Blade Cascades of Axial Turbomachines and the Possibility of Reducing its Unfavourable Effects".
Second International JSME Symposium, Fluid Machinery and Fluids, Tokyo, September, 1972, p. 41.

BĚLIK, L. (1973)
"The Secondary Flow About Circular Cylinder Mounted Normal to a Flat Plate".
Aero. Quart., Vol. 24, p. 47.

BOOTH, T. C. (1975)
"An Analysis of the Turbine Endwall Boundary Layer and Aerodynamic Losses".
ASME Paper No. 75-GT-23, March.

BOUSSINESQ, J. (1877)
"Théorie de l'écoulement tourbillant".
Mémoires Présentés par Divers Savants a l'Académie des Sciences, Vol. 23, p. 46.

BRADSHAW, P. (1965)
" 'Inactive' Motion and Pressure Fluctuations in Turbulent Boundary Layers".
NPL Aero. Report 1172, ARC 27, 338 and JFM, Vol. 30, Part 2, 1967, p. 241.

BRADSHAW, P. (1966)
"A Low-Turbulence Wind Tunnel Driven by an Aerofoil-Type Centrifugal Blower".
J. Roy. Aero. Soc., Vol. 71, p. 132.

BRADSHAW, P. (1968)
"Outlook for Three-Dimensional Procedures".
(Computation of Turbulent Boundary Layers, AFOSR-IFP-Stanford Conf., Vol. 1, "Methods, Predictions, Evaluation and Flow Structure", Editors: S. J. Kline, M. V. Morkovin, C. Sovran and D. J. Cockrell, p. 4.27).

BRADSHAW, P. (1970)
"Wind Tunnels and Test Rigs of the Department of Aeronautics, Imperial College".
IC Aero. Report 70-01.

BRADSHAW, P. (1971)
"An Introduction to Turbulence and its Measurement".
Pergamon Press.

BRADSHAW, P. (1972)
"Two More Wind Tunnels Driven by Aerofoil-Type Centrifugal Blowers".
IC Aero. Report 72-10.

BRADSHAW, P. (1973 - updated 1977)
"Aerodynamic Equipment Instruction Manual".
IC Aero. TN73-105.

BRADSHAW, P. (1975a)
"The Imperial College Aero Department Digital Magtape Data-Logging System".
IC Aero. TN72-101, (revised 1975).

BRADSHAW, P. (1975b)
"Turbulence".
M.Sc. Lecture Course, IC Aero. Dept.

BRADSHAW, P. (1976)
"Complex Turbulent Flows".
14th IUTAM Congress, Theoretical and Applied Mechanics,
editor: Koiter, W. T., North-Holland Publishing Co.

BRADSHAW, P. (1977)
" 'Discussion' - A Length-Scale Model for Developing
Turbulent Flow in a Rectangular Duct".
J. of Fluids Eng., Trans. ASME, Series I, Vol. 99, p. 784.

BRADSHAW, P., CEBECI, T. and WHITELAW, J. H. (1977)
"Engineering Calculation Methods for Turbulent Flows".
Lecture Series, Mech. Eng. Dept. of the California State
University, Long Beach, June, 1977 and Aero. Dept.,
Imperial College, London, October, 1977.

BRADSHAW, P. and FERRISS, D. H. (1965)
"The Response of a Retarded Equilibrium Turbulent Boundary
Layer to a Sudden Removal of Pressure Gradient".
NPL Aero. Report 1145, ARC 26 758-FM-3577.

BRADSHAW, P., FERRISS, D. H. and ATWELL, N. P. (1967)
"Calculation of Boundary-Layer Development Using the
Turbulent Energy Equation".
JFM, Vol. 28, Part 3, p. 593.

BRADSHAW, P. and GOODMAN, Miss D. G. (1966)
"The Effect of Turbulence on Static-Pressure Tubes".
ARC Reports & Memoranda No. 3527.

BRAGG, G. M. (1965)
"The Turbulent Boundary Layer in a Corner".
Ph. D. Thesis, University of Cambridge.

BRAGG, G. M. (1969)
"The Turbulent Boundary Layer in a Corner".
JFM, Vol. 36, p. 485.

BRAY de, B. G. (1967)
"Some Investigations into the Spanwise Non-Uniformity of
Nominally Two-Dimensional Incompressible Boundary Layers
Downstream of Gauze Screens".
ARC Reports & Memoranda No. 3578.

BREDERODE de, V. A. S. L. (1973)
" 'VELPROF' - A Boundary Layer Data Analysis Program".
IC Aero. TN73-107.

BREDERODE de, V. A. S. L. (1975)
"Three-Dimensional Effects in Nominally Two-Dimensional Flows".
Ph. D. Thesis, University of London.

BRUNDRETT, E. (1963)
"The Production and Diffusion of Vorticity in Channel Flow".
Ph. D. Thesis, University of Toronto, TP6302.

BRUNDRETT, E. and BAINES, W. D. (1964)
"The Production and Diffusion of Vorticity in Duct Flow".
JFM, Vol. 19, p. 375.

BULEEV, N. I. (1963)
"Theoretical Model of the Mechanism of Turbulent Exchange in Fluid Flows".
AERE Translation 957, Atomic Energy Research Establishment, Harwell, England.

CAME, P. M. (1973)
"Secondary Loss Measurements in a Cascade of Turbine Blades".
Instn. Mechanical Engineers, Conference, Publ. 3, p. 75.

CARRICK, H. B. (1974)
"Calculation of End-Wall Flow in Turbine Cascades".
ARC 35.916 Turbo 353, Cambridge Univ., SRC Turbomachinery Lab., March, 1975.

CARRICK, H. B. (1975)
"Preliminary Experimental Results on the Effect of Skew in the Boundary Layer on the Secondary Flow in an Impulse Turbine Cascade".
ARC 35 915, Turbo. 352.

CARRIER, G. (1947)
"The Boundary Layer in a Corner".
Quart. of Appl. Math., Vol. 4, No. 4, p. 367.

CARTER, A. D. S. and COHEN, E. M. (1946)
"Preliminary Investigation Into the Three-Dimensional Flow Through a Cascade of Aerofoils".
ARC Report and Memo. No. 2339.

CASTRO, I. P. (1973)
"A Highly-Distorted Turbulent Free Shear Layer".
Ph. D. Thesis, University of London.

CEBECI, T. and BRADSHAW, P. (1977)
"Momentum Transfer in Boundary Layers".
Hemisphere Publishing Corporation, McGraw Hill Book Co.

CHAMPAGNE, F. H., SCHLEICHER, C. A. and WEHRMANN, O. H. (1967)
"Turbulence Measurements with Inclined Hot Wires".
Parts 1 and 2, JFM, Vol. 28, p. 153.

CHANDRSUDA, C. (1976)
"A Reattaching Turbulent Shear Layer in Incompressible Flow".
Ph.D. Thesis, University of London.

CHU, J. K. and YOUNG, A. D. (1975)
"A Further Investigation of Viscous Effects in a Wing-Plate Junction".
Queen Mary College Departmental Rept., ER 1003.

CLAUSER, F. H. (1956)
"The Turbulent Boundary Layer".
Advances in Applied Mech., Vol. 4, p. 1.

COLES, D. E. (1956)
"The Law of the Wake of the Turbulent Boundary Layer".
JFM, Vol. 1, p. 191.

COLES, D. E. and HIRST, E. A. (Editors) (1968)
"Proceedings Computation of Turbulent Boundary Layers - 1968".
AFOSR-IFP-Stanford Conference, Vol. II, Compiled Data, Held at Stanford University, California, August 18 - 25.

DAVIES, T. W. and PATRICK, M. A. (1972)
"A Simplified Method of Improving the Accuracy of Hot-Wire Anemometry".
Fluid Dynamic Measurements in the Industrial and Mechanical Environments, Proc. DISA Conf., Vol. 1, Editor: D. J. Cockrell, Leicester University Press.

DEISSLER, R. G. and TAYLOR, M. F. (1959)
"Analysis of Turbulent Flow and Heat Transfer in Non-Circular Passages".
NASA, TR-31.

DESAI, S. S. and MANGLER, K. W. (1974)
"Incompressible Laminar Boundary-Layer Flow Along a Corner Formed by Two Intersecting Planes".
RAE Tech. Report 74062.

DOWDELL, R. B. (1952)
"Corner Boundary Layer".
M. Sc. Thesis, Brown University.

DOWDELL, R. B. (1968)
"Incompressible Boundary Layer Flow Along Interior Corners".
Proceedings 10th Midwestern Conf. on Mechanics, Colorado State University, Fort Collins, Colorado, August 21 - 28, p. 1355

DRING, R. P. (1971)
"A Momentum-Integral Analysis of the Three-Dimensional Turbine Endwall Boundary Layer".
J. of Engineering for Power, Trans. ASME Series C, Vol. 93, p. 386

DRYDEN, H. L. (1947)
"Some Recent Contributions to the Study of Transition and Turbulent Boundary Layers".
NACA Tech. Note No. 1168.

DUNHAM, J. (1970)
"A Review of Cascade Data on Secondary Losses in Turbines".
J. Mechanical Engineering Science, Vol. 12, No. 1, p. 48.

EAST, L. F. and HOXEY, R. P. (1968)
"Boundary Layer Effects in an Idealized Wing-Body Junction at Low Speed".
Royal Aircraft Establishment, Tech. Report TR68161.

EAST, L. F. and HOXEY, R. P. (1969)
"Low-Speed Three-Dimensional Turbulent Boundary Layer Data Part 2".
Royal Aircraft Establishment Tech. Report TR69137.

ECKERT, E. R. G. and IRVINE, T. F. (1955)
"Simultaneous Turbulent and Laminar Flow in Ducts With Non-Circular Cross-Section".
J. of the Aeronautical Sciences, Vol. 22, p. 65.

EICHELBRENNER, E. A. (1961)
"La Couche-Limite Turbulente a l'Interieur d'un Diedre".
La Recherche Aeronautique, Vol. 83, p. 3.

EICHELBRENNER, E. A. (1965)
"On the Determination of the Cross Flow Within the Turbulent Boundary Layer Along a Corner".
La Recherche Aérospatiale No. 104.

EINSTEIN, H. A. and LI, H. (1958)
"Secondary Currents in Straight Channels".
American Geophysical Union, Vol. 39, p. 1085.

EL-GAMAL, H. A. (1977)
"Laminar Flow Along a Corner With Boundary Layer Suction".
Ph. D. Thesis, University of London.

EL-GAMAL, H. A. and BARCLAY, W. H. (1978)
"Experiments on the Laminar Flow in a Rectangular Streamwise Corner".
Aero. Quart., Vol. 29, Part 2, p. 75.

FLAX, A. H. and LAWRENCE, H. R. (1951)
"The Aerodynamics of Low-Aspect-Ratio Wings and Wing-Body Combinations".
Proc. Third Anglo-American Aeronaut. Conf., Brighton, p. 363.

FRIEHE, F. H. and SCHWARZ, W. H. (1968)
"Deviation from Cosine-Law for Yawed Cylindrical Anemometer Sensors".
Trans. ASME, Series E, No. 35, p. 655.

GERARD, R. (1970)
"Turbulent Flow in Non-Circular Conduits".
Ph. D. Thesis, University of Newcastle, New South Wales, Australia.

GERSTEN, K. (1959)
"Corner Interference Effects".
AGARD Report 299.

GESSNER, F. B. (1964)
"Turbulence and Mean-Flow Characteristics of Fully-Developed Flow in Rectangular Channels".
Ph. D. Thesis, Purdue University.

GESSNER, F. B. (1973)
"The Origin of Secondary Flow in Turbulent Flow Along a Corner".
JFM, Vol. 58, Part 1, p. 1.

GESSNER, F. B. and EMERY, A. F. (1976)
"A Reynolds Stress Model for Turbulent Corner Flows - Part 1 : Development of the Model".
J. of Fluids Eng., Trans. ASME., Series I, Vol. 98, p. 261.

GESSNER, F. B. and EMERY, A. F. (1977)
"A Length-Scale Model for Developing Turbulent Flow in a Rectangular Duct".
J. of Fluids Eng., Trans. ASME, Series I, Vol. 99, p. 347.

GESSNER, F. B. and JONES, J. B. (1961)
"A Preliminary Study of Turbulence Characteristics of Flow Along a Corner".
ASME, J. of Basic Engineering, Vol. 83, p. 657.

GESSNER, F. B. and JONES, J. B. (1965)
"On Some Aspects of Fully Developed Turbulent Flow in Rectangular Channels".
JFM, Vol. 23, p. 689.

GESSNER, F. B. and PO, J. K. (1976)
"A Reynolds Stress Model for Turbulent Flows - Part II : Comparisons Between Theory and Experiment".
J. of Fluids Eng., Trans. ASME., Series I, Vol. 98, p. 269.

GHIA, K. N. (1975)
"Streamwise Flow Along an Unbounded Corner".
AIAA Journal, Vol. 13, No. 7, p. 902.

GHIA, K. N. and DAVIS, R. T. (1974a)
"Corner Layer Flow : Optimization of Numerical Methods of Solution".
Computers and Fluids, Vol. 2, p. 17.

GHIA, K. N. and DAVIS, R. T. (1974b)
"A Study of Compressible Potential and Asymptotic Viscous Flows for Corner Region".
AIAA Journal, Vol. 12, p. 355.

GILBERT, G. B. (1960)
"Secondary Flows in Straight Rectangular Ducts".
SM Thesis, MIT, July.

GOLDTEIN, S. (1936)
"A Note on the Measurements of Total Head and Static Pressure in Turbulent Stream".
Proc. Roy. Soc. (A), No. 155, p. 570.

GOLDSTEIN, S. (1965)
"Modern Developments in Fluid Dynamics".
Vol. 1, Dover Publications, New York, p. 208.

HANJALIC, K. and LAUNDER, B. E. (1972)
"A Reynolds Stress Model of Turbulence and its Application to Thin Shear Flows".
JFM, Vol. 52, Part 4, p. 609.

HAWTHORNE, W. R. (1951)
"Secondary Circulation in Fluid Flow".
Proc. Roy. Soc., Series A., No. 206, p. 374.

HERZIG, H. Z., HANSEN, A. G. and COSTELLO, G. R. (1953)
"A Visualization Study of Secondary Flows in Cascades".
NACA Report 1163.

HEY, R. D. and THORNE, C. R. (1975)
"Secondary Flows in River Channels".
Institute of British Geographers, Vol. 7, No. 3.

HINZE, J. O. (1967)
"Secondary Currents in Wall Turbulence".
Physics of Fluids, Supplement Vol. 10, p. S122.

HINZE, J. (1975)
"Turbulence".
McGraw-Hill Inc., Second Edition.

HOAGLAND, L. C. (1960)
"Fully Developed Turbulent Flow in Straight Rectangular Ducts - Secondary Flow, its Cause and Effect on the Primary Flow".
Sc.D. Thesis, MIT.

HUFFMAN, G. D. and BRADSHAW, P. (1972)
"A Note on von Kármán's Constant in Low Reynolds Number Turbulent Flows".
JFM, Vol. 53, Part 1, p. 45.

IBRAGIMOV, M. K., PETRISCHCHEV, V. S. and SABELEV, G. I. (1969)
"Calculation of Secondary Flow in a Turbulent Fluid Stream".
Fluid Dynamics (Translation of Mekhanika Zhidkosti I. Gaza), Vol. 4, No. 4, p. 114.

IRVINE, T. F. and ECKERT, E. R. G. (1959)
"Laminar Skin Friction and Heat Transfer on Flat Plates with Wedge-Shaped Grooves in Flow Direction".
ASME Paper 59-A-143.

JOHNSTON, J. P. (1960)
"On the Three-Dimensional Turbulent Boundary Layer Generated by Secondary Flow".
J. of Basic Eng., Trans. ASME, Series D, Vol. 82, No. 1, p. 233.

KACKER, S. C. (1973)
" ' Discussion' of Prediction of Flow and Heat Transfer in Ducts of Square Cross-Section ".
Proceedings of the Institution of Mechanical Engineers, Vol. 187, p. D147.

KEMP, N. (1951)
"The Laminar Three-Dimensional Boundary Layer and a Study of the Flow Past a Side Edge".
M. Ae. S. Thesis, Cornell University.

KLEBANOFF, P. S. (1954)
"Characteristics of Turbulence in a Boundary Layer with Zero Pressure Gradient".
NACA TN3178.

KLEBANOFF, P. S. (1955)
"Characteristics of Turbulence in a Boundary Layer with Zero Pressure Gradient".
NACA Report 1247.

KLINKSIEK, D. (1972)
"An Implicit Numerical Solution for the Axis of a 90-Degree Corner".
Ph. D. Thesis, Department of Mech. Eng., Virginia Polytechnic Institute and State University.

LANGSTON, L. S., NICE, M. L. and HOOPER, R. M. (1975 and 1977)
"Three-Dimensional Flow Within a Turbine Cascade Passage".
ASME Paper No. 76-GT-50, December, 1975 and J. of Engineering for Power, January, 1977, p. 21.

LAUNDER, B. E. and YING, W. M. (1971)
"Fully Developed Turbulent Flow in Ducts of Square Cross Section".
Report TM/TN/A/11, Department of Mech. Eng., Imperial College of Science & Technology, London (also Proceedings of the Institution of Mechanical Engineers, Vol. 187, p. 455, 1973).

LAUNDER, B. E. and YING, W. M. (1972)
"Secondary Flows in Ducts of Square Cross-Section".
JFM, Vol. 54, p. 289.

LAUNDER, B. E. and YING, W. M. (1973)
"Prediction of Flow and Heat Transfer in Ducts of Square Cross-Section".
Heat & Fluid Flow, Vol. 3, p. 115.

LEUTHEUSSER, H. J. (1963)
"Turbulent Flow in Rectangular Ducts".
J. of Hydraulics Division, Proc. ASCE, Vol. 89, p. 1.

LIGGETT, J. A., CHIU, C. L. and MIAO, L. S. (1965)
"Secondary Currents in a Corner".
J. of Hydraulics Division, Proc. ASCE, Vol. 91, p. 99.

LOITSIANSKII, L. G. (1936)
"Interference of Boundary Layers".
Central Aero-Hydrodynamical Institute, Moscow, Report 249 (English Translation - ARC 3186-FM342).

LOITSIANSKII, L. G. and BOLSHAKOV, V. P. (1951)
"On Motion of Fluid in a Boundary Layer Near Line of Intersection of Two Planes".
NACA TM1308.

LOUIS, J. F. (1958)
"Secondary Flow and Losses in a Compressor Cascade".
ARC Report & Memo 3136.

LUDWEG, H. and TILLMAN, W. (1949)
"Untersuchungen über die Wandschubspannung in turbulenten Reibungsschichten".
Ing.-Arch. 17, p. 288 - 299; ZAMM 29, p. 15 - 16. English translation: Investigations of the Wall-Shearing Stress in Turbulent Boundary Layers, NACA TM1285, 1950.

MAHGOUB, H. E. (1978)
"Calculation of the Interaction Between a Complex Turbulent Shear Layer and an External Inviscid Stream".
Ph. D. Thesis, University of London.

MARCHAL, P. H. and SIEVERDING, C. H. (1977)
"Secondary Flows Within Turbomachinery Bladings".
AGARD C P-214 on Secondary Flows in Turbomachinery, No. 11.

MAUER, J. C. (1961)
"An Examination of Fully-Developed Turbulent Flow in a Square Duct".
The Aerophysics Dept., Mississippi State University, Research Report No. 33.

MELLING, A. (1975)
"Investigation of Flow in Non-Circular Ducts and Other Configurations by Laser Doppler Anemometry".
Ph. D. Thesis, University of London.

MELLING, A. and WHITELAW, J. H. (1973)
"Measurements in Turbulent Water Flows by Laser Anemometry".
ARC 36 093, FM4555, Report No. HTS/73/44.

MOIN, P., REYNOLDS, W. C. and FERZIGER, J. H. (1978)
"Large Eddy Simulation of Incompressible Turbulent Channel Flow".
Stanford University, Thermosciences Division, Rept. TF-12.

MOJOLA, O. O. (1972)
"Turbulent Boundary Layer Along a Streamwise Corner".
Ph. D. Thesis, University of London.

MOJOLA, O. O. and YOUNG, A. D. (1971)
"An Experimental Investigation of Turbulent Shear Flows".
AGARD Conf. Proc. (C P-93), p. 12.1.

MURLIS, J. (1975)
"The Structure of a Turbulent Boundary Layer at Low Reynolds Number".
Ph. D. Thesis, University of London.

NAOT, D., SHAVIT, A. and WOLFSHTEIN, M. (1974)
"Numerical Calculation of Reynolds Stresses in a Square Duct with Secondary Flow".
Wärme und Stoffübertragung, Vol. 7, No. 3, p. 151.

NARANJIT, S. (1976)
"An Investigation of the Flow Over a Wing-Body Combination".
Ph. D. Thesis, University of London.

NIKURADSE, J. (1926)
"Untersuchungen über die Geschwindigteitsverteilung in Turbulenten Strömungen".
Thesis, Gottingen V.D.I - Forsch. 281.

NIKURADSE, J. (1930)
"Turbulente Strömung in nicht Kreisformigen Rohren".
Ing. - Arch. 1, pp. 306.

NOMURA, Y. (1962)
"Theoretical and Experimental Investigations on the Incompressible Viscous Flow Around the Corner".
Memo. of the Defence Academy of Japan, Vol. 2, No. 3.

OMAN, R. A. (1959)
"The Three-Dimensional Laminar Boundary Layer Along a Corner".
D. Sc. Thesis, MIT.

OWCZAREK, J. A. and ROCKWELL, D. O. (1972)
"An Experimental Study of Flows in Planar Nozzles".
Trans. ASME J. of Basic Eng., Vol. 94, Series D, No. 3, p. 682.

OWCZAREK, J. A., ROCKWELL, D. O. and CHA, Y. S. (1970)
"A Study of Flow From Two Planar Nozzles".
Lehigh University, Tech. Report No. 1.

PAL, A. and RUBIN, S. G. (1971)
"Asymptotic Features of the Viscous Flow Along a Corner".
Quart. of Applied Math., Vol. 29, p. 91.

PATEL, V. C. (1965)
"Calibration of the Preston Tube and Limitations on its Use in Pressure Gradients".
JFM, Vol. 23, Part 1, p. 185.

PATEL, D. K. and GOGLIA, G. L. (1977)
"Investigation of an Incompressible Flow Along a Corner by an Alternating Direction Implicit Method".
NASA-CR-154648, N77-30409.

PEACEMAN, D. W. and RACHFORD, H. H. (Jr.) (1955)
"The Numerical Solution of Parabolic and Elliptic Differential Equations".
J. Soc. Ind. and Appl. Math., Vol. 3, No. 1, p. 28.

PEARSON, J. R. A. (1957)
"Homogeneous Turbulence and Laminar Viscous Flow".
Ph. D. Thesis, Cambridge University.

PENKEN, J. H. (1977)
"Corner Layer and Secondary Flow Within a Straight Compressor Cascade".
Paper 21, AGARD-CP-214, on "Secondary Flows in Turbomachines".

PERKINS, H. J. (1967)
"A Study of Turbulent Flow in a Superelliptic Conduit".
M. A. Sc. Thesis, University of Waterloo.

PERKINS, H. J. (1970a)
"The Turbulent Corner Boundary Layer".
Ph. D. Thesis, University of Cambridge.

PERKINS, H. J. (1970b)
"The Formation of Streamwise Vorticity in Turbulent Flow".
JFM, Vol. 44, Part 4, p. 721.

PO, J. K. (1975)
"Developing Turbulent Flow in the Entrance Region of a Square Duct".
M.S. Thesis, Depart. of Mech. Eng., University of Washington.

PRANDTL, L. (1926)
"Über die ausgehildete Turbulenz".
Verhandlungen des zweithen Internationalen Kongresses für Tecknische Mechanik, Zurich. Translated as "Turbulent Flow" NACA TM435 (1926).

PRANDTL, L. (1927)
"Über den Reibungwiderstand Stromender Luft".
Ergeb. Aerodyn. Versuch, Göttingen, III Series.

PRÜMPER, H. (1972)
"Methoden zur Verminderung der Sekundärverluste in axialen Turbinenstufen".
Zeitschrift fur Flügwissenschaften, 20, p. 60.

RODET, E. (1958)
"Étude de l'écoulement turbulent dans un tunnel section non-circulaire".
Courtes Rendus 246, 3214, 3314 and 3578.

RODET, E. (1960)
"Étude de l'écoulement d'un fluide dans un tunnel primatique de section trapezoidale".
Publications Scientifiques et Techniques du Ministère de l'Air, No. 369.

RUBIN, S. G. (1966)
"Incompressible Flow Along a Corner".
JFM, Vol. 26, Part 1, p. 97.

RUBIN, S. G. and GROSSMAN, B. (1971)
"Viscous Flow Along a Corner : Numerical Solution of the Corner Layer Equations".
Quart. of Applied Math., Vol. 29, No. 2, p. 169.

SALVAGE, J. W. (1974)
"Investigation of Secondary Flow Behaviour and the Endwall Boundary Layer Development Through Compressors' Cascades".
VKI, TN107.

SCHILLER, L. (1923)
"Uber den Strömungswiderstand von Rohren Verschiedenen Querschnitts und Rauhigkeitsgrades".
ZAMM, Vol. 3, p. 2.

SCHLICHTING, H. (1946)
"Aerodynamics of the Mutual Influence of Aircraft Parts (Interference)".
Völkenrode R & T No. 171, (RAE Library Translation No. 275, ARC 12, 669, October, 1948).

SENOO, Y. (1958a)
"The Boundary Layer on the End Wall of a Turbine Nozzle Cascade".
Trans. Am. Soc. Mech. Engrs., Vol. 80, p. 1711.

SENOO, Y. (1958b)
"Three-Dimensional Laminar Boundary Layer in Curved Channel with Acceleration".
Trans ASME, Vol. 80, p. 1721.

SEPRI, P. (1973)
"An Investigation of the Flow in the Region of the Junction of a Wing and a Flat Surface Normal to the Wing Span".
Queen Mary College Departmental Report, QMC ER-1002.

SHABAKA, I. M. M. A. (1975)
"A Preliminary Experimental Investigation of Turbulent Flow in a Simplified Wing-Body Junction".
IC Aero Report 75-05.

SJOLANDER, S. A. (1975)
"The End-wall Boundary Layer in an Annular Cascade of Turbine Guide Vanes".
Carleton University, Dept. Mech. & Aerosp. Engng., Ottawa, Canada, TR ME/A 75-4.

SMITH, L. H. (1955)
"Secondary Flow in Axial-Flow Turbomachinery".
Trans. ASME., Vol. 77, p. 1065.

SO, R. M. C. (1977)
"A Note in Comment on (A Reynolds Stress Model for Turbulent Corner Flows)".
J. of Fluids Engng., Trans ASME, Vol. 99, Series I, No. 3, p. 593

SOWERBY, L. (1951)
"The Unsteady Flow of a Viscous Incompressible Fluid Inside an Infinite Channel".
Philosophical Magazine, Vol. 42, 7th Series, p. 176.

SQUIRE, H. B. and WINTER, K. G. (1951)
"The Secondary Flow in a Cascade of Aerofoils in a Non-Uniform Stream".
J. Aero. Sci., Vol. 18, p. 271.

STANBROOK, A. (1957)
"Experimental Observation of Vortices in Wing-Body Junctions".
RAE Aero. Report 2589 (also ARC Report & Memo No. 3114, 1959).

STEWART, W. L., WHITNEY, W. J. and WONG, R. Y. (1960)
"A Study of Boundary Layer Characteristics of Turbomachine Blade Rows and Their Relation to Overall Blade Loss".
J. Basic Engng., Trans. ASME, Vol. 82, Series D, p. 588.

TATCHELL, D. G. (1975)
"Convection Processes in Confined Three-Dimensional Boundary Layers".
Ph. D. Thesis, University of London.

TOAN, N. K. (1968)
"Couche Limite Turbulente a l'Interieur d'un Diedre avec Gradient de Pression".
M. A. Sc. Thesis, University of Laval, Canada.

TOAN, N. K. (1971)
"Application of Integral Methods to the Turbulent Corner Flow Problem".
ASME Paper No. 71-WA/FE36.

TOWNSEND, A. A. (1956)
"The Structure of Turbulent Shear Flow".
Cambridge University Press.

TRACY, H. J. (1965)
"Turbulent Flow in a Three-Dimensional Channel".
J. of Hydraulic Division, Proc. ASCE, Vol. 91, HY-6, p. 9.

TURNER, J. R. (1957)
"An Investigation of the End-Wall Boundary Layer of a Turbine-Nozzle Cascade".
Trans. ASME., Vol. 79, p. 1801.

VASANTA RAM, V. (1963a)
"Untersuchungen über die Eckengrenzschicht an einem Kreiszylinder mit Seitenwand".
Report 63/46, Institute of Fluid Mechanics, Technische Hochschule, Braunschweig.

VASANTA RAM, V. (1963b)
"Experimentelle Untersuchungen der Strömung entlang einer rechtwinkligen Ecke zwischen einem Profil und einer ebenen Seitenwand".
Institut für Strömungsmechanick, Technische Hochschule Braunschweig Bericht 63/17.

WAGNER, W. B. and OWCZAREK, J. A. (1974)
"An Investigation of the Corner Secondary Flows Generated in Planar Nozzles".
J. of Fluids Engineering, Trans. ASME, p. 234.

WALLIS, B. W. (1968)
"Some Measurements of the Laminar Boundary Layer in the Flow Along a Corner".
M. Phil. Thesis, University of London.

WEBER, J. (1975)
"Interference Problems in Wing-Fuselage Combinations - Part 1 : Lifting Unswept Wing Attached to a Cylindrical Fuselage at Zero Incidence in Midwing Position".
ARC Current Papers, C.P.No. 1331.

WEIR, A. D. (1976)
"Program 'TUVTER' - A Guide to Selecting Intermittency Criteria".
IC Aero TN 76-103.

WEIR, A. D. and BRADSHAW, P. (1974)
"Apparatus and Programs for Digital Analysis of Fluctuating Quantities in Turbulent Flow".
IC Aero Report 74-09.

WERLÉ, H. (1975)
"Ecoulements Décolles : Etude Phénoménologique at Partie de Visualisations Hydrodynamiques".
AGARD CP-168, Paper 39.

WINKELMANN, E. (1971)
"Aerodynamic Interaction Phenomena Produced by a Fine Protuberance Partially Immersed in a Turbulent Boundary Layer at Mach 5".
Paper No. 12, AGARD Conf. C P No. 71 on Aerodynamic Interference CP-71-71.

WOLF, H. (1961)
"Die Randverluste in geraden Schaufelgittern".
Wiss. Z. Tech. Hochsch. Dresden, 10, No. 2, RAE Library Translation No. 1336.

WOOD, D. H. (1978)
Private Communication.

YOUNG, A. D. (1977)
"Some Special Boundary Layer Problems".
Z. Flugwiss. Weltraumforsch. 1, Heft 6, p. 401.

ZAMIR, M. (1968)
"Boundary Layer Flow in Streamwise Corners".
Ph. D. Thesis, University of London.

ZAMIR, M. (1970)
"Boundary Layer Theory and the Flow in a Streamwise Corner".
Aeron. J. of the Roy. Aeron. Soc., Vol. 74, p. 330.

ZAMIR, M. (1972)
"On the Corner Boundary Layer with Favourable Pressure Gradient".
Aeron. Quart., Vol. 23, p. 161.

ZAMIR, M. (1973)
"Further Solution of the Corner Boundary Layer Equations".
Aeron. Quart., Vol. 24, p. 219.

ZAMIR, M. and YOUNG, A. D. (1970)
"Experimental Investigation of the Boundary Layer in a Streamwise Corner".
Aeron. Quart., Vol. 21, p. 313.

APPENDIX A

CROSS-WIRE YAW CALIBRATION

As explained in Chapter 2, a constant temperature hot-wire obeys the relation (2.2):-

$$E^2 = A + BU_{eff}^n$$

derived from King's law of cooling. Assuming the validity of the "cosine law", the effective cooling velocity over a wire at angle $(90 - \psi)$ to the flow is:-

$$U_{eff} = U \cos \psi \qquad (A.1)$$

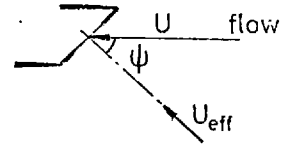

if V = 0. The cosine law has been shown not to be a good approximation for a single slant wire, by Champagne et al (1967) and Friehe et al (1968). They showed that the wire is significantly cooled by the longitudinal velocity component (U sin ψ). This problem, together with the practical difficulty of accurate measurement of the wire geometric angle to the flow, have been solved by determining the "effective" angle of the wire (ψ_{eff}), as suggested by Bradshaw (1971), described hereafter. The study of Wood (1978) carried out in this Department has shown that, for the particular X-wire probes used in the present work, the cosine law is adequate, i.e. the effect of the longitudinal velocity component is negligible, when the wires' effective angles are used.

If ψ_1 and ψ_2 are the effective angles of wires 1 and 2 relative to the X-wire probe centre line, not necessarily coinciding with their geometrical angles, and δ is the yaw

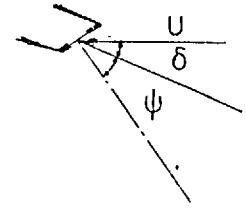

angle, then:-

$$E_1^2 = A_1 + B_1 \left[U \cos (\psi_1 + \delta)\right]^n \quad , \quad \text{and}$$
$$E_2^2 = A_2 + B_2 \left[U \cos (\psi_2 + \delta)\right]^n \quad . \qquad (A.2)$$

Assuming that A_1 and A_2 do not change with δ, for $\delta = 0$, we obtain:-

$$E_{1\delta=0}^2 = A_1 + B_1 \left[U \cos \psi_1\right]^n \quad , \quad \text{and}$$
$$E_{2\delta=0}^2 = A_2 + B_2 \left[U \cos \psi_2\right]^n \qquad (A.3)$$

Hence:-

$$\frac{\cos(\psi_1 + \delta)}{\cos \psi_1} = \left[\frac{E_1^2 - A_1}{E_{1\delta=0}^2 - A_1}\right]^n \quad , \quad \text{and}$$
$$\frac{\cos(\psi_2 - \delta)}{\cos \psi_2} \left[\frac{E_2^2 - A_2}{E_{2\delta=0}^2 - A_2}\right]^n \qquad (A.4)$$

i.e:-

$$\cos \delta - \left[\frac{E_1^2 - A_1}{E_{1\delta=0}^2 - A_1}\right]^{\frac{1}{n}} = \tan \psi_1 \sin \delta \quad , \quad \text{and} \qquad \text{(A.5) to be continued}$$

$$\cos\delta - \left[\frac{E_2^2 - A_2^2}{E_{\delta=0}^2 - A_2^2}\right]^{\frac{1}{n}} = \tan\psi_2 \sin\delta \qquad \text{(A.5) continued}$$

Knowing A_1 and A_2 from the velocity calibration and plotting the left hand sides of the last equations against sin δ usually gives straight lines of slope tan ψ_1 and tan ψ_2; departures from straight lines indicate misreading, drift or malfunction. A typical example of the yaw calibration is given in Fig. (2.11).

Useful comments on the limitations and errors of the above-described techniques, in high intensity flows where pitch and yaw response is more critical than in the present flow, are given by Castro (1973).

APPENDIX B

DEDUCTION OF TURBULENCE QUANTITIES FROM CROSS-WIRE SIGNALS

All the turbulence quantities could be deduced at a given point in the flow from the cross-wire measurements by rotating the planes of the wires about the x-axis so that it intersected the y-z plane at four different angles (usually the lines of intersection were chosen parallel to the y and z axes the bisectors of the angles between them). Recorded signals were analyzed using the standard "DIG2U" program as explained in Chapter 2 and in detail by Weir and Bradshaw (1974).

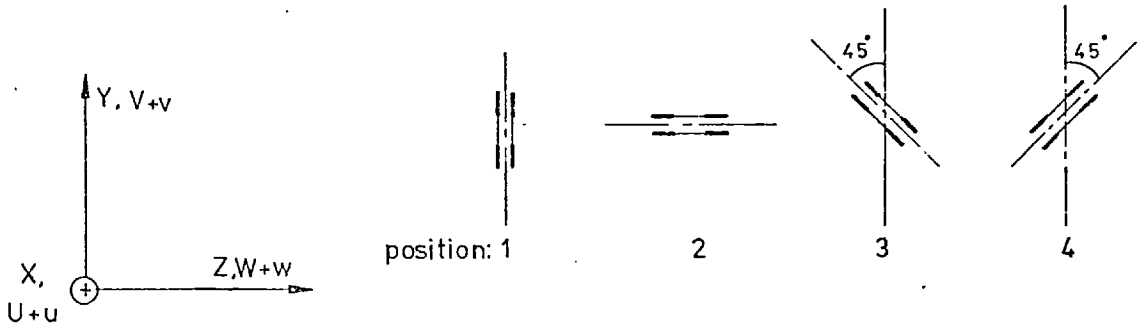

Aligning the plane of the wires in the (x-y) plane (position 1), yields the quantities: $\overline{u^2}$, $\overline{v^2}$, $\overline{uv}$, $\overline{u^3}$, $\overline{v^3}$, $\overline{u^2v}$ and $\overline{v^2u}$ in addition to the mean flow components U and V. Similarly, with the plane of the wires in the (x-z) plane (position 2), at the same point, the "DIG2U" output comprises $\overline{u^2}$, $\overline{w^2}$, $\overline{uw}$, $\overline{u^3}$, $\overline{w^3}$, $\overline{u^2w}$, $\overline{w^2u}$, U and W. When the wires are set at $\pm 45^{\circ}$ to the vertical (looking downstream - position 3), the wires respond to the two velocity components (U + u) and $\frac{(V + v) + (W + w)}{\sqrt{2}}$. In this case, the program gives:-

$\overline{u^2}$, $\overline{\frac{(v+w)^2}{2}}$, $\overline{u\frac{(v+w)}{\sqrt{2}}}$, $\overline{u^3}$, $\overline{\frac{(v+w)^3}{2\sqrt{2}}}$, $\overline{\frac{u^2(v+w)}{\sqrt{2}}}$, $\overline{\frac{(v+w)^2u}{2}}$, U and $\frac{V+W}{\sqrt{2}}$

Similarly, for the -45^0 setting (position 4), we get: $\overline{u^2}$, $\overline{\frac{(v-w)^2}{2}}$, ... , etc.

It is thus evident that all the six elements of the Reynolds stress tensor $\overline{u_iu_j}$, except $\overline{vw}$, follow directly from the vertical and horizontal setting the wires (positions 1 and 2). The secondary shear stress $\overline{vw}$ is deduced from the two inclined settings by subtracting $\overline{\frac{(v-w)^2}{2}}$ obtained with the wires at -45^0 from $\overline{\frac{(v+w)^2}{2}}$ obtained from the $+45^0$ setting (positions 3 and 4).

The triple products $\overline{u^3}$, $\overline{v^3}$, $\overline{w^3}$, $\overline{u^2v}$, $\overline{v^2u}$, $\overline{u^2w}$, $\overline{w^2u}$ are obtained directly from the vertical and horizontal wire positions, and the remaining three triple products $\overline{v^2w}$, $\overline{w^2v}$ and $\overline{uvw}$ are obtained as follows:-

(i) Subtracting $\overline{\left(\frac{v-w}{\sqrt{2}}\right)^3}$ from $\overline{\left(\frac{v+w}{\sqrt{2}}\right)^3}$, we get $\frac{\overline{w^3}+\overline{3v^2w}}{\sqrt{2}}$ and subtracting $\frac{\overline{w^3}}{\sqrt{2}}$ obtained from the horizontal wires' setting $\overline{v^2w}$ can be deduced.

(ii) Similarly adding $\overline{\left(\frac{v+w}{\sqrt{2}}\right)^3}$ to $\overline{\left(\frac{v-w}{\sqrt{2}}\right)^3}$, we get $\frac{\overline{v^3}+\overline{3wv^2}}{\sqrt{2}}$ and using the $\overline{v^3}$ from the vertical wires' setting we get $\overline{wv^2}$.

(iii) $\overline{uvw}$ is obtained from the two inclined wire setting by subtracting $u\left(\frac{v-w}{\sqrt{2}}\right)^2$ from $u\left(\frac{v+w}{\sqrt{2}}\right)^2$.

A brief discussion of the errors is given in the following Appendix.

APPENDIX C

A BRIEF ANALYSIS OF SOME ERRORS IN THE CROSS-WIRE MEASUREMENTS

C.1 The Effect of the Third Velocity Component

As has already been explained in Appendix A, the effect of the longitudinal component relative to wire centre-line is eliminated by the effective angle yaw-calibration of the X-wires. Here, we consider the effect of the third velocity component normal to the wire centre-line or normal to the plane of the X.

Setting the cross-wire probe with its wires in the (x-y) plane subjects the sensing wires 1 and 2 to the normal velocity components $V_{eff,1}$ and $V_{eff,2}$ respectively, where:-

$$V_{eff,1} = \sqrt{\left[(U + u)\cos\psi_1 + (V + v)\sin\psi_1\right]^2 + (W + w)^2} \qquad (C.1)$$

$$V_{eff,2} = \sqrt{\left[(U + u)\cos\psi_2 - (V + v)\sin\psi_2\right]^2 + (W + w)^2} \qquad (C.2)$$

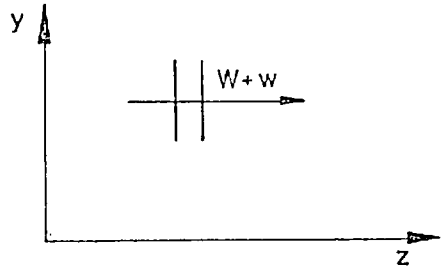

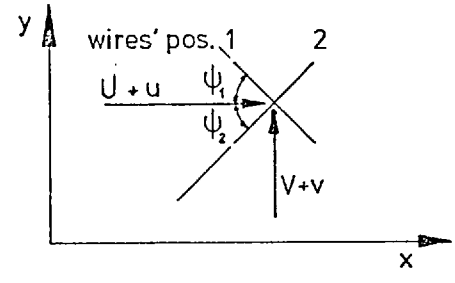

i.e.:-

$$V_{eff,1} = \left[(U + u)\cos\psi_1 + (V + v)\sin\psi_1\right] .$$

$$\cdot \sqrt{\left\{1 + \frac{(W + w)^2}{\left[(U + u)\cos\psi_1 + (V + v)\sin\psi_1\right]^2}\right\}} \qquad (C.3)$$

and:-

$$V_{eff,2} = \left[(U + u)\cos\psi_2 - (V + v)\sin\psi_2\right] \cdot$$

$$\cdot \sqrt{\left\{1 + \frac{(W + w)^2}{\left[(U + v)\cos\psi_2 + (V + v)\sin\psi_2\right]^2}\right\}} \qquad (C.4)$$

The measurements showed a maximum of $\sim 7\%$ for $\left[(W + w)/(U + u)\right]$ giving $(W + w)^2/(U + u)^2 \simeq 5\%$ at most. Hence, the relations used in the present work, namely:-

$$V_{eff,1} = (U + u)\cos\psi_1 + (V + v)\sin\psi_1 \quad , \quad \text{and} \qquad (C.5)$$

$$V_{eff,2} = (U + u)\cos\psi_2 - (V + v)\sin\psi_2 \qquad (C.6)$$

result in a maximum error of only 2.5% in $V_{eff,1}$ and $V_{eff,2}$ and in a negligible percentage error in the turbulence quantities.

C.2 Errors in the v-w Correlations

Appendix B explains the method used in deducing the v-w correlations from the X-wire measurements in planes inclined $\pm 45^{o}$ to the (x-y) plane. The error that results from inaccurate setting of the wires to $\pm 45^{o}$ relative to the vertical direction is discussed here.

If the wires are set at angles θ_1 and θ_2 to the vertical as sketched below, then they are measuring $v \sin\theta_1 + w \cos\theta_1$ and

$v \sin \theta_2 - w \cos \theta_2$ respectively corresponding to $(v + w)/\sqrt{2}$ and $(v - w)/\sqrt{2}$ for $\theta_1 = \theta_2 = 45^0$ as assumed.

C.2.1 Error in the Secondary Shear Stress - $\overline{vw}$

The measured value $\overline{vw_m}$, based on the assumption $\theta_1 = \theta_2 = 45^0$, is related to the actual value $\overline{vw}$ in the form:-

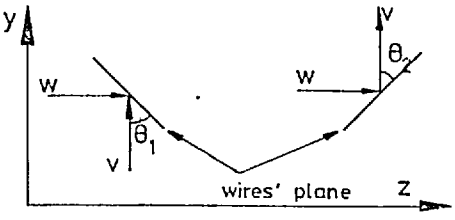

$$\overline{vw_m} = \frac{\overline{v^2}}{2} (\sin^2 \theta_1 - \sin^2 \theta_2) + \frac{\overline{w^2}}{2} (\cos^2 \theta_1 - \cos^2 \theta_2) + \overline{vw} \sin (\theta_1 + \theta_2) \quad (C.7)$$

For an exaggerated error of $\pm 5^0$ in θ_1 and θ_2 (> ± 10% error), we get:-

(a) If the errors lie in the same side, i.e. $\theta_1 = \theta_2$, then:-

$$\overline{vw_m} = 0.985\ \overline{vw}\ , \quad \text{i.e. - 1.5\% error in } \overline{vw}$$

(b) If the errors lie in the opposite sides, i.e. $\theta_1 + \theta_2 = 90^0$, then:-

$$\overline{vw_m} = \overline{vw} \left[1 \pm 0.0868\ (\overline{v^2} - \overline{w^2})/\overline{vw}\right]$$

The present measurements indicated a maximum value of about 1.75 for $|(\overline{v^2} - \overline{w^2})/\overline{vw}|$ near the walls. This results in a 15% error in the $\overline{vw}$ measurements at most.

C.2.2 Errors in the Triple Products

(i) For $\overline{v^2w}$ and $\overline{w^2v}$, we have:-

$$(3\overline{v^2w} + \overline{w^3})_m /\sqrt{2} = \overline{v^3} (\sin^3 \theta_1 - \sin^3 \theta_2) + 3\overline{v^2w} (\sin^2 \theta_1 \cos \theta_1 +$$

$$+ \sin^2 \theta_2 \cos \theta_2) + 3\overline{w^2v} (\sin \theta_1 \cos^2 \theta_1 - \sin \theta_2 \cos^2 \theta_2) +$$

$$+ \overline{w^3} (\cos^3 \theta_1 + \cos^3 \theta_2) \quad , \quad \text{and} \qquad (C.8)$$

$$(3\overline{w^2v} + \overline{v^3})_m /\sqrt{2} = \overline{v^3} (\sin^3 \theta_1 + \sin^3 \theta_2) + \overline{v^2w} (\sin^2 \theta_1 \cos \theta_1 -$$

$$- \sin^2 \theta_2 \cos \theta_2) + 3\overline{w^2v} (\sin \theta_1 \cos^2 \theta_1 + \sin \theta_2 \cos^2 \theta_2) +$$

$$+ \overline{w^3} (\cos^3 \theta_1 - \cos^3 \theta_2) \qquad (C.9)$$

Neglecting the error in $\overline{v^3}$ and $\overline{w^3}$, i.e. assuming $\overline{v_m^3} = \overline{v^3}$ and $\overline{w_m^3} = \overline{w^3}$, then for a $\pm 5^o$ setting error we get:-

(a) for $- 5^o$ error in both angles:-

$$\overline{v^2w_m} = \overline{v^2w} \left(0.895 + 0.091 \frac{\overline{w^3}}{\overline{v^2w}} \right), \text{ and}$$

$$\overline{w^2v}_m = \overline{w^2v} \left(1.067 - 0.083 \frac{\overline{v^3}}{\overline{w^2v}} \right)$$

Close to the wall an estimated error of - 16% and - 5% is found in $\overline{v^2w}$ and $\overline{w^2v}$ respectively when the measured values of $\overline{v^2w}$, ... there are used.

(b) for + 5^0 error in both angles:-

$$\overline{v^2 w_m} = \overline{v^2 w} \left[1.067 - 0.083 \frac{\overline{w^3}}{\overline{v^2 w}} \right] , \text{ and}$$

$$\overline{w^2 v_m} = \overline{w^2 v} \left[0.865 + 0.091 \frac{\overline{v^3}}{\overline{w^2 v}} \right]$$

resulting in an error of + 13% and + 0.2% in $\overline{v^2 w}$ and $\overline{w^2 v}$ close to the wall respectively.

(c) For $\mp 5^0$ and $\pm 5^0$ errors in θ_1 and θ_2 respectively:-

$$\overline{v^2 w_m} = \overline{v^2 w} \left[0.981 + (0.004\ \overline{w^3} \mp 0.087\ \overline{v^3} \pm 0.086\ \overline{w^2 v}) / \overline{v^2 w} \right] , \text{ and}$$

$$\overline{w^2 v_m} = \overline{w^2 v} \left[0.981 + (0.004\ \overline{v^3} \pm 0.087\ \overline{w^3} \mp 0.086\ \overline{v^2 w}) / \overline{w^2 v} \right]$$

Close to the solid surfaces the estimated errors are + 0.03% or - 4% in $\overline{v^2 w}$ and + 13% or - 15% in $\overline{w^2 v}$.

(ii) For $\overline{uvw}$, we have:-

$$\overline{uvw_m} = 0.5 \left[\overline{uv^2} (\sin^2 \theta_1 - \sin^2 \theta_2) + \overline{w^2 u} (\cos^2 \theta_1 - \cos^2 \theta_2) + \right.$$

$$\left. + \overline{uvw} (\sin 2\theta_1 + \sin 2\theta_2) \right] \qquad (C.10)$$

(a) For an error $\pm 5^0$ in both θ_1 and θ_2 (i.e. $\theta_1 = \theta_2$), we get:-

$\overline{uvw_m} = 0.985\ \overline{uvw}$ i.e. an error of only 1.5%

(b) For $\mp 5^0$ error in θ_1 and $\pm 5^0$ in θ_2, we get:-

$$\overline{uvw_m} = \left[0.985 \pm \frac{0.087}{\overline{uvw}} \left(\overline{uv^2} - \overline{uw^2}\right)\right] \overline{uvw}$$

The resulting errors close to the solid surface are + 8% or - 11%.

Taking into consideration that the above rough estimates of errors were made for an exaggerated error in setting the wires using the experimental data that almost give the highest error, it is seen that the present technique is reliable if the wires' plane was set reasonably accurately to the $\pm 45^0$ planes (within $\pm 2^0$ say).

APPENDIX D

PLOTS OF TRIPLE PRODUCTS OF TURBULENT VELOCITY COMPONENTS AND TURBULENT TRANSPORT VELOCITIES

The relegated isometric graphs of the triple products at stations 2, 5 and 9 (x = 15.7, 61.4, 122.3 cm) are displayed in this Appendix to complete the set of data. Figs. (D.1) - (D.30) show the computer-plotted experimental points. No connecting curves were traced, to save effort and time. However, values can be read easily from the graphs using the read-out sheet supplied with the thesis, as explained in Section 3.3. Some of the above figures (those of triple products at station 5) were retraced manually in a clearer form and have been presented in Chapter 4 (Figs. (4.25) - (4.34)), where the triple products results were discussed (Section 4.3).

This Appendix also includes the turbulent transport velocities of the shear stresses ($-\overline{uv}$ and $-\overline{uw}$) in the three x-, y- and z-directions at stations 2 and 9 (Figs. (D.31) - (D.42)). The corresponding figures of the transport velocities at station 5 have been displayed in Figs. (4.35) - (4.40) where they were discussed (in Section 4.3). The transport velocities of the secondary shear stress $-\overline{vw}$ in the three directions at stations 2, 5 and 9 are given in Figs. (D.43) - (D.51).

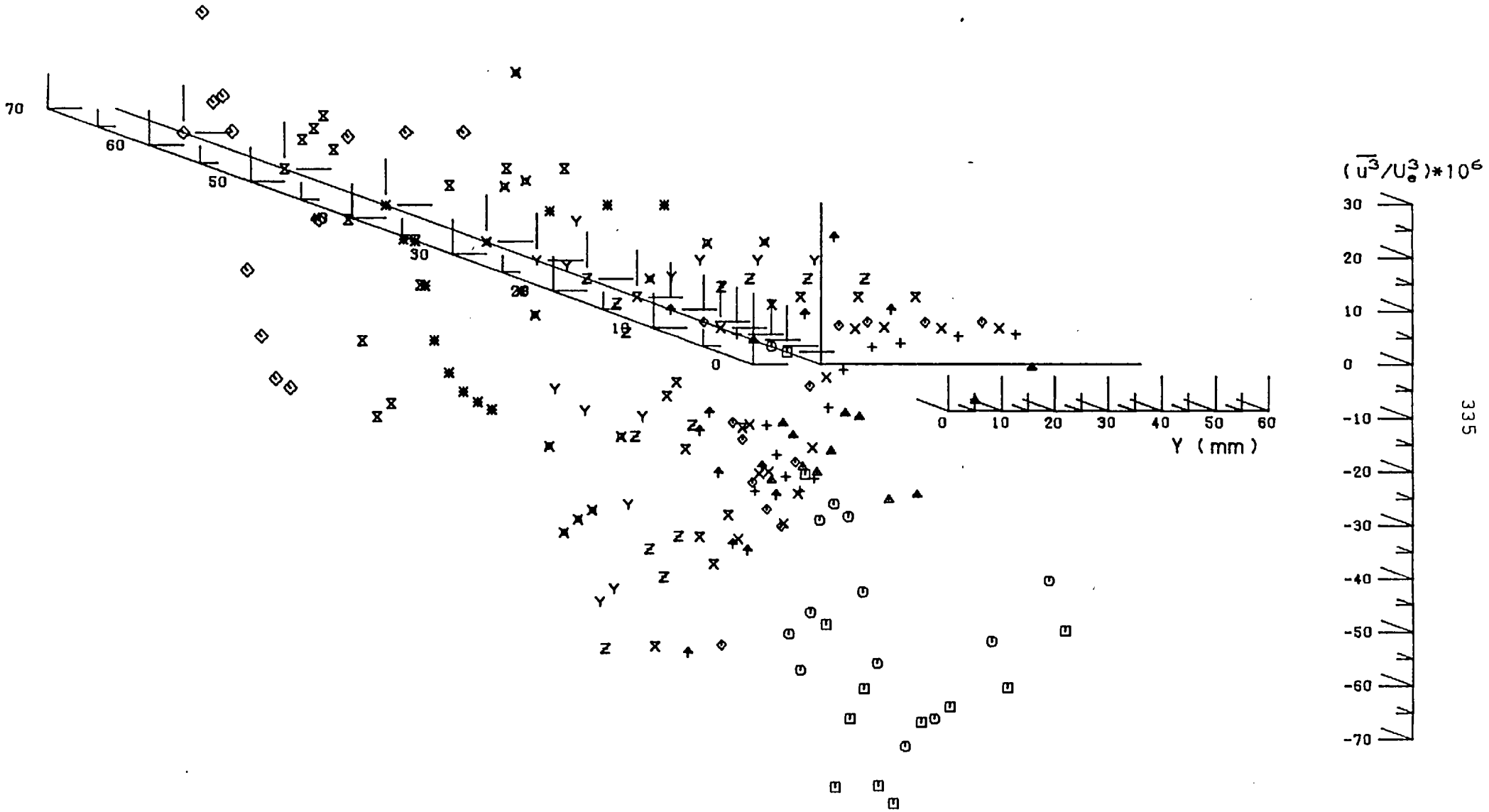

FIG.(D.1) PLOTS OF TRIPLE PRODUCT ($\overline{u^3}$) AT STATION 2 (X= 156.6mm)

Results of Cross Wire in Vertical (U-V) Position

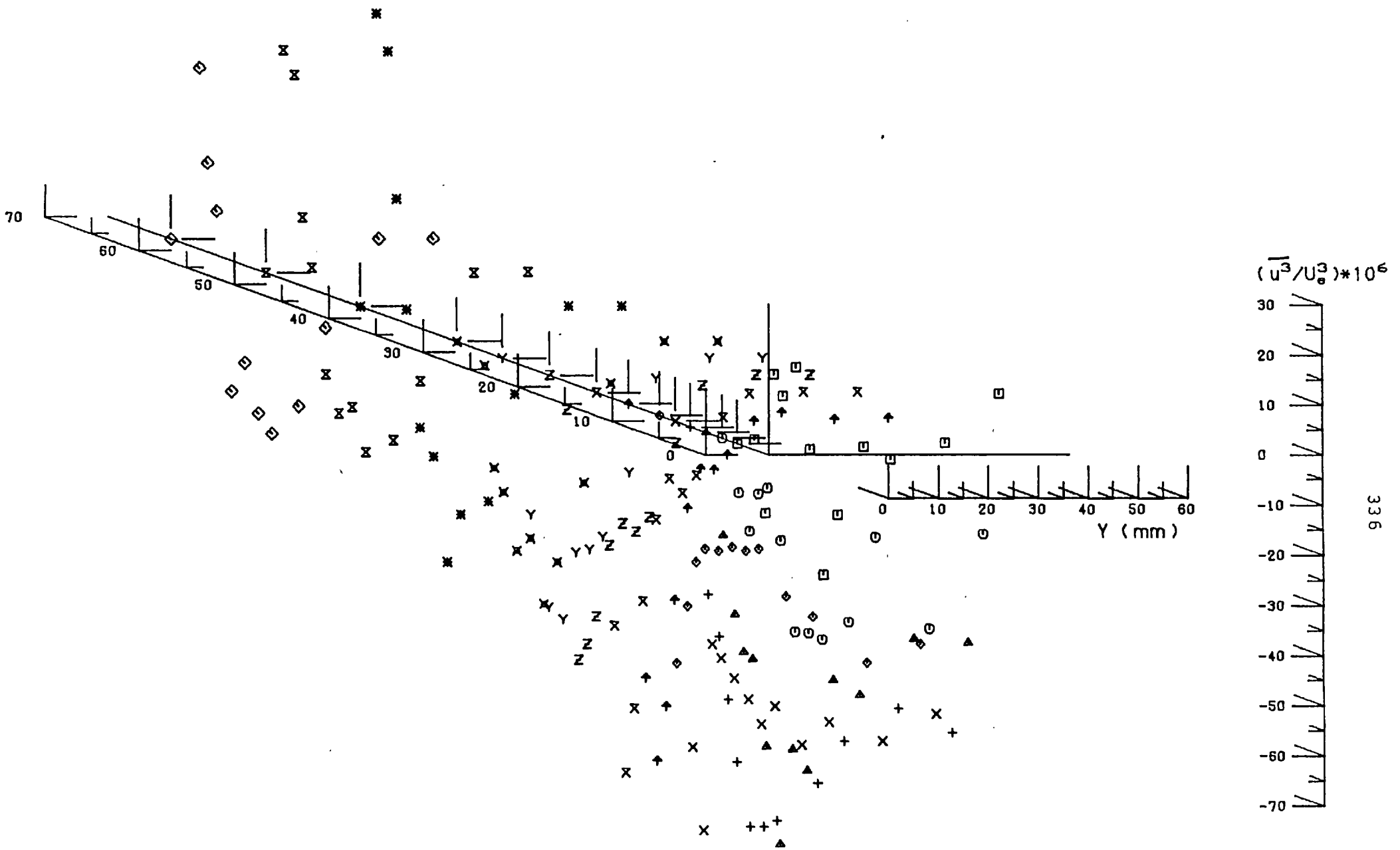

FIG.(D.2) PLOTS OF TRIPLE PRODUCT ($\overline{u^3}$) AT STATION 5 (X= 613.8mm)
Results of Cross Wire in Vertical (U-V) Position

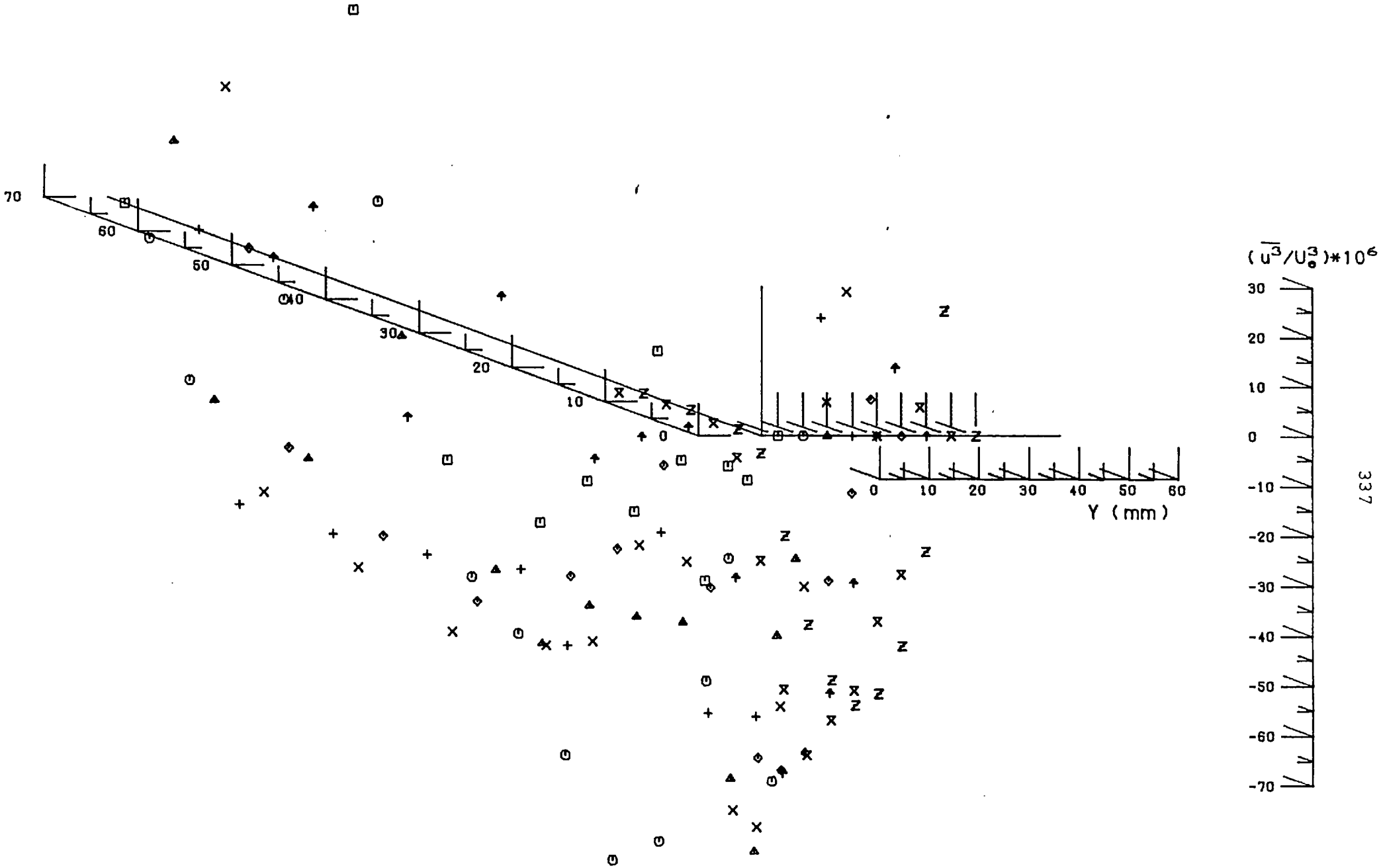

FIG.(D.3) PLOTS OF TRIPLE PRODUCT ($\overline{u^3}$) AT STATION 9 (X=1223.4mm)

Results of Cross Wire in Vertical (U-V) Position

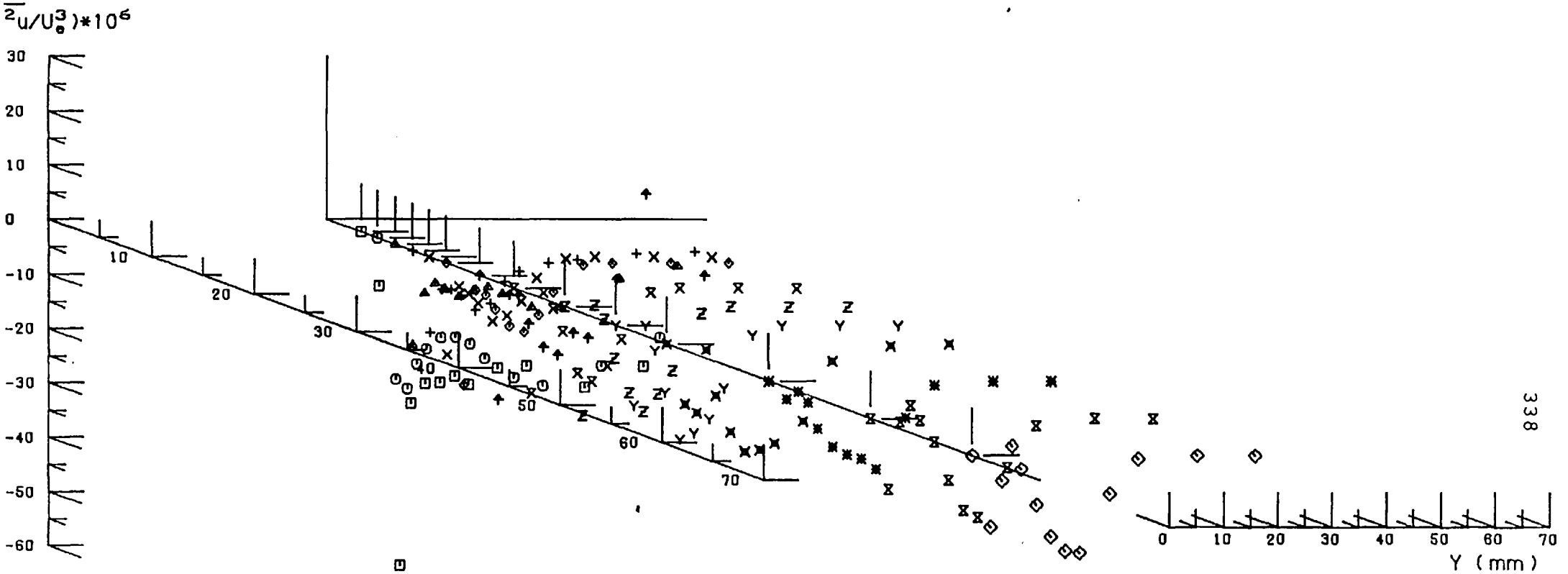

FIG.(D-4) PLOTS OF TRIPLE PRODUCT ($\overline{v^2u}$) AT STATION 2 (X= 156.6mm)
Results of Cross Wire in Vertical (U-V) Position

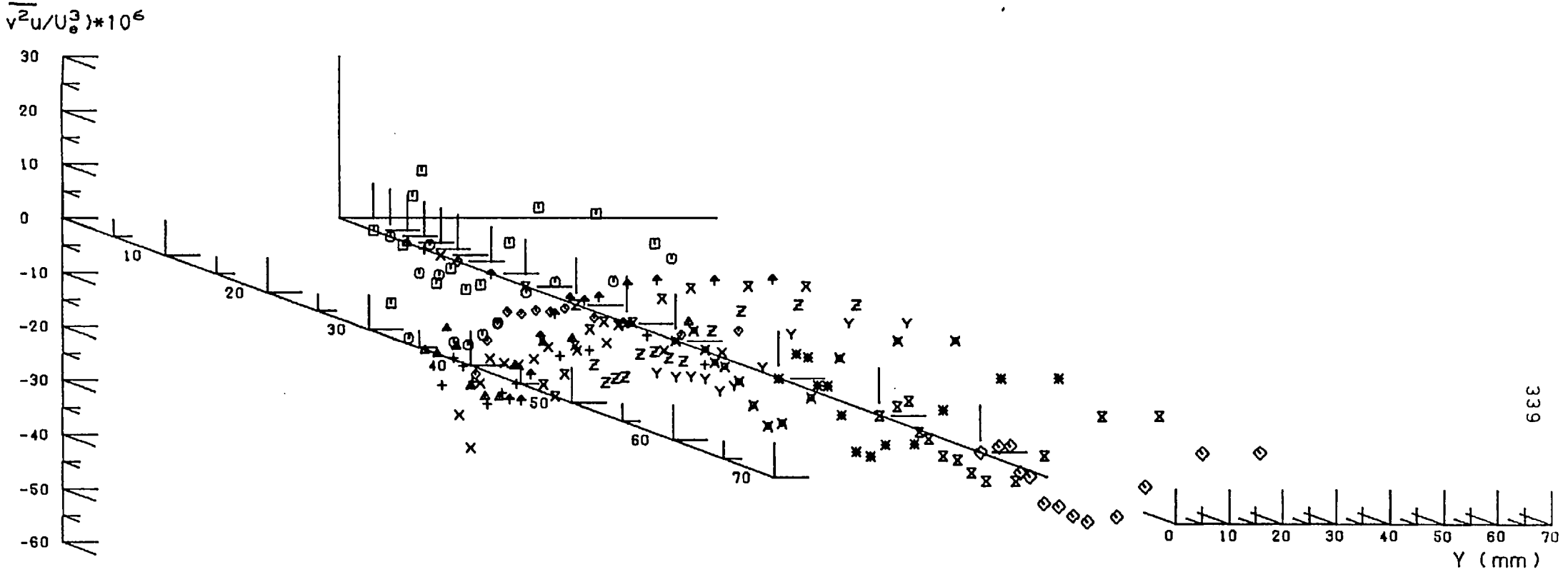

FIG.(D.5) PLOTS OF TRIPLE PRODUCT ($\overline{v^2u}$) AT STATION 5 (X= 613.8mm)

Results of Cross Wire in Vertical (U-V) Position

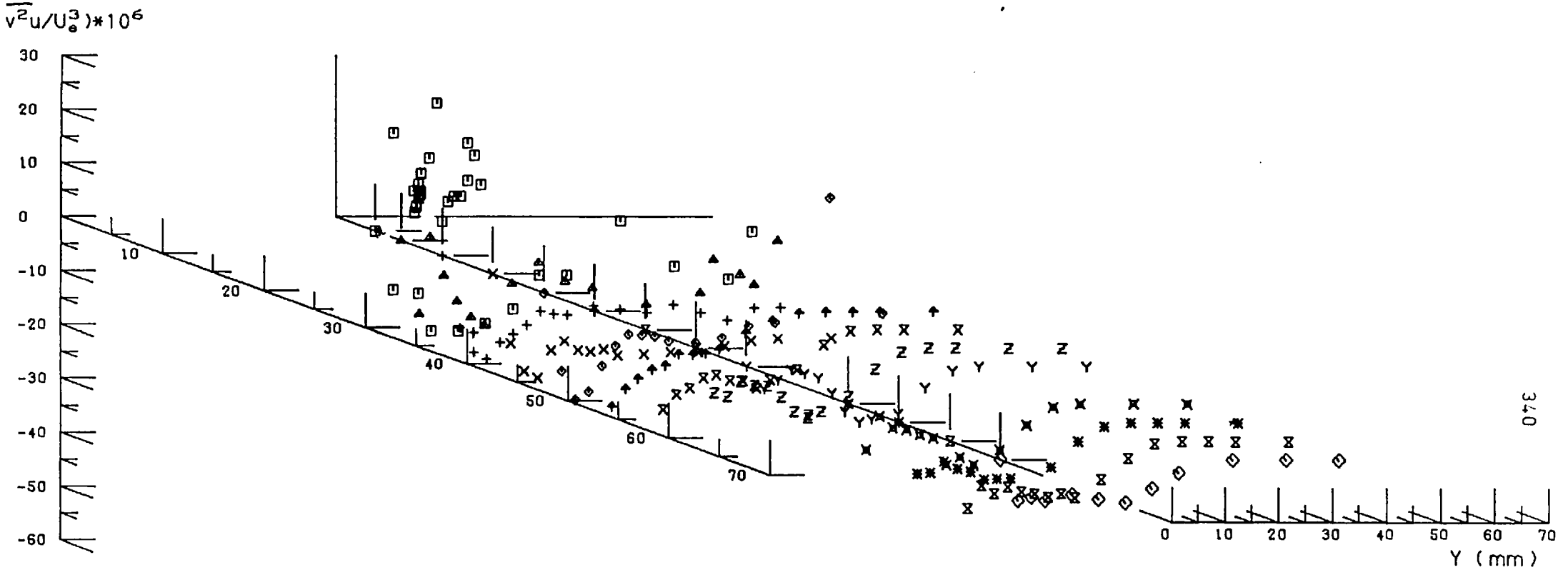

FIG.(D.6) PLOTS OF TRIPLE PRODUCT ($\overline{v^2u}$) AT STATION 9 (X=1223.4mm)

Results of Cross Wire in Vertical (U-V) Position

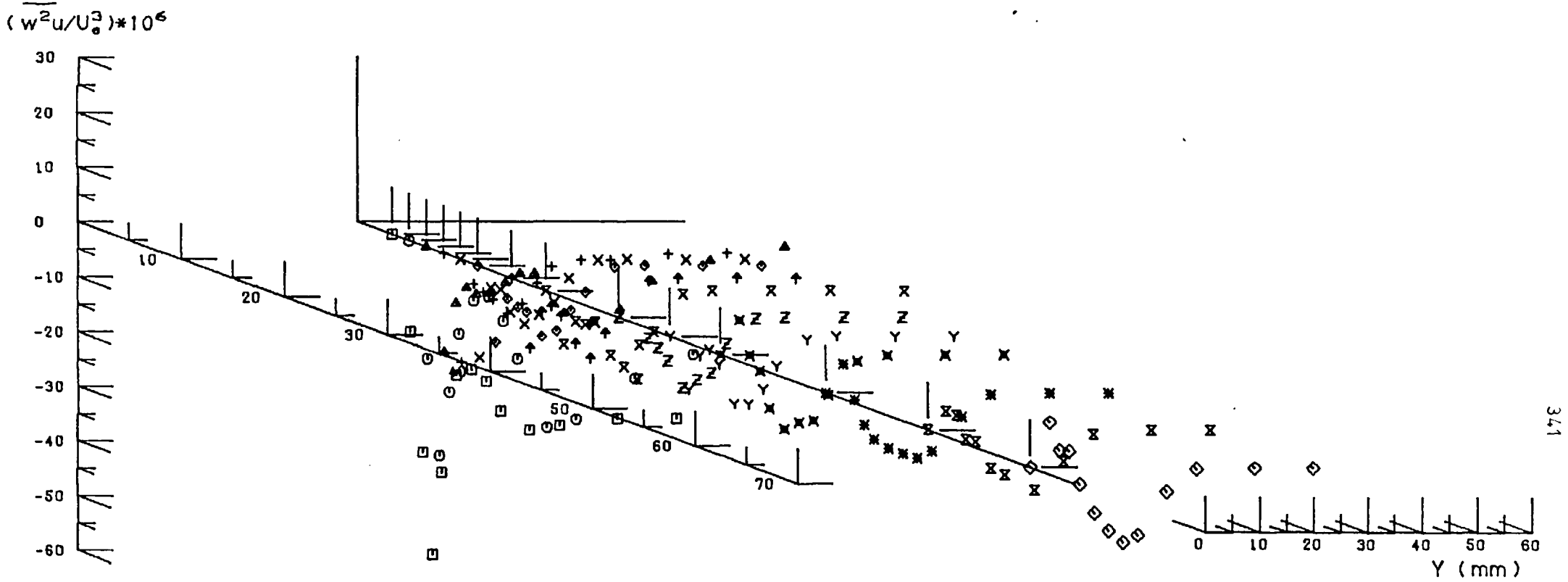

FIG.(D.7) PLOTS OF TRIPLE PRODUCT $(\overline{w^2u})$ AT STATION 2 (X= 156.6mm)

Results of Cross Wire in Horizontal (U-W) Position

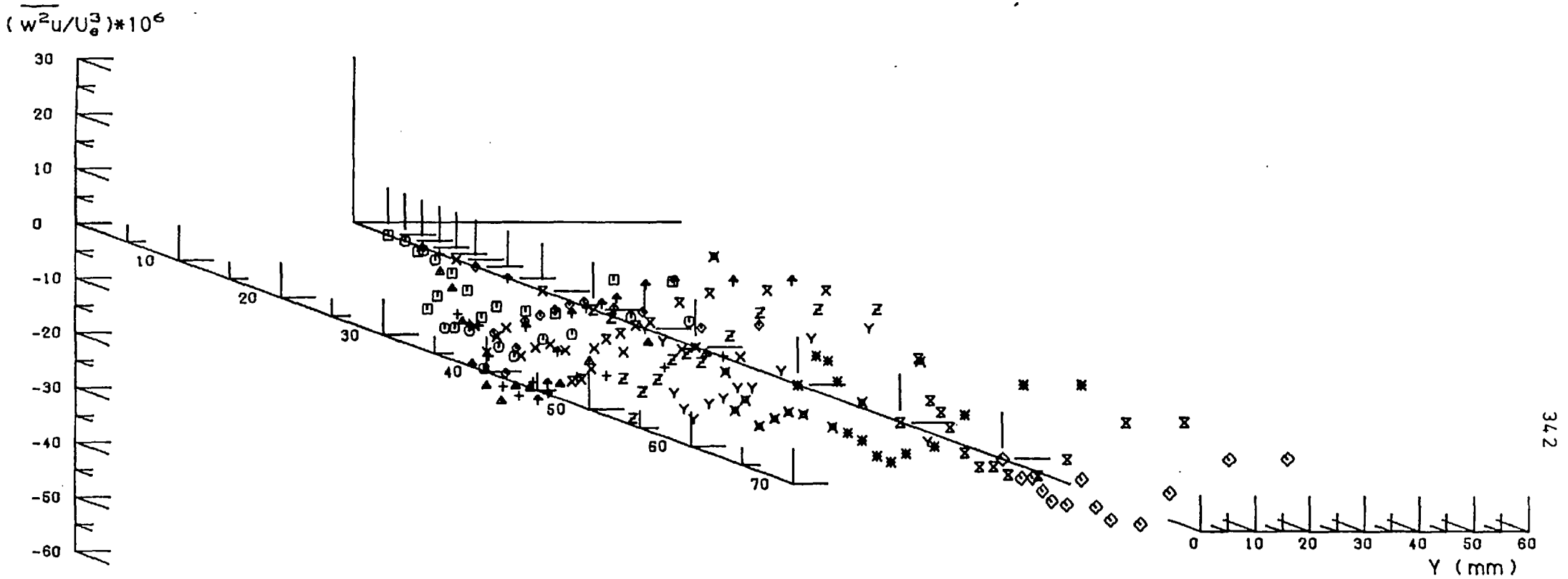

FIG.(D.8) PLOTS OF TRIPLE PRODUCT ($\overline{w^2u}$) AT STATION 5 (X= 613.8mm)

Results of Cross Wire in Horizontal (U-W) Position

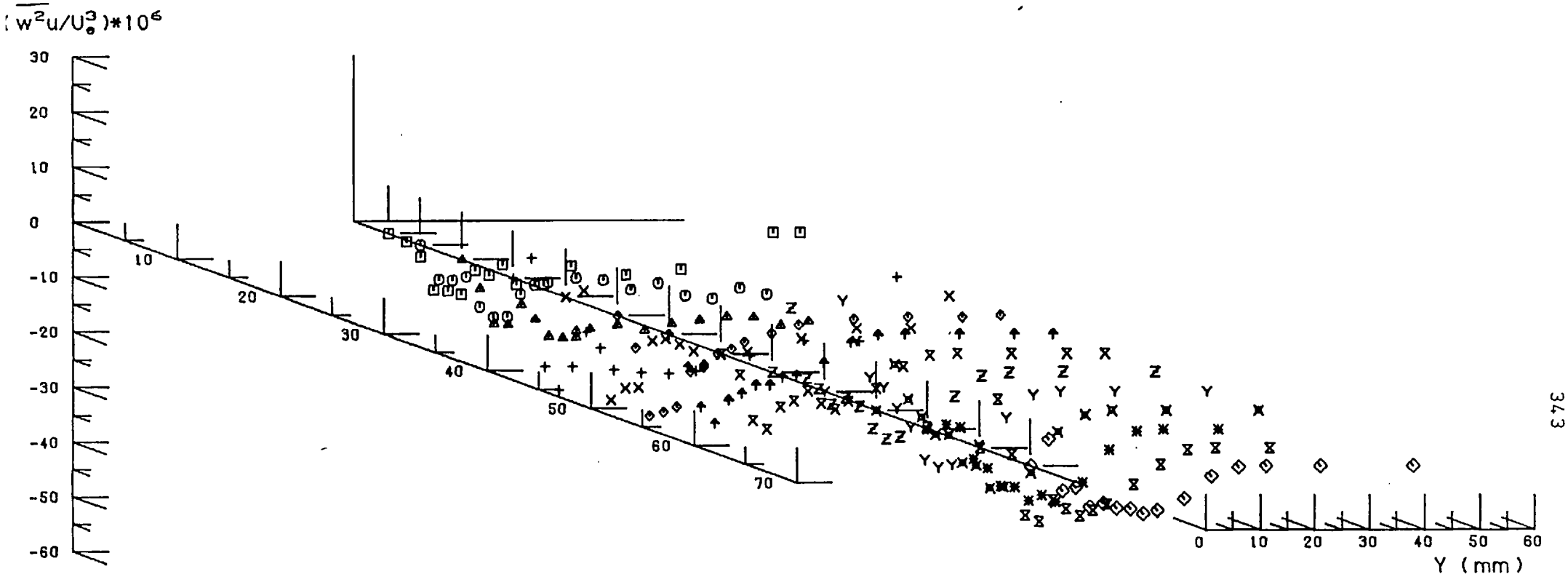

FIG.(D.9) PLOTS OF TRIPLE PRODUCT ($\overline{w^2u}$) AT STATION 9 (X=1223.4mm)

Results of Cross Wire in Horizontal (U-W) Position

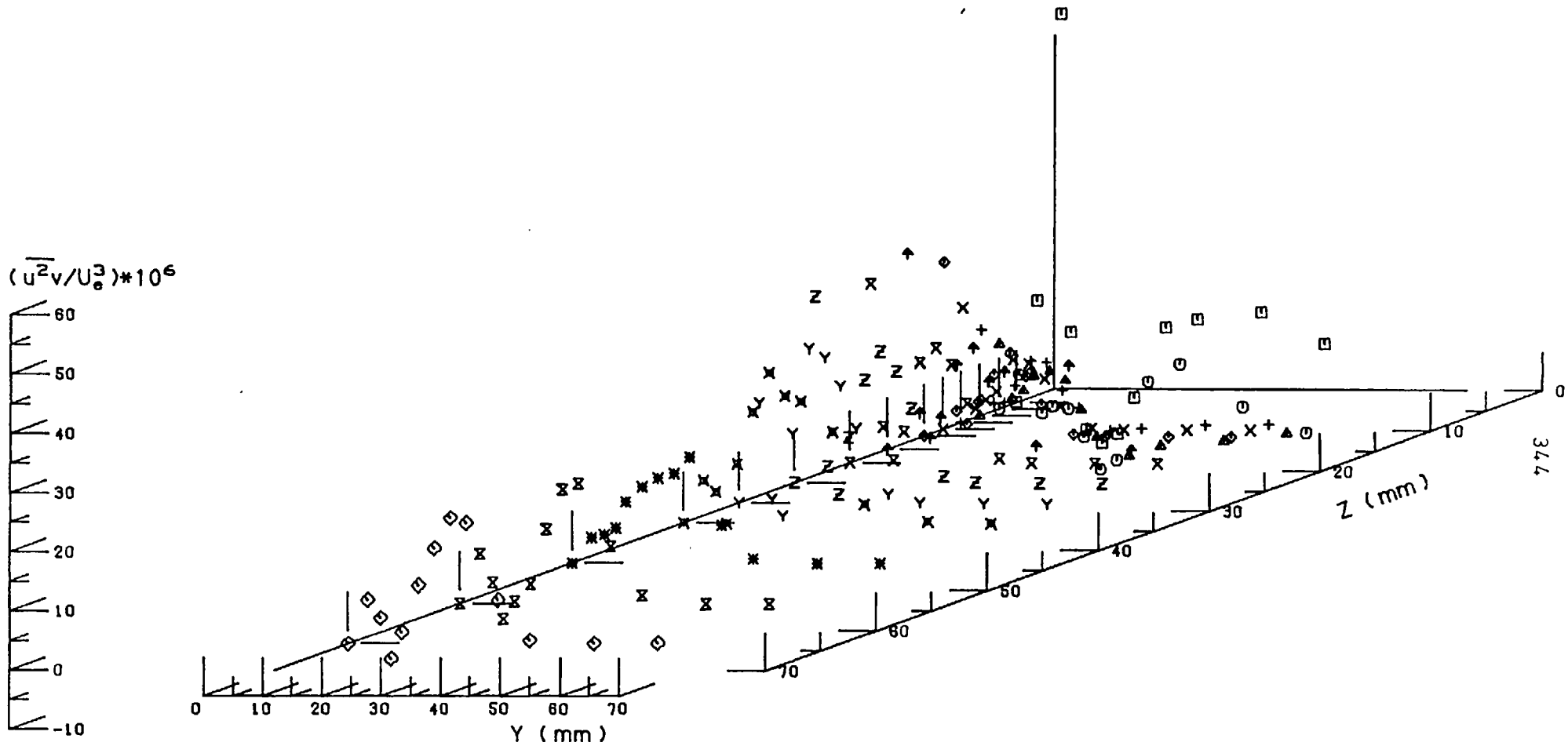

FIG.(D.10) PLOTS OF TRIPLE PRODUCT $(\overline{u^2v})$ AT STATION 2 (X= 156.6mm)

Results of Cross Wire in Vertical (U-V) Position

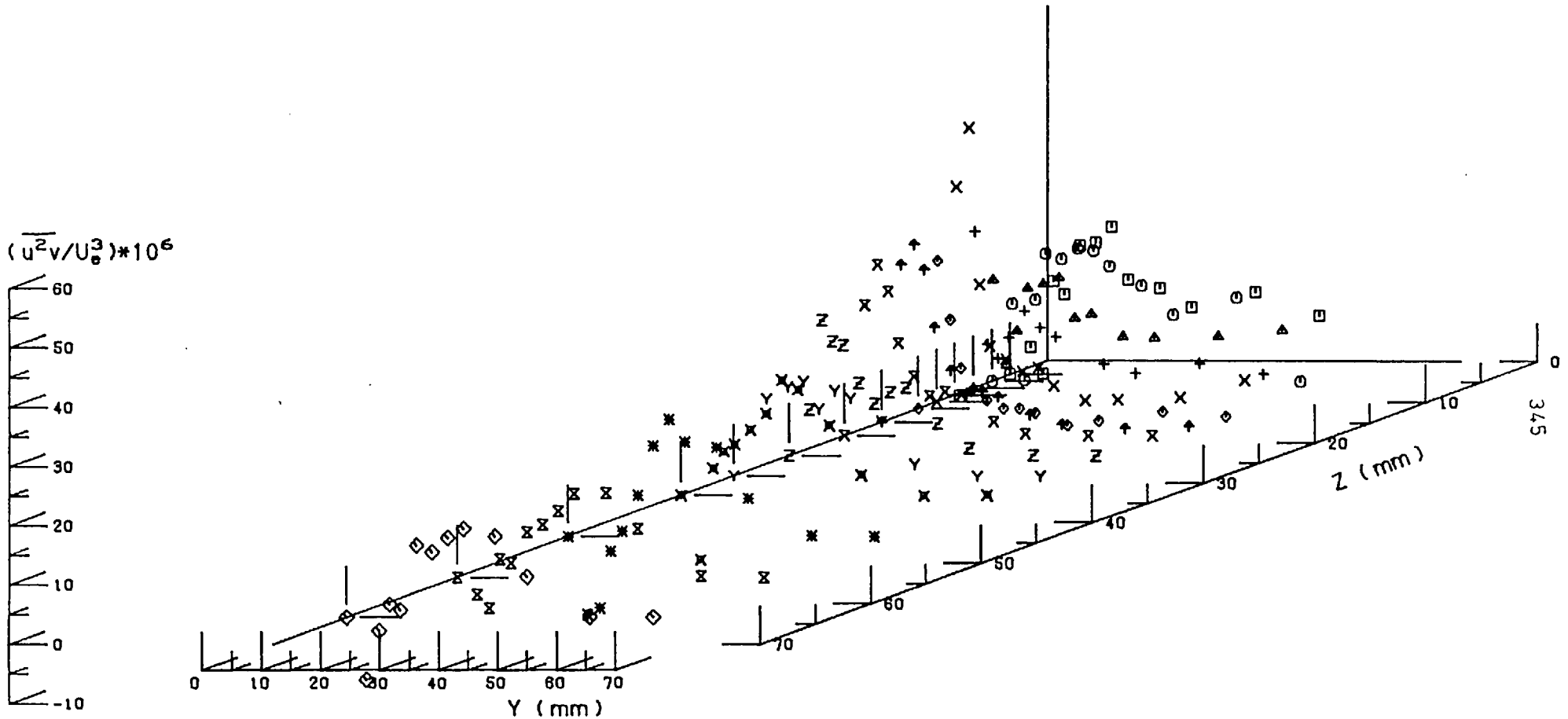

FIG.(D.11) PLOTS OF TRIPLE PRODUCT $(\overline{u^2v})$ AT STATION 5 (X= 613.8mm)

Results of Cross Wire in Vertical (U-V) Position

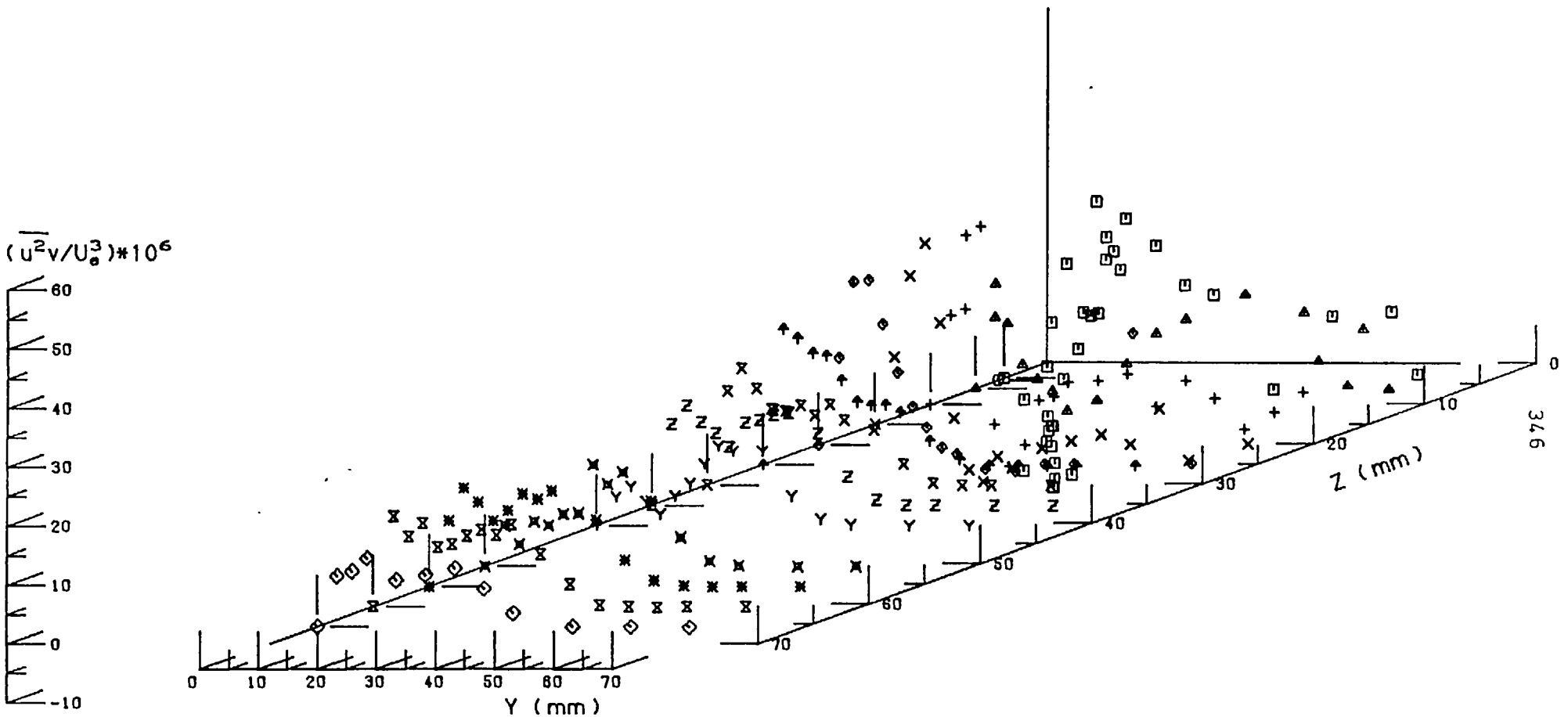

FIG.(D.12) PLOTS OF TRIPLE PRODUCT $(\overline{u^2v})$ AT STATION 9 (X=1223.4mm)

Results of Cross Wire in Vertical (U-V) Position

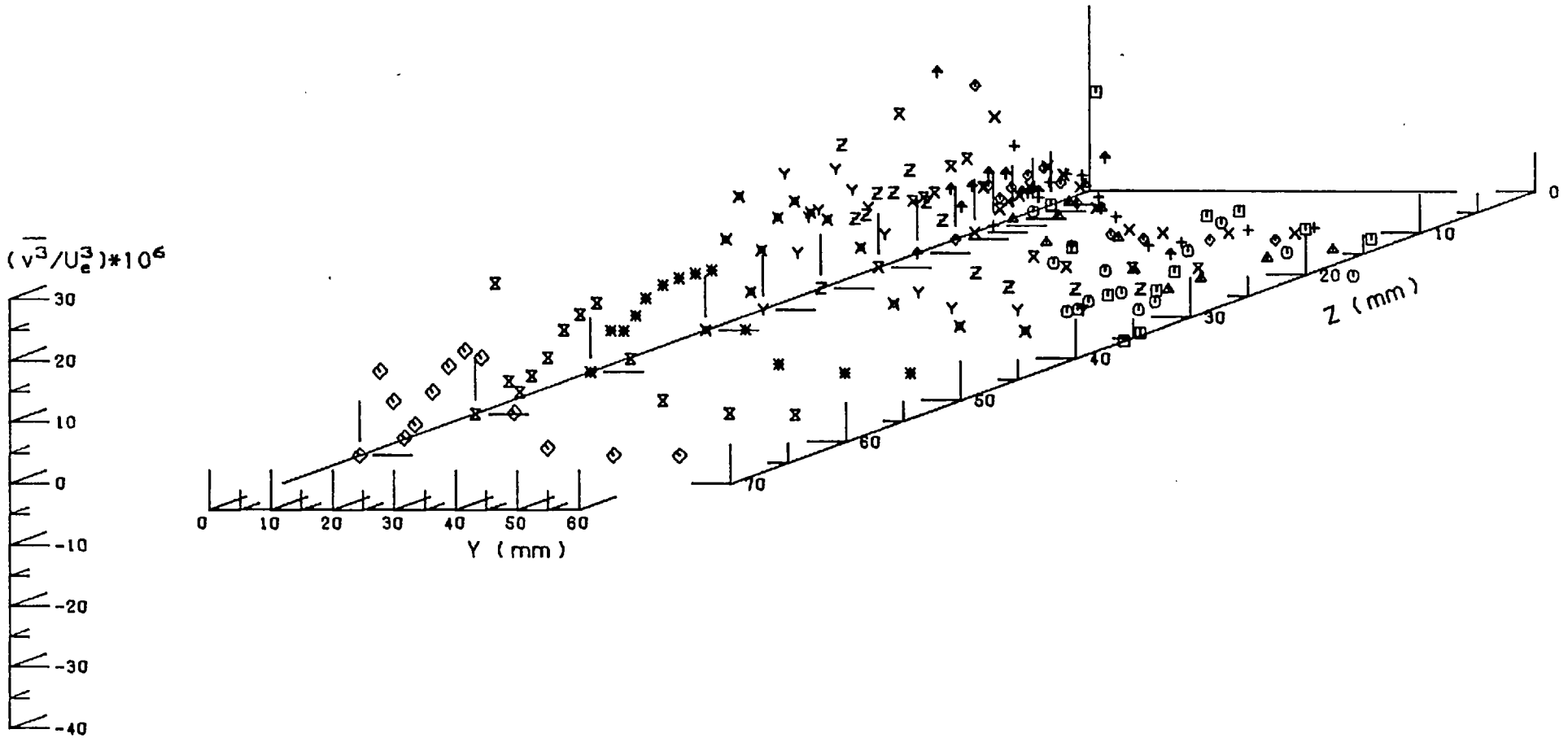

FIG.(D.13) PLOTS OF TRIPLE PRODUCT ($\overline{v^3}$) AT STATION 2 (X= 156.6mm)
Results of Cross Wire in Vertical (U-V) Position

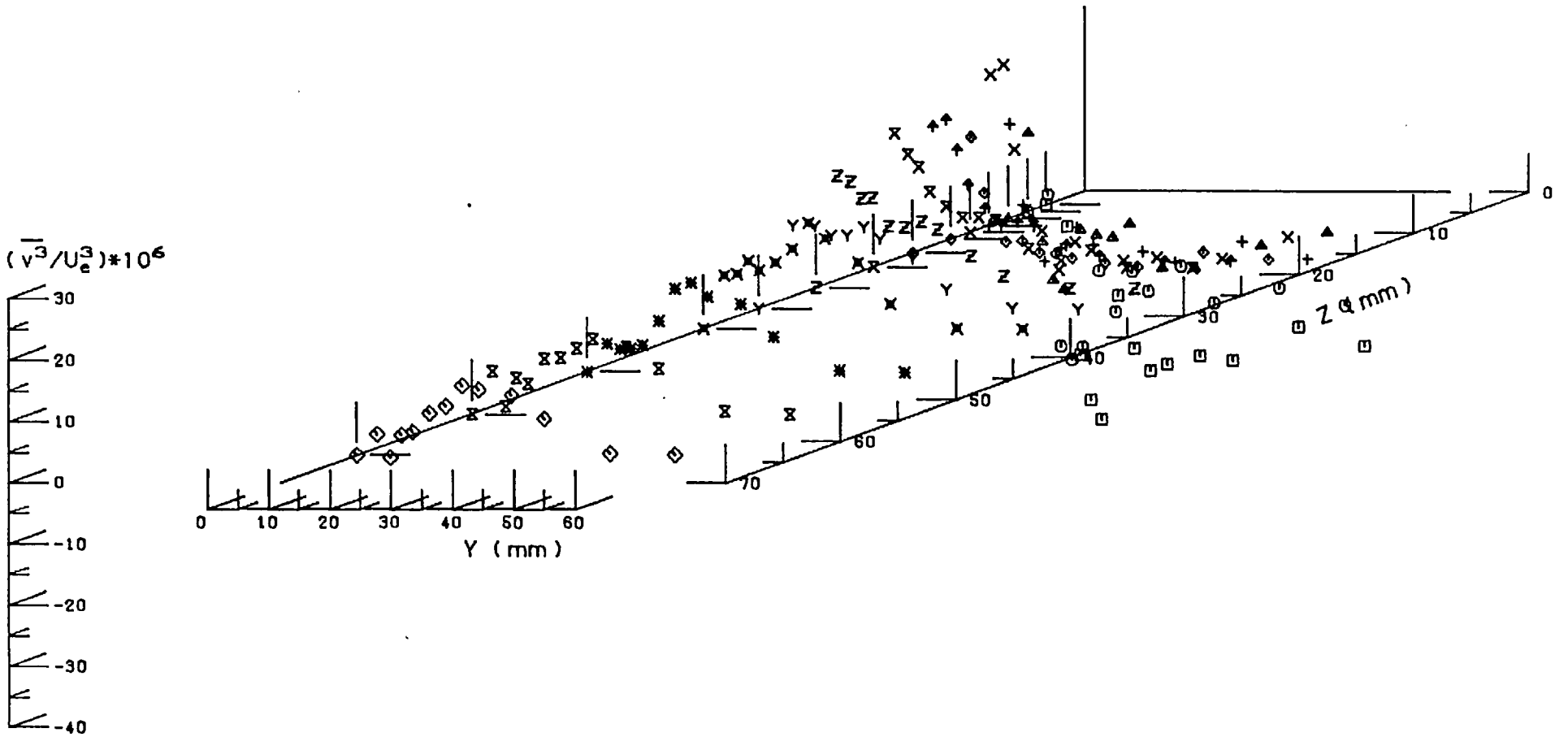

FIG.(D.14) PLOTS OF TRIPLE PRODUCT $(\overline{v^3})$ AT STATION 5 (X= 613.8mm)

Results of Cross Wire in Vertical (U-V) Position

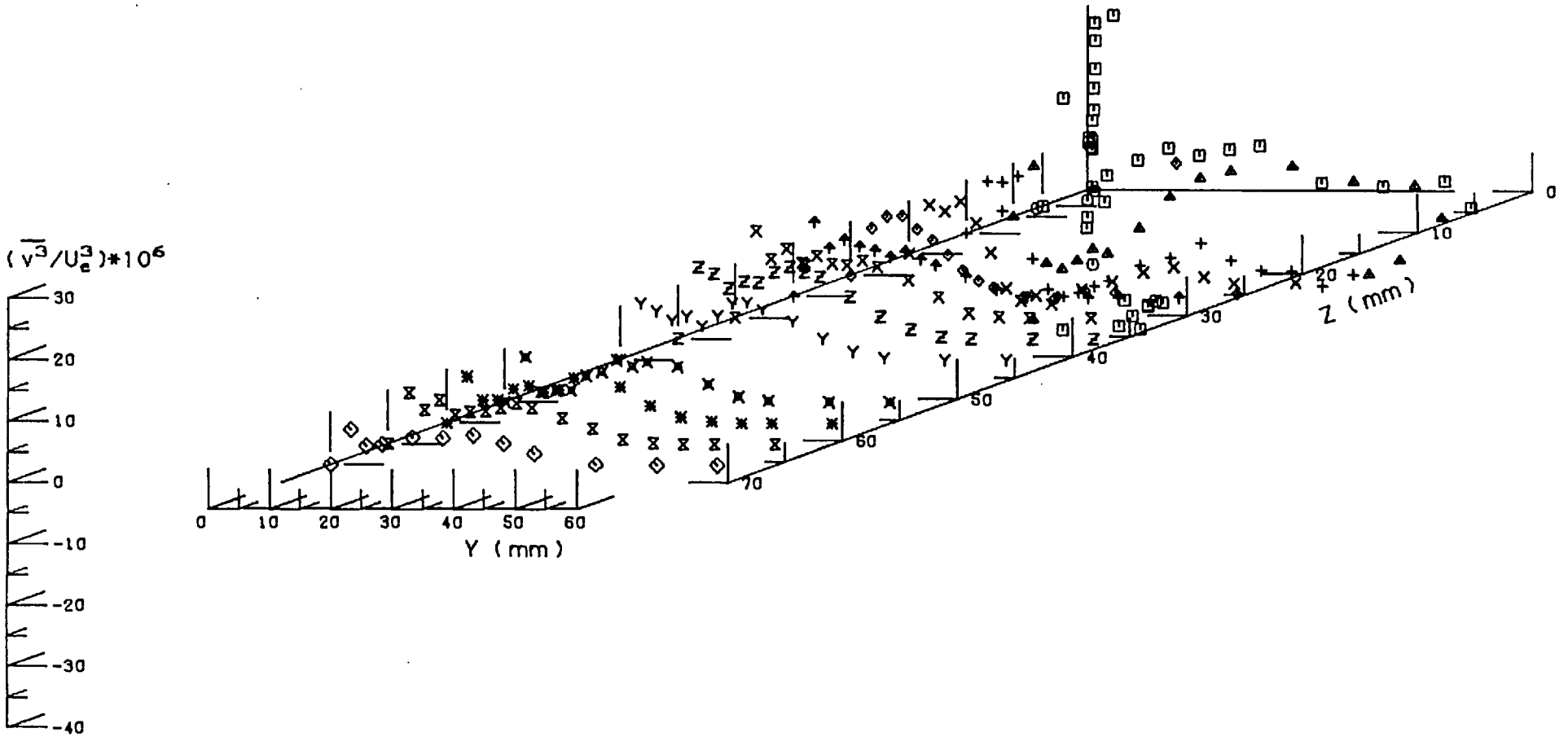

FIG.(D.15) PLOTS OF TRIPLE PRODUCT ($\overline{v^3}$) AT STATION 9 (X=1223.4mm)

Results of Cross Wire in Vertical (U-V) Position

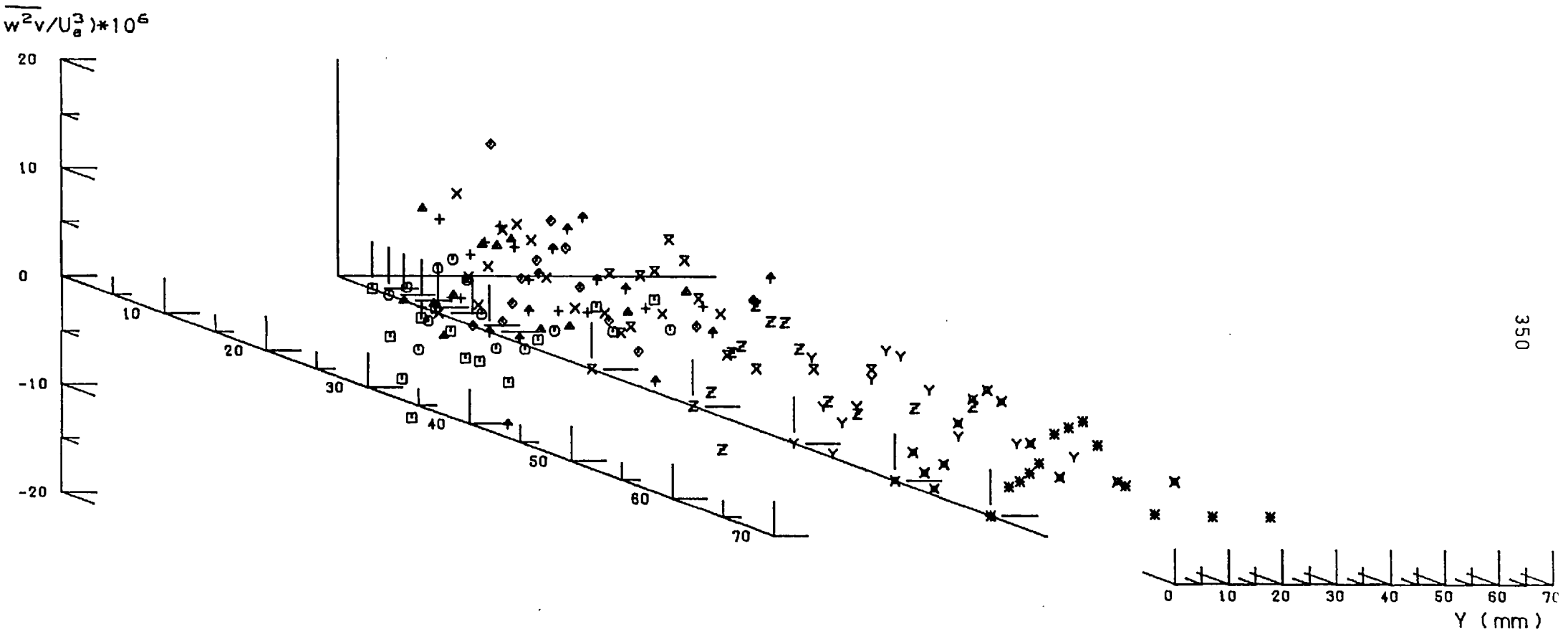

FIG.(D·16) PLOTS OF TRIPLE PRODUCT ($\overline{w^2v}$) AT STATION 2 (X= 156.6mm)

Results of Cross Wire

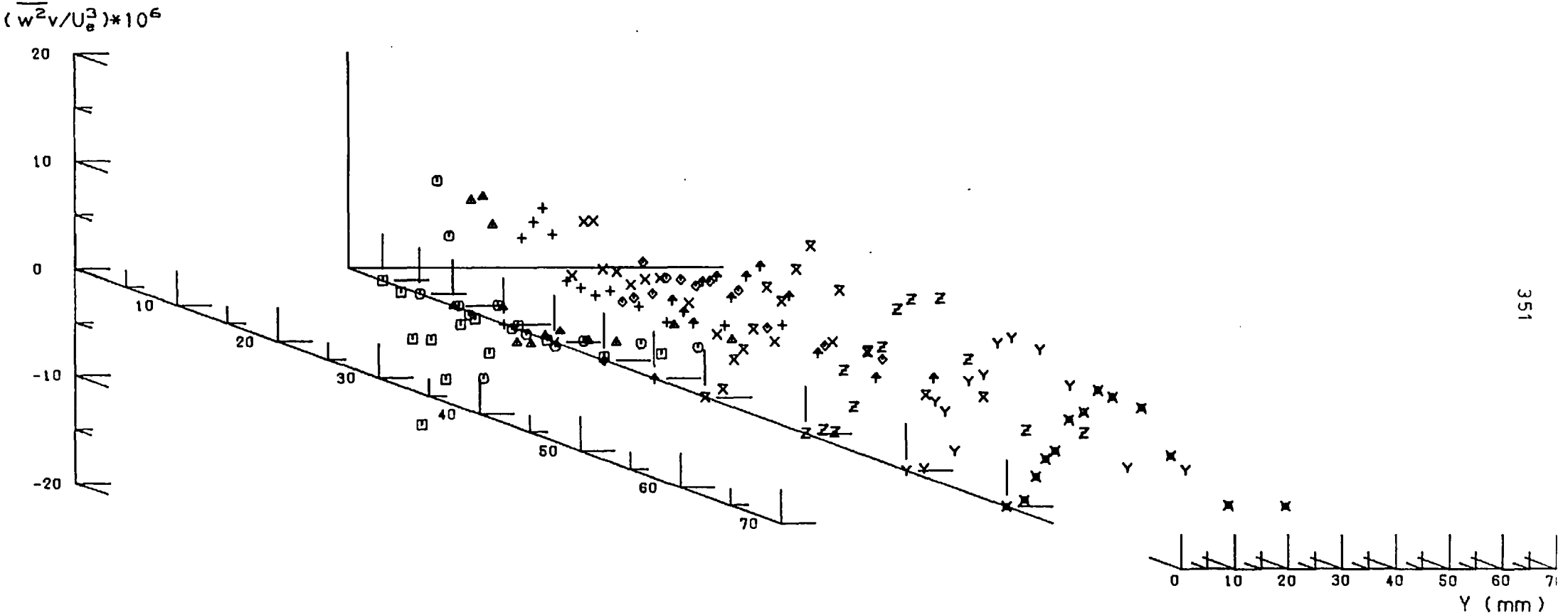

FIG.(D.17) PLOTS OF TRIPLE PRODUCT $(\overline{w^2v})$ AT STATION 5 (X= 613.8mm)

Results of Cross Wire

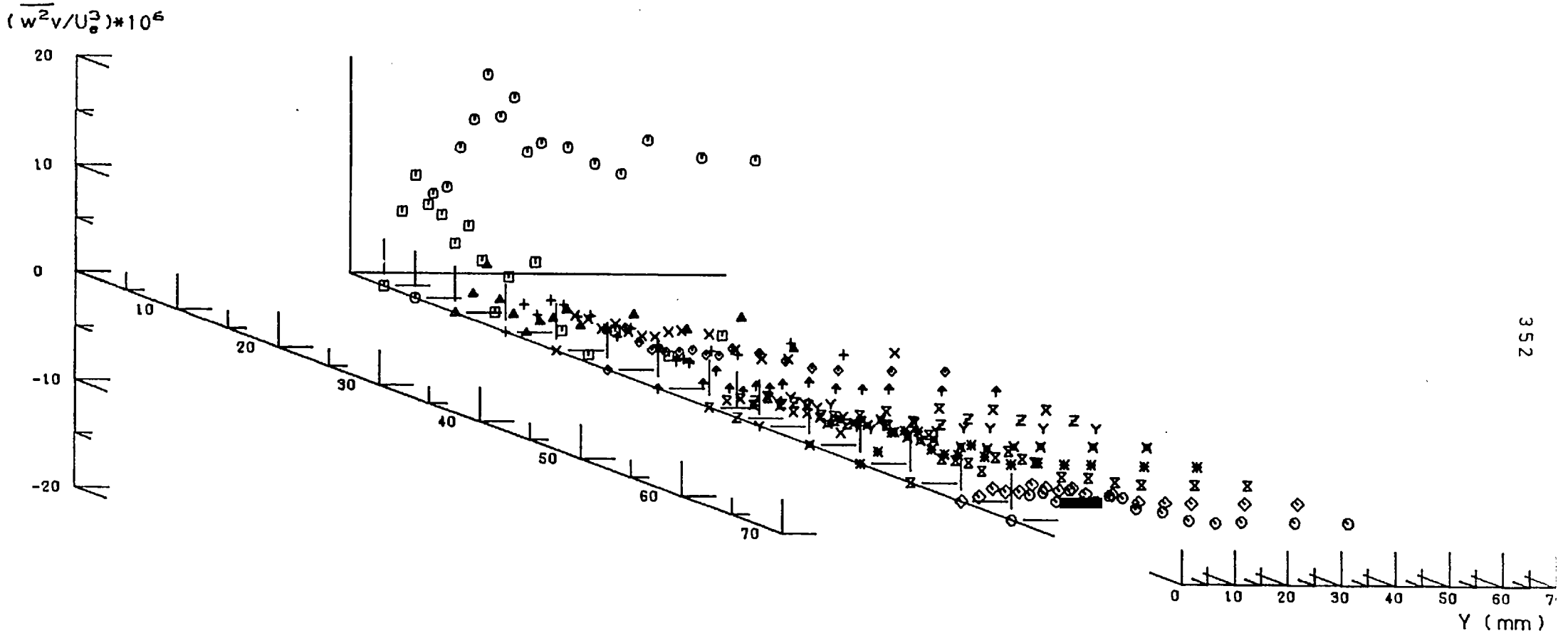

FIG.(D.18) PLOTS OF TRIPLE PRODUCT ($\overline{w^2v}$) AT STATION 9 (X=1223.4mm)
Results of Cross Wire

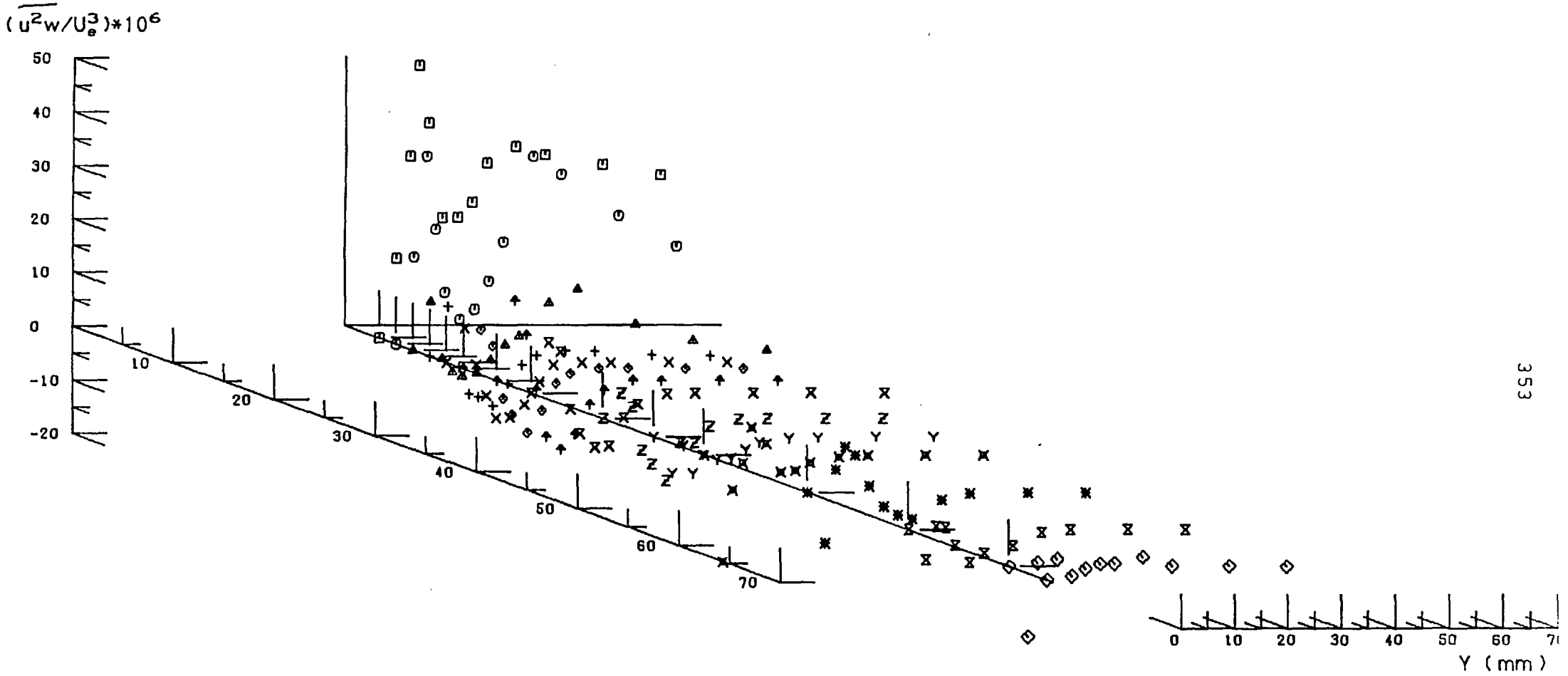

FIG.(D.19) PLOTS OF TRIPLE PRODUCT ($\overline{u^2w}$) AT STATION 2 (X= 156.6mm)

Results of Cross Wire in Horizontal (U-W) Position

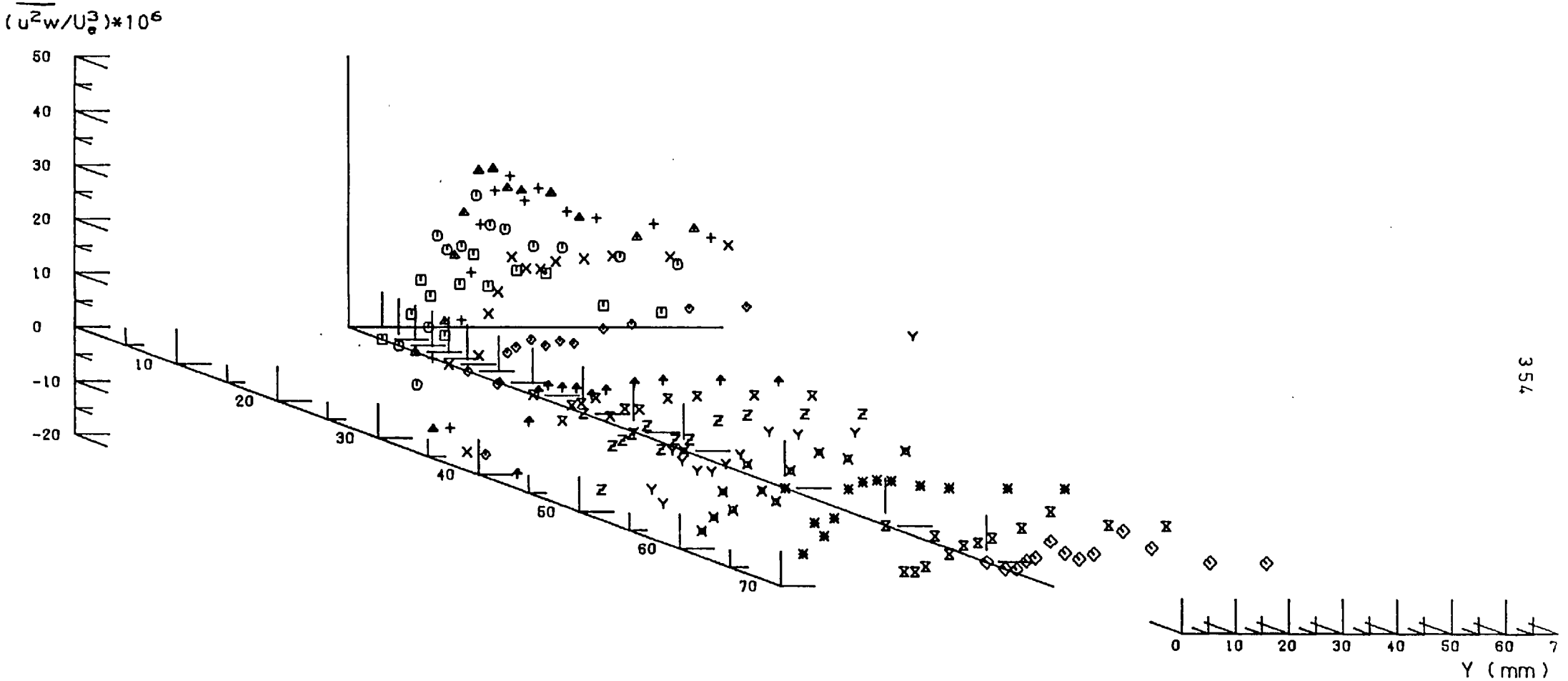

FIG.(D.20) PLOTS OF TRIPLE PRODUCT $(\overline{u^2w})$ AT STATION 5 (X= 613.8mm)

Results of Cross Wire in Horizontal (U-W) Position

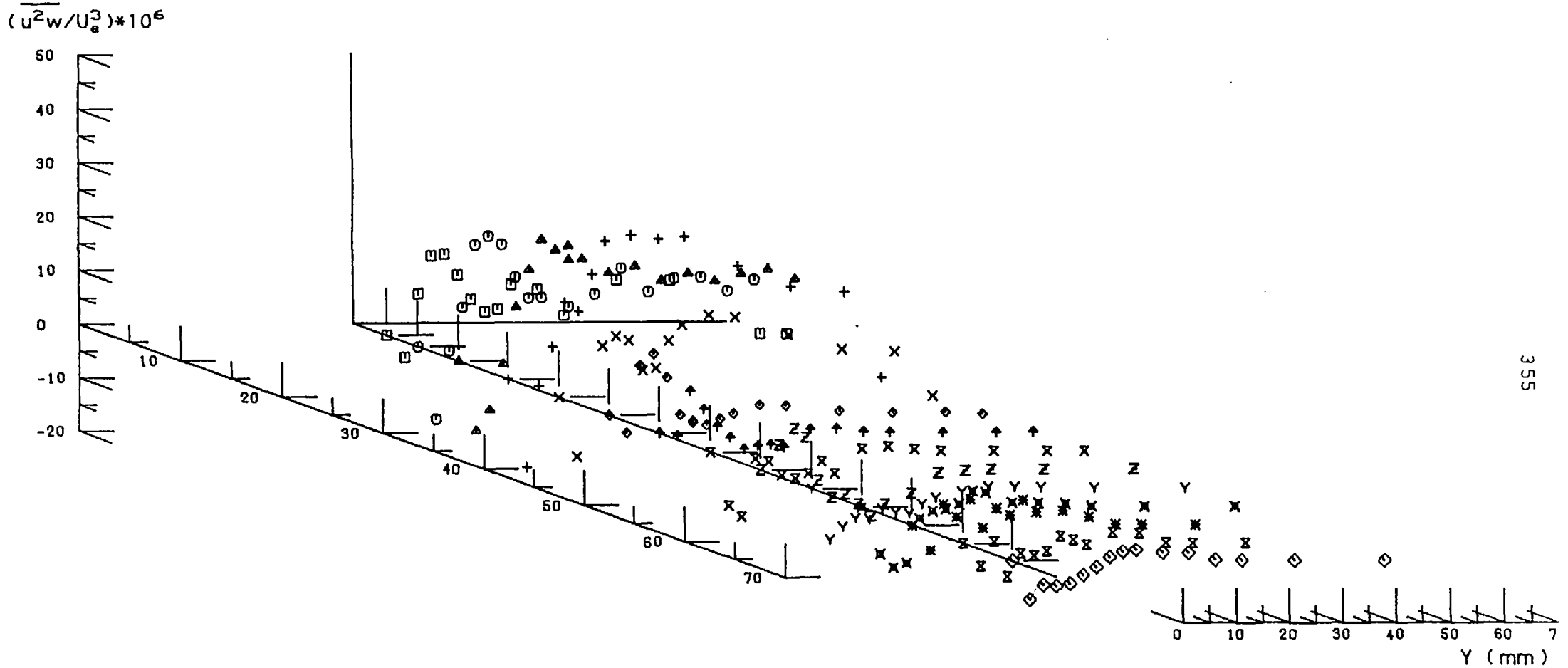

FIG.(D.21) PLOTS OF TRIPLE PRODUCT ($\overline{u^2w}$) AT STATION 9 (X=1223.4mm)

Results of Cross Wire in Horizontal (U-W) Position

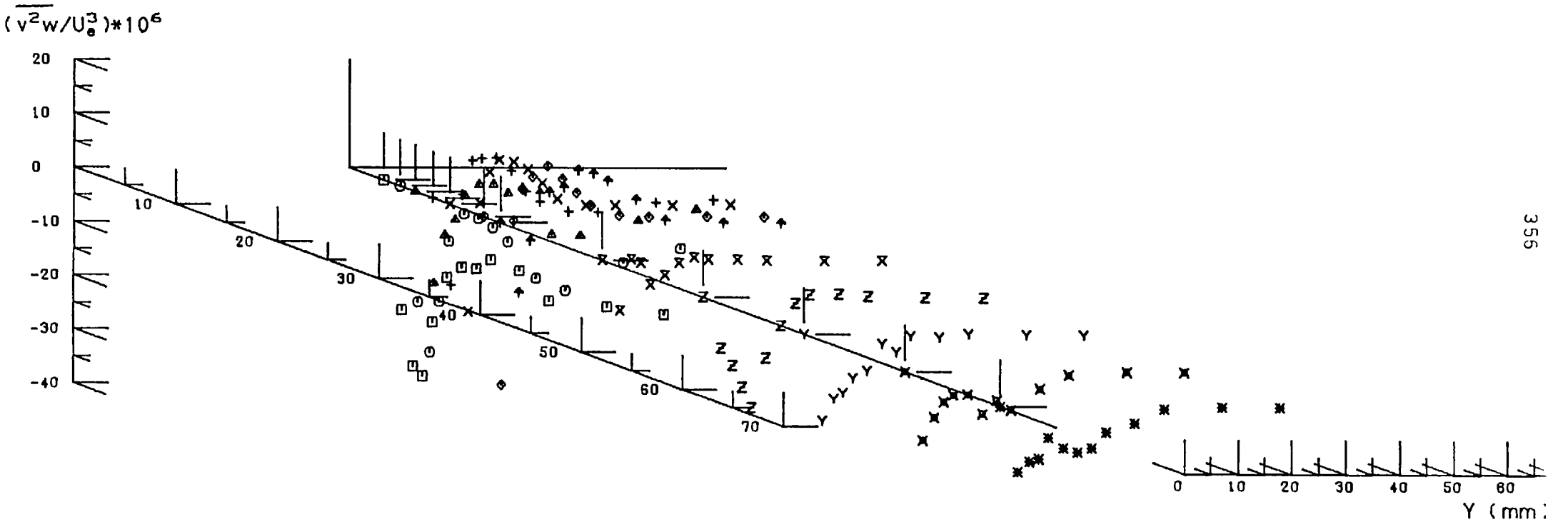

FIG.(D.22) PLOTS OF TRIPLE PRODUCT $(\overline{v^2w})$ AT STATION 2 (X= 156.6mm)
Results of Cross Wire

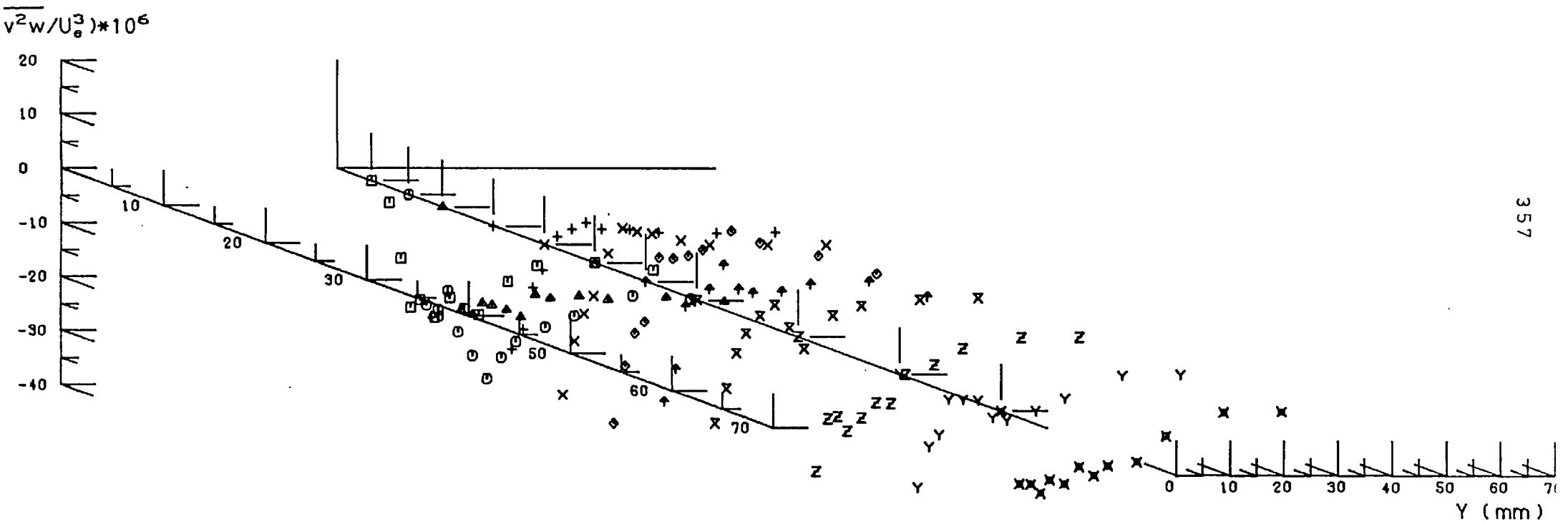

FIG.(D.23) PLOTS OF TRIPLE PRODUCT ($\overline{v^2w}$) AT STATION 5 (X= 613.8mm)
Results of Cross Wire

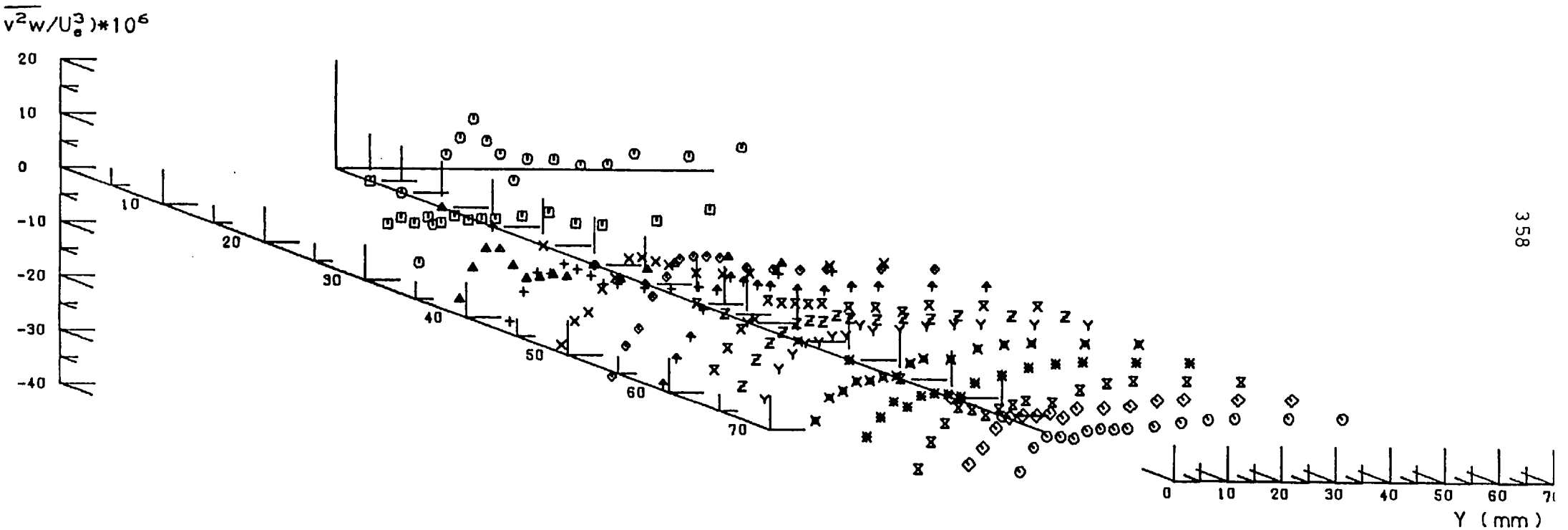

FIG.(D.24) PLOTS OF TRIPLE PRODUCT ($\overline{v^2w}$) AT STATION 9 (X=1223.4mm)

Results of Cross Wire

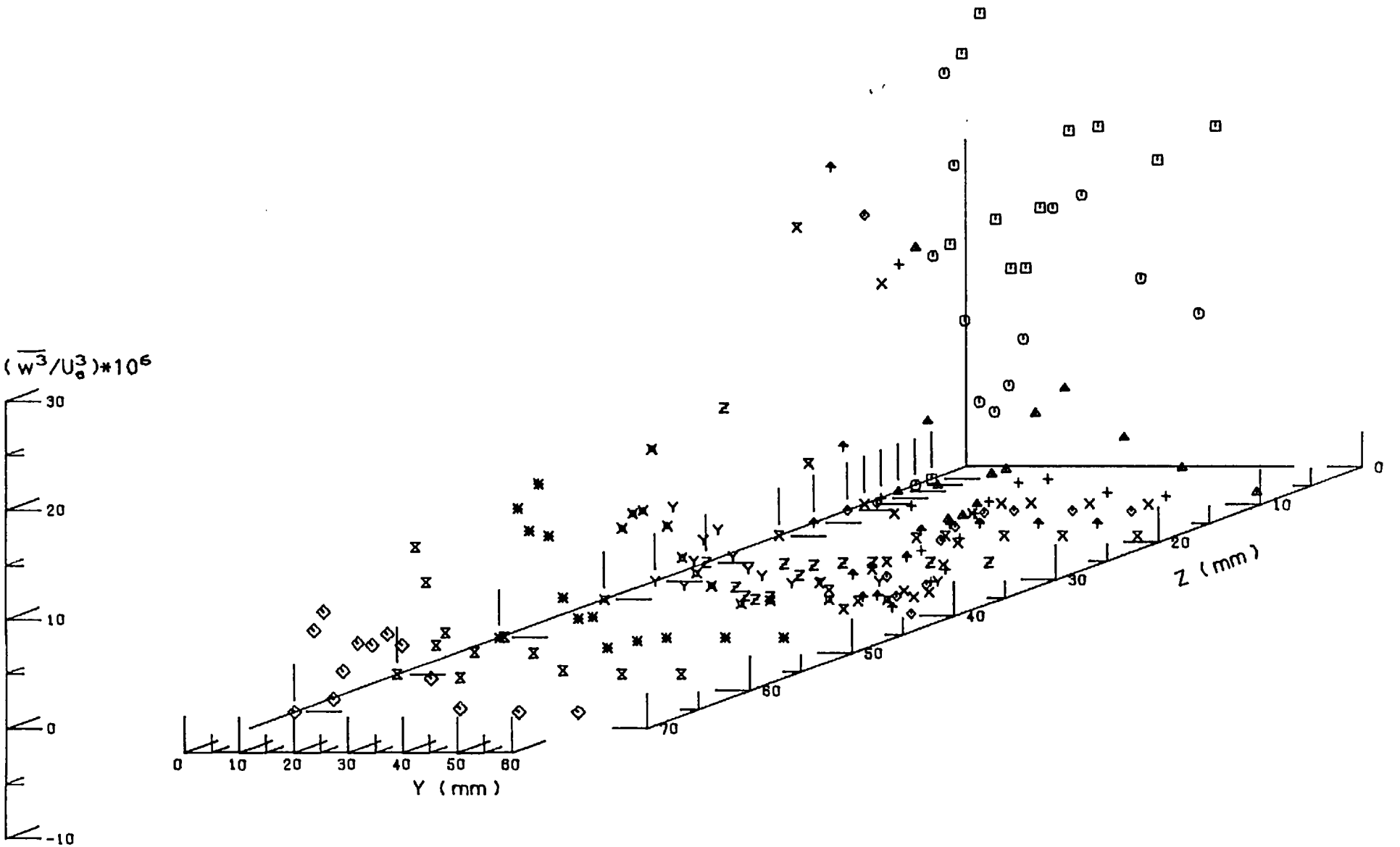

FIG.(D.25) PLOTS OF TRIPLE PRODUCT $(\overline{w^3})$ AT STATION 2 (X= 156.6mm)
Results of Cross Wire in Horizontal (U-W) Position

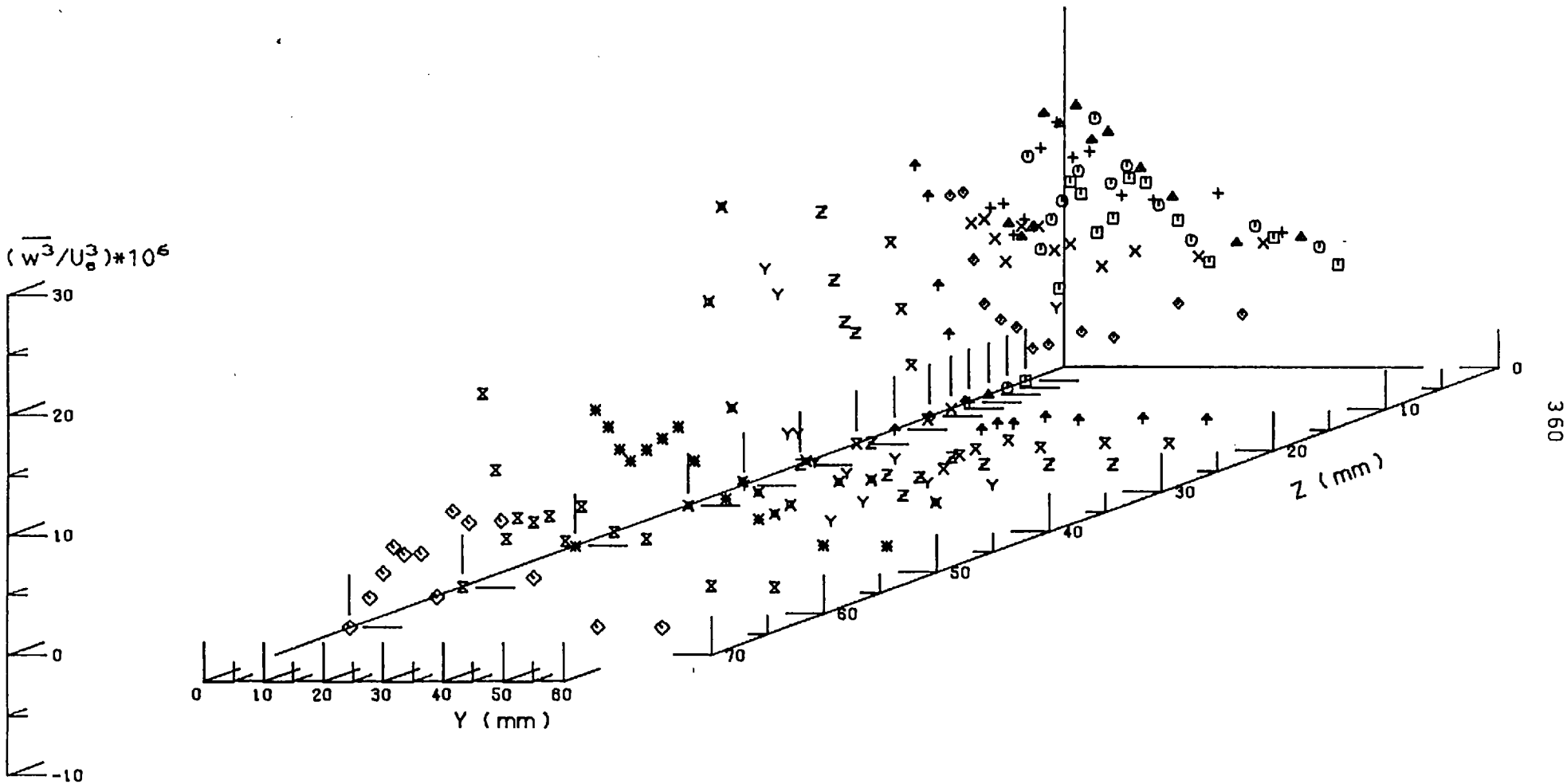

FIG.(D.26) PLOTS OF TRIPLE PRODUCT ($\overline{w^3}$) AT STATION 5 (X= 613.8mm)

Results of Cross Wire In Horizontal (U-W) Position

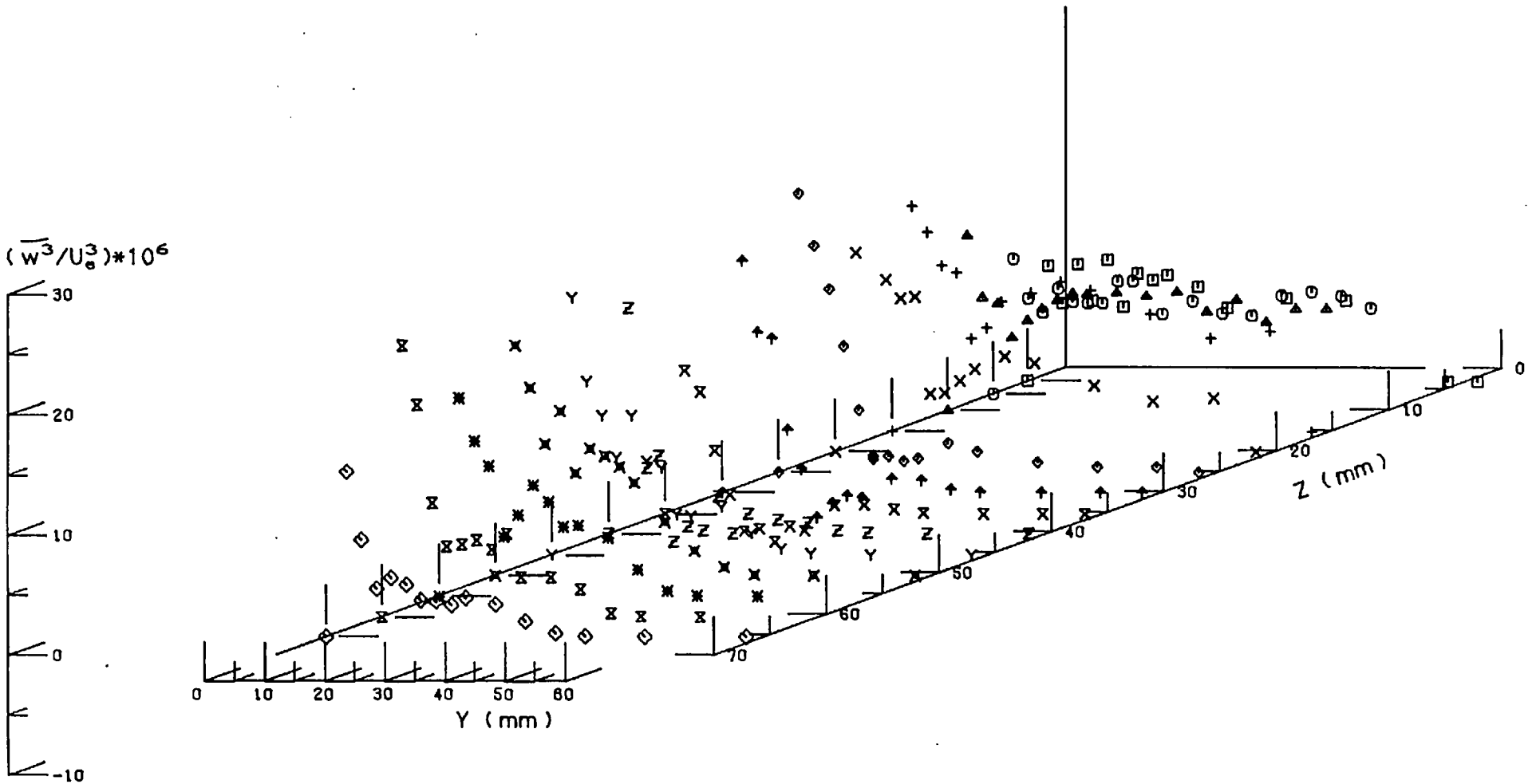

FIG.(D.27) PLOTS OF TRIPLE PRODUCT $(\overline{w^3})$ AT STATION 9 (X=1223.4mm)

Results of Cross Wire in Horizontal (U-W) Position

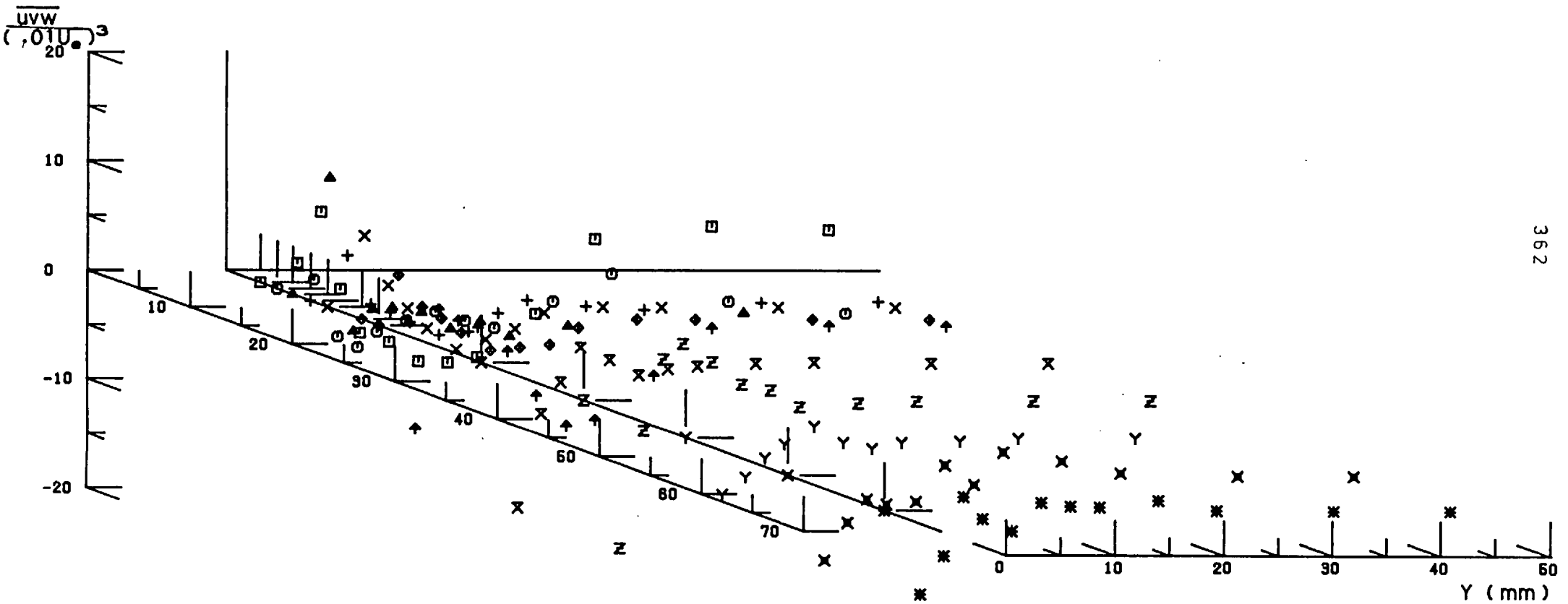

FIG.(D.28) $\overline{uvw}/(.01U_\infty)^3$ AT STATION 2 (X= 156.6 mm)
Results Of Cross Wire

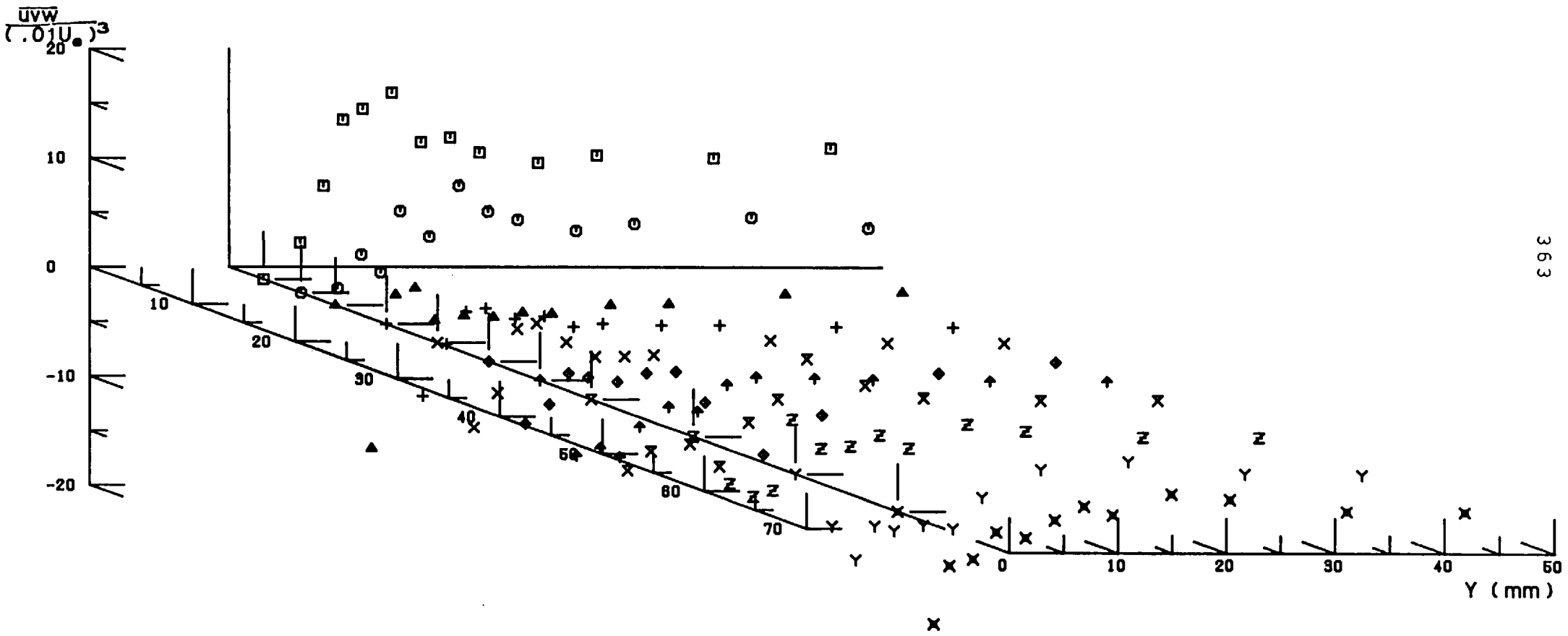

FIG.(D.29) $\overline{uvw}/(.01U_\infty)^3$ AT STATION 5 (X= 613.8 mm)
Results Of Cross Wire

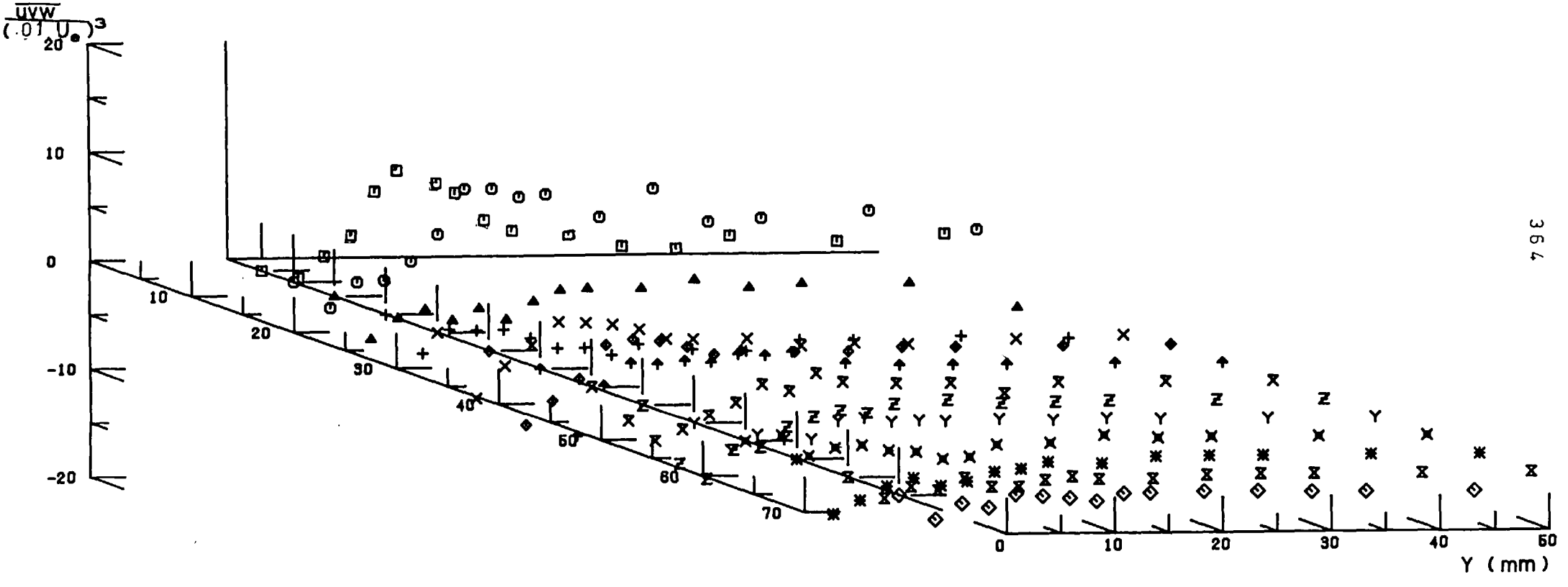

FIG.(D.30) $\overline{uvw}/(.01U_e)^3$ AT STATION 9 (X=1223.4 mm)
Results Of Cross Wire

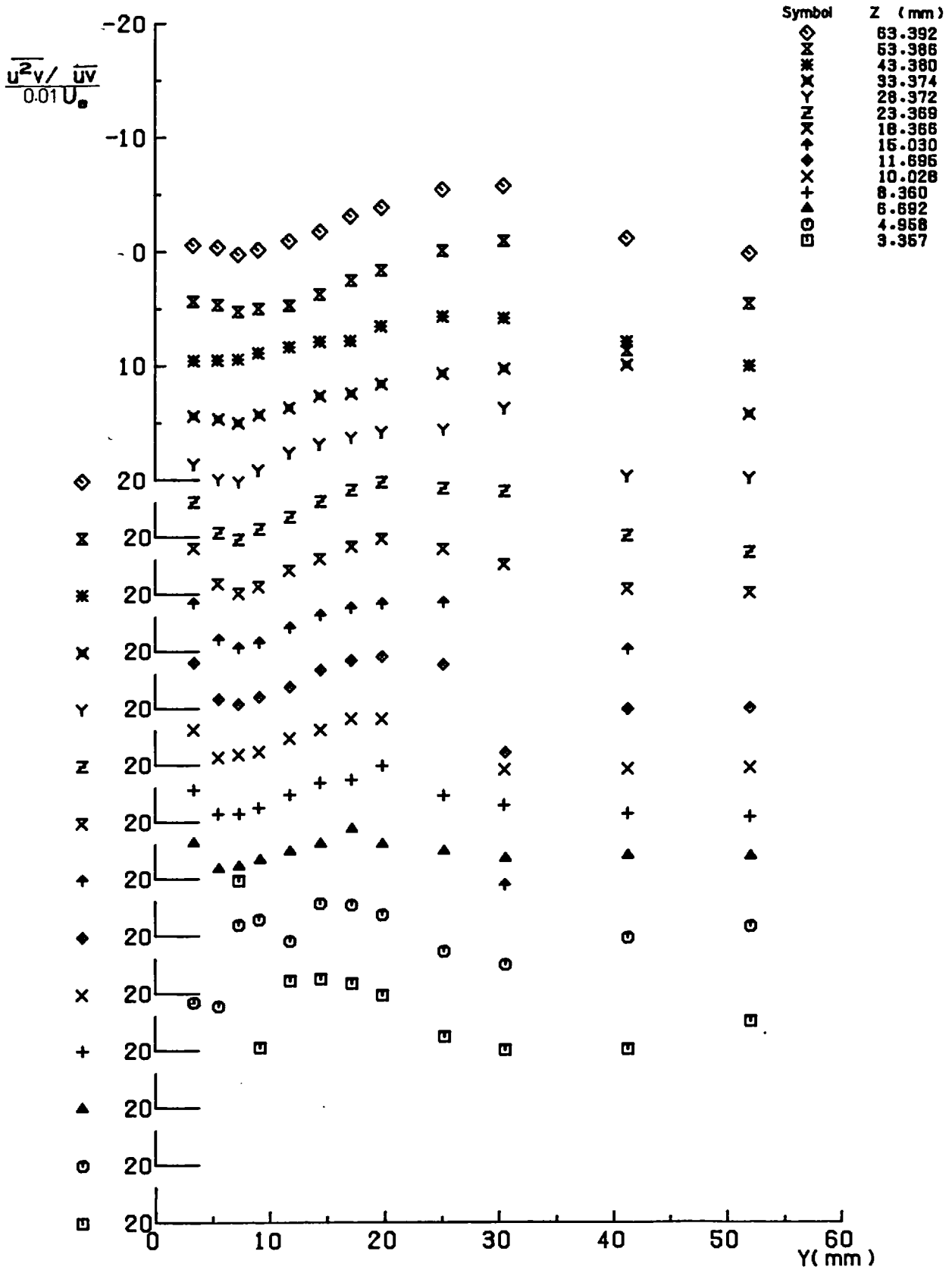

FIG.(D.31) $\overline{u^2v}/\ \overline{uv}$ AT STATION 2 (X= 156.6 mm)

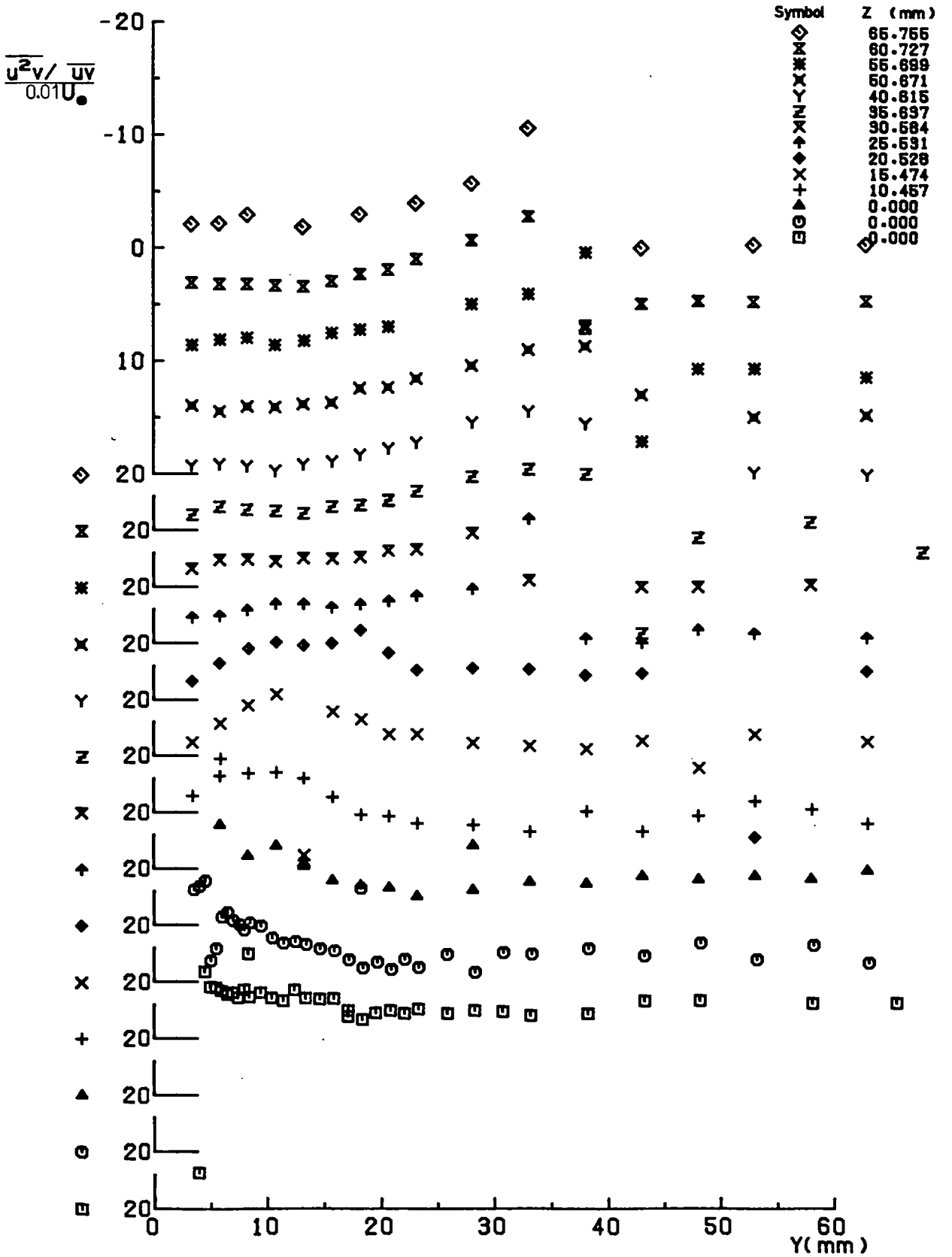

FIG.(D.32) $\overline{u^2v}/\overline{uv}$ AT STATION 9 (X=1223.4 mm)

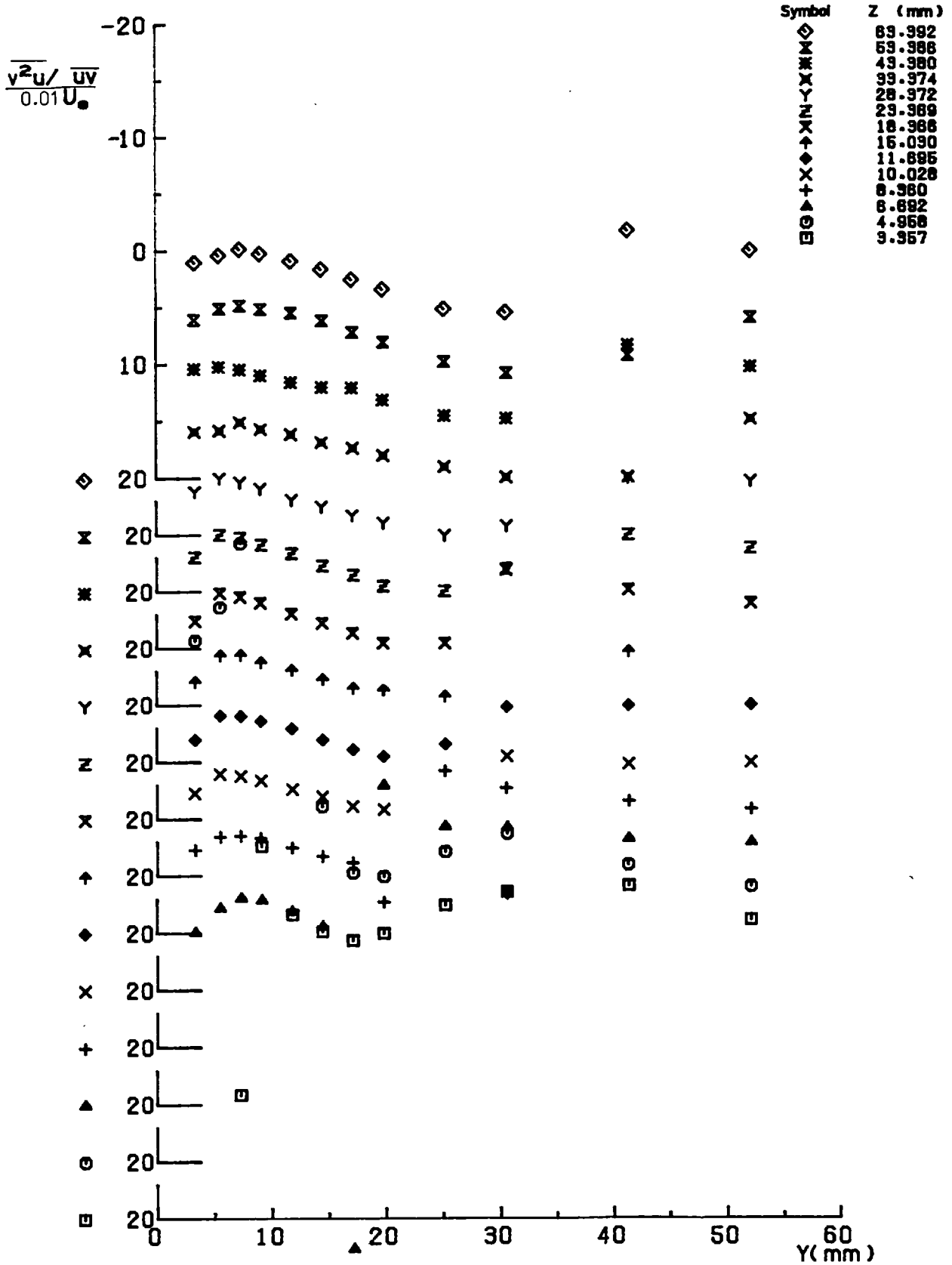

FIG.(D-33) $\overline{v^2u}/\ \overline{uv}$ AT STATION 2 (X= 156.6 mm)

Cross Wire Measurements

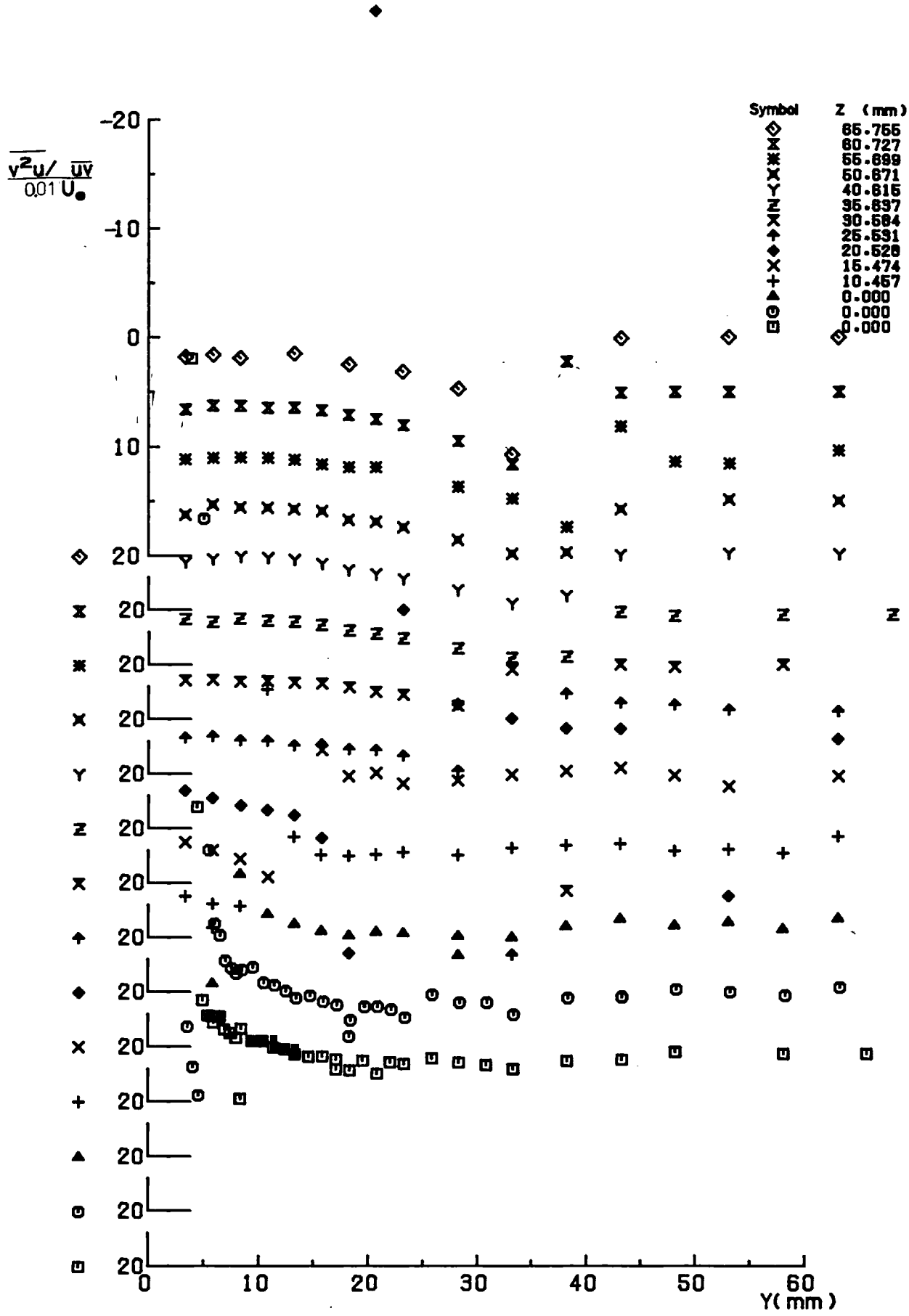

FIG.(D.34) $\overline{v^2u}/\ \overline{uv}$ AT STATION 9 (X=1223.4 mm)

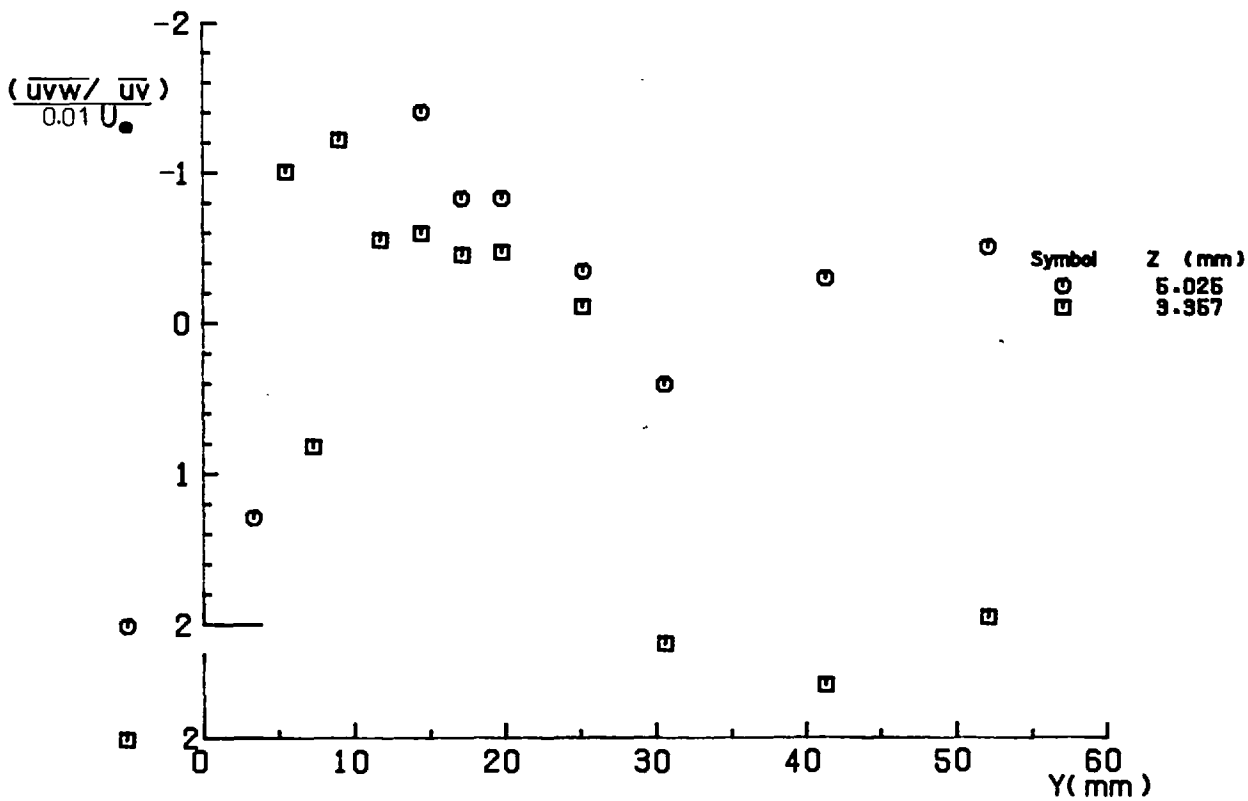

FIG.(D.35.a) $\overline{uvw}/\overline{uv}$ AT STATION 2 (X= 156.6 mm)

Cross Wire Measurements

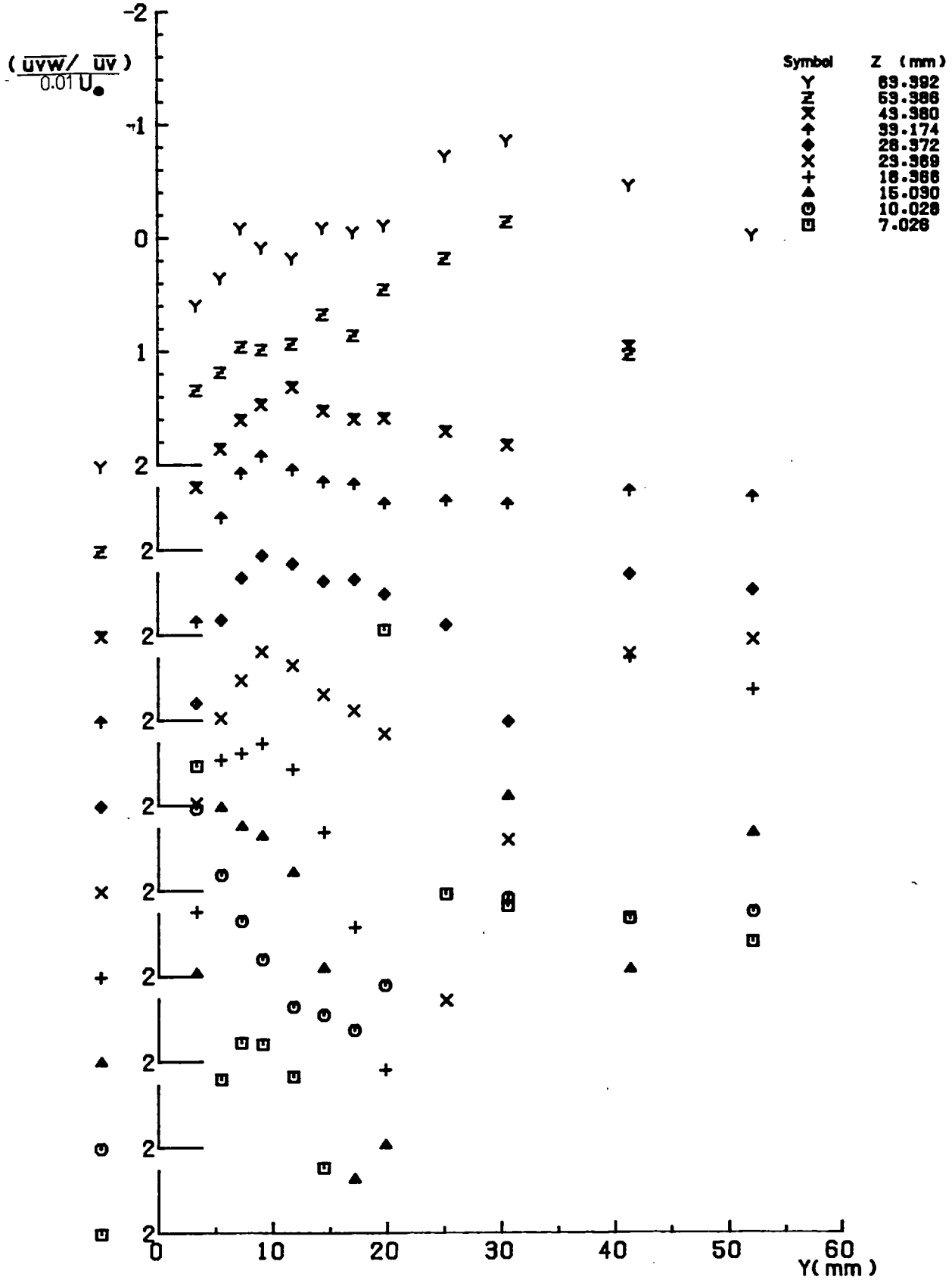

FIG.(D.35.b) $\overline{uvw}/\overline{uv}$ AT STATION 2 (X= 156.6 mm)

Cross Wire Measurements

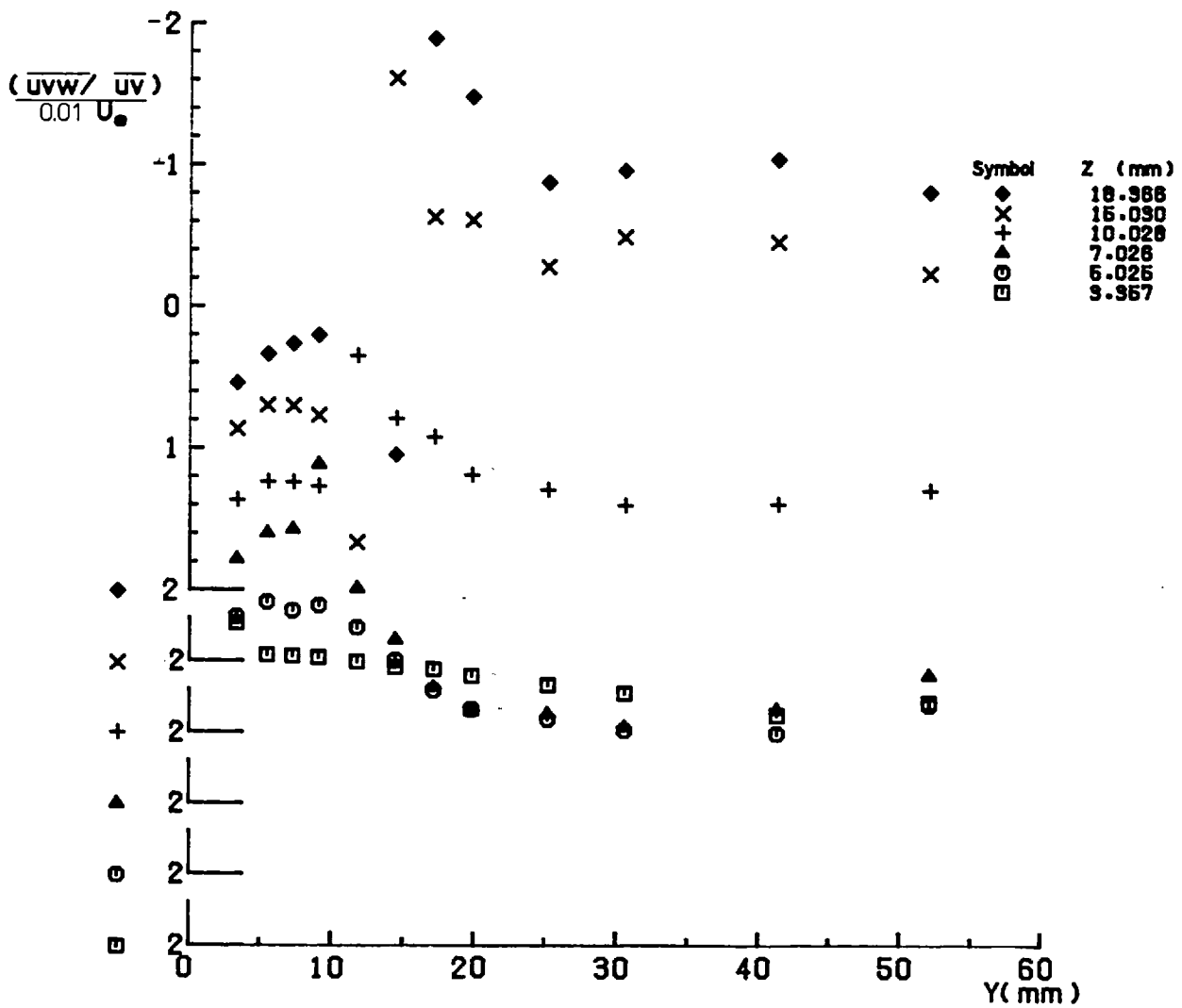

FIG.(D.36-a) $\overline{uvw}/\overline{uv}$ AT STATION 9 (X=1223.4 mm)

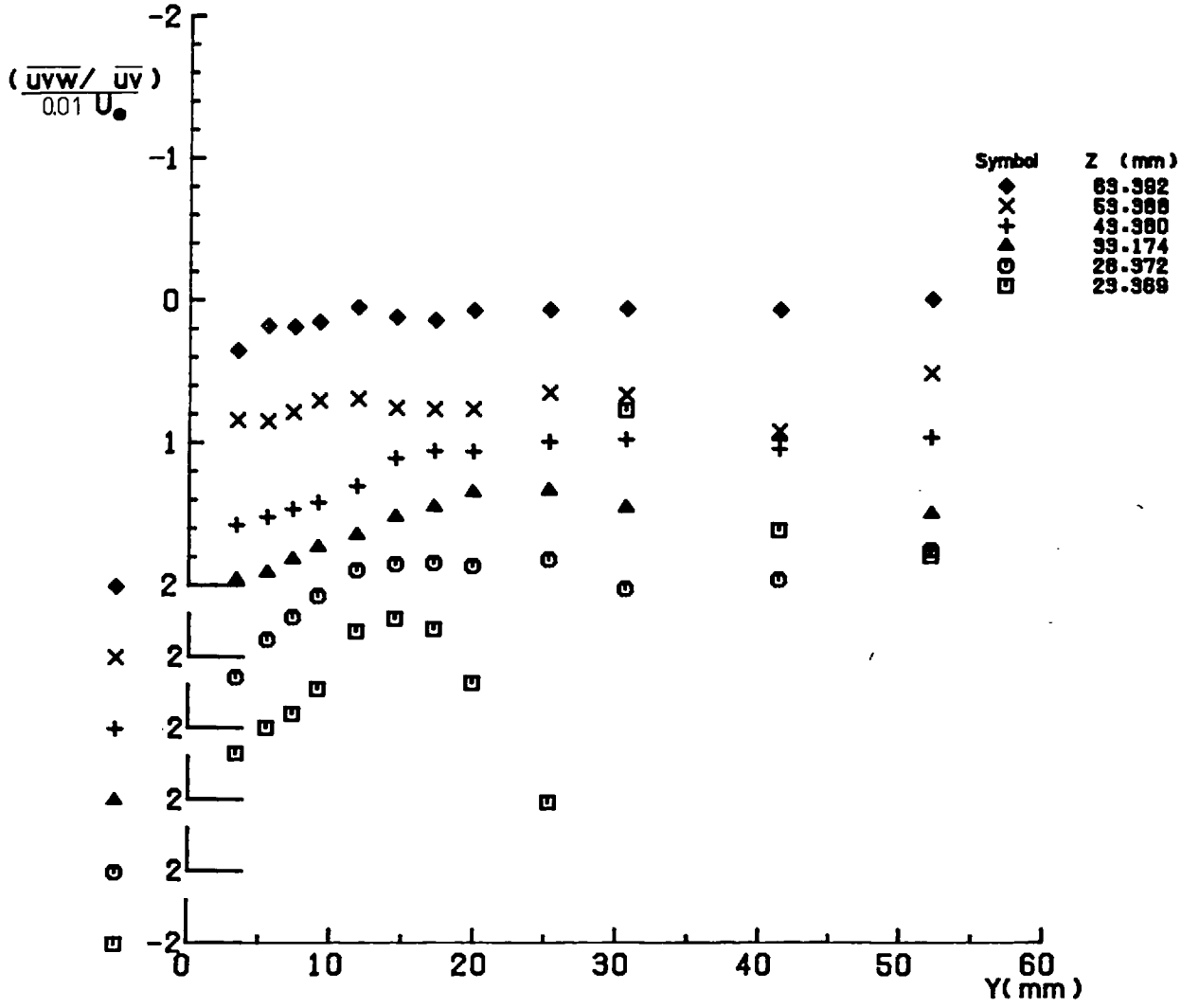

FIG.(D.36.b) $\overline{uvw}/\ \overline{uv}$ AT STATION 9 (X=1223.4 mm)

Cross Wire Measurements

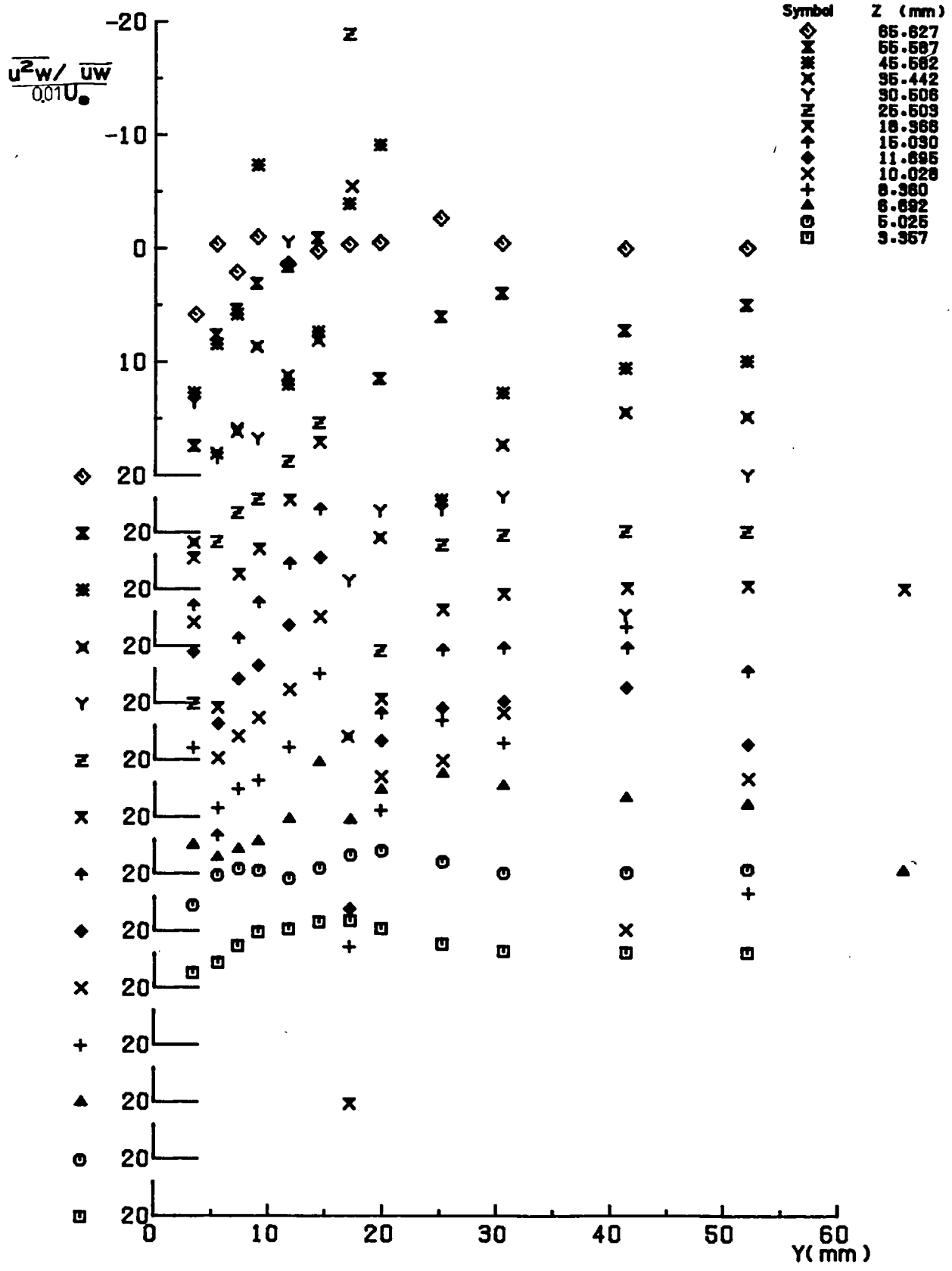

FIG.(D.37) $\overline{u^2w}/\overline{uw}$ AT STATION 2 (X= 156.6 mm)

Cross Wire Measurements

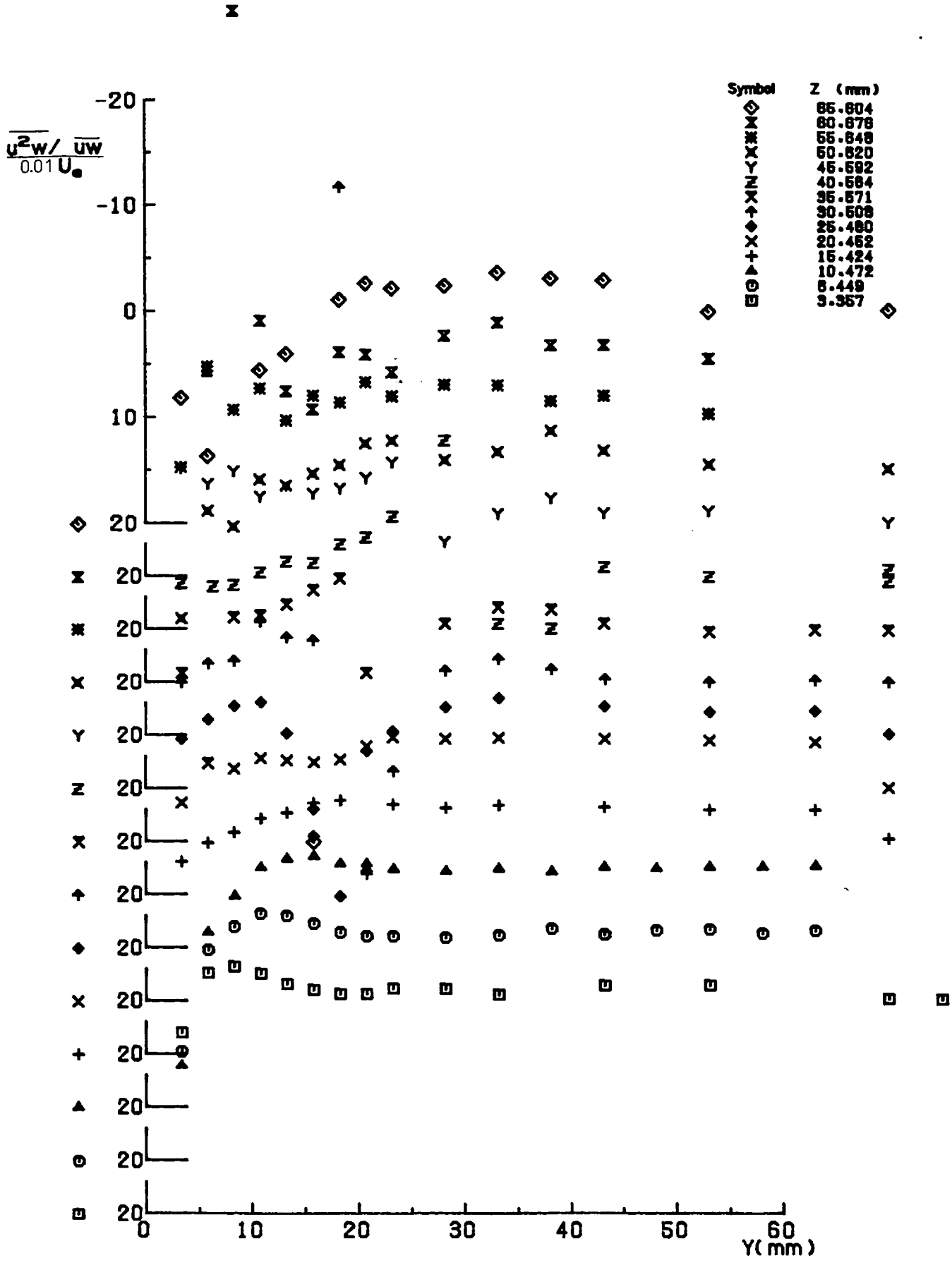

FIG.(D-38) $\overline{u^2w}/\ \overline{uw}$ AT STATION 9 (X=1223.4 mm)

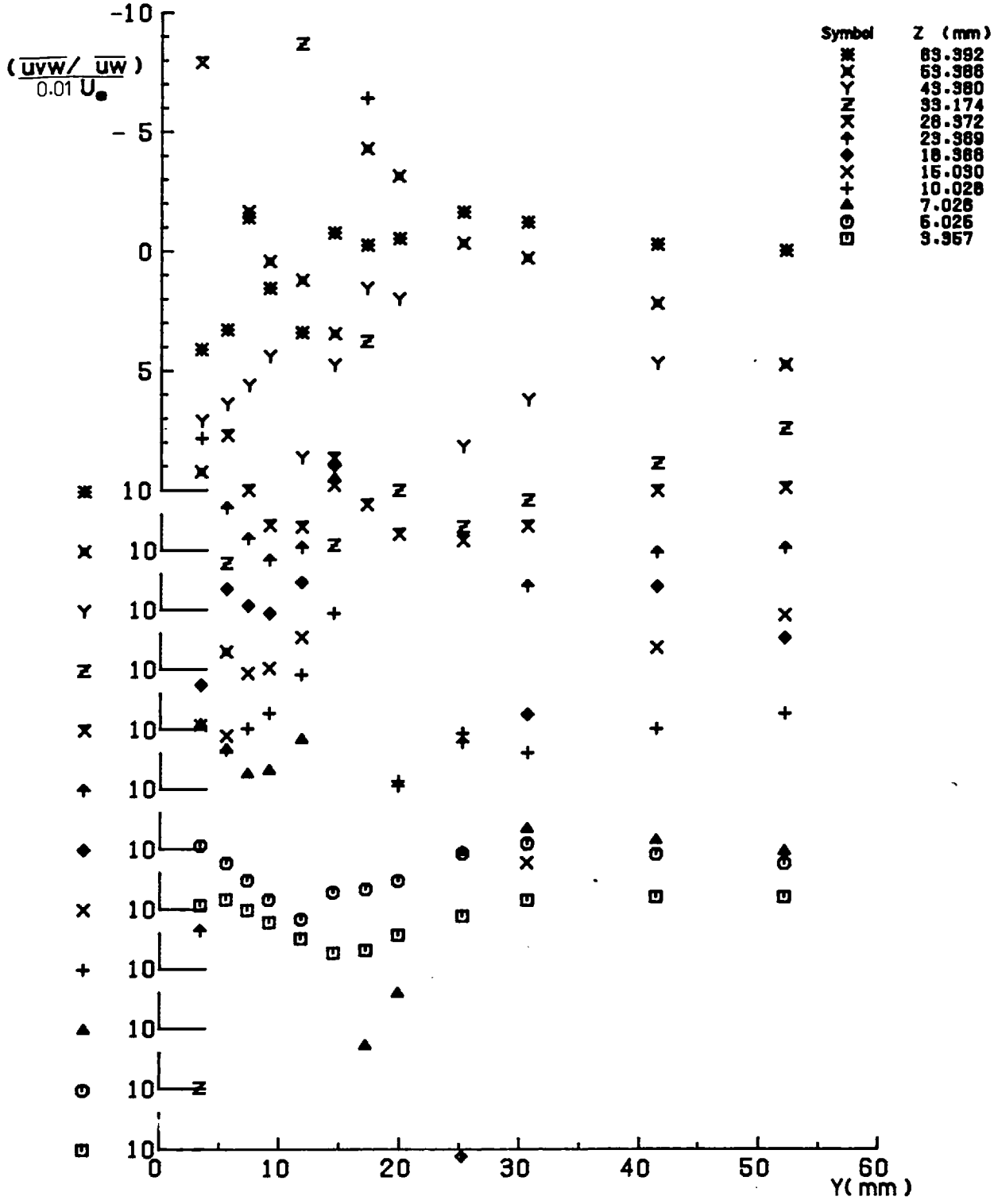

FIG.(D.39) $\overline{uvw}/\overline{uw}$ AT STATION 2 (X= 156.6 mm)

Cross Wire Measurements

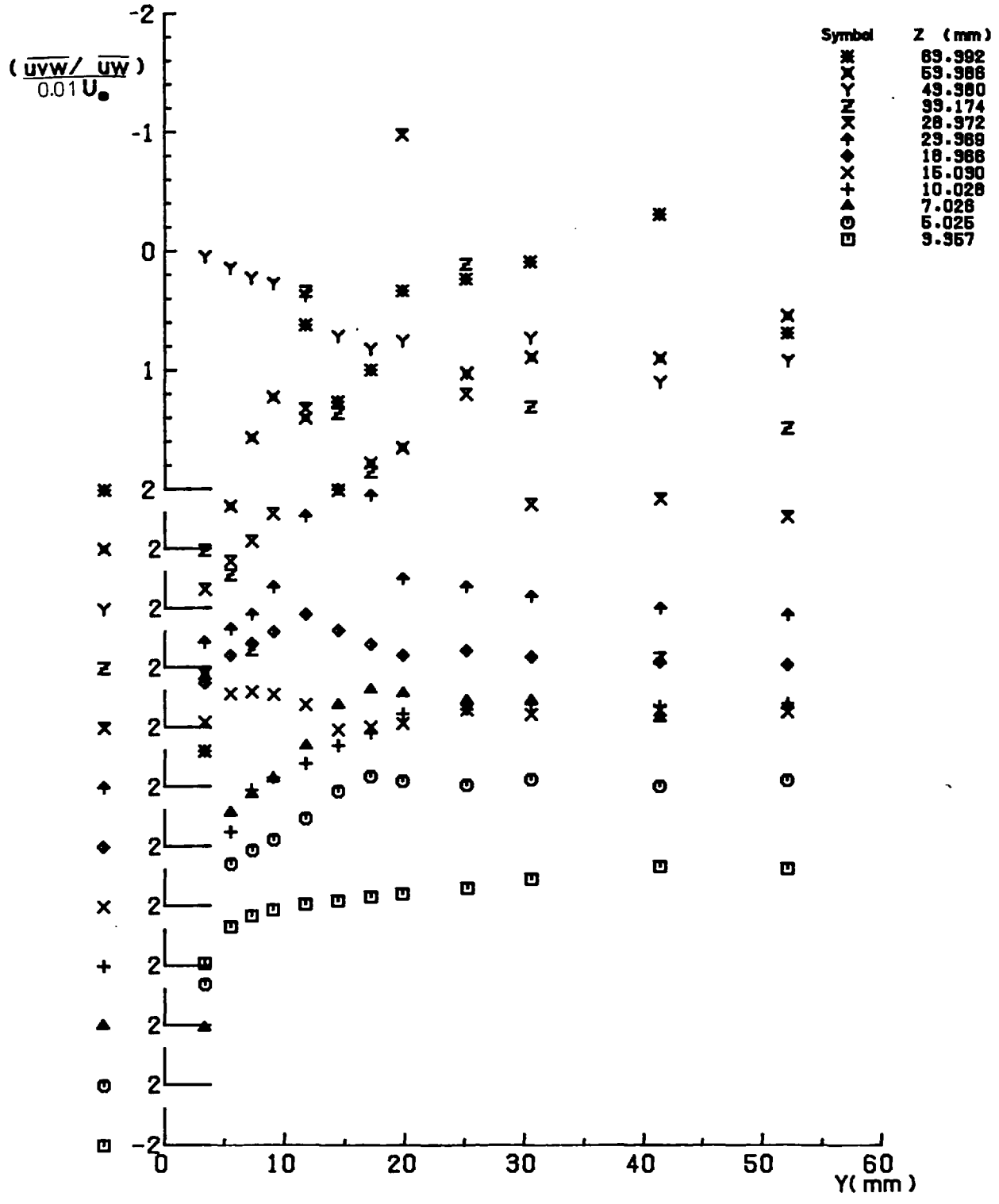

FIG.(D.40) $\overline{uvw}/\overline{uw}$ AT STATION 9 (X=1223.4 mm)

Cross Wire Measurements

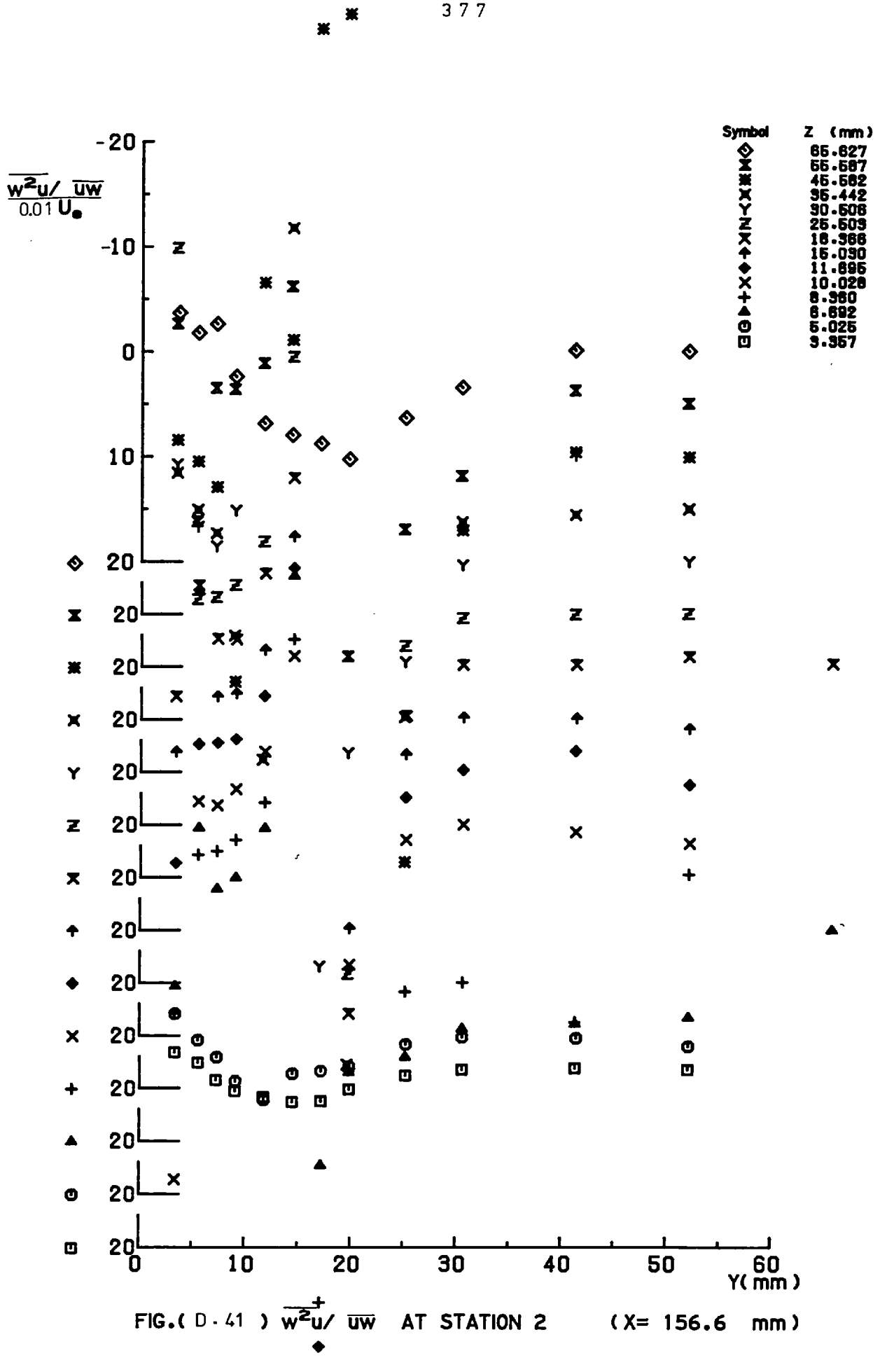

FIG.(D-41) $\overline{w^2u}/\overline{uw}$ AT STATION 2 (X= 156.6 mm)

Cross Wire Measurements

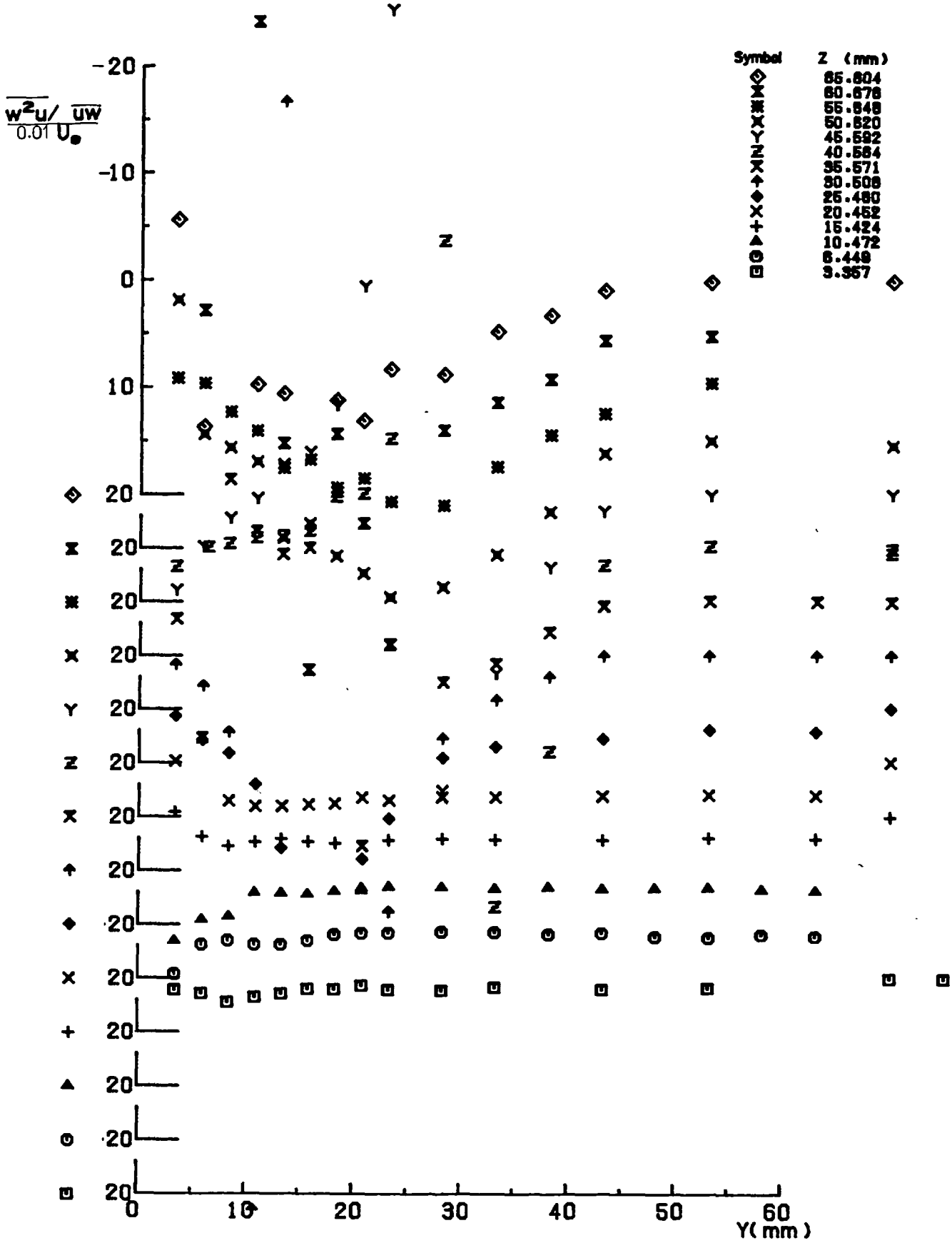

FIG.(D·42) $\overline{w^2u}/\overline{uw}$ AT STATION 9 (X=1223.4 mm)

Cross Wire Measurements

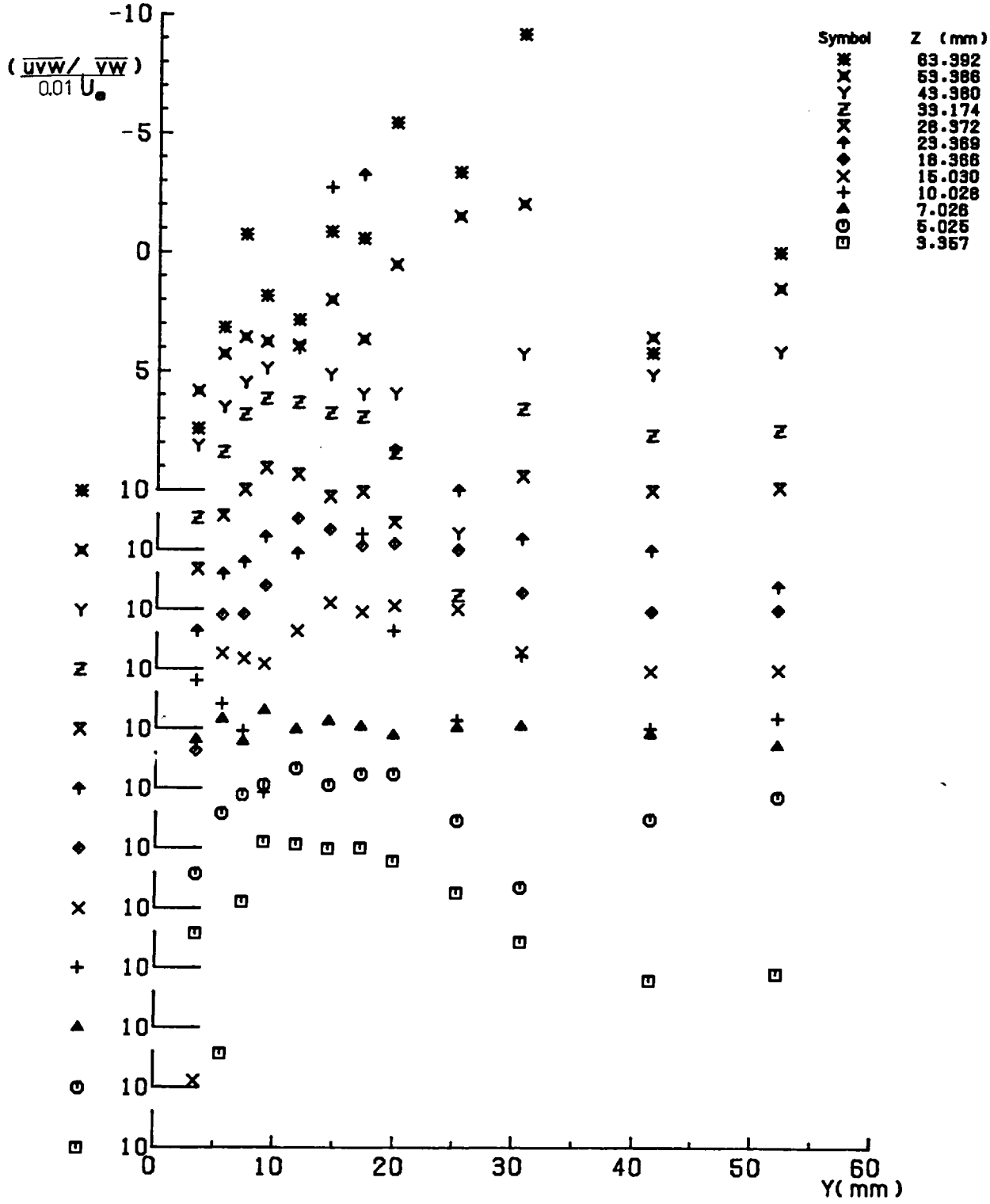

FIG.(D·43) $\overline{uvw}$/ $\overline{vw}$ AT STATION 2 (X= 156.6 mm)

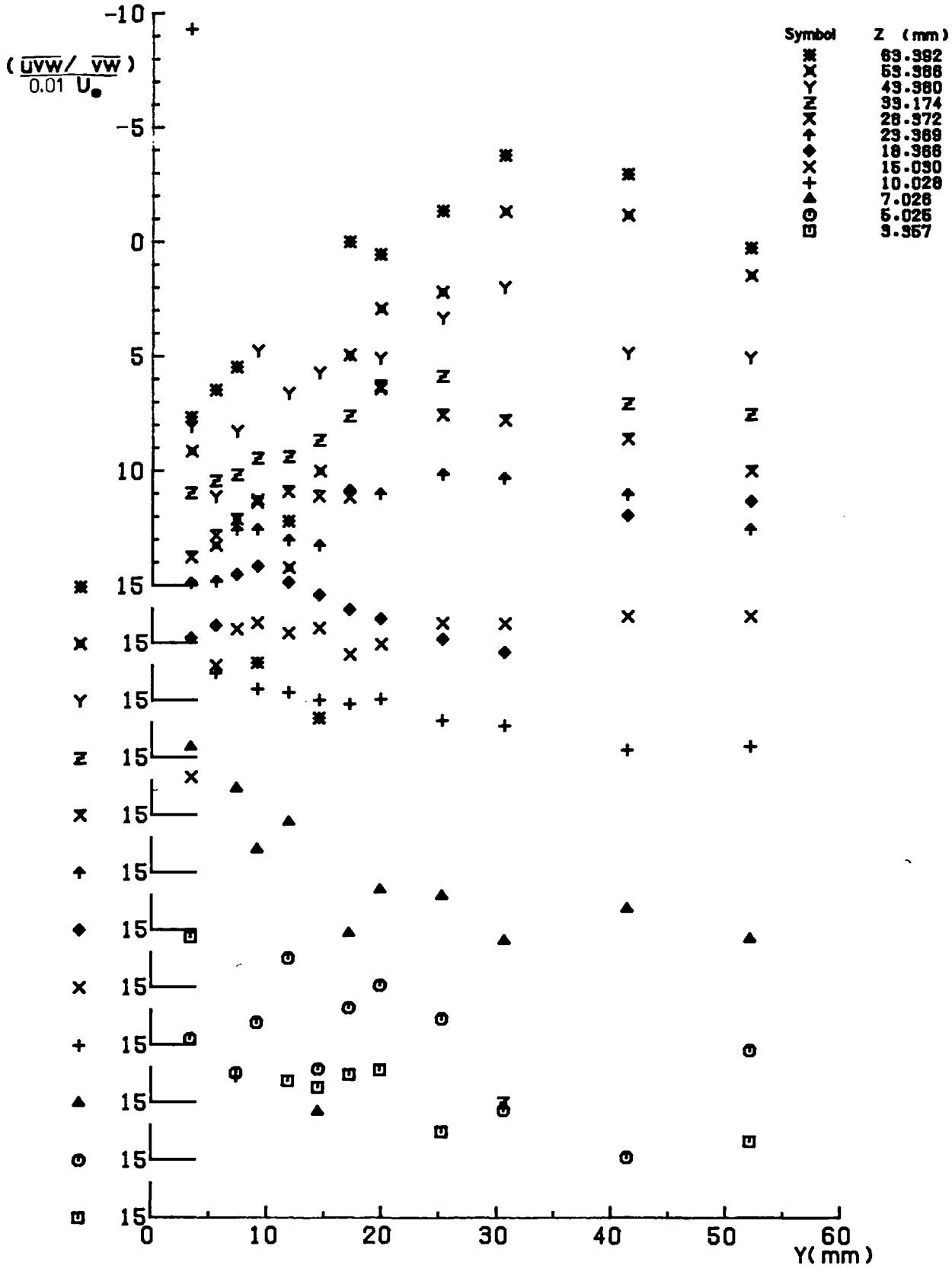

FIG.(D.44) $\overline{uvw}/\overline{vw}$ AT □ STATION 5 (X= 613.8 mm)

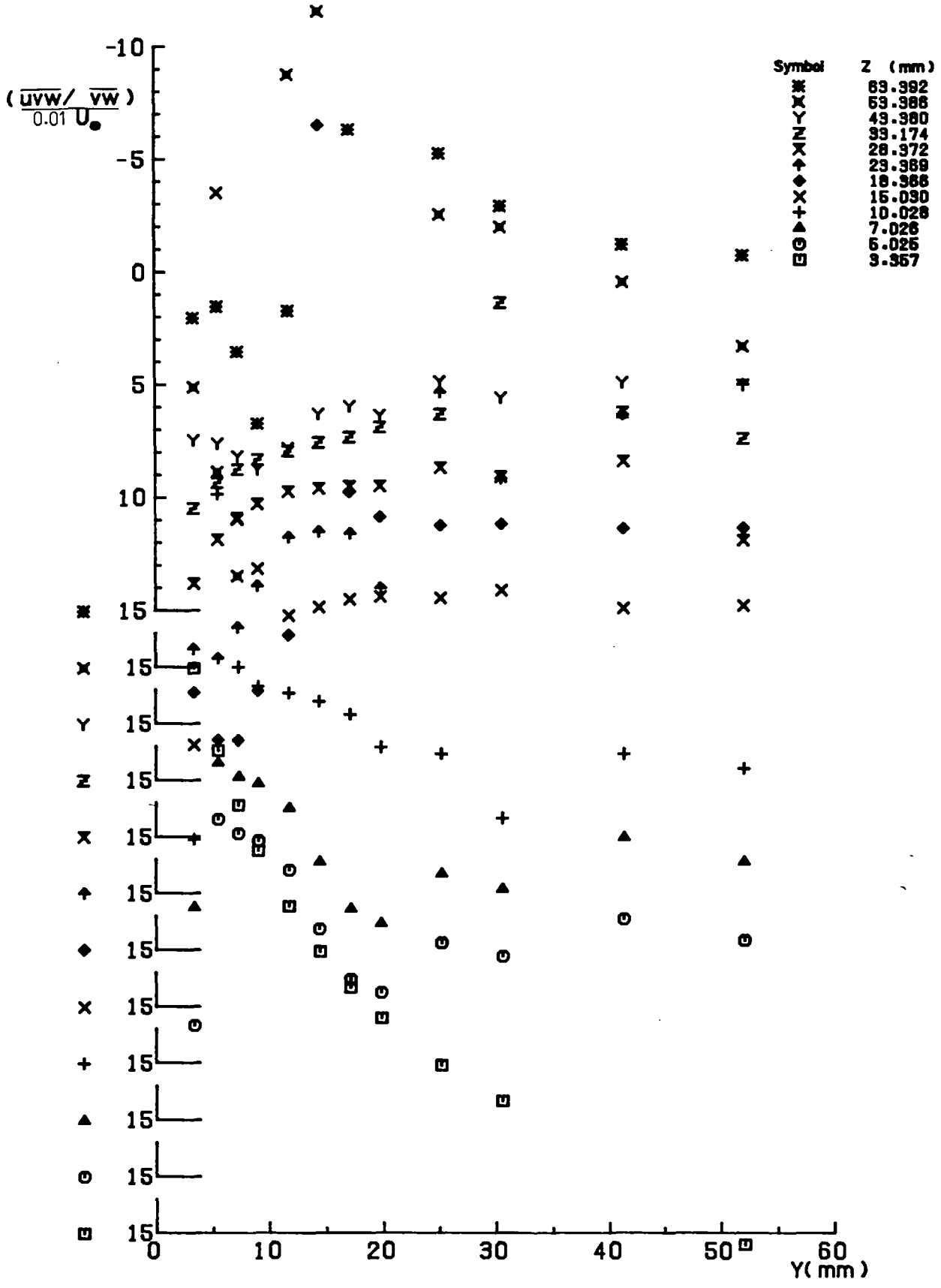

FIG.(D.45) $\overline{uvw}/\overline{vw}$ AT STATION 9 (X=1223.4 mm)

Cross Wire Measurements

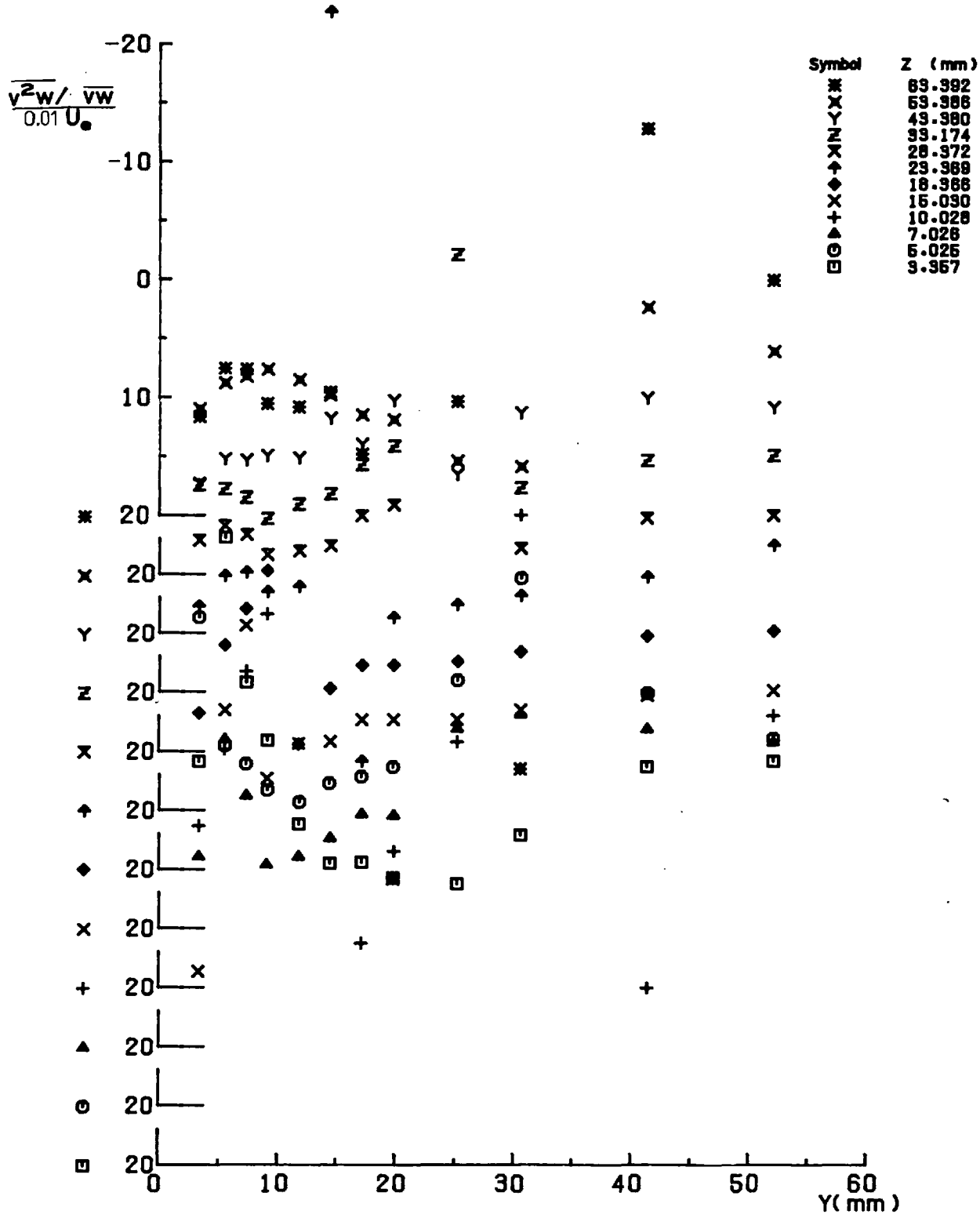

FIG.(D·46) $\overline{v^2w}/\ \overline{vw}$ AT STATION 2 (X= 156.6 mm)

Cross Wire Measurements

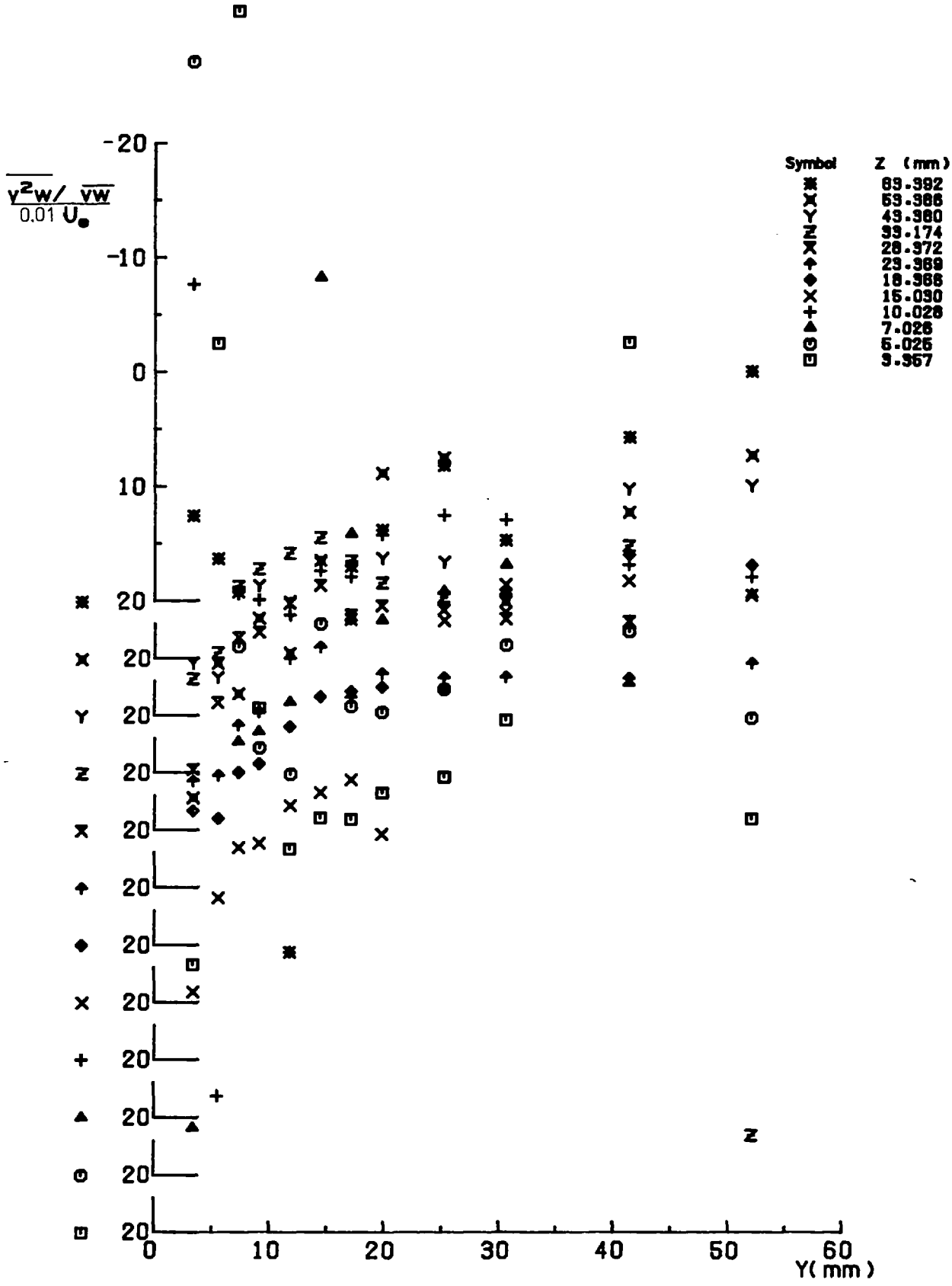

FIG.(D·47) $\overline{v^2w}/\overline{vw}$ AT STATION 5 (X= 613.8 mm)

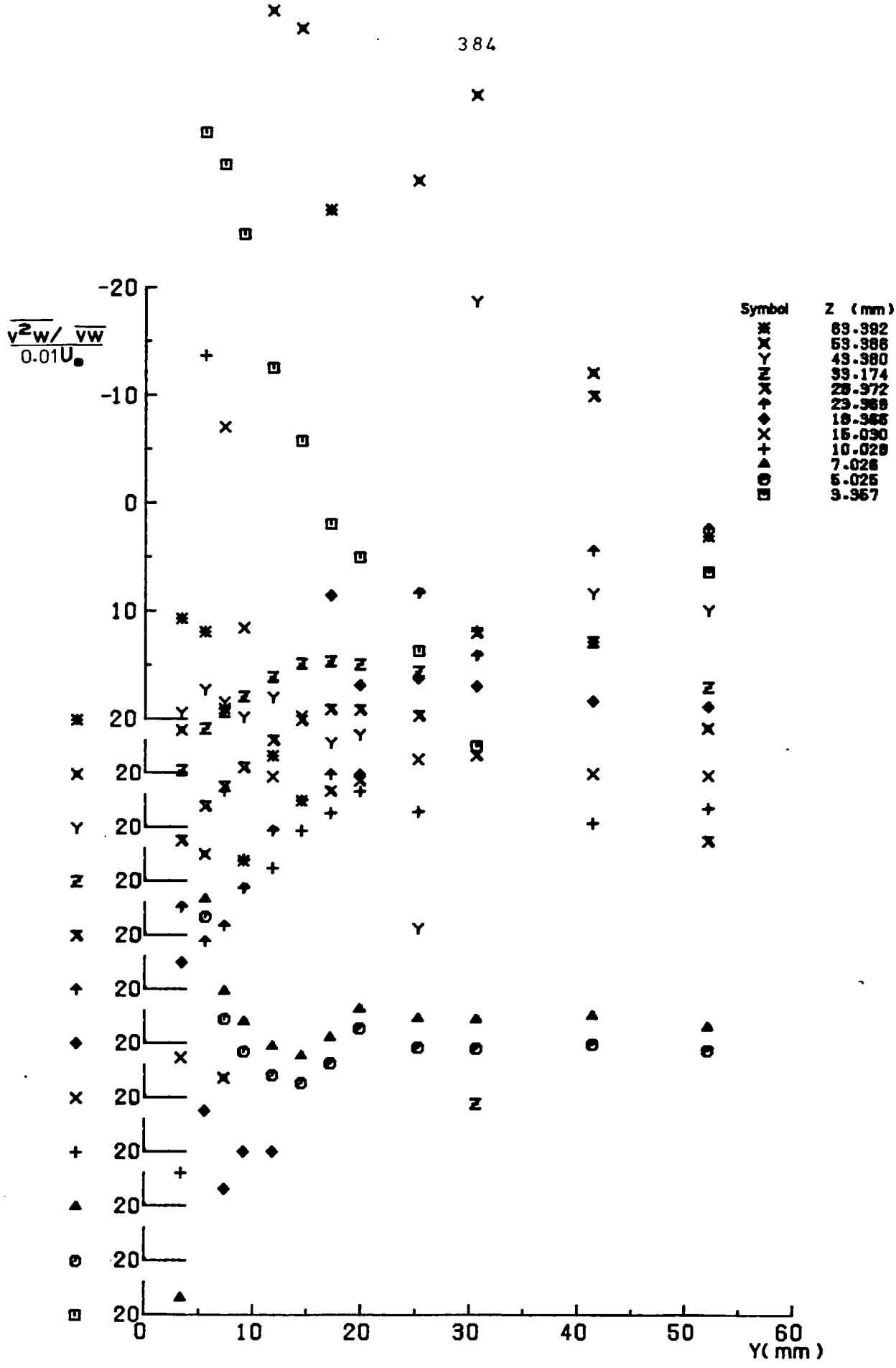

FIG.(D.48) $\overline{v^2w}/\ \overline{vw}$ AT STATION 9 (X=1223.4 mm)

Cross Wire Measurements

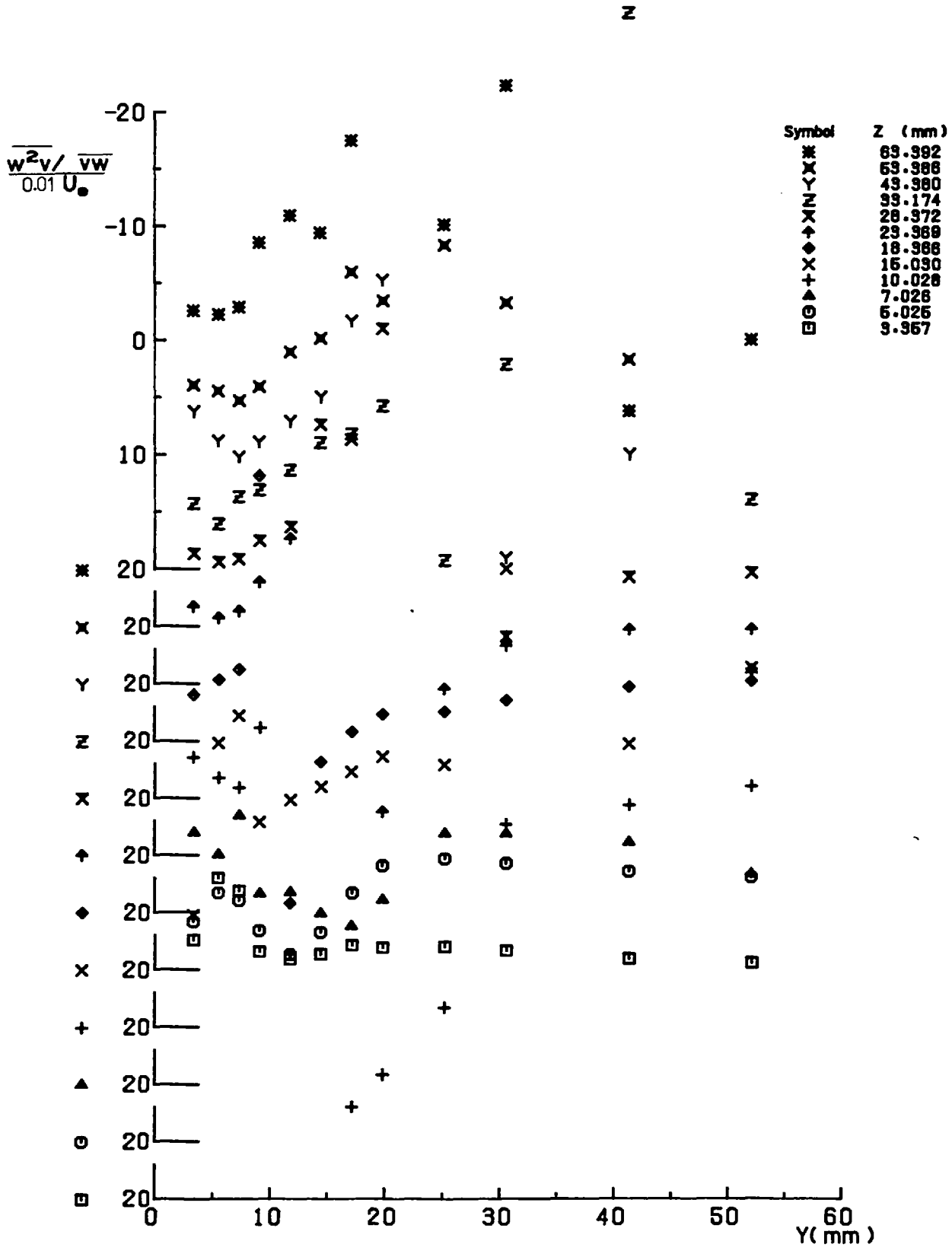

FIG.(D.49) $\overline{w^2v}/\overline{vw}$ AT STATION 2 (X= 156.6 mm)

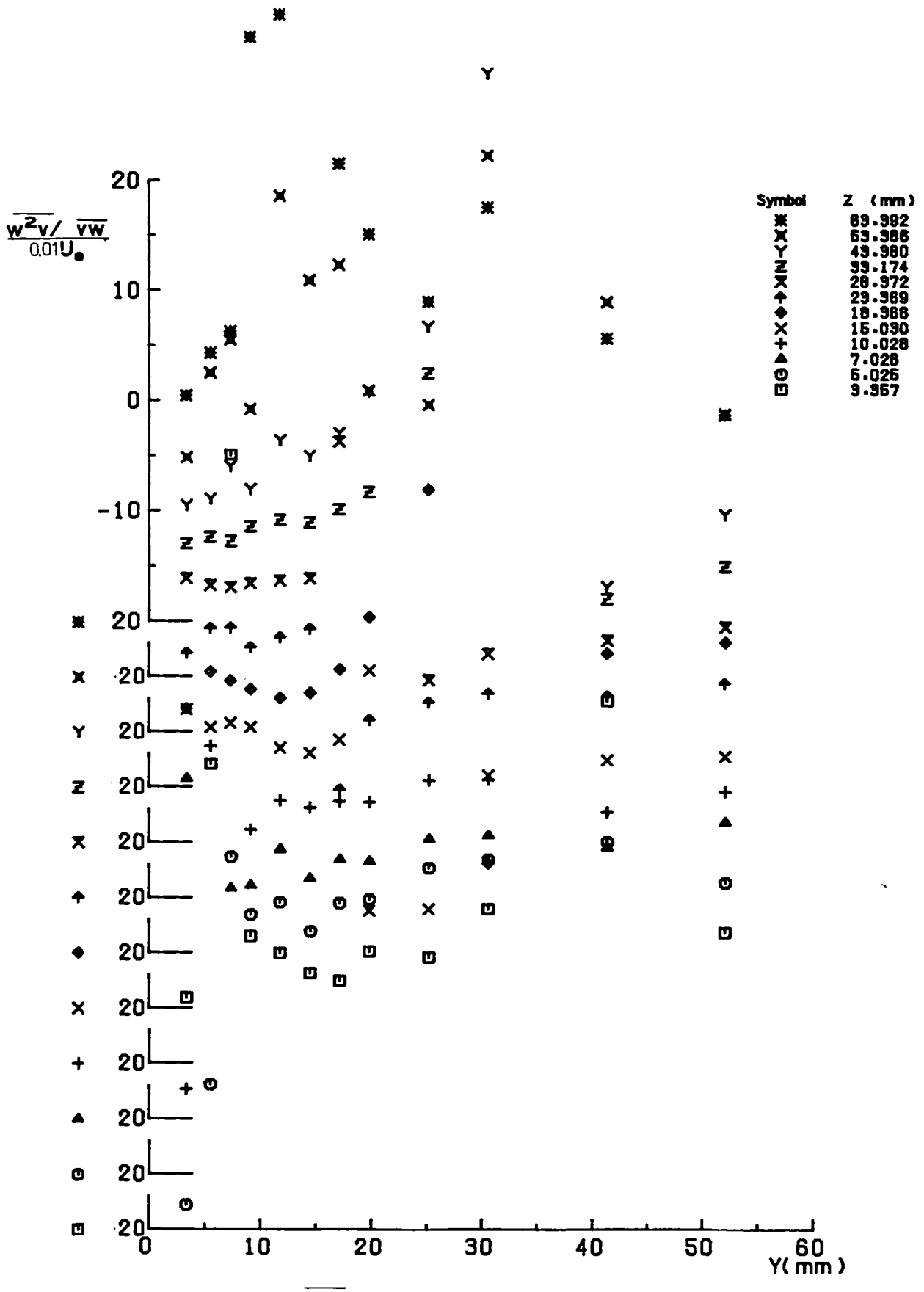

FIG.(D . 50) $\overline{w^2v}/\ \overline{vw}$ AT STATION 5 (X= 613.8 mm)

Cross Wire Measurements

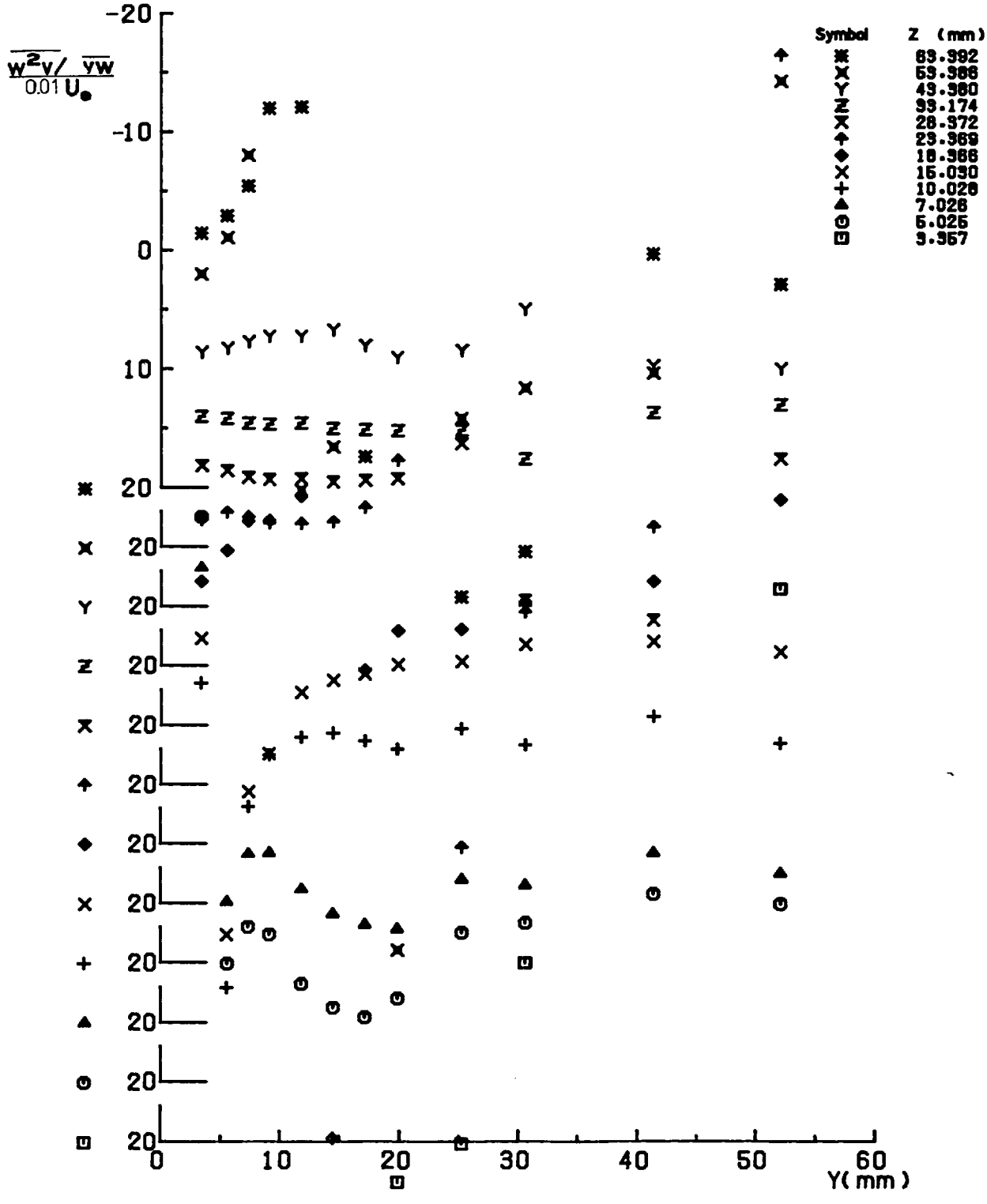

FIG.(D.51) $\overline{w^2v}/\ \overline{vw}$ AT STATION 9 (X=1223.4 mm)

APPENDIX E

NUMERICAL DIFFERENTIATION USING THE THREE-POINT LAGRANGE INTERPOLATION FORMULA

All the differentiations needed in the present work, for deducing the terms in the turbulent kinetic energy balance (Equation (4.6)), the shear stress transport equations (Equation (4.9)), and the streamwise vorticity equation (Equation (1.3)) were performed on the College CDC computer using the three-point Lagrange interpolation formulae (see Cebeci and Bradshaw (1977), page 261).

(a) For $1 < n < N$

$$\left(\frac{df}{dx}\right)_n = -\frac{f_{n-1}\,A_2}{A_1 \cdot A_3} + \frac{f_n(A_2 - A_1)}{A_1 \cdot A_2} + \frac{f_{n+1}\,A_1}{A_2 \cdot A_3} \qquad \text{(E.1)}$$

where:-

$$A_1 = (x_n - x_{n-1})$$

$$A_2 = (x_{n+1} - x_n)$$

$$A_3 = (x_{n+1} - x_{n-1})$$

(b) At the last point ($n = N$):-

$$\left(\frac{\partial f}{\partial x}\right)_N = \frac{f_{N-2}}{A_1 A_3} A_2 - \frac{f_{N-1}}{A_1 A_2} A_3 + \frac{f_N}{A_2 A_3} (A_2 + A_3) \qquad \text{(E.2)}$$

where:-

$$A_1 = x_{N-1}\ x_{N-2}$$

$$A_2 = x_N - x_{N-1}$$

$$A_3 = x_N - x_{N-2}$$

(c) At the first point (n = 1):-

$$\left(\frac{\partial f}{\partial x}\right)_1 = \frac{f_3}{A_1 A_3} A_2 - \frac{f_2}{A_1 A_2} A_3 + \frac{f_1}{A_2 A_3} (A_2 + A_3) \qquad (E.3)$$

where:-

$$A_1 = x_2 - x_3$$

$$A_2 = x_1 - x_2$$

$$A_3 = x_1 - x_3$$

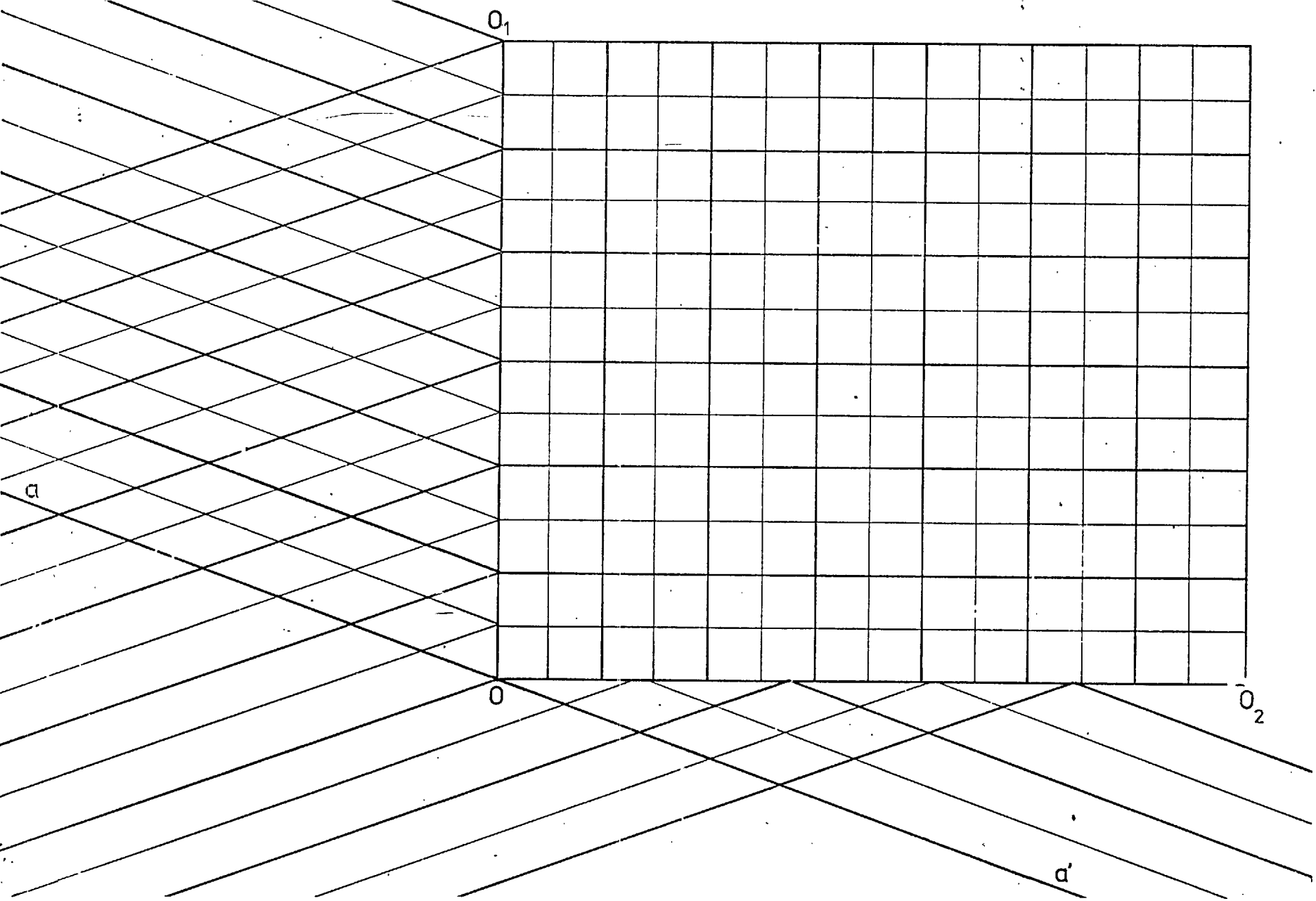
O_1
a
O
O_2
a'